

10-21-2015 12:00 AM

Nitrogen Abundances in Early-Type Be Stars

Ahmed Ahmed, *The University of Western Ontario*

Supervisor: Dr. T.A.A. Sigut, *The University of Western Ontario*

A thesis submitted in partial fulfillment of the requirements for the Doctor of Philosophy degree
in Astronomy

© Ahmed Ahmed 2015

Follow this and additional works at: <https://ir.lib.uwo.ca/etd>



Part of the [Stars, Interstellar Medium and the Galaxy Commons](#)

Recommended Citation

Ahmed, Ahmed, "Nitrogen Abundances in Early-Type Be Stars" (2015). *Electronic Thesis and Dissertation Repository*. 3354.

<https://ir.lib.uwo.ca/etd/3354>

This Dissertation/Thesis is brought to you for free and open access by Scholarship@Western. It has been accepted for inclusion in Electronic Thesis and Dissertation Repository by an authorized administrator of Scholarship@Western. For more information, please contact wlsadmin@uwo.ca.

NITROGEN ABUNDANCES IN EARLY-TYPE BE STARS
(Thesis format: Monograph)

by

Ahmed Ahmed

Graduate Program in Astronomy

A thesis submitted in partial fulfillment
of the requirements for the degree of
Doctor of Philosophy

The School of Graduate and Postdoctoral Studies
The University of Western Ontario
London, Ontario, Canada

© Ahmed M. H. Ahmed 2015

Abstract

A sample of 26 Be stars from the *Magnetism in Massive Stars* (MiMeS) spectroscopic survey are analyzed for their photospheric nitrogen abundances in an effort to detect rotational mixing in the Be stars. Be stars are massive stars, between 3 and 20 times the mass of the Sun, that are surrounded by a thin, equatorial disk of gas that produces emission lines in their optical and near-infrared spectra. Be stars are the most rapidly-rotating stellar population on the main sequence, where stars produce energy by core hydrogen burning. New, non-LTE line transfer calculations are performed for the N II ion, the dominant ionization stage in the photospheres of the B stars, and an extensive error analysis is performed via Monte Carlo simulation to determine the achievable accuracy of nitrogen abundances among these stars. To analyze the measured N II equivalent widths from the MiMeS survey, the effects of both gravitational darkening, due to the rapid rotation of the central B star, and the veiling effect of emission from the Be star circumstellar disk are considered. Both of these effects are found to be small for the sample population, affecting the final nitrogen abundances at the level $\approx \pm 0.1$ dex. The final, average nitrogen abundance for the MiMeS sample, $A_{\text{N}}^{\text{MiMeS}} = 7.78$, has a value in good agreement with the solar abundance, $A_{\text{N}}^{\odot} = 7.83$, and recent, high-precision abundance measurements for main sequence B stars. Nevertheless, the MiMeS sample standard deviation is over a factor of two larger than that of the observed nitrogen abundances in the atmospheres of B stars in the solar neighbourhood, with many low abundance objects and a few high abundance objects. No discernible trend of the nitrogen abundance can be seen with stellar gravity, $\log g$ (as a proxy for stellar age), or stellar equatorial velocity in the MiMeS survey. It is suggested that possible disk emission in the N II line transitions may explain the lower abundance objects, and this will be the subject of future work.

Keywords: stars: abundances - stars: atmospheres - stars: rotation - radiative transfer - line: formation

Acknowledgements

I would like express my sincere gratitude to my supervisor Aaron Sigut for his expertise and patience. Also, I would like to thank my advisory committee members Martin Houde and John D. Landstreet for their continuous support and suggestions. Finally, I would like to thank my examiners for their helpful comments and suggestions, Drs Gregg Wade, Jan Cami, John D. Landstreet, and Paul Ragona.

Contents

Abstract	ii
Acknowledgements	iii
List of Figures	vii
List of Tables	xii
List of Appendices	xv
1 Introduction and Overview	1
2 Early-Type Stars	5
2.1 Introduction	5
2.2 Physical Characteristics of Massive Stars	6
2.3 Surface Abundances of B-type stars	6
2.4 Evolution of Massive Stars on The Main Sequence	9
2.4.1 Effects of Rotation on Massive Star Evolution on the Main-Sequence . .	11
Rotational Mixing	11
Modelling Results	14
2.4.2 Observational Constraints on Rotational Mixing in Massive stars	22
3 The Classical Be stars	28
3.1 Introduction	28
3.2 Spectral features of Be Stars	30
3.3 Possible Formation Mechanisms of Be Star Disks	33
3.4 Disk structure	34
3.5 Be Stars and Rotational Mixing	36
4 The Non-LTE Radiative Transfer Problem	37
4.1 Introduction	37
4.2 The Radiative Transfer Equation	38
4.2.1 Local Thermodynamic Equilibrium	41
4.2.2 non-Local Thermodynamic Equilibrium	42
4.2.3 Numerical Solution of The Non-LTE Radiative Transfer Problem	42
5 Non-LTE for Calculation N II	45

5.1	Introduction	45
5.2	Previous Works	46
5.3	Nitrogen Atomic Data	49
5.3.1	N II	49
5.3.2	N III and N IV	56
5.4	Calculations	56
5.4.1	Ionization Balances and Departure Coefficients	57
5.4.2	Equivalent Widths	61
5.5	Multi-MULTI Analysis	71
5.6	The Accuracy of the Predicted non-LTE Equivalent Widths	77
5.6.1	Random Errors	77
5.6.2	Systematic Errors	81
6	Non-LTE Calculation for He I	87
6.1	Introduction	87
6.2	Previous works	88
6.3	He I Atomic data	92
6.4	Calculation Grid of He I Atom	97
6.4.1	Ionization Balances and Departure Coefficients	97
6.4.2	Equivalent Widths	99
6.5	The Accuracy of the Predicted non-LTE Equivalent Widths	106
7	Gravitational Darkening	108
7.1	Introduction	108
7.2	Gravitational Darkening Assuming Solid Body Rotation	108
7.3	Gravitational Darkening Effects on Spectral Lines	113
7.3.1	Gravitational Darkening Effects on N II λ 3995Å	114
7.3.2	Gravitational Darkening effects on He I λ 6678Å	117
7.3.3	Gravitational Darkening effects on Mg II λ 4481Å	118
7.3.4	Gravitational Darkening Effects on $v \sin i$ Measurements	119
8	Nitrogen Abundances for a Sample of Be Stars from the MiMeS Survey	122
8.1	Introduction	122
8.2	The Be star Sample	123
8.2.1	Spectra Normalization	123
8.2.2	Stellar Parameters	134
8.2.3	Equivalent Width Measurements	146
8.3	Estimations of Disk Parameters	151
8.4	Nitrogen Abundances	159
8.4.1	Estimations of Nitrogen Abundances Based Solely on the Observed Equivalent Widths	159
8.4.2	Corrections for Circumstellar Disks Effects on the Measured Nitrogen Abundances	167
8.5	Discussion	174

9	Conclusions	175
9.1	Results of Non-LTE calculations	175
9.2	Gravitational Darkening Effects	176
9.3	Results of the Abundance Analysis	177
9.4	Future Directions	178
	Bibliography	179
A	List of Constants and Abbreviations	187
A.1	Constants	187
A.2	Abbreviations	187
B	MULTI Results of Selected N II lines	188
C	Monte Carlo Results	218
D	Hα Fitting Figures	234
E	N II Normalized Spectra	254
	Curriculum Vitae	276

List of Figures

2.1	The evolution of the rotational profile of a $9 M_{\odot}$ star	15
2.2	The evolution of the H, He, C, N, and O surface abundances of a $9 M_{\odot}$ star . . .	16
2.3	The evolution of a rotating $9 M_{\odot}$ star on the main-sequence	17
2.4	The evolutionary track with and without rotation for stars with masses between $9 M_{\odot}$ and $120 M_{\odot}$	18
2.5	Evolutionary tracks of the atmospheric nitrogen abundance in massive stars . .	19
2.6	Evolutionary tracks of the ratio of the carbon abundance to the nitrogen abun- dance in massive stars.	20
2.7	Isochrones for rotating and non rotating models	21
2.8	The change of the ratio of the angular rotational velocity to the critical value . .	22
2.9	The increase of nitrogen abundance with stellar age	24
2.10	The nitrogen abundances for a sample of MagellC B and Be stars (Dunstall et al., 2011)	25
2.11	The change of the atmospheric nitrogen abundances with the change of the rotational velocity	26
3.1	The dependence of the observed line profiles of Be stars on the stellar inclination	32
3.2	colour-colour diagram for a number of Be stars	35
5.1	N II Grotrian diagram	50
5.2	Quadratic stark width ratios of N II lines versus the effective quantum number of the upper level	54
5.3	The fraction of singly ionized nitrogen as a function of the optical depth	57
5.4	Radiation temperature of the ionizing mean intensity for the first ten levels of N II	58
5.5	Non-LTE departures coefficients for the first sixteen energy levels of N II plus the ground level of N III	59
5.6	The predicted LTE (dashed lines) and non-LTE equivalent (solid lines) widths of N II λ 3995 Å and λ 6482 Å	64
5.7	The line source function of N II λ 3995 Å λ 6482 Å	65
5.8	Hydrogen opacity effects on the computed equivalent widths of N II λ 6482 Å and λ 3995 Å	66
5.9	Curves of growth for N II λ 6482 Å and λ 3995 Å	67
5.10	The source function of the N II λ 3995 Å & λ 6482 Å for different nitrogen abun- dances	71
5.11	The line source function of N II λ 3995 Å line from the results of the multi- MULTI analysis	74

5.12	The line source function of N II λ 6482 Å line from the results of the multi-MULTI analysis	75
5.13	The distribution of the equivalent widths results of the Monte-MULTI analysis for λ 6482 Å and λ 3995 Å	80
5.14	The uncertainties of the estimated nitrogen abundances due to inaccuracies in the atomic data	82
5.15	The change of the computed equivalent widths of λ 3995 Å and λ 6482 Å with the change of the size of the nitrogen atom	85
6.1	He I Grotrian diagram showing the singlet and triplet spin systems.	92
6.2	The stark width ratios of He I lines versus the effective quantum number of the upper LS state	96
6.3	The ionization Balances of He I and He II	98
6.4	The radiation temperature of the photoionizing radiation at the threshold wavelength for the lowest 10 LS states of the He I	99
6.5	The non-LTE departure coefficients of the population numbers of the lowest 15 LS states of He I plus the ground level of He II	100
6.6	The computed equivalent widths of a number of He I (I)	102
6.7	The computed equivalent widths of a number of He I lines (II)	103
6.8	The computed equivalent widths of a number of He I λ 10830 Å line.	104
7.1	The Distribution of the effective temperature over the surface of a rotating star .	113
7.2	The gravitational darkening effects on the predicted equivalent widths of the N II 3995 Å and 6482 Å lines.	115
7.3	Gravitationally darkening effects on the predicted equivalent widths of λ 3995 and λ 6482 Å N II lines for $v_{\text{frac}} = 0.85$	116
7.4	The gravitational darkening effects on the equivalent width of the He I λ 6678 Å	117
7.5	The gravitational darkening effects on the predicted equivalent widths of the Mg II λ 4481 Å	119
7.6	The gravitational darkening effects on the estimated $v \sin i$ using measured equivalent widths of the He I λ 6678 Å and the Mg II λ 4481 Å.	120
8.1	Normalization process of the H α line profile of the Be star HD 143275	126
8.2	Normalized H α of the Be star HD 143275	127
8.3	Normalization process of the N II λ 3995.0 Å line of the Be star HD 143275 . .	128
8.4	Normalization process of the N II λ 4447.0 Å line of the Be star HD 143275 . .	129
8.5	Normalization process of the N II λ 5679.0 Å line of the Be star HD 143275 . .	130
8.6	Normalized N II lines of the Be star HD 143275	131
8.7	Normalized N II lines of the Be star HD 11415	132
8.8	Normalized N II lines of the Be star HD 143275	133
8.9	Comparison of the T_{eff} estimates of Levenhagen & Leister (2006) for 22 Be stars in the sample with the corresponding values of Frémat et al. (2005)	137
8.10	Comparison of the T_{eff} estimates of Catanzaro (2013) for seven Be stars in the sample with the corresponding values of Frémat et al. (2005)	138
8.11	$v \sin i$ distribution for the Be stars sample	141

8.12	Fitting of the observed He I λ 4471 Å, Mg II λ 4481 Å and He I λ 6678 Å lines with synthetic non-LTE line profiles of the Be star HD 11415.	143
8.13	Fitting of the observed He I and Mg II lines with synthetic non-LTE line profiles of the Be star HD 174237	143
8.14	Fitting of the observed He I and Mg II lines with synthetic non-LTE line profiles of the Be star HD 65875	144
8.15	Fitting of the observed He I and Mg II lines with synthetic non-LTE line profiles of the Be star HD 45725	144
8.16	Fitting of the observed He I and Mg II lines with synthetic non-LTE line profiles of the Be star HD 203467	145
8.17	Comparison of the current estimates of log g with the available values in literature	145
8.18	Measuring equivalent widths of observed N II lines in the spectra of the Be star HD 11415.	147
8.19	Measured equivalent widths of observed N II lines in the spectra of the Be star HD 67698	148
8.20	Measured equivalent widths of observed N II lines in the spectra of the Be star HD 58343	149
8.21	Normalized H α of the Be star HD 49567	152
8.22	H α line fitting of the Be star HD189687	154
8.23	H α line fitting of the Be star HD 143275	154
8.24	H α line fitting of the Be star HD 45725	155
8.25	Comparison of current inclination estimations with those of Frémat et al. (2005) for the common objects.	157
8.26	Results of KS test result for current inclination estimations and those of Frémat et al. (2005)	158
8.27	Results of KS test result for the entire sample of Frémat et al. (2005)	159
8.28	The estimation of the nitrogen abundance of the Be star HD56139 based on the measured equivalent width of the N II 3995 Å line.	161
8.29	Nitrogen abundance estimations of the sample of Be stars versus their effective temperatures	162
8.30	Results of KS test result for the estimated nitrogen abundances of the sample. .	163
8.31	Comparison of the estimated nitrogen abundances from λ 3995 Å N II line with the results of the abundance analysis including all observed N II lines	165
8.32	Relation between the estimated nitrogen abundances of the Be stars sample and their gravities	166
8.33	Figure shows relation between the estimated nitrogen abundances of the Be stars sample and their equatorial rotational velocities	167
8.34	Figure shows the disk contamination as function of the wavelength for B3-type Be star	169
8.35	Figure shows the disk contamination as function of the wavelength for B4-type Be star	169
8.36	Corrections of the measured nitrogen abundances for disk contamination effect	172
8.37	Histograms of measured B and Be star nitrogen abundances from several sources	173
D.1	H α line fitting of the Be star HD 33328	234

D.2	H α line fitting of the Be star HD 56139	235
D.3	H α line fitting of the Be star HD 58050	236
D.4	H α line fitting of the Be star HD 58343	237
D.5	H α line fitting of the Be star HD 67698	238
D.6	H α line fitting of the Be star HD 120324	238
D.7	H α line fitting of the Be star HD 187811	239
D.8	H α line fitting of the Be star HD 191610	240
D.9	H α line fitting of the Be star HD 192685	241
D.10	H α line fitting of the Be star HD 205637	242
D.11	H α line fitting of the Be star HD 212076	243
D.12	H α line fitting of the Be star HD 212571	244
D.13	H α line fitting of the Be star HD 20336	245
D.14	H α line fitting of the Be star HD 54309	246
D.15	H α line fitting of the Be star HD 58978	247
D.16	H α line fitting of the Be star HD 65875	248
D.17	H α line fitting of the Be star HD 178175	249
D.18	H α line fitting of the Be star HD 187567	250
D.19	H α line fitting of the Be star HD 203467	251
D.20	H α line fitting of the Be star HD 217050	252
D.21	H α line fitting of the Be star HD 174237	253
E.1	Measured equivalent widths of observed N II lines in the spectra of the Be star HD	255
E.2	Measured equivalent widths of observed N II lines in the spectra of the Be star HD 65875	256
E.3	Measured equivalent widths of observed N II lines in the spectra of the Be star HD 189687	257
E.4	Measured equivalent widths of observed N II lines in the spectra of the Be star HD 54309	258
E.5	Measured equivalent widths of observed N II lines in the spectra of the Be star HD 178175	259
E.6	Measured equivalent widths of observed N II lines in the spectra of the Be star HD 192685	260
E.7	Measured equivalent widths of observed N II lines in the spectra of the Be star HD 120324	261
E.8	Measured equivalent widths of observed N II lines in the spectra of the Be star HD 58050	262
E.9	Measured equivalent widths of observed N II lines in the spectra of the Be star HD 174237	263
E.10	Measured equivalent widths of observed N II lines in the spectra of the Be star HD 187811	264
E.11	Measured equivalent widths of observed N II lines in the spectra of the Be star HD 187567	265
E.12	Measured equivalent widths of observed N II lines in the spectra of the Be star HD 33328	266

E.13	Measured equivalent widths of observed N II lines in the spectra of the Be star HD 203467	267
E.14	Measured equivalent widths of observed N II lines in the spectra of the Be star HD 49567	268
E.15	Measured equivalent widths of observed N II lines in the spectra of the Be star HD 212076	269
E.16	Measured equivalent widths of observed N II lines in the spectra of the Be star HD 56139	270
E.17	Measured equivalent widths of observed N II lines in the spectra of the Be star HD 191610	271
E.18	Measured equivalent widths of observed N II lines in the spectra of the Be star HD 20336	272
E.19	Measured equivalent widths of observed N II lines in the spectra of the Be star HD 58978	273
E.20	Measured equivalent widths of observed N II lines in the spectra of the Be star HD 212571	273
E.21	Measured equivalent widths of observed N II lines in the spectra of the Be star HD 45725	274
E.22	Measured equivalent widths of observed N II lines in the spectra of the Be star HD 205637	274
E.23	Measured equivalent widths of observed N II lines in the spectra of the Be star HD 217050	275

List of Tables

2.1	Average elemental abundances of Galactic, main-sequence B stars.	9
5.1	Energy Levels included in the N II atom model	51
5.2	Atomic data for several N II multiplets of interest.	52
5.3	Calculated Stark width ratios to experimental values	53
5.4	MULTI results for N II λ 3995 Å at $\xi_t = 5 \text{ km s}^{-1}$	69
5.5	MULTI results for N II λ 6482 Å at $\xi_t = 5 \text{ km s}^{-1}$	70
5.6	A multi-MULTI Analysis at $T_{\text{eff}} = 23000 \text{ K}$, $\log g = 4.0$, and $\xi_t = 5.0 \text{ km s}^{-1}$	72
5.7	A multi-MULTI Analysis at $T_{\text{eff}} = 15000 \text{ K}$, $\log g = 4.0$, and $\xi_t = 5.0 \text{ km s}^{-1}$	76
5.8	A multi-MULTI Analysis at $T_{\text{eff}} = 29000 \text{ K}$, $\log g = 4.0$, and $\xi_t = 5.0 \text{ km s}^{-1}$	77
5.9	Rates of variation of the atomic data	78
5.10	Results of Monte Carlo Simulations for N II atom at $\log g = 4.0$, and $\xi_t = 5.0 \text{ km s}^{-1}$	83
5.11	Results of Monte Carlo Simulations for N II at $\log g = 4.0$, $\xi_t = 5.0 \text{ km s}^{-1}$, and solar nitrogen abundance ($\epsilon_{N, \text{solar}} = 7.83$): Correlation Coefficients	84
6.1	Atomic data for the lowest 15 LS states of He I and the ground state of He II.	93
6.2	Atomic data for the He I multiplets of interest	94
6.3	Average ratios of theoretically calculated stark widths to experimental mea- sured values	95
6.4	MULTI results for He I λ 4471 and λ 6678 Å	105
6.5	Results of Monte-Carlo MULTI analysis for selected He I lines at $\xi_t = 5 \text{ km s}^{-1}$ (Equivalent widths, W_λ , are in mÅ and the uncertainties in %)	107
8.1	Adopted Stellar Parameters of the MiMeS Be stars Sample	139
8.2	Measured equivalent widths of observed N II lines in the spectra of the sample (in mÅ), and their uncertainties due to errors in the continuum normalization.	150
8.3	Adopted Stellar Parameters of the Central Stars	151
8.4	Most Probable Disk Parameters of Be Stars Sample	156
8.5	Measured Nitrogen Abundances of Be Stars Sample	164
8.6	Disk Contamination of the Spectra of Be Stars Sample	171
B.1	MULTI results for N II λ 3995 Å at $\xi_t = 0 \text{ km s}^{-1}$	189
B.2	MULTI results for N II λ 3995 Å at $\xi_t = 5 \text{ km s}^{-1}$	190
B.3	MULTI results for N II λ 3995 Å at $\xi_t = 10 \text{ km s}^{-1}$	191
B.4	MULTI results for N II λ 4447 Å at $\xi_t = 0 \text{ km s}^{-1}$	192
B.5	MULTI results for N II λ 4447 Å at $\xi_t = 5 \text{ km s}^{-1}$	193
B.6	MULTI results for N II λ 4447 Å at $\xi_t = 10 \text{ km s}^{-1}$	194

B.7	MULTI results for N II λ 4601.5 Å at $\xi_t = 0 \text{ km s}^{-1}$	195
B.8	MULTI results for N II λ 4601.5 Å at $\xi_t = 5 \text{ km s}^{-1}$	196
B.9	MULTI results for N II λ 4601.5 Å at $\xi_t = 10 \text{ km s}^{-1}$	197
B.10	MULTI results for N II λ 4607.2 Å at $\xi_t = 0 \text{ km s}^{-1}$	198
B.11	MULTI results for N II λ 4607.2 Å at $\xi_t = 5 \text{ km s}^{-1}$	199
B.12	MULTI results for N II λ 4607.2 Å at $\xi_t = 10 \text{ km s}^{-1}$	200
B.13	MULTI results for N II λ 4621.4 Å at $\xi_t = 0 \text{ km s}^{-1}$	201
B.14	MULTI results for N II λ 4621.4 Å at $\xi_t = 5 \text{ km s}^{-1}$	202
B.15	MULTI results for N II λ 4621.4 Å at $\xi_t = 10 \text{ km s}^{-1}$	203
B.16	MULTI results for N II λ 4630.6 Å at $\xi_t = 0 \text{ km s}^{-1}$	204
B.17	MULTI results for N II λ 4630.6 Å at $\xi_t = 5 \text{ km s}^{-1}$	205
B.18	MULTI results for N II λ 4630.6 Å at $\xi_t = 10 \text{ km s}^{-1}$	206
B.19	MULTI results for N II λ 4643.1 Å at $\xi_t = 0 \text{ km s}^{-1}$	207
B.20	MULTI results for N II λ 4643.1 Å at $\xi_t = 5 \text{ km s}^{-1}$	208
B.21	MULTI results for N II λ 4643.1 Å at $\xi_t = 10 \text{ km s}^{-1}$	209
B.22	MULTI results for N II λ 5005.1 Å at $\xi_t = 0 \text{ km s}^{-1}$	210
B.23	MULTI results for N II λ 5005.1 Å at $\xi_t = 5 \text{ km s}^{-1}$	211
B.24	MULTI results for N II λ 5005.1 Å at $\xi_t = 10 \text{ km s}^{-1}$	212
B.25	MULTI results for N II λ 5679.6 Å at $\xi_t = 0 \text{ km s}^{-1}$	213
B.26	MULTI results for N II λ 5679.6 Å at $\xi_t = 5 \text{ km s}^{-1}$	214
B.27	MULTI results for N II λ 5679.6 Å at $\xi_t = 10 \text{ km s}^{-1}$	215
B.28	MULTI results for N II λ 6482 Å at $\xi_t = 0 \text{ km s}^{-1}$	216
B.29	MULTI results for N II λ 6482 Å at $\xi_t = 10 \text{ km s}^{-1}$	217
C.1	Results of Monte Carlo Simulations for N II atom at $\log(g)=3.5$, and $\xi_t = 0.0 \text{ km s}^{-1}$	218
C.2	Results of Monte Carlo Simulations for N II atom at $\log(g)=4.0$, and $\xi_t = 0.0 \text{ km s}^{-1}$	219
C.3	Results of Monte Carlo Simulations for N II atom at $\log(g)=4.5$, and $\xi_t = 0.0 \text{ km s}^{-1}$	220
C.4	Results of Monte Carlo Simulations for N II atom at $\log(g)=3.5$, and $\xi_t = 5.0 \text{ km s}^{-1}$	221
C.5	Results of Monte Carlo Simulations for N II atom at $\log(g)=4.5$, and $\xi_t = 5.0 \text{ km s}^{-1}$	222
C.6	Results of Monte Carlo Simulations for N II atom at $\log(g)=3.5$, and $\xi_t = 10.0 \text{ km s}^{-1}$	223
C.7	Results of Monte Carlo Simulations for N II atom at $\log(g)=4.0$, and $\xi_t = 10.0 \text{ km s}^{-1}$	224
C.8	Results of Monte Carlo Simulations for N II atom at $\log(g)=4.5$, and $\xi_t = 10.0 \text{ km s}^{-1}$	225
C.9	Results of Monte Carlo Simulations for N II atom at $\log(g)=3.5$, and $\xi_t = 0.0 \text{ km s}^{-1}$: Correlation Coefficients	226
C.10	Results of Monte Carlo Simulations for N II atom at $\log(g)=4.0$, and $\xi_t = 0.0 \text{ km s}^{-1}$: Correlation Coefficients	227

C.11 Results of Monte Carlo Simulations for N II atom at $\log(g)=4.5$, and $\xi_t a = 0.0$ km s ⁻¹ : Correlation Coefficients	228
C.12 Results of Monte Carlo Simulations for N II at $\log g=3.5$, and $\xi_t = 5.0$ km s ⁻¹ : Correlation Coefficients	229
C.13 Results of Monte Carlo Simulations for N II at $\log g=4.5$, and $\xi_t = 5.0$ km s ⁻¹ : Correlation Coefficients (r)	230
C.14 Results of Monte Carlo Simulations for N II atom at $\log(g)=3.5$, and $\xi_t = 10.0$ km s ⁻¹ : Correlation Coefficients	231
C.15 Results of Monte Carlo Simulations for N II atom at $\log(g)=4.0$, and $\xi_t = 10.0$ km s ⁻¹ : Correlation Coefficients	232
C.16 Results of Monte Carlo Simulations for N II atom at $\log(g)=4.5$, and $\xi_t = 10.0$ km s ⁻¹ : Correlation Coefficients	233

List of Appendices

Appendix A List of Constants and Abbreviations	187
Appendix B MULTI Results of Selected N II lines	188
Appendix C Monte Carlo Results	218
Appendix D H α Fitting Figures	234
Appendix E N II Normalized Spectra	254

Chapter 1

Introduction and Overview

Stellar Evolutionary models of rotating, massive stars show that rotation affects a star's life-time, geometry, chemical composition, and many of its observed parameters, such as effective temperature (T_{eff}), gravity ($\log g$), colour, etc., (Maeder & Meynet, 2012, Palacios, 2013). One of these predicted changes (which is the subject of the current study) is an increase in nitrogen abundance in their atmospheres. This nitrogen increase is associated with changes in the abundances of a number of other elements, such increased helium and decreased carbon and oxygen abundances (Meynet & Maeder, 2000, Heger et al., 2000, Heger & Langer, 2000, Maeder & Meynet, 2001, Brott et al., 2011, Ekström et al., 2012). These changes are caused by a large scale, rotationally induced, circulation within the stellar envelopes, known as meridional circulation, that brings CNO processed material from the stellar core up to the surface and fresh hydrogen from the stellar envelope into the core (Eddington, 1925, Talon, 2008). Such models predict that these abundance changes are related to the stellar rotational velocity, and that the effects will be amplified with increased stellar rotation.

Although evolutionary models of rotating, massive stars are successfully able to explain the observed helium enrichment in O-type stars and the mass discrepancy of massive stars (Maeder, 1995), the predicted nitrogen enrichment is still a matter of debate. While several observational studies provide evidence of the predicted nitrogen enrichment (e.g. Maeder et al. (2014), Nieva & Przybilla (2014) Maeder et al. (2009), and Gies & Lambert (1992)), others do not find any significant nitrogen enrichment, (e.g. Hunter et al. (2009), Dunstall et al. (2011),

and Lyubimkov et al. (2012)). However, many of the studies that did not find the predicted nitrogen enrichment were performed on objects with low projected rotational velocities; a large fraction of these objects may be slowly-rotating objects, and rotational mixing is inefficient at low rotational velocities. For example, no nitrogen enrichment was found for models with an initial rotational velocity of 100 km s^{-1} by Talon et al. (1997) (see their Figure 10). Many theoretical models find that the stellar rotational velocity needs to be higher than a threshold value in order to produce a significant mixing.

For this study, I will look at Be stars with moderate to high projected rotational velocity. The consensus is that all Be stars are really rapidly rotating objects (Townsend et al., 2004, Frémat et al., 2005), although some will appear as slower rotators (low $v \sin i$ due to low inclination angle i). As the fastest rotating main-sequence stars, Be stars might be expected to have significant nitrogen enrichment in their atmospheres (Fukuda, 1982). Be stars are defined as “non-supergiant B-type stars whose spectra have, or had at one time, one or more Balmer lines in emission” (Slettebak, 1988). They are characterized with (usually) doubly-peaked Balmer emission lines, excess IR emission, and intrinsic polarization. These are explained by the existence of a rotationally-supported, circumstellar disk (Porter & Rivinius, 2003). Be stars have measured rotational velocities that average $\approx 80 \%$ of their critical rotational velocities, and they may rotate even faster (Cranmer, 2005). Finally, Be stars represent a significant fraction of the B spectral type stars with an average fraction of $\approx 17 \%$ which reaches $\approx 34\%$ in the B2 subclass (Zorec & Briot, 1997).

The spectral analysis of early-type Be stars is very challenging due to various effects that need to be properly considered and accounted for, such as non-LTE effects, rotational broadening, gravitational darkening, and circumstellar emission. Radiative transitions dominate in the atmospheres of early-type stars driven by photons from deeper and hotter regions, and photon losses from the outer boundary; these can cause a significant change in the ionization and excitation balances in the line formation region (Kurucz, 1979). As a result, assuming local thermodynamic equilibrium (LTE) will not be suitable for this analysis.

In addition to non-LTE effects, rotation changes the observed spectral profiles from deep and narrow Voigt profiles to broad and shallow rotation profiles with low continuum contrast. Rapid rotation can also cause strong line blending. Consequently, just a few strong lines of each element can be detected and used for measuring abundances. Our ability to model these lines can be highly affected by the accuracy of the atomic data. As a result, a detailed calculation of the error bounds on the estimated abundances will be required, instead of the traditional way of estimating the errors from the scatter of the estimated abundances using weak lines.

In the current work, the MULTI code (v2.0) of Carlsson (1992) was used to solve the non-LTE problem of N II in order to get grids of equivalent widths of the lines of interest over grids of stellar parameters suitable for B-type stars. MULTI solves the radiative transfer equation coupled with the statistical equilibrium equations simultaneously and can be used to get the emergent photospheric line profiles in non-LTE. Also, estimates of the uncertainties of the equivalent widths due to errors in the atomic data were obtained through a series of Monte-Carlo MULTI calculations following Sigut (1996).

Another effect of rapid rotation is the oblateness of the stellar surface resulting in a latitudinal dependent temperature and gravity: the temperature and gravity will be higher in the polar regions and lower at equatorial regions instead of the uniform stellar temperature and gravity of a non-rotating star with the same mass. This phenomenon is known as gravitational darkening, first suggested by von Zeipel (1924). This effect now has direct interferometric confirmation for nearby stars (see the review of van Belle 2012). As a result, the observed spectral line profiles will be dependent on the stellar rotational velocity and inclination of the stellar rotation axis to the line of sight. Gravitational darkening effects on the observed lines were studied using the STAR_GD code of Sigut (2014, private communication). The non-LTE line profiles computed using MULTI were used as inputs for these codes in order to represent the local photospheric emission.

Finally, emission from the circumstellar disk can affect the observed photospheric spectra. Due to the difficulty of the treatment of the disk emission, in addition to the expected rotational

broadening and gravitational darkening, Be stars have been excluded in many of the previous studies of the nitrogen abundances in B-type stars (e.g. Lyubimkov et al. (2012); Gies & Lambert (1992)). In other studies, Be stars were included, but their disk emission was corrected for in a approximate way that might cause significant uncertainties in the estimated nitrogen abundances (e.g. Lennon et al. (2005); Dunstall et al. (2011)). However, computational tools are now available for a more accurate spectral analysis. The `BEDISK` and `BERAY` codes (Sigut & Jones (2007); Sigut (2011), respectively) solve the radiative transfer equation within the circumstellar disk and can be used to provide a proper treatment of the disk emission. The photospheric lines computed using `MULTI` can again be used to represent the local, photospheric spectrum of the central star.

Chapter 2

Early-Type Stars

2.1 Introduction

Massive stars have great importance in astrophysics; their formation and evolution have a drastic influence on their parent galaxy's physical, chemical, and morphological characteristics. Energetic, ionizing photons and strong stellar winds from massive stars inject energy into the interstellar medium and provide it with metals synthesized within stellar cores through thermonuclear reactions (Crowther, 2004). As these stars evolve, their strong radiation and stellar winds cause the photo-evaporation of any remaining circumstellar material, forming compact HII regions which will expand away from the star, causing shock waves in the parent molecular cloud and triggering further star formation (Kennicutt, 2005). The death of these stars through powerful supernova explosions will also provide the interstellar medium with heavy elements and will trigger further star formation (Preibisch & Zinnecker, 2006). Massive stars are the progenitors of black holes and neutron stars. Cosmological observations of high redshift galaxies show that massive stars play a crucial role in the re-ionization of the early universe (Kennicutt, 2005).

2.2 Physical Characteristics of Massive Stars

Massive stars are defined as stars that have masses high enough to end with supernova and correspond to main sequence stellar masses equal to or greater than $\approx 8 M_{\odot}$ (Langer, 2012). This includes the early-B type stars, B0 through B3 ($8-16 M_{\odot}$) and O type stars ($16-128 M_{\odot}$) (Zinnecker & Yorke, 2007). Massive stars have high effective temperatures, from $\approx 19,000$ K for B3 stars (Habets & Heintze, 1981) up to $\approx 50,000$ K for O2 stars (Crowther, 2004).

Massive stars have absolute visual magnitudes equal to or less than -1.49 mag and bolometric magnitudes equal to or less than -3.39 mag (Habets & Heintze, 1981). The initial mass function with a Salpeter slope predicts that for every ≈ 1000 low-mass stars with masses less than $2 M_{\odot}$, there are only sixteen early B-type stars and 10 O-type stars (Zinnecker & Yorke, 2007). Although massive stars are rare, they provide most of the emitted UV radiation in the universe (Zinnecker & Yorke, 2007).

2.3 Surface Abundances of B-type stars

The measurement of atmospheric abundances of Galactic B-type stars has been the objective of many studies (Schönberner (1988); Langer (1992); Gies & Lambert (1992); Fierro & Georgiev (2008); Lyubimkov et al. (2012)). These measurements can test the efficiency of rotational mixing in massive stars and place constraints on evolutionary models of massive stars. Gies & Lambert (1992) studied 39 Galactic, early B-type stars, O9 through B3, and their measured (LTE) abundances of some B stars showed an increase in nitrogen surface abundance and a decrease in carbon and oxygen surface abundances. However, recently, the CNO abundances of 22 Galactic B-type stars with masses between 5 and $11 M_{\odot}$ were measured by Lyubimkov et al. (2012) and the results (presented in Table (2.1)) do not show the predicted changes of the CNO abundances via rotational mixing by theoretical models (e.g Brott et al. (2011) and Ekström et al. (2012)).

Nieva & Simón-Díaz (2011) studied 13 narrow-lined, early B-type stars with $v \sin i \leq 60 \text{ km s}^{-1}$ in the Ori OB1 association. This study did not find the predicted changes of the surface abundances by rotational mixing. Nieva & Przybilla (2012) measured the elemental abundances of 27 early B-type stars in the solar neighbourhood, within 500 pc from the sun, using echelle spectra with high resolution, $R \geq 40000$, and high signal-to-noise ratio, 250-800. Nitrogen enrichment was found in one third of B stars studied in this work. The average abundances of these 27 stars, plus 9 stars from Nieva & Simón-Díaz (2011), are shown in Table (2.1) from Nieva & Przybilla (2012). Note that the table abundances are expressed in the logarithmic measure, defining an abundance A for each element ϵ as

$$A_{\epsilon} \equiv \log \left(\frac{N_{\epsilon}}{N_{\text{H}}} \right) + 12 , \quad (2.1)$$

where N_{H} is the total number density of hydrogen atoms and ions. Hence the abundance of hydrogen is $A = 12$ on this scale and all other elements have smaller A values. Typically, the logarithmic units of abundance are measured in “dex.”

The metallicity of early, B-type, main-sequence stars in the Magellanic Clouds has been measured in many studies, such as Korn et al. (2000) and Hunter et al. (2005). Recently, a large, spectroscopic survey for massive stars in the fields of a number of stellar clusters in the Milky Way and the Magellanic Clouds was carried out using the Fibre Large Array Multi-Element Spectrograph (FLAMES-Giraffe) on the Very Large Telescope (VLT). (Evans et al., 2005). More than 50 O-type and 500 B-type stars were included in this survey. The stellar parameters $\log g$, $v \sin i$, T_{eff} , and the elemental abundances of the B-type stars, were published by Hunter et al. (2007), Hunter et al. (2009), and Trundle et al. (2007). These works give the extensive measurements of elemental abundances of B stars in the Magellanic Clouds and the Milky-Way.

The predicted nitrogen enrichment in a sample of early B-type main-sequence stars in the Magellanic Clouds and in the Milky-Way from the VLT-FLAMES survey was investigated

by Hunter et al. (2008b) and Hunter et al. (2009). Hunter et al. (2008b) show that 20% of a sample of 100 early B-type stars in the Small Magellanic Cloud (SMC) stars are rapid rotators with nitrogen enrichments in agreement with the predicted nitrogen enrichment by rotational mixing. A further 40% of the sample are slow rotators, $v \sin i \leq 50 \text{ km s}^{-1}$, with nitrogen enrichments that cannot be explained by rotational mixing. Instead, different mechanisms, like mass transfer in close binaries, are suggested. Similarly, Hunter et al. (2009) investigated the predicted nitrogen enrichment by rotational mixing in a sample of 135 early B-type stars in the Large Magellanic Cloud (LMC) and 50 early B-type stars in the Milky Way. About 20% of the LMC sample were rapidly rotating and nitrogen enriched, and another 20% of the sample were slowly rotating and nitrogen enriched; no nitrogen enrichment was found in the Galactic sample. Dunstall et al. (2011) studied the nitrogen abundances in a sample of Be stars in the Magellanic Clouds from the VLT-FLAMES survey. No nitrogen enrichment was detected, i.e. the nitrogen surface abundances of Be stars were similar to those of normal B stars. A major defect of this work; however, is that the disk emission in the Be star spectrum was corrected in an ad-hoc way by forcing the silicon abundance of each star to match the expected LMC/SMC average by addition of a featureless disk continuum. The disk emission is wavelength dependent as will be discussed later in Chapter 8. Stellar continuum dilutions of up to 60% were used.

These studies show that B stars in the LMC have overall metallicities close to one third of those in the solar neighbourhood, and B stars in the SMC have metallicities close to one tenth of those in the Milky Way solar neighbourhood.

Table 2.1: Average elemental abundances of Galactic, main-sequence B stars.

Element	Solar		Milky-Way				mean
	Aspl05	Lyub12	Nieva12	Nieva11	Hun09	Gies92	
He	10.93		10.99 ± 0.01			11.00	11.00 ± 0.00
C	8.39	8.31 ± 0.13	8.33 ± 0.04	8.35 ± 0.03	8.00 ± 0.19	8.20	8.24 ± 0.10
N	7.78	7.80 ± 0.12	7.79 ± 0.04	7.82 ± 0.07	7.62 ± 0.12	7.81	7.77 ± 0.06
O	8.66	8.73 ± 0.13	8.76 ± 0.05	8.77 ± 0.03	8.63 ± 0.19	8.68	8.71 ± 0.05
Ne	7.84		8.09 ± 0.05	8.09 ± 0.05		7.97	8.05 ± 0.05
Mg	7.53		7.56 ± 0.05	7.57 ± 0.06	7.25 ± 0.17		7.46 ± 0.14
Al	6.37					6.45	6.45 ± 0.00
Si	7.51		7.50 ± 0.05	7.50 ± 0.06	7.42 ± 0.07	7.58	7.50 ± 0.04
S	7.14					7.21	7.21 ± 0.00
Fe	7.45		7.52 ± 0.03	7.52 ± 0.06		7.72	7.59 ± 0.04

Sources: Lyub12, Lyubimkov et al. (2012); Nieva12, Nieva & Przybilla (2012); Nieva11, Nieva & Simón-Díaz (2011); Hun09, Hunter et al. (2009); Gies92, Gies & Lambert (1992); Aspl05, Asplund (2005).

2.4 Evolution of Massive Stars on The Main Sequence

Evolution on and after the main sequence stage depends on star's mass, rotation, composition, and mass loss history. The latter is sensitive to the metallicity and initial main-sequence mass (Woosley et al., 2002, Heger et al., 2003, Langer, 2006, Ekström et al., 2010). Massive stars, like all stars, reach the main-sequence once the temperature and the pressure of their cores become high enough to start hydrogen burning. Unlike low-mass stars, massive stars burn hydrogen through the carbon-nitrogen-oxygen (CNO) cycle, with the reaction sequence

$$^{12}\text{C}(p, \gamma)^{13}\text{N}(e^+ \nu)^{13}\text{C}(p, \gamma)^{14}\text{N}(p, \gamma)^{15}\text{O}(e^+ \nu)^{15}\text{N}(p, \alpha)^{12}\text{C}, \quad (2.2)$$

rather than the p-p chain, releasing ≈ 24.97 MeV per helium atom.

During their main sequence phase, stars remain in hydrostatic equilibrium by the support of the gas pressure and the radiation pressure maintained by the energy generated by thermonuclear reactions in their cores. Unlike low mass stars, radiation pressure in massive stars represents a significant fraction of the total core pressure and this fraction increases with stellar

mass. For a $9M_{\odot}$ star, the core ratio of radiation pressure to gas pressure is close to 15%. This rises to 46% for a $40M_{\odot}$ star, and dominates in very massive stars, $M \geq 120M_{\odot}$.

Massive stars have convective cores due to the steep temperature gradient in their core. In the core, the radiative gradient, ∇_{rad} , is greater than the adiabatic gradient, ∇_{ad} , satisfying the Schwarzschild criterion for convection. The radiative gradient is defined as

$$\nabla_{rad} = \frac{3}{16\pi a c G} \frac{\kappa L_r P}{M_r T^4}, \quad (2.3)$$

and the adiabatic gradient, as

$$\nabla_{ad} = \left(\frac{\partial \ln T}{\partial \ln P} \right)_{ad} = \frac{P \delta}{C_P \rho T}. \quad (2.4)$$

Here κ is the Rosseland mean opacity, M_r is the mass enclosed within a sphere of radius r , L_r , is the luminosity at the surface of this sphere, and δ is given by $\delta = -(\partial \ln \rho / \partial \ln T)_{P\mu}$. The radiative gradient, ∇_{rad} , represents the thermal gradient required to carry the total flux by radiation only. The adiabatic gradient, ∇_{ad} , represents the thermal gradient inside a moving fluid parcel that does not exchange heat with the surrounding medium. When ∇_{rad} is greater than ∇_{ad} , an outwardly displaced fluid parcel will be hotter than the surrounding medium and will continue to rise. On the other hand, ∇_{rad} is less than ∇_{ad} in the envelopes of massive stars due to the weak temperature gradient; as a result, no convection occurs and the energy will be transported by radiation (Maeder, 2009).

Due to the convective nature of the cores of massive stars, the chemical composition of the core will remain homogeneous because convection timescales are much shorter than the timescale of thermonuclear reactions (Carroll & Ostlie, 2007). The cessation of the hydrogen burning in the core represents the end of the main-sequence stage.

2.4.1 Effects of Rotation on Massive Star Evolution on the Main-Sequence

The study of the evolution of massive stars with rotation was an important step, and the inclusion of rotation solved many contradictions between observations and the predictions of theoretical models of evolution of massive stars, like the extended cluster main-sequence, the observed helium enrichment in fast rotating O-type stars, and the discrepancy between the spectroscopic and evolutionary mass of massive stars (Maeder, 1995).

In general, the inclusion of rotation leads to the deformation of the surfaces of massive stars that increases with increasing rotational velocities. As a result, the assumption of spherical symmetry will not be realistic for rapid rotation. The centrifugal force reduces the effective stellar gravity, and the reduction is latitude dependent, with its maximum at the stellar equator and a zero reduction at the pole. This reduction in the stellar gravity affects the stellar radiative flux, and therefore the local T_{eff} , that is now dependent on the stellar effective gravity through von Zeipel's relation

$$T_{\text{eff}}(\theta) = C_{\omega} |g_{\text{eff}}(\theta)|^{(1/4)}, \quad (2.5)$$

where C_{ω} is a constant and $g_{\text{eff}}(\theta)$ is the effective gravitational acceleration at stellar co-latitude θ . The implication of von Zeipel's relation is that rotating stars are distorted, with $R_{\text{eq}} > R_p$ and have an effective temperature that varies with latitude. Gravitational darkening and its effects will be discussed in much more detail in Chapter 7.

Rotational Mixing

Theoretical studies predict that rotating stars undergo mixing that can bring processed material from the core to the surface and unprocessed material from the envelope into the core (e.g. Brott et al. (2011), Ekström et al. (2012)). This mixing results from rotationally-induced instabilities within the envelope, such as the meridional circulation and shear turbulence. Consequently, massive stars are expected to show changes in their atmospheric abundances due to this rotational mixing, such as the increase of helium, nitrogen abundances and the decrease of the

carbon and oxygen abundances with age during the main-sequence. The net predicted abundance changes can depend on the treatment of the matter transport by meridional circulation as either an advection or diffusive process.

Meridional circulation, or Eddington-Sweet circulation, is a large-scale motion that is capable of transporting angular momentum and matter within stars (Eddington, 1925). This circulation results from the latitude dependence of the potential gradient within rotating stars that leads to the non-coincidence of the isobaric surfaces and the isothermal surfaces.

Assuming stars are born on the main-sequence with rotational profiles close to that of rigid body rotation, meridional circulation will transport the angular momentum from the stellar surfaces to the stellar cores until an equilibrium rotational profile is reached. Such an assumption is usually taken in theoretical models (Talon et al., 1997, Meynet & Maeder, 2000, Heger et al., 2000). Consequently, the rotational velocity will be a function of radius, and stars will have a differential rotation profile. Differential rotation introduces shear mixing that can also transport matter and angular momentum. As a result, the net transport of matter and angular momentum can be treated as the sum of these two effects (Maeder & Zahn, 1998). If the transport of matter by meridional circulation is an advective process, meridional circulation could lead to drastic changes in the surface abundances of He and CNO in massive stars. However, observed abundances in O and B type star do not support such large changes, and therefore, the efficiency of matter transported by rotational mixing must be lower than expected.

Chaboyer & Zahn (1992) suggested that strong horizontal turbulence can suppress the transport of matter by meridional circulation. They invoked this effect to explain observed abundances in giant stars with masses between one and two solar masses that do not show any boron depletion expected from rotational mixing. Chaboyer & Zahn (1992) argued that this assumption can explain the observed thickness of the tachocline layer in the sun (the layer between the radiative core and the convective envelope) as detected by helioseismological studies. Consequently, the transport of matter by meridional circulation should be treated as a diffusive process. Although this assumption was based on observations of low mass stars, Zahn (1992)

argued that this assumption can be valid in massive stars due to the stable vertical thermal gradient in the radiative envelopes of massive stars which suppress any vertical turbulence.

However, this is not the case for the transport of angular momentum. Zahn (1992) showed that the transportation of angular momentum by meridional circulation can still be treated as an advective process. In this case, meridional circulation and horizontal turbulence act on different physical quantities: horizontal turbulence affects the angular velocity and meridional circulation affects the specific angular momentum. For the transport of matter, however, meridional circulation and horizontal turbulence act on the same physical quantity, the element concentration. Consequently, if strong horizontal turbulence can homogenize the angular velocity over horizontal surfaces, it cannot suppress the advective transportation of angular momentum by meridional circulation (Zahn, 1992).

During early stages on the main sequence, stars are nearly chemically homogeneous and rotational mixing will therefore not be efficient. However, as thermonuclear reactions within the cores lead to significant changes in composition, the strong mean molecular weight gradient established suppresses meridional circulation, an effect known as the μ -barrier. This reduces differential rotation within the star and weakens the shear mixing, due to the density stratification that induces a buoyancy force prohibiting any vertical motion, *i.e.*, parallel to the rotational axis (Maeder & Zahn, 1998). However, horizontal turbulence induced by the strong differential rotation within the star, as suggested by Chaboyer & Zahn (1992), reduces the molecular weight gradient by homogenizing the chemical composition over the horizontal surfaces (Chaboyer & Zahn, 1992, Zahn, 1992). This reduces its prohibiting effects on the transport of matter and angular momentum. Also, if horizontal turbulence is not strong enough to overcome the prohibiting effects of the μ -barrier, it can cause mixing by enhancing other existing turbulence like, the shear turbulence (Maeder & Zahn, 1998).

In conclusion, the transport of matter by meridional circulation and shear mixing represents a diffusive process that depends on the rotational profile and the mean molecular weight gradient within a star. On the other hand, the transport of angular momentum within a star

should be treated as an advective-diffusive process, where meridional circulation will advect the angular momentum inward and the shear turbulence will diffuse it outward. The transport of angular momentum also depends on the rotational profile and the mean molecular weight gradient within the stars (Maeder, 2009, Zahn, 1992).

Modelling Results

Including rotation in the models of massive star evolution can lead to significant changes when compared to non-rotating models, such as the increase of the main-sequence lifetimes, the increase of the luminosity at the end of the main-sequence, and the change of surface abundances. Rotating models predict that massive stars will appear fainter on the zero age main-sequence (ZAMS) due to surface oblateness and gravity darkening. Massive stars appear brighter at the terminal main sequence (TAMS) because of the reduced opacity due to the increase in helium abundance in the atmosphere. Rotating models predict the increase of the nitrogen and helium surface abundances and the decrease of carbon and oxygen abundances by rotational mixing. In addition, rotating models predict longer main-sequence lifetimes for massive stars, due to fresh hydrogen brought from the envelope to the core by the rotationally induced mixing.

The evolution of a $9 M_{\odot}$ star with rotation on the main-sequence is given by Talon et al. (1997). This study investigated how rotation affects evolutionary tracks in the HR diagram, in addition to the rotational profiles within the stars and the atmospheric chemical composition. Stars were assumed to be born on the main sequence with rotational profiles close to that of rigid body rotation and with homogeneous composition, and models were computed for two initial surface equatorial rotational velocities, 100 km s^{-1} and 300 km s^{-1} .

Models with fast rotation (300 km s^{-1}) have a strong, differential rotational profile at the TAMS, compared with those with slow rotation (100 km s^{-1}). This is explained by the increase of the efficiency of the transport of angular momentum by meridional circulation with increasing the initial stellar rotation-see Figure (2.1). Also, this study shows that models with fast rotation have significant changes in surface abundances at the end of the main-sequence

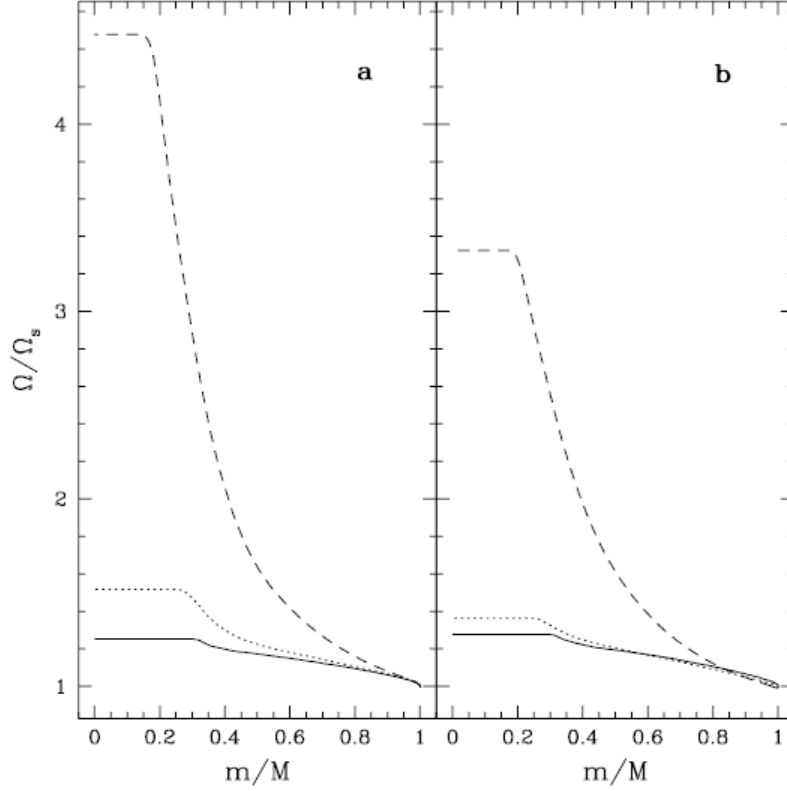


Figure 2.1: The evolution of the rotational profile of a $9 M_{\odot}$ star during the main-sequence as a function of the Lagrangian mass coordinate. Panel (A) shows models with high initial rotational velocity, 300 km s^{-1} , and Panel (B) represents models with low initial velocities, 100 km s^{-1} . In both panels, the solid line represents the rotational profile on the ZAMS, the dotted line, the rotational profile at the middle of the main-sequence, and the dashed line, the rotational profile at the TAMS. Figure from Talon et al. (1997).

as compared with those with slow rotation. Figure (2.2), shows the increase of helium and nitrogen abundances and the decrease of hydrogen, carbon and oxygen abundances for the two initial rotation rates.

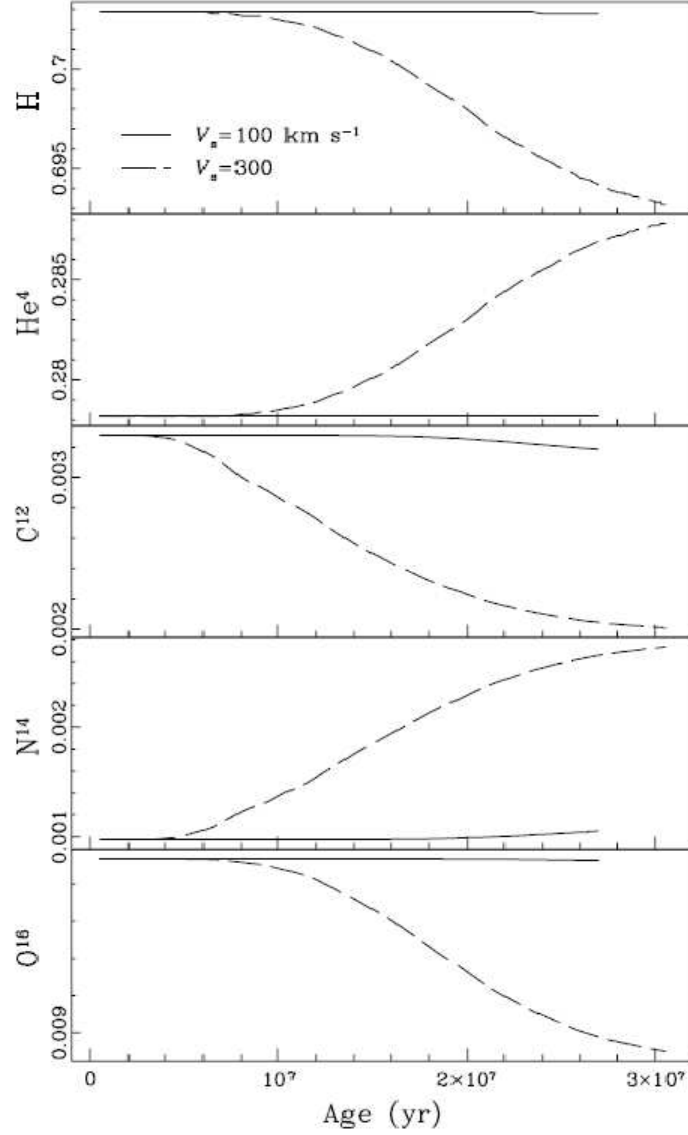


Figure 2.2: The evolution of the H, He, C, N, and O surface abundances of a $9 M_{\odot}$ star during the main-sequence for two different initial rotational rates. Figure from Talon et al. (1997).

Talon et al. (1997) also show that rotation affects the evolutionary tracks of massive stars in the HR diagram, as reproduced in Figure (2.3). As noted before, models with fast rotation (300 km s^{-1}) appear fainter on the ZAMS and have longer main-sequence lifetimes. The evolutionary tracks of slowly rotating models (100 km s^{-1}) were similar to those of non-rotating models with a moderate overshooting. Convective overshooting represents the extension of convective flows beyond the formal boundaries predicted by the Schwarzschild criterion (Maeder, 2009).

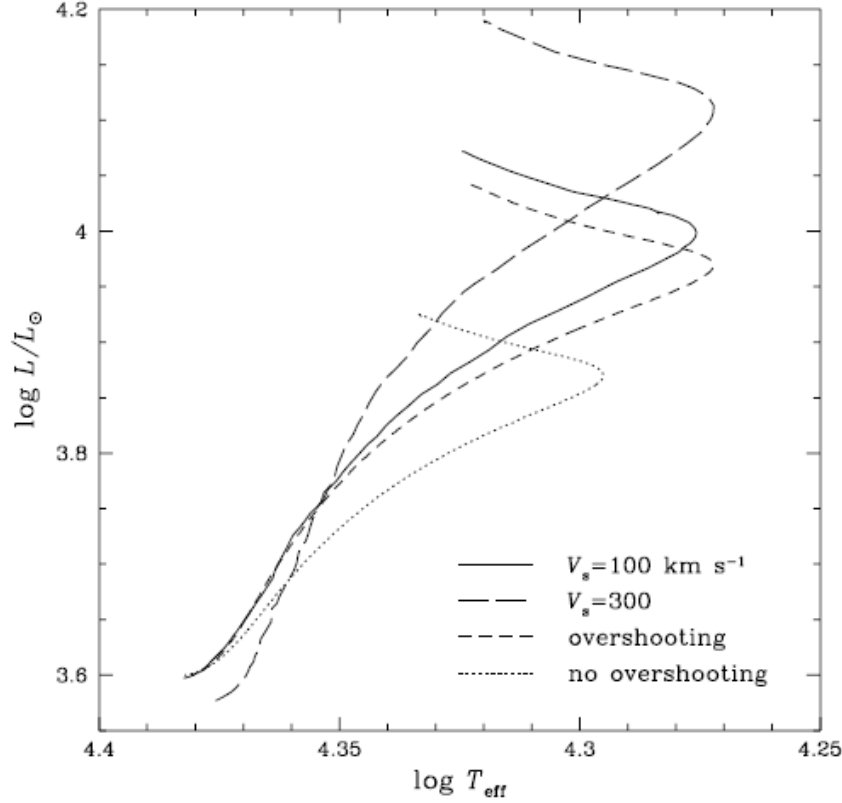


Figure 2.3: Evolutionary tracks of a $9 M_{\odot}$ star on the main-sequence for different initial velocities. Figure from Talon et al. (1997).

Also, models with fast rotation are brighter at the end of the main-sequence due to the decrease of the opacity of the stellar atmosphere that results from the increase of the helium surface abundance by rotational mixing.

Meynet & Maeder (2000) studied the evolution of rotating massive stars with masses between 9 and 120 solar masses. The evolutionary tracks on the HR diagram for rotating models with initial rotational velocities equal to 300 km s^{-1} and non-rotating models are shown Figure (2.4). Rotating models tend to be fainter on the ZAMS and brighter at the TAMS. Also, rotating models with initial masses equal to or less than $40 M_{\odot}$ have longer main-sequence lifetimes, such that the main-sequence lifetime of a $12 M_{\odot}$ star with initial rotational velocity equal to 300 km s^{-1} increases by close to 20%, in agreement with the results of Talon et al. (1997). This can explain the observed extended cluster main-sequence. Also, rotating models with initial stellar masses higher than $40 M_{\odot}$ have shorter main-sequence lifetimes due to the

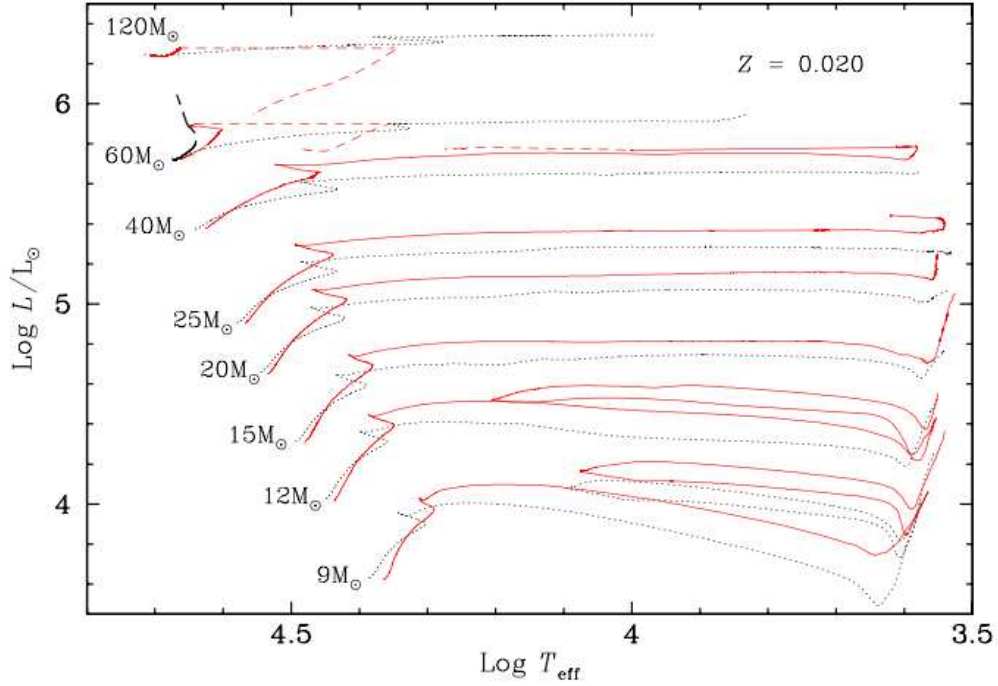


Figure 2.4: Evolutionary tracks with and without rotation for stars with masses between $9 M_{\odot}$ and $120 M_{\odot}$. The dotted lines represent non-rotating models, the solid lines, rotating models with initial rotational velocity equal to 300 km s^{-1} , and the long dashed lines, rotating models with initial rotational velocity equal to 400 km s^{-1} . The dashed part of the evolutionary tracks with initial stellar masses represent the WR stage. Figure from Meynet & Maeder (2000).

large mass loss rates, such that they evolve to the Wolf-Rayet stage from the main-sequence directly.

Meynet & Maeder (2000) also find significant changes in the elemental abundances in the atmosphere of rapidly rotating stars which increases with increasing the initial rotational velocities and initial stellar masses, as shown in Figures (2.5) and (2.6). Figure (2.5) shows the increase of the (N/H) ratio for a $20 M_{\odot}$ star due to rotational mixing with increasing initial rotational velocity. This demonstrates how rotational mixing can significantly enhance atmospheric nitrogen abundances in rotating stars.

Similarly, the mass fraction of helium, and the (N/O) ratio increase with initial rotational velocity. Such behaviour reflects the increase of the efficiency of rotational mixing with initial rotational velocities. Figure (2.6) shows the increase of the (N/C) ratio with initial stellar

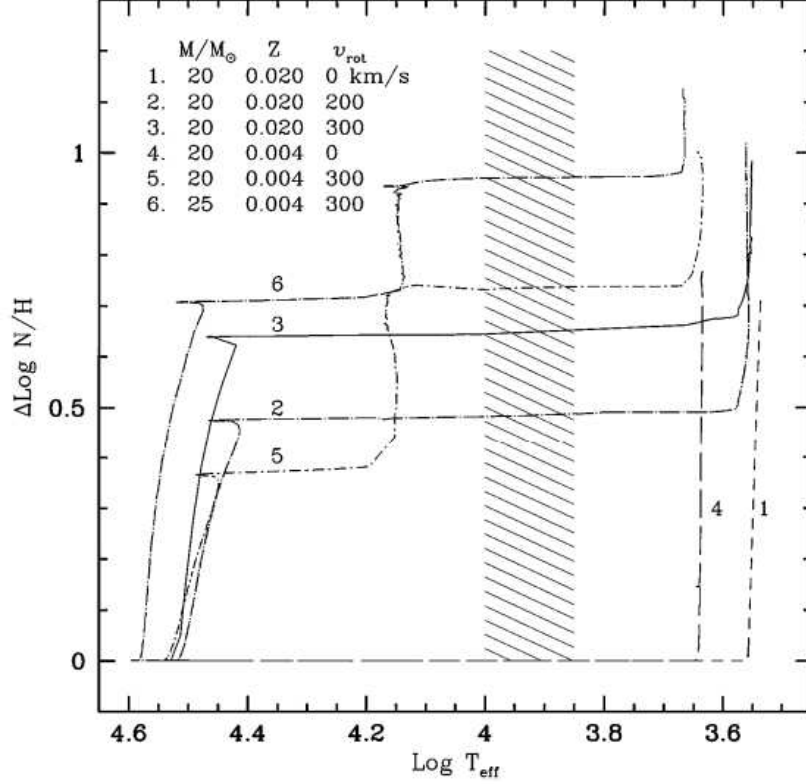


Figure 2.5: Evolutionary tracks of the atmospheric nitrogen abundance in massive stars. Note that $\Delta \log(N/H) \equiv \log(N/H) - \log(N/H)_i$. Figure from Maeder & Meynet (2000).

rotation and the initial rotational velocity. For a $20 M_{\odot}$ star, the (N/C) ratio increases from 0.25 to 1.77 on the TAMS as the initial rotational velocity increases from 0 to 300 km s^{-1} . Also, this figure shows that the predicted nitrogen enrichment and carbon depletion in the stellar atmospheres due to rotational mixing can explain the observed nitrogen and carbon abundances in the atmospheres of blue supergiants. The observed nitrogen abundances in blue supergiants are lower than those observed in stars that have undergone dredge up phases, while the observed carbon abundances in blue supergiants are higher (Meynet & Maeder, 2000).

Figure (2.7) shows predicted isochrones for rotating and non-rotating models of different initial stellar masses. Note the coincidence of the isochrones of rotating and non-rotating models within 0.1 dex in age. This result reflects the fact that the position in the HR diagram is not unique; a high mass star with low initial rotational velocity can have the same place on the HR diagram as a lower mass, more slowly rotating star, but both objects reach this point

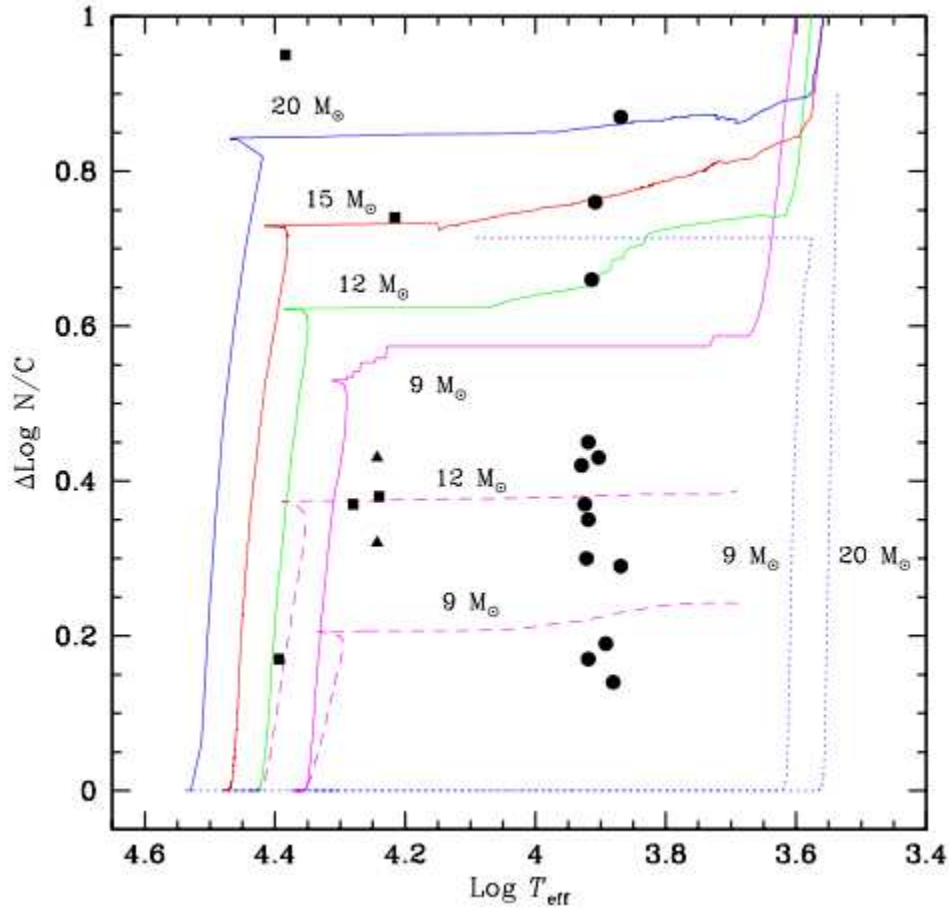


Figure 2.6: Evolutionary tracks of the ratio of the carbon abundance to the nitrogen abundance, $\log(N/C)$, as a function of the effective temperature, $\log T_{\text{eff}}$. Solid lines represent rotating models with initial stellar rotation equal to 300 km s^{-1} , dotted lines represent non-rotating models, and dashed lines represent rotating models with initial stellar rotation equal to 200 km s^{-1} . The black squares and triangles represent observational measurements of blue supergiants and the black circles represent observational measurements of A-type, galactic supergiants. Figure from Maeder & Meynet (2000).

at different ages. This result may explain the mass discrepancy between the evolutionary mass and spectroscopic mass of massive stars.

Including mass loss in evolutionary models significantly affects the surface angular velocity and the ratio of the surface angular velocity to the critical velocity, as shown in Figure (2.8). This behaviour depends strongly on the initial stellar mass; mass loss increases with initial stellar mass, and as a result, stars with masses higher than $12 M_{\odot}$ lose a larger portion of their surface angular momentum and slow down very quickly. Stars with masses less than or equal $12 M_{\odot}$, however, have lower mass loss rates and preserve most of their surface angular

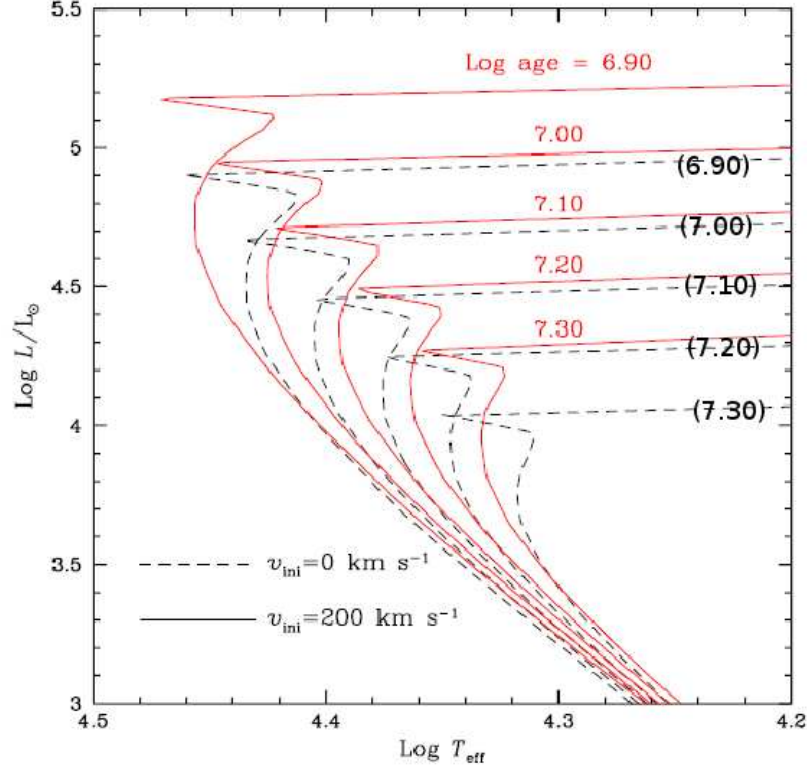


Figure 2.7: Predicted isochrones for rotating and non-rotating models of different initial masses with ages, $\log(\text{Age})$ between 6.9 and 7.3. Figure from Meynet & Maeder (2000).

momentum. As a result, stars with masses less than or equal to $12 M_{\odot}$ will have high surface angular velocities close to the critical values, and they will go through strong anisotropic mass loss in the equatorial region close to the end of the main-sequence. This might provide an explanation of the occurrence of the Be phenomenon (Meynet & Maeder, 2000). The recent work of Ekström et al. (2010) gives further support for this interesting result. Observations of Be stars in young open clusters (Keller et al. (1999); Martayan et al. (2007); Mathew et al. (2008)) show that this explanation can be a possible scenario for the formation of Be stars, but not the only one. Also, the sharp peaks shown in Figure (2.8) can be interpreted by the increase of the rotational velocity at the end of the main sequence due to the overall contraction of the stars. Also, the second peak shown in the $12 M_{\odot}$ model can be explained by the increase of the stellar rotational velocity as the star evolves on the blue side of the central helium burning, i.e. the blue loop.

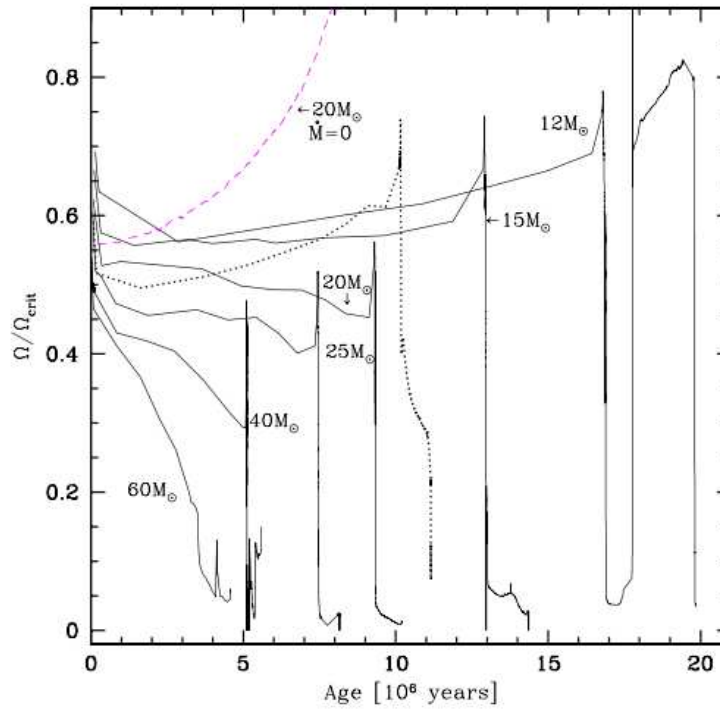


Figure 2.8: The change of the ratio of the angular rotational velocity to the critical value during the main-sequence stage for different initial stellar masses. Figure from Meynet & Maeder (2000).

2.4.2 Observational Constraints on Rotational Mixing in Massive stars

Observations of early B-type stars in the Milky Way and in the Magellanic Clouds have not provided clear evidence for efficient rotational mixing in massive stars. For example, some observational works agree with the predicted surface enrichment of nitrogen and helium and the depletion of carbon by rotational mixing (Maeder et al. (2009); Fierro & Georgiev (2008); Lyubimkov (1991); Herrero et al. (1992); Schönberner (1988)), while other studies do not find the predicted changes in the surface CNO abundances (Lyubimkov et al. (2012); Nieva & Przybilla (2012); Dunstall et al. (2011); Hunter et al. (2009))

However, most of the works that did not find evidence for a change in the surface abundances used samples of stars with low projected rotational velocities (i.e. low $v \sin i$) which may not have efficient rotational mixing. Although these are just projected rotational velocities, only a few percent of each sample could be nearly pole-on rotators, assuming random distribution of inclinations. Low projected rotational velocity objects were selected in order to get

narrow-lined spectra where elemental abundances can be measured with high precision. Stars with high projected rotational velocities, however, have very wide and shallow spectral lines, and as a result, accurate line equivalent widths are difficult to obtain in this case. In addition, gravitational darkening must be considered in any analysis of rapidly rotating stars.

Schönberner (1988) investigated the CNO abundances in four nitrogen rich OB stars, OBN stars, using the coude spectrograph of the ESO 1.5 m telescope at La Silla, Chile, and a coude spectrograph of the MPG 2.0 m telescope at Calar Alto, Spain. The results show that the N abundances in OBN stars are 10 to 30 times larger than those of the comparison stars, while the C abundances of OBN stars are close to 10 times lower than those of normal stars. Also, it was found that the O abundances in OBN stars are solar. Similar results were obtained by Lyubimkov (1991), who aimed to review the recent measurements of the surface abundances of B-type stars from literature. He found a trend of increasing nitrogen and helium abundances, with a slight decrease in the carbon and oxygen abundances, with age, in agreement with predicted rotational mixing- see Figure (2.9).

Among the 27 B stars included in the recent study of Nieva & Przybilla (2012), it was found that one third of the sample have higher nitrogen abundances that can be explained by surface enrichment through rotational mixing. On the other hand, recent measurements of the surface abundances of early B-type stars in the solar neighbourhood obtained by Lyubimkov et al. (2012) and Nieva & Simón-Díaz (2011) do not show the predicted abundances changes of rotational mixing. However, such studies were done for stars with low projected rotational velocities, $v \sin i \leq 66 \text{ km s}^{-1}$.

Similar studies were done for early B-type stars in the Magellanic Clouds (Dunstall et al. (2011); Hunter et al. (2009); Hunter et al. (2008b)) who did not find the predicted nitrogen abundance enrichment in early B-type stars with high rotational velocities. Dunstall et al. (2011) show that there is no difference in the observed nitrogen abundances in the atmospheres of Magellanic Clouds B and Be stars (Figure 2.10). This is surprising because Be stars, as a population, are the fastest rotating main-sequence stars (Yudin 2001, Fukuda 1982). Rapid

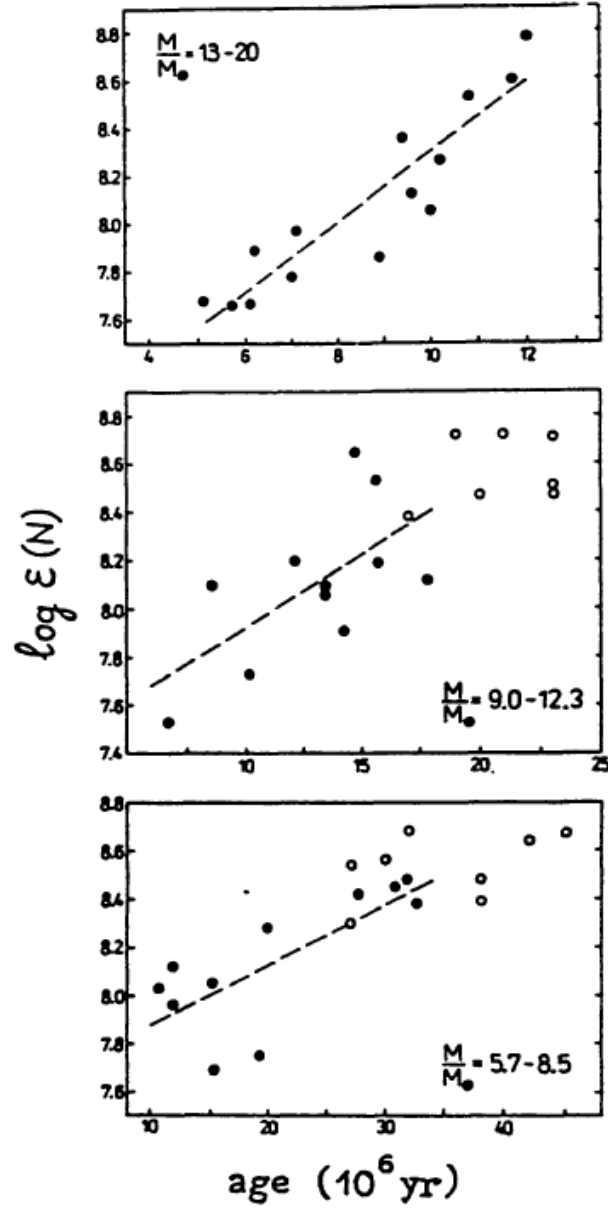


Figure 2.9: Observed increase in nitrogen abundance with age for three ranges of stellar masses, where the filled circles represent main-sequence early B-type stars and the filled circles represent yellow supergiants. Figure from Lyubimkov (1991).

rotation is thought to be the key driver of the Be phenomena; therefore, low $v \sin i$ Be stars are still expected to be rapidly rotating stars but seen at low inclination angle i .

Nevertheless, Maeder et al. (2009) emphasize that nitrogen enrichment is a function of stellar mass, rotation, metallicity, age, and multiplicity, and not just a function of stellar rotation alone, as assumed by Hunter et al. (2008b). As a consequence, Maeder et al. (2009) argued

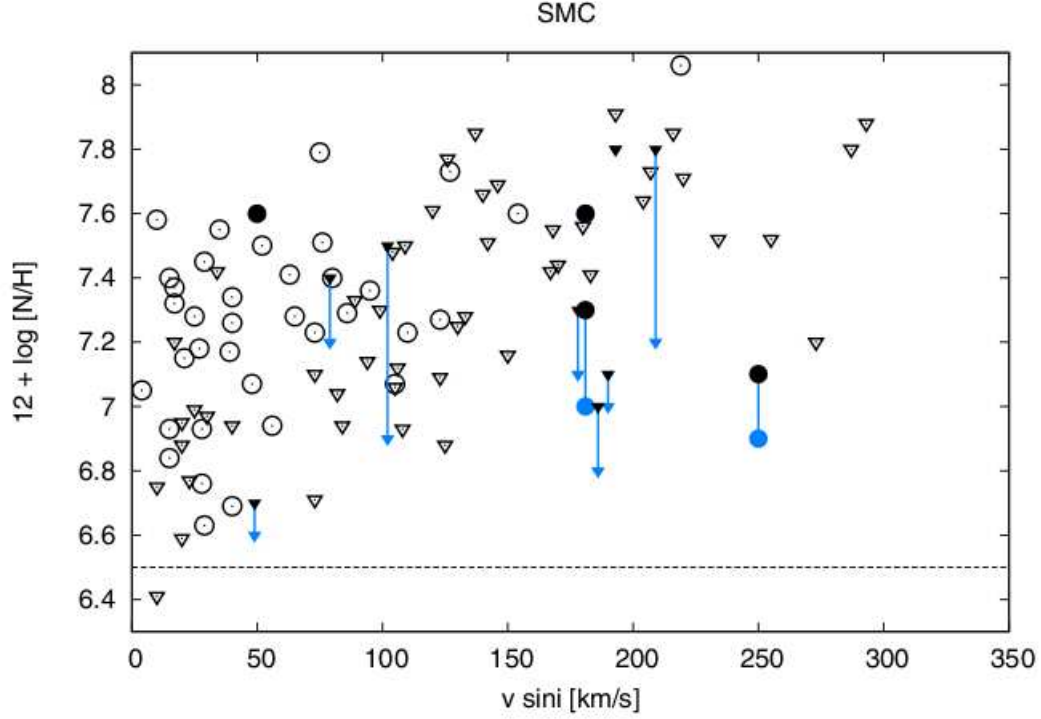


Figure 2.10: Dunstall et al. (2011) show that both Be and normal B stars have similar nitrogen abundances. Open circles represent normal B stars and the black and blue filled circles represent the nitrogen abundances of Be stars, post and pre removal of the disk contamination respectively. The black and blue triangles represent upper limit measurements from a number of Be stars and the colours have the same convention. Figure from Dunstall et al. (2011).

that the inclusion of field stars, the broad mass range of the stars ($10 - 30M_{\odot}$), the low number of B stars with projected rotational velocities higher than 250 km s^{-1} , and the expected binary error, significantly bias the results of Hunter et al. (2008b). Consequently, Maeder et al. (2009) reanalyzed the data from Hunter et al. (2008b) and showed that the atmospheric nitrogen abundances increase with increasing stellar rotation for B stars with masses within a narrow mass range and with the same metallicity and age. This gives support for rotational mixing, as shown in Figure (2.11). This point is still a matter of debate, and further investigations are required.

This work was complemented by another study for a larger sample of B stars from Hunter et al. (2009) by Maeder et al. (2014). Again, Maeder et al. (2014) argued that observed nitrogen abundances provide some evidence, and the observed scatter in the abundances is attributed to the low quality of data. Maeder et al. (2014) reinvestigated the accuracy of the estimated stellar

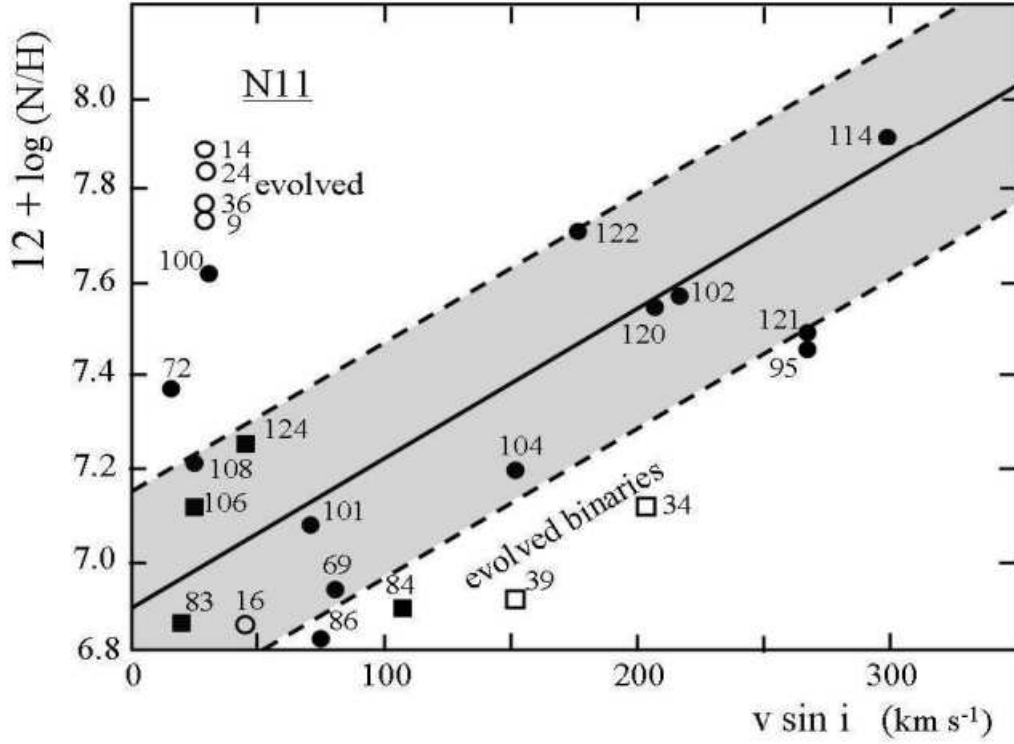


Figure 2.11: The increase of the atmospheric nitrogen abundance with increasing stellar rotational velocities for stars with masses between 14 and 20 M_{\odot} . The filled circles represent main-sequence objects, the open circles represent post main-sequence objects, and the squares represent the binaries. Figure from Maeder et al. (2009).

parameters and abundances for a subsample of 31 B stars from Hunter et al. (2009), $\approx 10\%$ of the sample, by comparing the observed spectra with non-LTE synthetic spectra, where the stellar parameters and abundances of Hunter et al. (2009) were adopted in the computation of these spectra. Results show that they did not get a good match in many cases, e.g. they did not get a good match for the observed $N\text{ II}$ lines in 6 cases. Also, they found that many of the stars in this sample have a binarity signature. Consequently, the authors suggested a careful reassessment for the results of Hunter et al. (2009).

Recently, Köhler et al. (2012) introduced a new method of testing the predicted nitrogen enrichment due to rotational mixing in early B-type stars by comparing their ages measured using evolutionary tracks in the HR diagram with the predicted ages assuming that the stars were enriched due to rotational mixing on the main-sequence. The latter ages were calculated based on their measured masses, nitrogen surface abundances, and rotational velocities. In this study, the

rotational velocities were measured by the profile fitting method using the non-LTE TLUSTY models from Hunter et al. (2008a). The objects included in the study were selected such that their nitrogen abundances are not larger than the maximum predicted nitrogen abundances enhancements by rotational mixing at velocities equal to their measured rotational velocities. It was found that the ages calculated for 7 out of 17 stars agree with those measured using the evolutionary tracks, i.e. an observed nitrogen enrichment of less than a half of these stars can be explained by rotational mixing.

Chapter 3

The Classical Be stars

3.1 Introduction

Classical Be stars are defined as non-supergiant, B spectral type stars which have, or had at some time in the past, one or more Balmer emission lines (Slettebak, 1988). Although the Be phenomenon is dominated by the B-type stars, it can also be found in late O-type and early A-type stars (Porter & Rivinius, 2003). The emission lines reflect the existence of circumstellar material, and these lines have different profile shapes: singly-peaked profiles or symmetric, although sometimes asymmetric, doubly-peaked profiles. Assuming that the circumstellar material of all Be stars has the same geometry, the different profile shapes represent different projections on the sky giving an indication that the circumstellar envelopes of Be stars are not spherically symmetric.

The Be phenomenon was first interpreted as the existence of a nebulous ring around the central B-type star in the work of Struve (1931). The first suggested mechanism for the formation of Be star disks was the ejection of matter from the equatorial regions of rapidly rotating stars that have rotational velocities close to their critical velocities, v_{crit} (Struve, 1931), which corresponds to the circular orbital velocity at the equator on the stellar surface. Using equation (7.12), the critical velocity for a B0 star is $\approx 490 \text{ km s}^{-1}$. The rapid rotation of Be stars is confirmed by many studies (Porter, 1996, Keller, 2004). Porter (1996) shows that Be stars have rotational velocities in the range of 70%-80% of their critical velocities. Recently, the

study of Townsend et al. (2004) shows that the observed rotational velocities of Be stars can be significantly underestimated due to gravitational darkening, and Be stars may have rotational velocities equal to or exceeding 95% of their critical velocities. The conclusion is disputed, however, by the statistical study of Cranmer (2005).

In addition to the observed optical emission lines, Be stars show polarized light which gives further confirmation of the disk-like structure of the circumstellar material of Be stars (Poeckert et al., 1979). Also, Be stars show an IR excess emission in their continuum energy distributions (Gehrz et al., 1974, Singh, 1985, Tur et al., 1995). This can be interpreted as free-free emission from circumstellar material with a disk-like structure around the central B-type star (Coté & Waters, 1987). In addition, interferometric studies for many Be stars confirm the disk-like structure of their circumstellar material directly (Kraus et al., 2012, Meilland et al., 2012).

Be stars represent a large fraction of the Galactic B-type stars, close to 17% overall, with a maximum fraction of 34% at the B1 spectral type (Zorec & Briot, 1997). Recent observational studies for open clusters in the Magellanic Clouds (Maeder et al., 1999, Martayan et al., 2010) show that the fraction of Be stars increases with decreasing metallicity. These studies reflect the important role that metallicity may play in the Be phenomenon.

Be stars undergo long and short period spectroscopic and photometric variations with time scales from hours to decades (Porter & Rivinius, 2003). Hanuschik et al. (1988) showed that one third of Be stars have asymmetric, doubly-peaked $H\alpha$ profiles and found that the violet to red peak intensity ratio, V/R , of the lines undergo long period, cyclic variations with timescales of years to decades. Recent studies show that V/R variability can be interpreted by the existence of one-armed spiral density waves (Porter & Rivinius, 2003, Kraus et al., 2012). Also, most Be stars show long period variability from years to decades as $H\alpha$ goes either from emission to absorption or absorption to emission, which is interpreted as the dissipation or formation of the disk, respectively.

The precise evolutionary stage of Be stars is still a matter of debate. Are Be stars born on

the main sequence as rapid rotators or do they spin up during their main sequence lifetimes as supported by the previous models? Spectroscopic and photometric studies of open clusters play an important role in answering this question because studying Be stars in stellar clusters provides the age of the stars with reasonable accuracy. Many studies have shown that the Be phenomenon can be seen at any age on the main sequence, i.e. they can be born on the main sequence as rapid rotators (Keller et al., 1999, Martayan et al., 2007, Mathew et al., 2008). Other studies suggest that the Be phenomenon is restricted to the second half of the main sequence with a maximum fraction at ages between 13-25 Myr (Fabregat & Torrejon (2000), Martayan et al. (2006)). Other observations show that Be stars can be found in young clusters, ≤ 10 Myr, with large enhancements of Be stars among evolved clusters, 10 - 30 Myr (McSwain & Gies, 2005, Wisniewski & Bjorkman, 2006, Tarasov & Malchenko, 2012).

The exact mechanism for the formation of Be star disks is still a matter of debate, but it is speculated that the rapid rotation of the central B star plays an important role in the formation of the disk. However, is the rotation the only factor affecting the Be phenomenon or are there other important factors such as the metallicity? What is the evolutionary stage of Be stars? Are they born on the main sequence as rapid rotators or do they spin up on the main sequence stage? All of these questions do not have clear answers.

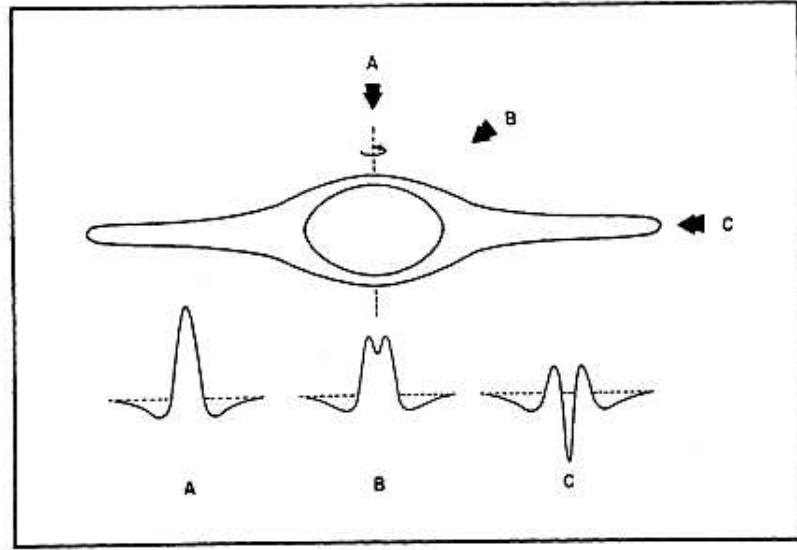
In the following subsections, I discuss the spectral features of Be stars, possible mechanisms of the formation of the disks, and the disk geometry.

3.2 Spectral features of Be Stars

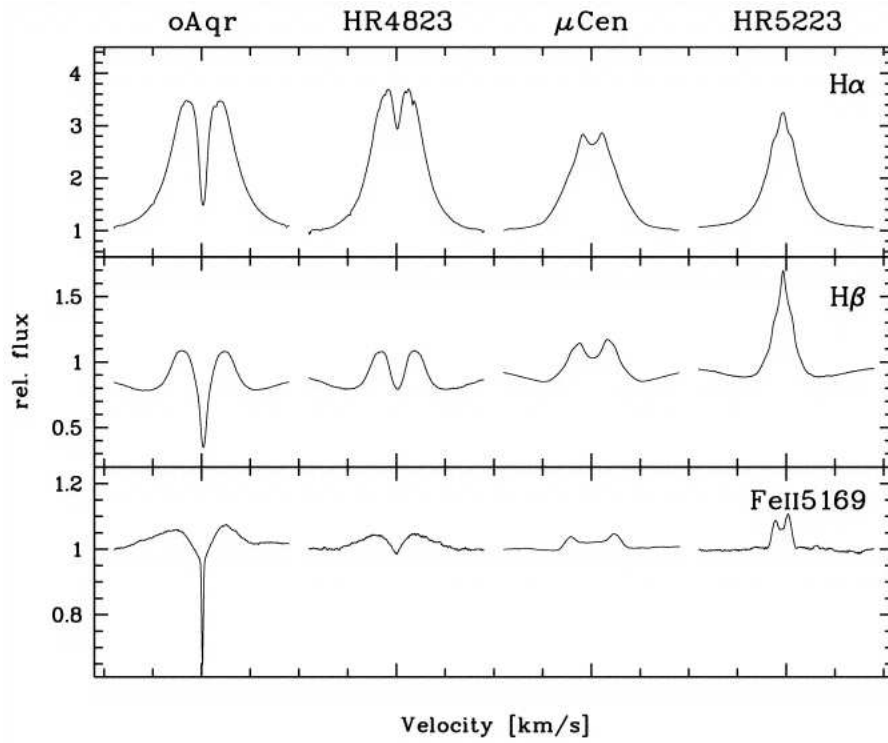
Observed emission lines in Be stars have well-defined profile shapes: singly-peaked profiles, symmetric and asymmetric doubly-peaked profiles, and lines with deep central absorption. Typical examples of these line profiles are shown in Figure 3.1(b). Most of the observed Be stars, ≈ 50 -70%, have symmetric, doubly-peaked emission lines (Hanuschik et al., 1988, Dachs et al., 1992). The different shapes of the observed emission lines can be explained by the

different inclinations of the observed Be stars, *i.e.*, the angle, i , between the stellar rotation axis (assumed perpendicular to the disk) and the line of sight. Be stars with low inclination angles i will show singly-peaked lines, while stars with larger inclination angles will show doubly-peaked features (Struve, 1931, Hanuschik et al., 1988), as shown in Figure 3.1(a). In addition to the observed Balmer emission lines, many Be stars can show emission in Fe II, Mg II, and other metals (Dachs et al., 1992, Hanuschik, 1987).

Emission lines in some Be stars have doubly-peaked profiles with central depressions that go below the continuum. This results from disk absorption, and these stars are called Be shell stars. They represent a significant fraction of all Be stars, close to 20% (Hanuschik et al., 1988). The relation between Be stars and Be shell stars was investigated by Porter (1996) who made a comparison between the $v \sin i$ distribution of all Be stars with a distribution of Be shell stars convolved with the distribution function for random inclinations (*i.e.* $p(i) di = \sin i di$). He found the resultant distributions are essentially the same, confirming that Be shell stars are Be stars that are seen nearly edge-on.



(a)



(b)

Figure 3.1: Panel (a) shows the dependence of the observed line profiles on the stellar inclination; observer (A) is viewing the system pole-on while observer (C) is viewing the system equator, or disk, on. Figure adopted from (Slettebak, 1988). Panel (b) shows example observed $H\alpha$, $H\beta$, and Fe II emission lines for four Be stars (Porter & Rivinius, 2003).

3.3 Possible Formation Mechanisms of Be Star Disks

There are many proposed mechanisms for the formation of Be star disks, namely the wind-compressed disk model, the magnetic-torqued disk model, and the viscous excretion disk model. A critical observational test for all models is that they need to produce dense, equatorial disk ($\rho \approx 10^{-11} - 10^{-10} \text{ g/cm}^3$ near the star) in Keplerian rotation with little radial flow. Below, I will give a brief description of each model. However, most of the recent observational studies of Be stars give strong support to the viscous excretion disk model.

One suggested disk-formation mechanism was the wind-compressed disk model (Bjorkman & Cassinelli, 1993). In this model, a supersonic, radiatively-driven, polar wind in a rapidly rotating B spectral type star ($v \geq 0.6v_{crit}$) is responsible for the formation of the circumstellar disk. The rapid stellar rotation will drift the polar winds towards the equator under the influence of gravity. When the supersonic, highly-ionized, polar wind from both poles of the star approach the equatorial region, they will cross the low-velocity, low-ionized equatorial wind causing shocks that will increase the temperature and the density of the shocked region and form a thin equatorial disk.

Cassinelli et al. (2002) introduced another mechanism for disk formation known as the magnetic-torqued disk model. In this model, a stellar magnetic field and rotation play an important role. A stellar wind ejected from the star at latitudes up to 45 degrees is confined by magnetic field loops and will drift to the equatorial regions. The magnetic field loops rotate with the underlying star as a rigid body. This will exert a torque on the confined equatorial matter, enhancing their azimuthal velocities until Keplerian velocities are reached, and the disk becomes centrifugally supported. In this model, the inner edge of the disk will be the first point at which the gas attains Keplerian rotation, and the outer boundary will be the point at which the magnetic energy density is equal to the wind energy density. Beyond the outer boundary, material can be driven away from the star by the stellar wind.

Both of the previous mentioned models are able to reproduce the observed dependence of the Be phenomenon on spectral type, namely the maximum frequency of Be stars at B2

spectral type. However, two-dimensional hydrodynamic simulations show that these models are unlikely to be valid scenarios of the formation of Be star disks (Owocki et al., 1996, Owocki & Ud-Doula, 2003).

Formation of Be star disks through the mass transfer in a close binary was suggested by Pols et al. (1991). They argued that this model can account for disk formation in up to 60% of observed Be stars. However, this mechanism cannot explain the disk formation in single, isolated Be stars.

Finally, the viscous excretion disk (VED) model was introduced by Lee et al. (1991) as a possible mechanism for the formation of Be star disks. In this model, matter will drift outward by exchanging angular momentum fed into the inner edge of the disk (in ad-hoc manner) via viscous stress, similar to what is happening in accretion disks but in the opposite direction. on a viscous timescale, $\tau_v = R^2/\nu$, where R is the radial distance and ν is the viscosity, typically assumed to be given by $\nu = \alpha c_s H$ where α is the ad-hoc viscosity parameter, c_s is the sound speed of the medium, and H is the scale height of the disk.

The basic VED model is supported by the results of many studies, such as Porter (1999) and Carciofi et al. (2012). Porter (1999) was able to reproduce the observed IR emission excess of χ Oph using a non-isothermal VED model with power-law density and thermal structure using a plausible disk densities of $\log \rho_0 = -11.2$. Carciofi et al. (2012) show that the viscosity parameter, α , has a value close to 1 in the Be star 28 CMa. They were able to reproduce the observed decline in the V-band magnitude of that Be star, representing a disk dissipation episode, using the viscous disk model with $\alpha = 1$ and estimated the mass injection rate in to the disk as $(3.5 \pm 1.3) \times 10^{-8} M_\odot/\text{yr}$.

3.4 Disk structure

The first speculation about the geometry of Be star disks was by Struve (1931); he suggested that Be stars possessed thin, circular, equatorial rings. The fact that Be stars have equatorial

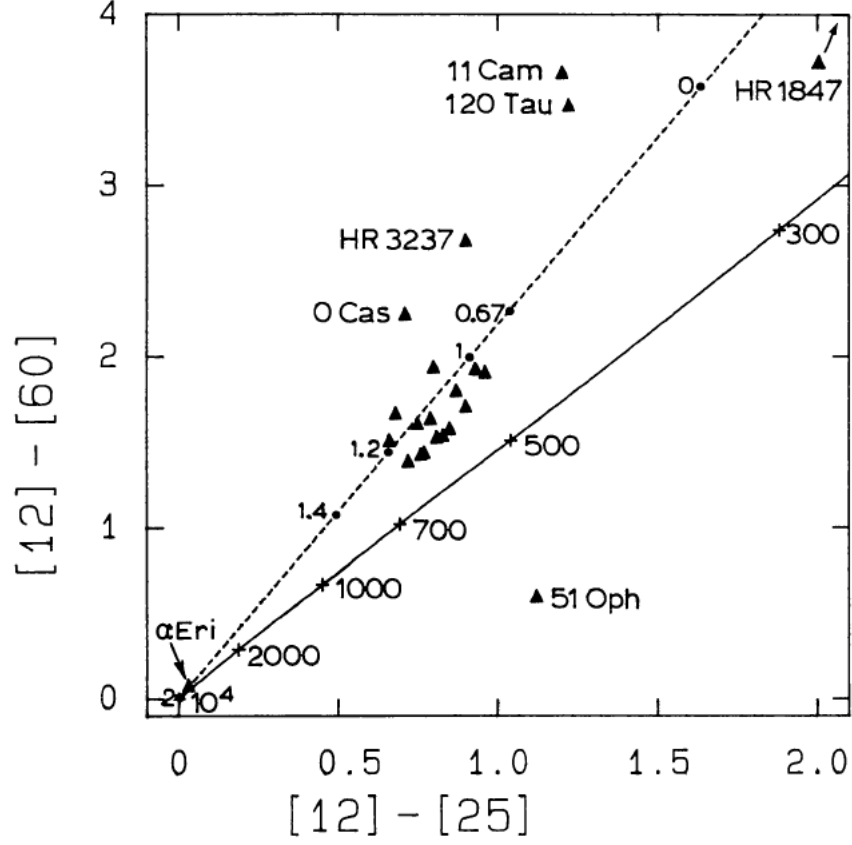


Figure 3.2: A [12]-[60] colour vs [12]-[25] colour diagram (numbers in brackets are wavelength in microns) for a number of Be stars. The solid line represents the predicted colours from the Planck function and the dotted line represents $F_\nu \propto \nu^a$, for free-free emission. Figure from (Coté & Waters, 1987).

disks, and not spherically symmetric envelopes, was confirmed by the existence of polarization in the continuum emission from the Be stars caused by electron scattering (Poeckret et al., 1979), and the different profiles of the observed emission lines as discussed in the previous section.

Coté & Waters (1987) used a geometrically thin disk model and showed that the observed near IR emission excess in Be stars, shown in Figure 3.2, is best fitted with a power-law energy distribution, $F_\nu \propto \nu^a$, where a is a constant that has a value close to 1, representing free-free and bound-free emission from the disk with a power-law density structure, $\rho \propto r^{-n}$, where r is the radial distance and the index n was found to have value between 2.5 and 3.25.

Observations of Be stars at cm and mm wavelengths give further confirmation to the pro-

posed power-law density structure of Be star disks and give estimations for the range of values of the density at the inner edge of the disk, $\log \rho_0$, between -10.7 and -11.9 g/cm^3 , the disk radius, R_d , between 31 and $108 R_*$, and the power law index, n , between 2.5 and 3.3 (Waters et al., 1991, Waters & Marlborough, 1994). van Kerkwijk et al. (1995) argued that the value of the power law index, n , should be greater than 3.5 to match the observed correlation between $W(H\alpha)$ and (J-L) colour of the observed Be stars.

Finally, Carciofi (2010) suggests that the value of n lies between 2.0 and 5.0 and explains this large scatter in the value of n by a deviation of the disk's density structure from the power-law form to a more complicated function due to non-isothermal, viscous diffusion effects or tidal interactions in close binaries.

3.5 Be Stars and Rotational Mixing

As discussed earlier in this chapter, Be stars are the fastest rotating stars on the main-sequence. In addition, they mostly represent a more evolved stage on the main-sequence, i.e. Be phenomenon mainly exist in the second half of the main-sequence. Consequently, they are expected to show higher nitrogen abundances compared to normal B-type stars. However, Be stars are usually excluded in the abundance analysis studies due to the difficulty of treating their spectra. Surprisingly, no significant nitrogen enrichment was found in the recent studied sample of Be stars in the Large Magellanic Cloud by Dunstall et al. (2011). They found that the surface nitrogen abundances in Be stars are similar to those of normal, slowly rotating B stars. However, their treatment of the disk contamination seems to be a significant source of error. They treated the disk contamination as a featureless disk emission, while it could be dependent on the wavelength. In addition, the disk contamination could be either emission or absorption, as will be discussed later in Chapter (8).

Chapter 4

The Non-LTE Radiative Transfer Problem

4.1 Introduction

The goal of solving the non-LTE radiative transfer problem within a stellar atmosphere is to obtain the atomic level populations, consistent with the radiation field, as a function of depth. These populations are needed to compute the opacity and the emissivity of the gas in order to predict the emergent radiation. Prior to solutions of this form, the atomic level populations were determined under the simplification of local thermodynamic equilibrium (LTE) through the use of the Saha ionization and Boltzmann excitation equations which are functions solely of the local temperature and electron density. The LTE approximation is of acceptable accuracy in many cases for low and intermediate mass main-sequence stars where the radiation field does not dominate the rates of population and depopulation of atomic levels. However, this is not the case for massive, main-sequence stars and evolved stars with much lower density atmospheres. In the atmospheres of early, main sequence B-type stars, the LTE assumption can be a poor approximation due to the presence of strong UV photoionizing radiation emitted from deeper layers. This non-local radiation from hot, deep regions can alter the populations of the energy levels in the line forming region from those computed in LTE. As a result, this radiation alters the populations of the atomic levels which itself affects the radiative transfer, resulting in a highly non-linear system. Consequently, the radiative transfer equation must be solved simultaneously with the statistical equilibrium equations that determine the atomic level

populations by requiring the rates into and out of each atomic level to balance.

For the B stars, radiative equilibrium, hydrostatic equilibrium, and plane-parallel geometry are still valid approximations. For the most massive main-sequence stars, the O-type stars, strong radiation pressure drives strong stellar winds and as a result, hydrostatic equilibrium and plane-parallel geometry are not valid assumptions. Similarly, evolved stars with low gravity have extended atmospheres.

4.2 The Radiative Transfer Equation

*

In a stellar atmosphere, energy is transferred by radiation. The change in the intensity of monochromatic radiation, I_ν , over a physical step ds along a ray in some direction is defined by the radiative transfer equation,

$$\frac{dI_\nu}{ds} = \eta_\nu - \chi_\nu I_\nu , \quad (4.1)$$

where I_ν is the specific intensity, η_ν is the emissivity in units of $\text{erg cm}^{-3} \text{ s}^{-1} \text{ Hz}^{-1} \text{ ster}^{-1}$, and χ_ν is the opacity with units of cm^{-1} . The transfer equation can be written as

$$\mu \frac{dI_{\mu\nu}}{d\tau_\nu} = I_\nu - S_\nu , \quad (4.2)$$

where S_ν is the monochromatic source function, $S_\nu \equiv \eta_\nu/\chi_\nu$, and τ_ν is the vertical (opposite to the gravitational acceleration) optical depth given by,

$$\tau_\nu = - \int_{-\infty}^z \chi_\nu dz , \quad (4.3)$$

where z direction represents the normal to the stellar surface. Here μ is the cosine of the angle

*The material in this section is mainly based on Mihalas (1978), Scharmer (1985) and Rutten, R.J. (2003).

between the line of the sight and the surface normal, $\mu \equiv \cos \theta$ such that

$$ds = \frac{dz}{|\mu|} \quad (4.4)$$

This second form of the radiative transfer, Equation (4.2), is the standard form. It relates the specific intensity to the thermodynamic and atomic properties of the medium represented by the source function, S_ν , and the optical depth $d\tau_\nu$.

If the source function is known, then the transfer equation can be formally solved for the intensity as

$$I^+(\tau_\nu, \mu \geq 0) = \int_{\tau_\nu}^{\infty} S_\nu(t_\nu) e^{(t_\nu - \tau_\nu)/\mu} \frac{dt_\nu}{\mu}, \quad (4.5)$$

for outgoing rays, and

$$I^-(\tau_\nu, \mu < 0) = \int_0^{\tau_\nu} S_\nu(t_\nu) e^{(t_\nu - \tau_\nu)/\mu} \frac{dt_\nu}{|\mu|}, \quad (4.6)$$

for incoming rays. Note that zero incident external radiation has been assumed for the second of these equations.

Given the intensity we can compute the moments of the radiation field, namely the mean intensity

$$J_\nu = \frac{1}{2} \int_{-1}^{+1} I_{\mu\nu} d\mu, \quad (4.7)$$

the (Eddington) flux,

$$H_\nu = \frac{1}{2} \int_{-1}^{+1} I_{\mu\nu} \mu d\mu, \quad (4.8)$$

and the radiation pressure moment

$$K_\nu = \frac{1}{2} \int_{-1}^{+1} I_{\mu\nu} \mu^2 d\mu. \quad (4.9)$$

These moments are required for several quantities on interest that depend on the radiation field. For example, the mean intensity determines the rate of all atomic processes depending

on a photon through

$$R_{ij} \equiv \int_0^\infty J_\nu \sigma_{ij}(\nu) \frac{d\nu}{h\nu}, \quad (4.10)$$

where R_{ij} is the rate of the radiative transition from i^{th} to j^{th} levels, $\sigma_{ij}(\nu)$ is the atomic cross section for the process and $h\nu$ is the photon energy. The radiative flux is closely associated with radiative equilibrium, *i.e.*, the conservation of energy as a whole through the stellar atmosphere. If we integrate H_ν over all frequencies to obtain the total flux H , then $dH/dz = 0$ is a statement of radiative equilibrium. Similarly if we integrate K_ν over all frequencies, then the total radiation pressure is just $4\pi/c K$ which is in a direction opposite to that of the gravitational acceleration.

In general, the source function is not known at the start because it depends on the atomic level populations and therefore the radiation field. However, in the idealized case of LTE, the source function is given by the Planck function,

$$S_\nu = B_\nu(T) \equiv \frac{2h\nu^3}{c^2} \frac{1}{e^{h\nu/kT} - 1}, \quad (4.11)$$

which is a function of only the local (electron) temperature.

Useful insight into the relation between I_ν and S_ν can be obtained by assuming the source function is a linear function of optical depth,

$$S_\nu = a_0 + a_1 \tau_\nu, \quad (4.12)$$

where a_0 and a_1 are two constants. In this case, the emergent radiation at $\tau_\nu = 0$ is

$$I^+(0, \mu \geq 0) = a_0 + a_1 \mu \equiv S_\nu(\tau_\nu = \mu). \quad (4.13)$$

This approximate solution is known as the Eddington-Barbier relation and illustrates that the emergent intensity is characteristic of the source function at an optical depth of order unity along the ray.

4.2.1 Local Thermodynamic Equilibrium

Local thermodynamic equilibrium can be realized in two ways: detailed balance in which the rate of each atomic process is balanced by its inverse, or by the dominance of collisional processes. The latter always enforce LTE if the particle velocity distributions are Maxwellian at the local electron temperature. The former is enforced deep within the stellar envelope and core where all photons are trapped locally.

In LTE, the Boltzmann equation can be used to compute the population of atomic levels of energies E_i and E_j with statistical weights g_i and g_j , respectively:

$$\frac{n_j}{n_i} = \frac{g_j}{g_i} e^{-(E_j-E_i)/kT}. \quad (4.14)$$

The Saha equation gives the ratio of the populations of two consecutive ionization states in of a specific element:

$$\frac{n_{i+1}}{n_i} = \frac{1}{N_e} \left(\frac{2\pi m_e kT}{h^2} \right) \frac{2U_{i+1}}{U_i} e^{-I/kT}. \quad (4.15)$$

In the Saha equation, N_e is the electron number density, and I is the ionization energy. The quantities U_i and U_{i+1} are the thermodynamic partition functions defined as

$$U_i = \sum_{n=1}^{n_{max}} g_n e^{-E_n/kT}, \quad (4.16)$$

summed over all levels of the ionization state i , with a similar equation for U_{i+1} , summed over all levels of ionization state $i + 1$.

The Saha and Boltzmann equations can be combined together to give the ratios of the population of any two excited states in any two adjacent ionization stages. Such calculations of the level populations need only the electron density and temperatures as function of depth within the atmosphere.

4.2.2 non-Local Thermodynamic Equilibrium

In the non-LTE case, the atomic level populations are determined by the requirement of statistical equilibrium in which the rate out of any atomic level i is balanced by net rate into that level, namely

$$\sum_{j \neq i}^{N_{\max}} n_i P_{ij} = \sum_{j \neq i}^{N_{\max}} n_j P_{ji} . \quad (4.17)$$

There is one such rate equation for every level i , $i=1,2,\dots, N_{\max}$. Here N_{\max} is the maximum number of atomic levels considered and P_{ij} and P_{ji} are the total transition rates from level i to j and j to i , respectively. The rates P_{ij} and P_{ji} can be decomposed into radiative and collisional parts, i.e.,

$$P_{ij} = R_{ij} + C_{ij} . \quad (4.18)$$

The radiative rate R_{ij} depends on the local radiation field through the mean intensity J_ν integrated over the atomic cross section. The collisional rate C_{ij} depends on the cross section for the collisional process integrated over the velocity distribution of the particles. In a stellar atmosphere, this distribution can always be taken to be a Maxwell-Boltzmann distribution at the local electron temperature. For this reason, the collisional rates are always in detailed balance, i.e.,

$$n_i^* C_{ij} = n_j^* C_{ji} , \quad (4.19)$$

where n_i^* and n_j^* are the LTE level populations that follow from the Saha-Boltzmann equations. For this reason, if collisional processes dominate all rates, it can be shown that the statistical equilibrium equations above recover the LTE populations, $n_i = n_i^*$.

4.2.3 Numerical Solution of The Non-LTE Radiative Transfer Problem

The numerical solution of the non-LTE line formation problem starts with initial estimates of the atomic level populations, such as their LTE values, and these estimates are substituted in the statistical equilibrium equations. Also, initial estimates of the mean intensities are obtained

from the Planck function. However, these values will not satisfy the statistical equilibrium equations. To overcome this problem, the atomic level populations are perturbed by δn_i^m , representing the required corrections for the atomic level populations to satisfy the statistical equilibrium equations. The superscript m represents the m^{th} iteration of the numerical solution. The initial statistical equilibrium equation can be written as

$$n_i^m \sum_{j \neq i}^{N_{max}} P_{ij}^m - n_i^m \sum_{j \neq i}^{N_{max}} P_{ji}^m - E_i^m = 0, \quad (4.20)$$

where E_i^m is the error in the net rate, which should be zero. Introducing the corrections δn_i^m and linearizing, the rate equation becomes

$$-E_i^m = \delta n_i^m \sum_{j \neq i}^{N_{max}} P_{ij}^m + n_i^m \sum_{j \neq i}^{N_{max}} \delta P_{ij}^m - \sum_{j \neq i}^{N_{max}} \delta n_j^m P_{ji}^m - \sum_{j \neq i}^{N_{max}} n_j^m \delta P_{ji}^m. \quad (4.21)$$

The corresponding corrections for the rates, δP_{ij} , are given by

$$\delta P_{ij}^m = \delta R_{ij}^m = \frac{B_{ij}}{2} \int_{-1}^{+1} \int_0^\infty \phi_\nu \delta I_{\nu\mu}^m d\nu d\mu, \quad (4.22)$$

in the case where the rate i to j is a bound-bound radiative transition with Einstein absorption coefficient B_{pij} . $\delta I_{\nu\mu}$ is the corresponding change of the specific intensity of the radiative field. This change in the intensity can be related to the source function through

$$\delta I_{\nu\mu}(\tau_{\nu\mu}) = \Lambda_{\nu\mu}[\delta S_\nu(\tau_{\nu\mu})], \quad (4.23)$$

where $\Lambda_{\nu\mu}$ is known the “lambda operator” which represents as an integral over frequency and optical depth of the formal solution of the radiative transfer equation. As the source function perturbation $\delta S_\nu(\tau_{\nu\mu})$ can be related to the perturbations to the upper and lower levels of the transition involved,

$$\delta S_\nu^m = c_i^m \delta n_i^m + c_j^m \delta n_j^m, \quad (4.24)$$

where c_i^m and c_j^m are coefficients determined numerically, Equations 4.21 can be cast as a system of linear equations for the population corrections δn_i^m that can be solved by standard techniques.

This is only a brief sketch of the numerical solution to the line transfer problem. The reader is referred to Carlsson (1992) for the specific implementation in the case of the MULTI code used in the current work. An entire field of radiative transfer was started by Scharmer (1981) who first suggested that great computational advantage could be gained by using not the full Λ -operator occurring in Equation 4.23 but a well-constructed approximate operator that nevertheless retains the essential physics. Approximate Λ -operators are further discussed by Hubeny (1992).

Chapter 5

Non-LTE for Calculation N II*

5.1 Introduction

The departure from LTE is a well known occurrence in the atmospheres of B-type stars (Kurucz 1979). Consequently, it is important to solve the non-LTE radiative transfer problem of the singly ionized nitrogen atom in order to obtain accurate nitrogen abundances for the B stars. This was done using the MULTI code (v.2) of Carlsson (1992). The goal of such a calculation is to compute grids of the non-LTE equivalent widths of the strongest optical N II lines commonly used in abundance analysis. Also, an important additional goal is to obtain estimates of the error bounds in the computed equivalent widths due to errors in the atomic data. This was done via Monte Carlo simulation following the procedure of Sigut (1996). This method is useful for cases where the traditional way of estimating uncertainties from the dispersion of the measured elemental abundance using many weak spectral lines is not applicable.

The structure of this chapter is as follows: In Section (5.2), I give a brief summary of previous, non-LTE calculations for N II and in Section (5.3) I discuss the atomic data used to construct the nitrogen atom. In Section (5.4), the results of the current, non-LTE nitrogen calculations are given, and the error bounds on the predicted equivalent widths due to random errors and systematic errors are discussed. The results of the multi-MULTI analysis are presented in Section (5.5). Section (5.6) discusses the achievable accuracy of nitrogen abundance

*A version of this chapter is a published article in the Monthly Notices of Royal Astronomical Society; "Non-LTE equivalent widths for N II with error estimates" Ahmed, A. & Sigut, T.A.A. 2016, MNRAS, 455, 1099A

determinations in B-type stars.

5.2 Previous Works

The N II non-LTE problem has been the subject of many previous works (Dufton (1979); Becker & Butler (1988); Becker & Butler (1989); and Przybilla & Butler (2001)) which differ both in the technique used for the line formation calculation and in the accuracy of the atomic data. This section aims to give a brief summary of these previous non-LTE line formation calculations for N II available in literature. Dufton (1979) investigated the atmospheric nitrogen abundance for a number of main-sequence B-type stars using the non-LTE line formation code of Auer (1973), which is based on the complete linearization method (Auer & Mihalas, 1969). A singly-ionized nitrogen atom was constructed that included the lowest 13 singlet energy levels; the other spin systems were omitted to save computation time. For reference, Figure (5.1) (page 50) shows a Grotrian diagram for N II containing the energy levels used in the present work. Among the 26 permitted radiative transitions considered by Dufton (1979), ten were included in the linearization method and another seven transitions were kept at fixed rates at the local electron temperature. The remaining transitions did not have accurate oscillator strength values, so they were omitted from the calculation.

Dufton & Hibbert (1981) extended this work by including the 14 lowest triplet energy levels, and they recalculated the oscillator strengths for 6 multiplets used in the non-LTE line formation calculation. In total, 44 allowed radiative transitions were considered, all with wavelengths less than $2 \mu m$. The transition rates of 9 of them were included in the linearization methods, while the rates of another 14 were kept fixed at the local electron temperature. The remaining transitions did not have reliable f -values, so they were omitted from the calculation. The photoionization rates from the ground states of N II and N III, and those from the N II excited levels $2p\ 3s\ ^3P^o$ and $2p\ 3p\ ^3P$, were included in the linearization technique, while the photoionization rates of the other excited states of N II were kept fixed at the local electron

temperature. The predicted non-LTE and LTE equivalent widths of three singlet lines (3995, 4447, and 4228 Å), and three triplets lines (4631, 5045 and 5680 Å) were calculated for T_{eff} between 20,000 and 32,500 K, microturbulent velocities between 0 and 10 km s⁻¹, and nitrogen abundances, ϵ_N , between 7.4 and 8.6 (where $\epsilon_N \equiv \log(N/H) + 12$, and N and H are the number densities of hydrogen and nitrogen, respectively). In general, the predicted non-LTE equivalent widths were significantly stronger than the corresponding LTE values, and the difference increased with T_{eff} . For example, the predicted equivalent width of λ 3995 Å was stronger by \approx 10% at 20,000 K, rising to \approx 30% stronger at 30,000 K. This line strengthening was explained by the overpopulation, relative to LTE, of the lower levels of the considered transitions due to non-LTE effects. Consequently, this non-LTE line strengthening resulted in lowering estimated nitrogen abundances by 0.1-0.2 dex at 20000K and by 0.3-0.5 dex at 30000K.

An extensive, singly-ionized nitrogen atom was constructed by Becker & Butler (1989, 1988). They aimed for a more accurate treatment of the non-LTE effects in ionized nitrogen in the atmospheres of B-type stars. They constructed non-LTE and LTE equivalent width grids of 35 radiative transitions in the wavelength region between 4000 Å and 5000 Å, calculated for T_{eff} between 24,000 and 33,000 K, $\log g$ between 3.5 and 4.5, microturbulent velocities between 0 and 10 km s⁻¹, and ϵ_N between 7.449 and 8.449. In this work, the non-LTE populations of energy levels with Principal quantum number up to 4 for the N I and N II, the lowest five levels of N III, and the ground level of N IV were explicitly considered. The remaining energy levels of N I, N II, and N III, up to $n=10$, were kept fixed at their LTE values. Their results showed strong non-LTE strengthening of the predicted equivalent widths for some lines (e.g. λ 4630.5 Å and 4242.0 Å) that could lower estimated nitrogen abundances by up to 0.25 dex, while there was significant non-LTE line strengthening for most of the lines that could lower estimated nitrogen abundances by 0.1-0.2 dex, on average (e.g. 4096.08 Å and 4446.96 Å). Becker & Butler (1989) compared their estimated equivalent widths with Dufton & Hibbert (1981) for common transitions. This comparison showed that their predicted equivalent widths were smaller than those of Dufton & Hibbert (1981). Becker & Butler (1989) argued that this

difference was due to the overestimation of the N II population by Dufton & Hibbert (1981) because of the lower number of N III energy levels (ground level only) which led to redistribution of population to N II. It should be noted that Becker & Butler (1989) have an important limitation in that they used LTE model atmospheres blanketed by only the 100 strongest lines. In the non-LTE problem for a trace element, the background photospheric model sets not only $T_e(\tau)$ and $N_e(\tau)$, but also the photoionizing radiation field, and a complete treatment of line blanketing can be an important ingredient in such calculations.

Korotin et al. (1999) (K99, hereafter) investigated the nitrogen abundance of γ Peg, a B2V type star, in order to test nitrogen enrichment due to rotational mixing. In this work, the non-LTE line formation was calculated using the MULTI code of Carlsson (1992). For this purpose, a nitrogen atom was constructed which consisted of 109 levels: 3 ground levels of N I, the 93 lowest energy levels of N II, the 12 lowest levels of N III, and the ground state of N IV.

K99 included all allowed radiative transitions with wavelengths less than $10 \mu m$. Ninety-two transitions computed in detail and the rates of the rest kept fixed. All N II energy levels with principal quantum number up to $n = 6$ and angular quantum number up to $\ell = 4$ were included. The estimated non-LTE equivalent widths were larger than the LTE equivalent widths for all observed lines except for $\lambda 4227.74 \text{ \AA}$ ($3p \ ^1P - 3d \ ^1D^0$) where they were equal. Non-LTE and LTE equivalent width grids for 23 transitions at T_{eff} between 16,000-32000 K were calculated, similar to those of Becker & Butler (1988). In general, there was good agreement between both works but with some differences. Firstly, the difference between the LTE and non-LTE equivalent widths in K99 were larger than those of Becker & Butler (1988), and the maximum differences occurred at lower T_{eff} . Secondly, the maximum calculated equivalent widths occur at lower T_{eff} , and this was attributed to the different model atmospheres. K99 used the fully line-blanketed, LTE atmospheres of Kurucz (1993a), while lightly line-blanketed LTE model atmospheres were used by Becker & Butler (1988), as previously noted by Becker & Butler (1988).

Przybilla & Butler (2001) aimed to perform non-LTE line formation for N I/N II in order to

determine the nitrogen abundance of a number of A and B type stars: Vega (A0V), and four late-A and early-B supergiants. In this work, an extensive nitrogen atom was used with recent and more accurate atomic data. The non-LTE level populations included energy levels with $n \leq 7$, plus the 8s level for N I, and energy levels with $n \leq 6$ for N II; the LTE populations for n up to 10 were calculated and included in the equation of particle conservation. Also, the non-LTE population of N III ground level was included. All bound-bound radiative transitions between the set of non-LTE levels were included, and the f -values were obtained from the opacity project (Cunto & Mendoza, 1992). This work was focused mainly on studying objects with lower T_{eff} , $\leq 12,000$, where N I is the dominant ionization stage. Consequently, there were only weak non-LTE effects on the N II lines, and the authors suggested further investigation at higher effective temperatures.

In conclusion, many previous studies have investigated the non-LTE problem of N II aiming to get accurate equivalent widths using improved techniques and more accurate atomic data. However, none of these works presented a detailed analysis of the uncertainties in the estimated equivalent widths, which is the main objective of the current work.

5.3 Nitrogen Atomic Data

5.3.1 N II

The N II atom used in the current calculation was composed of 106 LS states (lowest 93 N II LS states plus the lowest 12 N III LS states and ground state of N IV) with a total of 580 allowed radiative transitions, 563 allowed radiative transitions between N II LS states and 17 allowed radiative transitions between N III LS states. All N II and N III transitions with f -value greater than or equal to 1.0×10^{-3} are included in the current calculation. The 93 N II LS states represent all states with $n \leq 6$ plus the two LS states of $2p\ 7s$ configuration and the lowest LS state of the $2p\ 7p$ configuration. The experimental values for the N II energy levels were taken from Moore (1993) (listed in Table 5.1) available through the NIST on-line database. A Grottrian

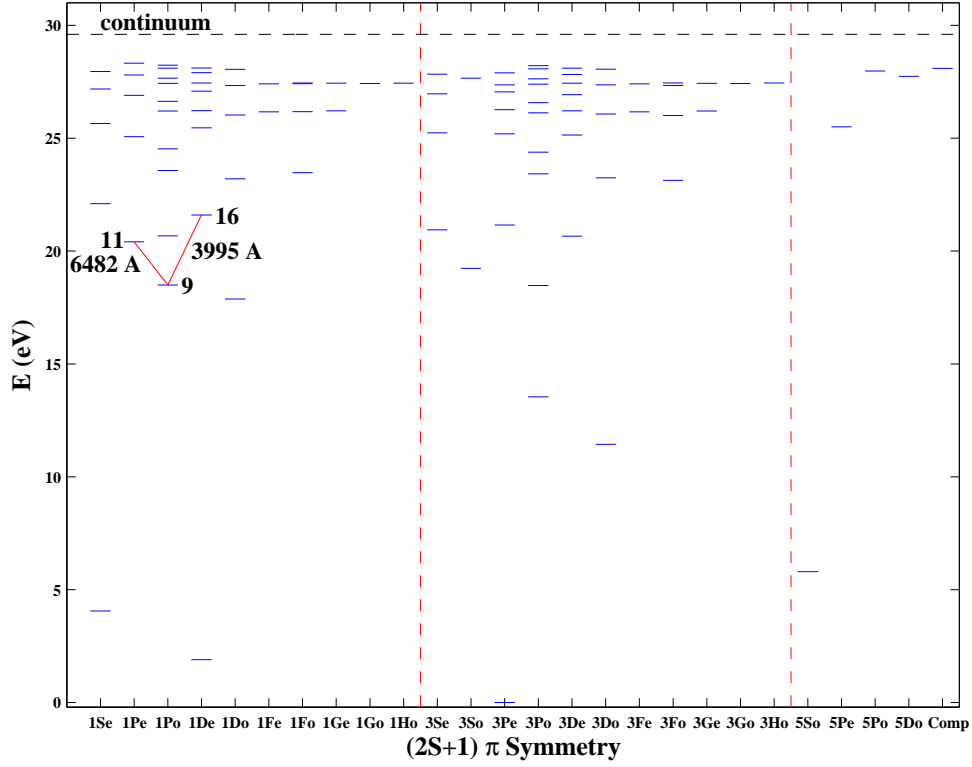


Figure 5.1: N II Grotrian diagram showing the singlet, triplet and quintet spin systems.

diagram for N II is shown in Figure (5.1): The λ 3995 Å and 6482 Å radiative transitions are shown as they are of main interest in this work. The oscillator strengths and photoionization cross-sections were taken from the Opacity Project (Luo & Pradhan, 1989), through the TOP-BASE on-line database (Cunto et al., 1993). Table (5.2) lists the atomic data for a number of bound-bound radiative transitions of interest that are commonly used in nitrogen abundance determinations.

Table 5.1: Energy Levels included in the N II atom model

No.	Energy (cm^{-1})	g	configuration	No.	Energy (cm^{-1})	g	configuration
1	0.000	9.0	$2p^2 \ ^3P$ (N II)	48	216953.141	3.0	$5p \ ^1P$
2	15316.200	5.0	$2p^2 \ ^1D$	49	217194.969	15.0	$5p \ ^3D$
3	32688.801	1.0	$2p^2 \ ^1S$	50	217487.641	3.0	$5p \ ^3S$
4	46784.602	5.0	$2p^3 \ ^5S^o$	51	218232.875	9.0	$5p \ ^3P$
5	92244.484	15.0	$2p^3 \ ^3D^o$	52	218421.266	5.0	$5p \ ^1D$
6	109217.922	9.0	$2p^3 \ ^3P^o$	53	219196.312	1.0	$5p \ ^1S$
7	144187.938	5.0	$2p^3 \ ^1D^o$	54	220472.359	21.0	$5d \ ^3F^o$
8	149012.406	9.0	$3s \ ^3P^o$	55	220495.359	5.0	$5d \ ^1D^o$
9	149187.797	3.0	$3s \ ^1P^o$	56	220693.594	15.0	$5d \ ^3D^o$
10	155126.734	3.0	$2p^3 \ ^3S^o$	57	220709.125	9.0	$2p^4 \ ^3P$
11	164610.766	3.0	$3p \ ^1P$	58	220946.188	9.0	$5d \ ^3P^o$
12	166615.188	15.0	$3p \ ^3D$	59	221054.500	7.0	$5f \ ^1F$
13	166765.656	3.0	$2p^3 \ ^1P^o$	60	221068.078	21.0	$5f \ ^3F$
14	168892.203	3.0	$3p \ ^3S$	61	221141.609	7.0	$5d \ ^1F^o$
15	170636.375	9.0	$3p \ ^3P$	62	221163.703	9.0	$5g \ ^1G^o$
16	174212.031	5.0	$3p \ ^1D$	63	221166.500	27.0	$5g \ ^3G^o$
17	178273.375	1.0	$3p \ ^1S$	64	221246.172	3.0	$5d \ ^1P^o$
18	186591.766	21.0	$3d \ ^3F^o$	65	221258.734	27.0	$5f \ ^3G$
19	187091.375	5.0	$3d \ ^1D^o$	66	221305.484	15.0	$5f \ ^3D$
20	187470.922	15.0	$3d \ ^3D^o$	67	221311.109	9.0	$5f \ ^1G$
21	188883.516	9.0	$3d \ ^3P^o$	68	221322.859	11.0	$5g \ ^1H^o$
22	189335.156	7.0	$3d \ ^1F^o$	69	221351.812	21.0	$5g \ ^3F^o$
23	190120.234	3.0	$3d \ ^1P^o$	70	221352.750	33.0	$5g \ ^3H^o$
24	196652.688	9.0	$4s \ ^3P^o$	71	221354.469	5.0	$5f \ ^1D$
25	197858.688	3.0	$4s \ ^1P^o$	72	221380.297	7.0	$5g \ ^1F^o$
26	202170.625	3.0	$4p \ ^1P$	73	222818.734	9.0	$6s \ ^3P^o$
27	202799.875	15.0	$4p \ ^3D$	74	223069.016	3.0	$3p \ ^3S^o$
28	203224.938	9.0	$4p \ ^3P$	75	223101.812	3.0	$6s \ ^1P^o$
29	203537.656	3.0	$4p \ ^3S$	76	223730.078	25.0	$3p \ ^5D^o$
30	205350.188	5.0	$4p \ ^1D$	77	224245.703	3.0	$6p \ ^1P$
31	205675.906	15.0	$3s \ ^5P$	78	224371.906	15.0	$6p \ ^3D$
32	206910.234	1.0	$4p \ ^1S$	79	224534.875	3.0	$6p \ ^3S$
33	209759.484	21.0	$4d \ ^3F^o$	80	224980.031	9.0	$6p \ ^3P$
34	209925.766	5.0	$4d \ ^1D^o$	81	225039.609	5.0	$6p \ ^1D$
35	210277.438	15.0	$4d \ ^3D^o$	82	225479.891	1.0	$6p \ ^1S$
36	210728.562	9.0	$4d \ ^3P^o$	83	225643.094	15.0	$3p \ ^5P^o$
37	211030.062	7.0	$4f \ ^1F$	84	226245.844	5.0	$6d \ ^1D^o$
38	211052.406	21.0	$4f \ ^3F$	85	226280.703	15.0	$6d \ ^3D^o$
39	211103.625	7.0	$4d \ ^1F^o$	86	226430.719	9.0	$6d \ ^3P^o$
40	211331.625	27.0	$4f \ ^3G$	87	226624.688	332.0	$n = 6, high$
41	211336.156	3.0	$4d \ ^1P^o$	88	226685.312	15.0	$6f \ ^3D$
42	211402.031	9.0	$4f \ ^1G$	89	226687.828	3.0	$6d \ ^1P^o$
43	211427.250	15.0	$4f \ ^3D$	90	226720.797	5.0	$6f \ ^1D$
44	211490.297	5.0	$4f \ ^1D$	91	227557.484	9.0	$7s \ ^3P^o$
45	211802.891	9.0	$3s \ ^3P$	92	227747.484	3.0	$7s \ ^1P^o$
46	214322.859	9.0	$5s \ ^3P^o$	93	228416.844	3.0	$7p \ ^1P$
47	214829.188	3.0	$5s \ ^1P^o$				
94	238866.594	6.0	$2p \ ^2P^o$ (N III)	100	441830.594	10.0	$2p^3 \ ^2D^o$
95	296027.688	12.0	$2p^2 \ ^4P$	101	460052.500	2.0	$3s \ ^2S$
96	339776.906	10.0	$2p^2 \ ^2D$	102	469157.500	6.0	$2p^3 \ ^2P^o$
97	369754.594	2.0	$2p^2 \ ^2S$	103	484439.594	6.0	$3p \ ^2P^o$
98	384699.375	6.0	$2p^2 \ ^2P$	104	505992.125	10.0	$3d \ ^2D$
99	425547.375	4.0	$2p^3 \ ^4S^o$	105	526389.125	12.0	$3s \ ^4P^o$

Table 5.2: Atomic data for several N II multiplets of interest.

λ (Å)	g_l	g_u	$A_{ul}(s^{-1})$	Transition	Multiplet Number	Stark Width (Å) $T_e = 1.0E4$ K $3.0E4$ K	
3955.0	3	5	1.203^{+07}	$3s^3P^o(1) \rightarrow 3p^1D(2)$ (8 – 16)	6	3.59^{-02}	3.87^{-02}
3995.0	3	5	1.386^{+08}	$3s^1P^o(1) \rightarrow 3p^1D(2)$ (9 – 16)	12	3.68^{-02}	3.86^{-02}
4601.5	3	5	2.325^{+07}	$3s^3P^o(1) \rightarrow 3p^3P(2)$ (8 – 15)	5	4.10^{-02}	4.45^{-02}
4607.2	1	3	3.310^{+07}	(0) (1)			
4613.9	3	3	2.227^{+07}	(1) (1)			
4621.4	3	1	9.474^{+07}	(1) (0)			
4630.5	5	5	7.878^{+07}	(2) (2)			
4643.1	5	3	4.611^{+07}	(2) (1)			
4447.0	3	5	1.174^{+08}	$3p^1P(1) \rightarrow 3d^1D^o(2)$ (11 – 19)	15	9.61^{-02}	8.95^{-02}
4987.4	3	1	7.474^{+07}	$3p^3S(1) \rightarrow 3d^3P^o(0)$ (14 – 21)	24	7.19^{-02}	6.96^{-02}
4994.4	3	3	7.583^{+07}	(1) (1)			
5007.3	3	5	7.956^{+07}	(1) (2)			
5001.1	3	5	9.719^{+07}	$3p^3D(1) \rightarrow 3d^3F^o(2)$ (12 – 18)	19	6.33^{-02}	6.73^{-02}
5001.5	5	7	1.046^{+08}	(2) (3)			
5005.1	7	9	1.155^{+08}	(3) (4)			
5016.4	5	5	1.581^{+07}	(2) (2)			
5025.7	7	7	1.055^{+07}	(3) (3)			
5040.7	7	5	4.722^{+05}	(3) (2)			
5002.7	1	3	8.661^{+06}	$3s^3P^o(0) \rightarrow 3p^3S(1)$ (8 – 14)	4	4.20^{-02}	4.96^{-02}
5010.6	3	3	2.165^{+07}	(1) (1)			
5045.1	5	3	3.481^{+07}	(2) (1)			
5666.6	3	5	3.608^{+07}	$3s^3P^o(1) \rightarrow 3p^3D(2)$ (8 – 12)	3	5.27^{-02}	6.12^{-02}
5676.0	1	3	2.916^{+07}	(0) (1)			
5679.6	5	7	5.194^{+07}	(2) (3)			
5686.2	3	3	1.875^{+07}	(1) (1)			
5710.8	5	5	1.229^{+07}	(2) (2)			
5730.7	5	3	1.221^{+06}	(2) (1)			
6482.1	3	3	2.913^{+07}	$3s^1P^o(1) \rightarrow 3p^1P(1)$ (9 – 11)	8	1.60^{-01}	1.27^{-01}

Note: Stark widths were calculated assuming electron number density of $1.0^{+16} cm^{-3}$.

Thermally-averaged collision strengths for bound-bound collisional transitions between the lowest 23 LS states of N II were taken from Hudson & Bell (2004, 2005a). These were calculated in a 23 state, close-coupling calculation using the R-Matrix method. The impact parameter approximation of Seaton (1962) was used for the remaining bound-bound collision strengths for allowed transitions. The collision strengths for forbidden transitions were assumed to be 0.1. The rates of collisional ionization of N II energy levels to the N III ground state

were estimated using the procedure of Seaton (1962) (see Mihalas (1978)).

The line profiles for the radiative transitions included natural broadening, thermal broadening, and pressure broadening due to collisions with charged and neutral particles. Quadratic Stark broadening, due to quasi-elastic collisions with electrons, represents the most important contributor to the line width in the atmospheres of hot stars. As the N II transitions are often strong, it is important to have accurate stark widths. For this reason, we have calculated the Stark width using three different approximations: the semi-classical approximation of Sahal-Br  chot & Segre (1971), the Kurucz (1979) formula that represents a fit of the estimated widths using Sahal-Br  chot & Segre (1971), and the method of Seaton (1988) developed for the Opacity Project and based on more accurate R-matrix collision strengths.

The ratios of these calculated stark widths to the experimentally measured values of Konjevi   et al. (2002) are shown in Figure (5.2). The plot assumes $T_e = 28,000$ K and shows Stark width versus the effective principal quantum number of the upper level, n_i^{eff} , defined as

$$n_i^{\text{eff}} = Z \sqrt{\frac{Ry}{(I - E_i)}}, \quad (5.1)$$

where Ry is the Rydberg constant, I and E_i are the ionization energy of the atom and the energy of the i^{th} state, and Z is the core charge. The figure shows that the Stark widths calculated following Seaton (1988) are the closest ones to the experimental values. The average ratios at several temperatures are given in Table (5.3).

Table 5.3: Average ratios of theoretically calculated stark widths to experimental values over a number of transitions for different temperatures. Seaton88 refers to Seaton (1988), Kur75 refers to Kurucz (1979), and SBS71 refers to Sahal-Br  chot & Segre (1971). Arrows point to the average ratio of each approximation.

Temperature (K)	$(\gamma_{\text{theo}}/\gamma_{\text{exp}})_{\text{av}}$		
	(Seaton88)	(Kur79)	(SBS71)
8000	2.12	0.23	0.50
15000	1.92	0.22	0.39
28000	1.55	0.21	0.18

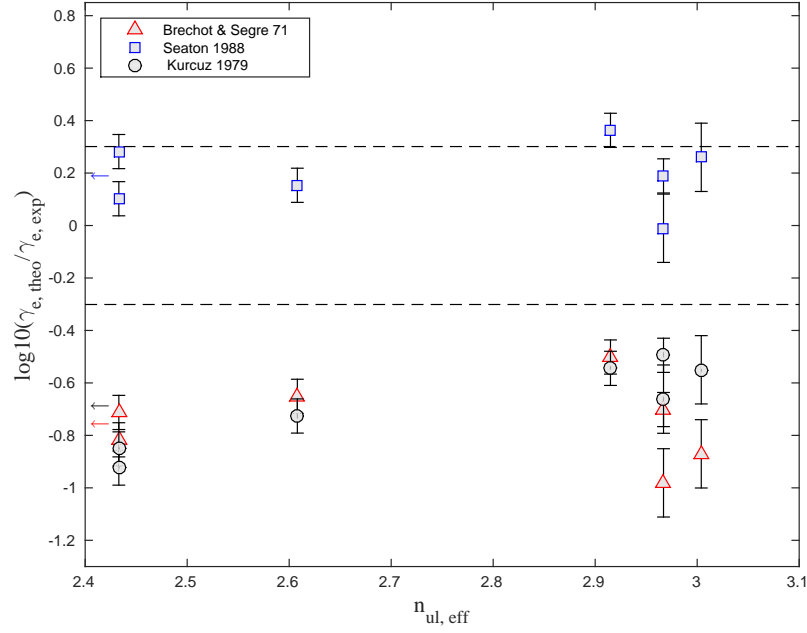


Figure 5.2: Ratio of theoretical to experimental quadratic stark width versus the effective quantum number of the upper level. The theoretical quadratic stark widths were calculated using three different approximations: Sahal-Bréchet & Segre (1971), Kurucz (1979), and Seaton (1988). The experimental widths are from Konjević et al. (2002). The dashed lines represent a factor of two uncertainty.

Collisional broadening results in a Lorentzian profile for the line, and the total line profile is found by the convolution of the Lorentzian with a Gaussian distribution of thermal velocities along the line of sight, resulting in a Voigt profile. The Voigt profile defined by,

$$\phi_\nu = \frac{a}{\pi} \int_{-\infty}^{\infty} \frac{e^{-y^2}}{(v-y)^2 + a^2} dy, \quad (5.2)$$

where a is equal to

$$a = \frac{\gamma}{4\pi \Delta\nu_D}, \quad (5.3)$$

γ is the total damping constant ($\gamma = \gamma_{rad} + \gamma_{vdw} + \gamma_{stk}$), and $\Delta\nu_D$ is the frequency Doppler shift the resulting from motion along the line of sight due to random motion which is given by

$$\Delta\nu_D = \frac{v_0}{c} \nu = \frac{v}{c} \sqrt{(2kTm)} \quad (5.4)$$

and y is equal to $\Delta\nu/\Delta\nu_D$ (Mihalas, 1978). Included in the thermal velocity of the line was microturbulence which is an important physical phenomenon that can strongly affect the strength of observed spectral lines. Microturbulence represents a nonthermal velocity field on a scale smaller than unit optical depth, that acts to broaden the atomic absorption. Weak lines, which lie in the linear part of the curve of growth, formed under LTE conditions are insensitive to variations in the microturbulence velocity. On the contrary, strong lines, which lie in the saturation part of the curve of growth, are very sensitive for small changes of the microturbulence velocity (Gray, 1992). Consequently, using only the strongest lines in the abundance analysis results in high uncertainties. This problem is solved by using both weak and strong lines to fix the value of the microturbulence velocity. The recent work of Cantiello et al. (2009) shows that the iron-peak in stellar opacities can lead to the formation of convective cells close to the surface of hot stars which could be the origin of such microturbulence, through energy dissipated from gravitational and pressure waves propagating outwardly from these convective cells.

5.3.2 N III and N IV

The N III and N IV energy levels were also taken from Moore (1993) (listed in Table 5.1). Oscillator strengths for the radiative bound-bound transitions of N III were obtained from Bell et al. (1995) and Fernley et al. (1999), available from the NIST database. The photoionization cross-sections were also taken from the Opacity Project. As with N II, the collision strength of excitation and ionization were calculated using impact parameter approximation of Seaton (1962).

5.4 Calculations

The N II non-LTE line formation calculation was carried out for nine values of T_{eff} , between 15,000 and 31,000 K (with a step of 2000 K), three surface gravities, $\log g$, 3.5, 4.0 and 4.5, four microturbulent velocities, ξ_t , 0, 2, 5 and 10 km s⁻¹, and selected nitrogen abundances between 6.83 and 8.13 dex. The MULTI code, v2, (Carlsson, 1992) was used. MULTI solves the statistical equilibrium and radiative transfer equations simultaneously in an iterative method using the approximate lambda-operator technique. A solar nitrogen abundance $\epsilon_N = 7.83$ was adopted from Grevesse et al. (2010).

For the calculation, the LTE, line-blanketed atmospheres of ATLAS9 were used (Kurucz, 1993a). ATLAS9 was also used to provide the mean intensity within the stellar atmosphere as a function of optical depth. This mean intensity was used to compute all of the photoionization and recombination rates which were kept fixed during the calculation. Using LTE atmospheres can be a source of error, particularly for hot stars; however, previous studies have shown that line-blanketing is more important than non-LTE effects up to a stellar effective temperatures of $\approx 30,000$ K (Przybilla & Butler (2001); Sigut (1996); Becker & Butler (1989)). This was recently discussed in Przybilla et al. (2011). As MULTI was originally developed for the atmospheres of cool stars, modification to the background continuous opacities are required in order to be suitable for early-type stars; the opacity package was replaced with the extensive package

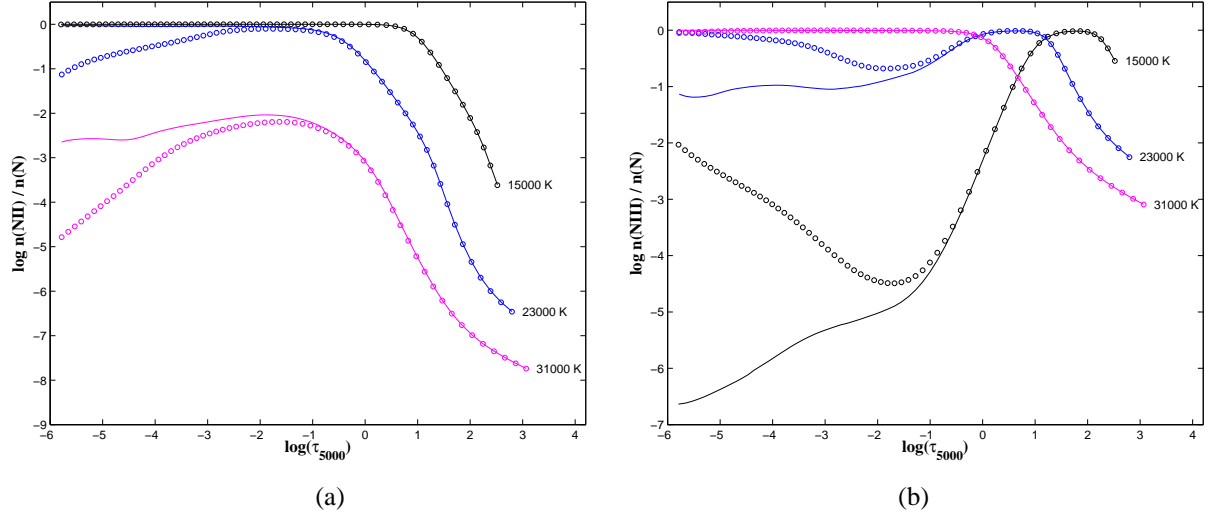


Figure 5.3: Panel (a) shows the fraction of singly ionized nitrogen as a function of the optical depth, τ_{5000} , for several stellar effective temperatures and $\log g = 4.0$ ($\xi_t = 5 \text{ km s}^{-1}$, and $\epsilon_N = 7.83$). The circles represent the predicted non-LTE fractions using MULTI and the solid lines represent the predicted LTE fractions. Panel (b) is the same but for doubly-ionized nitrogen.

that is available through ATLAS9 (see Sigut & Lester (1996)).

5.4.1 Ionization Balances and Departure Coefficients

Figure (5.3) shows the predicted LTE and non-LTE ionization fractions of singly and doubly ionized nitrogen as a function of optical depth, τ_{5000} , for the range of the T_{eff} considered, for $\log g = 4.0$, $\xi_t = 5.0 \text{ km s}^{-1}$ and the solar nitrogen abundance. At T_{eff} less than 21,000 K, N II is the dominant ionization stage in the line formation region, $\log \tau_{5000}$ between 0 and -2, approximately. Also, there is almost no deviation from LTE, and this can be explained by the absence of a strong non-local photoionizing radiation field for the low N II levels. Figure (5.4) shows the radiation temperature, T_{rad} of the photoionizing mean intensity as a function of the optical depth at the threshold wavelength of the lowest ten energy levels of N II; they are combined into three groups having similar T_{rad} values. This was done in a model atmosphere with T_{eff} equal to 15,000 K and $\log g = 4.0$. The radiation temperature, T_{rad} , was estimated by equating the mean intensity at threshold wavelength with Planck function, $J_\nu(\tau_\nu) = B_\nu(T_{\text{rad}})$. Deep in the stellar atmosphere, the optical depths are high enough that photons are trapped and photons

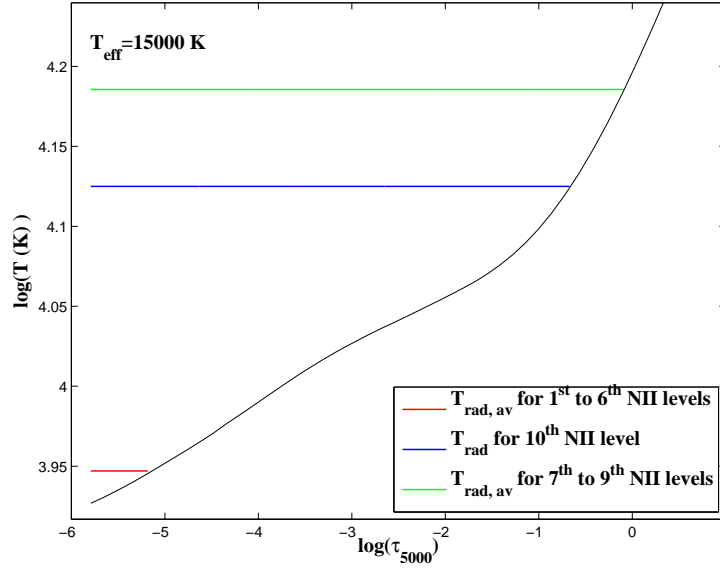


Figure 5.4: Radiation temperature, T_{rad} , at the threshold wavelength of the ionizing mean intensity for the first ten levels of N II, combined into three groups shown in the legends of the figure, as a function τ_{5000} , for T_{eff} equal to 15000, $\log g = 4.0$, and $\xi_t = 5 \text{ km s}^{-1}$. The black line represents the local electron temperature as a function of τ_{5000} .

and electrons will be in equilibrium and have the same temperature. As we proceed outward in the atmosphere, the density drops and a point will be reached from which photons can escape. The electron temperature then drops below the radiation temperature, and medium becomes optically thin for the radiation. The depth at which the medium changes from optically thick to optically thin depends on the wavelength of the radiation through the continuous opacity sources. The figure shows where the photoionizing radiation field of the specified energy levels will become optically thin. Note that the full, depth-dependent mean intensity was used in the MULTI calculation, and the assignment of radiation temperatures to the various photoionizing continua in Figure (5.4) is for illustrative purposes only.

Figure (5.4) shows that at T_{eff} of 15,000 K, the bound-free continua of the lowest N II levels are optically thick through almost the entire atmosphere. Note that on the τ_{5000} optical depth scale, the N II line formation region lies between 0 and -2, approximately. On the other hand, the photoionization threshold of the higher energy levels lie in the Balmer continuum which is optically thin in the line formation region. Hence, in the N II line formation region, $T_{\text{rad}} > T_e$

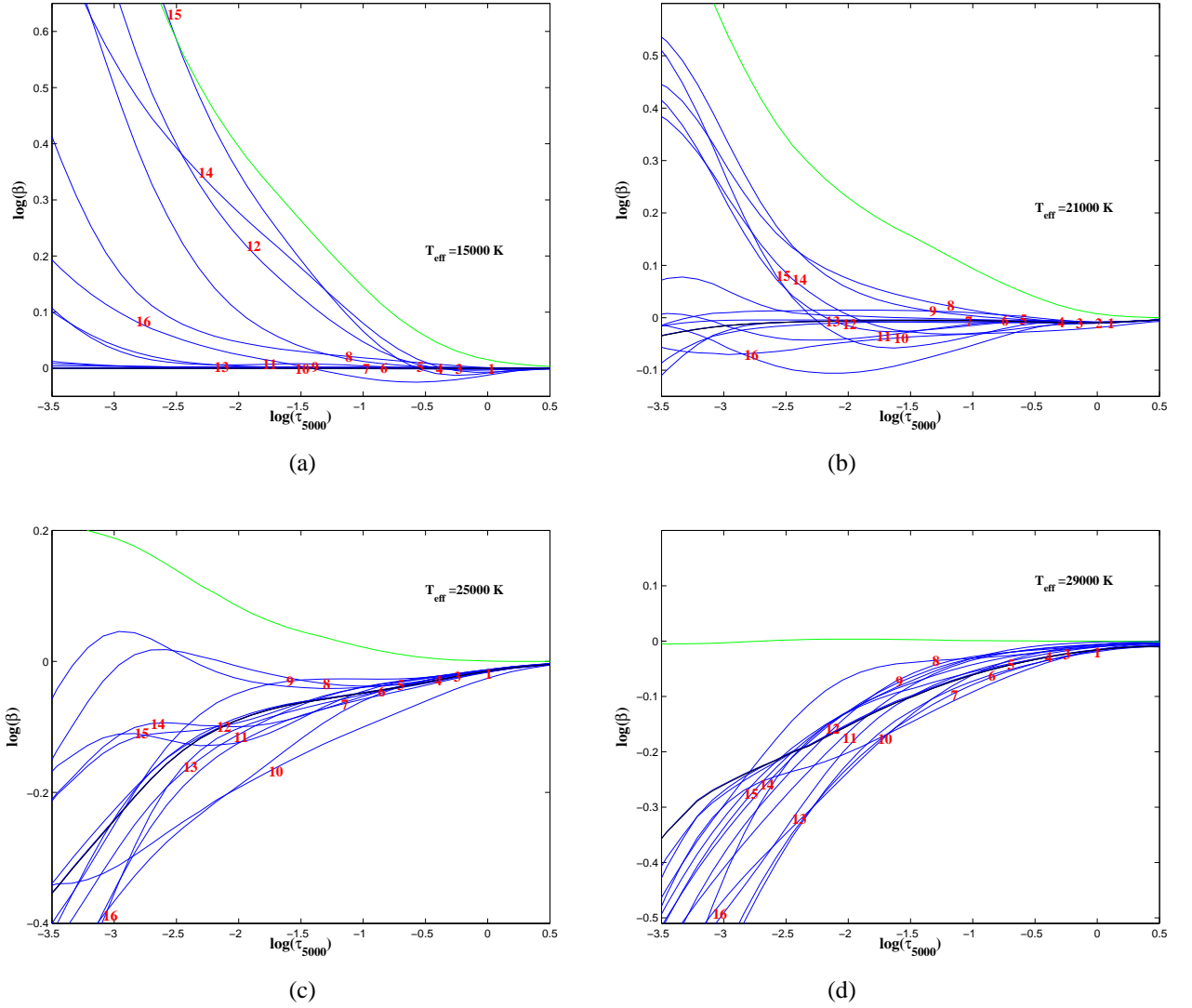


Figure 5.5: Non-LTE departures coefficients for the first sixteen energy levels of N II plus the ground level of N III (94th level, the green line) as a function of τ_{5000} at stellar effective temperatures equal to 15000, 19000, 23000, and 29000 K, surface gravity, $\log g$, equal to 4.0, microturbulent velocity equal to 5 km s⁻¹ and the solar nitrogen abundance.

only for the upper N II levels. Despite this, the populations of these levels at $T_{\text{eff}} = 15,000$ K are so small relative to the ground state that overionization of these levels will not result in a significant change in the ionization balance of N II, i.e. $n_{\text{NII}}/n_{\text{tot}}$.

Similar behaviour is seen for T_{eff} of 25,000 K; however, due to the larger population of the upper N II levels relative to the ground state, overionization of these levels leads to significant decrease of N II ionization balance, and significant increase of N III ionization balance, i.e.

$n_{\text{NIII}}/n_{\text{tot}}$, as shown in Figure (5.3).

The departure of the ionization balance from LTE of N II and N III becomes larger and begins deeper in the atmosphere for higher T_{eff} . Panel (b) of Figure (5.3) shows that for temperatures less than 25,000 K, there is strong deviation of the N III ionization balance from LTE in the optically thin region. This behaviour is a result of the overionization of N II due to non-LTE effects, resulting in a decrease in the ionization balance of N II and an increase of the ionization balance of N III compared with LTE. For higher T_{eff} , there is also strong deviation of the N III ionization balance from LTE.

The predicted departure coefficients of the 16 lowest LS states of N II and the ground state of N III, for four T_{eff} values (15,000, 21,000, 25,000 and 29,000 K), $\log g = 4.0$, $\xi_t = 5.0 \text{ km s}^{-1}$ and solar nitrogen abundance, are shown in Figure 5.5. The departure coefficient of the i^{th} energy level, β_i , is defined as the ratio of the predicted non-LTE number density to the corresponding LTE value computed for the local values of T_e and N_e , i.e.

$$\beta_i = n_i/n_i^*(N_e, T_e), \quad (5.5)$$

where n_i^* and n_i are the predicted LTE and non-LTE number densities of the i^{th} level. respectively.

For $T_{\text{eff}} \leq 21,000 \text{ K}$, the number density of N II ground state and the first and the second excited states (that are only collisionally coupled with the ground state because the radiative transitions are forbidden) remain almost at their LTE values. The ionization threshold of the lowest six N II levels lie in the Lyman continuum, $\lambda < 912 \text{ \AA}$, that is optically thick throughout the entire atmosphere. On the other hand, the ionization threshold of the higher excited states lie in the Balmer continuum that becomes optically thin in the line formation region, as shown in Figure (5.4). The overionization of the upper N II LS states, which lie in the optically thin Balmer continuum, lead to underpopulations in these states and overpopulations in the N III ground state for $\log(\tau_{5000})$ between 0 and -0.5, approximately. As we proceed outward through

the atmosphere, the photoionizing radiation of the upper N II LS levels becomes optically thin, and the overpopulation of the ground level of N III is shared with these high N II LS states through strong collisional coupling with N III ground state. For higher T_{eff} , the photoionizing non-local radiation of the lowest six N II levels is still optically thick in the line formation regions. However, in this case, the populations of the upper N II LS levels are high compared with the ground state. This results in strong underpopulation of these the upper N II LS levels that is driven by the strong non-local photoionizing radiation field at the line formation regions. The underpopulation of the low-lying N II levels is driven by collisional coupling with the upper levels.

5.4.2 Equivalent Widths

Figure (5.6) shows the predicted LTE and non-LTE equivalent widths for λ 3995 Å and λ 6482 Å N II lines, representing radiative bound-bound transitions from levels 9 to 16 ($3s^1P^o \rightarrow 3p^3D$) and levels 9 to 11 ($3s^1P^o \rightarrow 3p^1P$), respectively. The equivalent width is the width of a perfectly black spectral line that blocks the same amount of flux, i.e.

$$W = \int_{\text{line}} \frac{F_c - F_\lambda}{F_c} d\lambda, \quad (5.6)$$

where F_c and F_λ are continuum and line fluxes. Typically, equivalent widths are measured in milli-Å or 10^{-3} Å. For comparison, the predicted equivalent widths of these two lines from K99 are also shown. In general, there is acceptable agreement between the current results and those of K99.

Figure 5.6(a) shows that the predicted LTE equivalent widths of N II λ 3995 Å are in agreement with those of K99, except for an unexplained decrease of the K99 equivalent width at 21,000 K. However, for the λ 6482 Å transition, the agreement between our estimated LTE equivalent widths and those of K99 is not as good. As the background model atmospheres are the same in both the current calculation and K99, the only plausible explanation for the differ-

ences is the different Stark widths adopted in this works. As previously discussed, the current calculation uses the best available Stark widths, whereas K99 used the quadratic stark broadening constants available through ATLAS9 (Kurucz , 1993b), and adopted a value of 1.0×10^{-6} for the missing values

In general, the current predicted non-LTE equivalent widths are larger than the corresponding LTE values. Such differences between non-LTE and LTE equivalent width can be explained by non-LTE effects at the line formation depths, $\log \tau_{5000} \approx -1$.[†] Panels (a) and (b) of Figure (5.7) show the ratio of the line source function to Planck function for N II λ 3995 Å as a function of τ_{5000} at two T_{eff} , 21,000 and 25,000 K. The line source function is the ratio of the line emissivity, j_ν^l , to the line opacity, α_ν^l , which is generally given by,

$$S_\nu = j_\nu^l / \alpha_\nu^l = \frac{n_u A_{ul} \psi_\nu}{(n_l B_{lu} - n_u B_{ul}) \phi_\nu}, \quad (5.7)$$

where n_u and n_l are the number density of upper and lower levels of the radiative transitions, A_{ul} , B_{ul} and B_{lu} are Einstein's coefficients of spontaneous emission, induced emission and absorption, respectively, and ϕ_ν and ψ_ν are the line profiles for absorption and emission, respectively. In the case of complete redistribution, $\psi_\nu = \phi_\nu$, and the line source function will be frequency independent,

$$S_l = j_\nu^l / \alpha_\nu^l = \frac{n_u A_{ul}}{n_l B_{lu} - n_u B_{ul}} = \frac{A_{ul}}{B_{ul}} \frac{1}{\frac{n_l}{n_u} \frac{B_{lu}}{B_{ul}} - 1}, \quad (5.8)$$

as assumed in the current work. The Einstein coefficients are related with each other by $\frac{A_{ul}}{B_{ul}} = \frac{2h\nu^3}{c^2}$, and $\frac{B_{lu}}{B_{ul}} = \frac{g_u}{g_l}$, where g_u and g_l are the statistical weights of the upper and the lower levels, so the previous equation can be expressed as

$$S_l = j_\nu^l / \alpha_\nu^l = \frac{2h\nu^3}{c^2} \frac{1}{\frac{n_l}{n_u} \frac{g_u}{g_l} - 1}. \quad (5.9)$$

By expressing the number densities in terms of the departure coefficients, β_i 's, and using the

[†]The depth of formation of the line was computed using the contribution function following Achmad et al. (1991).

Boltzmann equation for the LTE population ratio,

$$\left(\frac{n_l}{n_u}\right)^* = \left(\frac{g_u}{g_l}\right) e^{\frac{h\nu}{kT}}, \quad (5.10)$$

we can write

$$S_l = \frac{2h\nu^3}{c^2} \frac{1}{\frac{\beta_u}{\beta_l} e^{\frac{h\nu}{kT}} - 1}. \quad (5.11)$$

Also, the line opacity is given by

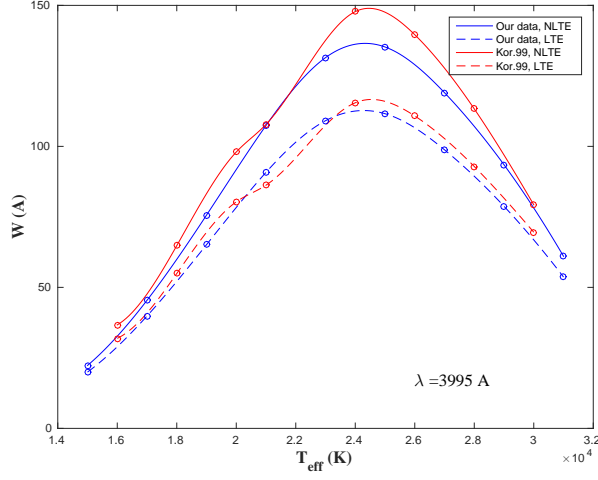
$$d\tau_\nu^l = -\frac{h\nu}{4\pi} (\beta_l n_l^* - \beta_u n_u^*) \phi_\nu dz. \quad (5.12)$$

The last two equations show how the departure coefficients strongly affect the line source function and opacity. In case of $h\nu \gg kT$, (i.e. photon energy is higher than the local kinetic energy) the line source function is proportional to β_u/β_l ratio, while the line opacity is proportional to β_l .

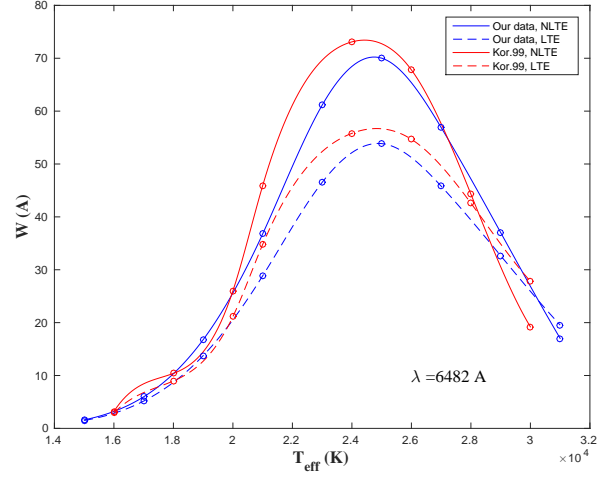
The departure coefficients of the upper and lower levels of the N II multiplets are shown in the Figure 5.7. At T_{eff} of 21,000 K, there is an overpopulation of the the ninth energy level, and an underpopulation of the sixteenth level, while at a T_{eff} of 25,000 K, there is an underpopulation of both levels. However, in both cases, the departure of the upper energy level is larger than that of the lower level. This reduces the line source function in the line formation region and leads to non-LTE strengthening of the line.

The difference between the non-LTE and LTE equivalent width of λ 3995 Å line increases with the increase of the stellar effective temperature and reaches maximum at a temperature of ≈ 24000 K due to the increase of the N II ionization balance and the strengthening of the non-LTE effects. It then decreases for higher T_{eff} due to the overionization of N II in the line formation depths. A similar behaviour is observed in the equivalent width of the λ 6482 Å line, as shown in Figure 5.6.

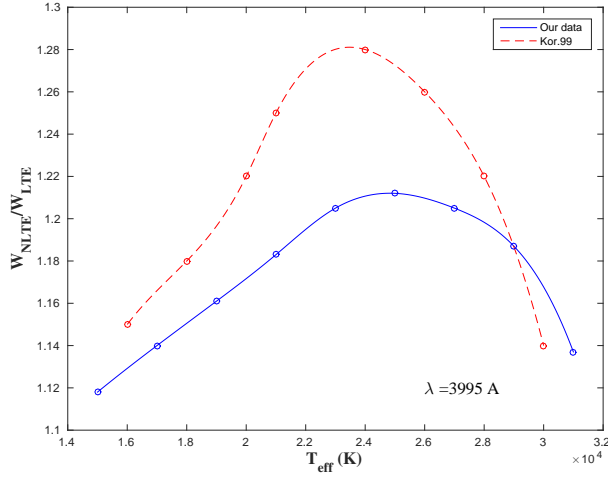
The ratios of the predicted non-LTE equivalent widths to the corresponding LTE values



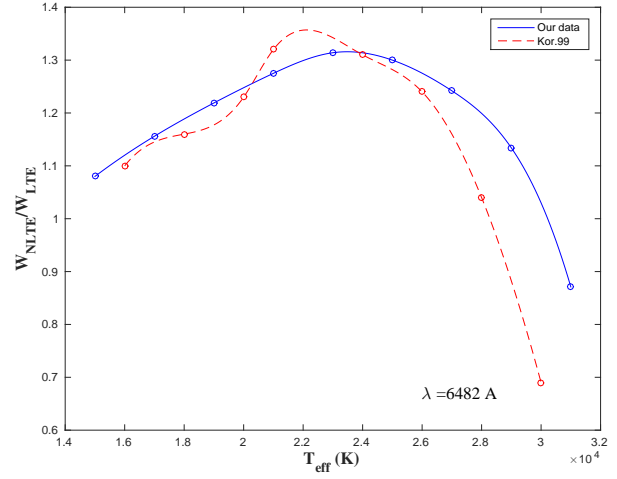
(a)



(b)



(c)



(d)

Figure 5.6: The LTE and non-LTE equivalent widths of N II λ 3995; (panel a) and λ 6482, (panel b) respectively, as a function of T_{eff} for $\log g = 4.0$, $\xi_t = 5 \text{ km s}^{-1}$ and the solar nitrogen abundance. The blue symbols are the current results and the red symbols are K99. The two bottom panels, (c) and (d), give the ratio of the non-LTE and LTE equivalent widths.

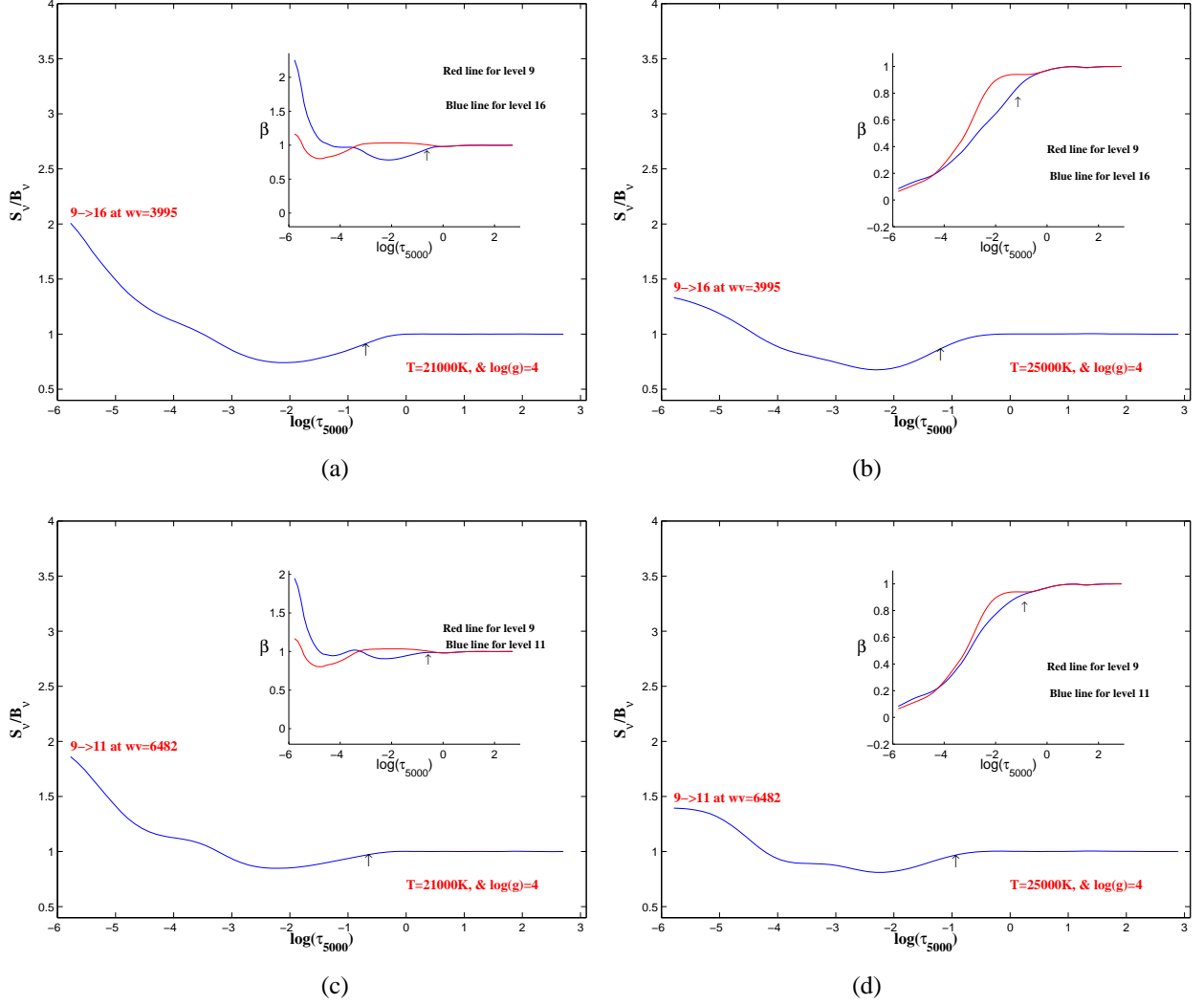


Figure 5.7: Panels (a) and (b) show the predicted line source function of $N \text{ II } 3995 \text{ \AA}$ for stellar effective temperatures equal to 21000 and 25000 K, $\log g = 4.0$, $\xi_t = 5 \text{ km s}^{-1}$ and $\epsilon_{N, \text{solar}} = 7.83$, as a function of τ_{5000} . The departure coefficients of the upper and lower energy levels are shown in the upper right corner of the panels (as a function of τ_{5000}), as the blue line and the red line, respectively. Panels (c) and (d) are the same, but for $N \text{ II } \lambda 6482 \text{ \AA}$. The arrows point to the depth of the line formation region using the contribution function of Achmad et al. (1991).

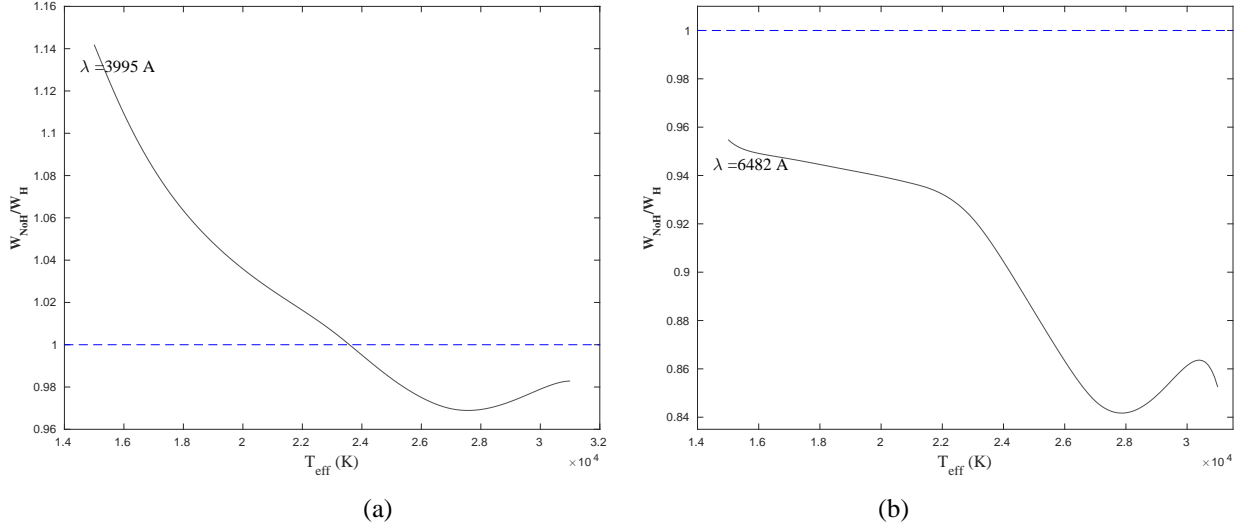


Figure 5.8: Figure shows the ratios of the computed non-LTE equivalent widths of N II λ 6482 Å and λ 3995 Å in the case of discarding and including the hydrogen line opacity as a function of the effective temperatures, $\log g = 4.0$, and $\xi_t = 5 \text{ km s}^{-1}$.

of these two multiplets are shown in panels (c) and (d) of Figure 5.6. Again, the non-LTE enhancement increases until $\approx 24000 \text{ K}$, as shown in Figure (5.6), and then decreases for the previously mentioned reason. Finally, λ 6482 Å undergoes non-LTE line weakening at high effective temperatures (above $T_{\text{eff}} \approx 30,000 \text{ K}$) which can be explained by the higher value of the departure coefficient of the upper level comparing with that of the lower level as shown in Figure (5.7). Such behaviour is shown in the results of K99 for λ 6482 Å line.

Overall, K99 show stronger non-LTE line strengthening compared with our results, as shown in panels (c) and (d) of Figure (5.6). The main difference between the current calculation and K99, besides the different Stark widths, is the lower number of bound-bound radiative transitions that were included in the K99 calculation: 266 transitions in total, with 92 linearized and the rest kept at fixed rates.[‡] In the current work, all radiative transitions with oscillator strengths greater than or equal to 10^{-3} were included in the non-LTE calculation, for a total of 580. All 580 were allowed to determine their own radiation fields- i.e. none were treated with fixed rates.

Figure (5.8) shows how the inclusion of hydrogen line opacity can affect the computed

[‡]It is not specified by K99 how the rates were fixed.

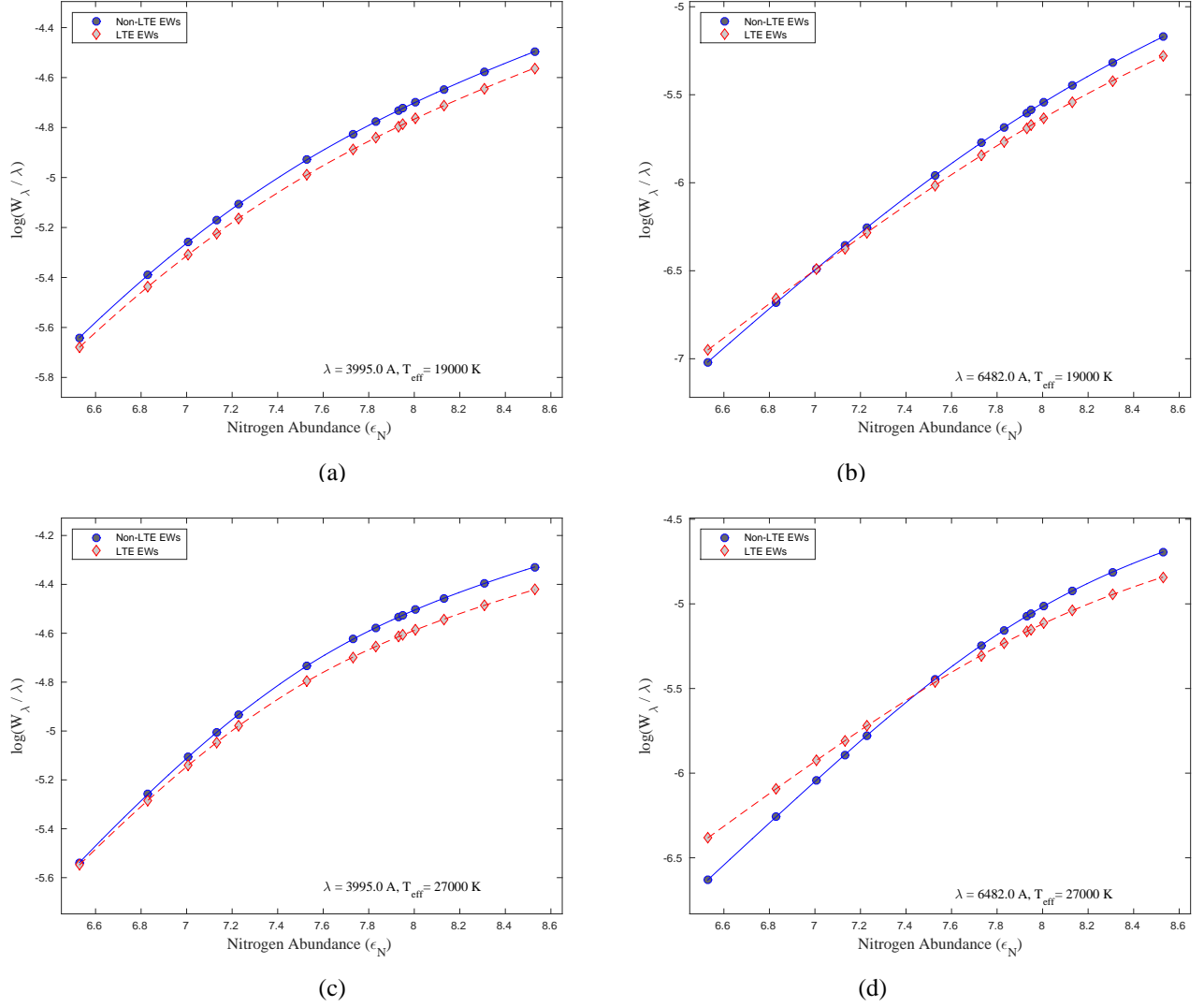


Figure 5.9: The predicted LTE (dashed lines) and non-LTE (solid lines) curves of growth for N II λ 6482 Å and λ 3995 Å as a function of the nitrogen abundance, ϵ_N , at two effective temperatures, 19000 and 27000 K, for $\log g = 4.0$ and $\xi_t = 5 \text{ km s}^{-1}$.

non-LTE equivalent widths of N II lines. The ratios of the computed equivalent widths in the case of excluding the hydrogen line opacity to that of including it are shown for λ 3995 Å and λ 6482 Å in panels (a) and (b) respectively. The inclusion of the hydrogen line opacity causes a significant reduction of the computed non-LTE equivalent widths of λ 3995 Å at low effective temperature, which decrease with the increase of the temperature, while it reduces the non-LTE equivalent widths of λ 3995 Å for $T_{\text{eff}} \lesssim 24,000$ K. On the other hand, including the hydrogen line opacity strengthens the non-LTE equivalent widths of λ 6482 Å over all T_{eff} .

Curves of growth for λ 3995 Å and λ 6482 Å are shown in Figure (5.9), which illustrate the change in the equivalent width with increasing nitrogen abundances, ϵ_N , at two effective temperatures, 19,000 and 27,000 K, for $\log g = 4$ and $\xi_t = 5 \text{ km s}^{-1}$. This figure clearly illustrates that the size of the non-LTE effect can depend on the nitrogen abundance. For λ 3995 Å, the difference between the predicted LTE equivalent widths and the non-LTE values increases with increasing the nitrogen abundance. As shown in Figure (5.10), panels (a) and (c), the ratio of the line source function to Planck function at the local electron temperature at the line formation region decreases with increasing nitrogen abundance. Also, the underpopulation of the upper level and the overpopulation of the lower level are greater at the higher nitrogen abundance. And finally, the line formation region shifts to smaller optical depths in the atmosphere with the increase of the nitrogen abundance. As a result there is non-LTE line strengthening with increasing nitrogen abundance.

These effects are strongest in the case of λ 6482 Å which shows a transition from non-LTE weakening at the lowest nitrogen abundance to non-LTE strengthening at the highest nitrogen abundance. Again, this behaviour can be explained by changes of the line source function in the line formation depth as shown in Figure (5.10), panels (b) and (d). At $T_{\text{eff}} = 19,000 \text{ K}$, the overpopulation of the lower level of this transition in the line formation region changes slightly with the increase of abundance. In addition, there is overpopulation of the upper level at the lower nitrogen abundance, leading to non-LTE line weakening, while there is an underpopulation of this level at the higher nitrogen abundance, leading to non-LTE line strengthening. A similar behaviour is seen at $T_{\text{eff}} = 27,000 \text{ K}$.

A grid of the calculated non-LTE equivalent widths is shown in Tables (5.4) for λ 3995 Å, and (5.5) for λ 6482 Å, which present the calculated non-LTE equivalent widths and the corresponding non-LTE strengthening or weakening for all selected stellar effective temperatures, stellar gravities and nitrogen abundances at a microturbulent velocity of 5 km s^{-1} . A full grid of the predicted non-LTE equivalent widths of the 10 strongest N II lines for all selected stellar parameters, and nitrogen abundances are available in appendix (B).

Table 5.4: MULTI results for N II λ 3995 Å at $\xi_r = 5 \text{ km s}^{-1}$ (Equivalent widths, W_λ , are in mÅ).

$T_{\text{eff}}, \log g$	Nitrogen Abundance difference $\Delta\epsilon_N$, ($\Delta\epsilon_N = \epsilon_N - \epsilon_{N,\text{solar}}$, where $\epsilon_{N,\text{solar}} = 7.83$)													
	-1.00		-0.70		-0.60		-0.30		0.00		0.18		0.30	
	W_λ	W/W_*	W_λ	W/W_*	W_λ	W/W_*	W_λ	W/W_*	W_λ	W/W_*	W_λ	W/W_*	W_λ	W/W_*
15000, 3.5	6.4	1.11	11.2	1.13	13.2	1.14	21.2	1.16	32.1	1.17	40.1	1.18	46.4	1.18
17000, 3.5	14.9	1.14	24.4	1.16	28.2	1.17	42.3	1.18	60.0	1.19	72.1	1.20	81.4	1.20
19000, 3.5	26.1	1.15	41.6	1.17	47.5	1.18	68.3	1.20	92.6	1.21	108.4	1.22	120.4	1.22
21000, 3.5	35.3	1.13	56.4	1.17	64.3	1.18	91.3	1.21	121.1	1.23	139.9	1.24	153.9	1.24
23000, 3.5	35.3	1.07	58.4	1.11	67.3	1.13	98.0	1.18	131.9	1.22	152.7	1.24	168.0	1.25
25000, 3.5	25.7	1.02	45.1	1.06	53.0	1.08	82.0	1.13	115.7	1.19	136.7	1.21	152.1	1.23
27000, 3.5	14.1	0.96	27.5	1.03	33.4	1.05	57.0	1.11	87.2	1.16	106.7	1.19	121.0	1.21
29000, 3.5	3.1	0.50	8.8	0.73	11.8	0.79	25.5	0.93	47.4	1.04	63.7	1.09	76.3	1.11
31000, 3.5	-1.1	-0.66	-1.3	-0.41	-1.3	-0.30	0.4	0.05	6.4	0.37	12.9	0.52	19.3	0.61
15000, 4.0	3.6	1.07	6.6	1.08	7.9	1.08	13.3	1.10	21.3	1.11	27.3	1.12	32.3	1.12
17000, 4.0	9.0	1.08	15.4	1.10	18.1	1.11	28.5	1.12	42.4	1.13	52.3	1.14	60.1	1.14
19000, 4.0	17.3	1.09	28.6	1.12	33.0	1.12	49.5	1.14	69.9	1.15	83.7	1.16	94.2	1.16
21000, 4.0	26.7	1.09	43.4	1.13	49.8	1.14	72.5	1.16	98.8	1.17	115.8	1.18	128.6	1.18
23000, 4.0	32.4	1.07	53.2	1.11	61.2	1.12	88.9	1.16	119.7	1.19	138.9	1.20	153.2	1.20
25000, 4.0	29.3	1.01	49.9	1.06	58.1	1.08	87.2	1.13	119.9	1.17	140.1	1.19	154.9	1.20
27000, 4.0	20.7	0.97	37.3	1.02	44.3	1.04	70.5	1.09	101.9	1.14	121.6	1.16	136.0	1.17
29000, 4.0	11.2	0.86	22.4	0.94	27.5	0.96	48.2	1.03	75.7	1.08	93.8	1.11	107.2	1.13
31000, 4.0	2.9	0.44	7.9	0.63	10.4	0.68	22.4	0.81	41.7	0.91	56.2	0.96	67.5	0.99
15000, 4.5	2.1	1.03	3.9	1.04	4.7	1.05	8.3	1.06	14.0	1.07	18.4	1.07	22.2	1.08
17000, 4.5	5.4	1.04	9.6	1.06	11.4	1.06	18.9	1.07	29.5	1.08	37.4	1.09	43.7	1.09
19000, 4.5	11.1	1.05	19.0	1.07	22.2	1.08	34.9	1.09	51.5	1.10	63.1	1.11	72.3	1.11
21000, 4.5	18.6	1.06	31.2	1.08	36.2	1.09	54.7	1.11	77.3	1.12	92.5	1.13	104.1	1.13
23000, 4.5	25.7	1.05	42.8	1.08	49.5	1.09	73.4	1.12	101.1	1.14	118.8	1.15	132.2	1.15
25000, 4.5	27.9	1.02	47.3	1.06	54.9	1.07	82.1	1.11	112.8	1.14	132.0	1.15	146.3	1.15
27000, 4.5	23.0	0.97	40.6	1.01	47.8	1.02	74.5	1.07	105.5	1.11	124.9	1.12	139.1	1.13
29000, 4.5	15.3	0.91	28.6	0.96	34.4	0.98	57.3	1.03	86.0	1.07	104.4	1.09	117.8	1.10
31000, 4.5	7.4	0.73	15.7	0.83	19.5	0.86	36.1	0.93	59.5	0.99	75.6	1.02	87.7	1.04

Table 5.5: MULTI results for N II λ 6482 Å at $\xi_t = 5 \text{ km s}^{-1}$ (Equivalent widths, W_λ , are in mÅ)

$T_{\text{eff}}, \log g$	Nitrogen Abundance difference $\Delta\epsilon_N$, ($\Delta\epsilon_N = \epsilon_N - \epsilon_{N,\text{solar}}$, where $\epsilon_{N,\text{solar}} = 7.83$)													
	-1.00		-0.70		-0.60		-0.30		0.00		0.18		0.30	
	W_λ	W/W_*	W_λ	W/W_*	W_λ	W/W_*	W_λ	W/W_*	W_λ	W/W_*	W_λ	W/W_*	W_λ	W/W_*
15000, 3.5	0.2	0.90	0.5	0.98	0.6	1.00	1.2	1.07	2.5	1.13	3.7	1.17	4.8	1.19
17000, 3.5	0.9	0.96	1.9	1.05	2.4	1.08	4.8	1.15	9.0	1.21	12.7	1.24	16.1	1.26
19000, 3.5	2.7	0.98	5.7	1.09	7.2	1.12	13.8	1.21	24.4	1.28	32.9	1.31	40.2	1.33
21000, 3.5	5.8	0.96	12.2	1.09	15.3	1.14	28.8	1.25	49.2	1.34	64.5	1.39	76.9	1.42
23000, 3.5	7.3	0.88	16.0	1.03	20.3	1.08	39.6	1.24	68.7	1.36	89.9	1.43	106.5	1.46
25000, 3.5	5.0	0.74	11.5	0.90	14.9	0.95	31.7	1.14	59.8	1.30	81.6	1.39	99.0	1.44
27000, 3.5	2.0	0.50	5.4	0.69	7.3	0.76	17.4	0.97	37.2	1.18	54.6	1.29	69.6	1.36
29000, 3.5	-1.3	-0.70	-0.6	-0.17	-0.1	-0.01	3.9	0.42	13.7	0.80	24.0	0.98	33.8	1.10
31000, 3.5	-3.2	-5.00	-5.0	-3.84	-5.5	-3.42	-6.7	-2.08	-6.1	-0.94	-3.8	-0.40	-0.7	-0.06
15000, 4.0	0.1	0.84	0.2	0.91	0.3	0.93	0.6	1.00	1.2	1.06	1.8	1.09	2.4	1.11
17000, 4.0	0.4	0.91	0.9	0.98	1.1	1.01	2.3	1.08	4.6	1.14	6.7	1.16	8.6	1.18
19000, 4.0	1.3	0.95	2.9	1.04	3.6	1.07	7.2	1.14	13.3	1.20	18.6	1.23	23.2	1.24
21000, 4.0	3.3	0.95	7.0	1.06	8.8	1.10	16.9	1.19	30.0	1.25	40.3	1.28	48.9	1.30
23000, 4.0	5.6	0.91	12.1	1.04	15.2	1.09	29.2	1.20	50.6	1.29	66.5	1.33	79.2	1.35
25000, 4.0	5.6	0.81	12.5	0.95	16.0	1.00	32.1	1.15	57.4	1.26	76.3	1.32	91.3	1.35
27000, 4.0	3.6	0.68	8.3	0.83	10.8	0.88	23.3	1.04	45.2	1.19	62.9	1.26	77.3	1.31
29000, 4.0	1.4	0.43	4.0	0.62	5.4	0.69	13.0	0.88	28.2	1.07	41.8	1.16	53.7	1.22
31000, 4.0	-0.9	-0.50	-0.1	-0.04	0.4	0.10	3.8	0.46	11.8	0.77	20.0	0.92	27.8	1.01
15000, 4.5	0.1	0.81	0.1	0.86	0.1	0.88	0.3	0.94	0.6	0.99	0.9	1.02	1.2	1.04
17000, 4.5	0.2	0.86	0.4	0.93	0.6	0.95	1.2	1.01	2.4	1.06	3.5	1.09	4.6	1.11
19000, 4.5	0.7	0.91	1.4	0.98	1.8	1.01	3.7	1.07	7.2	1.12	10.3	1.15	13.2	1.16
21000, 4.5	1.8	0.93	3.8	1.02	4.8	1.05	9.4	1.12	17.4	1.17	24.1	1.20	29.9	1.21
23000, 4.5	3.6	0.92	7.7	1.03	9.7	1.06	18.8	1.15	33.3	1.21	44.6	1.23	53.9	1.25
25000, 4.5	4.9	0.86	10.7	0.98	13.5	1.02	26.5	1.13	46.7	1.20	61.9	1.23	74.1	1.25
27000, 4.5	4.2	0.75	9.3	0.88	11.9	0.92	24.5	1.05	45.1	1.15	61.1	1.19	74.1	1.22
29000, 4.5	2.5	0.63	5.8	0.76	7.6	0.81	16.6	0.95	33.0	1.08	46.7	1.14	58.3	1.17
31000, 4.5	0.7	0.30	2.4	0.53	3.4	0.59	8.6	0.79	19.2	0.96	28.9	1.04	37.7	1.09

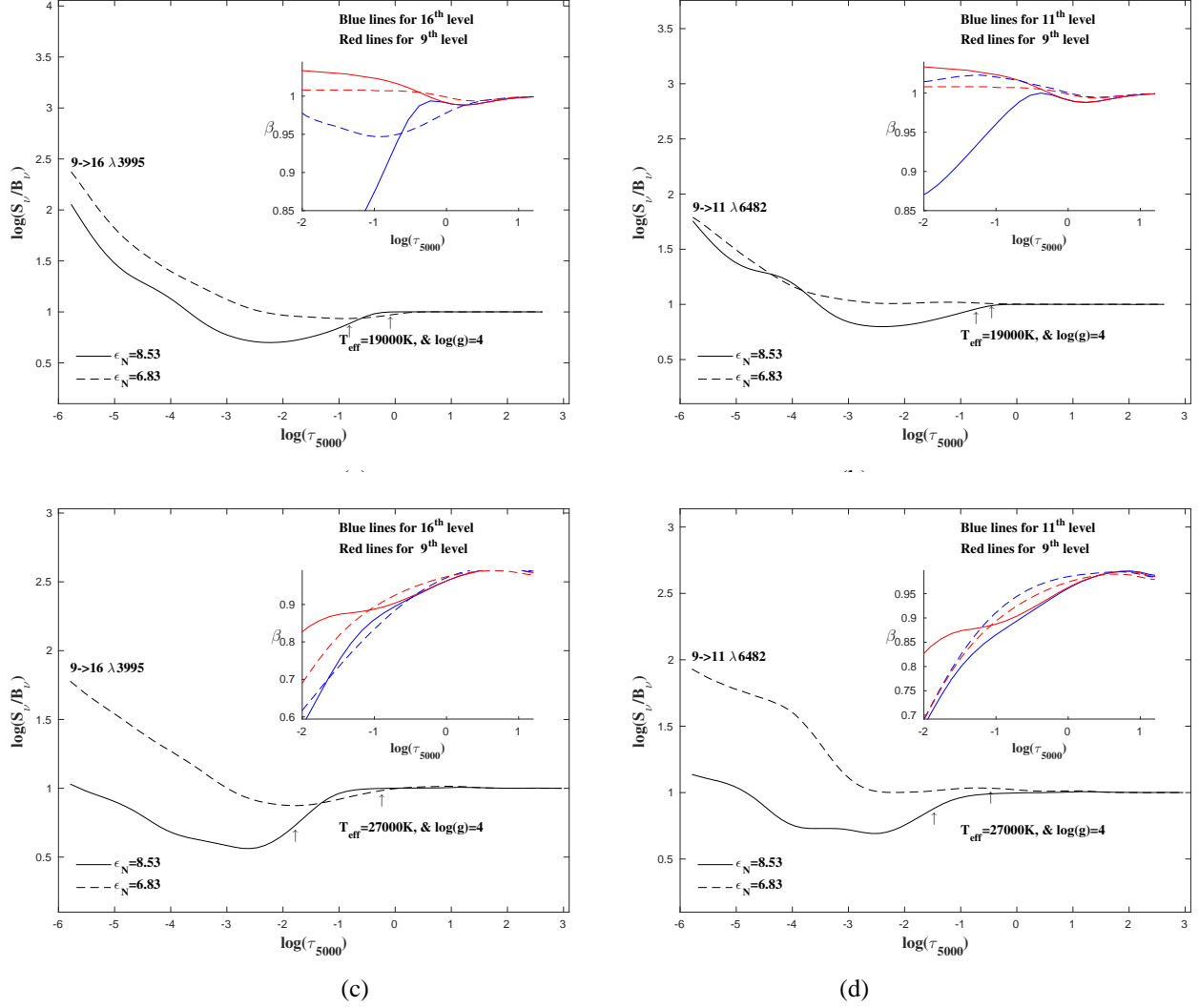


Figure 5.10: Panels (a), and (c) show the source function of N II λ 3995 Å at $T_{\text{eff}} = 19000$ and 27000 K, $\log g = 4.0$, $\xi_t = 5 \text{ km s}^{-1}$, and nitrogen abundances 6.83 and 8.53, as a function $\log \tau_{5000}$. The departure coefficients of the upper and lower energy levels are shown in the upper right corner of the panels for the two nitrogen abundances. Panels (b), and (d) are the same, but for N II λ 6482 Å. Solid and dashed lines for the higher and lower nitrogen abundances respectively.

5.5 Multi-MULTI Analysis

In order to investigate which of the radiative and collisional transitions included in the atom have the most significant effects on the predicted equivalent widths of the N II lines of interest, a series of multi-MULTI analysis were carried out (Carlsson et al., 1992). Multi-MULTI analysis is a good procedure that helps to provide a better understanding of the driving processes for the

Table 5.6: A multi-MULTI Analysis at $T_{\text{eff}} = 23000$ K, $\log g = 4.0$, and $\xi_t = 5.0$ km s $^{-1}$

Transition	Perturbed transition		Type	%
3995 Å	9 \rightarrow 16	($2p\ 3s\ ^1P^o$ - $2p\ 3p\ ^1D$)	rbb	35.22
	16 \rightarrow 94	($2p\ 3p\ ^1D$ - $2s^2\ 2p\ ^2P^o$ N III)	rbf	1.67
	9 \rightarrow 16	($2p\ 3s\ ^1P^o$ - $2p\ 3p\ ^1D$)	cbb	-1.43
	16 \rightarrow 87	($2p\ 3p\ ^1D$ - high l, n = 6)	rbb	-1.29
	16 \rightarrow 22	($2p\ 3p\ ^1D$ - $2p\ 3d\ ^1F^o$)	rbb	-1.21
	22 \rightarrow 87	($2p\ 3d\ ^1F^o$ - high l, n = 6)	rbb	-0.94
	8 \rightarrow 94	($2p\ 3s\ ^3P^o$ - $2s^2\ 2p\ ^2P^o$ N III)	rbf	-0.79
	16 \rightarrow 25	($2p\ 3p\ ^1D$ - $2p\ 4s\ ^1P^o$)	rbb	-0.75
	1 \rightarrow 94	($2p^2\ ^3P$ - $2s^2\ 2p\ ^2P^o$ N III)	rbf	0.71
	12 \rightarrow 16	($2p\ 3p\ ^3D$ - $2p\ 3p\ ^1D$)	cbb	-0.68
6482 Å	9 \rightarrow 11	($2p\ 3s\ ^1P^o$ - $2p\ 3p\ ^1P$)	rbb	71.67
	11 \rightarrow 19	($2p\ 3p\ ^1P$ - $2p\ 3d\ ^1D^o$)	rbb	-6.45
	11 \rightarrow 94	($2p\ 3p\ ^1P$ - $2s^2\ 2p\ ^2P^o$ N III)	rbf	3.95
	9 \rightarrow 16	($2p\ 3s\ ^1P^o$ - $2p\ 3p\ ^1D$)	rbb	3.41
	9 \rightarrow 11	($2p\ 3s\ ^1P^o$ - $2p\ 3p\ ^1P$)	cbb	-3.12
	11 \rightarrow 23	($2p\ 3p\ ^1P$ - $2p\ 3d\ ^1P^o$)	rbb	-2.95
	19 \rightarrow 87	($2p\ 3d\ ^1D^o$ - high l, n = 6)	rbb	-2.91
	7 \rightarrow 11	($2p^3\ ^1D^o$ - $2p\ 3p\ ^1P$)	rbb	2.92
	1 \rightarrow 6	($2p^2\ ^3P$ - $2p^3\ ^3P^o$)	rbb	-2.03
	1 \rightarrow 6	($2p^2\ ^3P$ - $2p^3\ ^3P^o$)	cbb	2.00

Note: rbb and rbf refer to bound-bound and bound-free radiative transitions, respectively, and cbb and cbf refer to bound-bound and bound-free collisional transitions, respectively.

departure from the LTE case in the line formation regions for the lines of interest. In a multi-MULTI analysis, a single radiative or collisional transition is perturbed by doubling its rate in the statistical equilibrium equations, and a new converged solution is obtained for the perturbed atom. The predicted equivalent widths from this new converged solution are compared with the reference solution of the unperturbed atom. Table (5.6) shows the top ten radiative/collisional transitions affecting the predicted equivalent widths of λ 6482 Å and λ 3995 Å for $T_{\text{eff}} = 23,000$ K, $\log g = 4.0$, $\xi_t = 5$ km s $^{-1}$, and a solar nitrogen abundance.

For λ 3995 Å, the calculated equivalent width was most sensitive to its own radiative transition rate controlled by the oscillator strength; e.g. doubling the oscillator strength leads to \approx 40% increase in the predicted equivalent width. This increase can be explained by the combination of the outward shift in the depth of formation and a larger non-LTE strengthening of

the line, as shown in Figure 5.11(a). Next was the photoionization rate from the upper level of λ 3995 Å (level 16). An increase in this rate by a factor of two leads to an increase in the predicted non-LTE equivalent width of $\approx 1.5\%$. This can be explained by the reduction of the population of the upper state through the increased rate of photoionization, which lowers the value of the line source function and causes further non-LTE line strengthening, as shown in Figure 5.11(b). Similarly, an increase in photoionization cross section of the ground state of N II leads to more non-LTE line strengthening. However, doubling the photoionization cross section of the eighth energy level ($2p\ 3s\ ^3P^o$), the lower level of this transition, causes a slight reduction of the predicted non-LTE line strengthening.

The collisional bound-bound transition between the lower and upper energy levels of the λ 3995 Å (9-16) is also one of the top transitions. Doubling the collision strength between these two levels increases the collisional coupling between them, and an increased collisional coupling tends to force LTE, i.e. S_ν comes closer to B_ν . In Figure 5.11(c), we see that this perturbation raises the source function in the line forming region, and, therefore the line is weaker.

Similar results were obtained for the multi-MULTI analysis of λ 6482 Å. Doubling the oscillator strength of the radiative transition itself causes an increase in the equivalent width by $\approx 70\%$, while doubling the collision strength of this transition reduces the predicted non-LTE line strengthening and the non-LTE equivalent width decrease by $\approx 3\%$. Panels (a) to (d) of Figure (5.12) show the line source function of λ 6482 Å for the converged solution of the perturbed and the unperturbed atom for the first four most effective transitions.

Tables (5.7) and (5.8) show the results of a multi-MULTI analysis for the same two N II transitions at $T_{\text{eff}} = 15,000$ and $29,000$ K, $\log g = 4.0$, and $\xi_t = 5\text{ km s}^{-1}$, respectively. At $T_{\text{eff}} = 15,000$ K, the radiative bound-free transitions play no important role as N II is the dominant ionization stage in the line forming region, and changes in the rbf rates have only a minor effect on the N II departure coefficients. On other side, radiative bound-free transitions play a more important role at $T_{\text{eff}} = 29,000$ K, where N III represents the most dominant ionization

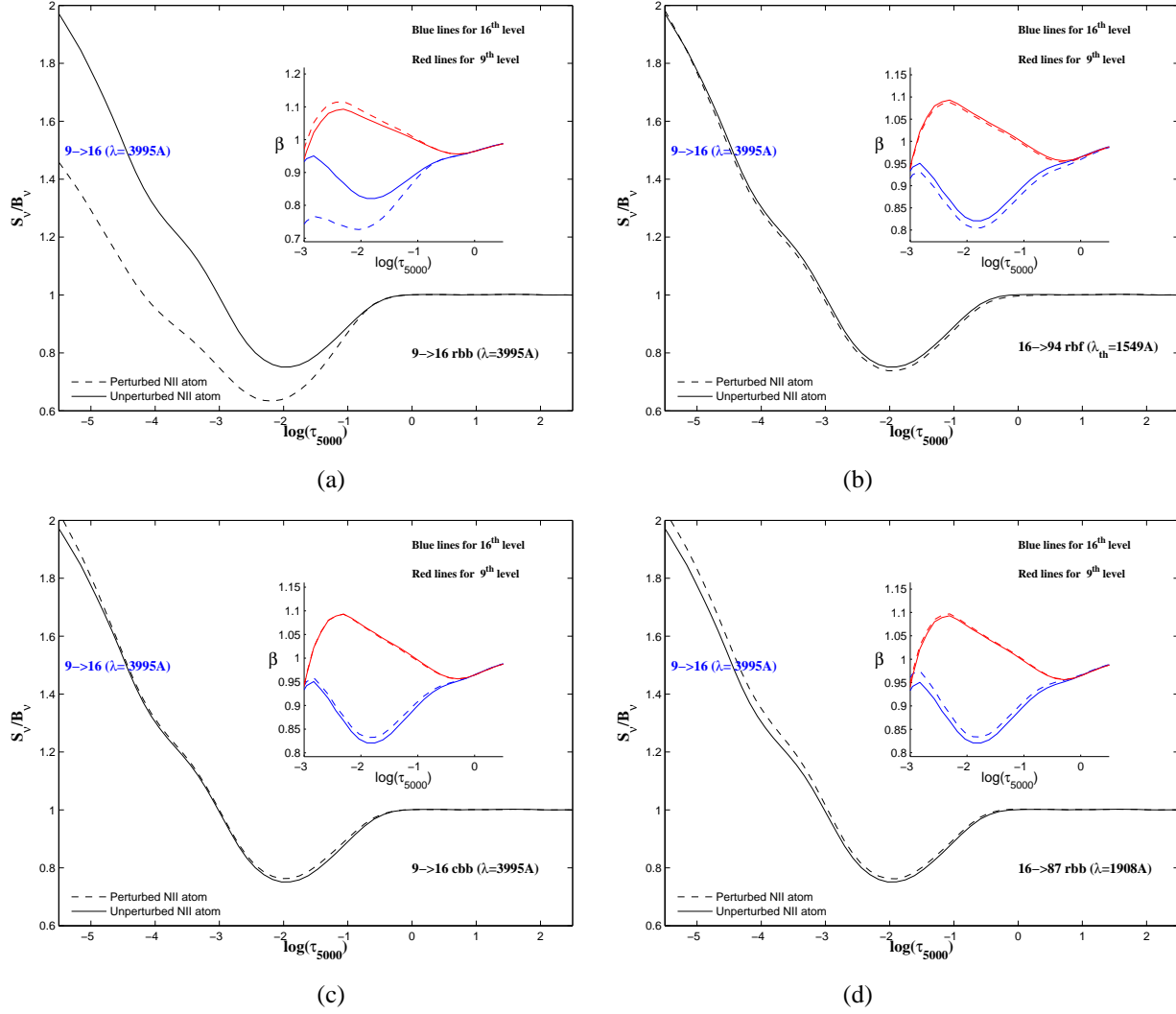


Figure 5.11: The line source function for N II λ 3995 Å for the perturbed nitrogen atom and the departure coefficients of the upper and lower energy levels of this transition (dashed lines) for $T_{\text{eff}} = 23000$ K, $\log g = 4.0$, $\xi_t = 5 \text{ km s}^{-1}$, and $\epsilon_{\text{N,solar}} = 7.83$. The perturbed transition is given in each panel. For comparison the results of the unperturbed atom were added (solid lines).

stage of the nitrogen atom and photoionization play more of a role in controlling the N II level populations.

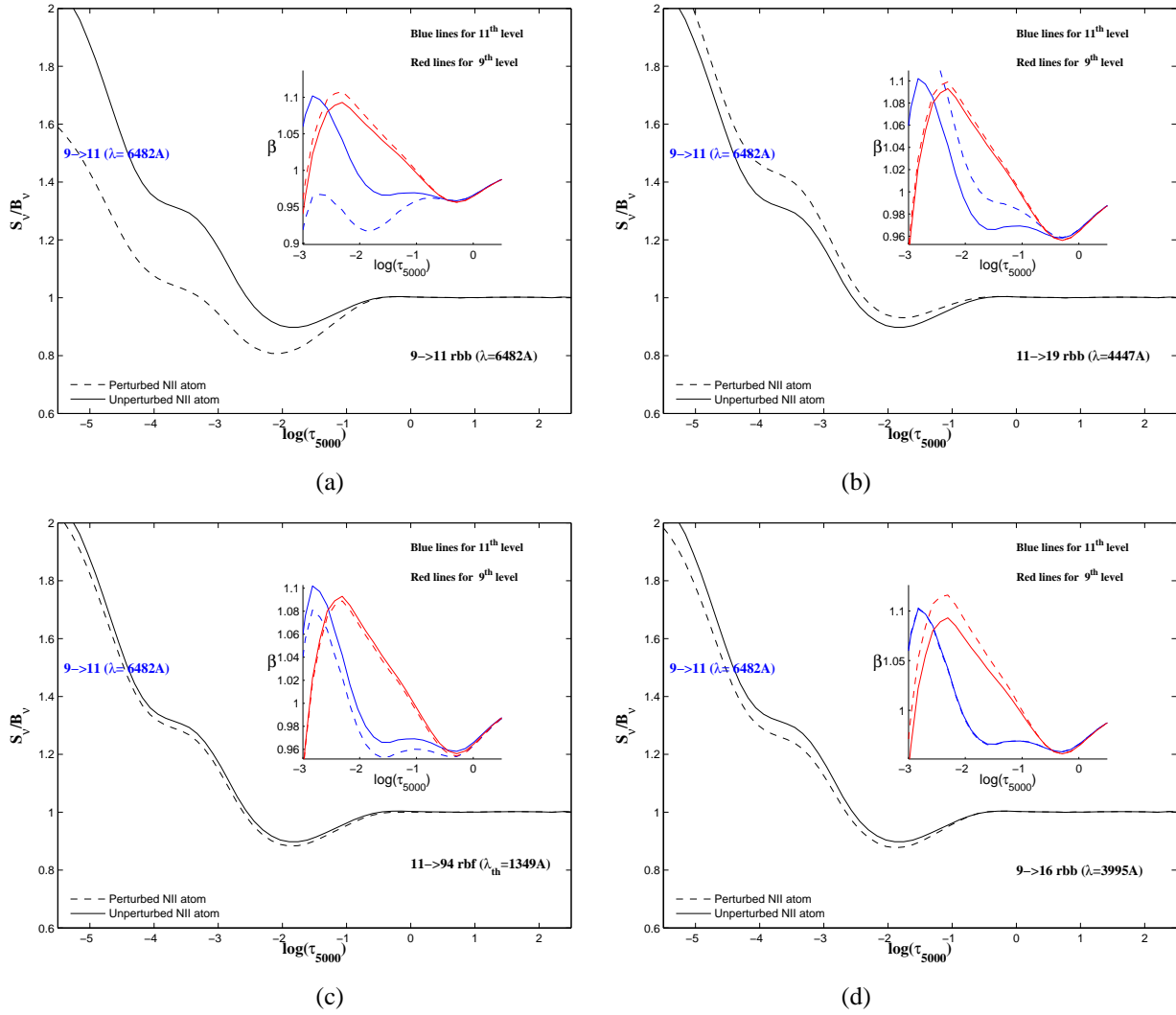
Figure 5.12: The same as Figure (5.11) but for N II λ 6482 Å.

Table 5.7: A multi-MULTI Analysis at $T_{\text{eff}} = 15000$ K, $\log g = 4.0$, and $\xi_t = 5.0$ km s $^{-1}$

Transition	Perturbed transition		Type	%
3995 Å	9 \rightarrow 16	($2p\ 3s\ ^1P^o$ - $2p\ 3p\ ^1D$)	rbb	59.47
	9 \rightarrow 16	($2p\ 3s\ ^1P^o$ - $2p\ 3p\ ^1D$)	cbb	-1.35
	12 \rightarrow 16	($2p\ 3p\ ^3D$ - $2p\ 3p\ ^1D$)	cbb	-0.75
	8 \rightarrow 16	($2p\ 3s\ ^3P^o$ - $2p\ 3p\ ^1D$)	rbb	0.52
	11 \rightarrow 16	($2p\ 3p\ ^1P$ - $2p\ 3p\ ^1D$)	cbb	-0.50
	8 \rightarrow 16	($2p\ 3s\ ^3P^o$ - $2p\ 3p\ ^1D$)	cbb	-0.43
	16 \rightarrow 22	($2p\ 3p\ ^1D$ - $2p\ 3d\ ^1F^o$)	rbb	-0.35
	16 \rightarrow 25	($2p\ 3p\ ^1D$ - $2p\ 4s\ ^1P^o$)	rbb	-0.33
	16 \rightarrow 22	($2p\ 3p\ ^1D$ - $2p\ 3d\ ^1F^o$)	cbb	-0.33
	15 \rightarrow 16	($2p\ 3p\ ^3P$ - $2p\ 3p\ ^1D$)	cbb	-0.25
6482 Å	9 \rightarrow 11	($2p\ 3s\ ^1P^o$ - $2p\ 3p\ ^1P$)	rbb	105.76
	11 \rightarrow 14	($2p\ 3p\ ^1P$ - $2p\ 3p\ ^3S$)	cbb	-4.30
	11 \rightarrow 19	($2p\ 3p\ ^1P$ - $2p\ 3d\ ^1D^o$)	rbb	-3.87
	8 \rightarrow 14	($2p\ 3s\ ^3P^o$ - $2p\ 3p\ ^3S$)	rbb	3.61
	9 \rightarrow 16	($2p\ 3s\ ^1P^o$ - $2p\ 3p\ ^1D$)	rbb	3.27
	1 \rightarrow 6	($2p^2\ ^3P$ - $2p^3\ ^3P^o$)	rbb	-2.15
	1 \rightarrow 6	($2p^2\ ^3P$ - $2p^3\ ^3P^o$)	cbb	2.15
	11 \rightarrow 16	($2p\ 3p\ ^1P$ - $2p\ 3p\ ^1D$)	cbb	2.06
	8 \rightarrow 12	($2p\ 3s\ ^3P^o$ - $2p\ 3p\ ^3D$)	rbb	1.89
	7 \rightarrow 11	($2p^3\ ^1D^o$ - $2p\ 3p\ ^1P$)	rbb	1.72

Table 5.8: A multi-MULTI Analysis at $T_{\text{eff}} = 29000$ K, $\log g = 4.0$, and $\xi_t = 5.0$ km s $^{-1}$

Transition	Perturbed transition		Type	%
3995 Å	9 \rightarrow 16	($2p\ 3s\ ^1P^o$ - $2p\ 3p\ ^1D$)	rbb	57.66
	16 \rightarrow 94	($2p\ 3p\ ^1D$ - $2s^2\ 2p\ ^2P^o$ N III)	rbf	7.95
	1 \rightarrow 94	($2p^2\ ^3P$ - $2s^2\ 2p\ ^2P^o$ N III)	rbf	6.83
	2 \rightarrow 94	($2p\ 2\ 0p\ ^1D$ - $2s^2\ 2p\ ^2P^o$ N III)	rbf	5.62
	9 \rightarrow 11	($2p\ 3s\ ^1P^o$ - $2p\ 3p\ ^1P$)	rbb	5.34
	9 \rightarrow 12	($2p\ 3s\ ^1P^o$ - $2p\ 3p\ ^3D$)	rbb	4.97
	11 \rightarrow 19	($2p\ 3p\ ^1P$ - $2p\ 3d\ ^1D^o$)	rbb	4.97
	4 \rightarrow 94	($2p^3\ ^5S^o$ - $2s^2\ 2p\ ^2P^o$ N III)	rbf	4.96
	8 \rightarrow 16	($2p\ 3s\ ^3P^o$ - $2p\ 3p\ ^1D$)	rbb	4.96
	9 \rightarrow 15	($2p\ 3s\ ^1P^o$ - $2p\ 3p\ ^3P$)	rbb	4.80
6482 Å	9 \rightarrow 11	($2p\ 3s\ ^1P^o$ - $2p\ 3p\ ^1P$)	rbb	125.08
	11 \rightarrow 94	($2p\ 3p\ ^1P$ - $2s^2\ 2p\ ^2P^o$ N III)	rbf	24.15
	9 \rightarrow 16	($2p\ 3s\ ^1P^o$ - $2p\ 3p\ ^1D$)	rbb	18.65
	1 \rightarrow 94	($2p^2\ ^3P$ - $2s^2\ 2p\ ^2P^o$ N III)	rbf	16.16
	19 \rightarrow 94	($2p\ 3d\ ^1D^o$ - $2s^2\ 2p\ ^2P^o$ N III)	rbf	14.79
	7 \rightarrow 11	($2p^3\ ^1D^o$ - $2p\ 3p\ ^1P$)	rbb	14.41
	2 \rightarrow 94	($2p^2\ ^1D$ - $2s^2\ 2p\ ^2P^o$ N III)	rbf	12.94
	9 \rightarrow 12	($2p\ 3s\ ^1P^o$ - $2p\ 3p\ ^3D$)	rbb	12.15
	8 \rightarrow 11	($2p\ 3s\ ^3P^o$ - $2p\ 3p\ ^1P$)	rbb	11.44
	9 \rightarrow 15	($2p\ 3s\ ^1P^o$ - $2p\ 3p\ ^3P$)	rbb	11.37

5.6 The Accuracy of the Predicted non-LTE Equivalent Widths

In this section, we will discuss estimated error bounds for the equivalent widths due to random errors and systematic errors. Random errors can result from the inclusion of atomic data from many sources with different accuracies, while systematic errors can result from the overall completeness of the model atom, and the use of LTE, line-blanketed, atmospheric models. Below we will discuss in detail how to estimate the errors due to the first two effects.

5.6.1 Random Errors

The accuracy of the non-LTE line formation calculation depends on many factors, and an important one is the accuracy of the atomic data. The inclusion of atomic data from different sources that have different accuracies represents a source of random errors in the estimated

Table 5.9: Rates of variation of the atomic data

Atomic parameter	uncertainty
f -value	$\pm 10\%$ f -value ≥ 0.1 $\pm 50\%$ f -value < 0.1
Stark widths	$\pm 40\%$
Photoionization cross section	$\pm 20\%$
Collision strength (Excitation)	
R-Matrix	$\pm 10\%$
Impact parameter approx.	Factor of 2
Collision strength (Ionization)	Factor of 5

equivalent widths. In order to quantify the errors, a series of Monte Carlo simulations were carried out following the procedure of Sigut (1996). In this simulation, two hundred random realizations of the nitrogen atom were generated where the various atomic data were changed within their estimated bounds shown in Table (5.9).

The oscillator strengths (f -values) of the bound-bound radiative transitions were allowed to change within $\pm 10\%$ for f -value equal to or greater than 0.1, and within $\pm 50\%$ for the transitions with smaller f -values. Such values were chosen because the OP length and velocity f -values differ by $\approx 10\%$ for f -values equal to or larger than 0.1, while the difference can be as high as $\approx 50\%$ for smaller f -values. The Stark widths were allowed to change within $\pm 40\%$, which is in the order of the difference between our calculated Stark widths and experimental values for a number of N II lines, see Table (5.3).[§] The photoionization cross sections were allowed to change within $\pm 20\%$. The photoionization cross sections have uncertainty of 10% (Luo & Pradhan, 1989), and an extra 10% was added to include possible uncertainty in the photoionizing mean intensity, J_ν (Sigut, 1996). The R-Matrix method represents the most accurate tool for the computation of the thermally-averaged collisional strengths, and Hudson & Bell (2004) show that their results agree with the the results of previous R-matrix calculations to within $\approx 10\%$. The impact approximation is not really as accurate as the R-Matrix

[§]The assumed error bound of Stark widths is smaller than the differences which lie between $\approx 50\% - 60\%$ in the temperature range of interest, but it is unlikely that this will cause significant effect.

procedure, and consequently, the collisional strengths of transitions computed with the impact approximation were allowed to vary by a factor of 2. Similarly, the collisional ionization rates computed using the procedure of Seaton (1962) are highly uncertain, and a factor of 5 was chosen as the error bound of their estimations.

A converged, non-LTE solution was found for each of the 200 randomly-realized atoms, and the distribution of each transition equivalent width was taken to estimate the uncertainty. The predicted distributions of equivalent widths (for λ 3995 Å and λ 6482 Å) are shown in Figure (5.13) for T_{eff} of 19,000 and 23,000 K, $\log g = 4.0$, and $\xi_t = 5 \text{ km s}^{-1}$. The figure shows that the distributions are nearly Gaussian, and the average value and the standard deviation represent the predicted equivalent width and the associated uncertainty due to random errors. The predicted equivalent widths and the expected errors due to uncertainties in the atomic data of these two lines (at $\log g = 4.0$, and $\xi_t = 5 \text{ km s}^{-1}$) with T_{eff} 's between 15000 and 31000 K and nitrogen abundances between 6.83 and 8.13, are given in Table (5.10).

Given in Table 5.11 are the correlations between the two hundred random realizations of each radiative and collision transition rate with the calculated equivalent widths of these two lines. The Pearson's correlation coefficient, r , was calculated in order to investigate the correlation between the random sets of the atomic data and the predicted equivalent widths. The correlation coefficients are similar to the multi-MULTI simulations of the previous section; however, the rates are now varied within their expected errors and not changed by an arbitrary factor of 2 one at a time. These correlations allow one to deduce which transitions are driving the uncertainty for a given line. Table (5.11) shows the correlation coefficients of the N II 3995 and 6482 Å lines at effective temperatures of 19,000, 23,000 and 27,000 K, gravity of 4.0, and microturbulent velocity of 5 km s^{-1} . For 200 random realization of the nitrogen atom, a correlation coefficient, r , of 0.18 is statistically significant at the 1 % level (Bevington, 1969). As shown in the Table, the error in the predicted equivalent widths is strongly affected by the uncertainties in the oscillator strength values of the radiative transition themselves and the accuracy of the collisional strength values. Tables C.1 to C.16 in Appendix C show the results of

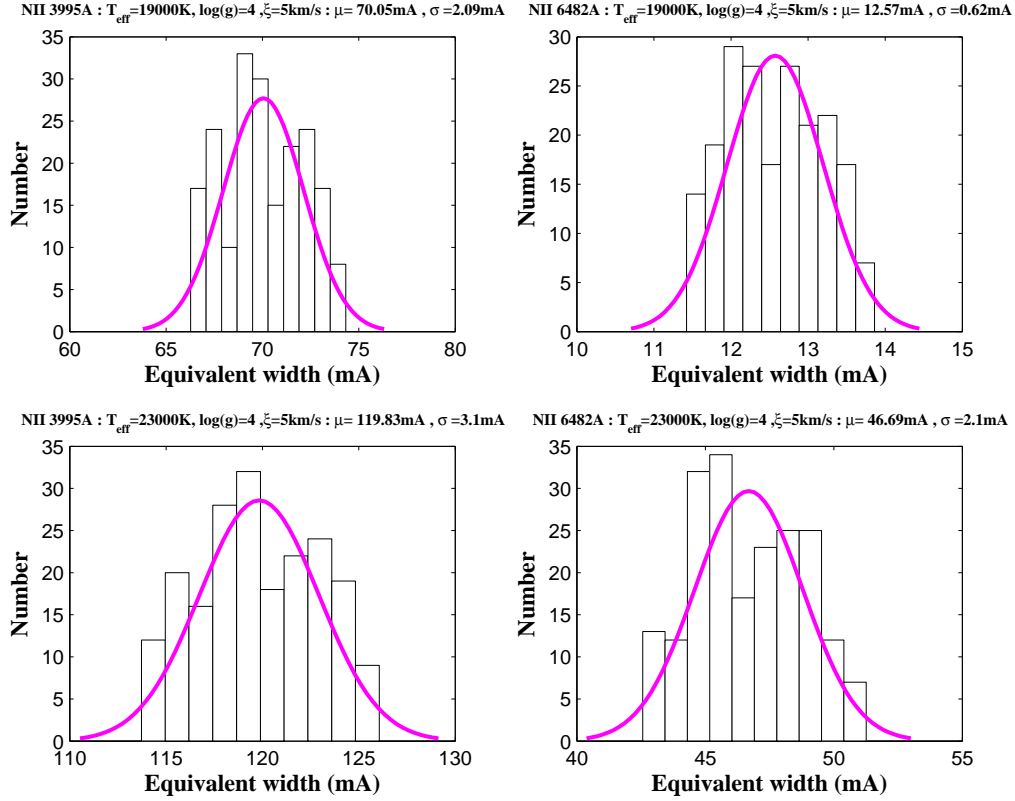


Figure 5.13: The predicted equivalent width distribution for λ 6482 Å and λ 3995 Å for $T_{\text{eff}} = 19000$ and 23000 K, $\log g$ equal to 4.0, $\xi_t = 5 \text{ km s}^{-1}$, and the solar nitrogen abundance. Two hundred randomly-realized atoms were used, and the mean and the standard deviation of the equivalent width distributions (in mÅ) are shown at the title of each panel.

the Monte Carlo simulations for the other combinations of $\log g$, (3.5, 4.0 and 4.5) and ξ (0.0, 5.0 and 10.0 km s^{-1}).

In order to test the accuracy of measuring the nitrogen abundances, given the above uncertainties, the equivalent widths of three singlet lines of N II, λ 3995 Å, λ 4447 Å and λ 6482 Å, computed for selected nitrogen abundances, $\epsilon_{N,MULTI}$, and the unperturbed, reference atoms were used for abundance estimations using the results of the Monte Carlo MULTI simulations, $\epsilon_{N,MC}$, for T_{eff} equal to 19,000 K, 23,000 K, 25,000 K and 31,000 K. In this test, nitrogen abundances were obtained from each of the curves of growth of the 200 random realizations of the nitrogen atom for the three singlet lines. Figure (5.14) shows how the estimated abundances based on the 200 random atoms differ from the original abundance values used in the reference

calculations. The computed abundances represent the mean of all abundance estimations using all Monte Carlo simulations. Also, the uncertainties of the estimated abundances due to inaccuracies in the atomic data are shown as error bars in the Figure which equal 2σ . The figure shows that abundances obtained using the results of the 200 Monte Carlo simulations match the original abundances, and that the expected errors in the estimated nitrogen abundances due to uncertain atomic data tend to increase with nitrogen abundance, e.g. for $T_{\text{eff}} = 23,000$ K, the uncertainty is ± 0.02 dex for $\epsilon_N = 6.83$ dex which rises to ± 0.11 dex for $\epsilon_N = 8.13$ dex. The figure also shows that the estimated errors vary with T_{eff} . At the same nitrogen abundance such as $\epsilon_N = 7.83$ dex, the uncertainty is ± 0.05 dex for $T_{\text{eff}} = 19,000$ K, rising to ± 0.07 dex for $T_{\text{eff}} = 23,000$ K and then falling to ± 0.05 dex for $T_{\text{eff}} = 29,000$ K. The highest error occurs for T_{eff} between 23,000 K and 25,000 K. This is in agreement with the observed behaviour of the equivalent widths with T_{eff} , where the maximum strengths of these lines occur at the same temperatures (see Figure 5.6).

5.6.2 Systematic Errors

Unlike random errors, systematic errors can be difficult to quantify. Systematic errors can originate from many sources, such as using LTE stellar atmospheres and using fixed photoionization rates. Available non-LTE stellar atmosphere models do not readily provide grids of the mean intensity, J_ν , as a function of optical depth, needed for calculating the photoionization rates. On the other side, the opacity distribution function treatment of Kurucz (1979) and the ATLAS9 code provides J_ν over manageable grids (see Przybilla & Butler (2001) for additional details). The adopted elemental abundances in the calculation of the atmosphere models can also be a source of error because the new elemental abundances will not be used to calculate more accurate stellar atmospheres with this process iterated to convergence.

Another source of systematic error is the completeness of the nitrogen atom. Using atomic models with only a few energy levels can result in large non-LTE effects, particularly for trace ions because collisional coupling to the dominant continuum is artificially suppressed (Sigut

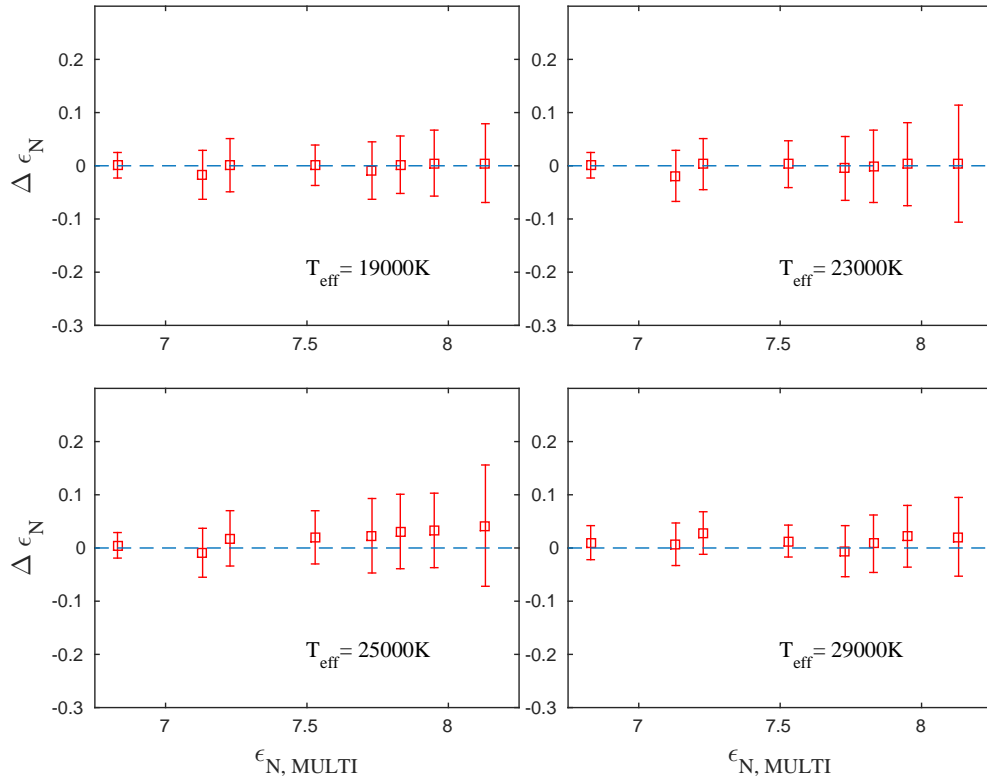


Figure 5.14: The difference between the estimated nitrogen abundances using the results of the 200 Monte Carlo simulations from the reference nitrogen abundance, $\Delta \epsilon_N$, as a function of the reference abundance. T_{eff} is indicated in each panel and $\log g = 4.0$, and $\xi_t = 5 \text{ km s}^{-1}$. The error bars represent the uncertainties of the estimated abundances due to inaccuracies in the atomic data at 2σ . Three lines were used (λ 3995, 4447 and 6482).

Table 5.10: Results of Monte Carlo Simulations for N II at $\log g=4.0$, and $\xi_t=5.0 \text{ km s}^{-1}$: average equivalent widths, $\langle W_\lambda \rangle$, and the expected error, 2σ

λ (Å)	ϵ_N	T_{eff} (K)	$\langle W_\lambda \rangle$ (mÅ)	σ (mÅ)	λ (Å)	ϵ_N	T_{eff} (K)	$\langle W_\lambda \rangle$ (mÅ)	2σ (mÅ)
3995	6.830	15000.0	3.0	0.32	6482	6.83	15000.0	0.1	0.01
		19000.0	16.1	1.56			19000.0	1.3	0.16
		23000.0	32.4	3.16			23000.0	5.3	0.74
		27000.0	21.1	2.45			27000.0	2.8	0.57
		31000.0	4.1	0.75			31000.0	-1.3	0.15
7.230	7.230	15000.0	6.6	0.66	7.23	7.23	15000.0	0.3	0.03
		19000.0	30.9	2.53			19000.0	3.6	0.41
		23000.0	60.6	4.68			23000.0	14.5	1.75
		27000.0	44.7	4.29			27000.0	8.9	1.48
		31000.0	12.7	1.87			31000.0	-0.8	0.37
7.530	7.530	15000.0	11.4	1.04	7.53	7.53	15000.0	0.6	0.07
		19000.0	46.6	3.34			19000.0	7.1	0.76
		23000.0	87.4	5.56			23000.0	28.0	2.98
		27000.0	70.7	5.55			27000.0	19.8	2.79
		31000.0	26.1	3.24			31000.0	1.4	0.86
7.830	7.830	15000.0	18.5	1.53	7.83	7.83	15000.0	1.2	0.14
		19000.0	66.1	4.19			19000.0	13.2	1.32
		23000.0	116.9	6.28			23000.0	48.7	4.46
		27000.0	101.4	6.42			27000.0	39.6	4.60
		31000.0	47.2	4.78			31000.0	7.4	1.87
8.130	8.130	15000.0	28.6	2.14	8.13	8.13	15000.0	2.4	0.26
		19000.0	89.4	5.12			19000.0	23.0	2.11
		23000.0	149.0	7.08			23000.0	76.6	5.98
		27000.0	134.4	7.05			27000.0	69.5	6.54
		31000.0	74.7	5.99			31000.0	20.7	3.54

Table 5.11: Results of Monte Carlo Simulations for N II at $\log g=4.0$, $\xi_t=5.0 \text{ km s}^{-1}$, and solar nitrogen abundance ($\epsilon_{N,solar} = 7.83$): Correlation Coefficients

λ (Å)	T_{eff} (K)	Perturbed Transition				Category	r
3995	19000	9	→	16	$(2p\ 3s\ ^1P^o \quad -2p\ 3p\ ^1D)$	rbb	0.988
		37	→	55	$(2p\ 4f\ ^1F \quad -2p\ 5d\ ^1D^o)$	cbb	-0.271
		28	→	35	$(2p\ 4p\ ^3P \quad -2p\ 4d\ ^3D^o)$	cbb	0.235
		9	→	16	$(2p\ 3s\ ^1P^o \quad -2p\ 3p\ ^1D)$	stk	0.222
		94	→	104	$(2s^2\ 2p\ ^2P^o\ \text{N III} \quad -2s^2\ 3d\ ^2D\ \text{N III})$	cbb	0.221
	23000	9	→	16	$(2p\ 3s\ ^1P^o \quad -2p\ 3p\ ^1D)$	rbb	0.983
		37	→	55	$(2p\ 4f\ ^1F \quad -2p\ 5d\ ^1D^o)$	cbb	-0.270
		28	→	35	$(2p\ 4p\ ^3P \quad -2p\ 4d\ ^3D^o)$	cbb	0.234
		94	→	104	$(2s^2\ 2p\ ^2P^o\ \text{N III} \quad -2s^2\ 3d\ ^2D\ \text{N III})$	cbb	0.228
		8	→	49	$(2p\ 3s\ ^3P^o \quad -2p\ 5p\ ^3D)$	cbb	-0.223
	27000	9	→	16	$(2p\ 3s\ ^1P^o \quad -2p\ 3p\ ^1D)$	rbb	0.967
		37	→	55	$(2p\ 4f\ ^1F \quad -2p\ 5d\ ^1D^o)$	cbb	-0.265
		94	→	104	$(2s^2\ 2p\ ^2P^o\ \text{N III} \quad -2s^2\ 3d\ ^2D\ \text{N III})$	cbb	0.234
		8	→	49	$(2p\ 3s\ ^3P^o \quad -2p\ 5p\ ^3D)$	cbb	-0.231
		28	→	35	$(2p\ 4p\ ^3P \quad -2p\ 4d\ ^3D^o)$	cbb	0.225
6482	19000	9	→	11	$(2p\ 3s\ ^1P^o \quad -2p\ 3p\ ^1P)$	rbb	0.988
		14	→	73	$(2p\ 3p\ ^3S \quad -2p\ 6s\ ^3P^o)$	cbb	-0.244
		55	→	94	$(2p\ 5d\ ^1D^o \quad -2s^2\ 2p\ ^2P^o\ \text{N III})$	cbf	0.227
		47	→	77	$(2p\ 5s\ ^1P^o \quad -2p\ 6p\ ^1P)$	rbb	-0.219
		56	→	94	$(2p\ 5d\ ^3D^o \quad -2s^2\ 2p\ ^2P^o\ \text{N III})$	cbf	-0.218
	23000	9	→	11	$(2p\ 3s\ ^1P^o \quad -2p\ 3p\ ^1P)$	rbb	0.969
		14	→	73	$(2p\ 3p\ ^3S \quad -2p\ 6s\ ^3P^o)$	cbb	-0.251
		55	→	94	$(2p\ 5d\ ^1D^o \quad -2s^2\ 2p\ ^2P^o\ \text{N III})$	cbf	0.231
		47	→	77	$(2p\ 5s\ ^1P^o \quad -2p\ 6p\ ^1P)$	rbb	-0.210
		56	→	80	$(2p\ 5d\ ^3D^o \quad -2p\ 6p\ ^3P)$	stk	-0.210
	27000	9	→	11	$(2p\ 3s\ ^1P^o \quad -2p\ 3p\ ^1P)$	rbb	0.910
		14	→	73	$(2p\ 3p\ ^3S \quad -2p\ 6s\ ^3P^o)$	cbb	-0.252
		55	→	94	$(2p\ 5d\ ^1D^o \quad -2s^2\ 2p\ ^2P^o\ \text{N III})$	cbf	0.225
		20	→	43	$(2p\ 3d\ ^3D^o \quad -2p\ 4f\ ^3D)$	rbb	-0.216
		56	→	80	$(2p\ 5d\ ^3D^o \quad -2p\ 6p\ ^3P)$	stk	-0.213

Notes: All correlation coefficients are statistically significant to less than 1% level, and "stk" refers to variation of the stark width of the radiative transition.

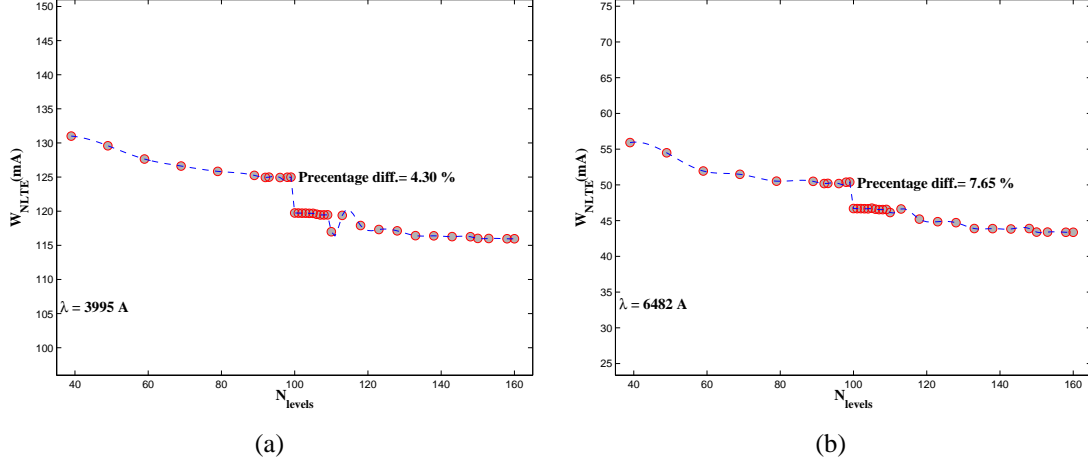


Figure 5.15: The change in the predicted equivalent widths of $\lambda 3995 \text{ Å}$ and $\lambda 6482 \text{ Å}$ with an increasing number of levels in the nitrogen atom at $T_{\text{eff}} = 23,000 \text{ K}$, $\log g = 4.0$, $\xi_t = 5 \text{ km s}^{-1}$, and solar nitrogen abundance.

, 1996). On the other hand, adding too many levels beyond a certain limit can be a source of error, especially highly excited levels with large statistical weights. Adding such levels can be unrealistic because the electrons in these levels can be easily perturbed and detached by the ions in the close neighbourhood (Hummer & Mihalas, 1988).

In order to investigate this issue, the non-LTE line formation calculation was performed for nitrogen atoms of different number of N II levels plus the lowest 12 LS states of N III and the ground state of N IV. Figure (5.15) panels (a) and (b) shows the change of the estimated non-LTE equivalent widths of $\lambda 3995$ and $\lambda 6482$, respectively, as the number of levels in the N II atom is increased. As shown in the figure, the non-LTE enhancement of the lines decreases as the number of N II levels is increased, but the effect is not large. The small discontinuity near the level 100 occurs because of the addition of a composite level representing $n=6$ and $\ell \geq 4$: this composite level has $g=332$ and includes many radiative transitions to other levels. Adding this level, which has high statistical weight, leads to a small decrease in the predicted non-LTE equivalent width by $\approx 4\%$ and 8% for the N II 3995 and 6482 Å lines, respectively. Then the predicted equivalent width changes slowly with the addition of the $n=7$ levels. Consequently, constructing a nitrogen atom of the lowest ninety-three LS states of N II plus the lowest twelve LS states of N III and the N IV ground energy state, was a suitable choice.

The uncertainties in the collision strengths for allowed transitions used in the nitrogen atom estimated using the impact parameter approximation of Seaton (1962) can be another source of systematic error. However, Sigut & Lester (1996) showed that the collision strengths calculated using the impact parameters are indeed within a factor of 2 of accurate *R*-matrix with no clear systematic trend. The expected uncertainty due to random errors in the collision strengths have been discussed earlier in section (5.6).

Chapter 6

Non-LTE Calculation for He I

6.1 Introduction

Helium is the second most abundant element in the universe, after hydrogen, and it is one of the very few atoms that were formed shortly after the big bang (Carroll & Ostlie, 2007). The solar value of the helium abundance is equal to 10.93 dex (Grevesse et al., 2010). Stars are expected to undergo many physical phenomena which alter their original helium abundances. Consequently, accurate estimations of helium abundances are important tests of current theoretical models of the evolution of stars and current cosmological models.

Helium absorption lines represent very prominent features in the spectra of OB stars. The strengths of many of the helium lines in the spectra of massive stars are indicators of their effective temperatures and gravities (e.g. Frémat et al. (2005); Levenhagen & Leister (2006)). However, the strengths of synthetic helium profiles used for spectral analysis are also dependent on the value of the helium abundance adopted in the calculation. Even though changing the helium abundance doesn't affect the background ionizing radiation in the atmospheres of B-type stars (except in the far UV), it affects the stellar opacity (Auer & Mihalas, 1973). Consequently, non-LTE line calculations for helium have been the subject of many previous works (Norris (1971); Auer (1973); Dufton & McKeith (1980); Leone & Lanzafame (1998); Przybilla (2005)). These works progressively aimed to reach the highest possible accuracy for the helium line transfer problem in order to match observed lines and to investigate how the de-

departure from local thermodynamic equilibrium affects the helium lines. However, many of the previous helium line calculations were not able to completely reproduce observed profiles. These discrepancies could be attributed to errors in the atomic data, especially in the collisional strengths and photoionization cross-sections, to the usage of unblanketed stellar atmospheres, and/or to errors in the broadening theory used in the calculation of the lines profiles (Leone & Lanzafame, 1998, Jaschek et al., 1994), especially of the forbidden components of many of the helium lines such as 4471 Å, and 4026 Å (Auer & Mihalas, 1973). In addition, massive stars have high rotational velocities that can result in strong line blending, which can significantly affect the measured equivalent widths of the observed helium lines. Such line blending might also contribute to the observed discrepancies between the equivalent widths of the observed helium lines and the theoretically computed values in many of the previous works (e.g. Jaschek et al. (1994); Leone & Lanzafame (1998)).

Results of previous calculations show that blue helium lines, with wavelength equal to or less than 4026 Å, are not sensitive to departures from LTE, while those with longer wavelengths can show significant departures from LTE, with the non-LTE effect increasing with wavelength (Auer & Mihalas (1973); Dufton & McKeith (1980)). An example is the He I 10830 Å transition which has $h\nu < kT$. Consequently, its line source function is sensitive to variations in the departure coefficients of the upper and lower levels (Przybilla, 2005). This effect will be discussed later in this chapter.

6.2 Previous works

Norris (1971) performed one of the earliest line calculations for the helium atom. This work aimed to get estimates of the helium abundances for a sample of eight B-type stars. For this purpose, grids of LTE line profiles for 11 He I lines (from λ 4009 through to λ 6678 Å) were computed. The LTE approach was adopted because previous studies showed that non-LTE effects cause changes in the computed equivalent widths by less than 10 %. Departure from LTE

causes changes in the line cores, while the line wings, which form deeper in the atmosphere, are formed under LTE conditions. Consequently, lines with strong wings are expected to show smaller changes, compared with lines with weak wings, such as He I λ 6678 Å.

The work of Auer & Mihalas (1973) is one of the earliest and most extensive non-LTE line calculations of He I lines over stellar parameters suitable for B-type stars. In this study, the stellar atmospheres were also computed assuming non-LTE line formation, assuming radiative and hydrostatic equilibrium. For this purpose, a hydrogen atom composed of 10 levels, where the lowest 5 levels were allowed to depart from LTE, was used. Five line transitions were allowed to depart from LTE: H α , H β , P α , P β and B α . Also, a helium atom consisting of the He I ground state and an excited level, and two continua, the ground states of He II and He III, was used. A helium abundance of 0.1 relative to hydrogen was assumed. The CNO elements were represented by a single light element with a total abundance of 1.15×10^{-3} relative to hydrogen. UV line-blanketing were ignored, which is one of the problems of early non-LTE calculations. Model atmospheres were computed for T_{eff} between 15,000 and 27,500 and $\log g$ between 2.5 and 4.5.

For the He line formation calculations, a helium atom with levels $n \leq 10$ was used. For $n \leq 4$ the individual LS states were treated explicitly, while for $n > 4$ states of the same ℓ in each spin system were represented with a single level, with the singlet and triplet spin systems treated separately. The states with $n \leq 4$ were allowed to depart from LTE. The radiative transitions between singlets with $n \leq 4$ were included in the linearization procedure, except for resonance transitions from $n = 1$ which were kept in detailed balance. The line profiles were calculated assuming pure thermal, Doppler profiles. A formal solution was then done with the line profiles represented by a Voigt profile, with a complete line broadening theory. The calculations were computed for He abundances of 0.05, 0.10 and 0.20 (relative to hydrogen, $N_{\text{He}}/N_{\text{H}}$).

Auer & Mihalas (1973) showed that non-LTE departures cause small changes in the computed helium equivalent widths, less than 10 %, for the He I blue lines with the exception of the

He I λ 3889 Å, which shares the same lower energy level as the He I 10830 Å (the metastable state $2s^3S$, which undergoes strong non-LTE departure). The equivalent widths of the He lines with wavelengths between 4026 and 5047 Å change by only 10 %. Larger changes for He I lines with longer wavelengths, up to $\approx 70\%$ for λ 6678 Å and λ 7281 and $\approx 30\%$ for λ 5876 Å. Some lines were went into emission at higher T_{eff} or lower $\log g$, such as He I λ 10830 Å.

The work of Dufton & McKeith (1980) aimed to compute a grid of LTE and non-LTE line profiles for three UV He I lines: λ 2829, λ 2945 and λ 3187 Å, over T_{eff} values between 15,000 K and 27,500 K. For this study, non-LTE line calculations were performed for a helium atom which was the same as used by Auer & Mihalas (1973) but with updated atomic data, i.e. new photoionization cross-sections and collision excitation strengths. Non-LTE model atmospheres were again computed assuming plane-parallel atmospheres in radiative and hydrostatic equilibrium. The lowest five states of hydrogen and the ground states of He I and He II were allowed to depart from LTE, and the CNO elements were represented by a composite element with an abundance representing an average abundance. The helium atom was constructed with 15 levels: the ground state, the lowest 14 triplet LS states with $n \leq 6$ and $\ell \leq 2$, and the ground state of He II. There were 45 allowed radiative transitions in total, 24 of them with $\lambda \leq 2\mu\text{m}$. Only 12 of them were included in the linearization procedure, chosen to have significant f -values and to be related to the levels of the studied UV lines. Results show strong non-LTE weakening of the three lines that increased until $T_{\text{eff}} \approx 20,500$ K. Comparison with observed equivalent widths show that the computed non-LTE equivalent widths of He I λ 2829 Å line was in acceptable agreement with observation. However, there is higher uncertainty in the measured equivalent widths in the UV due to uncertainties in determining the continuum level of the spectra and the background count rates. The measured equivalent widths of He I λ 2945 Å lies between their LTE and non-LTE results, while the measured equivalent widths of λ 3187 Å lie close to their LTE values. In general, the accuracy of the atomic data, the limited computational tools, and uncertainties in the measured equivalent widths represented significant sources of errors in the results of the study.

The work of Husfeld et al. (1989) represents another advancement in solving the non-LTE problem of He I, with more levels and transitions included in the linearization process, with updated atomic data. However, most of the details of this work will not be discussed, because it is not related to the topic of the current work. The work of Leone & Lanzafame (1998) is one of the most extensive non-LTE line calculations for the He I using updated atomic data. They solved the non-LTE line calculations of He I using the ATLAS9, line-blanketed, LTE, stellar atmospheres of Kurucz (1993a), treating helium as a trace element. This is good approximation because changing the He abundance in the stellar atmosphere will not significantly change the background photoionizing radiation field. The calculations were performed using the MULTI code, where all energy levels with principle quantum number satisfying $n \leq 5$ were included in the calculations. This work presented grids of non-LTE equivalent widths of helium lines over temperatures and gravities grids suitable for B-type stars. However, they were not able to match observed helium equivalent widths using Stark widths from Dimitrijević & Sahal-Bréchet (1990). In order to overcome this problem, they made an empirical correction to the Lorentzian broadening parameter, i.e Stark width, used in the non-LTE calculation to match the observed equivalent widths of main-sequence stars (Leone & Lanzafame, 1997). This is not explicitly mentioned in Leone & Lanzafame (1998), but supposedly they did the same. Their results are discussed in a more detailed way later in Section 6.4.

Finally, the recent work of Przybilla (2005) aimed to compute non-LTE grids of the equivalent width of He I λ 10830 Å, a multiplet that is very sensitive to departures from LTE, as mentioned before. All previous works failed to match the observed equivalent widths of this multiplet (Auer & Mihalas (1973); Leone & Lanzafame (1998)). Przybilla (2005) adopted an extended version of the helium atom of Husfeld et al. (1989). All LS states with $n \leq 5$ were included explicitly, and the atom was updated with accurate and recent atomic data. (The adopted atomic data in this work is almost the same as the atomic data used in the current calculations; This will be discussed in the next section. Also, they adopted the ATLAS9, line-blanketed, LTE, stellar atmospheres of Kurucz (1993a). Results show better agreement

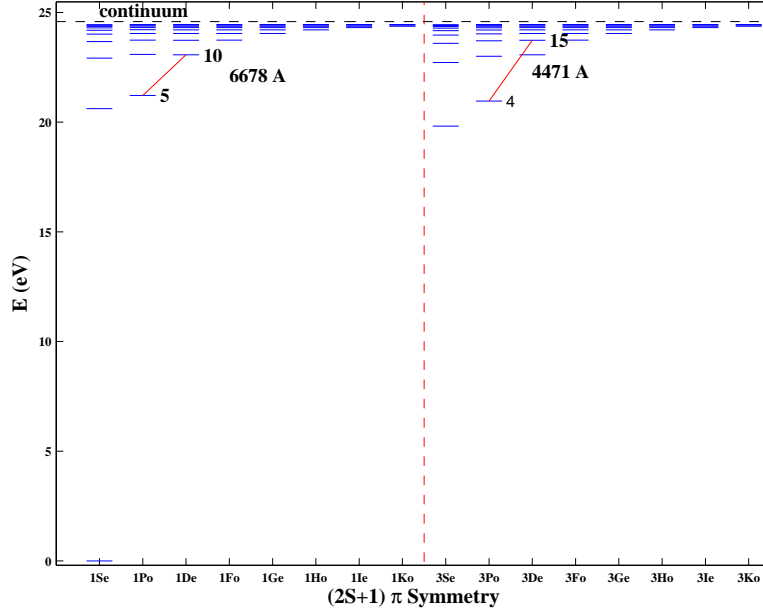


Figure 6.1: He I Grotrian diagram showing the singlet and triplet spin systems.

between the computed non-LTE equivalent widths and observations, and this will be discussed later in Section (6.4).

6.3 He I Atomic data

In the current non-LTE line calculation for He I, the atom was constructed consisting of the lowest 103 He I states (corresponding to $n \leq 10$) and the ground state of He II. The energies were taken from Morton et al. (2006), available through NIST database, and are shown in Figure (6.1). The energies, statistical weights, configurations, and the threshold wavelength of ionization of the lowest 15 LS states of He I and the ground state of He II are listed in Table (6.1). All allowed, bound-bound, radiative transitions with f -values equal to or greater than 0.001 were included, giving a total of 427 transitions. The oscillator strengths of the radiative transitions were taken from Drake (2006), which is also available through NIST database. The atomic data of the multiplets of interest are shown in Table (6.2). The photoionization cross-sections were taken from the Opacity Project (Fernley et al., 1987), available from the TOPBASE database (Cunto et al., 1993). For the He I levels which have no data available

Table 6.1: Atomic data for the lowest 15 LS states of He I and the ground state of He II.

n	Energy (cm^{-1})	g	$\lambda_{thres}(\text{\AA})$	configuration
1	0.000	1.0	504.3	$1s^2\ ^1S$ (He I)
2	159855.974	3.0	2600.3	$2s\ ^3S$
3	166277.440	1.0	3121.8	$2s\ ^1S$
4	169086.910	9.0	3421.9	$2p\ ^3P^o$
5	171134.897	3.0	3679.7	$2p\ ^1P^o$
6	183236.792	3.0	6634.0	$3s\ ^3S$
7	184864.829	1.0	1057.5	$3s\ ^1S$
8	185564.602	9.0	7437.2	$3p\ ^3P^o$
9	186101.556	15.0	7845.6	$3d\ ^3D$
10	186104.967	5.0	8190.6	$3d\ ^1D$
11	186209.365	3.0	8192.9	$3p\ ^1P^o$
12	190298.113	3.0	8263.6	$4s\ ^3S$
13	190940.226	1.0	12480.4	$4s\ ^1S$
14	191217.057	9.0	13567.7	$4p\ ^3P^o$
15	191444.485	15.0	14097.2	$4d\ ^3D$
\vdots	\vdots	\vdots	\vdots	\vdots
104	198310.666	2.0	227.8	$1s\ ^2S$ (He II)

in the Opacity Project, the photoionization cross-section at the threshold wavelength of these levels were computed using the Coulomb approximation, σ_{th} , and then the photoionization cross-sections for shorter wavelengths were computed using a hydrogen approximation,

$$\sigma = \sigma_{th} * \left(\frac{\lambda}{\lambda_{th}} \right)^3. \quad (6.1)$$

Thermally averaged collisional strengths of excitation were taken from many sources. Firstly, all collisional strengths available in Sawey & Berrington (1993) were adopted in this calculation. Sawey & Berrington (1993) performed a 29-state R-matrix calculation for He I in order to compute the collisional strengths for transitions between the lowest 19 LS states of He I for electron temperatures between 5,000 and 30,000 K. The Sawey & Berrington (1993) data represents the most accurate collisional strength available for He I (Bray et al., 2000). Secondly, the collisional strength values of Bray et al. (2000) were adopted for the other transitions not given in Sawey & Berrington (1993). Bray et al. (2000) computed collision strengths us-

Table 6.2: Atomic data for the He I multiplets of interest

λ (Å)	g_l	g_u	$A_{ul}(s^{-1})$	Transition	Multiplet Number	Stark Widths (Å) $T_e = 1.0E4$ K , $3.0E4$ K	
4471.48	5	3	6.828^{+05}	$2p^3P^o \rightarrow 4d^3D(15-4)$	14	2.678	2.057
4471.48	5	5	6.144^{+06}				
4471.48	5	7	2.458^{+07}				
4471.48	3	3	1.024^{+07}				
4471.48	3	5	1.843^{+07}				
4471.68	1	3	1.365^{+07}				
6678.15	3	5	6.370^{+07}	$2p^1P^o \rightarrow 3d^1D$ (5-10)	46	9.77^{-1}	8.79^{-01}

Note: Stark widths were calculated assuming electron number density of $1.0^{+16} \text{ cm}^{-3}$

ing the convergent, close coupling approximation (CCA) that included a frozen-core model for transitions from the ground state and the first and second excited states up to higher LS states with $n \leq 5$. This procedure has the advantage over the R-matrix technique in that it can be used to calculate collisional strengths for very high plasma temperatures. Many of Sawey & Berrington (1993) collisional strengths did not converge at high temperatures due to the poor convergence of the R-matrix method. Consequently, they provided no collisional strength values in these cases. In order to get the values for these missing collisional strengths, the values of Bray et al. (2000) for the same transitions were interpolated and scaled to the data points of Sawey & Berrington (1993), if available. Nevertheless, the accuracy of the CCA collisional strengths calculated at low temperatures near the threshold energy is less than those computed using the R-matrix method due to the lack of a sufficiently by fine energy grid.

The collisional strengths for all remaining allowed transitions were obtained following the impact parameter approximation of Seaton (1962), and the collisional strengths of radiatively forbidden transitions were kept constant at 0.1. The collisional strengths of ionization of the He I LS states were calculated the numerical procedure of Seaton (1962).

The Stark widths due to collision with electrons were computed using the approximate formula of Dimitrijević & Konjević (1986). Table (6.3) shows the average ratios of these theoretically calculated Stark widths to experimentally measured values obtained by Konjević et

Table 6.3: Average ratios of theoretically calculated stark widths to experimental measured values from Konjević et al. (2002) over a number of transitions for different temperatures. DK86 refers to Dimitrijević & Konjević (1986) and DS90 refers to Dimitrijević & Sahal-Bréchet (1990).

Temperature (K)	$(\gamma_{theo}/\gamma_{exp})_{av}$	
	(DK86)	(DS90)
20000	1.117	0.717
22000	1.126	0.703
25000	1.152	0.679
30000	1.116	0.711
35000	1.312	0.803
40000	1.220	0.763

al. (2002). The average ratios of theoretically calculated Stark widths results of Dimitrijević & Sahal-Bréchet (1990) to experimental measured values are also given in the table for comparison. The table shows that our computed Stark widths computed following Dimitrijević & Konjević (1986) are a factor of ≈ 2 higher than those of Dimitrijević & Sahal-Bréchet (1990)*. They are also somewhat higher than the experimentally measured values of Konjević et al. (2002), but they are closer to the observations than those of Dimitrijević & Sahal-Bréchet (1990). Figure (6.2) shows the ratios of the theoretically calculated Stark widths to experimental measured values versus the effective quantum number of the upper level of the radiative transitions for $T_e = 25,000 K$.

*Oddly, Dimitrijević & Sahal-Bréchet (1990) did not cite their previous work, Dimitrijević & Konjević (1986).

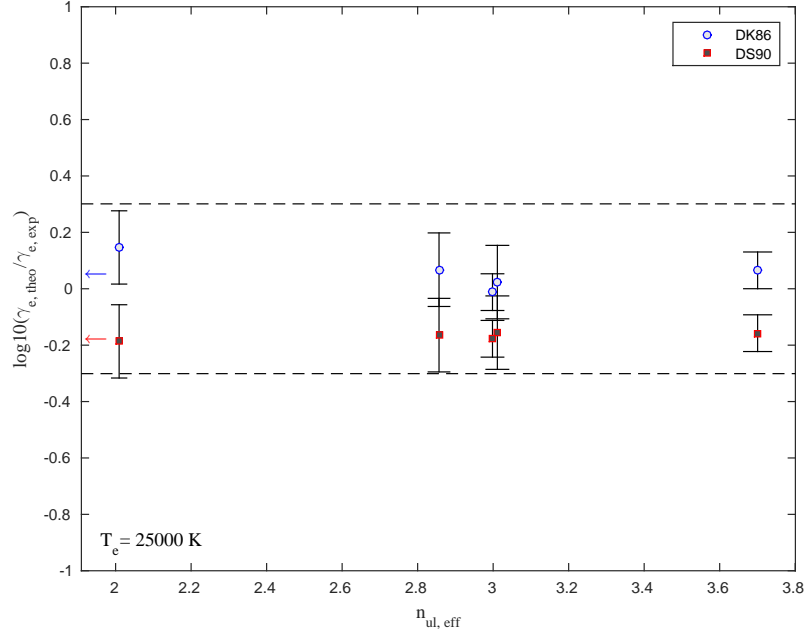


Figure 6.2: Ratios of theoretically calculated Stark widths computed using the approximate formula of Dimitrijević & Konjević (1986) to experimentally measured values from Konjević et al. (2002) versus the effective quantum number of the upper LS state of the transitions (blue circles) at $T_e = 25,000 \text{ K}$. The ratios of theoretically calculated stark widths of Dimitrijević & Sahal-Bréchet (1990) to the experimentally measured are shown for comparison (red squares). Arrows point to the average ratios of each technique. The dashed lines represent a factor of two uncertainty.

6.4 Calculation Grid of He I Atom

The non-LTE line formation calculation for He I was performed using the MULTI code v.2 of Carlsson (1992). Grids of the non-LTE equivalent widths and line profiles for the λ 4471 and λ 6678 Å were obtained over T_{eff} and $\log(g)$ ranges suitable for B-type stars. The calculations were carried out over nine selected T_{eff} between 15,000 K and 31,000 K, $\log g$ equal to 3.5, 4.0 and 4.5 dex, and microturbulence velocities of 0, 5 and 10 km s⁻¹. A solar helium abundance of 10.93 dex was adopted (Grevesse et al., 2010). Similar to the non-LTE line calculation for N II atom, ATLAS9 LTE, line blanketed atmospheres were used for the calculations, and provided not only $T(\tau)$ and $N_e(\tau)$, but also the photoionizing mean intensity, $J_\nu(\tau)$.

6.4.1 Ionization Balances and Departure Coefficients

Figure (6.3) shows the predicted LTE and non-LTE ionization balances of He I and He II, for T_{eff} of 15,000 K, 23,000 K and 29,000 K, $\log g = 4.0$, and $\xi_t = 5.0$ km s⁻¹. At T_{eff} of 15,000 K, He I represents the dominant ionization stage in the line formation region, and there is no significant deviation from LTE due to the lack of a strong and non-local non-LTE photoionizing radiation field. Figure (6.4) shows the radiation temperature of the photoionizing mean intensity at the threshold wavelength for the lowest ten LS states of He I atom for T_{eff} of 15,000 K and 23,000 K. The figure shows where the radiation temperature of the photoionizing radiation field is hotter than the local electron temperature, i.e. optically thin. At $T_{\text{eff}} = 15,000$ K, the photoionizing radiation field of the ground state is almost optically thick throughout the entire atmosphere, while photoionizing radiation field of the first to the fifth excited states becomes optically thin deeper in the stellar atmosphere. However, at such low T_{eff} , the populations of the excited states are so small compared with that of the ground state that no significant deviation from the predicted LTE ionization balance is possible.

He I is the dominant helium ionization stage for $T_{\text{eff}} \leq 19,000$ K, and then He II starts to dominate for higher T_{eff} , as shown in Figure (6.4). For $T_{\text{eff}} = 23,000$ K, the behaviour of

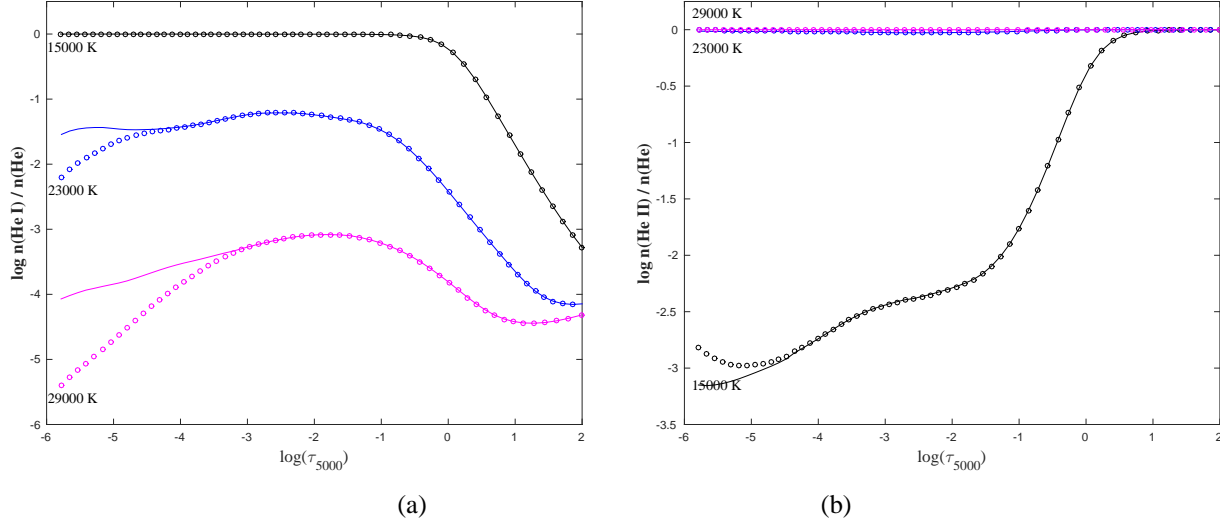


Figure 6.3: The ionization balance of He I and He II, panels ((a)) and ((b)) respectively, as function of τ_{5000} for three T_{eff} of 15,000, 23,000 and 29,000 K, $\log g = 4.0$ and $\xi_t = 5.0 \text{ km s}^{-1}$. The circles represent the predicted non-LTE ionization balances, and the solid lines represent the predicted LTE ionization balance computed using Saha equation at the local electron temperature and number density.

the radiation temperature of the photoionizing radiation field is similar to that of the lower T_{eff} . However, at these high temperatures, the population of the higher excited states are larger and overionization of these levels leads to a lower He I ionization balance, compared with the corresponding LTE values, for $\tau_{5000} \lesssim -4$. Such decrease in the ionization balance of He I is accompanied by an increase of the ionization balance of He II compared with its LTE values. The deviation of the ionization balance of He I and He II from the corresponding LTE values becomes stronger and goes deeper at higher T_{eff} .

Figure (6.5) shows the departure coefficients of the lowest 15 LS states of He I and the ground state of He II as a function of τ_{5000} for T_{eff} of 15,000, 21,000, 25,000 and 29,000 K (assuming $\log g = 4.0$ & $\xi_t = 5.0 \text{ km s}^{-1}$). At $T_{\text{eff}} = 15,000 \text{ K}$, there is no departure from LTE of the ground state of He I through the entire photosphere. This is in agreement with the local nature of the photoionizing radiation field (see Figure 6.4). On the other side, there is a slight underpopulation of the ground state of He II between ≈ 0 and -4 in $\log \tau_{5000}$, which associated with overpopulation of He I excited states. The maximum overpopulation of low LS states of He I and maximum underpopulation of the He II ground state occurs at $\log \tau_{5000} \approx -2.5$. At

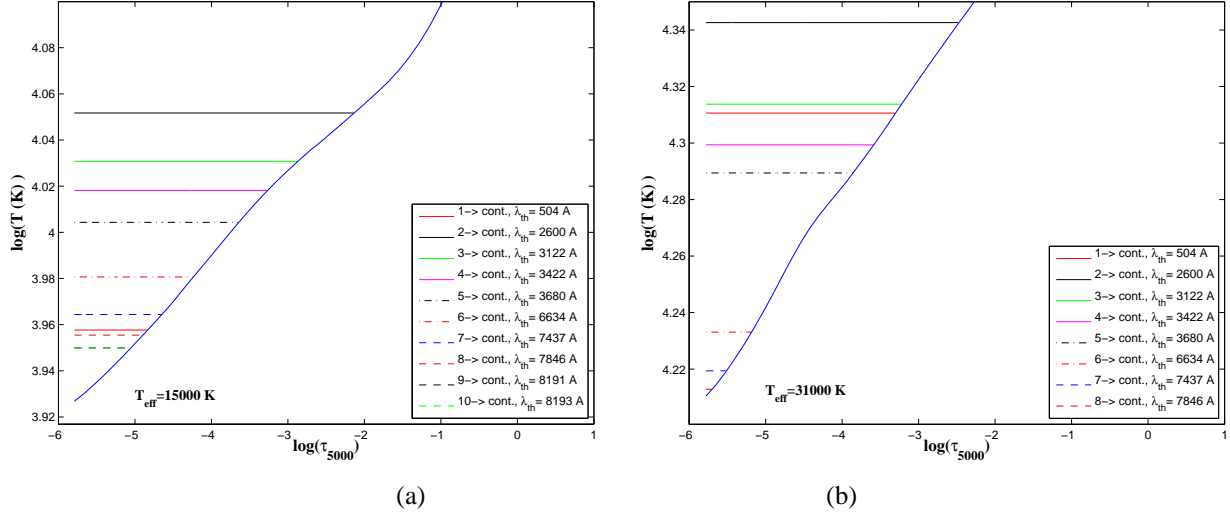


Figure 6.4: Panels (a) and (b) show T_{rad} of the photoionizing radiation at the threshold wavelength for the lowest 10 LS states of the He I atom as a function of τ_{5000} for T_{eff} of 15,000 K and 31,000 K respectively ($\log g = 4.0$ and $\xi_t = 5.0 \text{ km s}^{-1}$). The blue solid line represent the local electron temperature as a function of τ_{5000} .

$\log \tau_{5000} \approx -4$, all He I excited states become optically thin and show underpopulation, and there is an overpopulation of the ground state of He II which increases outward. The observed behaviour at higher effective temperatures can be interpreted in a similar way. Also, the ground state starts to underpopulate high in the atmosphere, $\log \tau_{5000} \approx -4.0$ for $T_{\text{eff}} = 21,000 \text{ K}$, where the underpopulation of the ground state starts deeper in the atmosphere as the photoionizing radiation field of the ground starts becomes optically thin at larger $\log \tau_{5000}$ values, as seen in Figure (6.4).

6.4.2 Equivalent Widths

The computed grids of the non-LTE equivalent widths and their ratios relative to the LTE values of He I $\lambda 4471 \text{ \AA}$ and $\lambda 6678 \text{ \AA}$ are listed in Table (6.4). The current results show that lines with wavelengths equal to or less than 5074 \AA show slight non-LTE strengthening, less than 10 %, for $T_{\text{eff}} < 25,000 \text{ K}$, similar to the observed behaviour of the He I $\lambda 4471 \text{ \AA}$ listed in the table. This behaviour agrees with the results of Auer & Mihalas (1973) and Dufton & McKeith (1980). However, departure from LTE becomes more important for higher effective

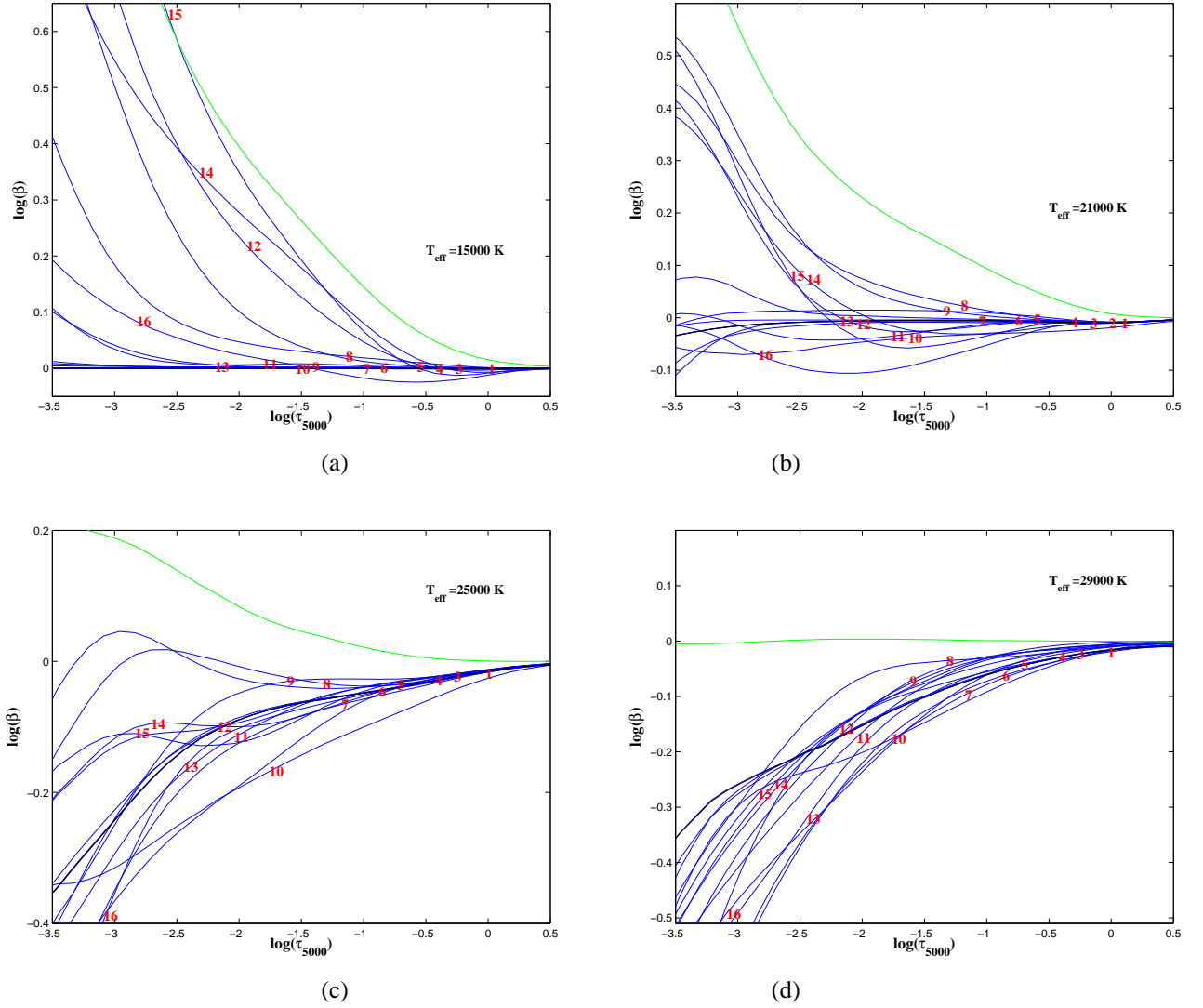


Figure 6.5: The non-LTE departure coefficients of the lowest 15 LS states of He I plus the ground level of He II (state number 104 represented by the green line) as a function of the optical depth at T_{eff} of 15000, 19000, 23000, and 29000 K, $\log g = 4.0$, $\xi_t = 5 \text{ km s}^{-1}$ and solar abundance.

temperatures. The He I $\lambda 5074 \text{ \AA}$ transition shows stronger non-LTE strengthening between 10 and 20 %, for $T_{\text{eff}} < 25,000 \text{ K}$, and then it shows stronger non-LTE changes for higher T_{eff} . Helium transitions with longer wavelengths show strong non-LTE effects over all effective temperatures, similar to the observed behaviour of $\lambda 6678 \text{ \AA}$ listed in Table (6.4).

Figure (6.6) and (6.7) show the computed non-LTE equivalent widths for six He I lines: $\lambda 6678$, $\lambda 7281$, $\lambda 7065$, $\lambda 5047$, $\lambda 5015$ and $\lambda 4471 \text{ \AA}$, as a function of effective temperature for

a microturbulent velocity of 0 km s^{-1} and gravities of 3.5, 4.0 and 4.5 dex. For comparison, the calculations of Leone & Lanzafame (1998) are also shown. Observed equivalent widths for the He I lines were taken from number of previous works that studied different samples over the whole spectral range of B-type stars: Leone & Lanzafame (1998), Leone & Lanzafame (1997), Wolff & Heasley (1982), and Gies & Lambert (1992).

Compared to Leone & Lanzafame (1998), the non-LTE equivalent widths of most of the He I lines agree well at lower effective temperatures, $< 20,000$ K, but the agreement at higher effective temperatures is not good. There are some exceptions, the He I λ 7065.0 Å line shows better agreement at higher temperatures. Also, our computed equivalent widths are generally higher than those of Leone & Lanzafame (1998). These differences could be due to differences in the atomic data, especially the Stark broadening constants as they adopted the calculations of Dimitrijević & Sahal-Bréchet (1990) while the procedure of Dimitrijević & Konjević (1986) was adopted in the current calculation. Both calculations of the Stark broadening constants differ significantly, as mentioned in section (6.3). In addition, the previous work of Leone & Lanzafame (1997) noted that the computed helium line profiles did not match the observed equivalent widths for main-sequence B-type stars. Their computation seemed to underestimate the equivalent widths, similar to the results of Auer & Mihalas (1973) and Dufton & McKeith (1980). In order to overcome this problem, Leone & Lanzafame (1997) empirically corrected their Stark broadening constants to match the observed equivalent widths of main-sequence B-type stars. Consequently, they were able to match the observed equivalent widths only in an ad-hoc way. On the other hand, our calculations were done in a consistent way without adopting such ad-hoc relation and we find acceptable agreement with the measured equivalent widths, in most cases, as shown in figures (6.6) and (6.7).

Also, Figures (6.6) and (6.7) show that the computed non-LTE equivalent widths increase only slightly with decreasing of gravity for lower effective temperatures, $\lesssim 20,000$ K, but then, increase strongly with gravity for higher temperatures, in most cases. It is important to note that part of the discrepancies between the observed equivalent widths and the computed ones

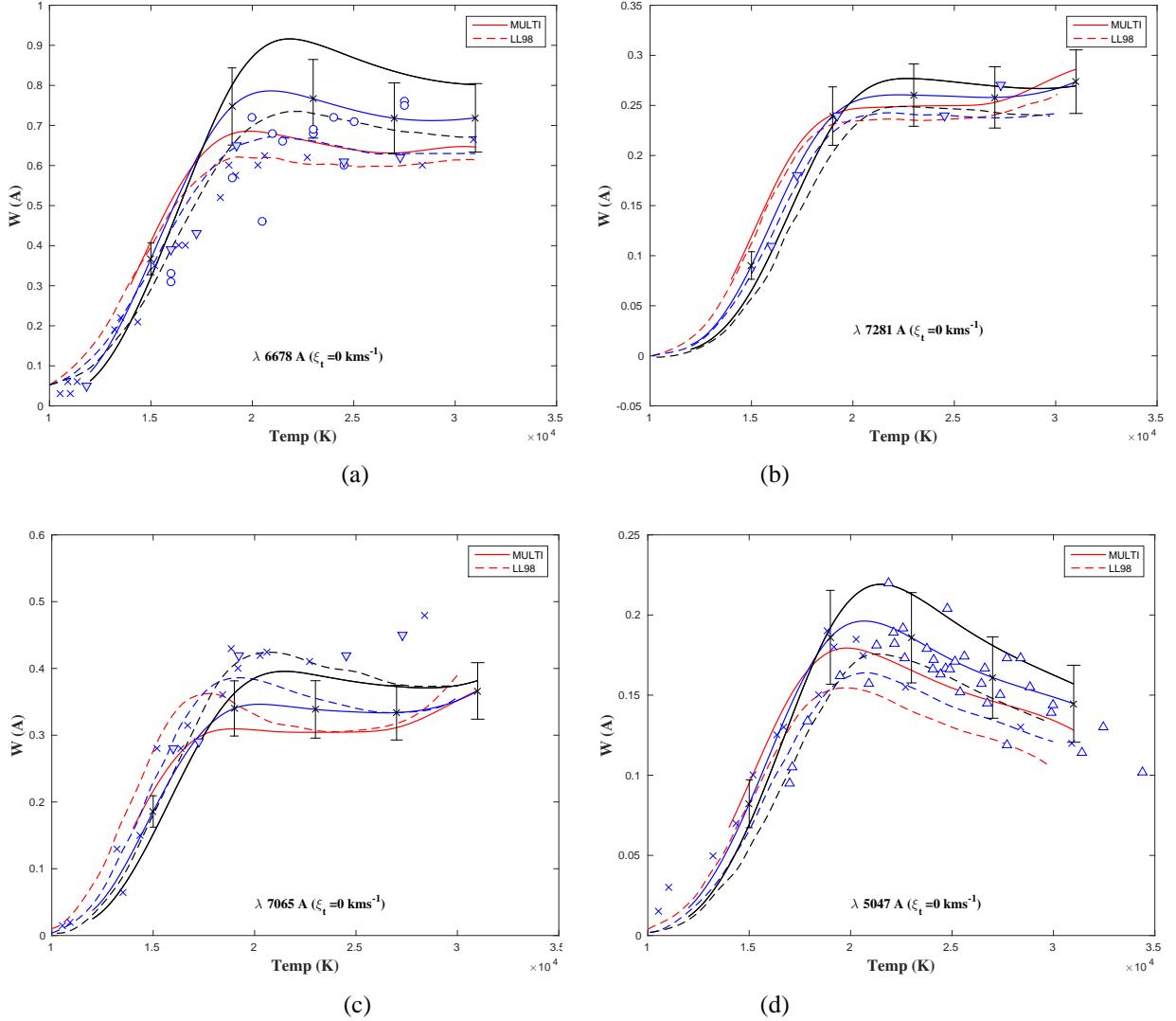


Figure 6.6: The computed non-LTE equivalent widths of the He I λ 6678, λ 7281, λ 7065 and λ 5047 Å lines, as a function of effective temperature for $\xi = 0.0 \text{ km s}^{-1}$ (solid lines), where the different colours represent different gravities: red ($\log g = 3.5$), blue ($\log g = 4.0$) and black ($\log g = 4.5$). The results of Leone & Lanzafame (1998) are added as dashed lines. The blue open circles represent measured equivalent widths from Wolff & Heasley (1982); the open triangles represent measured equivalent widths from the study of Gies & Lambert (1992); open inverted triangles represent measured equivalent widths from Leone & Lanzafame (1997); the crosses represent measured equivalent widths from the study of Leone & Lanzafame (1998). The error bars on MULTI results for $\log g = 4.0$ represents the uncertainty in the computed equivalent widths due to errors in the atomic data, 2σ as discussed in Section (6.5).

may reflect errors in the estimated effective temperatures for the stars that were included in these studies. Also, errors in the measured equivalent widths due to errors in continuum nor-

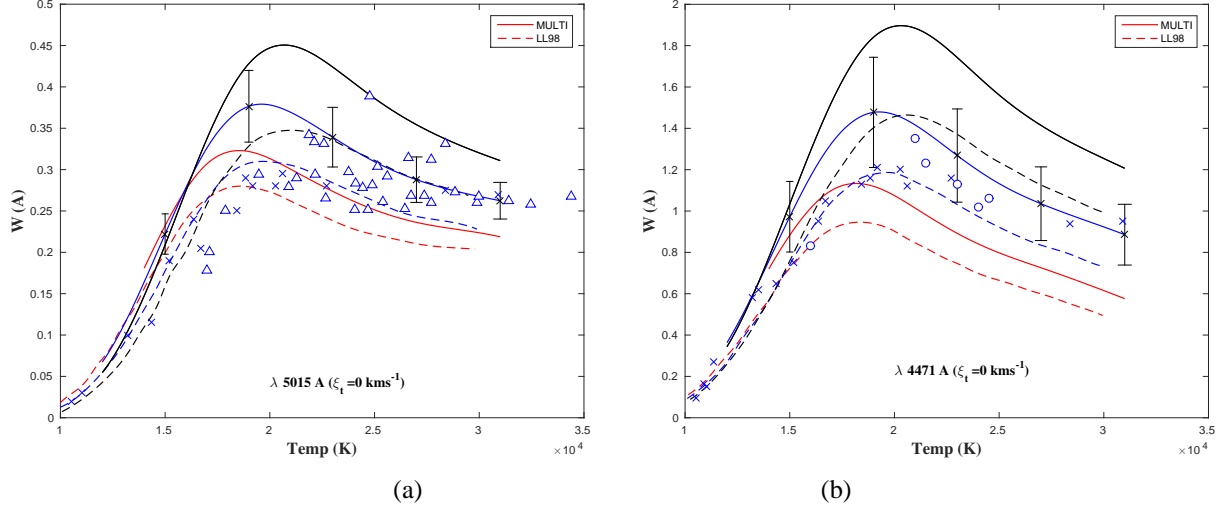


Figure 6.7: The same as Figure (6.6), but for the He I λ 5015 Å and λ 4471 Å lines.

malization and line blends could be another source of uncertainty (Jaschek et al. (1994); Leone & Lanzafame (1998)), due to their higher rotational velocities. B-type stars are rapid rotators with average projected rotational velocity ($v \sin i$) of $\approx 100 \text{ km s}^{-1}$ (Braganca, G. A., 2012). In addition, inclusion of He-weak and/or He-strong stars in the sample could contribute to the observed discrepancies between theory and observations.

The computed non-LTE equivalent width of He I λ 10830 Å is shown in Figure (6.8). This line is an important indicator of the accuracy of a He I line calculation because it is very sensitive to departures from LTE. This line has $h\nu \ll kT$ and its line source function is very sensitive to the departure coefficients of its upper and lower levels (Przybilla, 2005). Previous studies like Auer & Mihalas (1973) and Leone & Lanzafame (1998) failed to reproduce the measured equivalent width of this line due to errors in the atomic data. Figure (6.8) compares the current results to Przybilla (2005) and the results of Leone & Lanzafame (1998). This figure shows that the results of Leone & Lanzafame (1998) are lower than the observed equivalent widths of this line and their calculations show strong emission for effective temperatures higher than $\approx 22,000 \text{ K}$. On the other hand, the current results and those of Przybilla (2005) present a much better matching to the observed equivalent widths. However, the current results do not show such strong emission at the high effective temperatures as seen in Przybilla

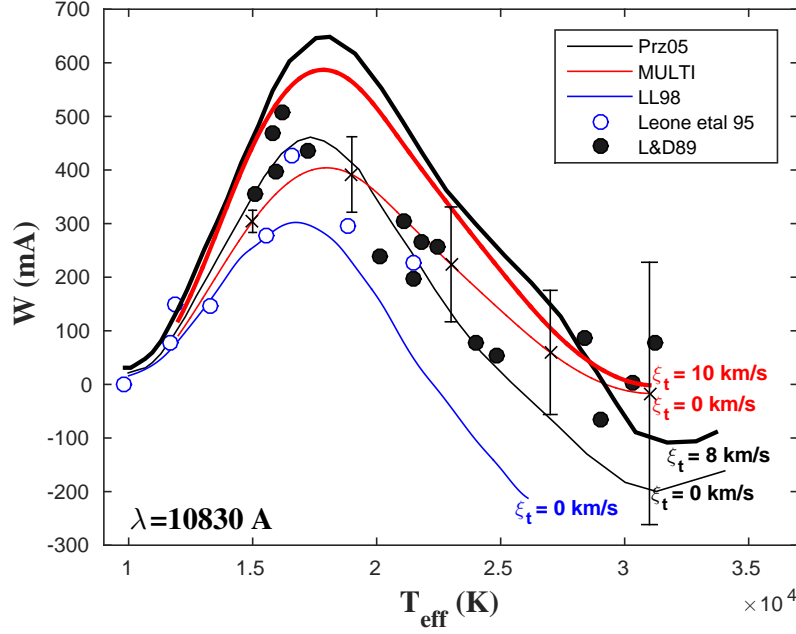


Figure 6.8: The computed non-LTE equivalent width of the He I λ 10830 Å line for $\log g = 4.0$ and microturbulent velocities of 0 km s^{-1} (thin red line) and 10 km s^{-1} (bold red line). The error bars show the uncertainties of the computed equivalent widths due to errors in the atomic data. The thin black and bold black lines represent the computed non-LTE equivalent widths of Przybilla (2005) for $\log g = 4.0$ and microturbulent velocities of 0 and 8 km s^{-1} , respectively. The blue lines represent the results of Leone & Lanzafame (1998) for $\log g = 4.0$ and $\xi_t = 0 \text{ km s}^{-1}$. Open and solid circles represent measured equivalent widths of this lines Leone et al. (1995) and Lennon & Dufton (1989), respectively.

(2005). Such differences may be attributed to differences in the atomic data, especially the collisional strengths of excitation and ionization and the damping constants. In the current work, the procedure of Seaton (1962) was used to compute the collisional strengths of ionization, while they adopted the procedure of Mihalas & Stone (1968). Also, Przybilla (2005) followed the theory of Allen (1973) to compute the line broadening. On the other hand, they adopted the energies of the helium LS states, the photoionization cross-sections and the f -values of the bound-bound radiative transitions from the same sources as the current calculation. Finally, the different codes used to perform the calculations: Przybilla (2005) used DETAIL and SURFACE (Giddings, 1981, Butler & Giddings, 1985). Finally, it should be noted that the current results and those of Przybilla (2005) agree within the error estimates of the current calculations as discussed in the next section.

Table 6.4: MULTI results for He I λ 4471 and λ 6678 Å (Equivalent widths, W_λ , are in mÅ)

$T_{\text{eff}}, \log g$	λ 4471 Å						λ 6678 Å					
	$\xi = 0 \text{ km s}^{-1}$		$\xi = 5 \text{ km s}^{-1}$		$\xi = 10 \text{ km s}^{-1}$		$\xi = 0 \text{ km s}^{-1}$		$\xi = 5 \text{ km s}^{-1}$		$\xi = 10 \text{ km s}^{-1}$	
	W_λ	W/W_*	W_λ	W/W_*	W_λ	W/W_*	W_λ	W/W_*	W_λ	W/W_*	W_λ	W/W_*
15000 , 3.5	883.2	1.07	903.8	1.08	951.1	1.09	410.4	1.51	449.4	1.55	535.2	1.62
17000 , 3.5	1100.3	1.05	1124.2	1.05	1180.7	1.07	594.4	1.37	645.3	1.42	762.1	1.50
19000 , 3.5	1119.6	1.03	1143.2	1.03	1200.2	1.05	679.3	1.29	732.5	1.33	857.9	1.41
21000 , 3.5	1013.5	1.05	1035.8	1.05	1091.0	1.07	679.2	1.30	730.3	1.34	852.7	1.41
23000 , 3.5	891.9	1.10	913.2	1.10	966.3	1.11	658.6	1.38	706.9	1.42	824.1	1.48
25000 , 3.5	797.8	1.17	818.0	1.17	869.1	1.18	639.3	1.50	684.9	1.53	796.7	1.59
27000 , 3.5	725.6	1.26	744.7	1.26	793.8	1.27	631.3	1.62	674.3	1.65	781.1	1.70
29000 , 3.5	653.2	1.46	671.7	1.46	719.6	1.46	641.9	1.85	682.7	1.87	785.2	1.90
31000 , 3.5	576.1	1.83	594.3	1.83	641.8	1.82	646.2	2.25	684.9	2.26	783.5	2.28
15000 , 4.0	972.5	1.07	988.0	1.07	1022.9	1.08	367.3	1.46	395.7	1.49	457.6	1.54
17000 , 4.0	1328.1	1.05	1348.3	1.06	1394.6	1.07	592.3	1.36	633.8	1.40	728.7	1.46
19000 , 4.0	1477.4	1.03	1498.2	1.04	1547.4	1.05	747.4	1.27	793.6	1.30	902.4	1.37
21000 , 4.0	1415.7	1.03	1435.4	1.04	1482.9	1.05	786.3	1.25	832.0	1.28	941.4	1.34
23000 , 4.0	1268.5	1.06	1286.9	1.06	1332.2	1.07	766.5	1.29	810.0	1.32	915.4	1.37
25000 , 4.0	1132.7	1.10	1149.9	1.10	1193.3	1.11	738.3	1.38	779.4	1.41	880.1	1.46
27000 , 4.0	1035.4	1.15	1051.7	1.15	1093.0	1.16	718.2	1.48	756.9	1.50	852.9	1.55
29000 , 4.0	959.2	1.22	974.5	1.23	1013.9	1.23	712.2	1.59	748.7	1.61	840.3	1.65
31000 , 4.0	885.7	1.38	900.3	1.38	938.3	1.38	719.0	1.80	753.4	1.81	840.7	1.85
15000 , 4.5	1034.1	1.06	1045.1	1.06	1069.0	1.06	320.8	1.37	339.4	1.39	379.6	1.42
17000 , 4.5	1527.2	1.05	1543.7	1.05	1580.1	1.06	574.6	1.32	605.9	1.34	677.0	1.39
19000 , 4.5	1840.8	1.04	1859.5	1.04	1901.8	1.05	800.7	1.25	838.6	1.27	927.5	1.32
21000 , 4.5	1883.9	1.03	1902.1	1.03	1944.2	1.04	907.8	1.21	947.2	1.23	1041.0	1.27
23000 , 4.5	1742.5	1.03	1759.2	1.04	1799.2	1.04	905.7	1.21	943.8	1.23	1035.8	1.28
25000 , 4.5	1561.3	1.06	1576.6	1.06	1614.1	1.06	868.9	1.27	905.0	1.29	993.2	1.33
27000 , 4.5	1414.4	1.09	1428.6	1.09	1464.0	1.10	835.1	1.34	869.0	1.36	953.2	1.40
29000 , 4.5	1302.7	1.13	1315.8	1.13	1349.1	1.14	812.0	1.42	843.9	1.44	923.8	1.48
31000 , 4.5	1206.7	1.21	1218.9	1.21	1250.4	1.22	802.0	1.56	832.0	1.57	907.7	1.61

6.5 The Accuracy of the Predicted non-LTE Equivalent Widths

Uncertainties in the computed equivalent widths due to errors in the atomic data included in the helium atom model were obtained following the Monte Carlo-MULTI analysis as the N II non-LTE line calculations in Subsection (5.6). For this analysis, 150 random realizations of the helium atom were generated with the atomic data changed within the same uncertainties as those of the N II atom (see Table (5.9)).

The analysis was performed for five effective temperatures between 15,000 K and 31,000 K with a step of 2000 K, and three gravities equal to 3.5, 4.0 and 4.5. All calculations were performed for a microturbulence of 5.0 km s^{-1} and the solar helium abundance. The average values of the computed equivalent widths and their dispersion are listed in Table (6.5), where the uncertainty in the computed equivalent width due to errors in the atomic data is set equal to twice the standard deviation. The uncertainties are shown as error bars in Figures (6.6), (6.7) and (6.8). The predicted uncertainties for the computed equivalent widths of the He I λ 4471, λ 5015, λ 5047, λ 6678, λ 7065 and λ 7281 Å lie between 10 and 20 %. However, for the He I λ 10830 Å, the uncertainty is much high due to the higher sensitivity for non-LTE effects which increases with T_{eff} . In general, the uncertainties of the non-LTE equivalent widths of He I lines due to errors in atomic data are larger than those of the N II lines, reflecting the higher sensitivity of the former for variations in the atomic data.

Table 6.5: Results of Monte-Carlo MULTI analysis for selected He I lines at $\xi_t = 5 \text{ km s}^{-1}$ (Equivalent widths, W_λ , are in mÅ and the uncertainties in %)

$T_{\text{eff}}(K) \& \log g$	$\lambda 4471 \text{ Å}$		$\lambda 5015 \text{ Å}$		$\lambda 5047 \text{ Å}$		$\lambda 6678 \text{ Å}$		$\lambda 7065 \text{ Å}$		$\lambda 7281 \text{ Å}$		$\lambda 10830 \text{ Å}$	
	$\langle W_\lambda \rangle$	2σ	$\langle W_\lambda \rangle$	2σ	$\langle W_\lambda \rangle$	2σ	$\langle W_\lambda \rangle$	2σ	$\langle W_\lambda \rangle$	2σ	$\langle W_\lambda \rangle$	2σ	$\langle W_\lambda \rangle$	2σ
15000.0 and 350.0	903.0	16.83	249.3	9.06	100.2	15.86	446.8	9.11	236.9	11.66	130.0	14.10	409.5	7.43
19000.0 and 350.0	1149.1	17.22	350.2	9.11	190.6	13.34	733.7	10.47	346.4	11.70	271.1	11.79	378.0	27.48
23000.0 and 350.0	917.3	16.40	297.5	8.15	176.3	13.45	707.6	10.11	335.2	11.94	276.7	11.70	169.3	84.79
27000.0 and 350.0	747.4	15.27	254.9	7.55	153.6	14.44	674.4	9.47	337.6	11.61	275.6	11.66	5.3	3162.21
31000.0 and 350.0	596.7	13.24	234.0	6.61	132.8	16.00	684.6	8.41	392.0	10.32	305.4	11.11	10.6	1529.45
15000.0 and 400.0	983.4	17.55	232.8	10.97	84.7	18.17	390.9	10.88	197.0	12.64	95.5	15.26	344.6	6.80
19000.0 and 400.0	1503.6	18.04	400.7	11.51	196.2	15.73	793.2	12.88	371.2	12.14	264.4	12.18	444.3	17.98
23000.0 and 400.0	1292.0	17.77	361.4	10.63	195.6	15.16	810.1	12.81	366.2	12.69	285.6	11.96	256.1	47.84
27000.0 and 400.0	1054.8	17.21	305.6	9.55	167.7	15.77	756.2	12.26	356.9	12.29	278.9	11.85	74.6	194.15
31000.0 and 400.0	902.3	16.59	277.1	8.44	149.2	16.61	752.2	11.89	386.5	11.55	291.4	11.59	-10.4	-1451.26
15000.0 and 450.0	1036.4	17.91	214.7	12.72	70.1	20.22	333.3	12.79	157.0	13.87	67.4	16.57	274.5	6.84
19000.0 and 450.0	1861.5	18.46	446.8	13.57	198.4	18.23	835.0	15.05	386.3	13.06	247.8	13.22	484.3	12.78
23000.0 and 450.0	1764.7	18.45	443.7	13.12	221.2	17.32	942.4	15.29	412.7	13.97	299.0	12.89	369.6	27.79
27000.0 and 450.0	1432.2	18.16	370.5	11.99	186.6	17.59	867.1	14.83	391.6	13.52	287.8	12.69	185.6	64.38
31000.0 and 450.0	1221.3	17.87	324.0	10.99	160.7	18.19	829.5	14.55	397.3	13.01	284.7	12.59	50.9	255.08

Chapter 7

Gravitational Darkening

7.1 Introduction

The temperature and gravity on the surface of a rotating star are dependent on its rotation rate and the latitude through the mathematical expressions mentioned in this part. In this chapter, the procedure used to account for gravitational darkening effects on the computed profiles will be explained, and a number of lines of interest (e.g. He I 6678 Å, Mg II 4482 Å) will be discussed.

7.2 Gravitational Darkening Assuming Solid Body Rotation

This section is based mainly on Maeder (2009). von Zeipel (1924) showed that rotating stars cannot be in hydrostatic and radiative equilibrium at the same time because rotation will lead to an oblate figure of the star and, as a consequence, the temperature gradient toward the equator will be shallower than that toward the pole, and the equator will be cooler. For a uniformly rotating star, the radiative flux is given by

$$\mathbf{F}(\omega, \theta) = -\chi \nabla T(\omega, \theta) , \quad (7.1)$$

where χ is the radiative conductivity, given by $\chi = \frac{4a c T^3}{3\kappa \rho}$ where a is the radiative constant, $a = 4\sigma/c$, σ is the Stefan-Boltzmann constant, c is the speed of light, κ is the Rossland mean

opacity. In this expression, ω is the angular rotation rate in rad/s (assuming solid-body rotation) and θ is the colatitude ($\theta = 0^\circ$ at the pole). In the case of a solid-body rotation, the equipotential surfaces coincidence with the isobar surfaces. As a consequence, Equation (7.1) can be written as

$$\mathbf{F}(\omega, \theta) = -\chi \left(\frac{d T}{d P} \right) \nabla P(\omega, \theta) . \quad (7.2)$$

In hydrostatic equilibrium,

$$\frac{1}{\rho} \nabla P = -\nabla \psi \equiv \mathbf{g}_{\text{eff}} , \quad (7.3)$$

where ψ is the total (gravitational and centrifugal) potential and is given by

$$\psi(\omega, \theta) = \varphi + V , \quad (7.4)$$

where φ is the gravitational potential,

$$\varphi = -\frac{GM_r}{r} , \quad (7.5)$$

and V is the centrifugal potential,

$$V = -\frac{1}{2} \omega^2 r^2 \sin^2 \theta . \quad (7.6)$$

Note that $r \sin \theta$ is the distance of the point (r, θ) from the rotation axis. The stellar luminosity of a rotating star could be obtained by integrating the above equation over the entire stellar surface. Using the StefanBoltzmann law, $F(\omega, \theta) = \sigma T_{\text{eff}}(\omega, \theta)^4$, we can get the relation between the local effective temperature and the local effective gravity,

$$T_{\text{eff}}(\omega, \theta) = \left(\frac{1}{4\pi\sigma G M_*} \right)^\beta [g_{\text{eff}}(\omega, \theta)]^\beta , \quad (7.7)$$

with $\beta = 1/4$, where $M_* = M \left(1 - \frac{\omega^2}{2\pi G \bar{\rho}_M} \right)$ and $\bar{\rho}_M$ is the average stellar density given by $\bar{\rho}_M = M/V$ of a star with mass M and volume V . More details are provided by Maeder (2009). The

effective gravity is given by

$$g_{\text{eff}} = \left[\left(-\frac{GM}{R^2} + \omega^2 R(\theta) \sin^2 \theta \right)^2 + \left(\omega^2 R(\theta) \sin \theta \cos \theta \right)^2 \right]^{1/2}, \quad (7.8)$$

assuming the polar radius is constant and the total potential, ψ , is constant on the stellar surface (Collins, 1966). The radial distance to a point on the surface of a distorted star could be obtained by equating equation 7.4 with its value in the pole, $-GM/R_p$, and rearranging the equation as follows,

$$R^3(\theta) - \frac{2GM_r}{\omega^2 \sin^2 \theta R_p} R(\theta) - \frac{2GM_r}{\omega^2 \sin^2 \theta} = 0. \quad (7.9)$$

The above equation can be solved analytically, and the solution is as follows

$$R(\theta) = \left(\frac{-3R_p}{\omega_{\text{frac}} \sin \theta} \right) \cos \left(\frac{\arccos(\omega_{\text{frac}} \sin \theta) + 4\pi}{3} \right), \quad (7.10)$$

where $\omega_{\text{frac}} = \omega/\omega_{\text{crit}}$ (McGill et al., 2011). The rotational velocity at which the centrifugal force is equal to the gravitational force, i.e. $g_{\text{eff}}=0$, is called the critical velocity, v_{crit} . The critical angular velocity at the equator, $\theta = \pi/2$, can be obtained from equation (7.8) by setting g_{eff} equal to zero,

$$\omega_{\text{crit}} = \left(\frac{GM}{R_{\text{e,crit}}^3} \right)^{1/2} = \left(\frac{8GM}{27R_p^3} \right)^{1/2}, \quad (7.11)$$

as $R_{\text{e,crit}} = 3/2R_p$. Also the stellar critical velocity at the equator can be obtained by

$$v_{\text{crit}} = \omega_{\text{crit}} R_{\text{e,crit}} = \left(\frac{2GM}{3R_p} \right)^{1/2}. \quad (7.12)$$

Thus rotating stars will both be non-spherical and have a T_{eff} that varies with latitude, with a dark equator and bright pole. These effects have direct, interferometric confirmation for nearby stars (van Belle, 2012). Note, however, such observations suggest $\beta = 1/4$, the canonical solution, is not the best fit to β , and the value of the power law index in equation (7.7), β , is a matter of debate. The recent work of Espinosa Lara & Rieutord (2011) showed that its

value was overestimated, and a value lower than 0.25 is required to match the interferometric observations which means a lower contrast in temperature and gravity between the stellar poles and stellar equators. This overestimation resulted from the assumption of barotropicity that was adopted by von Zeipel (1924), where density and pressure are constant over equipotential surfaces. This is a crude assumption that is valid in the case of slowly rotating objects, while for a rapidly rotating stars with a radiative envelope the isobar surfaces and equipotential surfaces do not coincide, which is known as baroclinicity (Espinosa Lara & Rieutord, 2011).

Consequently, Espinosa Lara & Rieutord (2011) tried solving the radiative flux but in a way which is less constrained than von Zeipel's treatment, and can match the observed dispersion of the values of β . Espinosa Lara & Rieutord (2011) started their solution from the equation of radiative flux under the assumption of hydrostatic equilibrium, Equation 7.2, similar to von Zeipel's standard method, but in their case the factor $\rho \chi \frac{dT}{dP}$ was not constant over equipotential surface. Instead, they assumed that the flux within the envelope could be expressed by the following relation,

$$\mathbf{F} = -f(r, \theta) \mathbf{g}_{\text{eff}}, \quad (7.13)$$

where $f(r, \theta)$ is an arbitrary function of radius and colatitude which satisfy the boundary condition $\eta = \frac{L}{4\pi G M}$ at $r = 0$. Because there is no heat generation in the envelope, we can write $\nabla \cdot \mathbf{F} = 0$, which implies

$$\mathbf{g}_{\text{eff}} \cdot \nabla f + f \nabla \cdot \mathbf{g}_{\text{eff}} = 0. \quad (7.14)$$

The temperature on the stellar surface according to the new solution under the assumptions of Roche model and solid body rotation is given by

$$T_{\text{eff}} = \left(\frac{L}{4\pi G M} \right)^{1/4} \sqrt{\frac{\tan \vartheta}{\tan \theta}} g_{\text{eff}}^{1/4}, \quad (7.15)$$

where ϑ is related to θ by

$$\frac{1}{3}\omega^2\tilde{r}^3\cos^3\theta + \cos\theta + \ln\tan\frac{\theta}{2} = \cos\vartheta + \ln\tan\frac{\vartheta}{2},$$

where $\tilde{r} = r/r_{eq}(\omega)$. This equation tends to the Von Zeipel Formula at low rotational rates when $\vartheta = \theta$. Also, the ratio of the equatorial to the polar temperatures is given by

$$\frac{T_{\text{eff}}^e}{T_{\text{eff}}^p} = \sqrt{\frac{2}{2+\omega^2}}(1-\omega^2)^{1/12}e^{-\frac{4}{3}\frac{\omega^2}{(2+\omega^2)^3}}. \quad (7.16)$$

More details are provided by Espinosa Lara & Rieutord (2011).

Figure (7.1) compares the Espinosa Lara & Rieutord (2011) gravitational darkening formalism to the standard Collins' implementation of von Zeipel's law with $\beta = 1/4$. Each panel shows the expected distribution of the emitted continuum emission at $\lambda = 5000 \text{ \AA}$ from each surface area element of a rotating star computed using the Planck function as a function of the local effective temperature. The calculations were performed for B3V star assuming rotational velocity, equal to 95.0 % of its critical velocity equal to $\approx 450.0 \text{ km s}^{-1}$. The star has $R_{eq}=6.87$ and $R_{eq}/R_p=1.43$, and the images are reproduced for a viewing inclination of 70° . The figure shows that the standard von Zeipel's relation results in a larger contrast in the effective temperature between the pole and the equator compared with the formulation of Espinosa Lara & Rieutord (2011). In the figure, the local temperature varies between $\approx 11,000 \text{ K}$ at the equator and $\approx 21,000 \text{ K}$ at the pole using Collins von Zeipel approach, and between $\approx 13,500 \text{ K}$ at the equator and $\approx 20,000 \text{ K}$ at the pole using the new Espinosa Lara & Rieutord (2011) formalism.

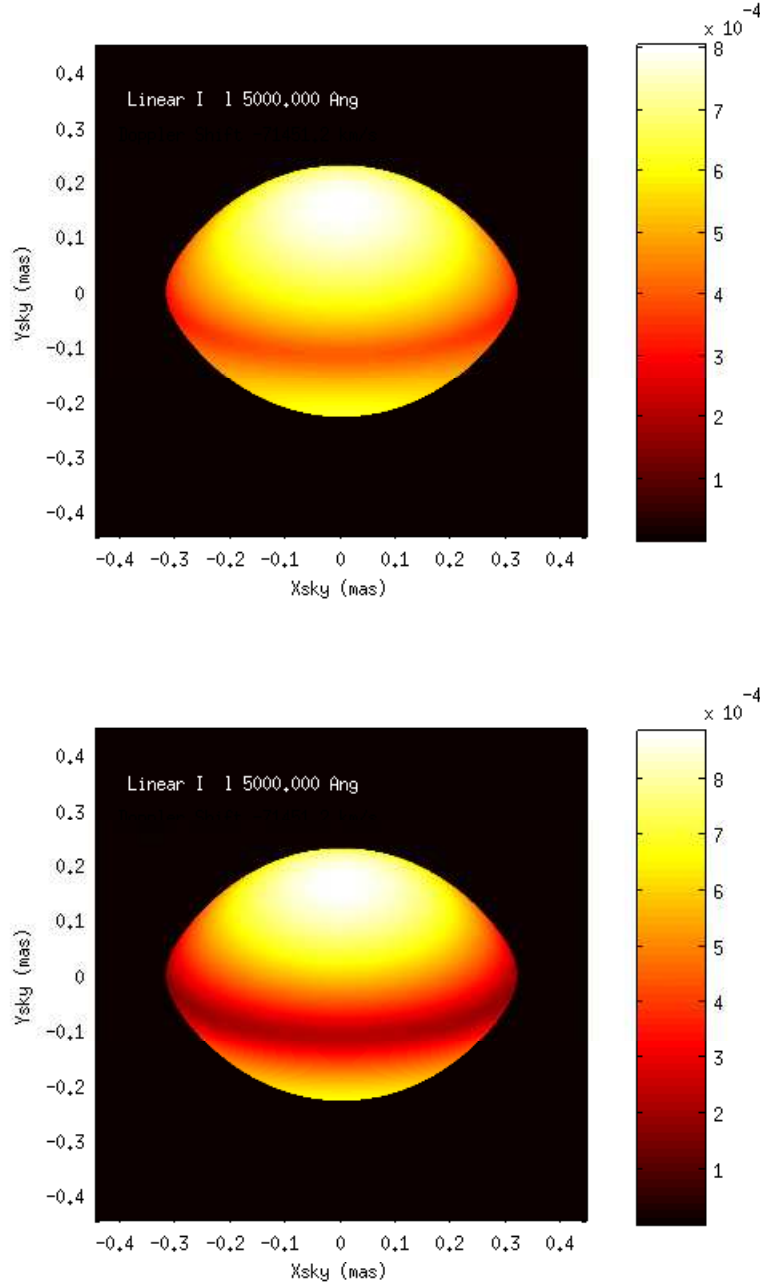


Figure 7.1: The distribution of continuum emission at 5000 Å computed using the Planck function at the local effective temperatures over the surface of a rotating, B3V type stellar model using von Zeipel's relation (lower panel) versus the treatment of Espinosa Lara & Rieutord (2011) (upper panel).

7.3 Gravitational Darkening Effects on Spectral Lines

To compute the effects of gravitational darkening on stellar spectra and on the measured equivalent widths, synthetic spectra for rotating stars were computed by dividing the (distorted)

stellar surfaces into small elements of area as function of the radial distance and the colatitude. The local emission from every element of area was estimated using a plane parallel atmosphere at the local temperature and gravity, approximated to the closest 200 K for effective temperature and 0.1 dex for gravity. Then the total emitted radiation from the stellar hemisphere seen by the observer at a specific wavelength was obtained by summing the local emitted radiation using a discretized form of

$$L_{\lambda}(i, \omega) = 2 \int_0^{\pi/2} d\phi \int_0^{\pi} R^2(\theta) I_{\mu\nu} \frac{|\mu|}{\cos(\delta)} \sin(\theta) d\theta, \quad (7.17)$$

where $R(\theta)$ is the radial distance, Equation (7.10), ϕ is the azimuthal angle, μ is the cosine of the viewing inclination angle, δ is angle between the radial direction and the normal to the surface, and $I_{\mu\nu}$ is the intensity of the emitted radiation at frequency ν from this element of area of the stellar surface seen at a viewing angle of μ (Maeder & Peytermann, 1970). More details on the calculation procedure are provided by McGill (2013).

7.3.1 Gravitational Darkening Effects on N II λ 3995Å

Panels (a) and (b) of Figure (7.2) show the predicted equivalent width of N II 3995 Å calculated from gravitationally darkened spectra of stars rotating at 99 % of their critical rotational velocities as a function of the stellar effective temperatures of the parent, non-rotating star with stellar gravity of 4.0, microturbulent velocity of 5.0 km s⁻¹, and solar nitrogen abundance. Three inclination angles are shown, 1, 60 and 90°. The left-hand panels show the results assuming the von Zeipel approach (Collins, 1965) and the right-hand panels, using the Espinosa Lara & Rieutord (2011) formulation. The figure also shows the predicted equivalent widths of the parent, non-rotating stars at solar nitrogen abundance, and ± 0.1 dex of the solar nitrogen abundance.

As shown in the figure, the non-LTE equivalent width increases with T_{eff} until they reach a maximum near $T_{\text{eff}} \approx 24,000$ K, then they decrease for higher T_{eff} 's because of the shift of

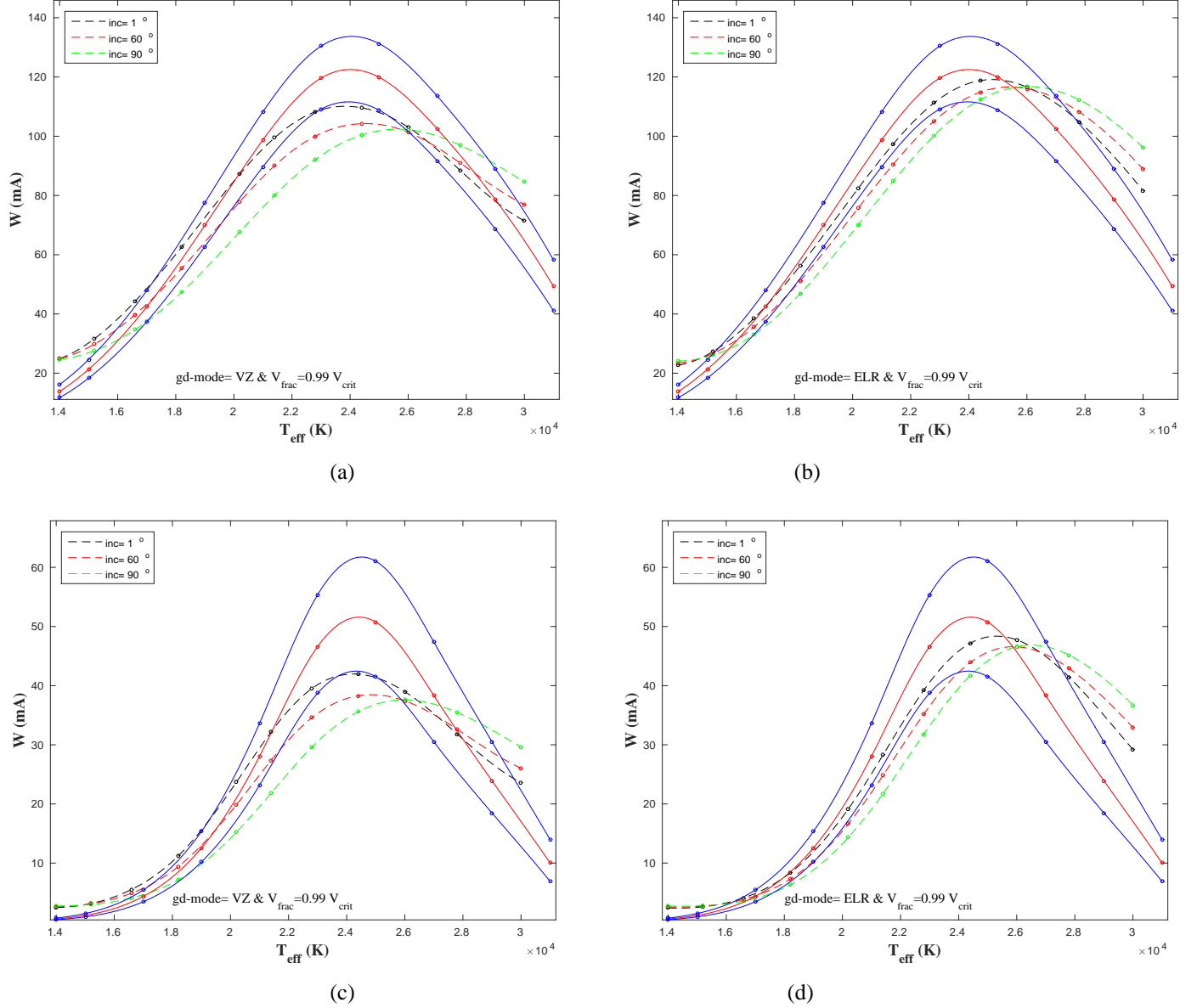


Figure 7.2: Panels (a) and (b) of Figure show the predicted equivalent widths of the N II 3995 Å transition including the gravitational darkening effects as a function of the stellar effective temperature of non-rotating stars with the same mass, for $\log(g) = 4.0$, $\xi_t = 5 \text{ km s}^{-1}$, rotational velocities equal to 0.99 of their critical velocities, and three inclinations angles (dashed lines). Panels (c), and (d) are the same, but for N II 6482 Å line. The equivalent widths of the non-rotating case computed assuming solar nitrogen abundance are represented by red lines, while blue lines represent equivalent widths of the non-rotating case computed assuming nitrogen abundance equal to ± 0.1 dex of the solar value. Note that the standard approach of von Zeipel (1924) was adopted in the calculations of the left-hand panels, while the approach of Espinosa Lara & Rieutord (2011) was adopted in the calculations of the right-hand panels.

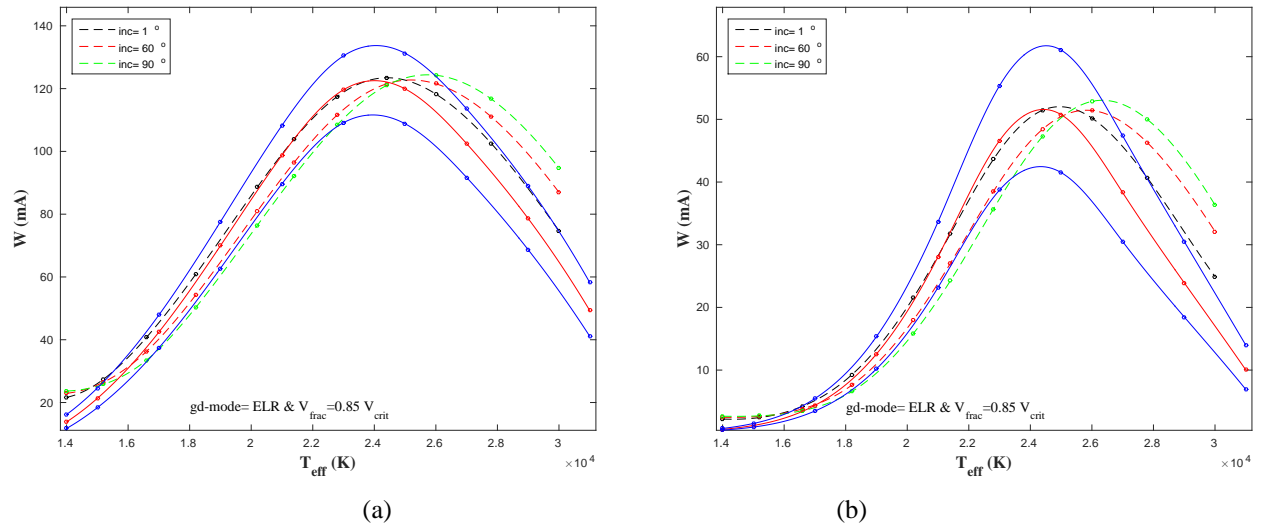


Figure 7.3: The same as Figure (7.2), for $v_{\text{frac}} = 0.85$. The approach of Espinosa Lara & Rieutord (2011) was adopted for the calculations.

the nitrogen ionization balance to N III, see Section (5.4.2). The observed behaviour of the equivalent widths for rotating stars depends on the inclination. For $T_{\text{eff}} \leq 24,000$ K, below the peak equivalent width, the equivalent widths increase with the decrease of the inclination. For pole on stars ($i = 0^\circ$), the major contribution comes from the hot polar regions which strengthens the lines compared to non-rotating stars. On the contrary, for edge on stars ($i = 90^\circ$), the major contribution comes from the cool equatorial regions that weakens the line profiles. This behaviour is reversed at higher T_{eff} where the N II line strengths now decrease for increasing temperature.

Note that the gravitational darkening effects estimated by adopting von Zeipel's treatment, in the left-hand panels are significantly different from those estimated by formalism of Espinosa Lara & Rieutord (2011). The latter approach gives a smaller temperature contrast between the pole and equator and higher temperatures in the equatorial regions (Section 7.2). Figure (7.2) does show that the computed equivalent widths of rotating stars assuming the solar nitrogen abundance go outside the equivalent widths of non-rotating stars computed at nitrogen abundances ± 0.1 dex of the solar value. However, it should be kept in mind that these figures are computed assuming the most extreme rotation, $v_{\text{frac}} = 0.99$. Figure 7.3 shows the behaviour

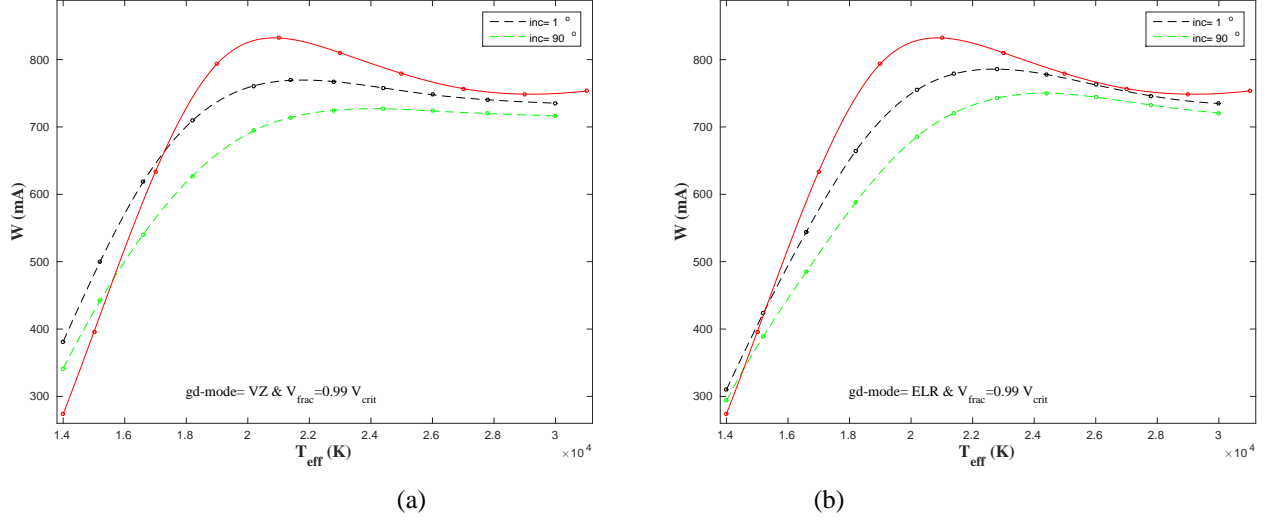


Figure 7.4: Gravitational darkening effects on the equivalent width of the He I 6678 Å computed using von Zeipel’s treatment (right panel) and Espinosa Lara & Rieutord (2011) treatment (left panel) as a function of T_{eff} at two inclination angles, dashed lines. Red lines represent the equivalent widths of the non-rotating case.

at the more realistic value of $v_f = 0.85$ or 85% of the critical rotation. A key result of this section is that both $\lambda 3995$ and $\lambda 6482$, the rotating equivalent widths be within ± 0.1 dex of the non-rotating widths for the most probable inclination (i.e. 60°) at all but the highest T_{eff} considered.

7.3.2 Gravitational Darkening effects on He I $\lambda 6678\text{\AA}$

Figure (7.4) shows the predicted equivalent widths of He I $\lambda 6678\text{\AA}$ for stellar models rotating at 99.0 % of their critical rotational velocities seen at two different inclination angles, 1° and 90° , that is, pole-on and edge on respectively. The calculations were performed for the two gravitational darkening models discussed in previous section, VZ and ELR.

Panel (a) shows that for pole-on stars with $T_{\text{eff}} \lesssim 18,000$ K gravitational darkening tends to strengthen the predicted equivalent widths of He I 6678 Å. At this temperature range the line strength increases rapidly with temperature, and as a consequence, the line strengthening in the radiation emergent from the hot, polar regions dominates over the the line weakening from the cool, equatorial regions. This behaviour results in overall line strengthening of the spectral

profiles.

For higher effective temperatures, $T_{\text{eff}} > 18,000$ K, the helium line strengths are nearly flat with T_{eff} and consequently, the line weakening in the equatorial regions (with the larger area due to the oblateness of a rotating star) dominates over the line strengthening in the polar regions. The figure also shows that the equivalent widths of rotating stars seen at high inclination angles, $i = 90^\circ$, are weaker than those computed for rotating models seen at low inclination angles, $i = 1^\circ$. The observed line weakening in both cases can be explained in the same manner as discussed before for the pole-on case. However, because the equatorial regions of these stars lie in the plane of the sky, the overall weakening of the line is stronger and starts at cooler effective temperatures.

The predicted gravitational effects on the strength of He I λ 6678 Å for the calculations performed by adopting the treatment of Espinosa Lara & Rieutord (2011), panel (b), can be explained in the same general way. However, they are weaker than those obtained by adopting von Zeipel's treatment due to the large amount of the gravitational darkening effects predicted by the latter.

7.3.3 Gravitational Darkening effects on Mg II λ 4481 Å

Similarly, the gravitational darkening effects on the observed strength of Mg II λ 4481.2 Å line were investigated, shown in Figure (7.5). To represent the stellar profile, the non-LTE calculations of Sigut & Lester (1996) were adopted. For this line, the gravitational darkening effects tend to strengthen the equivalent widths of this line as shown in the figure.

The expected gravitational darkening effects on the Mg II λ 4481 Å line can be explained in a similar manner to those of the He I λ 6678 Å line. However, an important difference is that the strengths of Mg II 4481 Å weakens with T_{eff} over the entire range of the B-stars. For pole on stars, the line strengthening in the cool, equatorial regions with the larger area dominates over the line weakening in the hot polar regions, resulting in overall line strengthening. This behaviour is largest for stars seen equator-on, i.e. $i = 90^\circ$. Also, the difference in the gravita-

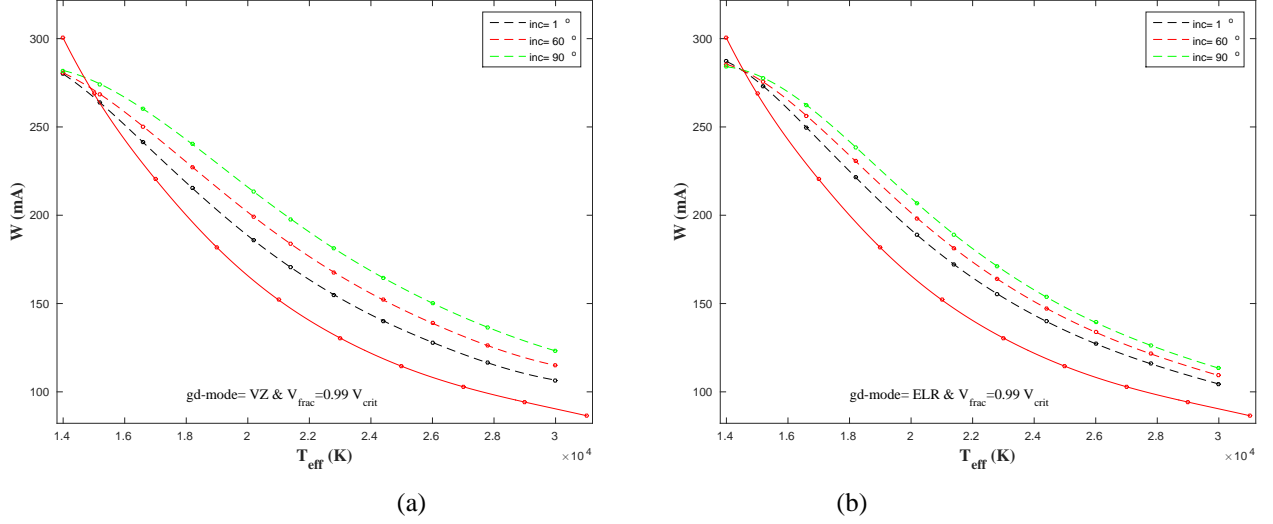


Figure 7.5: The same as Figure (7.4), but for the $\text{Mg II } \lambda 4481 \text{ \AA}$ line.

tional effects between stars seen pole-on and stars seen edge-on in the calculations performed by adopting the treatment of Espinosa Lara & Rieutord (2011) are smaller than that in the other set of calculations.

7.3.4 Gravitational Darkening Effects on $v \sin i$ Measurements

Figure (7.6) shows the measured projected rotational velocities (i.e. $v \sin i$) using gravitationally-darkened, synthetic $\text{He I } \lambda 6678 \text{ \AA}$ and $\text{Mg II } \lambda 4481 \text{ \AA}$ line profiles, panels (a) and (b) respectively, versus the projected rotational velocities adopted in the computation of these synthetic profiles. The gravitationally darkened, computed spectral lines were fit with pure rotation profiles to determine the $v \sin i$ from the line widths. Because of gravitational darkening and the low contrast of the equatorial regions, there have been suggestions that the use of gravitationally-darkened lines tend to systematically underestimate $v \sin i$ when fit with pure rotation profiles (Townsend et al., 2004).

Gravitationally-darkened, synthetic profiles were computed for a B2V stellar model (22808.0 K, 4.0) seen at nine inclination angles between 10° and 90° , with a step of 10° . The critical velocity of this model was 467 km s^{-1} . There are two sets of data for each line: the first were obtained by adopting von Zeipel's treatment, and the second set obtained with the treatment of

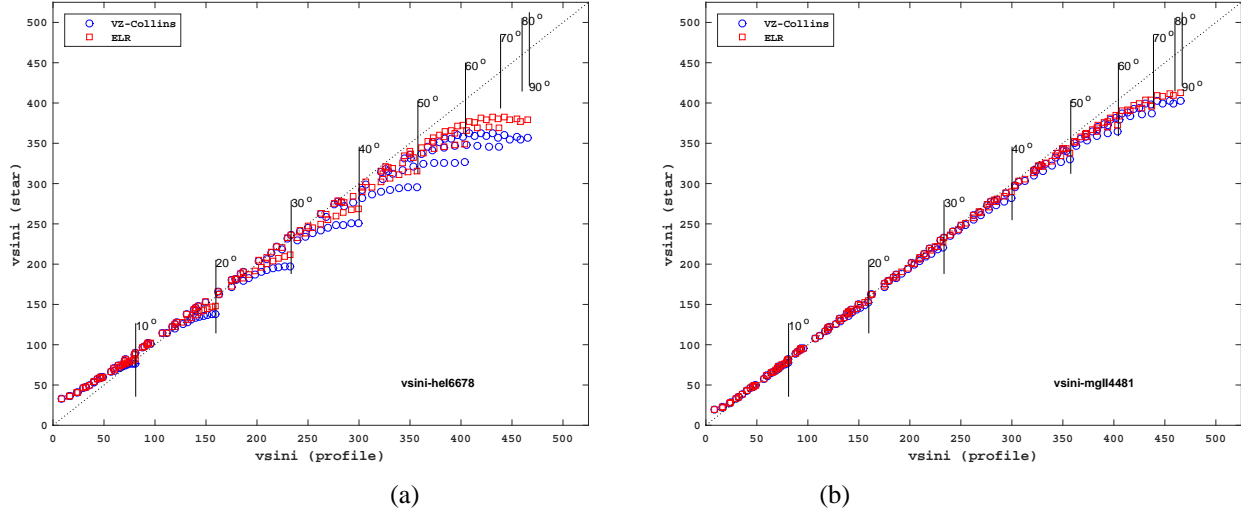


Figure 7.6: The estimated projected rotational velocities $v \sin i$ found by fitting pure rotational profiles to gravitationally darkened profiles. This is done for two sets of gravitationally darkened profiles, the standard von Zeipel’s treatment (blue circles), and the treatment of Espinosa Lara & Rieutord (2011) (red squares). The left panel shows the results for He I 6678 Å line, while the right panel shows the results for Mg II 4481 Å line.

Espinosa Lara & Rieutord (2011). Vertical lines in the figure mark the maximum $v_{\text{crit}} \sin i$ that could be obtained for models with the same inclination angle (see Section 8.2.2 in Chapter 8).

Panel (a) shows that gravitational darkening does not affect the $v \sin i$ estimations for the case of He I λ 6678 Å profiles with projected rotational velocities $\lesssim 70\%$ of $v_{\text{crit}} \sin i$. On the other hand, gravitational darkening results in significant underestimation of the measured rotational velocities for higher $v \sin i$ (profile) values. The amount of underestimation increases with the increase of $v \sin i$. The observed underestimation of the measured projected rotational can be explained as follows: For $v \sin i$ (profile) $\gtrsim 70\%$ of $v_{\text{crit}} \sin i$, darkening causes less contribution of the highest velocity portions of the stellar surface, the stellar equator, due to the significantly low T_{eff} there. Consequently, velocity estimations based on the profiles without proper treatment of this effect will underestimate the true projected rotational velocities of the observed star. The expected line weakening increases with the increase of the inclination angle that results in a larger underestimation of the measured $v \sin i$ (star), as shown in Figure (7.4). On the contrary, for lower $v \sin i$ (profile) the gravitational darkening has no significant effect on the computed line profiles. Consequently, there is no underestimation of the measured

projected rotational velocities.

In addition, the observed underestimations of the projected rotational velocities of gravitationally-darkened profiles computed by adopting von Zeipel's standard treatment (Collins, 1965) are significantly larger than those of computed by adopting Espinosa Lara & Rieutord (2011) treatment.

Panel (b) shows that the underestimation of the measured projected rotational velocities from the Mg II λ 4481 Å are much less pronounced than those seen for He I 6678 Å. This behaviour results from the compensation of the gravitational effects on continuum and line in both the equator and the pole. In the polar regions, the Mg II line is weakened due to the higher temperature compared with the non-rotating models, while the Mg II line strengthens in the equatorial regions due to the lower temperature there. Thus with the more realistic treatment of Espinosa Lara & Rieutord (2011) of gravitational darkening, the Mg II line is predicted to be very robust diagnostic for $v \sin i$ measurement, with little bias introduced by gravitational darkening. Of course, in practice, measurement of $v \sin i$ in excess of $\approx 300 \text{ km s}^{-1}$ are very difficult due to the very wide and shallow nature of the profiles. However, gravitational darkening seems to be an important effect at the most extreme values of $v \sin i > 400 \text{ km s}^{-1}$.

Chapter 8

Nitrogen Abundances for a Sample of Be Stars from the MiMeS Survey

8.1 Introduction

In this chapter, the results of the abundance analysis of a sample of Be stars from the MiMeS Survey (Wade et al., 2014) are presented. The structure as follows: The first section will introduce the Be star sample and the stellar parameters, i.e. the stellar effective temperatures, gravities, and microturbulence velocities used in the analysis. Next is a discussion of the procedure followed for the continuum normalization of the observed spectra in order to reliably measure the equivalent widths of the N II lines. Next, the method followed to get estimations of the Be star disk parameters, i.e. the disk size, density and inclination, is discussed. This is an important step to investigate how the circumstellar disk affects the observed spectra. Finally, the determination of the nitrogen abundances are discussed. In the latter section, estimates of the abundances based only on the measured equivalent widths are presented without taking in consideration the impact of circumstellar disk emission on the estimated abundances. Then, the corrections of the estimated abundances due to circumstellar modification of the spectrum are discussed.

8.2 The Be star Sample

A sample of 26 Be stars was considered, covering spectral types between B0 and B7 and luminosity classes V and VI. High resolution spectra for these stars were taken as part of the MiMeS project, The Magnetism in Massive Stars Survey, (Wade et al., 2014). This project aims to study the magnetic properties of large sample (> 500) of massive stars through high resolution spectra taken with the Echelle spectropolarimeter ESPaDOnS on the Cassegrain focus of the ESO 3.6m Canada-France-Hawaii Telescope, CFHT, and NARVAL on the Télescope Bernard Lyot, TBL. ESPaDOnS spectra have a resolving power of 80,000 in the spectroscopy star only option, used for observing bright stars, and a resolving power of 68,000 in the spectroscopy + sky mode used for observations of faint stars and for spectroscopy in a polarimetric mode in which all Stokes parameters are measured. The latter mode was adopted in producing the spectra for the MiMeS survey. ESPaDOnS has a spectral coverage between 3700 to 10,500 Å in a single exposure, divided into 40 overlapped orders, with three gaps in the far red region of the spectrum between 9224-9234 Å, 9608-9636 Å, and 10026-10074 Å. The initial processing of spectra was done by specialists in the CFHT observatory using the Libre-Esprit software*, which performs bias subtraction, wavelength calibration, and flat field subtraction. The wavelength calibration was done by exposures of a thorium comparison lamp. Also, this software provide tools for normalizing the spectra, subtracting telluric lines, and calculating the polarization Stokes parameters.

8.2.1 Spectra Normalization

Because the $v \sin i$ of the sample of Be stars can be large (typically 150 km s^{-1} up, to 300 km s^{-1}), the spectra were continuum renormalized in the wavelength regions containing the spectral features of interest. The spectra normalization was carried out using the CONTINUUM package of the IRAF image reduction and analysis facility (Tody, 1993). This could be

*<http://www.cfht.hawaii.edu/Instruments/Spectroscopy/Espadons/>

done in either a manual mode or an automatic mode. In the manual mode, the program fits the spectrum with a polynomial function through continuum points determined by the user in an interactive mode. In the automatic mode, the program fits a polynomial function to the average fluxes over a specified number of wavelength points, determined by the user. Then, the spectral features with fluxes that differ from the average flux by a user-specified number of standard deviations will be identified as absorption or emission features, and the identified spectral features are excluded and the rest of the flux points are fitted by another polynomial function. This process is repeated until the best fit is obtained. The program offers various polynomial functions for the normalization process, namely Legendre, linear spline, cubic spline, and Chebyshev polynomials of different orders selected by the user. The continuum normalization of the spectral orders containing $H\alpha$ (λ 6563 Å) were done using the automatic mode, which is good in this case. The normalization of the other spectral orders were done in the manual mode. Cubic spline or Legendre polynomials of order less than three were used for all fits.

The observed spectral files contain overlapped orders from the echelle spectrograph of ESPaDOnS. The fitting of the spectra was done for the entire spectral orders that contained the spectral lines of interest. Also, the observed spectra were normalized over short ranges of wavelengths in each spectral order around the lines of interest that included a sufficient number of continuum points. This was done mainly using a first-order linear spline function and/or a third-order Legendre polynomial.

As an example, Figures 8.1, 8.3, 8.4, and 8.5 show the normalization process of the Be star, HD 143275, for the four spectral orders containing $H\alpha$, $N\text{II}$ λ 3995.0 Å, λ 4447.0 Å, and λ 5679.6 Å. In the figure, the fitting polynomial function is represented by a dashed line, while the selected continuum points are represented by horizontal lines above the wavelength axis. Each figure indicates the type and the order of the polynomial function used for the fitting (the top, right corner). Also, each figure gives the conditions of rejecting the data points for the continuum fitting, and the number of iteration as explained above (namely parameters `low_rej`,

high_rej, and niterate). Note that these parameters are not used in the manual mode. Figures (8.2) and (8.6) show the normalized spectral regions that include $H\alpha$ and selected $N\text{ II}$ lines. In these figures, normalization using a Legendre polynomial is compared to normalization using a spline polynomial. Good agreement in both are found.

Figures (8.7) and (8.8) show normalized spectral regions for two Be stars, HD 11415 and HD 45725 respectively. Figure 8.7 represents the Be stars with low projected rotational velocities with well defined spectral lines. Figure 8.8 is an example of the observed spectra of rapidly rotating Be stars, which is the case for the majority of Be stars in the sample. Rapid rotation results in strong line blending and low continuum contrast as discussed earlier, which affects the accuracy of continuum normalization and equivalent width measurements. Also, Figure (8.8) shows that the $N\text{ II } \lambda 4630.5 \text{ \AA}$ line is masked by emission by the circumstellar disk in the $\text{Fe II } \lambda 4629.3 \text{ \AA}$ line; this is the case for most of the Be stars included in the current analysis.

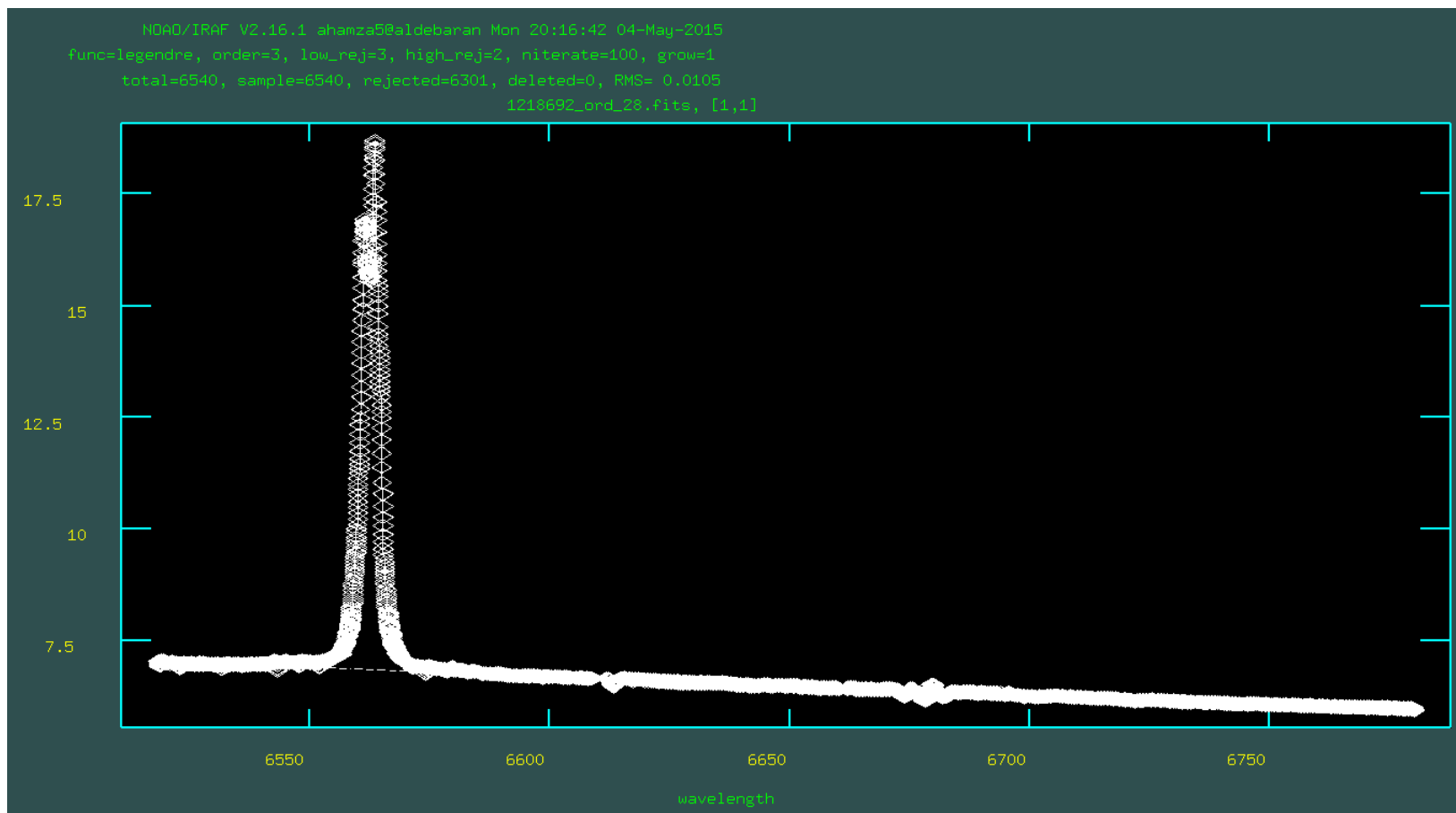


Figure 8.1: Continuum normalization of the spectral order that includes $H\alpha$ of the Be star HD 143275 by fitting the observed spectra by a Legendre polynomial function using the CONTINUUM package of the IRAF.

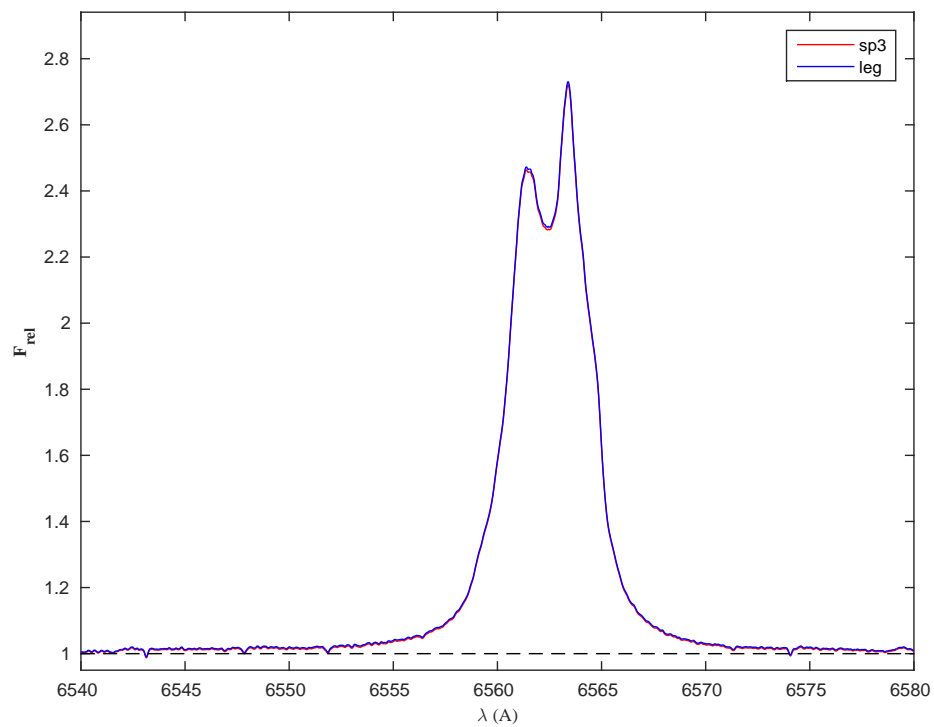


Figure 8.2: The normalized spectral order that includes H α line profile of the Be star HD 143275 using both cubic spline and Legendre polynomial functions, red and blue lines respectively.

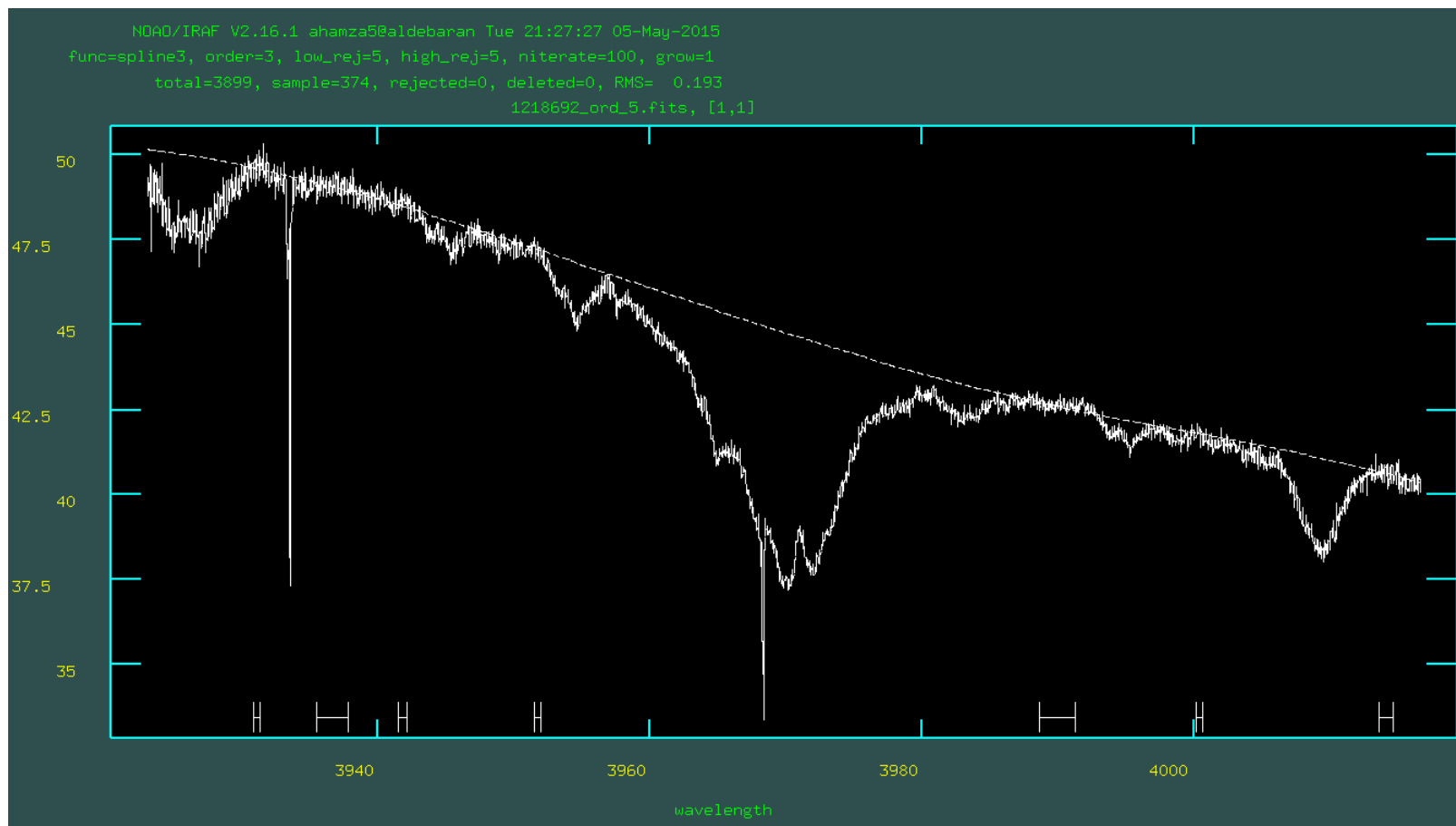


Figure 8.3: The same as Figure (8.1) but for the spectral order containing $\text{N II } \lambda 3995.0 \text{ \AA}$.

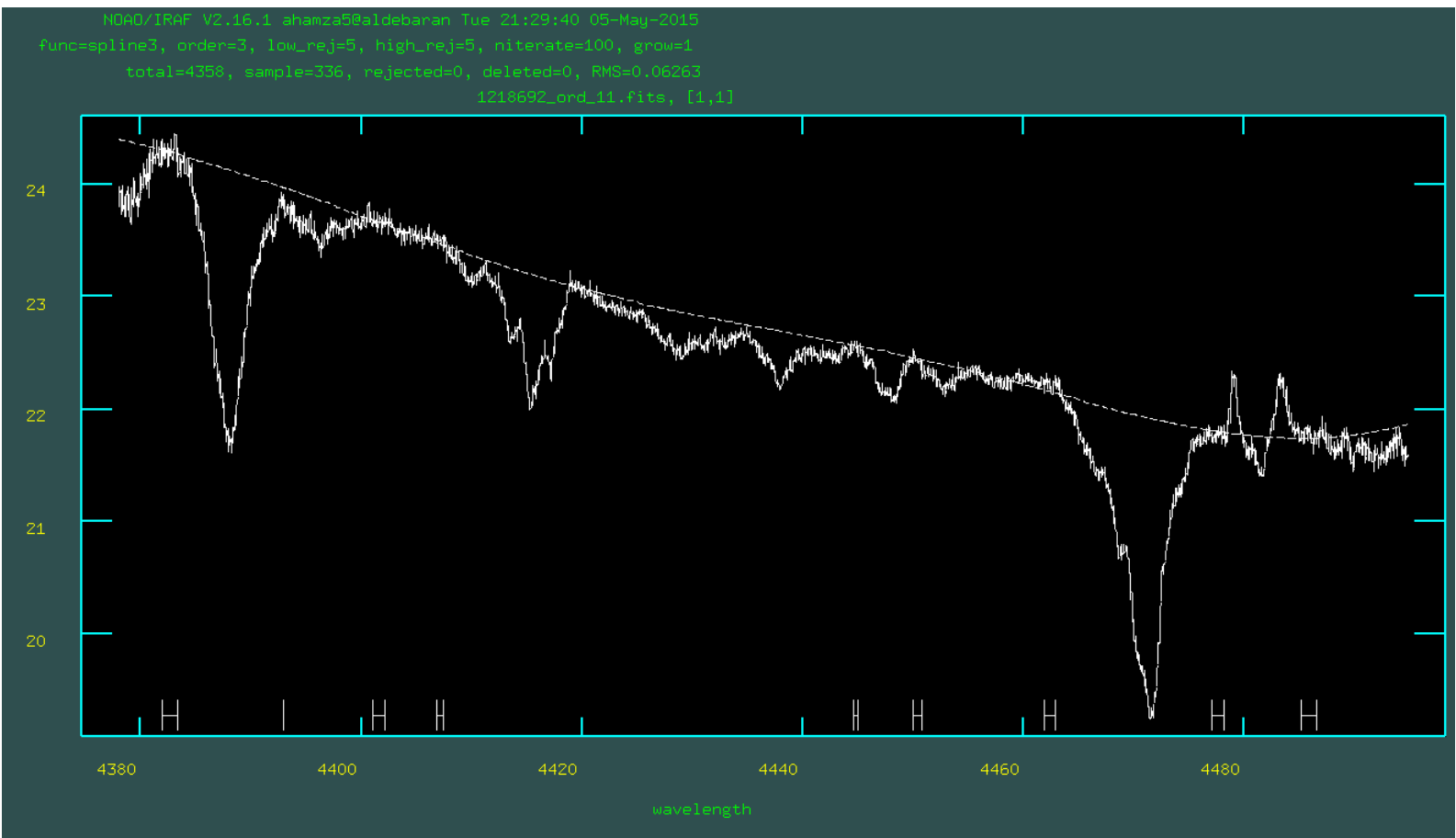


Figure 8.4: The same as Figure (8.1) but for the spectral order containing $\text{N II } \lambda 4447.0 \text{ \AA}$.

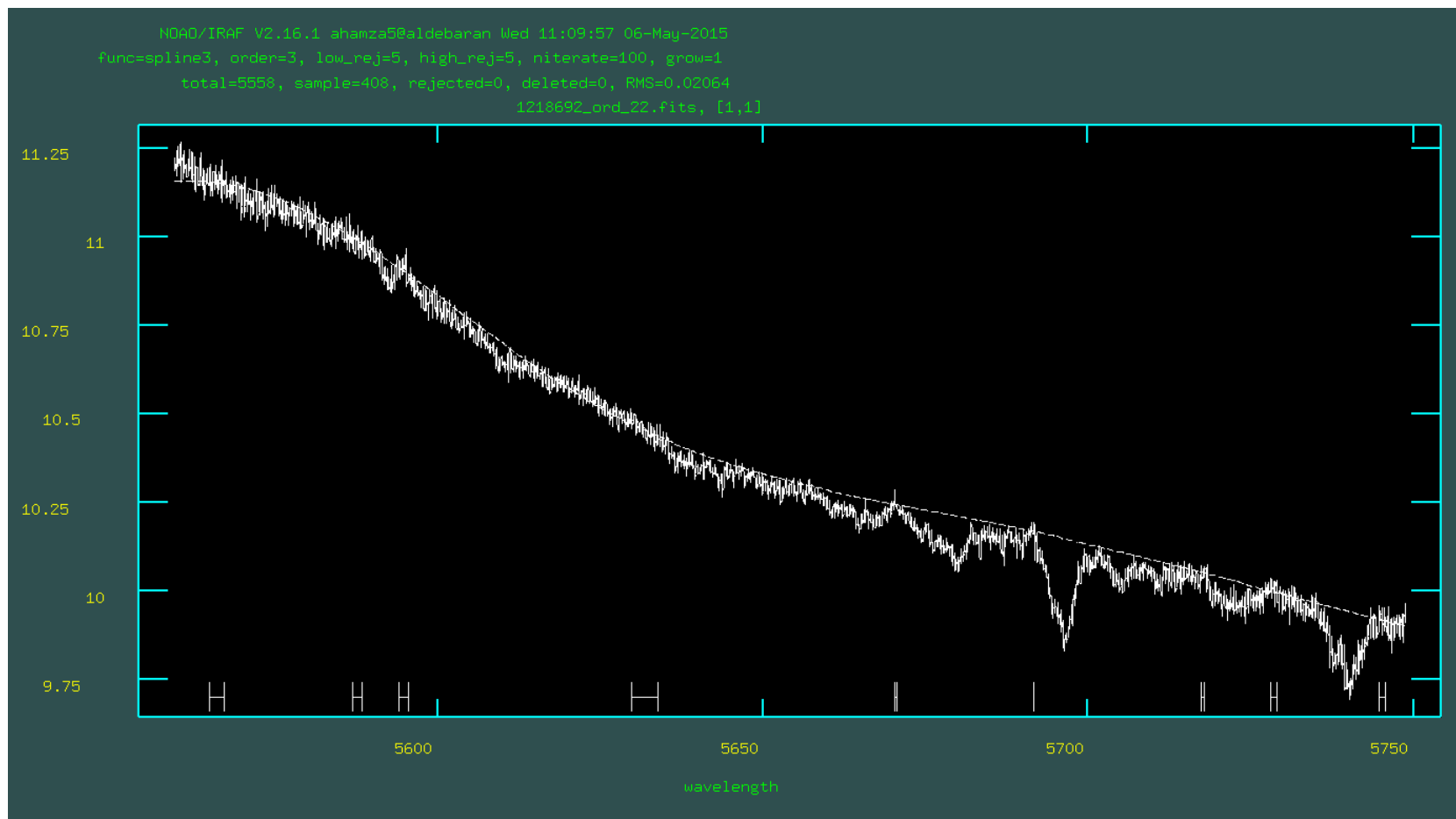


Figure 8.5: The same as Figure (8.1) but for the spectral order containing $\text{N II } \lambda 5679.0 \text{ \AA}$.

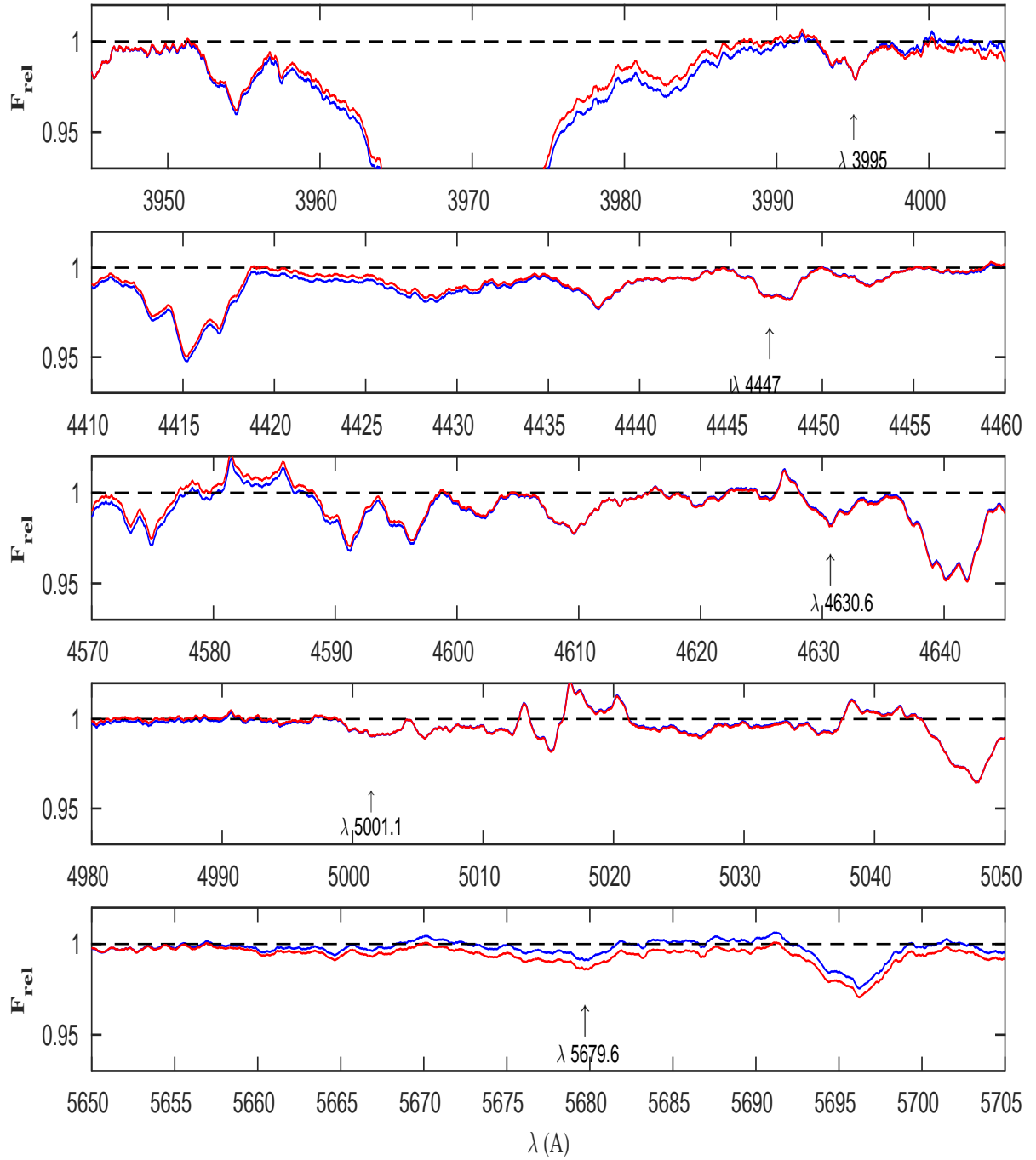


Figure 8.6: Figure shows the normalized spectral regions that contain a number of strong lines of N II of the Be star HD 143275. Blue lines represent spectra normalized using a Legendre polynomial, while red lines represent spectra normalized using a spline polynomial.

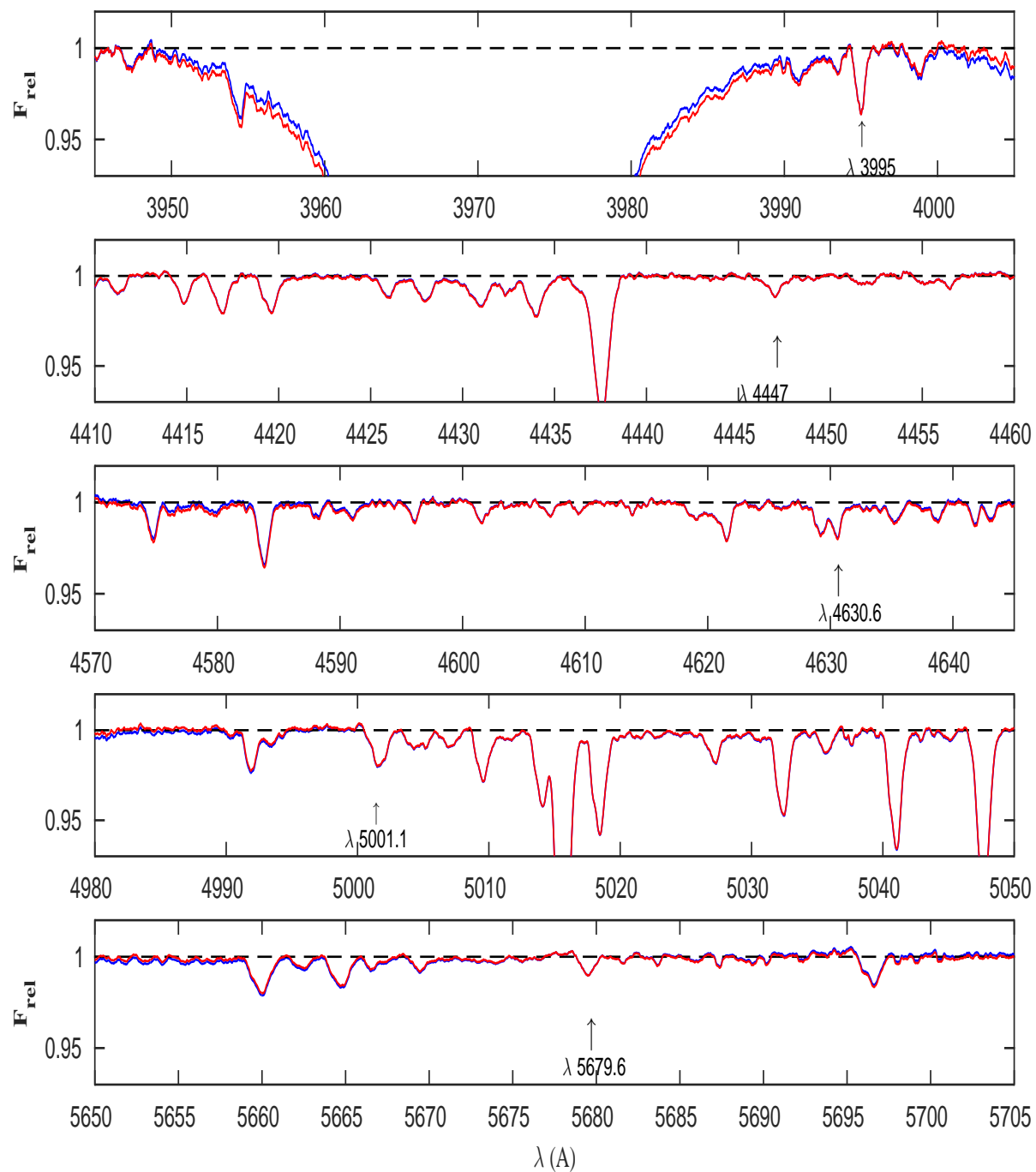


Figure 8.7: The same as Figure (8.6) but for the Be star HD 11415.

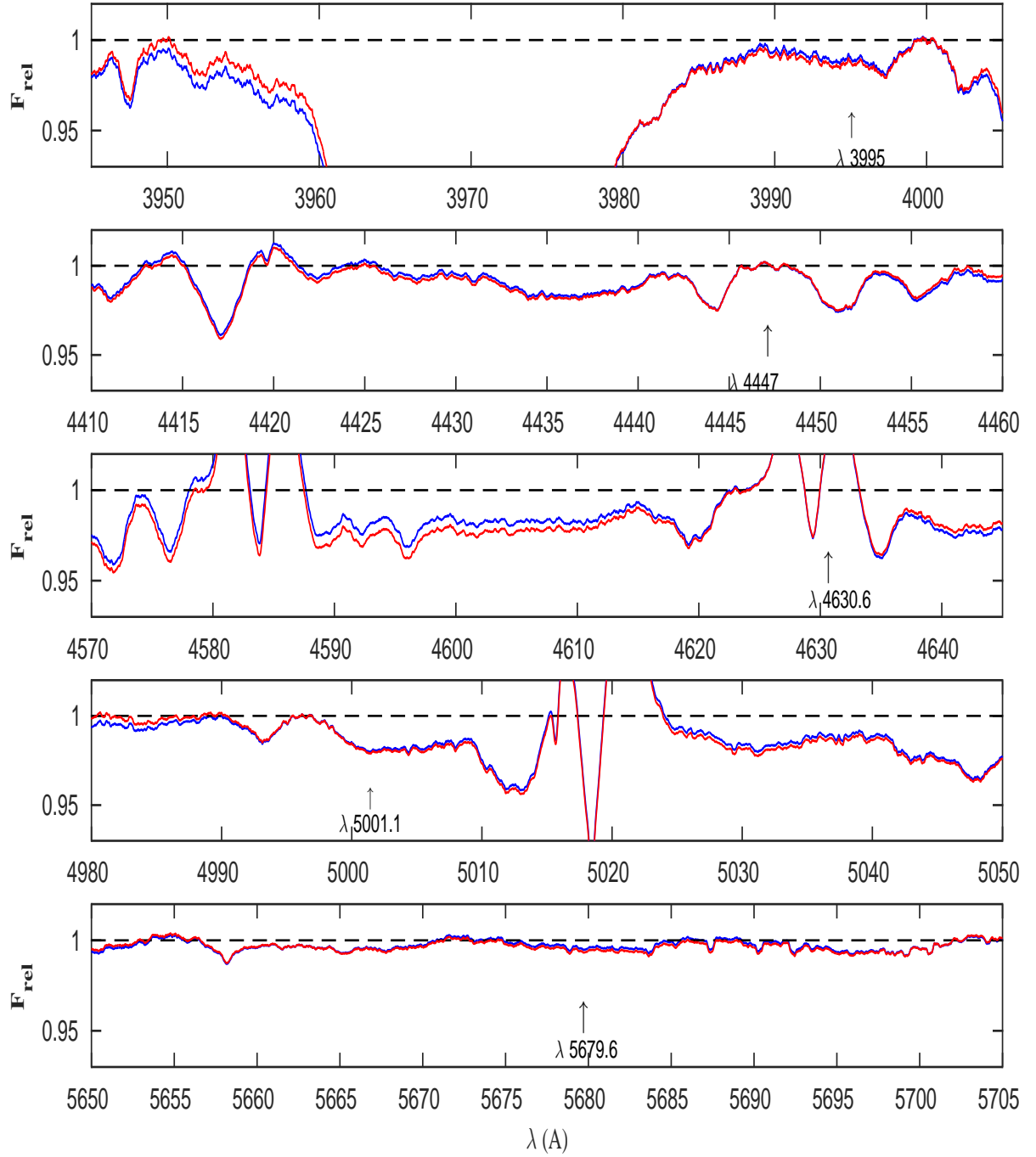


Figure 8.8: Figure shows the normalized, strong N II of the Be star HD 45725.

8.2.2 Stellar Parameters

The stellar parameters of the Be stars sample are shown in Table (8.1, page 142) and were adopted from the literature, mainly from the work of Frémat et al. (2005). In Frémat et al. (2005), the stellar effective temperatures and gravities were obtained by comparing observed spectra with synthetic ones over four wavelength ranges between 4300 and 4490 Å, which include lines sensitive to T_{eff} and $\log g$. These lines used were He I λ 4471 Å, and Mg II λ 4482 Å which are sensitive for variations of the stellar effective temperatures, and the Balmer H γ line which is sensitive for variations of the stellar gravities.

The study of Frémat et al. (2005) provides two sets of stellar parameters: the first set of stellar parameters was directly estimated from the observed spectral lines without corrections for gravitational darkening, i.e. the apparent stellar parameters. The other set were obtained where corrections for the effects of gravitational darkening were included. In the latter, the standard treatment of von Zeipel (1924) (Collins, 1965) was adopted. In the current work, the apparent parameters of Frémat et al. (2005) were adopted and not the ones corrected for gravitational darkening. The main reason for this decision is the overestimated effects of gravitational darkening of the standard von Zeipel's treatment compared with the recent treatment of Espinosa Lara & Rieutord (2011), as discussed in Chapter 7. Another aspect of the Frémat et al. (2005) work is that their estimated inclinations do not look right as they deviate significantly from the distribution expected from random inclinations to the line of sight, see subsection (8.3). The expected effects of gravitational darkening are dependent on the adopted viewing inclination angle.

The synthetic spectra used by Frémat et al. (2005) to get the apparent stellar parameters were computed using the non-LTE TLUSTY code of Lanz & Hubeny (2007) and the UV line-blanketed LTE stellar atmosphere models computed using ATLAS9 program of Kurucz (1993a). The computations were performed assuming plane-parallel atmospheres in radiative and hydrostatic equilibrium. The TLUSTY code was used to compute the non-LTE level populations, while the temperature and pressure structure of the atmosphere were obtained from

the LTE stellar atmosphere models.

Some notes on the parameters for specific stars are now given. Most of these notes are for stars for which Frémat et al. (2005) parameters were unavailable. Only one of the works below accounted for the effects of gravitational darkening which is Levenhagen & Leister (2006). The latter also adopted the standard von Zeipel's treatment.

The effective temperature and the gravity for the Be star HD 11415 of spectral type B3III was taken from Takeda et al. (2010). In this work, the temperature was obtained using the Strömgren *ubvyb* colour indexes obtained from the SIMBAD database. This was done using *uvbybetanew* program (Napiwotzki, R., 1993), which is based on Moon & Dworetsky (1985) *UVBYBETA* and *TEFFLOGG* programs. The adopted uncertainties of T_{eff} in Takeda et al. (2010) are $\pm 3\%$ of the measured values and the adopted uncertainties of $\log g$ are ± 0.2 dex.

The effective temperature and gravity of the Be star HD 49567 of spectral type B3 II/III was taken from Zorec et al. (2009). In this work, they developed a procedure to get the effective temperature and gravities using observed spectra and stellar atmosphere models. Their procedure starts with initial estimates of T_{eff} and $\log g$. Then, they pick a stellar atmosphere model with the same stellar parameters like these initial estimates, where LTE stellar atmospheres of Kurucz (1993a) were used. Next, they compute the bolometric flux by integration of the observed fluxes over the observed spectra. The observed spectra often extend from between 1200 -1300 Å to some wavelengths in the near IR. In this step, they add corrections for the missed fluxes in the far-UV, δ_{UV} , and IR spectral regions, δ_{IR} , from the adopted atmosphere model as follows,

$$f_{\text{bol}} = \int_{\lambda_a}^{\lambda_b} f(\lambda) d\lambda \times (\delta_{UV} + \delta_{IR}).$$

Then, a new estimate of T_{eff} is obtained using the StefanBoltzmann law as follows,

$$T_{\text{eff}} = \left[\frac{4 f_{\text{bol}}}{\sigma \theta^2} \right]^{1/4},$$

where θ is the angular diameter. The latter was obtained from observed near-IR fluxes

using the following relation,

$$\theta = 2 \left[\frac{f_{\lambda}^0}{F_{\lambda}} \right]^{1/2},$$

where f_{λ}^0 is the de-reddened observed flux and F_{λ} is the emitted flux at the stellar surface obtained from the adopted stellar atmosphere model. Also, a new estimate of $\log g$ is obtained using the $\log g(T_{\text{eff}}, \beta)$ calibration from synthetic stellar atmosphere models. This process is repeated in an iterative way until the difference in temperature between iterations becomes less than 1 K.

The effective temperatures and gravities of the Be stars HD 67698 (B3 III/IV) and HD 120324 (B2 V), were obtained from Levenhagen & Leister (2006). In this study, initial estimates of T_{eff} and $\log g$ were obtained from the available ionization balances of He II/He I, O III/O II, N III/N II and Si III/Si II, and the equivalent widths of hydrogen Balmer lines. The ratios of selected He I lines, which are weakly dependent on He abundance, were also used for stellar parameters for spectral types later than B2. This was done by comparing the observed profiles with the LTE, stellar atmospheres of Kurucz (1993a), where the T_{eff} and $\log g$ determinants from all available lines intercept in a narrow range for each star. They obtained estimations of T_{eff} and $\log g$ by matching the observed H and He lines with synthetic profiles computed using the SYNSPEC program of Hubeny et al. (1994) and the non-LTE model atmospheres from the TLUSTY program using the downhill simplex algorithm of Nelder & Mead (1985). Again, for the same reason as Frémat et al. (2005), their observed stellar parameters were adopted rather than their parameters corrected for gravitational darkening. There are twenty-two Be stars common in this study and Frémat et al. (2005), but none of these Be stars belong to the sample. Figure 8.9 shows comparison of the temperature estimates of Levenhagen & Leister (2006) with the corresponding values of Frémat et al. (2005) of the common Be stars. The temperature estimates of Levenhagen & Leister (2006) tend to be higher than those of Frémat et al. (2005), but overall, there is a good agreement between the temperature estimates of the two studies.

The effective temperature and gravity of the Be star HD 187567 (B2.5IV) were obtained

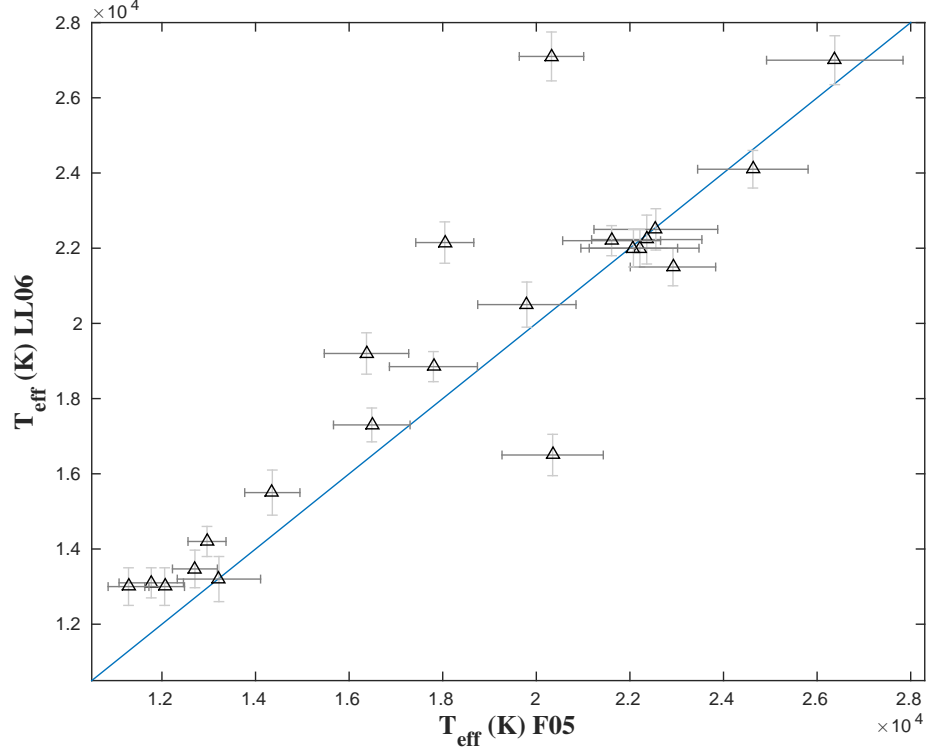


Figure 8.9: Figure shows comparison of the T_{eff} estimates from Levenhagen & Leister (2006) for twenty-two Be stars in the sample with the corresponding values from Frémat et al. (2005). The blue, dashed line is a unit slope, and zero intercept.

from Catanzaro (2013). In this work, effective temperatures were obtained using measured Strömgren colour indexes from literature following the Moon (1985) algorithm, while a value of gravity equal to 4.0 was adopted for stars with III/IV luminosity types.

This work provides estimated effective temperatures of seven Be stars common with the study of Frémat et al. (2005). Figure 8.10 shows comparison of the temperature estimates of Catanzaro (2013) with the corresponding values of Frémat et al. (2005).

For the Be stars HD 120324 (B2V) and HD 143275 (B0.2IV), the measurements of Harmanec (2000) were adopted. In this work, the temperatures were estimated photometrically following the procedures of Moon & Dworetzky (1985). Also, Catanzaro (2013) provides a T_{eff} estimation of the Be star HD 143275 (26700 K) which is much lower than the value (31478 K) of Harmanec (2000). However, the observed λ 4471 Å He I lines were best fitted with synthetic non-LTE profiles computed for stellar parameters close to those of Harmanec

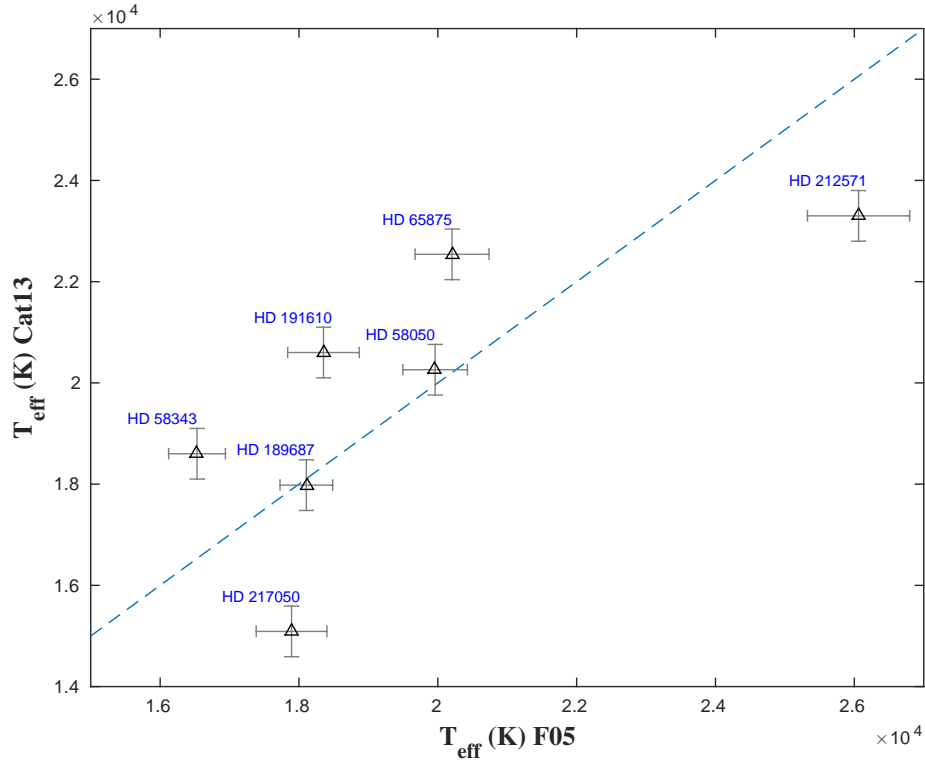


Figure 8.10: Figure shows comparison of the T_{eff} estimates from Catanzaro (2013) for 7 Be stars in the sample with the corresponding values from Frémat et al. (2005). The blue, dashed line is a unit slope, and the data points are labelled with the HD number of each Be star.

(2000), as will be discussed below, so the Harmanec (2000) values were adopted.

Finally, the effective temperature and gravity of the Be star HD 120324 (μCen , B2V) was obtained from Côté et al (1996). In this study, they estimated effective temperatures and gravities by comparing de-reddened observed spectra for $\lambda < 800$ nm with the LTE model atmospheres of Kurucz (1979).

Table 8.1: Adopted Stellar Parameters of the MiMeS Be stars Sample

HD	T_{eff} (K)	$\log g$	Spectral Type SIMBAD	F05	SIMBAD	$v \sin i$ (km s ⁻¹)			Source
						Current Estimations			
						λ 4471.5 Å	λ 4481.2 Å	λ 3995.0 Å	
11415	15147±455	3.50±0.20	B3 III	–	30.0	45.0	45.0	35.0	Tak10
20336	18684±517	3.87±0.07	B2.5 Vne	328.0±21.0	328.0	285.0	285.0	:220.0	F05
33328	21137±514	3.45±0.08	B2 IV ne	318.0±22.0	150.0	290.0	290.0	:265.0	F05
45725	17810±455	3.90±0.07	B3 Ve	330.0±20.0	260.0	285.0	:200.0	280.0	F05
49567	17270±1010	3.50±0.10*	B3 II-III	–	85.0	80.0	80.0	80.0	Zor09
54309	20859±397	3.59±0.05	B2 V:nn	195.0±10.0	195.0	205.0	150.0	220.0	F05
56139	19537±331	3.62±0.04	B2IV-Ve	85.0±4.0	105.0	100.0	50.0	75.0	F05
58050	19961±465	3.93±0.06	B2 Ve	130.0±8.0	130.0	130.0	130.0	115.0	F05
58343	16531±409	3.62±0.06	B2 Vne	43.0±2.0	43.0	50.0	50.0	40.0	F05
58978	24445±476	4.15±0.06	B1 II	370.0±21.0	155.0	280.0	200.0	115.0	F05
65875	20205±532	3.84±0.07	B2.5 Ve	153.0±10.0	140.0	:200.0	130.0	175.0	F05
67698	17400±500	3.60±0.10	B3 III/IV	–	150.0	–	70.0	75.0	LL06
120324	20000±500	4.00±0.20	B2V	–	155.0	140.0	140.0	135.0	H00
143275	31478±500	3.50±0.10*	B0.2IV	–	175.0	:190.0	–	165.0	H00
174237	17683±556	3.76±0.08	B2.5 Ve	163.0±11.0	163.0	150.0	150.0	145.0	F05
178175	18939±286	3.49±0.04	B2 V	105.0±5.0	105.0	150.0	110.0	145.0	F05
187567	23110±500	3.70±0.10*	B2.5 IV	–	140.0	195.0	130.0	165.0	Cat13
187811	18086±583	3.81±0.08	B2.5 Ve	245.0±17.0	245.0	235.0	200.0	:145.0	F05
189687	18106±379	3.46±0.05	B3IV	200.0±11.0	200.0	200.0	200.0	195.0	F05
191610	18353±516	3.72±0.07	B2.5 V	300.0±20.0	300.0	270.0	270.0	:170.0	F05
192685	18000±500	3.5±0.20	B3 V	–	160.0	180.0	180.0	150.0	Cote96
203467	17087±521	3.38±0.07	B3 IVe	153.0±10.0	120.0	–	150.0	170.0	F05
205637	17801±470	3.44±0.06	B3 Vpe	225.0±14.0	225.0	200.0	190.0	295.0	F05
212076	19270±326	3.73±0.04	B2 IV-Ve	98.0±5.0	98.0	130.0	:100.0	115.0	F05
217050	17893±509	3.57±0.07	B3IV	340.0±22.0	265.0	250.0	250.0	265.0	F05
212571	26061±736	3.92±0.09	B1Ve	230.0±17.0	215.0	215.0	215.0	:265.0	F05

Note: Tak10 refers to Takeda et al. (2010), F05 refers to Frémat et al. (2005), H00 refers to Harmanec (2000), Zor09 refers to Zorec et al. (2009), LL06 refers to Levenhagen & Leister (2006), Cat13 refers to Catanzaro (2013), and Cote96 refers to Coté et al (1996). $\log g$ values marked with an asterisk are current estimations and are not obtained from the referred sources. SIMBAD refers to spectral type classifications and $v \sin i$ estimates adopted from the SIMBAD database.

As a test of the adopted effective temperatures and gravities, the observed He I λ 4471 Å, λ 6678 Å, and Mg II λ 4481 Å lines were fitted with rotationally broadened, non-LTE, synthetic line profiles computed at these parameters, where the projected rotational velocity was allowed to vary to reach the best fit of the observed lines. This also represents a test of the reported values for $v \sin i$. In Frémat et al. (2005), projected rotational velocities ($v \sin i$) were obtained using the FFT method for He I λ 4471 Å, and Mg II λ 4482 Å lines. For comparison, especially for the Be stars not included in Frémat et al. (2005), the $v \sin i$ estimates available in the SIMBAD database were added to Table 8.1. Estimates of the projected rotational velocities were obtained by fitting the observed He I λ 4471 Å, Mg II λ 4481 Å, and N II 3995 Å lines. The $v \sin i$ estimates based on N II 3995 Å lines were obtained by fitting the observed profiles with pure rotational profiles computed using the approximation of Gray (1992), Equation (8.1). The values of the continuum linear limb darkening coefficient, ϵ , was obtained from Wade & Rucinski (1985) at the adopted temperature and the wavelength of the considered line.

$$G(\Delta\lambda) = \frac{2(1 - \epsilon)[1 - (\Delta\lambda/\Delta\lambda_L)^2]^{\frac{1}{2}} + \frac{1}{2}\pi\epsilon[1 - (\Delta\lambda/\Delta\lambda_L)^2]}{\pi\Delta\lambda_L(1 - \epsilon/3)}, \quad (8.1)$$

where $\Delta\lambda_L$ is the rotational broadening

$$\Delta\lambda_L = v \sin i,$$

where c is the speed of light. The estimates of $v \sin i$ from Mg II λ 4481 Å, and He I λ 4471 Å were obtained by fitting of the observed profiles with rotationally broadened, non-LTE, synthetic line profiles computed at the adopted T_{eff} and $\log g$. Table 8.1 contains $v \sin i$ estimates from each of the three lines for each star obtained in the current study. Figure (8.11) shows the distribution of the measured $v \sin i$ values for the sample. For comparison, the observed distribution of $v \sin i$ for two samples of 129 and 463 Be stars are taken from Frémat et al. (2005) and Yudin (2001), respectively. Note that 18 Be stars of the sample belong to the larger Be sample of Frémat et al. (2005). The figure shows that the sample of Be stars studied in

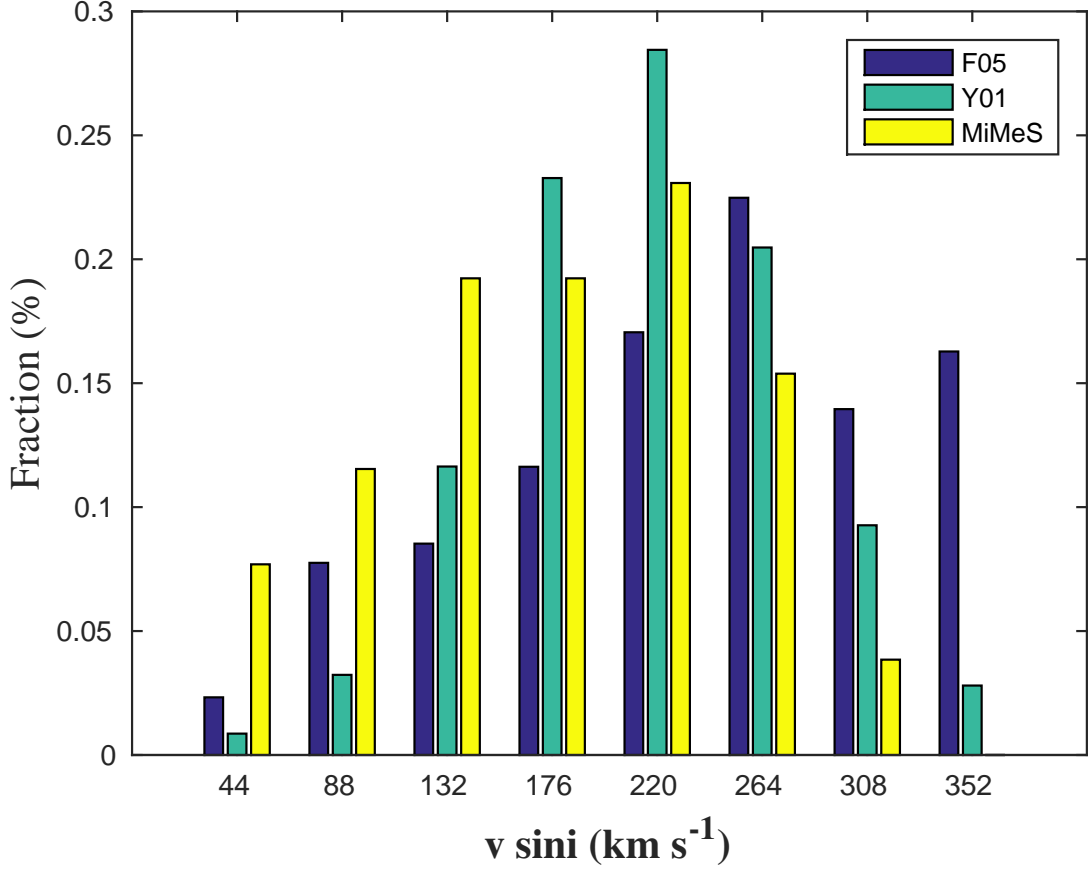


Figure 8.11: Figure shows the distribution of the Be stars sample from MiMeS survey (26 stars) labelled as MiMeS. The observed $v \sin i$ distribution for a sample of 129 Be stars from Frémat et al. (2005) (F05) and another $v \sin i$ distribution for 463 Be stars from Yudin (2001) (Y01) are shown for comparison

the MiMeS survey project represents a more slowly rotating sample, with a larger fraction of Be stars with rotational velocities lower than the average rotational velocities in the other two large $v \sin i$ distributions.

For all Be stars in the sample, except HD 203467 and HD 67698, a good fit to the observed He I λ 4471.5 Å line with a synthetic line computed at the adopted effective temperature was obtained, while the value of gravity was adjusted to get the best fit rather than adopting the measured value in literature. As discussed before in subsection (6.4.2), there are discrepancies between observed He I line profiles and synthetic non-LTE line profiles which could be attributed to errors in the line broadening theory. The latter is dependent on gravity. On the contrary, no acceptable fit was obtained for the observed He I λ 6678 Å line for the majority of

the stars in the sample, as it was affected by disk contamination.

Good fits for the He I λ 4471 Å, λ 6678 Å, and Mg II λ 4481 Å lines were obtained in five cases, HD 49567, HD 3328, HD 189687, HD 11415 and HD 191610. Figure (8.12) represents an example of this group. Next is Mg II λ 4481 Å for which acceptable fitting for this line was obtained beside He I λ 4471 Å line for most of Be stars in the sample, see Figures (8.13) & (8.14). Good fitting for He I λ 4471 Å and λ 6678 Å lines was obtained for 2 Be stars, HD 45725 & HD 58343. The fitting of the line profiles of HD 45725 are shown in Figure (8.15). For the Be stars HD 203467 and HD 67698, the observed He I λ 4471 Å and λ 6678 Å lines were poorly fit for these stars. However, acceptable fits of the observed Mg II λ 4481 Å lines with synthetic profiles computed at the adopted stellar parameters were obtained as shown in Figure (8.16). Note that observed He I λ 4471 Å and Mg II λ 4481 Å profiles of the Be star HD 65875 were fit with synthetic profiles that were rotationally broadened at two different rotational velocities, which suggests an error.

Figure (8.17) shows a comparison of the current estimates of $\log g$ with those obtained from literature. The current estimates represent the $\log g$ values adopted in the calculation of the synthetic line profiles that best fit the observed profiles. The figure shows that current estimations agree well with previous measurements obtained from literature, within ± 0.2 dex, for most of the sample. Consequently, the current measurements of gravity were adopted for the Be stars with no other measured value of gravity. They are marked with asterisk in Table (8.1). The vertical error bars represent the uncertainties in the differences due to uncertainties of the values of gravity obtained from literature.

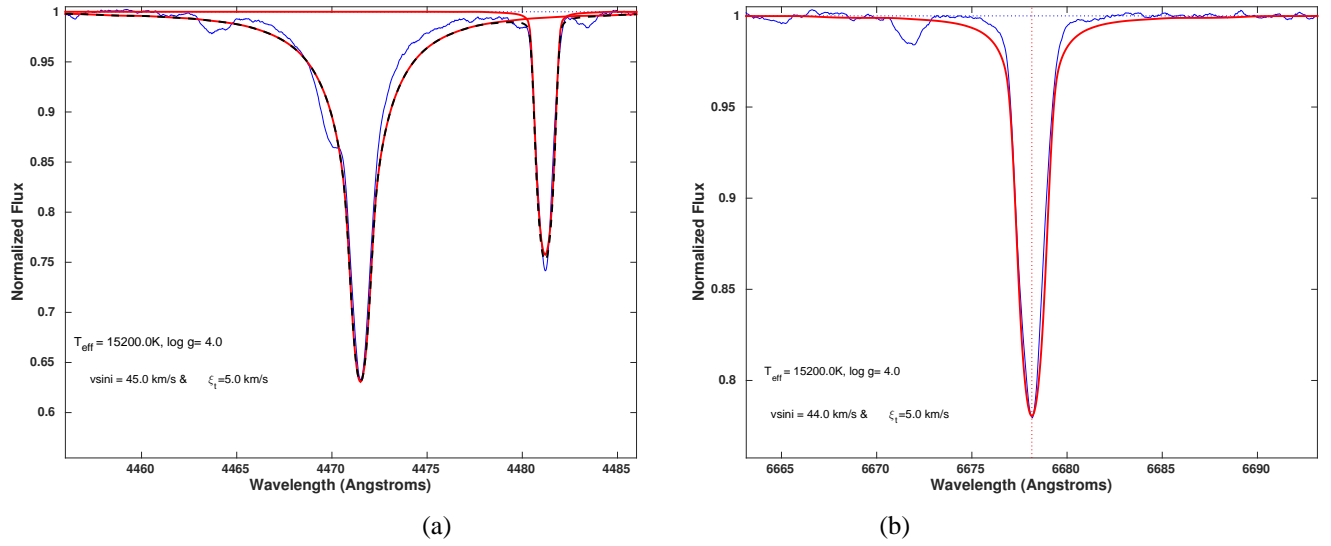


Figure 8.12: The Fitting of He I λ 4471 Å, Mg II λ 4481 Å and He I λ 6678 Å lines of the Be star HD 11415 with synthetic non-LTE line profiles computed at stellar parameters shown at the bottom, left corner of each panel. In the figure, blue lines represent the observed spectral lines, red lines the rotationally broadened non-LTE synthetic profiles computed, and the dashed black line in panel (b) is the sum of the two synthetic profiles.

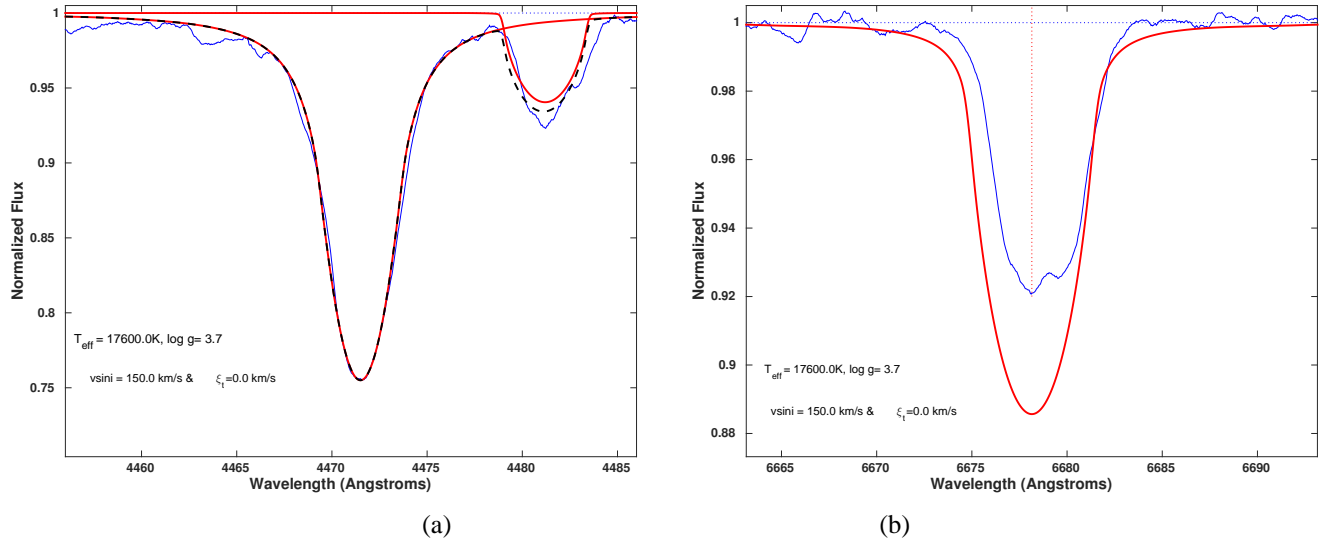
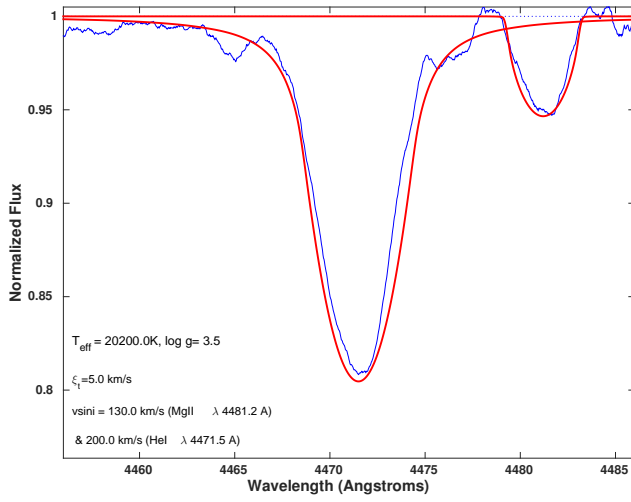
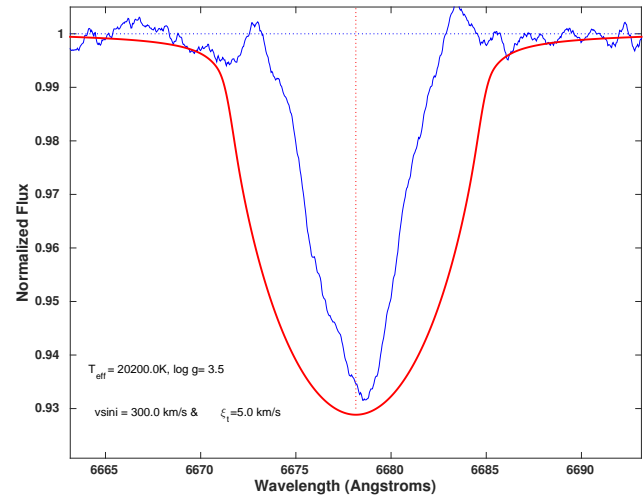


Figure 8.13: The same as Figure (8.12), but for the Be star HD 174237.

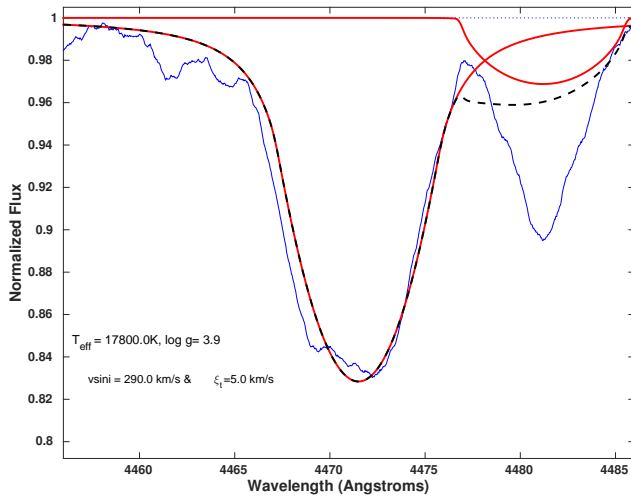


(a)

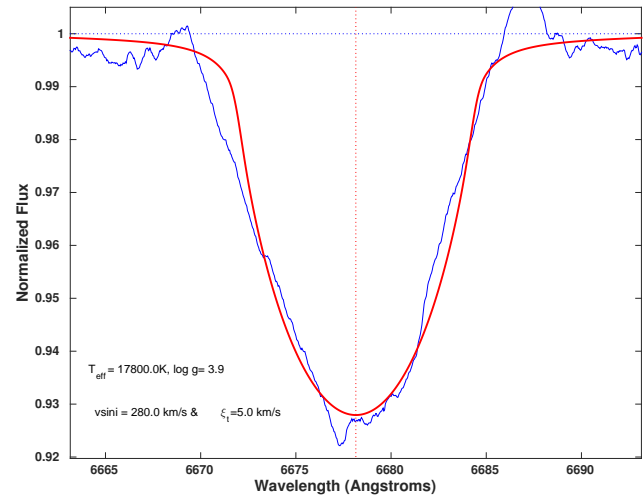


(b)

Figure 8.14: The same as Figure (8.12), but for the Be star HD 65875.



(a)



(b)

Figure 8.15: The same as Figure (8.12), but for the Be star HD 45725.

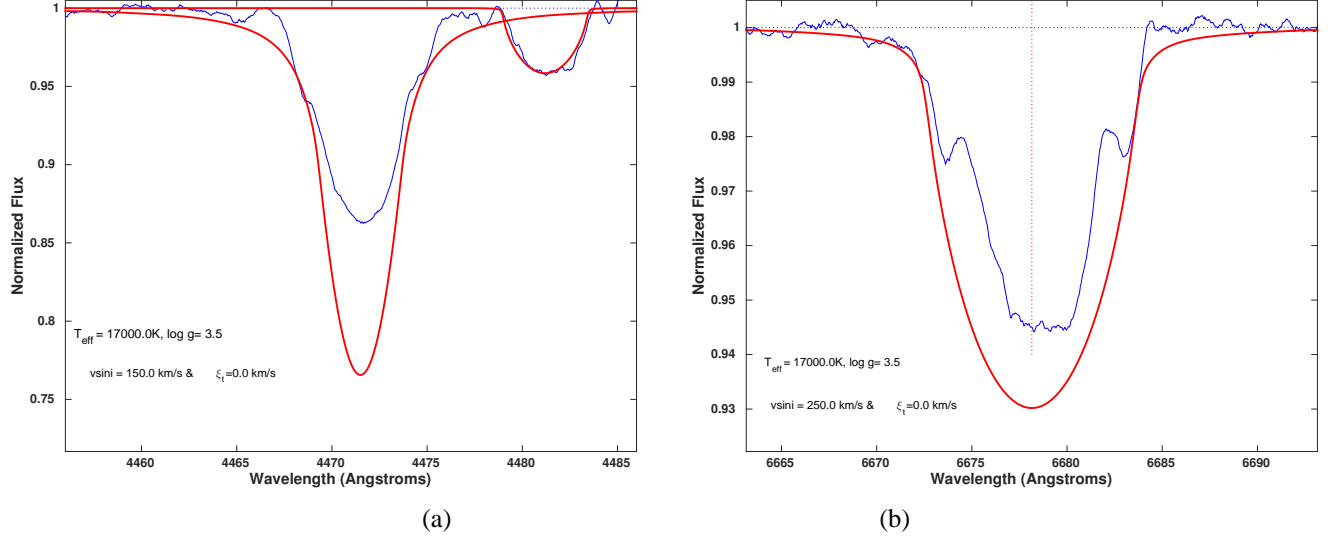


Figure 8.16: The same as Figure (8.12), but for the Be star HD 203467.

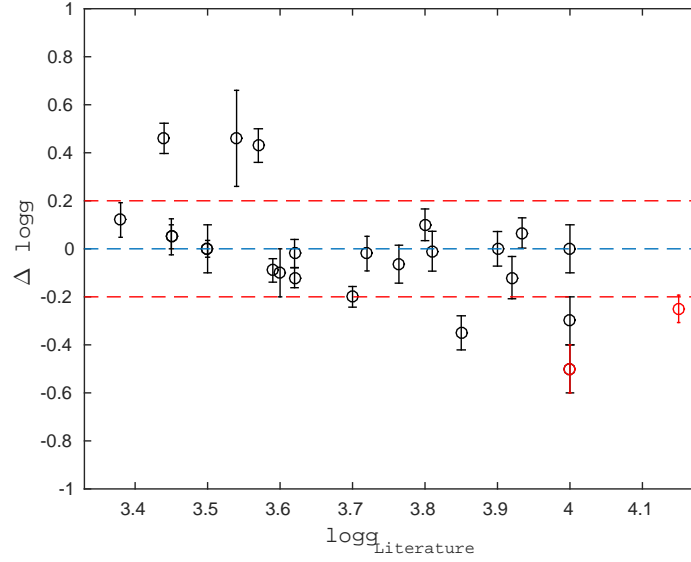


Figure 8.17: The difference between the current estimates of $\log g$ and the available estimates in literature versus the $\log g$ values in literature for the Be stars with available $\log g$ estimates in literature. The red dashed lines represents a difference with a factor of ± 0.2 dex. The red symbols represent Be stars that were poorly fitted with the synthetic line profiles.

8.2.3 Equivalent Width Measurements

Estimations of equivalent widths were obtained by integration over the observed spectral lines. In addition, the observed lines were fitted with pure rotational profiles computed using Equation (8.1). The last step had two important purposes; first, it constrains the shape of the line profiles, especially in case of blends. Secondly, it provides an estimate of the projected rotational velocity, $v \sin i$, which can be done for each line considered, and which acts as a consistency check. Another aspect is that the profile shapes can be significantly affected by noise in the case of weak or very shallow lines, and it is better to fit a template shape in this case.

Figures 8.18 to 8.20 show examples for the measured equivalent widths of the observed N II lines and their $v \sin i$ values used to compute the rotational profiles represented by red lines for three Be stars from the sample, HD11415 (B3III), HD67698 (B3III/IV), and HD58343 (B2Vne). The rest can be found in appendix (E). The measured equivalent widths of N II lines are listed in Table (8.2). The assigned uncertainties represent the change in the equivalent widths caused by changing the continuum level by 0.5 %. An important point to make is that the λ 3995 Å N II line itself is not significantly affected by line blending in most of the cases.

In cases of blends, estimates of the equivalent widths of the lines of interest were obtained in a way that preserves the same ratios of the line strengths of the N II lines as those observed in other stars with lower rotational velocities, i.e. for well defined lines at approximately the same stellar parameters or from the relative ratios of the computed non-LTE line profiles. Also, it matches either the red or the blue side of the line. As an example, Figure (E.1) shows the observed N II lines in the Be star HD 143275. In the figure, the λ 4447 Å N II line is blended with the line O II 4448.3 Å. The equivalent width was estimated such that the line strength ratio of this line relative to the λ 3995 Å line, which is around 50% and also the adopted rotational profile matches the blue side of the observed profile. Similarly, estimations of the equivalent widths of the other observed N II lines in the same star were obtained, λ 4630.5 Å, λ 5676.0 Å, and λ 5679.6 Å.

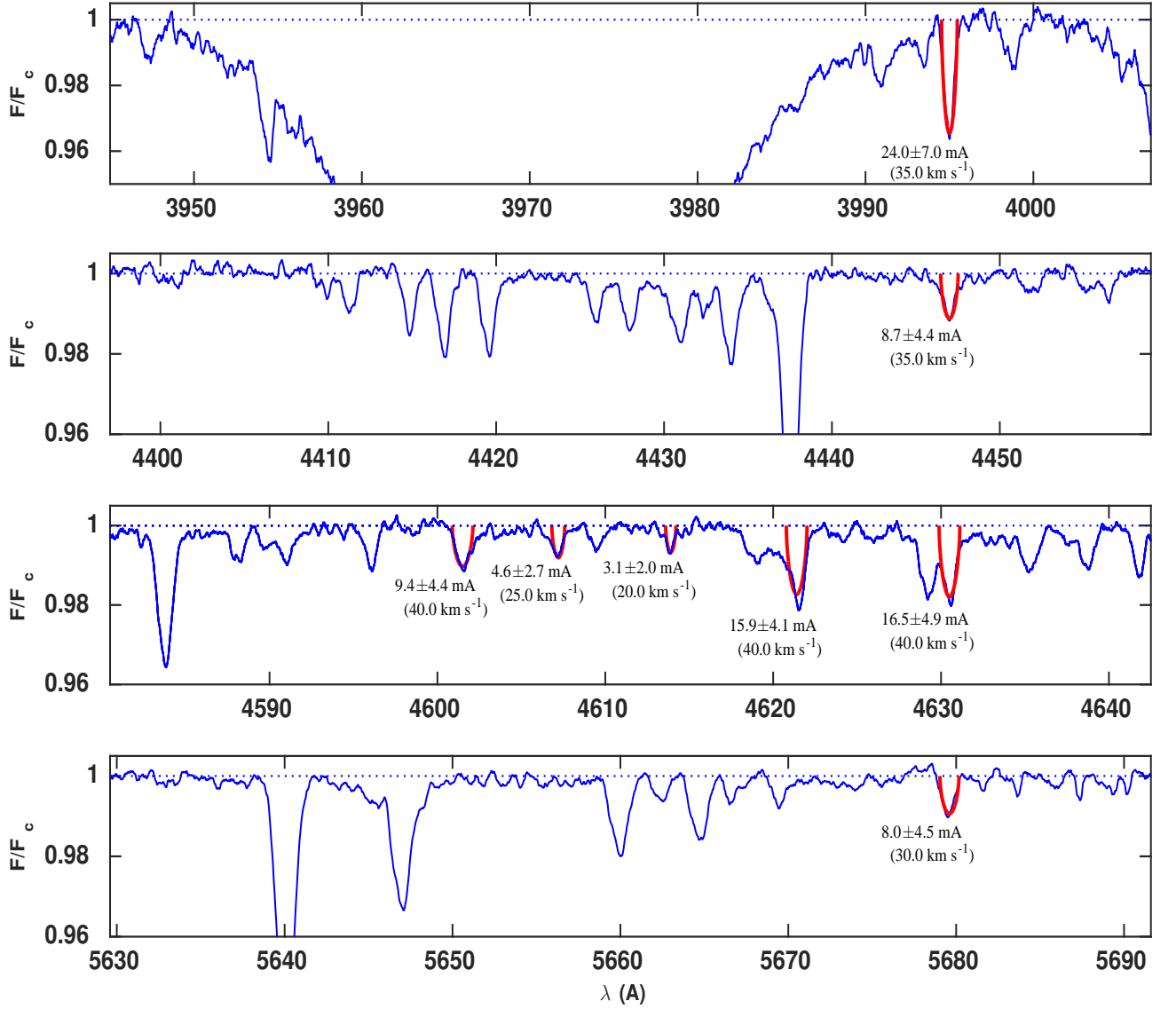


Figure 8.18: Estimating Equivalent widths of observed N II lines in the spectra of the Be star HD 11415. The blue lines represent the observed spectra, the blue dotted lines represents the continuum, and the red lines represent pure rotational profiles computed where the rotational velocities used for the calculation of the rotational profile is shown within brackets.

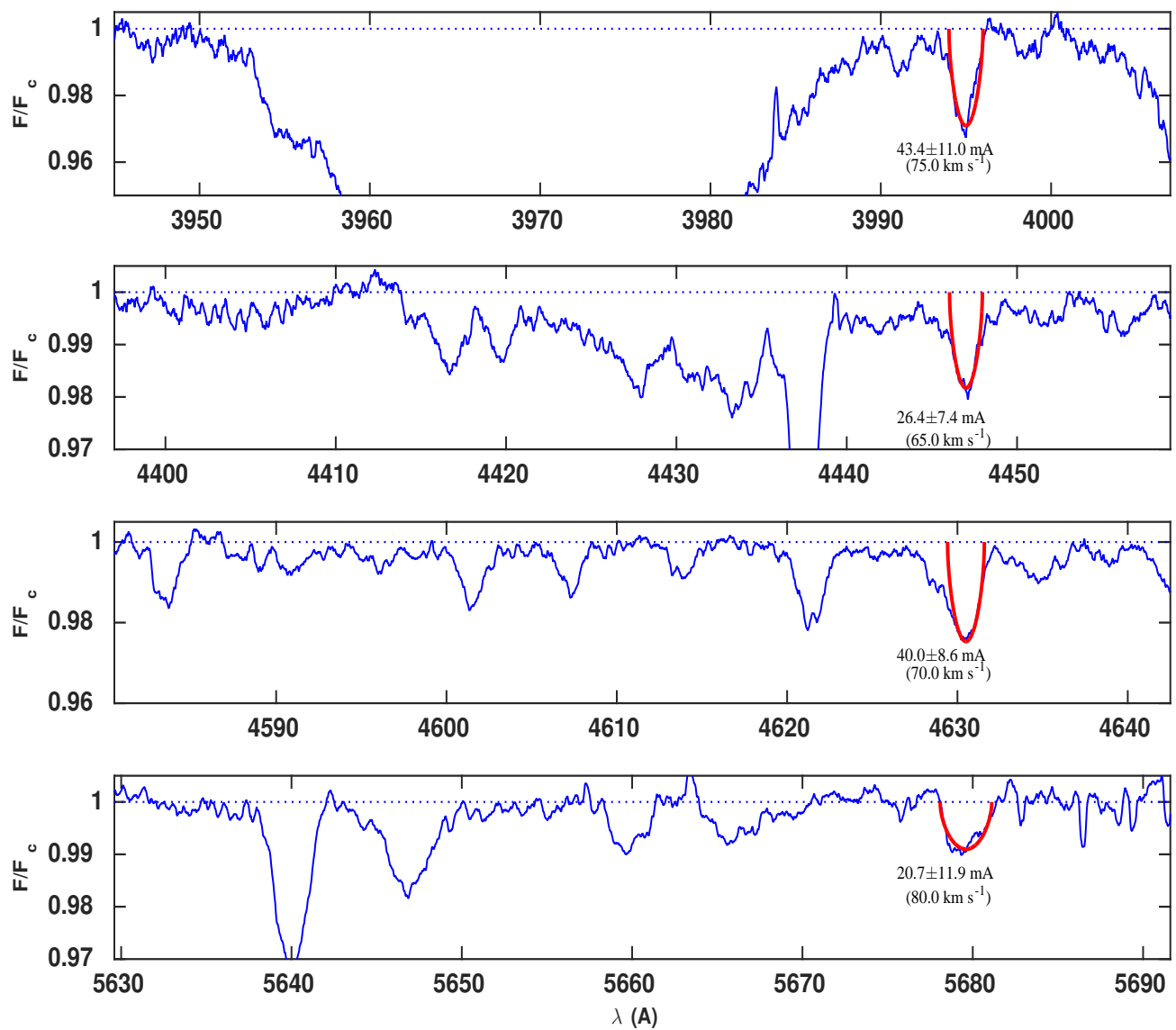


Figure 8.19: The same as Figure (8.18) but for the Be star HD 67698.

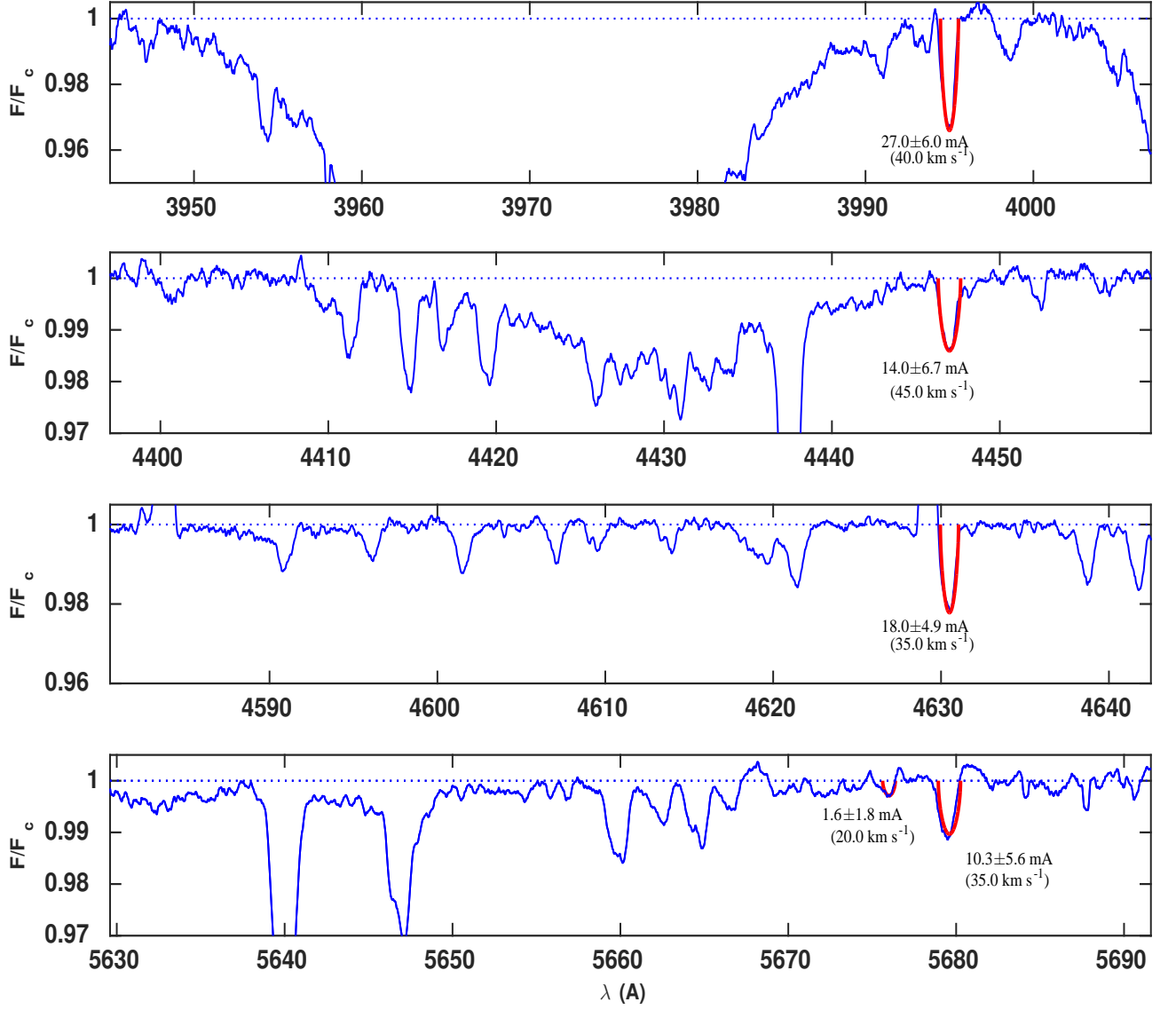


Figure 8.20: The same as Figure (8.18) but for the Be star HD 58343.

Table 8.2: Measured equivalent widths of observed N II lines in the spectra of the sample (in mÅ), and their uncertainties due to errors in the continuum normalization.

HD	Measured Equivalent Widths (mÅ)								
	λ 3995 Å	λ 4447 Å	λ 4601.5 Å	λ 4607.2 Å	λ 4613.9 Å	λ 4621.4 Å	λ 4630.5 Å	λ 5676 Å	λ 5679.6 Å
11415	24.0 ± 7.0	8.7 ± 4.4	9.4 ± 4.4	4.6 ± 2.7	3.1 ± 2.0	15.9 ± 4.9	16.5 ± 4.9	—	8.0 ± 4.5
20336	72.5 ± 24.4	38.6 ± 21.3	—	—	—	—	—	—	—
33328	85.1 ± 28.5	—	—	—	—	—	57.4 ± 29.3	—	—
45725	83.8: ± 25.0	—	—	—	—	—	—	—	40.8 ± 26.6
49567	88.7 ± 13.3	43.7 ± 11.7	44.9 ± 11.1	38.1 ± 10.2	30.6 ± 11.1	42.8 ± 11.7	71.7 ± 13.0	28.7 ± 12.8	64.1 ± 13.8
54309	67.5 ± 22.8	33.5 ± 19.5	—	—	—	—	—	13.8 ± 6.6	62.3 ± 21.7
56139	44.0 ± 11.7	25.1 ± 6.7	—	—	—	—	—	17.4 ± 8.8	41.1 ± 16.5
58050	57.4 ± 12.9	29.7 ± 10.4	—	—	—	—	46.9 ± 14.8	7.7 ± 6.3	36.7 ± 18.4
58343	27.0 ± 6.0	14.0 ± 6.7	13.9 ± 8.2	7.6 ± 6.0	5.7 ± 5.2	16.5 ± 7.5	18.0 ± 4.9	—	10.3 ± 5.6
58978	115.0 ± 33.4	—	—	—	—	—	—	—	—
65875	59.8 ± 18.9	32.1 ± 7.7	—	—	—	—	—	13.0 ± 5.8	43.6 ± 19.1
67698	43.4 ± 11.0	26.4 ± 7.4	—	—	—	—	40.0 ± 8.6	—	20.7 ± 11.9
120324	61.7 ± 20.4	36.3 ± 12.2	—	—	—	—	49.1 ± 12.7	13.4 ± 7.6	55.1 ± 20.0
143275	42.9 ± 17.2	18.0 ± 5.0	—	—	—	—	37.7 ± 12.2	17.9 ± 8.2	41.7 ± 15.8
174237	53.5 ± 15.1	32.4 ± 13.2	—	—	—	—	—	—	33.7 ± 20.5
178175	74.2 ± 20.9	38.1 ± 18.5	—	—	—	—	—	17.9 ± 8.2	63.1 ± 21.8
187567	113.9 ± 19.4	47.0 ± 14.1	—	—	—	—	—	35.9 ± 8.5	98.4 ± 21.6
187811	22.6 ± 14.6	12.5 ± 10.0	—	—	—	—	16.8 ± 11.6	3.1 ± 3.8	12.8 ± 12.6
189687	37.3 ± 18.5	17.8 ± 11.6	—	—	—	—	33.2 ± 17.9	—	24.3 ± 18.4
191610	35.0 ± 17.7	—	—	—	—	—	—	10.2 ± 6.1	35.2 ± 17.7
192685	41.1 ± 18.9	16.4 ± 12.3	—	—	—	—	—	5.7 ± 5.0	26.8 ± 17.7
203467	38.5 ± 16.9	20.7 ± 10.8	—	—	—	—	—	12.5 ± 7.2	27.0 ± 16.9
205637	163.7: ± 38.7	—	—	—	—	—	—	—	—
212076	65.8 ± 17.0	—	—	34.5 ± 12.1	25.9 ± 11.7	—	—	18.9 ± 10.6	58.7 ± 20.2
217050	78.5: ± 28.1	—	—	—	—	—	—	—	69.2: ± 31.7
212571	140.0: ± 30.4	—	—	—	—	—	—	—	—

Table 8.3: Adopted Stellar Parameters of the Central Stars

Spectral Type	$T_{\text{eff}}(K)$	$\log g$	$M(M_{\odot})$	$R(R_{\odot})$
B0V	30098.0	4.0	17.5	7.7
B1V	25978.0	4.0	12.5	6.3
B1.5V	24341.0	4.0	10.8	5.7
B2V	22808.0	4.0	9.6	5.4
B3V	20217.0	4.0	7.7	4.7
B4V	18203.0	4.0	6.4	4.2
B5V	16668.0	4.0	5.5	3.8

Source: Townsend et al. (2004).

8.3 Estimations of Disk Parameters

In order to account for the effects of the circumstellar disk on the emergent photospheric spectral lines, estimates of the most probable disk parameters are required. These parameters are ρ_0 , n and R that describe the density structure of the disk,

$$\rho(R, Z) = \rho_0 (R/R_*)^{-n} e^{-(z/H)^2}, \quad (8.2)$$

where (R, Z) are the cylindrical co-ordinates on the disk. The disk scale height, H , is of the form $H(R) = H_0 (R/R_*)^{3/2}$, and follows the assumption of vertical hydrostatic equilibrium (see Sigut et al. (2009)). In addition, the stellar inclination has an important affect on the appearance of the observed line profile, as discussed before in Section (3.2). To fix the disk density parameters for each star, model $H\alpha$ line profiles were fit to the observed $H\alpha$ profile.

Grids of synthetic $H\alpha$ line profiles were computed using the BEDISK code of Sigut & Jones (2007) and the BERAY code of Sigut (2011) for all combinations of the following disk parameters for central stars of spectral Types B0, B1, B1.5, B2, B3, B4 and B5. The selected values of ρ_0 were 1.0×10^{-12} , 2.5×10^{-12} , 5.0×10^{-12} , 7.5×10^{-12} , 1.0×10^{-11} , 2.5×10^{-11} , 5.0×10^{-11} , 7.5×10^{-11} , 1.0×10^{-10} and $2.5 \times 10^{-10} \text{ g/cm}^{-3}$. The selected values of the power-law index n were 2.0, 2.5, 3.0, 3.5 and 4.0. The selected values of disk radii were 6.0, 12.5, 25.0 and 50.0 stellar radii. Finally, 13 selected inclination angles 10, 18, 20, 30, 40, 45, 50, 60, 70, 72, 80, 84,

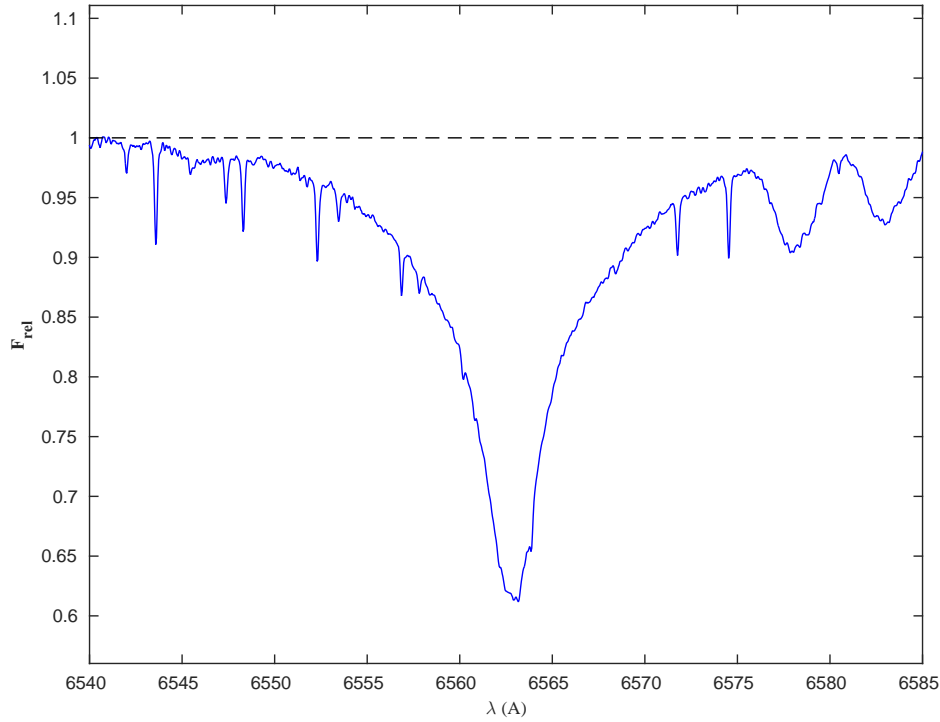


Figure 8.21: Observed $H\alpha$ line profile of the Be star HD 49567. Figure shows no observed emission in this line.

and 89 degrees were considered. All combinations of these parameters make a total of 3600 model $H\alpha$ line profiles for each spectral type. The physical parameters of the central stars, i.e. their masses, radii and temperatures, were taken from Townsend et al. (2004), listed in Table (8.3). Each star in the sample was assigned the same mass and radius as those of the spectral type with the closest T_{eff} value.

The BEDISK code takes the axisymmetric disk density of Equation (8.2) and enforces statistical and radiative equilibrium at many points in the disk to determine the temperature there. Then, the BERAY code performs a formal solution of the transfer equation in order to compute the $H\alpha$ line profile seen by a distant observer with the star-disk system seen at an inclination of i degrees.

The most probable disk parameters of each star of the sample are those of the synthetic $H\alpha$ profile that best match the observed $H\alpha$ line profile from the grid computed, assuming a central star model with the same spectral type as this star are listed in (Table 8.4). Two of the Be stars

in the sample, HD11415 and HD49567, do not show any sign of emission in the Balmer $H\alpha$ lines (the $H\alpha$ line of the Be star HD49567 shown in Figure 8.21). The rest of the Be stars in the sample are classified into three groups: good matching, acceptable matching, and poor matching. In the first group, the adopted disk models reproduce well the observed profiles, especially the peaks. They also have figure of merit, \mathfrak{F} , less than 0.1, e.g. Figure 8.23. The figure of merit could be computed in different ways as the sum of the absolute flux differences, the sum of the square of the flux differences, or the sum of the percentage flux differences, of which all lead to similar results, with a little difference in the order of the top ten models. The sum of the percentage flux difference was used in all cases, defined as

$$\mathfrak{F} = \frac{1}{N} \sum_i \frac{|F_i^{obs} - F_i^{Mod}|}{F_i^{obs}},$$

where the sum i is over the wavelength points between 6550 Å, and 6580 Å. The second group, the adopted models do not reproduce the observed profiles as well as the first group, especially the peaks. This affects the estimated value of their inclinations. Also, almost all of them have $\mathfrak{F} > 0.1$. Figure 8.24 represents an example of this group. The last group includes two Be stars with asymmetric doubly-peaked profiles, HD174237 and HD189687. The disk parameters of Be stars like these two are hard to determine, especially their inclinations, see Figure 8.22. Figures 8.22 to 8.24 show the top ten synthetic $H\alpha$ line profiles that best match the observed $H\alpha$ line profiles for four Be stars in the sample, HD189687, HD143237, and HD45725. The top left panel in each figure shows the the disk model that best reproduces the observed peaks of the line, while the top middle panel shows the disk model that best reproduces the observed central depressions.

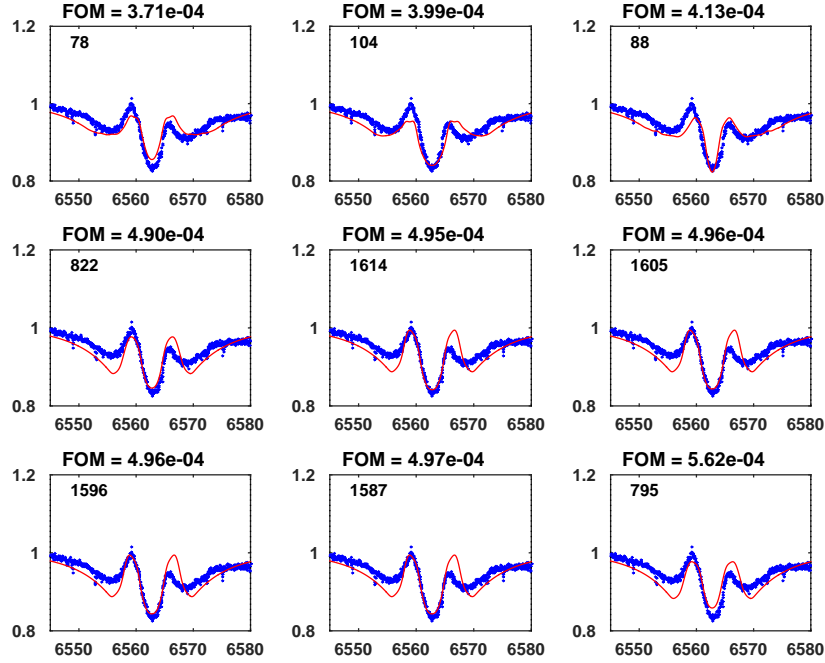


Figure 8.22: Figure shows the synthetic $H\alpha$ profiles of the top 10 disk parameters models computed using BEDISK/BERAY codes, red lines, that best match the observed $H\alpha$ line profile, blue lines, of the Be star HD 189687. The top left panel represents the disk model that best represents the observed peaks, while the top central panel shows the disk model that best matches the disk central depression.

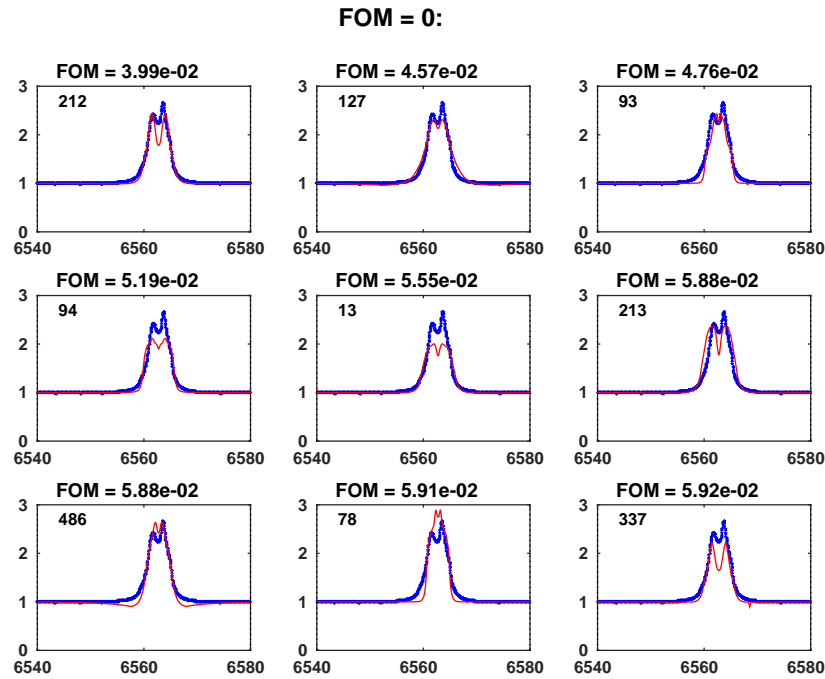


Figure 8.23: The same as Figure (8.22) but for the Be star HD 143275

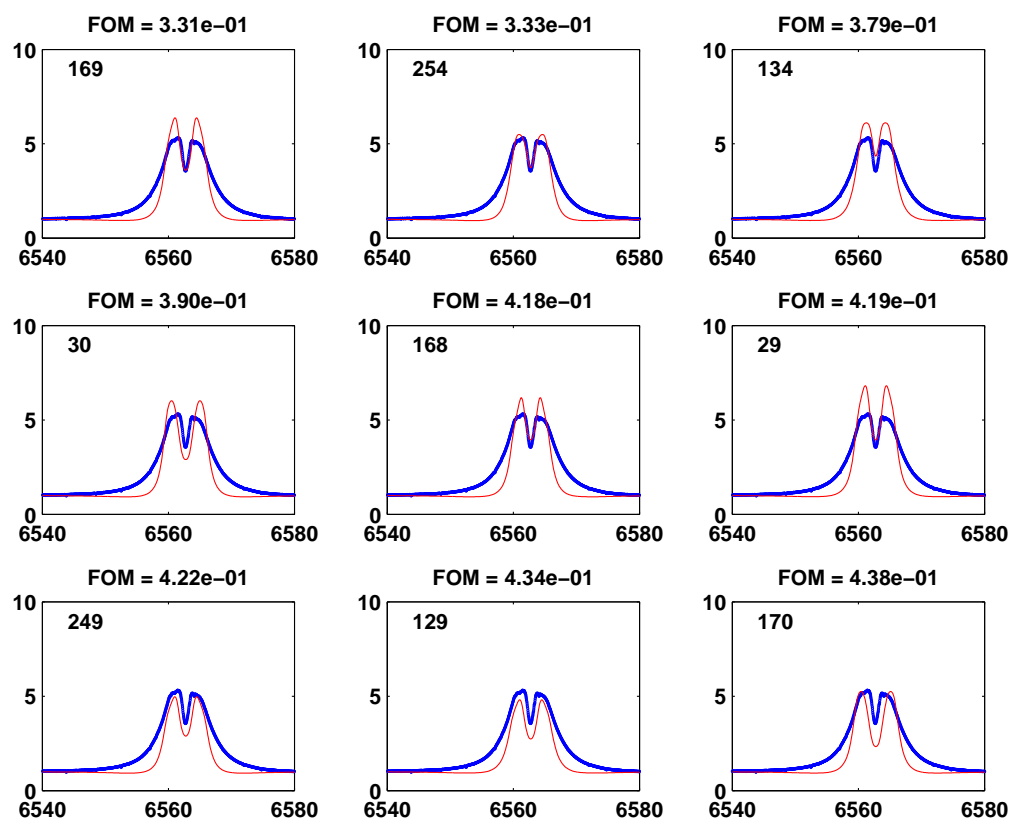


Figure 8.24: The same as Figure (8.22) but for the Be star HD 45725.

Table 8.4: Most Probable Disk Parameters of Be Stars Sample

HD	sp. type assigned	ρ_0	n	R_{disk}	i	i (F05)	Comments
Good Matching							
33328	B2V	1.00^{-12}	3.5	6.0	50.0	73.0	
56139	B3V	2.50^{-11}	2.5	25.0	30.0	16.6	
58050	B3V	1.00^{-12}	2.5	6.0	20.0	21.9	
58343	B5V	5.00^{-12}	2.0	50.0	20.0	9.7	F05
	B4V	1.00^{-11}	2.0	25.0	10.0		Cat13
67698	B5V	2.50^{-11}	3.0	12.5	20.0		
120324	B3V	7.50^{-12}	2.0	6.0	20.0		
	B2V	7.50^{-12}	2.5	12.5	20.0		
143275	B0V	7.50^{-12}	2.5	50.0	18.0		
187811	B4V	7.50^{-12}	2.5	6.0	50.0	48.9	
191610	B4V	7.50^{-12}	3.0	6.0	45.0	63.7	
192685	B4V	1.00^{-11}	3.0	6.0	50.0		
205637	B4V	5.00^{-11}	3.5	25.0	80.0	54.7	
212571	B1V	2.50^{-11}	3.0	12.5	60.0	33.6	
Acceptable Matching							
20336	B4V	5.00^{-11}	3.0	25.0	70.0	66.7	
45725	B4V	7.50^{-12}	2.0	25.0	72.0	66.6	
54309	B3V	1.00^{-10}	3.0	25.0	60.0	38.4	
58978	B1.5V	5.00^{-11}	3.5	50.0	60.0	55.2	
65875	B3V	7.50^{-12}	2.0	50.0	50.0	27.8	
178175	B4V	5.00^{-12}	2.0	12.5	30.0	22.4	
187567	B2V	5.00^{-12}	2.0	25.0	40.0		
203467	B5V	7.50^{-11}	2.5	50.0	60.0		
212076	B3V	5.00^{-12}	2.0	50.0	40.0	18.6	
217050	B4V	5.00^{-12}	2.0	25.0	84.0	78.5	Blue wing
		2.50^{-11}	2.5	50.0	84.0		Red wing
Poor Matching							
174237	B4V	1.00^{-12}	2.0	6.0	50.0	33.2	
189687	B4V	2.50^{-12}	3.0	6.0	30.0	46.6	
No Disk							
11415	B5V	—	—	—	—	—	
49567	B4V	—	—	—	—	—	

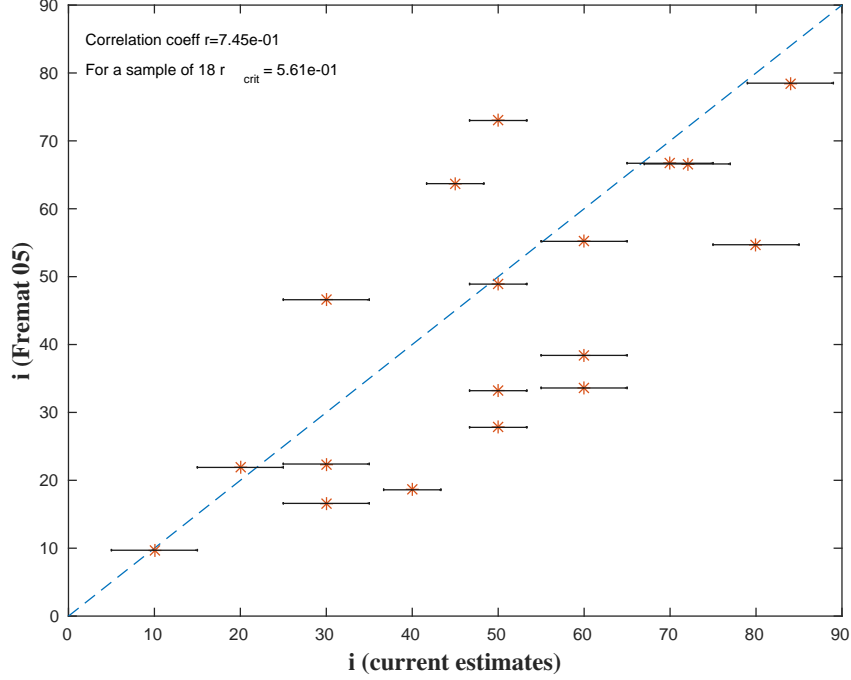


Figure 8.25: Figure shows current estimations of the stellar inclination versus those of Frémat et al. (2005) for the 18 common stars in the sample. In the figure, blue dashed line represents a unity slope line.

The best fit $H\alpha$ profile for each star yields an estimate of the system inclination. The reason for this can be seen in Figure 3.1; low i tends to give singly-peaked profiles, intermediate, doubly-peaked profiles, and large i , shell spectra. Comparison of the current estimations of stellar inclination with those of Frémat et al. (2005) for 18 common stars is shown in Figure (8.25), where the blue dashed line is a unit slope. Current estimates tend to be higher than those of Frémat et al. (2005). The inclination angles of Frémat et al. (2005) represent one of the parameters of non-rotating models that reproduce the observed stellar parameters of their sample when they rotate at ≈ 0.88 of their critical values. The correction process for the gravitational darkening effects was done in an iterative way.

In order to test the statistical significance of the inclination estimations, the Kolmogorov–Smirnov test was performed to compare current results and those of Frémat et al. (2005) to the expected inclination distribution for a random inclination angles following a $\sin(i) di$ distribution. In this

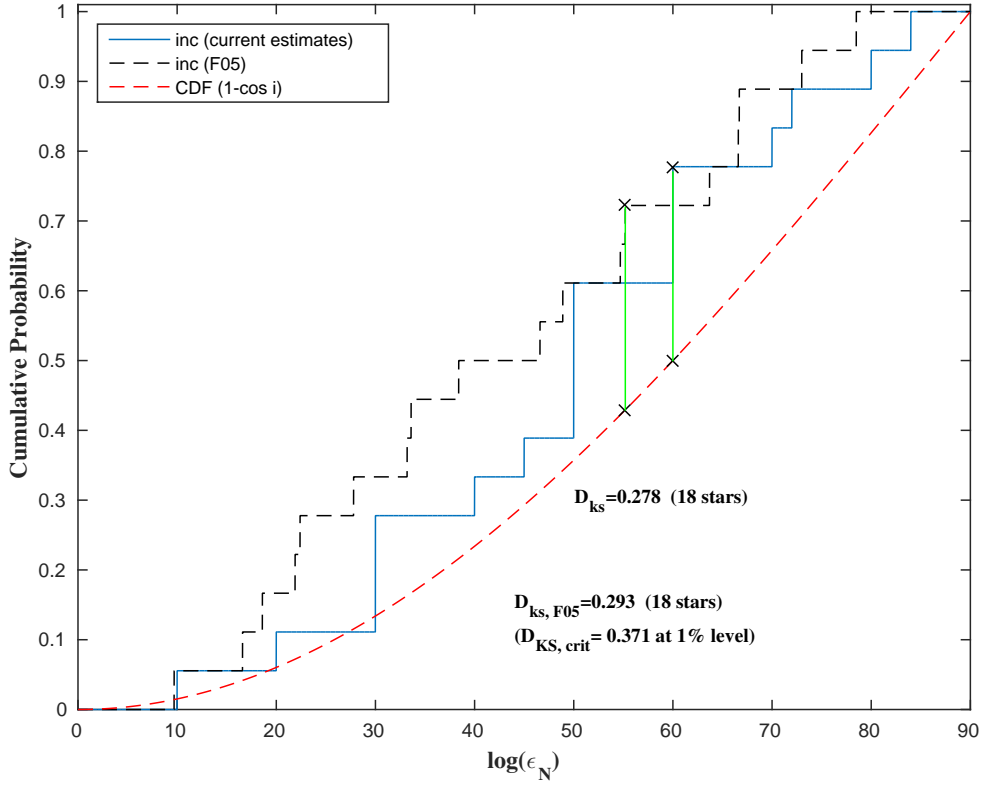


Figure 8.26: Figure shows the results of KS test for comparing current inclination estimations, and those of Frémat et al. (2005) with uniform distribution of inclination angles.

case the cumulative distribution function, CDF, of the inclination is just

$$CDF(i) = 1 - \cos i.$$

Results show that the current estimates of inclination and those of Frémat et al. (2005) are drawn from the expected distribution for random inclinations at the 1 % level ($D_{\text{ks}} < D_{\text{ks,crit}}$). However, the test was performed over small number of objects. Also, this test was performed for the entire results of Frémat et al. (2005), which included 129 Be stars, and this is shown in Figure (8.27). The distribution of the estimated inclinations in the study of Frémat et al. (2005) is not drawn from the expected random distribution, as their results have higher number of objects with low inclination angles than expected. The results of this test shows that the current inclination estimates seem to be more accurate than those of Frémat et al. (2005).

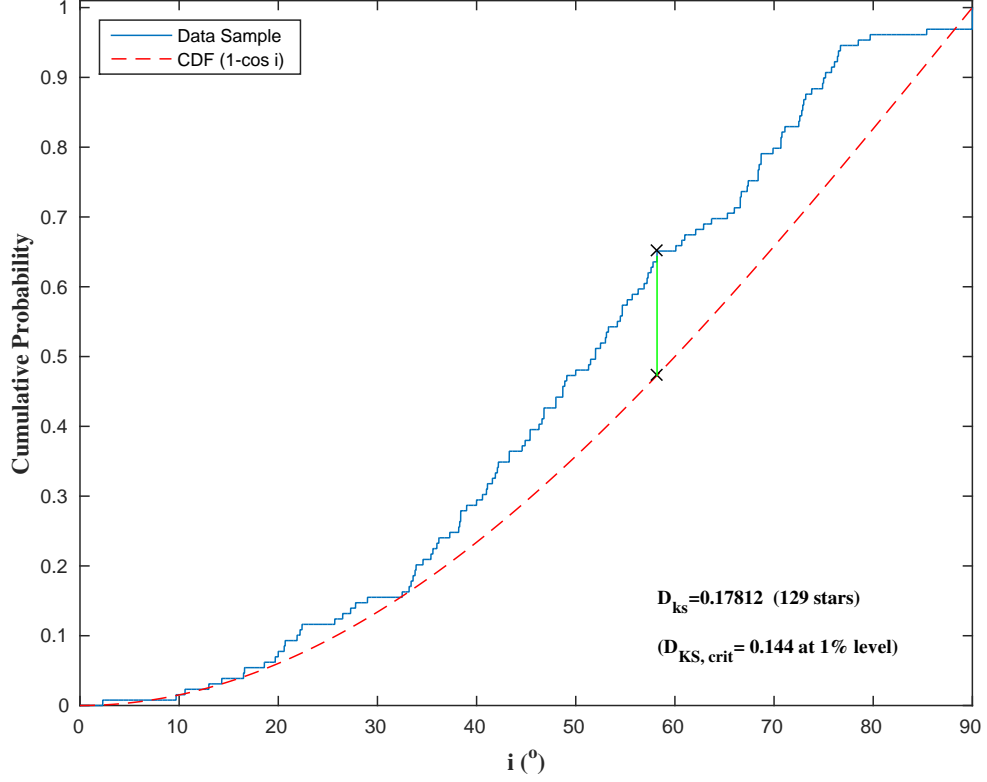


Figure 8.27: The same as Figure (8.26), but only for the results of Frémat et al. (2005) for all objects in this study.

8.4 Nitrogen Abundances

In this section, the estimated nitrogen abundances in the atmospheres of the sample of Be stars are discussed. First, results based solely on the equivalent widths of the observed N II lines without making any corrections are introduced. Then, the effects of gravitational darkening and circumstellar disk emission on the measured equivalent widths or the estimated abundances are investigated.

8.4.1 Estimations of Nitrogen Abundances Based Solely on the Observed Equivalent Widths

The process of determining the nitrogen abundances of the MiMeS sample of Be stars from the computed curves of growths of the N II Monte-MULTI analysis is discussed in subsection (5.6).

At this stage, neither the effect of gravitational darkening nor circumstellar emission will be included. As shown in Section 7.3.1, the expected correction for the realistic rotation ($v_f = 0.85$) and gravitational darkening is expected to be less than 0.1 dex for most of the objects in the sample.

The abundance analysis was done using the `PROG_ABUND` code of Sigut (2014, private communication). A total of 100 random sets of the stellar parameters and equivalent widths were used. The values of the stellar parameters were allowed to vary within the specified uncertainties given in Table 8.1, while the equivalent widths were allowed to vary within the specified uncertainties given in Table 8.2. Then, for each random set of stellar parameters and equivalent widths, the code interpolates in a randomly selected curve of growth of the Monte-MULTI analysis for the 100 random realizations of the nitrogen atom computed at this set of parameters. The final nitrogen abundance is the average of all abundances estimated for all random sets, and the dispersion of abundances represents its uncertainty due to errors in atomic data, stellar parameters, and the measured equivalent widths. Note that the latter is the main source of errors in the current study, as the measured equivalent widths are dominated by uncertainty in the continuum placement. Large rotational broadening, in addition to the strong line blending in many cases, can result in a scarcity of good continuum points for a reliable determination of the continuum. Figure (8.28) shows the estimation of the nitrogen abundance of the Be star HD56139 following the previously explained procedure using the measured equivalent width of the $N\text{ II } 3995 \text{ \AA}$ line. For stars with many observed $N\text{ II}$ lines this was repeated for each line and an average abundance is computed from all estimates obtained from all observed lines.

For microturbulent velocities, the code provides two options; it either uses a fixed value or it tries to determine the microturbulent velocity by forcing strong and weak lines to give the same abundance. However, in the current study, the latter method is not a reliable method of estimating the microturbulent velocity because the abundance analysis is mainly performed using strong lines which are all sensitive to variations of microturbulent velocity. Consequently, the microturbulent velocity was set at two fixed values, 2.0 and 5.0 km s^{-1} , where a microturbulent

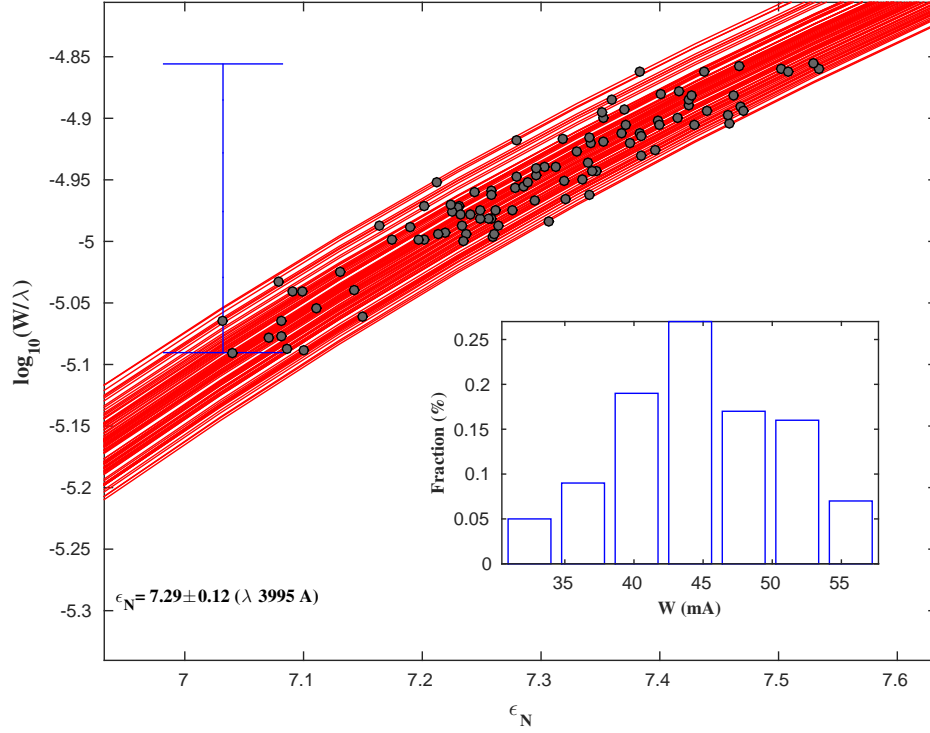


Figure 8.28: Figure shows the estimation of the nitrogen abundance of the Be star HD56139 based on the measured equivalent width of the N II 3995 Å line. This was done by interpolating the curves of growth of 100 Monte-MULTI runs computed for 100 random sets of effective temperatures and gravities (red solid lines), where the stellar effective temperature and gravity were varied within the uncertainties shown in Table 8.1, for 100 random realizations of the equivalent width of the N II 3995 Å line that was varied within the uncertainty listed in Table 8.2. The microturbulence velocity was kept fixed at 2.0 km s^{-1} . The average value of the nitrogen abundance and the dispersion are shown in the figure. In the figure, the circles represent the estimated nitrogen abundances for each random realization of the equivalent width from a randomly selected curve of growth, and the vertical line represents the full range of the random values of the equivalent width. The histogram in the lower right corner of the figure shows the distribution of the random realizations of the equivalent width.

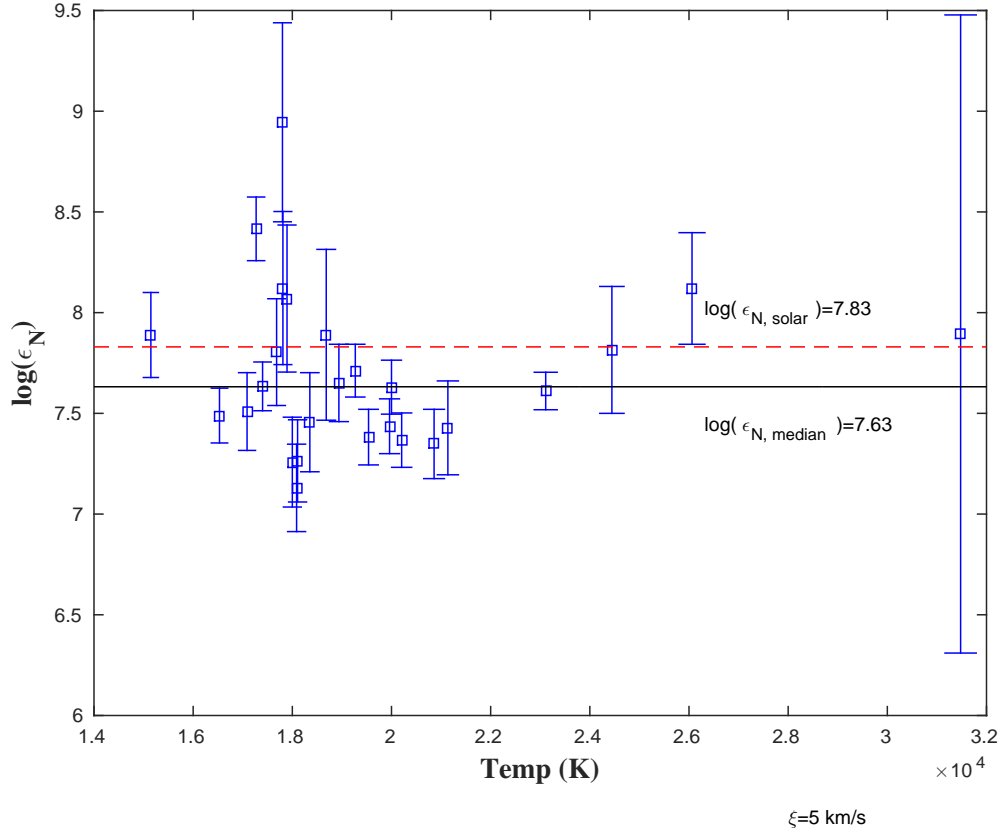


Figure 8.29: Estimated nitrogen abundances ($\xi_t = 5.0 \text{ km s}^{-1}$) of the sample is shown in the figure as a function of the effective temperatures. Red, dashed line marks the solar value of the nitrogen abundance, while the dashed, black line marks the the median value of the measured nitrogen abundances.

velocity of 5.0 km s^{-1} represents an average value over main-sequence B-type stars (Gies & Lambert, 1992).

Figure (8.29) shows the estimated nitrogen abundances for $\xi = 5.0 \text{ km s}^{-1}$ as a function of effective temperature for the sample. The abundance for each star is given in Table (8.5). The average nitrogen abundance is equal to $7.61 \pm 0.30 \text{ dex}$ and lower than the solar value by $\approx 0.2 \text{ dex}$ but in acceptable agreement with the solar value within the uncertainties. Adopting the smaller value of the microturbulent velocities increases the average nitrogen abundance by only 0.1 dex . On the individual level, there a few stars that have nitrogen abundances equal to or higher than the solar nitrogen abundance; although most have lower nitrogen abundance. However, further investigations for the effects of circumstellar disks should be performed (section

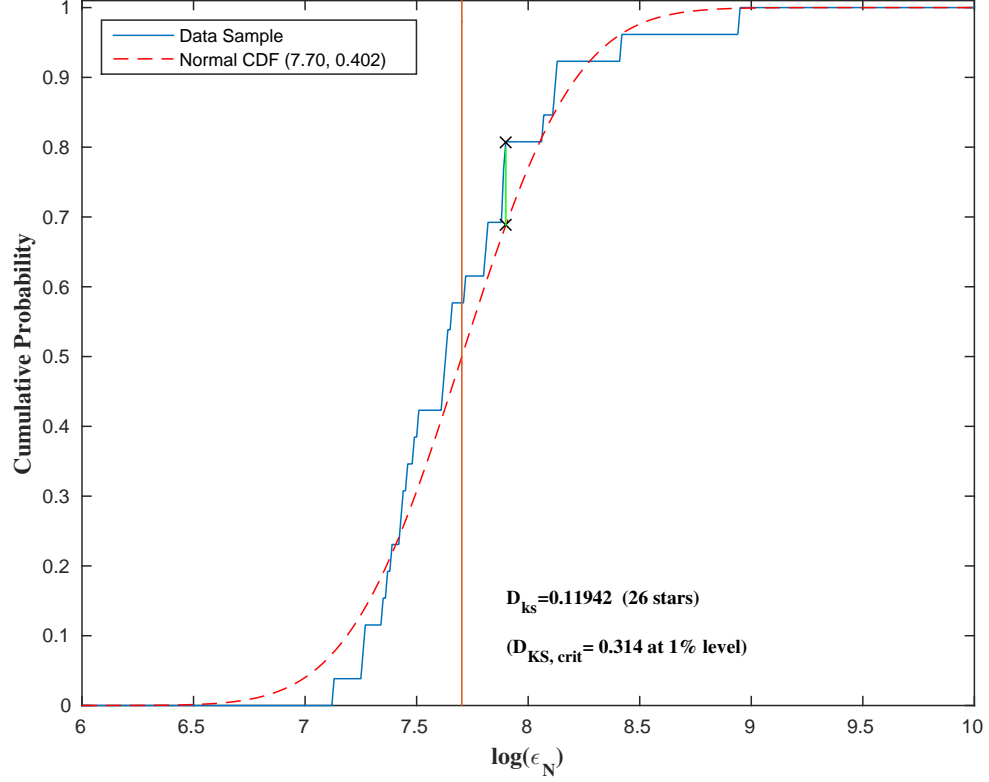


Figure 8.30: Figure shows results of KS test between the estimated nitrogen abundances ($\xi_t = 5.0 \text{ km s}^{-1}$) and cumulative normal distribution computed for a mean and standard deviations equal to those of the estimated nitrogen abundances. Red vertical line marks the average abundance, while the green vertical line and the crosses marks the maximum difference between the two cumulative distribution.

8.4.2) before deciding whether the observed nitrogen abundance is enriched or deficient. The estimated nitrogen abundance of the Be star HD 143275 is highly uncertain because its stellar parameters (31478 K , 3.5) lie close to the upper edge of the grid of the computed non-LTE N II profiles. Also, the N II lines are very weak at such a temperature and gravity and a small change in the equivalent width leads to a large change in the estimated abundance. In addition, in this range of the stellar parameters, some lines are in emission due to non-LTE effects.

A KS statistical test was performed in order to check whether the estimated abundances are normally distributed around the average value. In this test, the cumulative distribution of the nitrogen abundance is compared with a normal cumulative distribution computed using normcdf.m function of MATLAB. The mean and standard deviation of the distribution were

Table 8.5: Measured Nitrogen Abundances of Be Stars Sample

HD	T_{eff} (K)	$\log g$	$\epsilon_N \pm \Delta\epsilon_N$ (dex)	
			$\xi_t = 2.0 \text{ km s}^{-1}$	$\xi_t = 5.0 \text{ km s}^{-1}$
11415	15147.0	3.5	7.96 ± 0.20	7.89 ± 0.21
20336	18684.0	3.9	8.01 ± 0.41	7.89 ± 0.42
33328	21137.0	3.5	7.50 ± 0.26	7.43 ± 0.23
45725	17810.0	3.9	8.25 ± 0.49	8.12 ± 0.38
49567	17270.0	3.5	8.55 ± 0.17	8.42 ± 0.16
54309	20859.0	3.6	7.41 ± 0.16	7.35 ± 0.17
56139	19537.0	3.6	7.43 ± 0.14	7.38 ± 0.14
58050	19961.0	3.9	7.49 ± 0.15	7.44 ± 0.14
58343	16531.0	3.6	7.53 ± 0.17	7.49 ± 0.14
58978	24445.0	4.2	7.96 ± 0.36	7.82 ± 0.32
65875	20205.0	3.9	7.45 ± 0.16	7.37 ± 0.14
67698	17400.0	3.6	7.69 ± 0.16	7.63 ± 0.12
120324	20000.0	4.0	7.70 ± 0.16	7.63 ± 0.13
143275	31478.0	3.5	7.96 ± 0.68	7.89 ± 1.58
174237	17683.0	3.8	7.89 ± 0.29	7.80 ± 0.27
178175	18939.0	3.5	7.73 ± 0.19	7.65 ± 0.19
187567	23110.0	3.7	7.69 ± 0.10	7.61 ± 0.09
187811	18086.0	3.8	7.14 ± 0.24	7.13 ± 0.22
189687	18106.0	3.5	7.28 ± 0.24	7.26 ± 0.20
191610	18353.0	3.7	7.52 ± 0.24	7.46 ± 0.25
192685	18000.0	3.5	7.27 ± 0.20	7.26 ± 0.22
203467	17087.0	3.4	7.57 ± 0.26	7.51 ± 0.19
205637	17801.0	3.4	9.34 ± 0.59	8.95 ± 0.49
212076	19270.0	3.7	7.77 ± 0.15	7.71 ± 0.13
212571	26061.0	3.9	8.28 ± 0.31	8.12 ± 0.28
217050	17893.0	3.6	8.22 ± 0.43	8.07 ± 0.36

selected to be equal to those of the estimated values in Figure (8.30). Figure (8.30) shows that the maximum difference between the cumulative distribution of the sample and the normal cumulative distribution, D_{ks} , is less than the critical value at the 1 % level. Consequently, this supports the null hypothesis that the distribution of the abundance estimations of the sample is drawn from a normal distribution.

Because the λ 3995 Å N II line is less likely to be affected by line blends and measured for all objects, it is a more reliable line for nitrogen abundance analysis than the other N II lines in most cases. It is a good idea to check the estimated nitrogen abundance using all observed

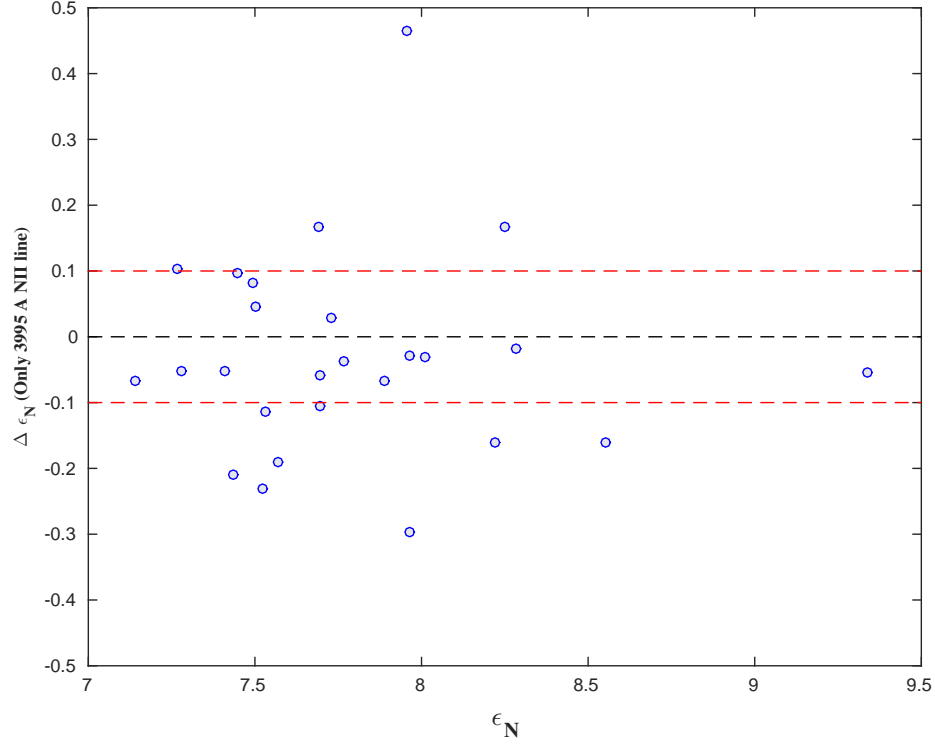


Figure 8.31: Figure shows the change of the estimated nitrogen abundances where the abundance analysis was done only for λ 3995 Å N II line compared to the results of abundance analysis where all observed N II lines were included.

N II lines with an estimate based only on the λ 3995 Å N II line. For this reason, the abundance analysis was reperformed with only this line included. Figure (8.31) shows the the nitrogen abundances based solely on the λ 3995 Å N II line differ only by ± 0.1 dex for most of the sample. The nitrogen abundances estimates based only on this line are lower than the results from the complete analysis of the six Be stars, HD 11415, HD 49567, HD 56139, HD 191610, HD 203467 and HD 217050, by more than 0.1 dex. This could be explained by a possible overestimation of the measured equivalent widths for any of the other N II lines due to line blending, or by a possible disk contamination at the λ 3995 Å line. On the other hand, the estimated nitrogen abundances were larger by more than 0.1 dex for three Be stars, HD 45725, HD 143275 and HD 187567. The higher nitrogen abundance of the Be star HD 143275, based on the λ 3995 Å N II line is attributed to possible line blending at this line. However, all of these differences are less than the proposed uncertainties of the measured nitrogen abundances.

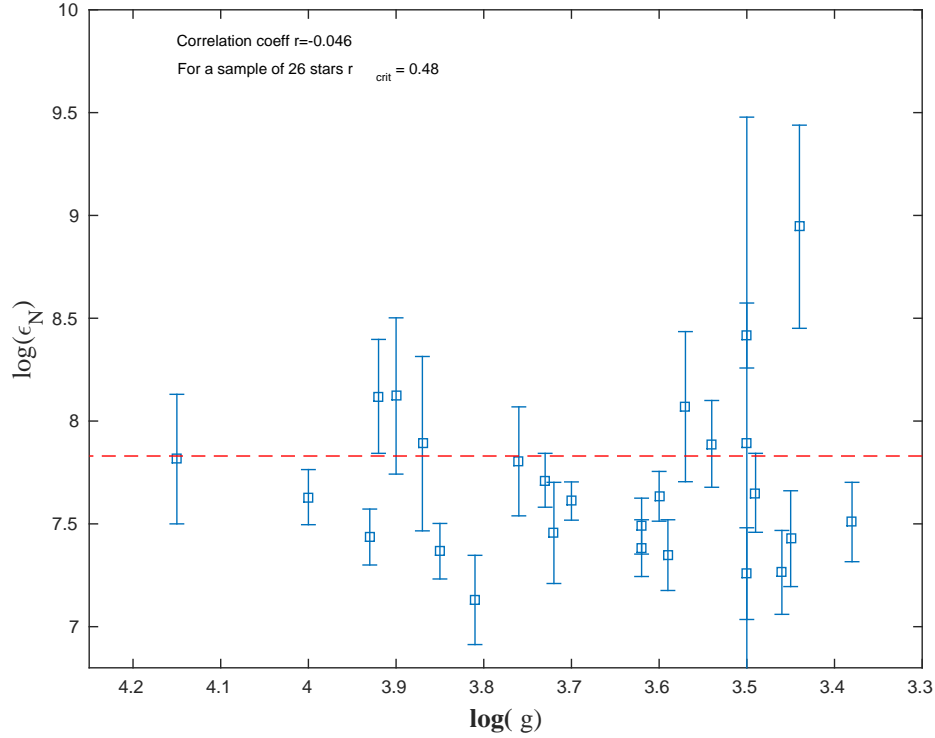


Figure 8.32: Figure shows the change of the estimated nitrogen abundances of the Be stars sample with their gravities. Dashed, red line represents the solar nitrogen abundance ($\epsilon_{N,solar} = 7.83$ dex).

Figures (8.32) and (8.33) shows the change of the measured nitrogen abundances of the Be stars sample with their gravities and equatorial rotational velocities, respectively. Theoretical models of the evolution of rotating massive stars on the main-sequence predict the increase of the nitrogen abundance with age and velocity. The age could be represented with the value of gravity, where the Be star with the smallest gravity is the oldest among them and vice versa. As Figure (8.32) shows there is no significant correlation or anti-correlation between the measured nitrogen abundances of the Be stars in the studied sample and their gravities. Also, there is no significant correlation with their equatorial rotational velocities, Figure (8.33). However, the results are not totally contradicting the predictions of these models, because there is a number of Be stars in the sample with low gravity values, i.e. they close to the TAMS, and they show enriched nitrogen abundances in their atmospheres.

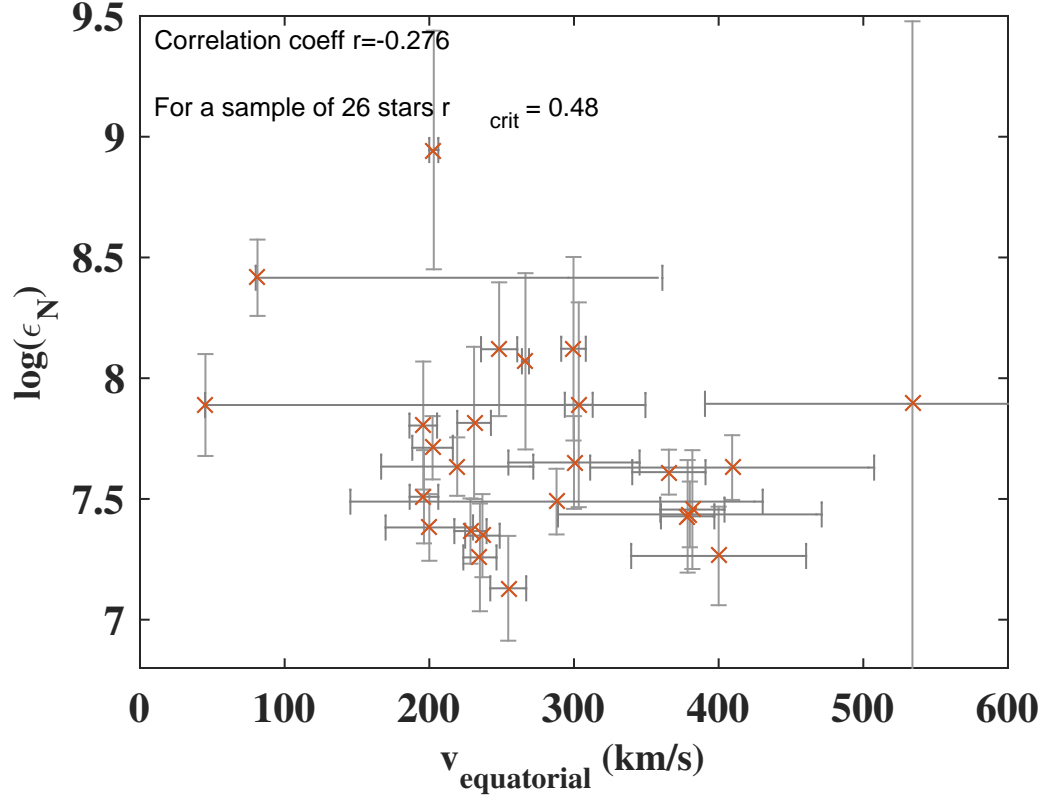


Figure 8.33: Figure shows the change of the estimated nitrogen abundances of the Be stars sample with their equatorial rotational velocities.

8.4.2 Corrections for Circumstellar Disks Effects on the Measured Nitrogen Abundances

The disk parameters obtained in section 8.3 were adopted to compute the expected disk contamination using the `BERAY` code. In these computations, the reference models for each spectral type were taken as the models with disk parameters equal to $\rho_0 = 1.0 \times 10^{-12} (\text{g cm}^{-3})$, $n = 4.0$, $R_{disk} = 6 R_*$ and $i = 60^\circ$. The computed fluxes of these models represent only the fluxes of their central stars, because they have small disks with very low mass that have almost no effect on the emitted stellar radiation.

Figures (8.34) and (8.35) show the expected disk contamination represented by the ratio of the total flux of the central star and the disk system to the emitted flux from central star as a function of wavelengths. Figures (8.34) shows the disk contamination for a model with a

B3-type central star and disk parameters $i = 30^\circ$, $n = 2.5$, and $R_{disk} = 25 R_*$ for 9 selected values of ρ_0 between 1.0×10^{-12} and $1.0 \times 10^{-10} \text{ (g cm}^{-3}\text{)}$ with a step of $2.5 \times 10^{-12} \text{ (g cm}^{-3}\text{)}$. As the figure shows, the model with the lowest ρ_0 value has no significant contribution to the total flux. The expected disk contamination increases with the increase of the disk's mass. In this case, the disk does not lie along the line of sight, and as a consequence the disk adds to the stellar flux by the emitted radiation by bound-free and free-free emission within the disk. The sharp peaks represents the peaks of the bound-free emission at the limits of the different hydrogen series, where the limits of Balmer ($\lambda_{th} = 364.6 \text{ nm}$) and Paschen ($\lambda_{th} = 820.4 \text{ nm}$) series are shown in the figure.

The expected disk contamination for a model with a B4-type central star and disk parameters $i = 80^\circ$, $n = 3.5$, and $R_{disk} = 25 R_*$ and for the same ρ_0 values as Figure (8.34) is shown in Figure (8.35). Again, the model with the lowest ρ_0 value has no effect on the observed stellar radiation. The predicted disk contamination increases with the increase of the value of ρ_0 , i.e. the increase of the disk's mass. In this case, the disk lies along the line of sight, and consequently, the stellar radiation passes through the disk. As a result, absorption by the disk reduces the flux of the emitted radiation from the central star. In contrast to Figure (8.34), there are sharp reduction of the stellar flux at the limits of Balmer and Paschen series due to the abrupt increase of the bound-free absorption rates at these wavelengths.

Table 8.6 shows the predicted disk contamination at 3 wavelengths computed for stellar models with disk parameters equal to those of the best fit for each Be star in the sample.

To correct the observed equivalent width, W_λ^{obs} , for the disk contribution, we use the fact that over the width of the N II spectral lines, the disk contributes a wavelength independent flux, F_D , making the observed flux at wavelength λ

$$F_\lambda = F_\lambda^* + F_D, \quad (8.3)$$

where F_λ^* is the stellar flux in the absence of the disk. Choosing a wavelength outside of the

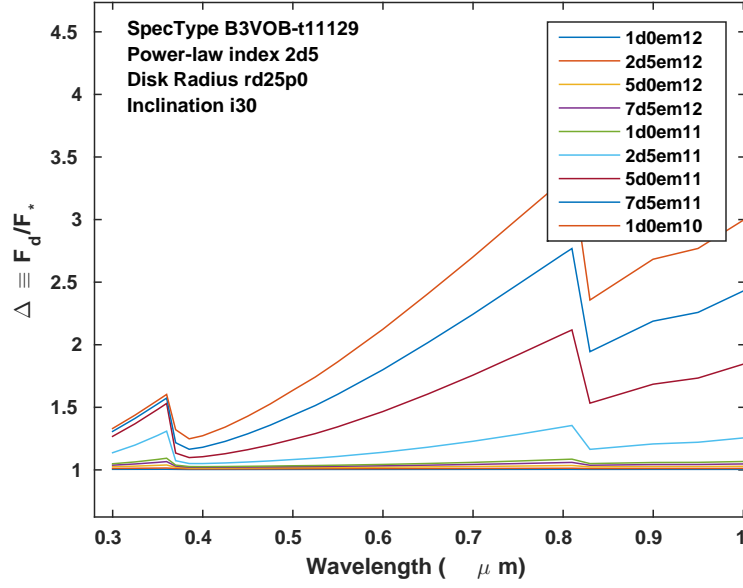


Figure 8.34: Figure shows the expected disk contamination as function of the wavelength for a Be model with a central star of B3 spectral type with viewing inclination angle equal to 30° and disk parameters with $n = 2.5$, $R_{disk} = 25 R_*$ for 9 selected values of ρ_0 between 1.0×10^{-12} and 1.0×10^{-10} (g cm^{-3}).

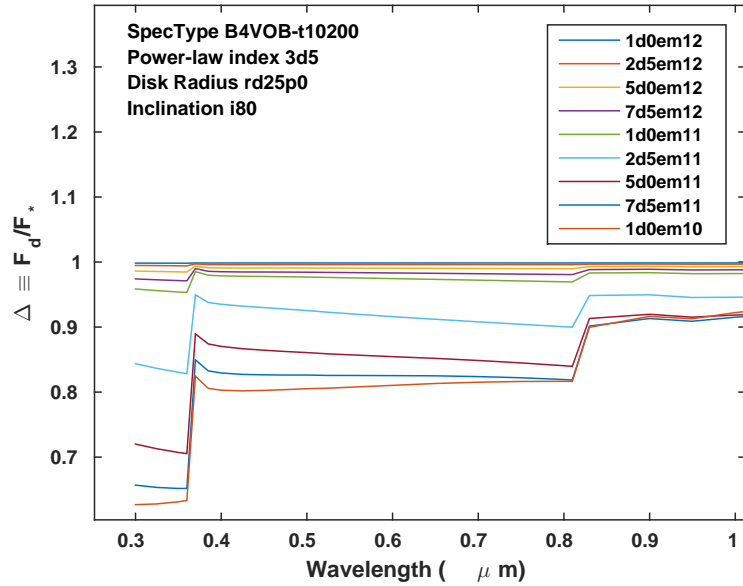


Figure 8.35: The same as Figure (8.34), but for B4-type Be model with disk parameters $i = 80^\circ$, $n = 3.5$, $R_{disk} = 25 R_*$.

line, we have the continuum flux

$$F_C = F_C^* + F_D, \quad (8.4)$$

where F_C^* is the stellar continuum flux in the absence of the disk. The observed equivalent width is

$$W_\lambda^{obs} \equiv \int_{\text{line}} \left(\frac{F_\lambda - F_C}{F_C} \right) d\lambda, \quad (8.5)$$

which includes the contribution of the disk and hence is not equal to the photospheric equivalent that we seek. Inserting the above relations, and using the definition of the photospheric equivalent width as

$$W_\lambda^{cor} \equiv \int_{\text{line}} \left(\frac{F_\lambda^* - F_C^*}{F_C^*} \right) d\lambda, \quad (8.6)$$

it is easy to show that the relation between W_λ^{obs} and W_λ^{cor} :

$$W_\lambda^{obs} = \frac{F_C^*}{F_C^* + F_D} W_\lambda^{cor}. \quad (8.7)$$

Model calculations with BEDISK and BERAY can provide the quantity $\Delta_D \equiv (F_C^* + F_D)/F_C^*$ at the wavelength of each line for the appropriate disk density model found by matching the H α profile. To obtain the photospheric equivalent, we correct the observed equivalent widths as

$$W_\lambda^{corr} = \Delta_D W_\lambda^{obs}. \quad (8.8)$$

While one may expect $\Delta_D > 1$, making the corrected equivalent widths larger than the observed ones, this is not necessarily the case. In shell stars, for example, the stellar continuum is seen through the disk and there is a reduction of the stellar flux associated with the optical depth of the disk. In this case, F_D will be negative, making $F_C^* + F_D < F_C^*$ and $\Delta_D < 1$. Finally, we note that for all of the N II lines, we have neglected line emission from the disk by the N II transitions.

After correcting the observed equivalent widths in this fashion, the abundances analysis was

Table 8.6: Disk Contamination of the Spectra of Be Stars Sample

HD	sp. type assigned	ρ_0	n	R_{disk}	i	$F_{\text{star}+\text{disk}}/F_{\text{star}}$		
						N II λ 3995	He I λ 4481	N II λ 5679.6 (Å)
Good Matching								
33328	B2V	1.00^{-12}	3.5	6.0	50.0	1.001	1.001	1.001
58343	B5V	5.00^{-12}	2.0	50.0	20.0	1.020	1.022	1.029
	B4V	1.00^{-11}	2.0	25.0	10.0	1.042	1.048	1.071
67698	B5V	2.50^{-11}	3.0	12.5	20.0	1.036	1.044	1.083
120324	B3V	7.50^{-12}	2.0	6.0	20.0	1.026	1.029	1.039
	B2V	7.50^{-12}	2.5	12.5	20.0	1.026	1.029	1.038
143275	B0V	7.50^{-12}	2.5	50.0	18.0	1.038	1.040	1.047
191610	B4V	7.50^{-12}	3.0	6.0	45.0	1.006	1.007	1.01
212571	B1V	2.50^{-11}	3.0	12.5	60.0	0.973	0.975	0.989
Acceptable Matching								
45725	B4V	7.50^{-12}	2.0	25.0	72.0	0.992	0.992	0.993
54309	B3V	1.00^{-10}	3.0	25.0	60.0	0.915	0.955	1.109
56139	B3V	2.50^{-11}	2.5	25.0	30.0	1.051	1.062	1.120
58050	B3V	1.00^{-12}	2.5	6.0	20.0	1.001	1.001	1.002
58978	B1.5V	5.00^{-11}	3.5	50.0	60.0	0.935	0.939	0.971
65875	B3V	7.50^{-12}	2.0	50.0	50.0	1.027	1.030	1.046
178175	B4V	5.00^{-12}	2.0	12.5	30.0	1.019	1.021	1.027
187811	B4V	7.50^{-12}	2.5	6.0	50.0	1.006	1.006	1.010
187567	B2V	5.00^{-12}	2.0	25.0	40.0	1.026	1.029	1.039
192685	B4V	1.00^{-11}	3.0	6.0	50.0	1.004	1.004	1.007
203467	B5V	7.50^{-11}	2.5	50.0	60.0	0.958	1.010	1.231
205637	B4V	5.00^{-11}	3.5	25.0	80.0	0.870	0.865	0.856
212076	B3V	5.00^{-12}	2.0	50.0	40.0	1.024	1.027	1.037
217050	B4V (B/W)	5.00^{-12}	2.0	25.0	84.0	0.941	0.938	0.929
	(R/W)	2.50^{-11}	2.5	50.0	84.0	0.892	0.886	0.870
20336	B4V	5.00^{-11}	3.5	25.0	70.0	0.886	0.884	0.903
Poor Matching								
174237	B4V	1.00^{-12}	2.0	6.0	50.0	1.002	1.003	1.003
189687	B4V	2.50^{-12}	3.0	6.0	30.0	1.004	1.005	1.006

reperformed where the corrected equivalent widths were adopted in the analysis. Figure(8.36) shows the change of the estimated nitrogen abundances after applying corrections for the expected disk contamination. As the figure shows, the expected corrections of the nitrogen abundance for the disk contamination lie within ± 0.1 dex for most of the sample. There is a number of stars with larger differences. However, all of these differences are smaller than the estimated

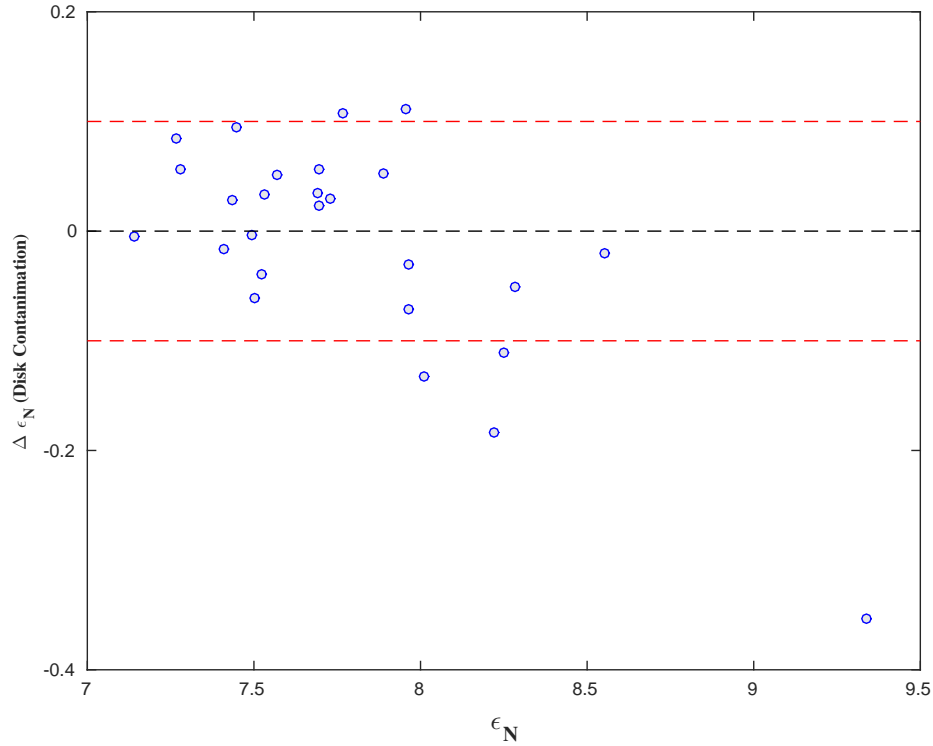


Figure 8.36: Figure shows the changes of the measured nitrogen abundances for the Be stars after implementing corrections for the disk contamination effect.

uncertainties of the nitrogen abundances due to errors in the continuum renormalization.

Finally in Figure 8.37, the obtained abundances are compared as histograms to the recent B-star nitrogen abundances of Lyubimkov et al. (2012) and Nieva & Przybilla (2012). While the mean nitrogen abundance agrees very well in all cases, it is clear that the dispersion in abundance is much larger for the current analysis, with the standard deviation being about a factor of two larger. In fairness to the current results, however, it should be noted that both the Lyubimkov et al. (2012) and Nieva & Przybilla (2012) works used carefully selected samples of stars to yield the most accurate abundance analysis possible— low $v \sin i$, for sharp, unblended lines and no Be stars. The current sample of Be stars used and analyzed here would be naturally excluded from such an analysis as too troublesome!

Nevertheless, there are some unsettling aspects to the current results. A significant number of stars have nitrogen abundances $A_N < 7.6$ dex whereas the previously mentioned B star samples have no such objects. It is difficult to easily reconcile a significant population of sub-

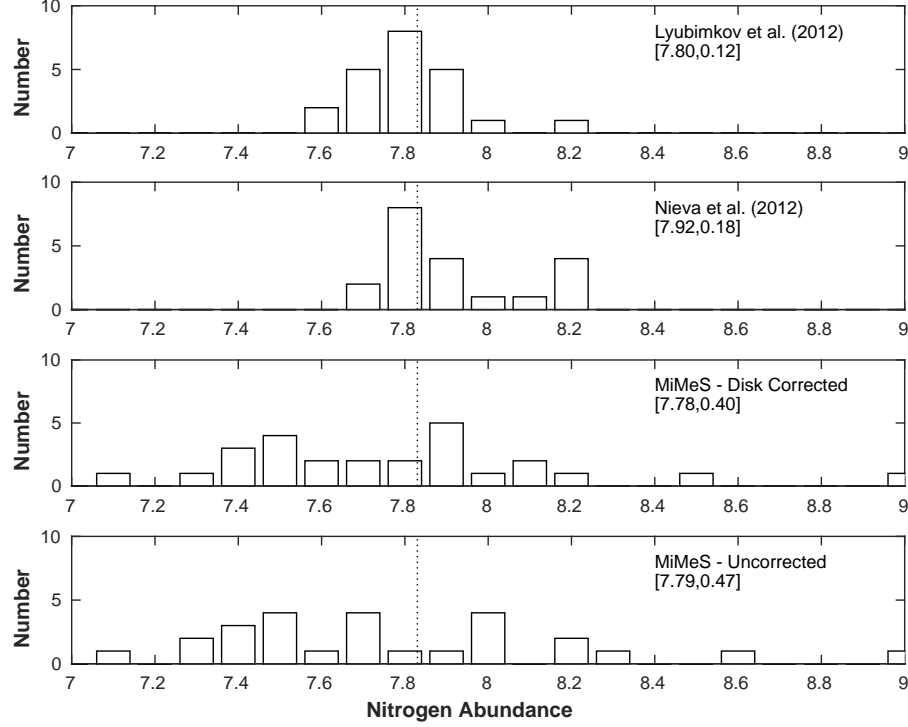


Figure 8.37: Histograms of the measured nitrogen abundances in B and Be stars. The top panel is the B star sample of Lyubimkov et al. (2012); the next lower panel is the B star sample of Nieva & Przybilla (2012); the next lower panel is the current MiMeS Be star sample, corrected for disk emission; the bottom panel is the current MiMeS Be star sample, uncorrected for disk emission. The mean and standard deviation of each sample is given in the panels. The solar nitrogen abundance is indicated by the dotted line in each panel.

solar abundance Be stars when no corresponding main sequence population of B stars exists. One clear source of uncertainty is the neglect of line emission in the N II transitions by the disk which would fill in the lines. This possibility can be checked via further calculation with the BEDISK and BERAY codes.

In addition, we have a small number of high nitrogen abundance objects. The highest abundance object, $A_N > 9$, has a very large uncertainty. The next highest nitrogen abundance, HD 49567, with $A_N = 8.55 \pm 0.17$ is an interesting case. With sharp lines due to its lower $v \sin i$, the abundance seems reliably determined. Nevertheless, this star is a member of a HMXB binary star system (Sterken & Manfroid, 1996) and hence its high nitrogen abundance may be due to mass transfer and not rotational mixing.

8.5 Discussion

Results of the abundance analysis based only on the observed spectral lines without correcting for the disk contamination shows that on average the nitrogen abundance of the sample agrees with the solar value. However, some Be stars of the sample have significantly higher nitrogen abundances compared with the solar value, while others have significantly lower nitrogen abundances. The largest source of uncertainty in the current analysis is the continuum determination of the observed spectra which is a consequence of the rapid rotation of the stars in the sample.

The order of the expected corrections for gravitational darkening effects lies within ± 0.1 dex for most of the stars included in this analysis, see Figure 7.3. This is smaller than the estimated uncertainties of all Be stars in the sample. As a result, it is not expected that correction of the gravitational darkening significantly changes the estimated nitrogen abundances.

Next, effects of the disk contamination on the observed spectral lines were checked, and consequently, the estimated nitrogen abundances. Results show that the expected disk contamination is less than 5% for most of the cases, and it can reach as high as $\approx 25\%$ in some cases. This is not as high as predicted in the previous work of Dunstall et al. (2011). The latter work predicted higher disk contamination that could reach 60% in some cases. The results show that including disk contamination corrections changes the estimated nitrogen abundance by $\approx \pm 0.1$ dex in most cases. Again, these corrections do not significantly change the estimated nitrogen abundances.

Chapter 9

Conclusions

In the current work, abundance analysis was performed for a sample of 26 Be stars using high resolution spectra taken from the MiMeS survey (Wade et al., 2014). This was done to test the expected nitrogen enrichment in their atmospheres by rotational mixing as predicted by theoretical models of the evolution of rotating massive stars (e.g. (Meynet & Maeder, 2000), (Brott et al., 2011) and (Ekström et al., 2012)). Be stars are the fastest rotating main-sequence stars, so measuring their nitrogen abundances represents an important test for the efficiency of matter transport by rotational mixing. However, due to the difficulty of performing abundance analysis for Be stars, they were either excluded in most of the previous spectroscopic analysis, or treated in an ad-hoc way that might affect the estimated abundances (Dunstall et al., 2011). In this current thesis, the accuracy estimates for the nitrogen abundances were obtained through a careful treatment of the departure from LTE in their atmospheres, the rotational effects, and disk contamination.

9.1 Results of Non-LTE calculations

Non-LTE calculations for N II were performed using the MULTI code (v2) of Carlsson (1992). Grids of non-LTE equivalent widths of N II lines over stellar parameters suitable for B-type stars were obtained. In addition to the computation of the non-LTE equivalent widths, estimates of the error bounds on the computed equivalent widths due to errors in the atomic data

were obtained. This is very important in many cases, like the current work, where the nitrogen abundances of many stars in the sample were only based on one line, λ 3995 Å. Consequently, the traditional way of estimating the uncertainties is not applicable, and an alternative procedure is needed. This was done using Monte Carlo simulations following the procedure of Sigut (1996). Results show that the current calculation has a good agreement with the previous calculation of Korotin et al. (1999), but the expected non-LTE effects in the current work are lower.

In addition, non-LTE calculations for He I were performed in order to obtain grids of the non-LTE equivalent widths and profiles of the λ 4471 and λ 6678 Å over stellar parameters suitable for B-type stars. They were used to test the estimated stellar parameters of the sample, and to get estimations of the projected rotational velocities ($v \sin i$) of stars in the sample. Also, they were used to test the effects of gravitational darkening. Results of the He I calculation are in a good agreement with previous calculations and with observed equivalent widths of B type stars adopted from literature. Also, estimates the error bounds on the computed equivalent widths of He I lines due to errors in the atomic data were obtained. Results show that the He I lines are very sensitive for the errors in the atomic data, especially lines with long wavelengths, i.e. $h\nu < kT$, like λ 10830 Å.

9.2 Gravitational Darkening Effects

Gravitational darkening affects the equivalent widths of the λ 3995 and λ 6482 Å N II lines and on the He I λ 6678 Å and Mg II λ 4481 Å lines. The non-LTE equivalent width grid of the Mg II λ 4481 Å line was taken from Sigut & Lester (1996) were investigated. This was done for two data sets; in the first set the standard treatment of von Zeipel was adopted (Collins, 1965), while the new formulation of Espinosa Lara & Rieutord (2011) was adopted in the other set.

Results show that the von Zeipel's standard treatment seems to estimate significantly higher gravitational darkening effects than the new treatment of Espinosa Lara & Rieutord (2011),

such that the expected change in the equivalent widths are smaller in case of adopting the new treatment of Espinosa Lara & Rieutord (2011). The expected changes of the equivalent width of λ 3995 N II line for stars with $T_{\text{eff}} \leq 26,000\text{K}$ and realistic rotational velocities equal to 0.85 of their critical velocities lies within ± 0.1 dex, that covers most of Be stars in the sample.

The gravitational darkening effects on the $v \sin i$ estimates using λ 6678 and λ 4481 Å line profiles were tested. Results show that the λ 4481 Å Mg II line is less affected by gravitational darkening than the other line, which makes it more reliable for $v \sin i$ estimations. Also, current results show that the expected underestimation of the measured projected rotational velocities by adopting the new, and more realistic treatment of Espinosa Lara & Rieutord (2011) is less pronounced than the expected underestimation obtained by adopting the standard treatment of von Zeipel.

9.3 Results of the Abundance Analysis

The results of the abundance analysis based solely on the observed equivalent widths show that the estimated nitrogen abundance have an average value of 7.61 ± 0.30 dex, which agrees with the solar value (7.83 dex) within the uncertainties. The average nitrogen abundance equal to the average measured nitrogen abundance of Lyubimkov et al. (2012), while it is lower than the average measured nitrogen abundance of Nieva & Przybilla (2012). However, the measured nitrogen abundances in the current work have a larger dispersion with a larger fraction of stars with low nitrogen abundances.

Corrections for gravitational darkening effects are of the order of ± 0.1 dex, smaller than the estimated uncertainties of the measured abundances. Consequently, corrections for gravitational darkening effects are not expected to change the measured nitrogen abundances significantly.

Calculations of the disk contamination were done using the BEDISK code of Sigut & Jones (2007) and the BERAY code of Sigut (2011). For this purpose, estimates of the disk parameters

were obtained by fitting the observed $H\alpha$ profiles with synthetic profiles computed using the `BEDISK` code. Then these estimates were used to compute the disk contamination to the observed continuum flux using the `BERAY` code. Results show that the expected disk contamination is less than 5% in most cases, which is not as high as the expected disk contamination in Dunstall et al. (2011).

The estimated nitrogen abundances post correction for the disk contamination changed by ≈ 0.1 dex for most Be stars in the sample. This did not significantly change the measured nitrogen abundances, or the observed distribution. In conclusion, results show that correction for gravitational darkening effects and disk contamination did not significantly change the measured nitrogen abundance that were based solely on the observed equivalent widths. The results do not oppose or support the prediction nitrogen enrichment in the atmospheres of rotating massive stars by rotational mixing.

9.4 Future Directions

Because the abundance analysis was done for a small sample of Be stars, it is suggested that the spectral analysis should be performed over a larger sample of Be stars. Also, including more accurate stellar masses and radii using grids of stellar evolution models in the computation of gravitational darkening and disk contamination may improve the results of the abundance analysis. The presence of a large fraction of Be stars in the sample with low nitrogen abundance may suggest a possible line emission by the disk that could affect the measured nitrogen abundances. This effect was not investigated in the current work, and it is recommended to be investigated in future studies.

Bibliography

- Achmad, L, de Jager, C., & Nieuwenhuijzen, H., 1991, A& A, 250, 445
- Allen, C. W. 1973, *Astrophysical Quantities*, 3rd edition (London: Athlone Press)
- Asplund, M. , Grevesse, N. & Sauval, A. J. 2005 in *Cosmic Abundances as Records of Stellar Evolution and Nucleosynthesis in Honour of David Lambert*, ed. T. G. Barnes III & F. N. Bash, ASP Conf. Ser. 336, 25
- Auer, Lawrence H. & Mihalas, Dimitri 1969, ApJ, 158, 641
- Auer, Lawrence 1973, ApJ, 180, 469
- Auer, Lawrence H. & Mihalas, Dimitri 1973, ApJSS, 25, 433
- Bell, K.L., Hibbert, A., Stafford, R.P., & Brage, T. 1995, MNRAS, 272, 909
- Becker & Butler 1989, A&A, 209, 244
- Becker & Butler 1988, A&A, 76, 331
- Bevington, P. R. 1969, *Data Reduction and Error Analysis for Physical Sciences*(New York: McGraw Hill)
- Bjorkman, J. E., & Cassinelli, J. P. 1993, ApJ, 409, 429
- Braganca, G. A., Daflon, S., Cunha, K., Bensby, T., Oey, M. S., and Walth, G. 2012, AJ, 144, 130
- Bray, I., Burgess, A., Fursa, D.V., & Tully, J.A. 2000, A&AS, 146, 481
- Brott et al., & 8 coauthors 2011, A&A, 530, A115
- Butler, K., & Giddings, J. R. 1985, in *Newsletter on Analysis of Astronomical Spectra*, No. 9 (London: Univ. London)
- Cantiello, M., & 8 co-authors 2009, A&A, 499, 279
- Carciofi, Alex C., & 7 co-authors 2012, ApJ, 744, L15
- Carciofi, Alex C. 2010, IAUS, 272, 325

- Carlsson, Mats 1992, ASP Conference Series, 26, 499C
- Carlsson, M., Rutten, R.J. & Shchukina, N.G. 1992, A&A, 253, 567
- Carroll, Bradley W., & Ostlie, Dale A. 2007, An introduction to modern astrophysics, 2nd edition. San Francisco: Pearson, Addison-Wesley
- Cassinelli, J. P., Brown, J. C., Maheswaran, M., Miller, N. A., & Telfer, D. C. 2002, ApJ, 578, 951
- Catanzaro, G. 2013, A&A, 550, A79
- Chaboyer, B. & Zahn, J.-P. 1992, A&A, 253, 173
- Collins, G. W., II. 1965, ApJ, 142, 265
- Collins, G. W., II. 1966, ApJ, 146, 914
- Coté, J. & Waters, L.B.F.M. & Marlborough, J.M. 1996, A&A, 307, 184
- Coté, J. & Waters, L.B.F.M. 1987, A&A, 176, 93
- Cranmer, Steven R. 2005, ApJ, 634, 585
- Crowther, P. A. 2004, EAS Publication Series, 13,1
- Cunto, W., Mendoza, C., Ochsenbein, F., and Zeippen, C. J. 1993, A&A, 275, L5
- Cunto, W., & Mendoza, C. 1992. Rev. Mexicana Astron. Astrof., 23, 107
- Dachs, J., Hummel, W., & Hanuschik, R. W. 1992, A&ASS, 95, 437
- Dimitrijević, M. S. & Konjević, N. 1986, A&A, 163, 297
- Dimitrijević, M. S. & Sahal-Bréchet, S. 1990, A&A, 82, 519
- Drake, Gordon 2006, Springer Handbook of Atomic, Molecular, and Optical Physics, Springer New York, 199-219
- Dufton & Hibbert 1981, A&A, 95, 24
- Dufton, P.L. & McKeith, C.D. 1980, A&A, 81, 8
- Dufton, P.L. 1979, A&A, 73, 203
- Duntsall, P. R., & 6 co-authors 2011, A&A, 536, A65
- Eddington, A. S. 1925, Obs., 48, 73E
- Ekström, S., & 11 co-authors 2012, A&A, 537, A146
- Ekström, Sylvia, Georgy, Cyril, Meynet, Georges, Maeder, André, & Granada, Anahí 2010, IAU Symposium, 272, 1

- Evans, C.J., & 25 co-authors 2005, A&A, 437, 467
- Fabregat, J., Torrijón, J. M. 2000, A&A, 357,451
- Fernley, J.A., Taylor, K. T., & Seaton, M. J. 1987, J. Phys. B: At. Mol. Opt. Phys., 20, 6457
- Fernley, J.A., Hibbert, A., Kingston, A E & Seaton, M J 1999, J. Phys. B: At. Mol. Opt. Phys., 32, 5507
- Fierro, C. R. & Georgiev, L. 2008, RMXAA, 44, 213
- Frémat, Y., Zorec, J., Hubert, A.-M. & Floquet, M. 2005, A&A, 440, 305
- Fukuda, Ichiro 1982, PASP, 94, 271
- Gehrz, R. D., Hackwell, J. A., & Jones, T.W. 1974, ApJ, 191, 675
- Giddings, J. R. 1981, Ph.D. Thesis, Univ. London
- Gies, Douglas R., & Lambert, David L. 1992, ApJ, 387, 673
- Gray, David F. 1992, The Observation and Analysis of Stellar Photospheres, Third Edition (Cambridge: Cambridge Univ. Press)
- Grevesse, N., & Sauval, A. J. 1998, Space Science Reviews, v. 85, Issue 1/2, p. 161
- Grevesse, N. et al. 2010, Ap&SS, 328, 179
- Habets, G. M. H. J., & Heintze, J. R. W. 1981, A&AS, 46, 193
- Hanuschik, R. W. 1987, A&A, 173, 299
- Hanuschik, R. W., Kozok, J. R., & Kaiser, D. 1988, A&A, 147, 162
- Harmanec, P. 2000, ASP Conference Series, 214, 13
- Heger, A., Fryer, C. L., Woosley, S. E., Langer, N., & Hartmann, D. H. 2003, ApJ, 591, 288
- Heger, A., Langer, N., & Woosley, S.E. 2000, ApJ, 528,368
- Heger, A., & Langer, N. 2000, ApJ, 544, 1016
- Heasley, J.N. & Wolf, Sidney C. 1982, ApJ, 262,663
- Herrero et al., & 5 co-authors 1992, A&A, 260, 209 ASP Conference Series, 214, 527
- Hubeny, I. 1992, LNP, 401, 377H
- Hubeny, I., Hummer, D. G., & Lanz, T. 1994, A&A, 282, 151
- Hummer, D. G. & Mihalas, Dimitri 1988, 331, 794
- Hunter, I., and 10 co-authors 2009, A&A, 496, 841

- Hunter, I., and 7 co-authors 2008, A&A, 479, 541
- Hunter, I., and 9 co-authors 2008, ApJ, 676, L29
- Hunter, I., and 8 co-authors 2007, A&A, 466, 277
- Hunter, I., and 6 co-authors 2005, A&A 436, 687
- Hudson, C. E. & Bell, K. L. 2004, MNRAS, 348, 1275
- Hudson, C. E. & Bell, K. L. 2005a, Phys. Scr., 71, 268
- Husfeld, D., Butler, K., Heber, U. & Drilling, J.S. 1989, A&A, 222, 150
- Jaschek, M., Andrillat, Y., Houziaux, L., & Jaschek, C. 1994, A&A, 282, 911
- Keller, S. C., Wood, P. R., & Bessell, M.S. 1999, A&ASS, 134, 489
- Keller, Stefan 2004, PASA, 21, 310
- Kennicutt, Robert C. 2005, IAUS, 227, 3
- Köhler, K., & 4 co-authors 2012, A&A, 544, A76
- Korn, A.J., Becker, S.R. , Gummersbach, C.A., & Wolf, B 2000, A&A, 353, 655
- Korn, A.J., Keller, & 6-co-authors 2002, A&A, 385, 143
- Korn, A.J., Nieva, M. F., Daflon, S., & Cunha, K. 2005, ApJ, 633, 899
- Kraus, S., & 13 co-authors 2012, ApJ, 744, 19
- Konjević, N., Lesage, A., Fuhr, J. R., & Wiese, W. L. 2002, J Phys Chem Ref Data, 31, pp. 819
- Korotin, S. A., Andrievsky, S. M. & Kostynchuk, L. Yu. 1999, A&A, 342, 756 (referred to as K99 in the text)
- Kurucz, R. F. 1979, Model atmospheres for G, F, A, B, and O stars, ApJS, 40, 1
- Kurucz, R. F. 1993, Kurucz CD-ROM 13, ATLAS9 Stellar Atmosphere Programs (Cambridge: SAO)
- Kurucz, R. F. 1993, Kurucz CD-ROM 23, ATLAS9 Stellar Atmosphere Programs (Cambridge: SAO)
- Langer, N. 2012, ARA&A, 50, 107
- Langer, N. 2006, ASP Conference series, 353, 15
- Langer, N. 1992, A&A, 265, L17
- Lanz, T. & Hubeny, I. 2007, ApJS, 83, 104.

- Espinosa Lara, F. & Rieutord, M. 2011, A&A, 533, A43
- Lee, Umin, Saio, Hideyuki, & Osaki, Yoji 1991, MNRAS, 250, 432
- Lennon, D. J., Lee, J.-K., Dufton, P. L., and Ryans, R. S. I. 2005, A&A, 438, 265
- Lennon, D.J., & Dufton, P.L. 1989, A&A, 225, 439
- Leone, F. & Lanzafame, A.C. 1998, A&A, 330, 306
- Leone, F. & Lanzafame, A.C. 1997, A&A, 320, 893
- Leone, F. & Lanzafame, A.C. & Pasquinni, L. 1995, A&A, 293, 457
- Levenhagen, R. S. & Leister, N. V. 2006, MNRAS, 371, 252
- Luo, D. ,& Pradhan, A. K. 1989, J. Phys. B: At. Mol. Opt. Phys., 22, 3377
- Lyubimokv, Leonid S., & 4 co-authors 2012, MNRAS, tmp, 222L
- Lyubimkov, L.S. 1991, IAUS, 145, 125L
- Maeder, André, & 6 co-authors 2014, A&A, 565, A39
- Maeder, A. & Meynet, G. 2012, RevModPhys., 84, 25
- Maeder, A. 2009, Physics, Formation and Evolution of Rotating Stars, Astronomy and Astrophysics Library. ISBN 978-3-540-76948-4. Springer Berlin Heidelberg.
- Maeder, A., Meynet, G., Ekström, S., & Georgy, C. 2009, CoAst, 158, 72
- Maeder, A., & Meynet, G. 2001, A&A, 373, 555
- Maeder, André, & Meynet, Georges 2001, ARAA, 38, 143
- Maeder, André, Grebel, Eva K., & Mermilliod, Jean-Claude 1999, A&A, 346, 459
- Maeder, André, & Zahn, Jean-Paul 1998, A&A, 334, 1000
- Maeder, André 1995, ASP Conference Series, 83, 1M
- Maeder, A., & Peytermann, E. 1970, A&A, 7, 120M
- Meynet, G., & Maeder, André 2000, A&A, 361, 101
- Martayan, C., & 5 co-authors 2006, A&A, 452, 273
- Martayan, C., & 5 co-authors 2007 , A&A, 462, 683
- Martayan, C., Baade, D., & Fabregat, J. 2010, A&A, 509, A11
- Mattew, Blessen, Subramaniam, Annapurni, & Bhatt, Chandra 2008, MNRAS, 388, 1879

- McGill, M. A. 2013, PhD Thesis, University of Western Ontario
- McGill, M. A., Sigut, T. A. A. & Jones, C. E. 2011, *ApJ*, 743, 111
- McSwain, M. Virginia, & Gies, Douglas R. 2005, *ApJSS*, 161, 118
- Meilland, A., & 7 co-authors 2012, *A&A*, 538, A110
- Mihalas, Dimitri 1978, *Stellar Atmospheres*, Second Edition, San Francisco, W. H. Freeman and Co., 1978. 650 p.
- Mihalas, D., & Stone, M. E. 1968, *ApJ*, 151, 293
- Moon, T. T. 1985, *Comm. from the Univ. of London Obs.*, 78
- Moon, T. T. & Dworetsky, M. M. 1985, *MNRAS*, 217, 305M
- Moore, C. E. 1993, *Tables of Spectra of Hydrogen, Carbon, Nitrogen and Oxygen Atoms and Ions*, ed. J. W. Gallagher (Boca Raton: CRC)
- Morton, Donald C., Wu, Qixue, & Drake, G.W.F. 2006, *Canadian Journal of Physics*, 84, 83
- Napiwotzki, R., Schoenberner, D. & Wenske, V., 1993, *A&A*, 268, 653N
- Nelder, J. A. & Mead, R. 1985, *The Computer Journal*, 308, 13
- Nieva, María-Fernnanda, & Przybilla, Norbert 2014, *A&A*, 566, A7
- Nieva, M.-F. & Przybilla, N. 2012, *A&A*, 539, A143
- Nieva, M.-F. & Simón-Díaz, S. 2011, *A&A*, 532, A2
- Norris, John 1971, *ApJSS*, 23, 193
- Owocki, S. P., Cranmer, S. R., & Gayley, K. G. 1996, *ApJ*, 472, L115
- Owocki, Stan, & Ud-Doula, Asif 2003, *ASP Conference Series*, 305, 350
- Palacios, A. 2013, *EAS Publications Series*, 62, 227
- Porter, John M., & Rivinius 2003, *PASP*, 115, 1153
- Poeckret, R., Bastien, P., & Landstreet, J. D. 1979, *AJ*, 84, 812
- Pols, O. R., Coté, J., Waters, L. B. F. M., & Heise, J. 1991, *A&A*, 241, 419
- Porter, John M. 1996, *MNRAS*, 250, L31
- Porter, John M. 1999, *A&A*, 348, 512
- Preibisch, Thomas, & Zinnecker, Hans 2008, *IAUS*, 237, 270
- Przybilla N., Nieva M.-F., & Butler K., 2011, *J. Phys.: Conf. Ser.*, 328, 012015

- Przybilla, N. 2005, A&A, 443, 293
- Przybilla, N. & Butler, K. 2001, A&A, 379, 955
- Rolleston, W. R. J., Tolstoy, K. Venn, E., & Dufton, P. L. 2003, A&A, 400, 21
- Rutten, R.J. 2003, Radiative Transfer in Stellar Atmospheres, Lecture Notes Utrecht University.
- Sahal-Br  chot, S. & Segre, E. R. A. 1971, A&A, 13, 161
- Sawey, P. M. J. & Berrington, K. A. 1993, Atomic Data and Nuclear Data Tables, 55, 81
- Scharmer, G.B. 1981, ApJ, 249, 720
- Scharmer G. B., & Carlsson M., 1985, J. Comput. Phys., 59, 56
- Sch  nberner, S., & 6 co-authors, A&A, 197, 209
- Seaton, M. J. 1962, Proc. Phys. Soc., 79, 1105
- Seaton, M. J. 1988 A&A, Mol. Opt. Phys., 21, 3033
- Sigut, T. A. A. 2010, in IAU Symp. 272, Active OB Stars: Structure, Evolution, Mass Loss, and Critical Limits, ed. C. Neiner, G. Wade, G. Meynet, & G. Peters (Cambridge: Cambridge Univ. Press), 426
- Sigut, T. A. A., McGill, M. A., & Jones, C. E. 2009, ApJ, 699, 1973
- Sigut, T. A. A., & Jones, C. E. 2007, ApJ, 668, 481
- Sigut, T. A. A. & Lester, John B. 1996, ApJ, 461, 972
- Sigut, T. A. A. 1996, ApJ, 473, 452
- Singh, Mahendra 1985, Ap&AA, 113, 325
- Slettebak, Arne 1988, PASP, 100, 770
- Sterken, C., & Manfroid, J. 1996, A&A, 305, 481
- Struve, Otto 1931, ApJ, 73, 94
- Takeda, Yoichi, Kambe, Eiji, Sadakane, Kozo & Masuda, Seiji 2010, PASJ , 62, 1239
- Talon, Suzanne, Zahn, Jean-Paul, Maeder, Andr  , & Meynet, Georges 1997, A&A, 322, 209
- Talon, S. 2008, EAS Publications Series, 32, 81
- Tarasov, A. E., & Malchenko, S. L. 2012, AstL, 38, 428
- Tody, Doug 1993, ASP Conference Series, 52, 173T

- Townsend, R. H. D., Owocki, S. P., & Howarth, I. D. 2004, MNRAS, 350, 189
- Trundle, C., & 6 co-authors 2007, A&A, 471, 625
- Tur, N. S., Goraya, P. S., & Sharma, S. D. 1995, PASP, 107, 730
- van Belle, Gerard T. 2012, A&AR, 20, 51
- van Kerkwijk, M. H., Waters, L.B.F.M., & Marlborough, J.M. 1995, A&A, 300, 259
- Von Zeipel, H. 1924, MNRAS, 48, 665V
- Wade G. A. et al. 2014, in Petit P., Jardine M., Spruit H., eds, Proc. IAU Symp. 302, Magnetic Fields throughout Stellar Evolution. Cambridge Univ. Press, Cambridge, p. 265.
- Wade, R. A. & Rucinski, S. M. 1985, A&ASS, 60, 471
- Waters, L.B.F.M., van der Veen, W.E.C.J., Taylor, A.R., Marlborough, J.M., & Dougherty, S. M. 1991, A&A, 244, 120
- Waters, L.B.F.M., & Marlborough, J.M. 1994, IAUS, 162, 399
- Wisniewski, J. P., & Bjorkman, K.S. 2006, ApJ, 652, 458
- Wolff, Sidney C. & Heasley, J.N. 1985, ApJ, 292,589
- Woosley, S. E., Heger, A., & Weaver, T. A. 2002, RvMP, 74, 1015
- Zinnecker, H., & Yorke, H. W. 2007, ARA&A ,45, 481
- Zorec, J. & 6 co-authors 2009, A&A, 501, 297
- Zorec, J., & Briot, D. 1997, A&A, 318, 443
- Zahn, J.-P. 1992, A&A, 265, 115
- Yudin, R. V. 2001, A&A, 368, 912

Appendix A

List of Constants and Abbreviations

A.1 Constants

Constant Name	Symbol	Value	unit
Planck's constant	h	6.6261×10^{-27}	$\text{m}^2 \text{g s}^{-1}$
Rydberg constant	R_y	1.0973×10^7	m^{-1}
Solar luminosity	L_\odot	3.8460×10^{34}	erg s^{-1}
Solar mass	M_\odot	1.9885×10^{33}	g
Solar radius	R_\odot	6.9634×10^{10}	cm
Speed of light	c	2.9979×10^{10}	cm s^{-1}
Stefan-Boltzmann constant	σ	5.6704×10^{-5}	$\text{erg cm}^{-2} \text{s}^{-1} \text{K}^{-4}$

A.2 Abbreviations

Phrase	Abbreviation
Korotin et al. (1999)	K99
Local thermodynamic equilibrium	LTE
Large Magellanic Cloud	LMC
Small Magellanic Cloud	SMC
Collisional bound-bound transition	cbb
Collisional bound-free transition	cbf
Radiative bound-bound transition	rbb
Radiative bound-free transition	rbf
Stark width	stk
Terminal age main-sequence	TAMS
Zero age main-sequence	ZAMS

Appendix B

MULTI Results of Selected NII lines

Table B.1: MULTI results for N II λ 3995 Å at $\xi_t = 0 \text{ km s}^{-1}$ (Equivalent widths, W_λ , are in mÅ)

$T_{\text{eff}}, \log(g)$	Nitrogen Abundance difference $\Delta\epsilon_N$, ($\Delta\epsilon_N = \epsilon_N - \epsilon_{N,\text{solar}}$, where $\epsilon_{N,\text{solar}} = 7.83$)													
	-1.00		-0.70		-0.60		-0.30		0.00		0.18		0.30	
	W_λ	W/W_*	W_λ	W/W_*	W_λ	W/W_*	W_λ	W/W_*	W_λ	W/W_*	W_λ	W/W_*	W_λ	W/W_*
15000, 3.5	5.5	1.13	9.4	1.14	11.0	1.15	17.2	1.16	25.6	1.17	31.6	1.17	36.3	1.17
17000, 3.5	13.0	1.16	20.6	1.17	23.5	1.18	34.3	1.19	47.6	1.19	56.6	1.19	63.6	1.19
19000, 3.5	23.2	1.18	35.3	1.20	39.8	1.20	55.4	1.21	73.3	1.21	85.0	1.21	93.9	1.20
21000, 3.5	32.4	1.18	49.0	1.21	55.0	1.21	74.8	1.23	96.4	1.23	110.2	1.23	120.7	1.23
23000, 3.5	34.4	1.16	53.6	1.20	60.6	1.21	83.6	1.24	108.0	1.25	123.2	1.26	134.5	1.26
25000, 3.5	26.4	1.13	44.0	1.17	50.8	1.19	74.3	1.23	99.8	1.26	115.3	1.27	126.7	1.28
27000, 3.5	15.7	1.11	28.7	1.16	34.2	1.17	55.0	1.21	79.5	1.25	94.7	1.27	105.7	1.28
29000, 3.5	5.4	0.88	12.2	1.03	15.4	1.07	29.7	1.16	50.3	1.23	64.4	1.26	74.9	1.27
31000, 3.5	-0.9	-0.55	0.0	0.01	0.8	0.19	5.7	0.66	16.0	0.96	25.3	1.07	33.3	1.13
15000, 4.0	2.9	1.08	5.2	1.09	6.2	1.10	10.4	1.11	16.4	1.12	20.9	1.12	24.6	1.13
17000, 4.0	7.5	1.10	12.6	1.12	14.7	1.12	22.7	1.13	33.3	1.14	40.7	1.14	46.6	1.14
19000, 4.0	15.0	1.12	24.0	1.14	27.4	1.14	40.1	1.15	55.4	1.16	65.7	1.16	73.7	1.16
21000, 4.0	23.9	1.14	37.2	1.16	42.1	1.16	59.2	1.18	78.7	1.18	91.4	1.18	101.1	1.18
23000, 4.0	30.2	1.14	47.2	1.17	53.3	1.17	74.0	1.19	96.5	1.20	110.8	1.20	121.5	1.20
25000, 4.0	28.8	1.11	46.6	1.15	53.2	1.16	75.7	1.19	99.9	1.21	114.8	1.21	125.8	1.22
27000, 4.0	21.2	1.08	36.5	1.12	42.6	1.13	64.5	1.17	88.8	1.20	103.6	1.21	114.4	1.22
29000, 4.0	12.7	1.02	23.9	1.08	28.7	1.09	47.4	1.14	70.5	1.19	84.9	1.20	95.3	1.21
31000, 4.0	5.1	0.79	11.3	0.93	14.3	0.97	27.4	1.06	46.4	1.14	59.6	1.17	69.4	1.19
15000, 4.5	1.4	1.04	2.6	1.06	3.2	1.06	5.7	1.07	9.7	1.08	12.8	1.08	15.5	1.09
17000, 4.5	4.0	1.06	7.1	1.07	8.5	1.08	14.0	1.09	21.8	1.10	27.6	1.10	32.3	1.10
19000, 4.5	8.9	1.08	15.0	1.09	17.5	1.10	27.2	1.11	39.6	1.11	48.4	1.12	55.2	1.12
21000, 4.5	15.8	1.09	25.8	1.11	29.7	1.12	43.8	1.13	60.9	1.13	72.3	1.13	81.1	1.13
23000, 4.5	22.9	1.10	36.8	1.12	42.0	1.13	60.1	1.15	80.8	1.15	94.1	1.15	104.3	1.15
25000, 4.5	26.1	1.09	42.3	1.12	48.4	1.13	69.2	1.15	92.0	1.16	106.4	1.16	117.2	1.16
27000, 4.5	22.5	1.05	38.1	1.09	44.2	1.10	65.6	1.13	89.2	1.15	103.7	1.16	114.5	1.16
29000, 4.5	15.8	1.02	28.3	1.06	33.6	1.07	53.3	1.11	76.2	1.14	90.4	1.15	100.8	1.16
31000, 4.5	9.0	0.93	17.5	1.00	21.4	1.02	37.1	1.08	57.7	1.12	71.1	1.14	80.9	1.15

Table B.2: MULTI results for N II λ 3995 Å at $\xi_t = 5 \text{ km s}^{-1}$ (Equivalent widths, W_λ , are in mÅ)

$T_{\text{eff}}, \log(g)$	Nitrogen Abundance difference $\Delta\epsilon_N$, ($\Delta\epsilon_N = \epsilon_N - \epsilon_{N,\text{solar}}$, where $\epsilon_{N,\text{solar}} = 7.83$)													
	-1.00		-0.70		-0.60		-0.30		0.00		0.18		0.30	
	W_λ	W/W_*	W_λ	W/W_*	W_λ	W/W_*	W_λ	W/W_*	W_λ	W/W_*	W_λ	W/W_*	W_λ	W/W_*
15000, 3.5	5.9	1.12	10.3	1.13	12.2	1.14	19.7	1.15	30.2	1.16	37.8	1.17	43.9	1.17
17000, 3.5	14.2	1.15	23.3	1.16	27.0	1.17	40.6	1.18	57.8	1.19	69.5	1.19	78.5	1.19
19000, 3.5	25.7	1.17	40.9	1.19	46.6	1.19	67.0	1.21	90.6	1.21	106.0	1.21	117.6	1.21
21000, 3.5	36.0	1.17	56.9	1.20	64.7	1.21	91.3	1.22	120.4	1.23	138.6	1.24	152.2	1.24
23000, 3.5	37.5	1.15	61.3	1.18	70.3	1.19	101.1	1.23	134.3	1.25	154.6	1.26	169.4	1.27
25000, 3.5	27.9	1.12	48.5	1.16	56.9	1.17	87.1	1.21	121.3	1.25	142.2	1.27	157.4	1.28
27000, 3.5	15.8	1.09	30.1	1.14	36.3	1.15	61.3	1.20	93.0	1.24	113.2	1.27	127.9	1.28
29000, 3.5	4.8	0.78	11.6	0.96	14.9	1.01	30.5	1.12	54.8	1.20	72.5	1.24	86.1	1.26
31000, 3.5	-1.2	-0.75	-0.8	-0.24	-0.2	-0.06	4.0	0.47	14.4	0.85	24.4	0.99	33.6	1.07
15000, 4.0	3.0	1.07	5.5	1.09	6.7	1.09	11.5	1.10	18.7	1.11	24.2	1.12	28.7	1.12
17000, 4.0	8.0	1.09	13.8	1.11	16.3	1.11	26.0	1.13	39.2	1.14	48.5	1.14	56.0	1.14
19000, 4.0	16.2	1.11	26.9	1.13	31.2	1.14	47.1	1.15	66.7	1.16	80.0	1.16	90.2	1.16
21000, 4.0	26.1	1.12	42.3	1.15	48.6	1.16	70.7	1.17	96.3	1.18	112.8	1.18	125.2	1.19
23000, 4.0	32.9	1.12	53.7	1.15	61.6	1.16	88.9	1.19	118.9	1.20	137.5	1.21	151.3	1.21
25000, 4.0	30.7	1.09	52.0	1.13	60.3	1.14	89.6	1.18	121.9	1.20	141.6	1.22	156.0	1.22
27000, 4.0	22.0	1.06	39.4	1.10	46.6	1.11	73.8	1.16	105.7	1.19	125.4	1.21	139.7	1.22
29000, 4.0	12.7	0.99	24.6	1.05	30.0	1.07	51.9	1.12	80.8	1.17	99.6	1.19	113.3	1.21
31000, 4.0	4.6	0.70	10.8	0.87	13.9	0.91	28.1	1.02	50.2	1.11	66.4	1.15	78.9	1.17
15000, 4.5	1.4	1.04	2.7	1.05	3.4	1.05	6.1	1.06	10.6	1.07	14.3	1.08	17.4	1.08
17000, 4.5	4.2	1.05	7.6	1.07	9.1	1.07	15.5	1.08	24.8	1.09	31.8	1.10	37.6	1.10
19000, 4.5	9.4	1.07	16.4	1.09	19.3	1.09	30.8	1.10	46.2	1.11	57.1	1.12	65.7	1.12
21000, 4.5	16.9	1.08	28.6	1.10	33.3	1.11	50.8	1.12	72.4	1.13	86.9	1.14	98.0	1.14
23000, 4.5	24.6	1.09	41.1	1.11	47.6	1.12	70.7	1.14	97.4	1.15	114.5	1.16	127.3	1.16
25000, 4.5	27.8	1.07	47.1	1.11	54.6	1.12	81.3	1.14	111.2	1.16	129.8	1.17	143.5	1.17
27000, 4.5	23.6	1.03	41.4	1.07	48.7	1.09	75.6	1.12	106.3	1.15	125.3	1.16	139.2	1.16
29000, 4.5	16.1	0.99	29.9	1.04	35.8	1.05	59.3	1.10	88.5	1.13	107.0	1.15	120.4	1.16
31000, 4.5	8.7	0.89	17.7	0.97	21.9	0.99	39.7	1.05	64.5	1.10	81.4	1.13	93.9	1.14

Table B.3: MULTI results for N II λ 3995 Å at $\xi_t = 10 \text{ km s}^{-1}$ (Equivalent widths, W_λ , are in mÅ)

$T_{\text{eff}}, \log(g)$	Nitrogen Abundance difference $\Delta\epsilon_N$, ($\Delta\epsilon_N = \epsilon_N - \epsilon_{N,\text{solar}}$, where $\epsilon_{N,\text{solar}} = 7.83$)													
	-1.00		-0.70		-0.60		-0.30		0.00		0.18		0.30	
	W_λ	W/W_*	W_λ	W/W_*	W_λ	W/W_*	W_λ	W/W_*	W_λ	W/W_*	W_λ	W/W_*	W_λ	W/W_*
15000, 3.5	6.3	1.11	11.3	1.12	13.6	1.13	22.8	1.14	36.3	1.16	46.3	1.16	54.5	1.17
17000, 3.5	15.5	1.13	26.7	1.15	31.4	1.16	49.3	1.17	72.7	1.19	88.9	1.19	101.5	1.19
19000, 3.5	28.6	1.15	47.9	1.17	55.6	1.18	83.7	1.20	117.5	1.21	139.5	1.21	156.1	1.21
21000, 3.5	39.9	1.16	67.0	1.18	77.6	1.19	115.5	1.21	158.6	1.23	185.4	1.24	205.2	1.24
23000, 3.5	40.9	1.13	70.7	1.16	82.8	1.17	126.5	1.21	176.2	1.24	206.7	1.25	228.8	1.26
25000, 3.5	29.5	1.10	53.7	1.14	64.1	1.15	104.6	1.19	154.4	1.23	185.8	1.26	208.6	1.27
27000, 3.5	15.7	1.04	31.2	1.10	38.4	1.12	68.9	1.17	111.9	1.22	141.3	1.25	163.2	1.26
29000, 3.5	3.9	0.63	10.4	0.84	13.8	0.90	30.4	1.05	59.2	1.15	82.4	1.20	101.2	1.23
31000, 3.5	-1.6	-1.00	-1.8	-0.57	-1.6	-0.40	1.3	0.15	10.8	0.63	21.3	0.84	31.6	0.95
15000, 4.0	3.1	1.06	5.9	1.08	7.2	1.08	12.7	1.09	21.5	1.11	28.5	1.11	34.3	1.12
17000, 4.0	8.5	1.08	15.3	1.10	18.2	1.10	30.3	1.12	47.3	1.13	59.8	1.14	69.8	1.14
19000, 4.0	17.6	1.10	30.6	1.12	36.0	1.12	56.8	1.14	83.6	1.15	102.0	1.16	116.2	1.16
21000, 4.0	28.5	1.11	48.8	1.13	57.0	1.14	87.3	1.16	123.7	1.18	147.3	1.18	165.0	1.19
23000, 4.0	35.8	1.10	61.7	1.13	72.2	1.14	110.4	1.17	154.4	1.19	181.8	1.20	201.9	1.21
25000, 4.0	32.8	1.07	58.3	1.10	69.0	1.12	109.2	1.16	156.6	1.19	186.0	1.21	207.3	1.22
27000, 4.0	22.8	1.03	42.5	1.07	51.2	1.09	86.3	1.13	131.3	1.17	160.3	1.20	181.6	1.21
29000, 4.0	12.5	0.94	25.2	1.01	31.2	1.03	57.2	1.09	95.1	1.15	121.7	1.17	141.8	1.19
31000, 4.0	3.8	0.58	9.8	0.77	12.9	0.82	28.1	0.96	54.2	1.06	75.1	1.11	92.1	1.14
15000, 4.5	1.5	1.03	2.8	1.04	3.5	1.05	6.5	1.06	11.7	1.07	16.0	1.07	19.9	1.08
17000, 4.5	4.3	1.05	8.1	1.06	9.8	1.06	17.2	1.08	28.7	1.09	37.6	1.09	45.0	1.10
19000, 4.5	9.9	1.06	17.9	1.07	21.5	1.08	35.7	1.09	55.7	1.11	70.1	1.11	81.6	1.12
21000, 4.5	18.1	1.07	32.0	1.09	37.9	1.10	60.6	1.11	89.9	1.13	109.8	1.13	125.1	1.14
23000, 4.5	26.4	1.07	46.4	1.10	54.7	1.11	85.8	1.13	123.4	1.15	147.7	1.15	165.9	1.16
25000, 4.5	29.6	1.05	52.7	1.09	62.4	1.10	98.6	1.13	141.6	1.15	168.6	1.16	188.4	1.17
27000, 4.5	24.6	1.01	45.2	1.05	54.1	1.06	89.3	1.10	132.9	1.13	160.7	1.15	181.0	1.16
29000, 4.5	16.3	0.96	31.4	1.01	38.3	1.03	67.1	1.07	106.5	1.11	133.0	1.13	152.6	1.15
31000, 4.5	8.3	0.82	17.6	0.92	22.1	0.94	42.4	1.02	73.6	1.08	96.4	1.10	114.1	1.12

Table B.4: MULTI results for N II λ 4447 Å at $\xi_t = 0 \text{ km s}^{-1}$ (Equivalent widths, W_λ , are in mÅ)

$T_{\text{eff}}, \log(g)$	Nitrogen Abundance difference $\Delta\epsilon_N$, ($\Delta\epsilon_N = \epsilon_N - \epsilon_{N,\text{solar}}$, where $\epsilon_{N,\text{solar}} = 7.83$)													
	-1.00		-0.70		-0.60		-0.30		0.00		0.18		0.30	
	W_λ	W/W_*	W_λ	W/W_*	W_λ	W/W_*	W_λ	W/W_*	W_λ	W/W_*	W_λ	W/W_*	W_λ	W/W_*
15000, 3.5	1.2	1.06	2.2	1.07	2.7	1.07	4.8	1.08	8.0	1.09	10.6	1.10	12.8	1.10
17000, 3.5	3.5	1.08	6.3	1.08	7.4	1.08	12.2	1.09	18.9	1.10	23.9	1.10	27.8	1.11
19000, 3.5	7.5	1.09	12.9	1.09	15.1	1.09	23.5	1.09	34.4	1.10	41.9	1.10	47.8	1.10
21000, 3.5	11.8	1.10	19.9	1.09	23.2	1.09	35.3	1.08	49.9	1.08	59.4	1.08	66.7	1.08
23000, 3.5	13.2	1.08	22.7	1.07	26.5	1.07	40.6	1.06	57.2	1.05	67.8	1.05	75.7	1.05
25000, 3.5	10.2	1.05	18.4	1.05	21.9	1.05	35.2	1.04	51.6	1.03	62.1	1.03	69.8	1.03
27000, 3.5	6.4	1.06	12.1	1.07	14.7	1.07	25.4	1.05	39.9	1.04	49.7	1.03	57.1	1.03
29000, 3.5	2.9	1.03	6.1	1.12	7.7	1.14	14.6	1.14	25.4	1.11	33.5	1.09	39.9	1.07
31000, 3.5	0.2	0.30	1.2	0.77	1.9	0.92	5.1	1.24	11.1	1.33	16.2	1.31	20.5	1.28
15000, 4.0	0.6	1.05	1.2	1.05	1.5	1.05	2.8	1.05	4.9	1.06	6.6	1.07	8.1	1.07
17000, 4.0	2.0	1.06	3.6	1.06	4.4	1.06	7.6	1.06	12.4	1.07	16.1	1.07	19.2	1.07
19000, 4.0	4.6	1.07	8.2	1.06	9.7	1.06	16.0	1.07	24.5	1.07	30.7	1.07	35.7	1.07
21000, 4.0	8.4	1.07	14.5	1.07	17.0	1.07	26.8	1.06	39.3	1.06	47.9	1.06	54.6	1.06
23000, 4.0	11.5	1.07	19.8	1.06	23.2	1.06	35.9	1.05	51.3	1.04	61.5	1.04	69.2	1.04
25000, 4.0	11.4	1.04	20.0	1.03	23.6	1.03	37.1	1.02	53.4	1.01	63.9	1.01	71.8	1.01
27000, 4.0	8.6	1.02	15.7	1.02	18.7	1.02	30.9	1.01	46.4	1.00	56.6	0.99	64.2	0.99
29000, 4.0	5.4	0.99	10.5	1.01	12.8	1.02	22.5	1.01	36.1	1.00	45.6	1.00	52.7	0.99
31000, 4.0	2.6	0.88	5.7	0.98	7.1	1.00	13.7	1.03	24.0	1.03	31.8	1.02	38.1	1.01
15000, 4.5	0.3	1.04	0.7	1.04	0.8	1.04	1.6	1.04	2.9	1.04	4.1	1.04	5.2	1.05
17000, 4.5	1.1	1.04	2.1	1.04	2.6	1.04	4.6	1.04	8.0	1.05	10.7	1.05	13.1	1.05
19000, 4.5	2.8	1.05	5.1	1.04	6.1	1.04	10.5	1.04	17.1	1.05	22.1	1.05	26.2	1.05
21000, 4.5	5.5	1.05	9.9	1.05	11.7	1.05	19.3	1.04	29.8	1.04	37.3	1.04	43.2	1.04
23000, 4.5	8.7	1.06	15.3	1.05	18.1	1.04	28.9	1.04	42.9	1.03	52.4	1.03	59.8	1.03
25000, 4.5	10.5	1.04	18.5	1.03	21.8	1.03	34.6	1.01	50.5	1.01	61.0	1.00	69.0	1.00
27000, 4.5	9.3	1.01	16.8	1.00	20.0	1.00	32.6	0.99	48.5	0.98	59.0	0.97	66.9	0.97
29000, 4.5	6.7	0.98	12.6	0.98	15.2	0.98	26.1	0.98	40.6	0.97	50.5	0.96	58.0	0.96
31000, 4.5	4.0	0.92	8.1	0.96	10.0	0.97	18.2	0.98	30.3	0.97	39.0	0.97	45.8	0.96

Table B.5: MULTI results for N II λ 4447 Å at $\xi_t = 5 \text{ km s}^{-1}$ (Equivalent widths, W_λ , are in mÅ)

$T_{\text{eff}}, \log(g)$	Nitrogen Abundance difference $\Delta\epsilon_N$, ($\Delta\epsilon_N = \epsilon_N - \epsilon_{N,\text{solar}}$, where $\epsilon_{N,\text{solar}} = 7.83$)													
	-1.00		-0.70		-0.60		-0.30		0.00		0.18		0.30	
	W_λ	W/W_*	W_λ	W/W_*	W_λ	W/W_*	W_λ	W/W_*	W_λ	W/W_*	W_λ	W/W_*	W_λ	W/W_*
15000, 3.5	1.2	1.06	2.3	1.07	2.9	1.07	5.1	1.08	8.8	1.09	11.9	1.09	14.5	1.10
17000, 3.5	3.7	1.08	6.7	1.08	8.0	1.08	13.6	1.09	21.7	1.10	27.8	1.10	32.8	1.10
19000, 3.5	7.9	1.10	14.0	1.09	16.6	1.09	26.9	1.09	40.6	1.10	50.2	1.10	57.7	1.10
21000, 3.5	12.5	1.11	21.9	1.10	25.8	1.10	40.9	1.09	59.8	1.09	72.4	1.09	82.0	1.09
23000, 3.5	13.8	1.08	24.6	1.08	29.2	1.08	46.8	1.07	68.6	1.06	82.8	1.06	93.3	1.06
25000, 3.5	10.5	1.05	19.5	1.05	23.5	1.05	39.5	1.05	60.5	1.04	74.4	1.04	84.8	1.04
27000, 3.5	6.4	1.05	12.4	1.07	15.2	1.07	27.3	1.06	45.0	1.05	57.6	1.04	67.2	1.04
29000, 3.5	2.7	0.96	6.0	1.09	7.6	1.11	15.0	1.14	27.2	1.12	36.8	1.11	44.7	1.09
31000, 3.5	0.1	0.12	0.9	0.56	1.4	0.72	4.6	1.11	10.9	1.30	16.5	1.32	21.4	1.30
15000, 4.0	0.7	1.05	1.3	1.05	1.5	1.05	2.9	1.05	5.2	1.06	7.2	1.06	8.9	1.07
17000, 4.0	2.0	1.06	3.8	1.06	4.6	1.06	8.2	1.06	13.7	1.07	18.1	1.07	21.8	1.07
19000, 4.0	4.8	1.07	8.7	1.06	10.5	1.06	17.7	1.07	28.0	1.07	35.6	1.07	41.8	1.07
21000, 4.0	8.8	1.08	15.6	1.07	18.6	1.07	30.3	1.07	45.9	1.06	56.8	1.06	65.3	1.07
23000, 4.0	12.1	1.08	21.5	1.07	25.5	1.06	41.0	1.05	60.7	1.05	73.9	1.05	83.9	1.05
25000, 4.0	11.8	1.04	21.4	1.04	25.6	1.04	41.9	1.03	62.8	1.02	76.6	1.02	86.9	1.02
27000, 4.0	8.8	1.01	16.4	1.02	19.9	1.02	34.1	1.01	53.4	1.01	66.5	1.00	76.4	1.00
29000, 4.0	5.4	0.97	10.7	1.01	13.2	1.01	24.0	1.02	40.1	1.01	51.8	1.00	60.9	1.00
31000, 4.0	2.4	0.81	5.5	0.94	7.0	0.97	14.0	1.02	25.5	1.03	34.7	1.03	42.3	1.02
15000, 4.5	0.4	1.04	0.7	1.04	0.9	1.04	1.6	1.04	3.1	1.04	4.3	1.04	5.5	1.04
17000, 4.5	1.1	1.05	2.2	1.04	2.7	1.04	4.9	1.04	8.6	1.05	11.7	1.05	14.4	1.05
19000, 4.5	2.9	1.05	5.3	1.05	6.5	1.05	11.3	1.04	18.9	1.05	24.7	1.05	29.6	1.05
21000, 4.5	5.7	1.06	10.4	1.05	12.5	1.05	21.2	1.05	33.6	1.04	42.7	1.04	50.0	1.05
23000, 4.5	9.1	1.06	16.3	1.05	19.5	1.05	32.2	1.04	49.3	1.03	61.2	1.03	70.5	1.03
25000, 4.5	10.9	1.04	19.7	1.04	23.5	1.03	38.7	1.02	58.5	1.01	71.9	1.01	82.0	1.01
27000, 4.5	9.6	1.01	17.7	1.00	21.3	1.00	36.0	0.99	55.7	0.98	69.0	0.98	79.1	0.98
29000, 4.5	6.8	0.97	13.0	0.98	15.9	0.98	28.1	0.98	45.5	0.98	57.8	0.97	67.3	0.97
31000, 4.5	3.9	0.88	8.1	0.94	10.1	0.95	19.0	0.97	32.9	0.98	43.4	0.97	51.7	0.97

Table B.6: MULTI results for N II λ 4447 Å at $\xi_t = 10 \text{ km s}^{-1}$ (Equivalent widths, W_λ , are in mÅ)

$T_{\text{eff}}, \log(g)$	Nitrogen Abundance difference $\Delta\epsilon_N$, ($\Delta\epsilon_N = \epsilon_N - \epsilon_{N,\text{solar}}$, where $\epsilon_{N,\text{solar}} = 7.83$)													
	-1.00		-0.70		-0.60		-0.30		0.00		0.18		0.30	
	W_λ	W/W_*	W_λ	W/W_*	W_λ	W/W_*	W_λ	W/W_*	W_λ	W/W_*	W_λ	W/W_*	W_λ	W/W_*
15000, 3.5	1.3	1.07	2.4	1.06	3.0	1.07	5.5	1.07	9.8	1.08	13.4	1.08	16.6	1.09
17000, 3.5	3.8	1.08	7.1	1.08	8.7	1.08	15.2	1.08	25.3	1.09	33.1	1.10	39.6	1.10
19000, 3.5	8.4	1.10	15.3	1.10	18.3	1.10	31.0	1.09	49.1	1.10	62.1	1.10	72.5	1.10
21000, 3.5	13.2	1.11	24.0	1.10	28.7	1.10	48.0	1.09	73.9	1.09	91.7	1.09	105.5	1.09
23000, 3.5	14.5	1.09	26.7	1.08	32.2	1.08	54.6	1.07	84.9	1.07	105.3	1.06	120.8	1.06
25000, 3.5	10.8	1.05	20.6	1.06	25.1	1.06	44.6	1.05	72.6	1.05	92.4	1.05	107.6	1.04
27000, 3.5	6.3	1.02	12.7	1.06	15.7	1.06	29.5	1.07	51.4	1.06	68.3	1.06	81.7	1.05
29000, 3.5	2.3	0.84	5.6	1.01	7.2	1.05	15.1	1.12	29.1	1.14	40.9	1.13	51.0	1.12
31000, 3.5	-0.1	-0.08	0.5	0.28	0.9	0.43	3.6	0.88	9.9	1.20	16.1	1.29	21.9	1.31
15000, 4.0	0.7	1.06	1.3	1.05	1.6	1.05	3.0	1.05	5.6	1.05	7.8	1.06	9.9	1.06
17000, 4.0	2.1	1.06	4.0	1.06	4.9	1.06	8.9	1.06	15.4	1.06	20.8	1.07	25.4	1.07
19000, 4.0	5.0	1.07	9.4	1.07	11.3	1.07	19.8	1.06	32.7	1.07	42.5	1.07	50.5	1.07
21000, 4.0	9.2	1.08	16.9	1.08	20.4	1.07	34.7	1.07	55.1	1.07	69.8	1.07	81.5	1.07
23000, 4.0	12.7	1.08	23.3	1.07	28.1	1.07	47.5	1.06	74.1	1.05	92.6	1.05	106.7	1.05
25000, 4.0	12.3	1.05	23.0	1.04	27.8	1.04	48.0	1.04	76.2	1.03	95.7	1.02	110.5	1.02
27000, 4.0	8.9	1.01	17.2	1.02	21.0	1.02	37.8	1.02	62.8	1.02	81.0	1.01	95.0	1.01
29000, 4.0	5.3	0.94	10.8	0.99	13.4	1.00	25.6	1.02	45.2	1.02	60.5	1.01	72.9	1.01
31000, 4.0	2.1	0.70	5.1	0.86	6.6	0.90	14.1	0.99	27.2	1.03	38.3	1.03	47.8	1.03
15000, 4.5	0.4	1.05	0.7	1.04	0.9	1.04	1.7	1.04	3.2	1.04	4.6	1.04	5.9	1.04
17000, 4.5	1.2	1.05	2.2	1.04	2.7	1.04	5.1	1.04	9.3	1.04	12.9	1.05	16.1	1.05
19000, 4.5	2.9	1.05	5.6	1.05	6.8	1.05	12.3	1.05	21.2	1.05	28.3	1.05	34.4	1.05
21000, 4.5	5.9	1.06	11.1	1.05	13.4	1.05	23.6	1.05	38.9	1.05	50.6	1.05	60.0	1.05
23000, 4.5	9.4	1.07	17.5	1.06	21.1	1.05	36.5	1.05	58.5	1.04	74.4	1.04	86.9	1.04
25000, 4.5	11.3	1.05	21.1	1.04	25.5	1.04	44.0	1.03	70.1	1.02	88.4	1.02	102.6	1.01
27000, 4.5	9.8	1.00	18.7	1.01	22.8	1.01	40.3	1.00	65.8	0.99	84.0	0.99	98.1	0.99
29000, 4.5	6.8	0.95	13.4	0.97	16.5	0.98	30.5	0.99	52.1	0.98	68.4	0.98	81.4	0.98
31000, 4.5	3.7	0.83	8.0	0.91	10.1	0.93	19.8	0.96	36.1	0.98	49.2	0.98	60.1	0.98

Table B.7: MULTI results for N II λ 4601.5 Å at $\xi_t = 0 \text{ km s}^{-1}$ (Equivalent widths, W_λ , are in mÅ)

$T_{\text{eff}}, \log(g)$	Nitrogen Abundance difference $\Delta\epsilon_N$, ($\Delta\epsilon_N = \epsilon_N - \epsilon_{N,\text{solar}}$, where $\epsilon_{N,\text{solar}} = 7.83$)													
	-1.00		-0.70		-0.60		-0.30		0.00		0.18		0.30	
	W_λ	W/W_*	W_λ	W/W_*	W_λ	W/W_*	W_λ	W/W_*	W_λ	W/W_*	W_λ	W/W_*	W_λ	W/W_*
15000, 3.5	0.8	0.98	1.6	1.07	1.9	1.09	3.6	1.14	6.4	1.16	8.6	1.16	10.5	1.16
17000, 3.5	2.3	1.04	4.5	1.12	5.5	1.14	9.5	1.16	15.5	1.18	19.9	1.18	23.4	1.18
19000, 3.5	4.9	1.05	9.4	1.14	11.4	1.16	19.0	1.18	29.1	1.19	36.1	1.19	41.5	1.19
21000, 3.5	7.3	0.99	14.5	1.12	17.6	1.14	29.0	1.17	43.3	1.18	52.6	1.18	59.6	1.18
23000, 3.5	6.5	0.83	15.0	1.05	18.6	1.08	32.2	1.14	48.8	1.15	59.4	1.15	67.2	1.15
25000, 3.5	3.1	0.52	9.1	0.82	12.0	0.90	24.1	1.04	39.8	1.08	50.2	1.09	57.9	1.09
27000, 3.5	1.2	0.35	3.8	0.59	5.2	0.67	12.6	0.88	25.0	1.00	34.1	1.03	41.1	1.04
29000, 3.5	0.2	0.16	1.4	0.50	2.0	0.58	5.0	0.75	11.0	0.88	16.7	0.93	21.7	0.97
31000, 3.5	-0.4	-0.45	-0.1	-0.12	0.1	0.04	1.2	0.53	3.5	0.82	5.6	0.90	7.5	0.93
15000, 4.0	0.4	0.90	0.8	1.00	1.0	1.02	2.0	1.07	3.6	1.10	5.1	1.11	6.3	1.11
17000, 4.0	1.2	0.98	2.4	1.06	3.0	1.08	5.5	1.11	9.5	1.13	12.6	1.13	15.3	1.13
19000, 4.0	2.9	1.01	5.6	1.09	6.9	1.11	12.0	1.13	19.4	1.14	24.9	1.15	29.2	1.15
21000, 4.0	5.1	1.01	10.1	1.10	12.3	1.12	20.8	1.14	32.2	1.15	40.0	1.15	46.1	1.15
23000, 4.0	6.5	0.93	13.5	1.07	16.5	1.09	28.0	1.13	42.6	1.13	52.2	1.13	59.4	1.13
25000, 4.0	5.1	0.77	12.0	0.97	15.0	1.02	27.1	1.08	42.4	1.09	52.6	1.09	60.1	1.09
27000, 4.0	2.7	0.57	7.1	0.79	9.3	0.85	19.2	0.99	33.1	1.03	42.6	1.04	49.8	1.04
29000, 4.0	1.4	0.46	3.6	0.64	4.7	0.69	10.7	0.85	21.2	0.96	29.4	0.99	35.8	1.00
31000, 4.0	0.5	0.36	1.7	0.59	2.2	0.65	5.2	0.78	10.8	0.87	16.1	0.92	20.8	0.95
15000, 4.5	0.2	0.80	0.4	0.91	0.5	0.94	1.1	1.01	2.1	1.05	3.0	1.06	3.8	1.07
17000, 4.5	0.6	0.89	1.3	0.98	1.6	1.00	3.2	1.05	5.7	1.07	7.9	1.08	9.7	1.09
19000, 4.5	1.6	0.94	3.3	1.03	4.0	1.04	7.4	1.08	12.5	1.09	16.6	1.10	19.9	1.10
21000, 4.5	3.2	1.00	6.4	1.07	7.9	1.08	13.9	1.11	22.6	1.11	28.9	1.11	33.9	1.11
23000, 4.5	4.9	0.97	10.0	1.07	12.2	1.09	21.2	1.11	33.4	1.11	41.8	1.11	48.2	1.11
25000, 4.5	5.3	0.88	11.4	1.02	14.1	1.04	24.9	1.08	39.1	1.08	48.7	1.08	56.0	1.08
27000, 4.5	3.8	0.72	8.9	0.89	11.3	0.94	21.4	1.01	35.4	1.03	45.0	1.04	52.3	1.04
29000, 4.5	2.2	0.60	5.3	0.76	6.9	0.81	14.4	0.93	26.2	0.99	34.8	1.00	41.6	1.00
31000, 4.5	1.2	0.55	2.9	0.68	3.8	0.72	8.2	0.83	16.3	0.92	23.1	0.96	28.8	0.97

Table B.8: MULTI results for N II λ 4601.5 Å at $\xi_t = 5 \text{ km s}^{-1}$ (Equivalent widths, W_λ , are in mÅ)

$T_{\text{eff}}, \log(g)$	Nitrogen Abundance difference $\Delta\epsilon_N$, ($\Delta\epsilon_N = \epsilon_N - \epsilon_{N,\text{solar}}$, where $\epsilon_{N,\text{solar}} = 7.83$)													
	-1.00		-0.70		-0.60		-0.30		0.00		0.18		0.30	
	W_λ	W/W_*	W_λ	W/W_*	W_λ	W/W_*	W_λ	W/W_*	W_λ	W/W_*	W_λ	W/W_*	W_λ	W/W_*
15000, 3.5	0.7	0.89	1.5	1.02	1.9	1.05	3.8	1.11	6.9	1.14	9.5	1.15	11.8	1.16
17000, 3.5	2.2	0.97	4.6	1.08	5.6	1.10	10.3	1.15	17.4	1.17	22.9	1.17	27.4	1.18
19000, 3.5	4.7	0.96	9.7	1.10	11.9	1.12	21.0	1.17	33.8	1.18	42.9	1.19	50.1	1.19
21000, 3.5	6.6	0.86	14.7	1.06	18.3	1.10	32.4	1.16	50.9	1.18	63.5	1.18	73.1	1.19
23000, 3.5	5.4	0.66	14.5	0.95	18.6	1.02	35.2	1.12	56.8	1.14	71.2	1.15	81.9	1.15
25000, 3.5	2.3	0.38	8.0	0.70	11.0	0.79	24.7	0.99	44.4	1.07	58.0	1.08	68.3	1.08
27000, 3.5	0.7	0.20	3.1	0.48	4.5	0.56	11.9	0.80	25.8	0.96	37.0	1.01	45.9	1.03
29000, 3.5	-0.2	-0.13	0.9	0.32	1.5	0.43	4.5	0.67	10.7	0.83	16.7	0.90	22.3	0.94
31000, 3.5	-0.6	-0.53	-0.5	-0.34	-0.3	-0.21	0.7	0.30	3.1	0.70	5.3	0.84	7.4	0.90
15000, 4.0	0.3	0.82	0.8	0.94	1.0	0.97	2.0	1.04	3.8	1.08	5.4	1.10	6.9	1.11
17000, 4.0	1.1	0.91	2.4	1.02	3.0	1.04	5.8	1.09	10.3	1.12	14.0	1.12	17.2	1.13
19000, 4.0	2.7	0.94	5.7	1.05	7.1	1.08	13.0	1.12	21.9	1.14	28.6	1.14	34.1	1.15
21000, 4.0	4.8	0.92	10.3	1.06	12.7	1.08	22.8	1.13	37.0	1.15	47.2	1.15	55.1	1.15
23000, 4.0	5.9	0.81	13.5	1.01	16.9	1.05	30.7	1.11	49.3	1.13	62.1	1.13	71.8	1.14
25000, 4.0	4.3	0.64	11.4	0.89	14.8	0.95	28.9	1.06	48.3	1.09	61.7	1.09	71.8	1.09
27000, 4.0	2.2	0.46	6.4	0.69	8.7	0.77	19.4	0.94	36.1	1.02	48.1	1.04	57.5	1.04
29000, 4.0	1.1	0.35	3.2	0.55	4.3	0.61	10.3	0.79	21.8	0.92	31.4	0.97	39.3	0.99
31000, 4.0	0.2	0.17	1.4	0.48	1.9	0.55	4.9	0.72	10.7	0.84	16.3	0.89	21.5	0.93
15000, 4.5	0.2	0.71	0.4	0.85	0.5	0.88	1.1	0.97	2.1	1.02	3.1	1.04	4.0	1.05
17000, 4.5	0.6	0.81	1.3	0.93	1.6	0.96	3.2	1.02	6.0	1.06	8.5	1.07	10.6	1.08
19000, 4.5	1.6	0.87	3.3	0.98	4.1	1.01	7.7	1.06	13.7	1.09	18.4	1.09	22.5	1.10
21000, 4.5	3.1	0.93	6.5	1.04	8.1	1.06	14.9	1.10	25.2	1.11	33.0	1.11	39.3	1.11
23000, 4.5	4.6	0.89	10.0	1.03	12.5	1.05	22.9	1.10	37.9	1.11	48.6	1.11	57.0	1.11
25000, 4.5	4.8	0.78	11.2	0.96	14.2	1.00	26.8	1.07	44.4	1.08	56.8	1.08	66.3	1.08
27000, 4.5	3.3	0.62	8.4	0.82	10.9	0.87	22.3	0.99	39.2	1.03	51.3	1.03	60.7	1.04
29000, 4.5	1.9	0.52	4.9	0.69	6.5	0.74	14.4	0.88	27.8	0.97	38.2	0.99	46.6	1.00
31000, 4.5	1.1	0.46	2.7	0.62	3.5	0.66	8.0	0.79	16.5	0.89	24.2	0.94	30.8	0.96

Table B.9: MULTI results for N II λ 4601.5 Å at $\xi_t = 10 \text{ km s}^{-1}$ (Equivalent widths, W_λ , are in mÅ)

$T_{\text{eff}}, \log(g)$	Nitrogen Abundance difference $\Delta\epsilon_N$, ($\Delta\epsilon_N = \epsilon_N - \epsilon_{N,\text{solar}}$, where $\epsilon_{N,\text{solar}} = 7.83$)													
	-1.00		-0.70		-0.60		-0.30		0.00		0.18		0.30	
	W_λ	W/W_*	W_λ	W/W_*	W_λ	W/W_*	W_λ	W/W_*	W_λ	W/W_*	W_λ	W/W_*	W_λ	W/W_*
15000, 3.5	0.6	0.78	1.5	0.94	1.9	0.98	3.9	1.07	7.4	1.12	10.5	1.14	13.2	1.15
17000, 3.5	2.0	0.85	4.5	1.01	5.7	1.05	11.0	1.12	19.7	1.16	26.6	1.17	32.5	1.17
19000, 3.5	4.2	0.82	9.6	1.02	12.1	1.06	23.1	1.14	39.4	1.17	51.8	1.18	61.7	1.19
21000, 3.5	5.4	0.67	14.1	0.95	18.2	1.01	35.6	1.12	60.4	1.17	78.1	1.18	92.0	1.18
23000, 3.5	3.6	0.43	12.6	0.79	17.2	0.88	37.4	1.06	66.4	1.13	86.9	1.14	102.7	1.15
25000, 3.5	1.1	0.17	6.1	0.51	9.0	0.61	23.8	0.88	48.8	1.03	67.5	1.07	82.2	1.08
27000, 3.5	-0.1	-0.04	2.0	0.30	3.2	0.39	10.3	0.66	25.3	0.87	39.0	0.96	50.7	1.00
29000, 3.5	-0.9	-0.56	0.0	0.01	0.6	0.17	3.5	0.52	9.8	0.74	16.0	0.83	22.2	0.88
31000, 3.5	-0.7	-0.51	-0.9	-0.54	-0.9	-0.47	-0.2	-0.06	2.1	0.46	4.5	0.68	6.7	0.80
15000, 4.0	0.3	0.71	0.7	0.86	0.9	0.90	2.0	1.00	3.9	1.06	5.7	1.08	7.4	1.09
17000, 4.0	1.0	0.81	2.3	0.95	3.0	0.98	6.0	1.06	11.2	1.10	15.7	1.11	19.6	1.12
19000, 4.0	2.5	0.83	5.6	0.99	7.1	1.02	13.9	1.09	24.7	1.13	33.3	1.14	40.5	1.14
21000, 4.0	4.2	0.77	10.0	0.97	12.8	1.02	24.7	1.10	42.9	1.14	56.5	1.15	67.5	1.15
23000, 4.0	4.8	0.62	12.7	0.89	16.5	0.96	33.2	1.08	57.6	1.12	75.3	1.13	89.2	1.13
25000, 4.0	3.2	0.46	9.9	0.74	13.4	0.82	30.0	1.00	55.1	1.07	73.6	1.09	88.0	1.09
27000, 4.0	1.5	0.29	5.2	0.55	7.3	0.62	18.5	0.84	38.6	0.98	54.5	1.02	67.4	1.04
29000, 4.0	0.5	0.17	2.5	0.41	3.5	0.48	9.3	0.68	21.5	0.85	32.8	0.92	42.8	0.96
31000, 4.0	-0.2	-0.14	0.8	0.27	1.3	0.38	4.2	0.61	10.2	0.77	16.1	0.83	21.8	0.88
15000, 4.5	0.2	0.60	0.4	0.76	0.5	0.80	1.0	0.91	2.1	0.99	3.2	1.02	4.2	1.03
17000, 4.5	0.6	0.71	1.2	0.86	1.6	0.89	3.3	0.98	6.3	1.04	9.1	1.06	11.6	1.07
19000, 4.5	1.4	0.77	3.2	0.92	4.0	0.95	8.0	1.03	14.9	1.07	20.6	1.08	25.7	1.09
21000, 4.5	2.8	0.83	6.3	0.97	8.0	1.01	15.8	1.07	28.2	1.10	38.2	1.11	46.5	1.11
23000, 4.5	4.0	0.76	9.7	0.95	12.4	0.99	24.5	1.07	43.2	1.11	57.5	1.11	69.0	1.11
25000, 4.5	4.0	0.63	10.4	0.85	13.6	0.91	28.2	1.03	50.6	1.08	67.4	1.08	80.7	1.08
27000, 4.5	2.7	0.49	7.4	0.70	9.9	0.76	22.4	0.92	43.2	1.01	59.2	1.03	72.2	1.03
29000, 4.5	1.5	0.40	4.2	0.58	5.7	0.63	13.7	0.80	28.9	0.92	41.8	0.97	52.8	0.99
31000, 4.5	0.8	0.31	2.3	0.51	3.1	0.56	7.4	0.71	16.3	0.83	24.9	0.89	32.7	0.93

Table B.10: MULTI results for N II λ 4607.2 Å at $\xi_t = 0$ km s⁻¹ (Equivalent widths, W_λ , are in mÅ)

T _{eff} , log(g)	Nitrogen Abundance difference $\Delta\epsilon_N$, ($\Delta\epsilon_N = \epsilon_N - \epsilon_{N,solar}$, where $\epsilon_{N,solar} = 7.83$)													
	-1.00		-0.70		-0.60		-0.30		0.00		0.18		0.30	
	W_λ	W/W_*	W_λ	W/W_*	W_λ	W/W_*	W_λ	W/W_*	W_λ	W/W_*	W_λ	W/W_*	W_λ	W/W_*
15000, 3.5	0.7	0.98	1.4	1.07	1.7	1.09	3.2	1.13	5.7	1.15	7.8	1.15	9.5	1.16
17000, 3.5	2.0	1.04	4.0	1.12	4.9	1.13	8.6	1.16	14.0	1.17	18.2	1.17	21.5	1.17
19000, 3.5	4.3	1.05	8.4	1.14	10.1	1.15	17.2	1.17	26.7	1.18	33.3	1.18	38.5	1.18
21000, 3.5	6.4	0.98	12.9	1.12	15.7	1.14	26.3	1.16	39.9	1.17	48.9	1.17	55.6	1.17
23000, 3.5	5.7	0.82	13.3	1.04	16.5	1.08	29.0	1.13	44.8	1.13	55.1	1.14	62.7	1.14
25000, 3.5	2.8	0.52	8.0	0.82	10.5	0.89	21.4	1.03	36.1	1.07	46.0	1.07	53.4	1.07
27000, 3.5	1.0	0.36	3.3	0.59	4.6	0.67	11.1	0.87	22.3	0.99	30.7	1.02	37.3	1.02
29000, 3.5	0.2	0.17	1.2	0.50	1.7	0.58	4.3	0.75	9.6	0.87	14.6	0.92	19.2	0.95
31000, 3.5	-0.3	-0.38	-0.1	-0.08	0.1	0.06	1.1	0.52	3.1	0.81	4.8	0.89	6.5	0.92
15000, 4.0	0.3	0.90	0.7	1.00	0.9	1.02	1.7	1.07	3.2	1.10	4.5	1.11	5.7	1.11
17000, 4.0	1.0	0.98	2.1	1.06	2.6	1.07	4.9	1.11	8.5	1.12	11.4	1.12	13.9	1.13
19000, 4.0	2.5	1.01	5.0	1.09	6.1	1.10	10.8	1.13	17.7	1.14	22.8	1.14	26.9	1.14
21000, 4.0	4.5	1.00	9.0	1.10	10.9	1.11	18.8	1.14	29.5	1.14	37.0	1.14	42.8	1.14
23000, 4.0	5.7	0.92	12.0	1.07	14.6	1.09	25.2	1.12	39.0	1.12	48.3	1.12	55.3	1.12
25000, 4.0	4.5	0.77	10.5	0.97	13.3	1.01	24.3	1.07	38.7	1.08	48.5	1.08	55.8	1.08
27000, 4.0	2.4	0.57	6.2	0.79	8.2	0.85	17.0	0.98	29.8	1.03	38.8	1.03	45.7	1.03
29000, 4.0	1.2	0.46	3.1	0.64	4.2	0.69	9.4	0.85	18.9	0.95	26.3	0.98	32.4	0.99
31000, 4.0	0.5	0.36	1.4	0.60	2.0	0.65	4.5	0.78	9.5	0.87	14.2	0.92	18.5	0.94
15000, 4.5	0.2	0.79	0.4	0.91	0.5	0.94	0.9	1.00	1.8	1.04	2.6	1.06	3.4	1.06
17000, 4.5	0.6	0.88	1.2	0.98	1.4	1.00	2.8	1.05	5.1	1.07	7.1	1.08	8.8	1.08
19000, 4.5	1.4	0.94	2.9	1.02	3.6	1.04	6.6	1.07	11.3	1.09	15.1	1.09	18.2	1.09
21000, 4.5	2.8	1.00	5.7	1.07	7.0	1.08	12.5	1.10	20.5	1.11	26.5	1.11	31.2	1.11
23000, 4.5	4.3	0.97	8.8	1.07	10.8	1.08	19.1	1.10	30.5	1.10	38.5	1.10	44.7	1.10
25000, 4.5	4.7	0.88	10.1	1.02	12.5	1.04	22.3	1.07	35.7	1.07	44.9	1.07	52.0	1.07
27000, 4.5	3.3	0.72	7.8	0.89	9.9	0.93	19.1	1.01	32.0	1.03	41.2	1.03	48.2	1.03
29000, 4.5	1.9	0.60	4.6	0.76	6.0	0.80	12.7	0.92	23.5	0.98	31.5	0.99	37.9	0.99
31000, 4.5	1.1	0.55	2.5	0.68	3.3	0.72	7.2	0.83	14.4	0.92	20.6	0.95	25.8	0.97

Table B.11: MULTI results for N II λ 4607.2 Å at $\xi_t = 5 \text{ km s}^{-1}$ (Equivalent widths, W_λ , are in mÅ)

$T_{\text{eff}}, \log(g)$	Nitrogen Abundance difference $\Delta\epsilon_N$, ($\Delta\epsilon_N = \epsilon_N - \epsilon_{N,\text{solar}}$, where $\epsilon_{N,\text{solar}} = 7.83$)													
	-1.00		-0.70		-0.60		-0.30		0.00		0.18		0.30	
	W_λ	W/W_*	W_λ	W/W_*	W_λ	W/W_*	W_λ	W/W_*	W_λ	W/W_*	W_λ	W/W_*	W_λ	W/W_*
15000, 3.5	0.6	0.89	1.4	1.02	1.7	1.05	3.4	1.11	6.2	1.14	8.5	1.15	10.6	1.15
17000, 3.5	1.9	0.97	4.0	1.08	5.0	1.10	9.2	1.14	15.7	1.16	20.8	1.17	25.0	1.17
19000, 3.5	4.1	0.96	8.6	1.09	10.6	1.12	18.9	1.16	30.7	1.17	39.3	1.18	46.2	1.18
21000, 3.5	5.8	0.86	13.0	1.06	16.2	1.09	29.1	1.15	46.5	1.17	58.5	1.17	67.7	1.17
23000, 3.5	4.8	0.67	12.7	0.95	16.4	1.01	31.4	1.11	51.6	1.13	65.4	1.13	75.8	1.14
25000, 3.5	2.0	0.38	7.0	0.69	9.7	0.78	21.8	0.98	39.9	1.05	52.6	1.07	62.5	1.07
27000, 3.5	0.6	0.21	2.7	0.48	3.9	0.56	10.4	0.79	22.8	0.95	32.9	1.00	41.2	1.02
29000, 3.5	-0.1	-0.11	0.8	0.33	1.3	0.43	3.9	0.67	9.3	0.82	14.6	0.89	19.6	0.93
31000, 3.5	-0.5	-0.45	-0.4	-0.29	-0.3	-0.17	0.7	0.30	2.7	0.69	4.6	0.83	6.4	0.89
15000, 4.0	0.3	0.82	0.7	0.94	0.9	0.97	1.8	1.04	3.4	1.08	4.8	1.10	6.1	1.10
17000, 4.0	1.0	0.91	2.1	1.01	2.7	1.04	5.1	1.09	9.2	1.11	12.6	1.12	15.6	1.12
19000, 4.0	2.4	0.94	5.0	1.05	6.3	1.07	11.6	1.11	19.7	1.13	26.0	1.14	31.2	1.14
21000, 4.0	4.2	0.91	9.1	1.05	11.2	1.08	20.4	1.12	33.6	1.14	43.2	1.14	50.8	1.14
23000, 4.0	5.2	0.81	11.9	1.01	14.9	1.04	27.5	1.11	44.8	1.12	57.0	1.12	66.3	1.12
25000, 4.0	3.8	0.64	10.0	0.89	13.0	0.95	25.7	1.05	43.7	1.08	56.3	1.08	66.1	1.08
27000, 4.0	1.9	0.46	5.6	0.69	7.6	0.77	17.1	0.94	32.2	1.01	43.5	1.03	52.3	1.03
29000, 4.0	0.9	0.35	2.8	0.55	3.8	0.61	9.1	0.78	19.3	0.92	27.9	0.96	35.2	0.98
31000, 4.0	0.2	0.17	1.2	0.48	1.7	0.55	4.2	0.72	9.4	0.83	14.3	0.89	19.0	0.92
15000, 4.5	0.2	0.70	0.4	0.84	0.5	0.88	0.9	0.96	1.9	1.02	2.7	1.04	3.5	1.05
17000, 4.5	0.5	0.81	1.1	0.93	1.4	0.96	2.8	1.02	5.4	1.06	7.6	1.07	9.5	1.08
19000, 4.5	1.4	0.87	2.9	0.98	3.6	1.00	6.8	1.06	12.2	1.08	16.6	1.09	20.4	1.09
21000, 4.5	2.7	0.94	5.7	1.04	7.1	1.06	13.2	1.09	22.7	1.11	30.0	1.11	36.0	1.11
23000, 4.5	4.0	0.89	8.8	1.03	11.0	1.05	20.5	1.10	34.3	1.11	44.4	1.11	52.4	1.10
25000, 4.5	4.2	0.78	9.9	0.96	12.5	1.00	23.8	1.06	40.1	1.08	51.9	1.08	61.0	1.08
27000, 4.5	2.9	0.62	7.3	0.82	9.6	0.87	19.8	0.98	35.2	1.02	46.6	1.03	55.6	1.03
29000, 4.5	1.7	0.52	4.3	0.69	5.7	0.74	12.6	0.88	24.7	0.96	34.3	0.98	42.2	0.99
31000, 4.5	0.9	0.46	2.4	0.62	3.1	0.66	7.0	0.79	14.6	0.89	21.4	0.93	27.5	0.95

Table B.12: MULTI results for N II λ 4607.2 Å at $\xi_t = 10 \text{ km s}^{-1}$ (Equivalent widths, W_λ , are in mÅ)

$T_{\text{eff}}, \log(g)$	Nitrogen Abundance difference $\Delta\epsilon_N$, ($\Delta\epsilon_N = \epsilon_N - \epsilon_{N,\text{solar}}$, where $\epsilon_{N,\text{solar}} = 7.83$)													
	-1.00		-0.70		-0.60		-0.30		0.00		0.18		0.30	
	W_λ	W/W_*	W_λ	W/W_*	W_λ	W/W_*	W_λ	W/W_*	W_λ	W/W_*	W_λ	W/W_*	W_λ	W/W_*
15000, 3.5	0.6	0.78	1.3	0.94	1.7	0.98	3.4	1.07	6.6	1.12	9.3	1.14	11.8	1.14
17000, 3.5	1.8	0.85	4.0	1.01	5.0	1.04	9.8	1.12	17.6	1.15	24.0	1.16	29.4	1.16
19000, 3.5	3.7	0.82	8.5	1.01	10.7	1.05	20.5	1.13	35.6	1.16	47.0	1.17	56.4	1.18
21000, 3.5	4.8	0.66	12.4	0.94	16.1	1.00	31.7	1.12	54.5	1.16	71.2	1.17	84.4	1.17
23000, 3.5	3.2	0.43	11.1	0.79	15.1	0.88	33.1	1.06	59.6	1.12	78.9	1.13	93.9	1.13
25000, 3.5	1.0	0.18	5.3	0.51	7.9	0.61	20.9	0.88	43.3	1.02	60.5	1.05	74.3	1.07
27000, 3.5	-0.1	-0.03	1.8	0.30	2.9	0.40	9.0	0.66	22.2	0.87	34.4	0.95	45.1	0.99
29000, 3.5	-0.7	-0.53	0.1	0.03	0.6	0.17	3.1	0.52	8.5	0.73	14.0	0.82	19.4	0.87
31000, 3.5	-0.6	-0.42	-0.8	-0.46	-0.7	-0.41	-0.1	-0.03	1.9	0.45	3.9	0.67	5.9	0.78
15000, 4.0	0.3	0.71	0.6	0.86	0.8	0.90	1.7	1.00	3.5	1.05	5.1	1.08	6.6	1.09
17000, 4.0	0.9	0.81	2.1	0.95	2.6	0.98	5.3	1.06	10.0	1.10	14.0	1.11	17.6	1.12
19000, 4.0	2.2	0.83	4.9	0.98	6.3	1.02	12.3	1.09	22.1	1.12	30.0	1.13	36.7	1.13
21000, 4.0	3.7	0.77	8.8	0.97	11.2	1.02	22.0	1.10	38.6	1.13	51.3	1.14	61.6	1.14
23000, 4.0	4.2	0.62	11.1	0.89	14.5	0.95	29.4	1.07	51.8	1.11	68.4	1.12	81.6	1.12
25000, 4.0	2.8	0.46	8.7	0.74	11.8	0.82	26.5	1.00	49.3	1.07	66.4	1.08	80.1	1.08
27000, 4.0	1.3	0.30	4.6	0.55	6.4	0.62	16.3	0.84	34.2	0.98	48.7	1.01	60.7	1.03
29000, 4.0	0.5	0.17	2.2	0.42	3.1	0.48	8.2	0.68	18.9	0.84	29.0	0.92	38.0	0.95
31000, 4.0	-0.2	-0.12	0.7	0.28	1.2	0.38	3.7	0.61	8.9	0.77	14.1	0.83	19.1	0.87
15000, 4.5	0.1	0.59	0.3	0.75	0.4	0.79	0.9	0.91	1.9	0.98	2.8	1.01	3.7	1.03
17000, 4.5	0.5	0.70	1.1	0.85	1.4	0.89	2.9	0.98	5.6	1.03	8.1	1.05	10.3	1.06
19000, 4.5	1.3	0.76	2.8	0.91	3.5	0.95	7.1	1.02	13.2	1.07	18.5	1.08	23.1	1.09
21000, 4.5	2.5	0.83	5.6	0.97	7.1	1.01	13.9	1.07	25.3	1.10	34.4	1.10	42.1	1.11
23000, 4.5	3.5	0.76	8.5	0.95	10.9	0.99	21.7	1.07	38.8	1.10	52.0	1.11	62.9	1.11
25000, 4.5	3.5	0.63	9.1	0.85	11.9	0.91	24.9	1.03	45.3	1.07	60.9	1.08	73.5	1.08
27000, 4.5	2.4	0.49	6.5	0.70	8.7	0.76	19.7	0.92	38.4	1.00	53.2	1.02	65.3	1.03
29000, 4.5	1.3	0.40	3.7	0.58	5.0	0.64	12.0	0.80	25.5	0.92	37.2	0.96	47.2	0.98
31000, 4.5	0.7	0.32	2.0	0.51	2.7	0.56	6.5	0.71	14.3	0.83	21.9	0.89	28.9	0.92

Table B.13: MULTI results for N II λ 4621.4 Å at $\xi_t = 0$ km s⁻¹ (Equivalent widths, W_λ , are in mÅ)

T _{eff} , log(g)	Nitrogen Abundance difference $\Delta\epsilon_N$, ($\Delta\epsilon_N = \epsilon_N - \epsilon_{N,solar}$, where $\epsilon_{N,solar} = 7.83$)													
	-1.00		-0.70		-0.60		-0.30		0.00		0.18		0.30	
	W_λ	W/W_*	W_λ	W/W_*	W_λ	W/W_*	W_λ	W/W_*	W_λ	W/W_*	W_λ	W/W_*	W_λ	W/W_*
15000, 3.5	0.7	0.98	1.4	1.07	1.7	1.09	3.2	1.13	5.7	1.14	7.8	1.15	9.5	1.15
17000, 3.5	2.0	1.04	4.0	1.11	4.8	1.13	8.5	1.15	14.0	1.16	18.1	1.16	21.5	1.16
19000, 3.5	4.3	1.05	8.3	1.13	10.1	1.14	17.1	1.17	26.6	1.17	33.2	1.17	38.4	1.17
21000, 3.5	6.3	0.98	12.8	1.11	15.5	1.13	26.1	1.16	39.6	1.16	48.6	1.16	55.4	1.17
23000, 3.5	5.7	0.83	13.2	1.04	16.4	1.07	28.8	1.12	44.4	1.13	54.7	1.13	62.4	1.13
25000, 3.5	2.8	0.54	7.9	0.82	10.5	0.89	21.2	1.02	35.8	1.06	45.7	1.07	53.1	1.07
27000, 3.5	1.1	0.38	3.3	0.60	4.6	0.68	11.0	0.87	22.1	0.99	30.4	1.01	37.0	1.02
29000, 3.5	0.3	0.20	1.3	0.52	1.8	0.59	4.4	0.76	9.6	0.87	14.5	0.92	19.1	0.95
31000, 3.5	-0.3	-0.35	-0.1	-0.05	0.1	0.09	1.1	0.54	3.1	0.82	4.9	0.89	6.5	0.92
15000, 4.0	0.3	0.90	0.7	1.00	0.9	1.02	1.7	1.07	3.2	1.09	4.5	1.10	5.7	1.10
17000, 4.0	1.0	0.98	2.1	1.05	2.6	1.07	4.9	1.10	8.5	1.12	11.4	1.12	13.8	1.12
19000, 4.0	2.5	1.01	5.0	1.09	6.1	1.10	10.7	1.12	17.6	1.13	22.7	1.13	26.8	1.13
21000, 4.0	4.5	1.00	8.9	1.09	10.8	1.11	18.6	1.13	29.3	1.14	36.8	1.14	42.6	1.14
23000, 4.0	5.7	0.93	11.8	1.06	14.5	1.09	25.0	1.11	38.8	1.12	48.0	1.12	55.0	1.12
25000, 4.0	4.4	0.77	10.4	0.97	13.1	1.01	24.0	1.07	38.4	1.07	48.1	1.07	55.5	1.07
27000, 4.0	2.4	0.58	6.2	0.80	8.1	0.85	16.8	0.98	29.5	1.02	38.5	1.03	45.4	1.03
29000, 4.0	1.2	0.47	3.1	0.65	4.1	0.70	9.4	0.85	18.7	0.95	26.1	0.98	32.1	0.99
31000, 4.0	0.5	0.38	1.5	0.61	2.0	0.66	4.5	0.78	9.5	0.87	14.1	0.92	18.3	0.94
15000, 4.5	0.2	0.80	0.4	0.91	0.5	0.94	0.9	1.00	1.8	1.04	2.6	1.05	3.4	1.06
17000, 4.5	0.6	0.89	1.2	0.98	1.4	1.00	2.8	1.05	5.1	1.07	7.0	1.08	8.8	1.08
19000, 4.5	1.4	0.94	2.9	1.02	3.5	1.04	6.5	1.07	11.3	1.09	15.0	1.09	18.1	1.09
21000, 4.5	2.8	1.00	5.6	1.07	6.9	1.08	12.4	1.10	20.4	1.10	26.3	1.10	31.1	1.10
23000, 4.5	4.3	0.97	8.7	1.07	10.7	1.08	18.9	1.10	30.2	1.10	38.3	1.10	44.5	1.10
25000, 4.5	4.6	0.88	10.0	1.02	12.3	1.04	22.1	1.07	35.4	1.07	44.6	1.07	51.7	1.07
27000, 4.5	3.3	0.72	7.7	0.89	9.8	0.93	18.9	1.01	31.7	1.02	40.9	1.02	47.9	1.02
29000, 4.5	1.9	0.61	4.6	0.76	6.0	0.81	12.6	0.92	23.2	0.98	31.2	0.99	37.6	0.99
31000, 4.5	1.1	0.56	2.5	0.69	3.3	0.72	7.1	0.83	14.3	0.92	20.4	0.95	25.6	0.96

Table B.14: MULTI results for N II λ 4621.4 Å at $\xi_t = 5 \text{ km s}^{-1}$ (Equivalent widths, W_λ , are in mÅ)

$T_{\text{eff}}, \log(g)$	Nitrogen Abundance difference $\Delta\epsilon_N$, ($\Delta\epsilon_N = \epsilon_N - \epsilon_{N,\text{solar}}$, where $\epsilon_{N,\text{solar}} = 7.83$)													
	-1.00		-0.70		-0.60		-0.30		0.00		0.18		0.30	
	W_λ	W/W_*	W_λ	W/W_*	W_λ	W/W_*	W_λ	W/W_*	W_λ	W/W_*	W_λ	W/W_*	W_λ	W/W_*
15000, 3.5	0.6	0.90	1.4	1.02	1.7	1.04	3.3	1.10	6.1	1.13	8.5	1.14	10.6	1.15
17000, 3.5	1.9	0.97	4.0	1.07	5.0	1.09	9.2	1.14	15.7	1.15	20.7	1.16	25.0	1.16
19000, 3.5	4.1	0.96	8.5	1.09	10.5	1.11	18.7	1.15	30.6	1.17	39.2	1.17	46.0	1.17
21000, 3.5	5.8	0.86	12.9	1.05	16.1	1.09	28.8	1.15	46.1	1.16	58.1	1.16	67.4	1.17
23000, 3.5	4.8	0.68	12.6	0.95	16.3	1.01	31.1	1.10	51.2	1.12	64.9	1.13	75.3	1.13
25000, 3.5	2.1	0.39	7.0	0.70	9.6	0.79	21.6	0.98	39.5	1.05	52.2	1.06	62.0	1.06
27000, 3.5	0.7	0.23	2.8	0.50	4.0	0.57	10.4	0.80	22.6	0.95	32.6	1.00	40.8	1.01
29000, 3.5	-0.1	-0.07	0.9	0.35	1.4	0.45	4.0	0.68	9.3	0.83	14.5	0.89	19.5	0.93
31000, 3.5	-0.4	-0.42	-0.3	-0.25	-0.2	-0.14	0.7	0.33	2.8	0.70	4.7	0.83	6.5	0.89
15000, 4.0	0.3	0.82	0.7	0.94	0.9	0.97	1.7	1.04	3.4	1.08	4.8	1.09	6.1	1.10
17000, 4.0	1.0	0.91	2.1	1.01	2.7	1.04	5.1	1.08	9.2	1.11	12.6	1.11	15.5	1.12
19000, 4.0	2.4	0.94	5.0	1.05	6.2	1.07	11.5	1.11	19.6	1.13	25.9	1.13	31.1	1.13
21000, 4.0	4.2	0.92	9.0	1.05	11.1	1.08	20.2	1.12	33.4	1.13	43.0	1.14	50.6	1.14
23000, 4.0	5.1	0.81	11.8	1.00	14.8	1.04	27.2	1.10	44.5	1.12	56.6	1.12	66.0	1.12
25000, 4.0	3.8	0.65	9.9	0.89	12.8	0.95	25.5	1.05	43.3	1.07	55.9	1.07	65.6	1.07
27000, 4.0	2.0	0.47	5.6	0.70	7.5	0.77	16.9	0.94	31.9	1.01	43.0	1.02	51.9	1.03
29000, 4.0	1.0	0.37	2.8	0.56	3.8	0.62	9.0	0.79	19.1	0.92	27.7	0.96	34.9	0.98
31000, 4.0	0.2	0.20	1.2	0.49	1.7	0.56	4.2	0.72	9.3	0.84	14.2	0.89	18.9	0.92
15000, 4.5	0.2	0.71	0.4	0.84	0.5	0.88	0.9	0.96	1.9	1.02	2.7	1.04	3.5	1.05
17000, 4.5	0.5	0.81	1.1	0.93	1.4	0.96	2.8	1.02	5.3	1.06	7.5	1.07	9.5	1.07
19000, 4.5	1.4	0.87	2.8	0.98	3.6	1.00	6.8	1.05	12.2	1.08	16.6	1.09	20.3	1.09
21000, 4.5	2.7	0.94	5.6	1.03	7.0	1.05	13.1	1.09	22.6	1.10	29.8	1.10	35.8	1.10
23000, 4.5	4.0	0.89	8.7	1.03	10.9	1.05	20.2	1.09	34.0	1.10	44.1	1.10	52.1	1.10
25000, 4.5	4.2	0.78	9.7	0.96	12.4	1.00	23.6	1.06	39.8	1.07	51.5	1.07	60.6	1.07
27000, 4.5	2.9	0.63	7.3	0.82	9.5	0.87	19.5	0.98	34.8	1.02	46.1	1.02	55.1	1.02
29000, 4.5	1.7	0.53	4.3	0.69	5.6	0.74	12.5	0.88	24.4	0.96	33.9	0.98	41.8	0.99
31000, 4.5	0.9	0.47	2.3	0.62	3.1	0.67	6.9	0.79	14.4	0.89	21.2	0.93	27.2	0.95

Table B.15: MULTI results for N II λ 4621.4 Å at $\xi_t = 10 \text{ km s}^{-1}$ (Equivalent widths, W_λ , are in mÅ)

$T_{\text{eff}}, \log(g)$	Nitrogen Abundance difference $\Delta\epsilon_N$, ($\Delta\epsilon_N = \epsilon_N - \epsilon_{N,\text{solar}}$, where $\epsilon_{N,\text{solar}} = 7.83$)													
	-1.00		-0.70		-0.60		-0.30		0.00		0.18		0.30	
	W_λ	W/W_*	W_λ	W/W_*	W_λ	W/W_*	W_λ	W/W_*	W_λ	W/W_*	W_λ	W/W_*	W_λ	W/W_*
15000, 3.5	0.6	0.79	1.3	0.94	1.7	0.98	3.4	1.06	6.5	1.11	9.3	1.13	11.8	1.14
17000, 3.5	1.8	0.86	4.0	1.01	5.0	1.04	9.8	1.11	17.5	1.14	23.9	1.15	29.3	1.16
19000, 3.5	3.7	0.82	8.4	1.01	10.6	1.05	20.4	1.13	35.3	1.16	46.8	1.17	56.1	1.17
21000, 3.5	4.8	0.67	12.4	0.94	15.9	1.00	31.4	1.11	54.0	1.15	70.7	1.16	83.8	1.16
23000, 3.5	3.3	0.45	11.1	0.80	15.0	0.88	32.7	1.06	59.0	1.11	78.2	1.12	93.2	1.13
25000, 3.5	1.1	0.20	5.4	0.52	7.9	0.62	20.8	0.88	42.9	1.02	59.9	1.05	73.6	1.06
27000, 3.5	0.0	0.00	1.9	0.32	3.0	0.41	9.1	0.67	22.1	0.87	34.1	0.95	44.6	0.99
29000, 3.5	-0.7	-0.48	0.2	0.06	0.6	0.20	3.2	0.53	8.6	0.74	14.0	0.83	19.3	0.88
31000, 3.5	-0.5	-0.40	-0.7	-0.42	-0.7	-0.37	0.0	0.01	2.0	0.47	4.0	0.68	6.0	0.79
15000, 4.0	0.3	0.73	0.6	0.87	0.8	0.90	1.7	0.99	3.5	1.05	5.1	1.07	6.6	1.08
17000, 4.0	0.9	0.81	2.1	0.95	2.6	0.98	5.3	1.05	9.9	1.09	13.9	1.11	17.5	1.11
19000, 4.0	2.2	0.83	4.9	0.98	6.2	1.02	12.2	1.09	22.0	1.12	29.8	1.12	36.5	1.13
21000, 4.0	3.7	0.78	8.7	0.97	11.1	1.02	21.7	1.10	38.2	1.13	50.9	1.13	61.2	1.14
23000, 4.0	4.2	0.63	11.0	0.89	14.4	0.95	29.1	1.07	51.3	1.11	67.8	1.12	81.0	1.12
25000, 4.0	2.8	0.47	8.6	0.75	11.7	0.82	26.2	1.00	48.8	1.06	65.8	1.07	79.4	1.07
27000, 4.0	1.3	0.32	4.6	0.56	6.4	0.63	16.1	0.84	33.8	0.98	48.2	1.01	60.0	1.02
29000, 4.0	0.5	0.19	2.2	0.43	3.1	0.50	8.1	0.69	18.7	0.85	28.7	0.92	37.6	0.95
31000, 4.0	-0.1	-0.10	0.7	0.30	1.2	0.40	3.7	0.62	8.9	0.77	14.0	0.83	19.0	0.88
15000, 4.5	0.1	0.60	0.3	0.76	0.4	0.80	0.9	0.91	1.9	0.98	2.8	1.01	3.7	1.03
17000, 4.5	0.5	0.71	1.1	0.85	1.4	0.89	2.9	0.98	5.6	1.03	8.0	1.05	10.3	1.06
19000, 4.5	1.3	0.77	2.8	0.91	3.5	0.95	7.0	1.02	13.2	1.06	18.4	1.08	23.0	1.08
21000, 4.5	2.5	0.84	5.5	0.98	7.0	1.01	13.8	1.07	25.1	1.09	34.2	1.10	41.9	1.10
23000, 4.5	3.5	0.77	8.4	0.95	10.7	0.99	21.4	1.07	38.4	1.10	51.6	1.10	62.4	1.10
25000, 4.5	3.5	0.64	9.0	0.85	11.8	0.91	24.6	1.03	44.8	1.07	60.3	1.07	72.8	1.07
27000, 4.5	2.4	0.50	6.4	0.70	8.6	0.77	19.5	0.92	38.0	1.00	52.6	1.02	64.6	1.02
29000, 4.5	1.4	0.41	3.7	0.59	5.0	0.64	11.9	0.80	25.2	0.92	36.7	0.96	46.7	0.98
31000, 4.5	0.7	0.33	2.0	0.52	2.7	0.57	6.5	0.71	14.2	0.83	21.7	0.89	28.6	0.92

Table B.16: MULTI results for N II λ 4630.6 Å at $\xi_t = 0$ km s⁻¹ (Equivalent widths, W_λ , are in mÅ)

T _{eff} , log(g)	Nitrogen Abundance difference $\Delta\epsilon_N$, ($\Delta\epsilon_N = \epsilon_N - \epsilon_{N,solar}$, where $\epsilon_{N,solar} = 7.83$)													
	-1.00		-0.70		-0.60		-0.30		0.00		0.18		0.30	
	W_λ	W/W_*	W_λ	W/W_*	W_λ	W/W_*	W_λ	W/W_*	W_λ	W/W_*	W_λ	W/W_*	W_λ	W/W_*
15000, 3.5	2.5	0.98	4.7	1.07	5.8	1.09	9.9	1.14	15.9	1.18	20.3	1.19	23.9	1.20
17000, 3.5	6.9	1.04	12.3	1.13	14.5	1.15	22.9	1.19	33.8	1.22	41.3	1.23	47.1	1.23
19000, 3.5	14.0	1.07	24.2	1.17	28.0	1.19	41.8	1.23	57.9	1.25	68.3	1.26	76.1	1.26
21000, 3.5	20.8	1.03	36.6	1.17	42.2	1.20	61.1	1.25	81.3	1.27	93.7	1.27	102.7	1.27
23000, 3.5	20.0	0.87	39.6	1.10	46.7	1.14	69.2	1.22	91.8	1.25	105.0	1.25	114.4	1.25
25000, 3.5	10.9	0.60	27.2	0.90	34.1	0.97	57.8	1.12	81.7	1.19	95.2	1.20	104.7	1.20
27000, 3.5	4.7	0.43	13.3	0.67	17.6	0.75	36.3	0.96	60.4	1.10	74.7	1.15	84.4	1.16
29000, 3.5	1.3	0.25	5.6	0.58	7.7	0.66	17.6	0.83	34.0	0.97	46.6	1.05	56.4	1.09
31000, 3.5	-1.5	-0.79	-0.3	-0.09	0.6	0.14	5.2	0.68	13.6	0.94	20.7	1.01	26.8	1.04
15000, 4.0	1.3	0.91	2.6	1.00	3.2	1.02	5.8	1.07	9.9	1.11	13.1	1.12	15.8	1.13
17000, 4.0	3.8	0.98	7.2	1.06	8.6	1.08	14.5	1.12	22.6	1.15	28.5	1.16	33.2	1.17
19000, 4.0	8.7	1.02	15.5	1.10	18.2	1.12	28.6	1.16	41.6	1.19	50.5	1.19	57.3	1.20
21000, 4.0	15.0	1.02	26.4	1.13	30.8	1.15	46.2	1.19	63.9	1.21	75.1	1.22	83.6	1.22
23000, 4.0	19.2	0.96	35.2	1.11	41.0	1.14	60.5	1.19	81.2	1.21	93.8	1.22	103.0	1.22
25000, 4.0	15.9	0.80	32.9	1.01	39.4	1.06	61.0	1.15	83.2	1.18	96.2	1.18	105.6	1.18
27000, 4.0	9.2	0.61	21.5	0.84	27.1	0.90	48.1	1.05	71.0	1.12	84.2	1.14	93.5	1.14
29000, 4.0	4.9	0.51	11.9	0.69	15.3	0.74	30.8	0.91	52.3	1.04	65.9	1.08	75.5	1.10
31000, 4.0	2.0	0.41	6.0	0.64	7.9	0.69	16.8	0.82	31.6	0.94	43.1	1.00	52.2	1.04
15000, 4.5	0.7	0.85	1.4	0.94	1.8	0.96	3.4	1.02	6.1	1.05	8.4	1.07	10.3	1.07
17000, 4.5	2.1	0.92	4.2	1.00	5.1	1.02	9.0	1.06	14.9	1.09	19.4	1.10	23.1	1.10
19000, 4.5	5.2	0.97	9.6	1.04	11.5	1.06	19.0	1.09	29.2	1.12	36.5	1.13	42.2	1.13
21000, 4.5	9.9	1.00	17.9	1.08	21.1	1.09	33.1	1.13	48.0	1.15	58.0	1.16	65.6	1.16
23000, 4.5	14.9	0.98	27.0	1.09	31.6	1.11	48.0	1.15	66.7	1.16	78.6	1.17	87.5	1.17
25000, 4.5	16.2	0.89	31.1	1.04	36.8	1.07	56.1	1.13	77.0	1.15	89.9	1.15	99.3	1.15
27000, 4.5	12.1	0.74	25.6	0.92	31.2	0.97	51.4	1.06	73.2	1.10	86.2	1.11	95.7	1.11
29000, 4.5	7.5	0.63	16.5	0.79	20.7	0.83	38.2	0.97	59.7	1.05	72.8	1.07	82.2	1.08
31000, 4.5	4.4	0.59	9.7	0.72	12.3	0.75	24.2	0.87	42.1	0.98	54.6	1.03	63.8	1.05

Table B.17: MULTI results for N II λ 4630.6 Å at $\xi_t = 5 \text{ km s}^{-1}$ (Equivalent widths, W_λ , are in mÅ)

$T_{\text{eff}}, \log(g)$	Nitrogen Abundance difference $\Delta\epsilon_N$, ($\Delta\epsilon_N = \epsilon_N - \epsilon_{N,\text{solar}}$, where $\epsilon_{N,\text{solar}} = 7.83$)													
	-1.00		-0.70		-0.60		-0.30		0.00		0.18		0.30	
	W_λ	W/W_*	W_λ	W/W_*	W_λ	W/W_*	W_λ	W/W_*	W_λ	W/W_*	W_λ	W/W_*	W_λ	W/W_*
15000, 3.5	2.4	0.90	4.9	1.02	6.0	1.04	10.8	1.11	18.1	1.16	23.6	1.17	28.3	1.18
17000, 3.5	6.9	0.97	13.2	1.08	15.8	1.11	26.2	1.17	40.1	1.20	50.0	1.22	57.8	1.23
19000, 3.5	14.2	0.98	26.4	1.11	31.3	1.14	49.2	1.21	70.8	1.24	85.1	1.26	95.9	1.26
21000, 3.5	20.2	0.90	39.8	1.10	47.2	1.14	73.0	1.22	101.4	1.26	118.9	1.27	131.6	1.28
23000, 3.5	17.8	0.71	41.3	1.00	50.5	1.07	81.8	1.19	114.2	1.24	133.2	1.25	146.6	1.26
25000, 3.5	8.7	0.45	25.8	0.77	33.8	0.86	64.5	1.07	98.3	1.17	117.7	1.19	131.2	1.20
27000, 3.5	3.2	0.28	11.7	0.56	16.1	0.64	37.0	0.88	67.7	1.06	87.5	1.12	101.4	1.15
29000, 3.5	-0.2	-0.04	4.1	0.42	6.2	0.52	16.7	0.75	35.1	0.92	50.2	1.00	62.6	1.05
31000, 3.5	-2.2	-1.05	-1.6	-0.46	-0.9	-0.22	3.5	0.45	12.5	0.84	20.4	0.96	27.5	1.01
15000, 4.0	1.2	0.84	2.6	0.95	3.2	0.97	6.1	1.04	10.9	1.09	14.7	1.10	18.0	1.12
17000, 4.0	3.8	0.92	7.5	1.02	9.1	1.04	16.0	1.10	25.9	1.13	33.4	1.15	39.4	1.16
19000, 4.0	8.7	0.95	16.5	1.06	19.8	1.08	32.6	1.14	49.4	1.17	61.0	1.19	70.1	1.19
21000, 4.0	14.9	0.93	28.5	1.08	34.0	1.11	53.9	1.17	77.7	1.20	93.0	1.22	104.5	1.22
23000, 4.0	18.3	0.84	37.5	1.04	45.0	1.09	71.2	1.17	100.0	1.21	117.6	1.22	130.3	1.22
25000, 4.0	14.3	0.67	33.4	0.92	41.5	0.99	70.3	1.11	101.3	1.17	119.5	1.18	132.5	1.19
27000, 4.0	7.9	0.50	20.5	0.73	26.7	0.81	52.2	1.00	83.2	1.10	101.6	1.13	114.6	1.14
29000, 4.0	4.0	0.40	10.9	0.60	14.5	0.66	31.3	0.84	57.4	0.99	75.5	1.05	88.6	1.08
31000, 4.0	1.1	0.23	5.1	0.53	7.0	0.60	16.4	0.76	32.9	0.89	46.4	0.96	57.6	1.01
15000, 4.5	0.7	0.80	1.4	0.89	1.8	0.92	3.5	0.98	6.5	1.03	9.1	1.05	11.3	1.06
17000, 4.5	2.1	0.87	4.2	0.96	5.2	0.98	9.6	1.03	16.5	1.07	21.9	1.09	26.4	1.09
19000, 4.5	5.1	0.91	10.0	1.00	12.1	1.02	21.0	1.07	33.4	1.11	42.6	1.12	49.9	1.13
21000, 4.5	9.8	0.93	18.9	1.04	22.7	1.06	37.5	1.11	56.5	1.14	69.5	1.15	79.5	1.16
23000, 4.5	14.6	0.90	28.6	1.04	34.4	1.07	55.3	1.13	80.2	1.16	96.1	1.17	107.9	1.17
25000, 4.5	15.4	0.79	32.4	0.98	39.4	1.02	64.7	1.10	93.0	1.14	110.3	1.15	123.0	1.16
27000, 4.5	11.2	0.64	25.4	0.84	32.0	0.90	57.2	1.03	86.5	1.09	104.3	1.11	117.1	1.11
29000, 4.5	6.8	0.55	15.9	0.71	20.4	0.77	40.3	0.92	67.7	1.02	85.2	1.06	97.8	1.07
31000, 4.5	3.8	0.51	9.2	0.66	11.9	0.70	24.5	0.82	45.3	0.94	60.8	1.00	72.7	1.03

Table B.18: MULTI results for N II λ 4630.6 Å at $\xi_t = 10 \text{ km s}^{-1}$ (Equivalent widths, W_λ , are in mÅ)

$T_{\text{eff}}, \log(g)$	Nitrogen Abundance difference $\Delta\epsilon_N$, ($\Delta\epsilon_N = \epsilon_N - \epsilon_{N,\text{solar}}$, where $\epsilon_{N,\text{solar}} = 7.83$)													
	-1.00		-0.70		-0.60		-0.30		0.00		0.18		0.30	
	W_λ	W/W_*	W_λ	W/W_*	W_λ	W/W_*	W_λ	W/W_*	W_λ	W/W_*	W_λ	W/W_*	W_λ	W/W_*
15000, 3.5	2.2	0.80	4.9	0.94	6.1	0.98	11.7	1.07	20.6	1.12	27.7	1.15	33.7	1.16
17000, 3.5	6.7	0.87	13.8	1.01	17.0	1.05	30.0	1.13	48.4	1.18	61.9	1.20	72.7	1.21
19000, 3.5	13.4	0.84	28.2	1.03	34.4	1.08	58.4	1.17	89.0	1.22	109.7	1.24	125.5	1.25
21000, 3.5	17.6	0.71	41.4	0.99	51.4	1.05	87.9	1.18	130.6	1.24	157.4	1.26	177.0	1.27
23000, 3.5	13.2	0.49	39.5	0.84	51.4	0.93	96.4	1.12	146.9	1.21	177.0	1.24	198.3	1.25
25000, 3.5	4.9	0.24	21.5	0.58	30.2	0.68	69.2	0.96	120.2	1.12	151.3	1.17	173.0	1.19
27000, 3.5	0.4	0.03	8.3	0.38	12.7	0.47	35.0	0.74	74.0	0.96	103.0	1.06	124.8	1.11
29000, 3.5	-2.6	-0.51	1.1	0.11	3.2	0.26	14.1	0.60	34.7	0.82	52.9	0.92	68.8	0.98
31000, 3.5	-2.9	-1.23	-3.4	-0.91	-3.2	-0.71	0.2	0.03	9.4	0.62	18.3	0.82	26.5	0.92
15000, 4.0	1.1	0.75	2.5	0.88	3.2	0.91	6.4	1.00	11.9	1.05	16.5	1.08	20.6	1.10
17000, 4.0	3.6	0.83	7.6	0.95	9.5	0.98	17.6	1.06	30.0	1.11	39.6	1.13	47.6	1.14
19000, 4.0	8.3	0.85	17.3	0.99	21.2	1.03	37.4	1.10	59.7	1.15	75.8	1.17	88.5	1.18
21000, 4.0	13.8	0.80	29.9	0.99	36.8	1.04	63.5	1.13	97.2	1.18	119.6	1.20	136.6	1.21
23000, 4.0	15.8	0.67	38.0	0.93	47.7	0.99	84.4	1.12	127.4	1.19	154.2	1.21	173.7	1.22
25000, 4.0	11.2	0.49	31.3	0.77	41.0	0.85	80.2	1.04	127.1	1.14	155.6	1.17	175.9	1.18
27000, 4.0	5.6	0.34	17.8	0.59	24.2	0.66	54.4	0.89	98.2	1.05	126.8	1.10	147.1	1.12
29000, 4.0	2.2	0.22	8.9	0.47	12.4	0.53	30.2	0.73	61.9	0.91	86.8	0.99	106.2	1.04
31000, 4.0	-0.4	-0.08	3.3	0.33	5.2	0.43	15.0	0.66	33.2	0.81	49.3	0.89	63.4	0.94
15000, 4.5	0.6	0.72	1.4	0.83	1.7	0.86	3.6	0.94	6.9	1.00	9.8	1.02	12.5	1.04
17000, 4.5	2.0	0.79	4.2	0.90	5.3	0.93	10.2	1.00	18.4	1.05	25.0	1.07	30.7	1.08
19000, 4.5	4.9	0.82	10.2	0.94	12.7	0.97	23.2	1.04	38.9	1.08	50.8	1.10	60.6	1.11
21000, 4.5	9.4	0.83	19.6	0.97	24.2	1.01	42.8	1.08	68.2	1.12	86.2	1.14	100.2	1.15
23000, 4.5	13.4	0.77	29.4	0.95	36.5	1.00	64.3	1.09	99.5	1.14	122.6	1.16	140.0	1.17
25000, 4.5	13.5	0.65	32.0	0.86	40.6	0.92	74.6	1.06	116.0	1.12	142.2	1.14	161.2	1.15
27000, 4.5	9.4	0.51	23.8	0.72	31.1	0.78	62.6	0.95	104.8	1.06	131.7	1.09	151.1	1.10
29000, 4.5	5.5	0.43	14.4	0.61	19.0	0.66	41.2	0.83	76.8	0.97	102.2	1.02	121.2	1.05
31000, 4.5	2.8	0.36	8.1	0.55	10.8	0.60	24.2	0.74	48.1	0.87	68.0	0.94	84.4	0.98

Table B.19: MULTI results for N II λ 4643.1 Å at $\xi_t = 0$ km s⁻¹ (Equivalent widths, W_λ , are in mÅ)

T _{eff} , log(g)	Nitrogen Abundance difference $\Delta\epsilon_N$, ($\Delta\epsilon_N = \epsilon_N - \epsilon_{N,solar}$, where $\epsilon_{N,solar} = 7.83$)													
	-1.00		-0.70		-0.60		-0.30		0.00		0.18		0.30	
	W_λ	W/W_*	W_λ	W/W_*	W_λ	W/W_*	W_λ	W/W_*	W_λ	W/W_*	W_λ	W/W_*	W_λ	W/W_*
15000, 3.5	1.0	0.98	2.0	1.06	2.5	1.08	4.7	1.12	8.0	1.14	10.7	1.15	12.9	1.15
17000, 3.5	3.0	1.04	5.7	1.11	6.9	1.13	11.8	1.16	18.7	1.17	23.8	1.17	27.8	1.17
19000, 3.5	6.3	1.05	11.8	1.14	14.1	1.15	23.0	1.18	34.5	1.19	42.2	1.19	48.2	1.19
21000, 3.5	9.3	1.00	18.1	1.12	21.7	1.14	34.8	1.18	50.5	1.19	60.6	1.19	68.1	1.19
23000, 3.5	8.6	0.85	18.9	1.05	23.2	1.09	38.8	1.14	57.0	1.15	68.4	1.16	76.7	1.16
25000, 3.5	4.4	0.57	11.8	0.84	15.4	0.91	29.8	1.05	47.6	1.09	58.9	1.10	67.1	1.10
27000, 3.5	1.8	0.41	5.2	0.64	7.1	0.70	16.3	0.90	31.1	1.01	41.5	1.04	49.3	1.05
29000, 3.5	0.5	0.24	2.0	0.55	2.8	0.62	6.8	0.78	14.6	0.90	21.5	0.95	27.6	0.98
31000, 3.5	-0.5	-0.46	-0.1	-0.04	0.2	0.13	1.9	0.60	4.9	0.86	7.8	0.93	10.4	0.95
15000, 4.0	0.5	0.91	1.1	1.00	1.3	1.02	2.6	1.07	4.7	1.09	6.4	1.10	8.0	1.11
17000, 4.0	1.6	0.98	3.1	1.05	3.9	1.07	7.0	1.10	11.7	1.12	15.4	1.12	18.5	1.13
19000, 4.0	3.7	1.02	7.2	1.09	8.7	1.10	14.8	1.13	23.4	1.14	29.6	1.14	34.5	1.14
21000, 4.0	6.6	1.01	12.7	1.10	15.3	1.12	25.2	1.14	38.1	1.15	46.7	1.15	53.3	1.15
23000, 4.0	8.4	0.94	16.9	1.07	20.4	1.10	33.7	1.13	49.9	1.14	60.2	1.14	67.9	1.14
25000, 4.0	6.7	0.79	15.1	0.98	18.8	1.02	32.9	1.08	50.0	1.10	61.0	1.10	69.1	1.10
27000, 4.0	3.7	0.60	9.2	0.81	12.0	0.87	23.9	1.00	39.8	1.04	50.4	1.05	58.2	1.05
29000, 4.0	1.9	0.50	4.8	0.67	6.3	0.72	13.8	0.87	26.4	0.97	35.8	1.00	43.1	1.01
31000, 4.0	0.8	0.41	2.3	0.63	3.0	0.68	6.8	0.80	14.0	0.89	20.4	0.94	26.1	0.96
15000, 4.5	0.3	0.83	0.6	0.93	0.7	0.95	1.4	1.01	2.7	1.04	3.8	1.06	4.9	1.06
17000, 4.5	0.8	0.91	1.7	0.99	2.2	1.01	4.1	1.05	7.2	1.07	9.8	1.08	12.0	1.08
19000, 4.5	2.1	0.95	4.2	1.03	5.2	1.04	9.3	1.08	15.4	1.09	20.1	1.10	24.0	1.10
21000, 4.5	4.2	1.00	8.2	1.07	9.9	1.08	17.1	1.10	27.1	1.11	34.3	1.11	39.9	1.11
23000, 4.5	6.3	0.98	12.6	1.07	15.3	1.08	25.8	1.11	39.5	1.11	48.8	1.11	55.8	1.11
25000, 4.5	6.9	0.89	14.4	1.02	17.6	1.04	30.2	1.08	46.2	1.09	56.6	1.09	64.4	1.09
27000, 4.5	5.0	0.73	11.3	0.90	14.2	0.94	26.3	1.02	42.2	1.04	52.8	1.04	60.7	1.05
29000, 4.5	2.9	0.63	6.9	0.77	8.9	0.82	18.1	0.93	31.9	0.99	41.7	1.01	49.2	1.01
31000, 4.5	1.7	0.58	3.8	0.70	5.0	0.74	10.5	0.85	20.4	0.93	28.4	0.97	34.9	0.98

Table B.20: MULTI results for N II λ 4643.1 Å at $\xi_t = 5 \text{ km s}^{-1}$ (Equivalent widths, W_λ , are in mÅ)

$T_{\text{eff}}, \log(g)$	Nitrogen Abundance difference $\Delta\epsilon_N$, ($\Delta\epsilon_N = \epsilon_N - \epsilon_{N,\text{solar}}$, where $\epsilon_{N,\text{solar}} = 7.83$)													
	-1.00		-0.70		-0.60		-0.30		0.00		0.18		0.30	
	W_λ	W/W_*	W_λ	W/W_*	W_λ	W/W_*	W_λ	W/W_*	W_λ	W/W_*	W_λ	W/W_*	W_λ	W/W_*
15000, 3.5	1.0	0.91	2.0	1.02	2.6	1.04	4.9	1.10	8.7	1.13	11.9	1.14	14.6	1.15
17000, 3.5	2.9	0.97	5.9	1.07	7.2	1.09	12.9	1.14	21.4	1.16	27.8	1.17	33.0	1.17
19000, 3.5	6.1	0.97	12.3	1.09	15.0	1.12	25.8	1.16	40.5	1.18	50.7	1.19	58.7	1.19
21000, 3.5	8.7	0.88	18.7	1.07	22.9	1.10	39.4	1.16	60.3	1.18	74.1	1.19	84.4	1.19
23000, 3.5	7.3	0.70	18.6	0.97	23.6	1.02	43.1	1.12	67.4	1.15	83.1	1.16	94.6	1.16
25000, 3.5	3.4	0.43	10.7	0.73	14.5	0.81	31.1	1.00	53.9	1.08	69.1	1.09	80.3	1.10
27000, 3.5	1.2	0.27	4.5	0.53	6.3	0.61	15.7	0.82	32.7	0.97	45.7	1.02	55.9	1.04
29000, 3.5	-0.1	-0.03	1.5	0.39	2.3	0.49	6.3	0.71	14.4	0.85	21.9	0.92	28.9	0.96
31000, 3.5	-0.7	-0.57	-0.5	-0.29	-0.3	-0.14	1.2	0.39	4.4	0.76	7.5	0.88	10.3	0.93
15000, 4.0	0.5	0.84	1.0	0.95	1.3	0.98	2.6	1.04	4.9	1.08	6.9	1.09	8.7	1.10
17000, 4.0	1.5	0.92	3.2	1.01	3.9	1.04	7.4	1.08	12.9	1.11	17.4	1.12	21.1	1.12
19000, 4.0	3.6	0.95	7.3	1.05	9.0	1.07	16.2	1.11	26.6	1.13	34.4	1.14	40.7	1.14
21000, 4.0	6.3	0.93	13.0	1.06	16.0	1.08	28.0	1.13	44.3	1.15	55.7	1.15	64.5	1.15
23000, 4.0	7.7	0.83	17.1	1.02	21.2	1.05	37.5	1.12	58.6	1.14	72.6	1.14	83.0	1.14
25000, 4.0	5.8	0.67	14.6	0.90	18.8	0.96	35.7	1.06	57.8	1.09	72.5	1.10	83.4	1.10
27000, 4.0	3.1	0.50	8.5	0.72	11.3	0.79	24.5	0.95	44.1	1.03	57.7	1.05	68.1	1.05
29000, 4.0	1.5	0.40	4.3	0.59	5.8	0.64	13.4	0.81	27.4	0.93	38.8	0.98	47.9	1.00
31000, 4.0	0.4	0.23	1.9	0.52	2.7	0.59	6.5	0.74	14.0	0.85	21.0	0.91	27.3	0.94
15000, 4.5	0.3	0.76	0.5	0.87	0.7	0.90	1.4	0.98	2.8	1.02	4.0	1.04	5.2	1.05
17000, 4.5	0.8	0.84	1.7	0.94	2.2	0.97	4.2	1.03	7.7	1.06	10.7	1.07	13.3	1.08
19000, 4.5	2.1	0.89	4.2	0.99	5.3	1.01	9.8	1.06	17.0	1.08	22.6	1.09	27.4	1.10
21000, 4.5	4.0	0.94	8.3	1.03	10.3	1.05	18.5	1.09	30.6	1.11	39.6	1.11	46.7	1.11
23000, 4.5	6.0	0.90	12.8	1.03	15.8	1.05	28.3	1.10	45.4	1.11	57.4	1.11	66.6	1.11
25000, 4.5	6.3	0.79	14.3	0.96	17.9	1.00	32.9	1.07	53.1	1.09	66.8	1.09	77.1	1.09
27000, 4.5	4.5	0.65	10.8	0.83	14.0	0.88	27.8	0.99	47.4	1.03	61.0	1.04	71.3	1.04
29000, 4.5	2.6	0.55	6.4	0.71	8.4	0.76	18.2	0.89	34.3	0.97	46.4	1.00	55.8	1.01
31000, 4.5	1.5	0.50	3.6	0.64	4.7	0.69	10.3	0.80	20.9	0.90	30.1	0.95	37.9	0.97

Table B.21: MULTI results for N II λ 4643.1 Å at $\xi_t = 10 \text{ km s}^{-1}$ (Equivalent widths, W_λ , are in mÅ)

$T_{\text{eff}}, \log(g)$	Nitrogen Abundance difference $\Delta\epsilon_N$, ($\Delta\epsilon_N = \epsilon_N - \epsilon_{N,\text{solar}}$, where $\epsilon_{N,\text{solar}} = 7.83$)													
	-1.00		-0.70		-0.60		-0.30		0.00		0.18		0.30	
	W_λ	W/W_*	W_λ	W/W_*	W_λ	W/W_*	W_λ	W/W_*	W_λ	W/W_*	W_λ	W/W_*	W_λ	W/W_*
15000, 3.5	0.9	0.81	2.0	0.95	2.5	0.98	5.1	1.06	9.5	1.11	13.3	1.13	16.6	1.14
17000, 3.5	2.7	0.87	5.9	1.01	7.4	1.04	14.1	1.11	24.5	1.15	32.7	1.16	39.6	1.16
19000, 3.5	5.6	0.84	12.4	1.02	15.6	1.06	28.9	1.13	48.1	1.17	62.2	1.18	73.4	1.18
21000, 3.5	7.3	0.70	18.3	0.96	23.3	1.02	44.1	1.13	72.8	1.17	92.7	1.18	107.9	1.19
23000, 3.5	5.3	0.48	16.7	0.81	22.3	0.90	46.8	1.07	80.4	1.13	103.4	1.15	120.7	1.15
25000, 3.5	1.9	0.23	8.5	0.55	12.2	0.65	30.8	0.90	60.6	1.04	82.2	1.08	98.7	1.09
27000, 3.5	0.2	0.04	3.1	0.36	4.8	0.45	14.0	0.69	32.9	0.89	49.4	0.98	63.2	1.02
29000, 3.5	-0.9	-0.45	0.4	0.11	1.2	0.25	5.2	0.57	13.5	0.77	21.6	0.85	29.4	0.90
31000, 3.5	-0.9	-0.59	-1.1	-0.54	-1.0	-0.45	0.1	0.04	3.3	0.54	6.5	0.74	9.6	0.84
15000, 4.0	0.4	0.75	1.0	0.88	1.3	0.91	2.6	1.00	5.1	1.05	7.4	1.07	9.5	1.08
17000, 4.0	1.4	0.83	3.1	0.95	3.9	0.99	7.8	1.05	14.2	1.09	19.6	1.11	24.3	1.11
19000, 4.0	3.4	0.85	7.3	0.99	9.2	1.02	17.6	1.09	30.5	1.12	40.6	1.13	49.0	1.14
21000, 4.0	5.6	0.80	12.9	0.98	16.3	1.02	30.9	1.10	52.2	1.14	67.8	1.15	80.1	1.15
23000, 4.0	6.4	0.66	16.4	0.91	21.1	0.97	41.3	1.08	69.6	1.12	89.6	1.14	105.0	1.14
25000, 4.0	4.5	0.49	13.0	0.76	17.5	0.84	37.7	1.01	67.3	1.08	88.2	1.09	104.2	1.10
27000, 4.0	2.2	0.34	7.1	0.58	9.8	0.65	23.9	0.86	48.1	0.99	66.7	1.03	81.4	1.04
29000, 4.0	0.9	0.22	3.5	0.46	4.9	0.52	12.4	0.71	27.6	0.86	41.3	0.94	53.2	0.97
31000, 4.0	-0.1	-0.06	1.2	0.33	2.0	0.42	5.8	0.64	13.5	0.79	21.0	0.85	28.1	0.89
15000, 4.5	0.2	0.67	0.5	0.80	0.7	0.83	1.4	0.93	2.8	0.99	4.2	1.02	5.4	1.03
17000, 4.5	0.8	0.76	1.7	0.88	2.1	0.91	4.3	0.99	8.2	1.04	11.6	1.05	14.7	1.06
19000, 4.5	1.9	0.80	4.2	0.93	5.3	0.96	10.3	1.03	18.7	1.07	25.7	1.08	31.6	1.09
21000, 4.5	3.7	0.85	8.2	0.98	10.4	1.01	19.9	1.07	34.9	1.10	46.5	1.11	56.0	1.11
23000, 4.5	5.4	0.78	12.5	0.95	15.8	0.99	30.7	1.07	52.8	1.10	69.0	1.11	82.0	1.11
25000, 4.5	5.4	0.66	13.4	0.86	17.4	0.92	35.3	1.03	61.7	1.08	80.7	1.09	95.5	1.09
27000, 4.5	3.7	0.52	9.7	0.72	12.9	0.78	28.4	0.93	53.2	1.01	71.7	1.03	86.3	1.04
29000, 4.5	2.1	0.44	5.7	0.60	7.6	0.66	17.6	0.81	36.2	0.93	51.6	0.97	64.4	0.99
31000, 4.5	1.1	0.36	3.1	0.55	4.2	0.59	9.8	0.73	21.0	0.85	31.4	0.90	40.9	0.94

Table B.22: MULTI results for N II λ 5005.1 Å at $\xi_t = 0$ km s⁻¹ (Equivalent widths, W_λ , are in mÅ)

T _{eff} , log(g)	Nitrogen Abundance difference $\Delta\epsilon_N$, ($\Delta\epsilon_N = \epsilon_N - \epsilon_{N,solar}$, where $\epsilon_{N,solar} = 7.83$)													
	-1.00		-0.70		-0.60		-0.30		0.00		0.18		0.30	
	W_λ	W/W_*	W_λ	W/W_*	W_λ	W/W_*	W_λ	W/W_*	W_λ	W/W_*	W_λ	W/W_*	W_λ	W/W_*
15000, 3.5	1.3	1.15	2.4	1.13	2.9	1.13	4.9	1.12	8.0	1.12	10.5	1.12	12.6	1.12
17000, 3.5	4.3	1.16	7.2	1.14	8.4	1.13	13.2	1.12	19.9	1.12	24.7	1.12	28.6	1.13
19000, 3.5	10.3	1.20	16.1	1.16	18.4	1.14	27.0	1.12	37.8	1.12	45.1	1.12	50.8	1.12
21000, 3.5	19.0	1.28	28.3	1.20	31.6	1.17	43.2	1.12	56.8	1.10	65.7	1.09	72.5	1.09
23000, 3.5	25.2	1.36	37.2	1.26	41.2	1.22	53.9	1.12	67.5	1.06	76.2	1.04	82.8	1.04
25000, 3.5	21.3	1.34	33.8	1.27	38.2	1.24	51.9	1.14	64.7	1.04	72.3	1.00	77.9	0.99
27000, 3.5	13.3	1.26	23.2	1.23	27.2	1.21	41.0	1.15	55.2	1.07	62.9	1.02	68.1	0.99
29000, 3.5	6.0	1.11	11.2	1.10	13.6	1.09	23.5	1.06	36.4	1.02	44.7	0.99	50.5	0.97
31000, 3.5	1.7	0.88	3.3	0.89	4.1	0.89	7.7	0.87	13.8	0.83	18.6	0.80	22.5	0.78
15000, 4.0	0.7	1.12	1.3	1.11	1.6	1.10	2.8	1.09	4.8	1.09	6.5	1.09	8.0	1.09
17000, 4.0	2.3	1.13	4.1	1.11	4.9	1.10	8.1	1.09	12.9	1.09	16.6	1.09	19.6	1.09
19000, 4.0	6.0	1.15	10.0	1.12	11.6	1.11	18.1	1.10	26.7	1.09	32.8	1.09	37.7	1.09
21000, 4.0	12.2	1.19	19.3	1.14	22.0	1.12	32.0	1.09	44.3	1.08	52.6	1.08	59.0	1.08
23000, 4.0	19.2	1.24	29.3	1.16	32.9	1.14	45.2	1.08	59.4	1.05	68.5	1.04	75.5	1.04
25000, 4.0	21.0	1.25	32.5	1.17	36.6	1.15	49.6	1.06	63.4	1.01	72.1	0.99	78.7	0.98
27000, 4.0	16.5	1.20	27.2	1.15	31.3	1.13	44.7	1.06	58.2	0.99	66.1	0.96	71.9	0.94
29000, 4.0	10.5	1.10	18.8	1.09	22.2	1.09	34.7	1.05	48.6	0.99	56.7	0.96	62.3	0.94
31000, 4.0	5.4	0.98	10.2	0.98	12.4	0.98	21.4	0.97	33.4	0.94	41.2	0.92	46.9	0.91
15000, 4.5	0.4	1.06	0.7	1.07	0.9	1.07	1.6	1.06	2.9	1.06	4.0	1.06	5.0	1.06
17000, 4.5	1.3	1.08	2.3	1.08	2.8	1.07	5.0	1.07	8.3	1.06	11.0	1.06	13.3	1.06
19000, 4.5	3.5	1.10	6.1	1.08	7.2	1.08	11.8	1.07	18.5	1.07	23.4	1.06	27.4	1.07
21000, 4.5	7.6	1.13	12.7	1.10	14.7	1.09	22.8	1.07	33.3	1.06	40.7	1.06	46.4	1.06
23000, 4.5	13.4	1.16	21.4	1.12	24.5	1.10	35.7	1.06	49.3	1.04	58.4	1.04	65.3	1.04
25000, 4.5	17.8	1.18	28.1	1.12	31.9	1.10	44.8	1.04	59.4	1.01	68.9	1.00	76.2	0.99
27000, 4.5	16.8	1.15	27.5	1.10	31.4	1.08	44.8	1.02	59.1	0.97	68.1	0.95	74.9	0.94
29000, 4.5	12.4	1.08	21.5	1.07	25.2	1.05	38.1	1.01	52.2	0.96	60.7	0.94	66.9	0.92
31000, 4.5	7.7	0.99	14.1	1.00	16.9	1.00	27.8	0.98	41.0	0.94	49.3	0.92	55.2	0.91

Table B.23: MULTI results for N II λ 5005.1 Å at $\xi_t = 5 \text{ km s}^{-1}$ (Equivalent widths, W_λ , are in mÅ)

$T_{\text{eff}}, \log(g)$	Nitrogen Abundance difference $\Delta\epsilon_N$, ($\Delta\epsilon_N = \epsilon_N - \epsilon_{N,\text{solar}}$, where $\epsilon_{N,\text{solar}} = 7.83$)													
	-1.00		-0.70		-0.60		-0.30		0.00		0.18		0.30	
	W_λ	W/W_*	W_λ	W/W_*	W_λ	W/W_*	W_λ	W/W_*	W_λ	W/W_*	W_λ	W/W_*	W_λ	W/W_*
15000, 3.5	1.4	1.16	2.5	1.15	3.1	1.14	5.4	1.13	9.1	1.12	12.0	1.12	14.6	1.12
17000, 3.5	4.6	1.18	7.9	1.15	9.3	1.15	15.2	1.13	23.5	1.13	29.6	1.13	34.6	1.13
19000, 3.5	11.4	1.23	18.5	1.18	21.4	1.17	32.2	1.14	46.3	1.13	56.0	1.12	63.6	1.13
21000, 3.5	21.4	1.32	33.4	1.24	37.8	1.22	53.4	1.15	71.8	1.12	84.0	1.11	93.2	1.10
23000, 3.5	27.9	1.40	43.9	1.31	49.6	1.28	67.9	1.17	87.0	1.10	99.0	1.07	108.0	1.06
25000, 3.5	22.8	1.36	38.2	1.31	44.1	1.28	63.6	1.19	82.7	1.09	93.5	1.05	101.3	1.02
27000, 3.5	13.8	1.27	24.9	1.25	29.7	1.24	47.3	1.18	67.2	1.11	78.6	1.06	86.3	1.03
29000, 3.5	6.1	1.12	11.7	1.11	14.3	1.11	25.4	1.08	41.3	1.04	52.1	1.01	60.0	0.99
31000, 3.5	1.8	0.88	3.4	0.90	4.2	0.90	8.1	0.89	14.8	0.85	20.3	0.83	25.0	0.81
15000, 4.0	0.7	1.13	1.3	1.12	1.6	1.11	3.0	1.10	5.3	1.09	7.2	1.09	8.9	1.09
17000, 4.0	2.4	1.14	4.4	1.12	5.3	1.11	9.0	1.10	14.7	1.10	19.2	1.10	22.9	1.10
19000, 4.0	6.4	1.16	11.0	1.13	13.0	1.12	20.8	1.11	31.5	1.10	39.4	1.10	45.7	1.10
21000, 4.0	13.4	1.21	21.9	1.16	25.3	1.15	38.1	1.11	54.1	1.09	65.1	1.09	73.5	1.09
23000, 4.0	21.2	1.26	33.9	1.20	38.7	1.18	55.3	1.11	74.3	1.07	86.7	1.06	96.0	1.05
25000, 4.0	22.8	1.27	37.3	1.21	42.7	1.19	60.8	1.11	80.0	1.04	91.8	1.02	100.6	1.00
27000, 4.0	17.4	1.21	30.1	1.18	35.2	1.16	53.0	1.10	72.1	1.03	83.2	1.00	91.1	0.97
29000, 4.0	10.9	1.10	20.0	1.10	23.9	1.10	39.2	1.07	57.7	1.02	69.0	0.99	76.9	0.97
31000, 4.0	5.5	0.98	10.5	0.99	12.9	0.99	23.0	0.98	37.6	0.96	47.6	0.94	55.2	0.93
15000, 4.5	0.4	1.04	0.7	1.06	0.9	1.07	1.7	1.07	3.1	1.06	4.3	1.06	5.5	1.06
17000, 4.5	1.3	1.08	2.4	1.08	3.0	1.08	5.3	1.07	9.2	1.07	12.3	1.07	15.0	1.07
19000, 4.5	3.6	1.10	6.5	1.09	7.8	1.09	13.1	1.08	21.1	1.07	27.1	1.07	32.1	1.07
21000, 4.5	8.1	1.15	13.9	1.12	16.4	1.11	26.1	1.08	39.2	1.07	48.5	1.07	55.9	1.07
23000, 4.5	14.4	1.19	24.1	1.14	27.9	1.13	42.1	1.09	59.6	1.06	71.4	1.05	80.5	1.05
25000, 4.5	19.2	1.20	31.8	1.15	36.6	1.13	53.7	1.08	73.1	1.03	85.6	1.02	95.0	1.01
27000, 4.5	17.9	1.16	30.5	1.12	35.5	1.11	53.1	1.05	72.6	1.00	84.6	0.98	93.4	0.96
29000, 4.5	12.9	1.09	23.2	1.08	27.5	1.07	43.7	1.03	62.5	0.99	74.0	0.96	82.3	0.94
31000, 4.5	7.8	0.99	14.8	1.00	17.9	1.00	30.6	0.99	47.2	0.96	58.0	0.94	65.9	0.93

Table B.24: MULTI results for N II λ 5005.1 Å at $\xi_t = 10 \text{ km s}^{-1}$ (Equivalent widths, W_λ , are in mÅ)

$T_{\text{eff}}, \log(g)$	Nitrogen Abundance difference $\Delta\epsilon_N$, ($\Delta\epsilon_N = \epsilon_N - \epsilon_{N,\text{solar}}$, where $\epsilon_{N,\text{solar}} = 7.83$)													
	-1.00		-0.70		-0.60		-0.30		0.00		0.18		0.30	
	W_λ	W/W_*	W_λ	W/W_*	W_λ	W/W_*	W_λ	W/W_*	W_λ	W/W_*	W_λ	W/W_*	W_λ	W/W_*
15000, 3.5	1.4	1.17	2.7	1.16	3.3	1.15	5.9	1.14	10.3	1.13	13.9	1.12	17.0	1.12
17000, 3.5	4.9	1.20	8.8	1.17	10.5	1.16	17.6	1.14	28.1	1.13	36.2	1.13	42.9	1.13
19000, 3.5	12.6	1.26	21.4	1.21	25.1	1.20	39.3	1.16	58.3	1.14	71.9	1.13	82.7	1.13
21000, 3.5	23.9	1.35	39.6	1.29	45.8	1.27	68.0	1.20	94.6	1.14	112.3	1.12	125.8	1.12
23000, 3.5	30.7	1.43	51.8	1.37	60.0	1.34	88.0	1.24	117.9	1.15	136.2	1.11	149.7	1.09
25000, 3.5	24.3	1.37	43.2	1.34	51.0	1.32	79.5	1.25	110.5	1.16	128.3	1.10	140.7	1.07
27000, 3.5	14.4	1.27	26.9	1.27	32.5	1.26	55.3	1.22	84.6	1.16	102.9	1.12	115.7	1.08
29000, 3.5	6.3	1.13	12.1	1.13	14.9	1.12	27.7	1.10	47.7	1.07	62.5	1.05	74.1	1.03
31000, 3.5	1.9	0.86	3.5	0.90	4.3	0.91	8.4	0.91	15.8	0.89	22.4	0.86	28.2	0.84
15000, 4.0	0.7	1.13	1.4	1.12	1.7	1.12	3.2	1.11	5.8	1.10	8.0	1.10	10.1	1.09
17000, 4.0	2.5	1.15	4.7	1.13	5.7	1.13	10.0	1.11	17.0	1.10	22.5	1.10	27.3	1.10
19000, 4.0	6.9	1.18	12.3	1.15	14.6	1.14	24.2	1.12	38.1	1.10	48.5	1.10	57.0	1.10
21000, 4.0	14.6	1.23	25.2	1.19	29.5	1.18	46.3	1.14	68.4	1.11	83.8	1.10	95.7	1.09
23000, 4.0	23.3	1.29	39.6	1.24	46.1	1.22	69.6	1.16	97.4	1.10	115.5	1.08	129.1	1.07
25000, 4.0	24.7	1.29	42.9	1.25	50.3	1.23	76.7	1.16	106.2	1.09	124.1	1.05	137.3	1.03
27000, 4.0	18.4	1.22	33.4	1.20	39.8	1.19	64.3	1.14	93.3	1.08	111.0	1.04	123.4	1.02
29000, 4.0	11.2	1.10	21.3	1.11	25.8	1.11	45.0	1.09	70.9	1.06	88.0	1.03	100.4	1.01
31000, 4.0	5.5	0.97	10.8	0.99	13.4	0.99	24.9	0.99	43.1	0.98	56.8	0.96	67.5	0.95
15000, 4.5	0.4	1.02	0.7	1.05	0.9	1.06	1.8	1.07	3.3	1.07	4.7	1.07	6.0	1.06
17000, 4.5	1.3	1.07	2.6	1.08	3.1	1.08	5.8	1.08	10.2	1.07	13.9	1.07	17.2	1.07
19000, 4.5	3.8	1.10	7.0	1.10	8.5	1.09	14.7	1.08	24.4	1.08	32.1	1.07	38.5	1.07
21000, 4.5	8.6	1.16	15.4	1.14	18.4	1.13	30.4	1.10	47.4	1.08	59.9	1.08	69.9	1.07
23000, 4.5	15.6	1.21	27.2	1.17	32.1	1.16	50.9	1.11	75.1	1.08	91.6	1.07	104.4	1.06
25000, 4.5	20.8	1.22	36.2	1.19	42.6	1.17	66.2	1.11	94.4	1.06	112.6	1.04	126.2	1.03
27000, 4.5	19.0	1.17	34.1	1.15	40.5	1.14	64.6	1.09	93.4	1.04	111.5	1.01	124.6	0.99
29000, 4.5	13.5	1.09	25.1	1.09	30.2	1.09	51.0	1.06	77.9	1.02	95.3	1.00	107.9	0.98
31000, 4.5	8.0	0.97	15.4	1.00	18.9	1.00	34.0	1.00	55.9	0.98	71.3	0.97	83.0	0.96

Table B.25: MULTI results for N II λ 5679.6 Å at $\xi_t = 0$ km s⁻¹ (Equivalent widths, W_λ , are in mÅ)

T _{eff} , log(g)	Nitrogen Abundance difference $\Delta\epsilon_N$, ($\Delta\epsilon_N = \epsilon_N - \epsilon_{N,solar}$, where $\epsilon_{N,solar} = 7.83$)													
	-1.00		-0.70		-0.60		-0.30		0.00		0.18		0.30	
	W_λ	W/W_*	W_λ	W/W_*	W_λ	W/W_*	W_λ	W/W_*	W_λ	W/W_*	W_λ	W/W_*	W_λ	W/W_*
15000 , 3.5	1.2	0.85	2.5	0.98	3.1	1.01	5.8	1.11	10.3	1.18	13.8	1.21	16.8	1.24
17000 , 3.5	4.2	0.96	8.1	1.09	9.9	1.13	17.0	1.22	27.1	1.29	34.4	1.31	40.2	1.33
19000 , 3.5	10.7	1.03	19.8	1.18	23.5	1.22	37.4	1.32	54.6	1.38	66.0	1.40	74.6	1.41
21000 , 3.5	19.7	1.05	35.4	1.22	41.5	1.27	62.7	1.37	85.9	1.42	100.1	1.43	110.4	1.44
23000 , 3.5	25.2	1.05	43.9	1.19	51.2	1.23	76.6	1.33	103.1	1.38	118.5	1.40	129.4	1.40
25000 , 3.5	21.6	1.06	37.4	1.13	43.7	1.15	66.6	1.23	93.0	1.29	108.7	1.31	119.8	1.32
27000 , 3.5	13.8	1.08	26.2	1.16	31.3	1.17	49.6	1.19	71.4	1.21	85.5	1.22	96.0	1.24
29000 , 3.5	5.5	0.88	13.2	1.11	16.8	1.16	31.5	1.24	50.2	1.24	62.0	1.23	70.6	1.22
31000 , 3.5	-0.9	-0.44	1.2	0.29	2.6	0.51	10.2	1.01	23.4	1.24	33.6	1.29	41.7	1.30
15000 , 4.0	0.6	0.81	1.3	0.91	1.6	0.94	3.2	1.02	5.8	1.09	8.1	1.12	10.1	1.14
17000 , 4.0	2.2	0.90	4.4	1.01	5.4	1.04	9.8	1.12	16.5	1.18	21.7	1.21	25.9	1.22
19000 , 4.0	6.0	0.98	11.4	1.09	13.8	1.13	23.2	1.21	35.9	1.26	44.9	1.28	51.9	1.30
21000 , 4.0	12.7	1.02	23.2	1.15	27.5	1.19	43.4	1.27	62.3	1.32	74.6	1.33	83.8	1.34
23000 , 4.0	20.0	1.04	35.3	1.16	41.3	1.20	62.6	1.28	85.8	1.32	99.9	1.33	110.2	1.34
25000 , 4.0	21.5	1.02	37.2	1.11	43.4	1.13	65.9	1.21	90.7	1.26	105.5	1.27	116.0	1.28
27000 , 4.0	16.6	1.00	29.6	1.06	34.8	1.08	54.2	1.12	77.2	1.17	91.7	1.19	102.1	1.20
29000 , 4.0	10.4	0.96	20.2	1.04	24.3	1.06	40.1	1.09	59.3	1.10	72.0	1.12	81.4	1.13
31000 , 4.0	4.5	0.76	10.5	0.95	13.3	0.99	25.2	1.07	41.2	1.10	51.8	1.10	59.7	1.10
15000 , 4.5	0.3	0.80	0.7	0.88	0.9	0.90	1.8	0.96	3.4	1.02	4.8	1.05	6.1	1.06
17000 , 4.5	1.2	0.87	2.4	0.95	3.0	0.98	5.6	1.04	10.0	1.09	13.5	1.11	16.6	1.13
19000 , 4.5	3.4	0.93	6.6	1.02	8.0	1.05	14.1	1.11	23.1	1.16	29.8	1.18	35.2	1.19
21000 , 4.5	7.7	0.98	14.4	1.08	17.3	1.11	28.5	1.17	43.3	1.22	53.4	1.23	61.2	1.24
23000 , 4.5	13.9	1.01	25.0	1.11	29.5	1.14	46.3	1.20	66.0	1.24	78.7	1.25	88.1	1.25
25000 , 4.5	18.5	1.01	32.3	1.09	37.8	1.11	57.8	1.17	80.5	1.21	94.5	1.22	104.7	1.22
27000 , 4.5	17.1	0.97	30.1	1.03	35.3	1.04	54.7	1.09	77.4	1.14	91.6	1.15	101.9	1.16
29000 , 4.5	12.2	0.94	22.6	0.99	26.9	1.01	43.3	1.04	63.4	1.07	76.5	1.09	86.3	1.10
31000 , 4.5	7.1	0.87	14.3	0.95	17.5	0.97	30.3	1.01	46.9	1.03	58.1	1.04	66.5	1.05

Table B.26: MULTI results for N II λ 5679.6 Å at $\xi_t = 5 \text{ km s}^{-1}$ (Equivalent widths, W_λ , are in mÅ)

$T_{\text{eff}}, \log(g)$	Nitrogen Abundance difference $\Delta\epsilon_N$, ($\Delta\epsilon_N = \epsilon_N - \epsilon_{N,\text{solar}}$, where $\epsilon_{N,\text{solar}} = 7.83$)													
	-1.00		-0.70		-0.60		-0.30		0.00		0.18		0.30	
	W_λ	W/W_*	W_λ	W/W_*	W_λ	W/W_*	W_λ	W/W_*	W_λ	W/W_*	W_λ	W/W_*	W_λ	W/W_*
15000, 3.5	1.1	0.78	2.4	0.90	3.0	0.94	6.0	1.05	11.1	1.13	15.3	1.17	19.0	1.20
17000, 3.5	4.0	0.88	8.3	1.02	10.3	1.06	18.6	1.17	31.0	1.25	40.3	1.28	47.9	1.30
19000, 3.5	10.6	0.93	20.8	1.10	25.3	1.15	42.7	1.27	65.3	1.34	80.8	1.38	92.7	1.40
21000, 3.5	19.9	0.96	38.1	1.14	45.7	1.19	73.8	1.32	106.2	1.40	126.5	1.43	141.2	1.44
23000, 3.5	26.2	0.99	48.1	1.13	57.2	1.17	90.7	1.29	128.4	1.37	150.7	1.39	166.4	1.40
25000, 3.5	22.2	1.02	41.0	1.11	48.7	1.14	77.7	1.20	113.1	1.27	135.2	1.30	150.9	1.32
27000, 3.5	13.3	1.00	27.3	1.13	33.3	1.15	56.3	1.19	84.7	1.21	103.3	1.22	117.3	1.24
29000, 3.5	4.4	0.69	12.3	1.00	16.1	1.07	32.9	1.21	56.5	1.25	72.2	1.25	83.8	1.24
31000, 3.5	-1.6	-0.74	-0.2	-0.05	1.0	0.19	8.3	0.81	22.7	1.16	34.8	1.26	44.8	1.29
15000, 4.0	0.6	0.76	1.2	0.85	1.6	0.88	3.2	0.97	6.1	1.04	8.7	1.08	11.0	1.10
17000, 4.0	2.1	0.84	4.4	0.95	5.4	0.98	10.3	1.07	18.2	1.14	24.5	1.18	29.8	1.20
19000, 4.0	5.9	0.91	11.8	1.03	14.5	1.07	25.6	1.16	41.4	1.23	53.0	1.26	62.2	1.28
21000, 4.0	12.8	0.95	24.6	1.08	29.7	1.13	49.6	1.23	74.7	1.30	91.5	1.32	104.1	1.34
23000, 4.0	20.5	0.97	38.2	1.10	45.5	1.14	73.1	1.24	105.2	1.31	125.0	1.33	139.4	1.34
25000, 4.0	22.3	0.98	40.6	1.07	48.2	1.10	76.7	1.18	110.5	1.24	131.2	1.27	146.0	1.28
27000, 4.0	16.7	0.96	31.7	1.04	37.9	1.06	61.9	1.11	91.8	1.16	111.2	1.18	125.4	1.20
29000, 4.0	9.9	0.89	20.5	1.01	25.3	1.03	44.3	1.08	68.7	1.10	85.0	1.11	97.3	1.12
31000, 4.0	3.7	0.63	9.9	0.87	12.9	0.92	26.1	1.04	45.5	1.09	59.0	1.10	69.2	1.10
15000, 4.5	0.3	0.76	0.7	0.83	0.8	0.86	1.7	0.93	3.4	0.99	5.0	1.02	6.4	1.04
17000, 4.5	1.1	0.82	2.4	0.91	3.0	0.93	5.8	1.00	10.7	1.06	14.8	1.09	18.4	1.11
19000, 4.5	3.3	0.88	6.7	0.97	8.2	1.00	15.1	1.07	25.7	1.13	34.0	1.16	40.8	1.17
21000, 4.5	7.7	0.93	15.0	1.03	18.2	1.06	31.6	1.14	50.1	1.19	63.2	1.22	73.4	1.23
23000, 4.5	14.2	0.96	26.6	1.06	31.9	1.09	52.7	1.17	78.7	1.23	95.7	1.24	108.4	1.25
25000, 4.5	19.1	0.97	34.9	1.05	41.5	1.07	66.6	1.15	96.9	1.20	115.9	1.22	129.8	1.23
27000, 4.5	17.5	0.94	32.3	1.00	38.5	1.02	62.4	1.07	92.0	1.12	110.9	1.14	124.8	1.16
29000, 4.5	12.2	0.90	23.6	0.97	28.6	0.99	48.2	1.03	73.5	1.06	90.5	1.08	103.2	1.09
31000, 4.5	6.8	0.81	14.3	0.92	17.8	0.94	32.5	1.00	52.8	1.02	66.8	1.03	77.5	1.04

Table B.27: MULTI results for N II λ 5679.6 Å at $\xi_t = 10 \text{ km s}^{-1}$ (Equivalent widths, W_λ , are in mÅ)

$T_{\text{eff}}, \log(g)$	Nitrogen Abundance difference $\Delta\epsilon_N$, ($\Delta\epsilon_N = \epsilon_N - \epsilon_{N,\text{solar}}$, where $\epsilon_{N,\text{solar}} = 7.83$)													
	-1.00		-0.70		-0.60		-0.30		0.00		0.18		0.30	
	W_λ	W/W_*	W_λ	W/W_*	W_λ	W/W_*	W_λ	W/W_*	W_λ	W/W_*	W_λ	W/W_*	W_λ	W/W_*
15000, 3.5	1.0	0.70	2.3	0.82	2.9	0.86	6.1	0.98	11.8	1.07	16.8	1.12	21.3	1.15
17000, 3.5	3.8	0.78	8.3	0.93	10.4	0.97	20.1	1.10	35.4	1.19	47.4	1.24	57.5	1.26
19000, 3.5	10.2	0.83	21.4	0.99	26.6	1.05	48.4	1.19	79.0	1.29	100.8	1.34	117.9	1.36
21000, 3.5	19.6	0.85	40.0	1.03	49.2	1.08	86.5	1.24	134.0	1.35	164.8	1.40	187.5	1.42
23000, 3.5	26.5	0.92	52.1	1.05	63.3	1.09	108.0	1.22	164.2	1.33	199.4	1.37	224.5	1.39
25000, 3.5	21.8	0.94	44.1	1.07	53.7	1.10	91.9	1.17	141.8	1.24	175.1	1.28	199.6	1.30
27000, 3.5	11.9	0.86	27.1	1.05	34.2	1.09	63.8	1.18	103.3	1.21	130.1	1.22	150.5	1.23
29000, 3.5	2.5	0.40	10.1	0.81	14.1	0.91	32.9	1.13	63.2	1.24	85.6	1.26	102.7	1.26
31000, 3.5	-2.3	-1.07	-2.1	-0.51	-1.4	-0.28	4.6	0.45	19.6	0.97	33.8	1.16	46.4	1.24
15000, 4.0	0.5	0.70	1.2	0.79	1.5	0.82	3.2	0.91	6.3	0.99	9.2	1.03	11.9	1.06
17000, 4.0	2.0	0.77	4.3	0.88	5.4	0.91	10.8	1.01	19.9	1.09	27.6	1.13	34.3	1.16
19000, 4.0	5.7	0.82	11.9	0.95	14.9	0.99	28.0	1.10	48.0	1.18	63.3	1.22	75.8	1.25
21000, 4.0	12.5	0.86	25.5	1.00	31.5	1.04	56.5	1.16	90.9	1.25	114.9	1.29	133.3	1.31
23000, 4.0	20.6	0.89	40.6	1.02	49.5	1.06	85.7	1.18	132.1	1.27	162.2	1.31	184.3	1.33
25000, 4.0	22.4	0.91	43.8	1.02	53.1	1.05	90.3	1.13	138.7	1.21	170.2	1.25	193.1	1.26
27000, 4.0	16.2	0.88	33.2	0.99	40.7	1.02	71.5	1.08	112.5	1.13	140.6	1.16	161.8	1.18
29000, 4.0	9.0	0.78	20.2	0.93	25.5	0.97	48.7	1.05	81.5	1.09	104.4	1.10	122.0	1.11
31000, 4.0	2.5	0.41	8.4	0.72	11.5	0.79	26.1	0.97	50.0	1.06	68.3	1.09	82.7	1.10
15000, 4.5	0.3	0.72	0.6	0.79	0.8	0.81	1.7	0.88	3.5	0.94	5.2	0.98	6.8	1.00
17000, 4.5	1.1	0.77	2.3	0.85	2.9	0.88	5.9	0.95	11.3	1.02	16.1	1.05	20.4	1.07
19000, 4.5	3.2	0.82	6.7	0.91	8.3	0.94	16.1	1.02	28.8	1.09	39.0	1.12	47.8	1.14
21000, 4.5	7.6	0.87	15.4	0.96	19.0	1.00	35.0	1.09	58.7	1.16	76.3	1.19	90.4	1.21
23000, 4.5	14.1	0.89	27.9	0.99	34.2	1.03	60.3	1.12	95.9	1.19	120.4	1.22	138.9	1.24
25000, 4.5	19.2	0.91	37.3	1.00	45.2	1.02	77.6	1.10	120.1	1.17	148.2	1.20	169.1	1.21
27000, 4.5	17.4	0.88	34.3	0.96	41.8	0.98	72.1	1.04	112.7	1.09	140.2	1.12	160.9	1.14
29000, 4.5	11.7	0.83	24.2	0.92	29.9	0.95	54.1	1.00	87.8	1.04	111.5	1.06	129.6	1.07
31000, 4.5	6.0	0.70	13.8	0.85	17.6	0.88	34.5	0.96	60.4	1.01	79.3	1.02	94.2	1.03

Table B.28: MULTI results for N II λ 6482 Å at $\xi_t = 0$ km s⁻¹ (Equivalent widths, W_λ , are in mÅ)

T _{eff} , log(g)	Nitrogen Abundance difference $\Delta\epsilon_N$, ($\Delta\epsilon_N = \epsilon_N - \epsilon_{N,solar}$, where $\epsilon_{N,solar} = 7.83$)													
	-1.00		-0.70		-0.60		-0.30		0.00		0.18		0.30	
	W_λ	W/W_*	W_λ	W/W_*	W_λ	W/W_*	W_λ	W/W_*	W_λ	W/W_*	W_λ	W/W_*	W_λ	W/W_*
15000, 3.5	0.2	0.95	0.5	1.02	0.6	1.05	1.3	1.11	2.5	1.17	3.6	1.20	4.6	1.21
17000, 3.5	0.9	1.01	1.9	1.10	2.4	1.12	4.7	1.19	8.6	1.24	11.9	1.27	14.7	1.28
19000, 3.5	2.8	1.04	5.8	1.15	7.1	1.18	13.1	1.25	22.3	1.31	29.4	1.34	35.4	1.36
21000, 3.5	6.0	1.03	12.2	1.16	15.0	1.20	27.0	1.30	43.9	1.38	56.1	1.42	65.8	1.44
23000, 3.5	7.6	0.94	16.2	1.10	20.2	1.16	37.4	1.30	61.2	1.41	77.8	1.46	90.5	1.49
25000, 3.5	5.3	0.80	12.0	0.97	15.4	1.03	31.1	1.21	55.2	1.36	72.8	1.44	86.5	1.48
27000, 3.5	2.4	0.59	6.0	0.79	8.0	0.85	18.1	1.06	36.4	1.25	51.5	1.35	63.9	1.41
29000, 3.5	-0.8	-0.43	0.2	0.07	1.0	0.21	5.4	0.60	15.5	0.93	25.2	1.09	34.2	1.19
31000, 3.5	-2.9	-4.55	-4.2	-3.26	-4.6	-2.82	-5.0	-1.54	-3.4	-0.53	-0.5	-0.05	3.0	0.24
15000, 4.0	0.1	0.88	0.2	0.95	0.3	0.97	0.6	1.04	1.2	1.09	1.8	1.12	2.4	1.14
17000, 4.0	0.4	0.95	0.9	1.03	1.2	1.05	2.4	1.12	4.5	1.17	6.4	1.19	8.2	1.20
19000, 4.0	1.4	1.00	2.9	1.09	3.6	1.11	7.0	1.18	12.6	1.23	17.2	1.25	21.1	1.26
21000, 4.0	3.4	1.01	7.1	1.12	8.8	1.15	16.2	1.23	27.4	1.28	36.0	1.30	43.0	1.32
23000, 4.0	5.9	0.97	12.2	1.11	15.1	1.15	27.6	1.25	45.4	1.32	58.1	1.35	68.1	1.37
25000, 4.0	5.9	0.87	12.9	1.02	16.2	1.07	30.9	1.20	52.2	1.30	67.3	1.34	78.9	1.37
27000, 4.0	3.9	0.75	8.8	0.90	11.3	0.95	23.3	1.11	42.7	1.24	57.3	1.30	69.0	1.34
29000, 4.0	1.7	0.53	4.5	0.72	6.0	0.78	13.7	0.96	28.0	1.13	40.0	1.22	50.2	1.27
31000, 4.0	-0.5	-0.27	0.5	0.16	1.2	0.28	4.8	0.60	13.0	0.88	20.8	1.01	28.1	1.09
15000, 4.5	0.1	0.84	0.1	0.90	0.1	0.92	0.3	0.97	0.6	1.02	0.9	1.05	1.3	1.07
17000, 4.5	0.2	0.90	0.5	0.96	0.6	0.99	1.2	1.04	2.4	1.09	3.5	1.11	4.5	1.13
19000, 4.5	0.7	0.95	1.5	1.02	1.9	1.05	3.7	1.10	7.0	1.15	9.8	1.17	12.4	1.18
21000, 4.5	1.8	0.98	3.8	1.07	4.8	1.09	9.2	1.15	16.4	1.19	22.2	1.21	27.1	1.22
23000, 4.5	3.7	0.97	7.8	1.08	9.7	1.11	18.0	1.18	30.6	1.23	40.0	1.25	47.6	1.26
25000, 4.5	5.2	0.92	10.9	1.04	13.6	1.07	25.4	1.16	42.5	1.23	54.9	1.25	64.6	1.26
27000, 4.5	4.4	0.81	9.6	0.94	12.2	0.98	23.9	1.09	41.9	1.18	55.1	1.22	65.5	1.24
29000, 4.5	2.7	0.69	6.2	0.83	8.0	0.87	16.8	1.01	31.7	1.12	43.6	1.17	53.3	1.20
31000, 4.5	1.0	0.41	2.8	0.62	3.9	0.68	9.2	0.86	19.4	1.01	28.3	1.09	36.0	1.13

Table B.29: MULTI results for N II λ 6482 Å at $\xi_t = 10 \text{ km s}^{-1}$ (Equivalent widths, W_λ , are in mÅ)

$T_{\text{eff}}, \log(g)$	Nitrogen Abundance difference $\Delta\epsilon_N$, ($\Delta\epsilon_N = \epsilon_N - \epsilon_{N,\text{solar}}$, where $\epsilon_{N,\text{solar}} = 7.83$)													
	-1.00		-0.70		-0.60		-0.30		0.00		0.18		0.30	
	W_λ	W/W_*	W_λ	W/W_*	W_λ	W/W_*	W_λ	W/W_*	W_λ	W/W_*	W_λ	W/W_*	W_λ	W/W_*
15000, 3.5	0.2	0.86	0.4	0.93	0.6	0.95	1.2	1.02	2.5	1.09	3.7	1.13	4.9	1.15
17000, 3.5	0.9	0.90	1.8	0.99	2.3	1.02	4.8	1.10	9.4	1.17	13.6	1.20	17.4	1.23
19000, 3.5	2.6	0.91	5.6	1.02	7.1	1.06	14.2	1.15	26.6	1.23	36.9	1.27	45.9	1.30
21000, 3.5	5.5	0.88	11.9	1.01	15.1	1.05	30.2	1.18	55.1	1.28	74.9	1.34	91.2	1.37
23000, 3.5	6.9	0.80	15.3	0.94	19.7	0.99	41.0	1.15	76.7	1.29	104.7	1.36	127.5	1.41
25000, 3.5	4.6	0.67	10.7	0.80	14.0	0.85	31.2	1.03	63.6	1.22	91.1	1.31	114.3	1.37
27000, 3.5	1.4	0.36	4.5	0.56	6.2	0.63	15.8	0.84	36.6	1.06	56.5	1.19	74.7	1.27
29000, 3.5	-2.1	-1.08	-2.0	-0.51	-1.6	-0.34	1.4	0.15	10.2	0.57	20.4	0.79	30.9	0.93
31000, 3.5	-3.6	-5.54	-5.9	-4.59	-6.8	-4.21	-9.4	-2.90	-10.5	-1.63	-9.5	-0.98	-7.4	-0.58
15000, 4.0	0.1	0.81	0.2	0.86	0.3	0.88	0.6	0.95	1.2	1.01	1.8	1.05	2.4	1.07
17000, 4.0	0.4	0.86	0.9	0.93	1.1	0.96	2.3	1.03	4.7	1.10	6.9	1.13	9.1	1.15
19000, 4.0	1.3	0.89	2.8	0.98	3.5	1.01	7.2	1.09	14.0	1.16	20.1	1.19	25.5	1.22
21000, 4.0	3.1	0.88	6.8	0.99	8.6	1.03	17.4	1.13	32.7	1.21	45.3	1.25	56.2	1.27
23000, 4.0	5.2	0.83	11.6	0.96	14.8	1.00	30.3	1.13	56.1	1.24	76.7	1.28	93.6	1.31
25000, 4.0	5.2	0.73	11.8	0.86	15.3	0.91	32.6	1.06	62.7	1.20	87.2	1.26	107.3	1.30
27000, 4.0	3.2	0.60	7.6	0.73	10.0	0.78	22.6	0.95	47.1	1.11	68.5	1.20	87.1	1.25
29000, 4.0	0.9	0.28	3.2	0.49	4.5	0.56	11.7	0.76	27.3	0.96	42.5	1.07	56.5	1.14
31000, 4.0	-1.4	-0.82	-1.1	-0.33	-0.8	-0.18	1.9	0.23	9.3	0.58	17.5	0.76	25.8	0.87
15000, 4.5	0.1	0.79	0.1	0.83	0.1	0.84	0.3	0.90	0.6	0.95	0.9	0.98	1.2	1.00
17000, 4.5	0.2	0.83	0.4	0.88	0.5	0.90	1.1	0.97	2.4	1.03	3.5	1.06	4.7	1.08
19000, 4.5	0.6	0.86	1.4	0.93	1.8	0.96	3.7	1.03	7.3	1.09	10.8	1.12	14.0	1.14
21000, 4.5	1.7	0.87	3.6	0.96	4.6	0.99	9.5	1.07	18.4	1.14	26.2	1.17	33.1	1.19
23000, 4.5	3.4	0.85	7.4	0.96	9.4	0.99	19.2	1.09	36.2	1.17	50.2	1.20	62.1	1.22
25000, 4.5	4.6	0.78	10.2	0.90	13.1	0.94	27.1	1.06	51.1	1.16	70.5	1.20	86.5	1.23
27000, 4.5	3.8	0.68	8.7	0.80	11.3	0.84	24.4	0.97	48.1	1.09	68.1	1.15	84.9	1.18
29000, 4.5	2.1	0.54	5.2	0.67	6.9	0.72	15.8	0.86	33.6	1.01	49.6	1.08	63.9	1.13
31000, 4.5	0.3	0.12	1.8	0.38	2.6	0.45	7.5	0.67	18.2	0.86	28.7	0.96	38.7	1.02

Appendix C

Monte Carlo Results

Table C.1: Results of Monte Carlo Simulations for N II atom at $\log(g)=3.5$, and $\xi_t=0.0 \text{ km s}^{-1}$: average equivalent widths, $\langle W_\lambda \rangle$, and the expected error, 2σ

λ (Å)	ϵ_N	T_{eff} (K)	$\langle W_\lambda \rangle$ (mÅ)	σ (mÅ)	λ (Å)	ϵ_N	T_{eff} (K)	$\langle W_\lambda \rangle$ (mÅ)	2σ (mÅ)
3995	6.830	15000.0	5.5	0.54	6482	6.83	15000.0	0.2	0.03
		19000.0	22.8	1.97			19000.0	2.8	0.34
		23000.0	33.2	3.08			23000.0	6.8	1.07
		27000.0	14.6	1.83			27000.0	1.4	0.47
		31000.0	-1.1	0.21			31000.0	-3.2	0.26
7.230	7.230	15000.0	10.9	0.95	7.23	7.23	15000.0	0.6	0.07
		19000.0	39.3	2.76			19000.0	7.0	0.77
		23000.0	58.5	4.13			23000.0	18.4	2.34
		27000.0	31.9	3.29			27000.0	5.5	1.25
		31000.0	0.1	0.65			31000.0	-5.4	0.41
7.530	7.530	15000.0	17.1	1.33	7.53	7.53	15000.0	1.3	0.14
		19000.0	54.6	3.34			19000.0	12.8	1.30
		23000.0	80.8	4.63			23000.0	34.3	3.61
		27000.0	51.4	4.29			27000.0	13.5	2.38
		31000.0	4.4	1.42			31000.0	-6.8	0.57
7.830	7.830	15000.0	25.4	1.80	7.83	7.83	15000.0	2.5	0.26
		19000.0	72.3	3.94			19000.0	21.8	1.99
		23000.0	104.6	5.06			23000.0	56.9	4.88
		27000.0	74.5	4.93			27000.0	28.9	3.94
		31000.0	14.1	2.64			31000.0	-6.6	1.00
8.130	8.130	15000.0	36.0	2.32	8.13	8.13	15000.0	4.6	0.46
		19000.0	92.8	4.68			19000.0	34.7	2.85
		23000.0	130.5	5.63			23000.0	84.9	6.03
		27000.0	99.5	5.33			27000.0	53.0	5.55
		31000.0	30.8	4.02			31000.0	-2.4	2.05

Table C.2: Results of Monte Carlo Simulations for N II atom at $\log(g)=4.0$, and $\xi_t=0.0 \text{ km s}^{-1}$: average equivalent widths, $\langle W_\lambda \rangle$, and the expected error, 2σ

λ (Å)	ϵ_N	T_{eff} (K)	$\langle W_\lambda \rangle$ (mÅ)	σ (mÅ)	λ (Å)	ϵ_N	T_{eff} (K)	$\langle W_\lambda \rangle$ (mÅ)	2σ (mÅ)
3995	6.830	15000.0	2.9	0.30	6482	6.83	15000.0	0.1	0.01
		19000.0	14.8	1.36			19000.0	1.4	0.17
		23000.0	29.8	2.69			23000.0	5.5	0.74
		27000.0	20.3	2.23			27000.0	3.0	0.58
		31000.0	4.6	0.77			31000.0	-1.0	0.14
7.230	7.230	15000.0	6.2	0.59	7.23	7.23	15000.0	0.3	0.03
		19000.0	27.2	2.09			19000.0	3.6	0.40
		23000.0	52.5	3.70			23000.0	14.5	1.65
		27000.0	40.8	3.61			27000.0	9.4	1.46
		31000.0	13.2	1.81			31000.0	-0.1	0.40
7.530	7.530	15000.0	10.3	0.90	7.53	7.53	15000.0	0.6	0.07
		19000.0	39.7	2.69			19000.0	6.9	0.72
		23000.0	72.8	4.29			23000.0	26.6	2.64
		27000.0	61.8	4.42			27000.0	20.1	2.60
		31000.0	25.6	2.94			31000.0	2.5	0.91
7.830	7.830	15000.0	16.3	1.29	7.83	7.83	15000.0	1.2	0.13
		19000.0	54.9	3.36			19000.0	12.4	1.20
		23000.0	95.0	4.90			23000.0	43.8	3.72
		27000.0	85.3	4.98			27000.0	37.8	4.01
		31000.0	43.8	4.06			31000.0	8.9	1.87
8.130	8.130	15000.0	24.4	1.75	8.13	8.13	15000.0	2.4	0.25
		19000.0	73.1	4.18			19000.0	20.9	1.84
		23000.0	119.8	5.74			23000.0	66.0	4.83
		27000.0	110.3	5.51			27000.0	62.5	5.37
		31000.0	65.9	4.83			31000.0	21.7	3.30

Table C.3: Results of Monte Carlo Simulations for N II atom at $\log(g)=4.5$, and $\xi_t=0.0 \text{ km s}^{-1}$: average equivalent widths, $\langle W_\lambda \rangle$, and the expected error, 2σ

λ (Å)	ϵ_N	T_{eff} (K)	$\langle W_\lambda \rangle$ (mÅ)	σ (mÅ)	λ (Å)	ϵ_N	T_{eff} (K)	$\langle W_\lambda \rangle$ (mÅ)	2σ (mÅ)
3995	6.830	15000.0	1.4	0.15	6482	6.83	15000.0	0.1	0.01
		19000.0	8.8	0.86			19000.0	0.7	0.08
		23000.0	22.7	2.11			23000.0	3.7	0.45
		27000.0	22.2	2.29			27000.0	4.0	0.59
		31000.0	8.6	1.12			31000.0	0.6	0.19
7.230	7.230	15000.0	3.2	0.33	7.23	7.23	15000.0	0.1	0.02
		19000.0	17.4	1.48			19000.0	1.8	0.21
		23000.0	41.7	3.12			23000.0	9.5	1.04
		27000.0	43.5	3.59			27000.0	11.3	1.44
		31000.0	20.7	2.31			31000.0	2.9	0.57
7.530	7.530	15000.0	5.7	0.55	7.53	7.53	15000.0	0.3	0.03
		19000.0	27.0	2.06			19000.0	3.7	0.39
		23000.0	59.7	3.85			23000.0	17.7	1.75
		27000.0	64.6	4.37			27000.0	22.6	2.49
		31000.0	36.0	3.39			31000.0	7.5	1.19
7.830	7.830	15000.0	9.6	0.85	7.83	7.83	15000.0	0.6	0.07
		19000.0	39.4	2.75			19000.0	6.9	0.70
		23000.0	80.2	4.67			23000.0	30.1	2.65
		27000.0	87.9	5.04			27000.0	40.0	3.74
		31000.0	56.1	4.31			31000.0	16.7	2.21
8.130	8.130	15000.0	15.4	1.24	8.13	8.13	15000.0	1.3	0.13
		19000.0	54.9	3.61			19000.0	12.3	1.15
		23000.0	103.6	5.83			23000.0	47.0	3.67
		27000.0	113.0	5.87			27000.0	63.3	4.98
		31000.0	78.9	5.00			31000.0	32.3	3.54

Table C.4: Results of Monte Carlo Simulations for N II at $\log g=3.5$, and $\xi_t= 5.0 \text{ km s}^{-1}$: average equivalent widths, $\langle W_\lambda \rangle$, and the expected error, σ

λ (Å)	ϵ_N	T_{eff} (K)	$\langle w_\lambda \rangle$ (mÅ)	2σ (mÅ)	λ (Å)	ϵ_N	T_{eff} (K)	$\langle w_\lambda \rangle$ (mÅ)	2σ (mÅ)
3995	6.830	15000.0	5.8	0.60	6482	6.83	15000.0	0.2	0.03
		19000.0	25.3	2.36			19000.0	2.7	0.34
		23000.0	36.3	3.65			23000.0	6.5	1.08
		27000.0	14.8	1.94			27000.0	1.1	0.45
		31000.0	-1.4	0.20			31000.0	-3.5	0.28
7.230	7.230	15000.0	12.1	1.11	7.23	7.23	15000.0	0.6	0.07
		19000.0	46.0	3.49			19000.0	7.0	0.81
		23000.0	67.9	5.32			23000.0	18.3	2.52
		27000.0	33.9	3.77			27000.0	4.8	1.24
		31000.0	-0.9	0.60			31000.0	-6.3	0.49
7.530	7.530	15000.0	19.6	1.62	7.53	7.53	15000.0	1.2	0.14
		19000.0	66.1	4.29			19000.0	13.4	1.43
		23000.0	97.7	6.16			23000.0	36.1	4.19
		27000.0	57.3	5.27			27000.0	12.6	2.47
		31000.0	2.7	1.38			31000.0	-8.5	0.66
7.830	7.830	15000.0	29.9	2.23	7.83	7.83	15000.0	2.5	0.27
		19000.0	89.5	5.07			19000.0	23.9	2.30
		23000.0	130.0	6.74			23000.0	63.5	6.03
		27000.0	87.0	6.36			27000.0	28.9	4.39
		31000.0	12.2	2.76			31000.0	-9.5	1.02
8.130	8.130	15000.0	43.5	2.92	8.13	8.13	15000.0	4.8	0.50
		19000.0	116.1	5.90			19000.0	39.3	3.42
		23000.0	164.3	7.28			23000.0	99.5	7.72
		27000.0	120.2	7.00			27000.0	56.8	6.63
		31000.0	30.4	4.58			31000.0	-6.7	2.03

Table C.5: Results of Monte Carlo Simulations for N II at $\log g=4.5$, and $\xi_t= 5.0 \text{ km s}^{-1}$: average equivalent widths, $\langle W_\lambda \rangle$, and the expected error, σ

λ (Å)	ϵ_N	T_{eff} (K)	$\langle w_\lambda \rangle$ (mÅ)	2σ (mÅ)	λ (Å)	ϵ_N	T_{eff} (K)	$\langle w_\lambda \rangle$ (mÅ)	2σ (mÅ)
3995	6.830	15000.0	1.4	0.16	6482	6.83	15000.0	0.1	0.01
		19000.0	9.3	0.95			19000.0	0.7	0.08
		23000.0	24.4	2.40			23000.0	3.5	0.44
		27000.0	23.2	2.53			27000.0	3.7	0.59
		31000.0	8.4	1.13			31000.0	0.3	0.18
7.230	7.230	15000.0	3.3	0.35	7.23	7.23	15000.0	0.1	0.02
		19000.0	19.1	1.71			19000.0	1.8	0.21
		23000.0	47.2	3.79			23000.0	9.5	1.08
		27000.0	48.0	4.29			27000.0	11.0	1.47
		31000.0	21.1	2.49			31000.0	2.4	0.54
7.530	7.530	15000.0	6.1	0.60	7.53	7.53	15000.0	0.3	0.03
		19000.0	30.6	2.43			19000.0	3.7	0.40
		23000.0	70.1	4.76			23000.0	18.4	1.92
		27000.0	74.4	5.46			27000.0	22.9	2.70
		31000.0	38.4	3.89			31000.0	6.8	1.18
7.830	7.830	15000.0	10.5	0.96	7.83	7.83	15000.0	0.6	0.07
		19000.0	45.9	3.26			19000.0	7.1	0.74
		23000.0	96.7	5.68			23000.0	32.8	3.04
		27000.0	104.7	6.32			27000.0	42.9	4.31
		31000.0	62.6	5.21			31000.0	16.2	2.31
8.130	8.130	15000.0	17.3	1.44	8.13	8.13	15000.0	1.2	0.14
		19000.0	65.2	4.22			19000.0	13.1	1.27
		23000.0	126.4	6.76			23000.0	53.3	4.35
		27000.0	137.2	7.13			27000.0	71.3	6.00
		31000.0	91.5	6.17			31000.0	33.4	3.94

Table C.6: Results of Monte Carlo Simulations for N II atom at $\log(g)=3.5$, and $\xi_t=10.0 \text{ km s}^{-1}$: average equivalent widths, $\langle W_\lambda \rangle$, and the expected error, 2σ

λ (Å)	ϵ_N	T_{eff} (K)	$\langle W_\lambda \rangle$ (mÅ)	σ (mÅ)	λ (Å)	ϵ_N	T_{eff} (K)	$\langle W_\lambda \rangle$ (mÅ)	2σ (mÅ)
3995	6.830	15000.0	6.2	0.67	6482	6.83	15000.0	0.2	0.03
		19000.0	28.2	2.85			19000.0	2.5	0.34
		23000.0	39.6	4.34			23000.0	6.0	1.09
		27000.0	14.6	2.04			27000.0	0.6	0.42
		31000.0	-1.7	0.19			31000.0	-3.8	0.32
7.230	7.230	15000.0	13.4	1.31	7.23	7.23	15000.0	0.6	0.07
		19000.0	54.8	4.61			19000.0	6.9	0.85
		23000.0	79.9	7.14			23000.0	17.6	2.67
		27000.0	35.8	4.36			27000.0	3.8	1.20
		31000.0	-2.2	0.53			31000.0	-7.5	0.59
7.530	7.530	15000.0	22.6	2.01	7.53	7.53	15000.0	1.2	0.14
		19000.0	82.6	5.93			19000.0	13.9	1.57
		23000.0	122.2	8.85			23000.0	37.1	4.81
		27000.0	64.3	6.69			27000.0	10.9	2.51
		31000.0	-0.1	1.27			31000.0	-11.1	0.84
7.830	7.830	15000.0	36.0	2.87	7.83	7.83	15000.0	2.5	0.28
		19000.0	115.9	7.15			19000.0	26.0	2.68
		23000.0	170.4	9.93			23000.0	70.3	7.59
		27000.0	104.6	8.82			27000.0	27.4	4.83
		31000.0	8.3	2.79			31000.0	-14.1	1.16
8.130	8.130	15000.0	54.1	3.88	8.13	8.13	15000.0	4.9	0.53
		19000.0	154.1	8.31			19000.0	44.9	4.19
		23000.0	221.6	10.66			23000.0	118.4	10.42
		27000.0	152.9	10.19			27000.0	59.4	8.08
		31000.0	27.5	5.22			31000.0	-14.0	1.99

Table C.7: Results of Monte Carlo Simulations for N II atom at $\log(g)=4.0$, and $\xi_t=10.0 \text{ km s}^{-1}$: average equivalent widths, $\langle W_\lambda \rangle$, and the expected error, 2σ

λ (Å)	ϵ_N	T_{eff} (K)	$\langle W_\lambda \rangle$ (mÅ)	σ (mÅ)	λ (Å)	ϵ_N	T_{eff} (K)	$\langle W_\lambda \rangle$ (mÅ)	2σ (mÅ)
3995	6.830	15000.0	3.1	0.35	6482	6.83	15000.0	0.1	0.01
		19000.0	17.4	1.81			19000.0	1.3	0.16
		23000.0	35.2	3.74			23000.0	4.9	0.74
		27000.0	21.9	2.68			27000.0	2.4	0.56
		31000.0	3.4	0.71			31000.0	-1.9	0.18
7.230	7.230	15000.0	7.1	0.74	7.23	7.23	15000.0	0.3	0.03
		19000.0	35.6	3.17			19000.0	3.5	0.41
		23000.0	71.0	6.18			23000.0	14.1	1.83
		27000.0	49.1	5.21			27000.0	8.0	1.47
		31000.0	11.7	1.90			31000.0	-2.0	0.35
7.530	7.530	15000.0	12.6	1.22	7.53	7.53	15000.0	0.6	0.07
		19000.0	56.2	4.37			19000.0	7.1	0.80
		23000.0	108.6	7.78			23000.0	28.9	3.35
		27000.0	82.6	7.37			27000.0	18.8	2.93
		31000.0	25.9	3.57			31000.0	-0.5	0.77
7.830	7.830	15000.0	21.3	1.88	7.83	7.83	15000.0	1.2	0.14
		19000.0	82.8	5.63			19000.0	13.8	1.46
		23000.0	151.8	8.96			23000.0	53.9	5.44
		27000.0	125.8	9.06			27000.0	40.5	5.29
		31000.0	50.6	5.81			31000.0	4.6	1.79
8.130	8.130	15000.0	34.1	2.70	8.13	8.13	15000.0	2.4	0.27
		19000.0	115.1	6.90			19000.0	25.2	2.45
		23000.0	198.6	9.93			23000.0	90.3	7.78
		27000.0	174.4	10.13			27000.0	77.2	8.23
		31000.0	86.8	7.99			31000.0	17.7	3.73

Table C.8: Results of Monte Carlo Simulations for N II atom at $\log(g)=4.5$, and $\xi_t=10.0 \text{ km s}^{-1}$: average equivalent widths, $\langle W_\lambda \rangle$, and the expected error, 2σ

λ (Å)	ϵ_N	T_{eff} (K)	$\langle W_\lambda \rangle$ (mÅ)	σ (mÅ)	λ (Å)	ϵ_N	T_{eff} (K)	$\langle W_\lambda \rangle$ (mÅ)	2σ (mÅ)
3995	6.830	15000.0	1.4	0.16	6482	6.83	15000.0	0.0	0.01
		19000.0	9.8	1.05			19000.0	0.6	0.08
		23000.0	26.2	2.77			23000.0	3.3	0.44
		27000.0	24.2	2.81			27000.0	3.4	0.58
		31000.0	7.9	1.13			31000.0	-0.1	0.16
7.230	7.230	15000.0	3.5	0.38	7.23	7.23	15000.0	0.1	0.02
		19000.0	21.3	2.02			19000.0	1.7	0.20
		23000.0	54.2	4.82			23000.0	9.2	1.10
		27000.0	53.3	5.28			27000.0	10.2	1.48
		31000.0	21.2	2.68			31000.0	1.6	0.49
7.530	7.530	15000.0	6.5	0.67	7.53	7.53	15000.0	0.3	0.03
		19000.0	35.4	3.01			19000.0	3.6	0.41
		23000.0	85.1	6.37			23000.0	18.9	2.08
		27000.0	87.9	7.27			27000.0	22.6	2.89
		31000.0	40.8	4.55			31000.0	5.6	1.12
7.830	7.830	15000.0	11.6	1.12	7.83	7.83	15000.0	0.6	0.07
		19000.0	55.2	4.15			19000.0	7.3	0.78
		23000.0	122.5	7.71			23000.0	35.6	3.54
		27000.0	130.8	8.80			27000.0	45.4	5.03
		31000.0	71.2	6.66			31000.0	14.8	2.36
8.130	8.130	15000.0	19.7	1.74	8.13	8.13	15000.0	1.2	0.14
		19000.0	81.0	5.41			19000.0	13.9	1.40
		23000.0	164.6	8.95			23000.0	61.2	5.38
		27000.0	178.2	9.87			27000.0	81.2	7.59
		31000.0	110.9	8.39			31000.0	33.4	4.40

Table C.9: Results of Monte Carlo Simulations for N II atom at $\log(g)=3.5$, and $\xi_t=0.0 \text{ km s}^{-1}$: Correlation Coefficients

λ (Å)	T_{eff} (K)	Perturbed Transition				Category	r
3995	19000	9	→	16	$(2p\ 3s\ ^1P^o \quad -2p\ 3p\ ^1D)$	rbb	0.984
		37	→	55	$(2p\ 4f\ ^1F \quad -2p\ 5d\ ^1D^o)$	cbb	-0.269
		28	→	35	$(2p\ 4p\ ^3P \quad -2p\ 4d\ ^3D^o)$	cbb	0.238
		9	→	16	$(2p\ 3s\ ^1P^o \quad -2p\ 3p\ ^1D)$	stk	0.236
		94	→	104	$(2s^2\ 2p\ ^2P^o\ \text{N III} \quad -2s^2\ 2p\ ^2P^o\ \text{N IV})$	cbb	0.224
	23000	9	→	16	$(2p\ 3s\ ^1P^o \quad -2p\ 3p\ ^1D)$	rbb	0.973
		37	→	55	$(2p\ 4f\ ^1F \quad -2p\ 5d\ ^1D^o)$	cbb	-0.264
		94	→	104	$(2s^2\ 2p\ ^2P^o\ \text{N III} \quad -2s^2\ 2p\ ^2P^o\ \text{N IV})$	cbb	0.236
		8	→	49	$(2p\ 3s\ ^3P^o \quad -2p\ 5p\ ^3D)$	cbb	-0.233
		28	→	35	$(2p\ 4p\ ^3P \quad -2p\ 4d\ ^3D^o)$	cbb	0.230
	27000	9	→	16	$(2p\ 3s\ ^1P^o \quad -2p\ 3p\ ^1D)$	rbb	0.965
		37	→	55	$(2p\ 4f\ ^1F \quad -2p\ 5d\ ^1D^o)$	cbb	-0.267
		94	→	104	$(2s^2\ 2p\ ^2P^o\ \text{N III} \quad -2s^2\ 2p\ ^2P^o\ \text{N IV})$	cbb	0.240
		8	→	49	$(2p\ 3s\ ^3P^o \quad -2p\ 5p\ ^3D)$	cbb	-0.230
		28	→	35	$(2p\ 4p\ ^3P \quad -2p\ 4d\ ^3D^o)$	cbb	0.226
	6482	9	→	11	$(2p\ 3s\ ^1P^o \quad -2p\ 3p\ ^1P)$	rbb	0.984
		14	→	73	$(2p\ 3p\ ^3S \quad -2p\ 6s\ ^3P^o)$	cbb	-0.247
		55	→	94	$(2p\ 5d\ ^1D^o \quad -2s^2\ 2p\ ^2P^o\ \text{N III})$	cbf	0.232
		56	→	94	$(2p\ 5d\ ^3D^o \quad -2s^2\ 2p\ ^2P^o\ \text{N III})$	cbf	-0.215
		47	→	77	$(2p\ 5s\ ^1P^o \quad -2p\ 6p\ ^1P)$	rbb	-0.214
		9	→	11	$(2p\ 3s\ ^1P^o \quad -2p\ 3p\ ^1P)$	rbb	0.942
		14	→	73	$(2p\ 3p\ ^3S \quad -2p\ 6s\ ^3P^o)$	cbb	-0.255
		55	→	94	$(2p\ 5d\ ^1D^o \quad -2s^2\ 2p\ ^2P^o\ \text{N III})$	cbf	0.229
		56	→	80	$(2p\ 5d\ ^3D^o \quad -2p\ 6p\ ^3P)$	stk	-0.225
		20	→	43	$(2p\ 3d\ ^3D^o \quad -2p\ 4f\ ^3D)$	rbb	-0.212
	27000	9	→	11	$(2p\ 3s\ ^1P^o \quad -2p\ 3p\ ^1P)$	rbb	0.887
		14	→	73	$(2p\ 3p\ ^3S \quad -2p\ 6s\ ^3P^o)$	cbb	-0.240
		11	→	19	$(2p\ 3p\ ^1P \quad -2p\ 3d\ ^1D^o)$	rbb	-0.235
		55	→	94	$(2p\ 5d\ ^1D^o \quad -2s^2\ 2p\ ^2P^o\ \text{N III})$	cbf	0.224
		56	→	80	$(2p\ 5d\ ^3D^o \quad -2p\ 6p\ ^3P)$	stk	-0.220

Table C.10: Results of Monte Carlo Simulations for N II atom at $\log(g)=4.0$, and $\xi_t=0.0 \text{ km s}^{-1}$: Correlation Coefficients

λ (Å)	T_{eff} (K)	Perturbed Transition				Category	r		
3995	19000	9	→	16	$(2p\ 3s\ ^1P^o)$	$-2p\ 3p\ ^1D)$	rbb	0.971	
		9	→	16	$(2p\ 3s\ ^1P^o)$	$-2p\ 3p\ ^1D)$	stk	0.310	
		37	→	55	$(2p\ 4f\ ^1F)$	$-2p\ 5d\ ^1D^o)$	cbb	-0.261	
		28	→	35	$(2p\ 4p\ ^3P)$	$-2p\ 4d\ ^3D^o)$	cbb	0.244	
		94	→	104	$(2s^2\ 2p\ ^2P^o\ \text{N III})$	$-2s^2\ 2p\ ^2P^o\ \text{N IV})$	cbb	0.212	
	23000	9	→	16	$(2p\ 3s\ ^1P^o)$	$-2p\ 3p\ ^1D)$	rbb	0.969	
		9	→	16	$(2p\ 3s\ ^1P^o)$	$-2p\ 3p\ ^1D)$	stk	0.288	
		37	→	55	$(2p\ 4f\ ^1F)$	$-2p\ 5d\ ^1D^o)$	cbb	-0.261	
		28	→	35	$(2p\ 4p\ ^3P)$	$-2p\ 4d\ ^3D^o)$	cbb	0.241	
		8	→	49	$(2p\ 3s\ ^3P^o)$	$-2p\ 5p\ ^3D)$	cbb	-0.222	
	27000	9	→	16	$(2p\ 3s\ ^1P^o)$	$-2p\ 3p\ ^1D)$	rbb	0.963	
		37	→	55	$(2p\ 4f\ ^1F)$	$-2p\ 5d\ ^1D^o)$	cbb	-0.262	
		8	→	49	$(2p\ 3s\ ^3P^o)$	$-2p\ 5p\ ^3D)$	cbb	-0.232	
		94	→	104	$(2s^2\ 2p\ ^2P^o\ \text{N III})$	$-2s^2\ 2p\ ^2P^o\ \text{N IV})$	cbb	0.231	
		28	→	35	$(2p\ 4p\ ^3P)$	$-2p\ 4d\ ^3D^o)$	cbb	0.227	
	6482	19000	9	→	11	$(2p\ 3s\ ^1P^o)$	$-2p\ 3p\ ^1P)$	rbb	0.987
			14	→	73	$(2p\ 3p\ ^3S)$	$-2p\ 6s\ ^3P^o)$	cbb	-0.246
			55	→	94	$(2p\ 5d\ ^1D^o)$	$-2s^2\ 2p\ ^2P^o\ \text{N III})$	cbf	0.227
			56	→	94	$(2p\ 5d\ ^3D^o)$	$-2s^2\ 2p\ ^2P^o\ \text{N III})$	cbf	-0.217
			47	→	77	$(2p\ 5s\ ^1P^o)$	$-2p\ 6p\ ^1P)$	rbb	-0.216
23000		9	→	11	$(2p\ 3s\ ^1P^o)$	$-2p\ 3p\ ^1P)$	rbb	0.968	
		14	→	73	$(2p\ 3p\ ^3S)$	$-2p\ 6s\ ^3P^o)$	cbb	-0.253	
		55	→	94	$(2p\ 5d\ ^1D^o)$	$-2s^2\ 2p\ ^2P^o\ \text{N III})$	cbf	0.230	
		56	→	80	$(2p\ 5d\ ^3D^o)$	$-2p\ 6p\ ^3P)$	stk	-0.212	
		20	→	43	$(2p\ 3d\ ^3D^o)$	$-2p\ 4f\ ^3D)$	rbb	-0.208	
27000		9	→	11	$(2p\ 3s\ ^1P^o)$	$-2p\ 3p\ ^1P)$	rbb	0.912	
		14	→	73	$(2p\ 3p\ ^3S)$	$-2p\ 6s\ ^3P^o)$	cbb	-0.252	
		55	→	94	$(2p\ 5d\ ^1D^o)$	$-2s^2\ 2p\ ^2P^o\ \text{N III})$	cbf	0.225	
		20	→	43	$(2p\ 3d\ ^3D^o)$	$-2p\ 4f\ ^3D)$	rbb	-0.217	
		56	→	80	$(2p\ 5d\ ^3D^o)$	$-2p\ 6p\ ^3P)$	stk	-0.217	

Table C.11: Results of Monte Carlo Simulations for N II atom at $\log(g)=4.5$, and $\xi_i a = 0.0$ km s^{-1} : Correlation Coefficients

λ (Å)	T_{eff} (K)			Perturbed Transition		Category	r
3995	19000	9	→	16	$(2p\ 3s\ ^1P^o - 2p\ 3p\ ^1D)$	rbb	0.954
		9	→	16	$(2p\ 3s\ ^1P^o - 2p\ 3p\ ^1D)$	stk	0.372
		37	→	55	$(2p\ 4f\ ^1F - 2p\ 5d\ ^1D^o)$	cbb	-0.252
		28	→	35	$(2p\ 4p\ ^3P - 2p\ 4d\ ^3D^o)$	cbb	0.248
		55	→	94	$(2p\ 5d\ ^1D^o - 2s^2\ 2p\ ^2P^o\ \text{N III})$	cbf	-0.208
	23000	9	→	16	$(2p\ 3s\ ^1P^o - 2p\ 3p\ ^1D)$	rbb	0.940
		9	→	16	$(2p\ 3s\ ^1P^o - 2p\ 3p\ ^1D)$	stk	0.408
		28	→	35	$(2p\ 4p\ ^3P - 2p\ 4d\ ^3D^o)$	cbb	0.250
		37	→	55	$(2p\ 4f\ ^1F - 2p\ 5d\ ^1D^o)$	cbb	-0.247
		8	→	49	$(2p\ 3s\ ^3P^o - 2p\ 5p\ ^3D)$	cbb	-0.209
	27000	9	→	16	$(2p\ 3s\ ^1P^o - 2p\ 3p\ ^1D)$	rbb	0.954
		9	→	16	$(2p\ 3s\ ^1P^o - 2p\ 3p\ ^1D)$	stk	0.300
		37	→	55	$(2p\ 4f\ ^1F - 2p\ 5d\ ^1D^o)$	cbb	-0.254
		28	→	35	$(2p\ 4p\ ^3P - 2p\ 4d\ ^3D^o)$	cbb	0.240
		8	→	49	$(2p\ 3s\ ^3P^o - 2p\ 5p\ ^3D)$	cbb	-0.225
	6482	9	→	11	$(2p\ 3s\ ^1P^o - 2p\ 3p\ ^1P)$	rbb	0.990
		14	→	73	$(2p\ 3p\ ^3S - 2p\ 6s\ ^3P^o)$	cbb	-0.244
		55	→	94	$(2p\ 5d\ ^1D^o - 2s^2\ 2p\ ^2P^o\ \text{N III})$	cbf	0.224
		56	→	94	$(2p\ 5d\ ^3D^o - 2s^2\ 2p\ ^2P^o\ \text{N III})$	cbf	-0.218
		47	→	77	$(2p\ 5s\ ^1P^o - 2p\ 6p\ ^1P)$	rbb	-0.216
		9	→	11	$(2p\ 3s\ ^1P^o - 2p\ 3p\ ^1P)$	rbb	0.977
		14	→	73	$(2p\ 3p\ ^3S - 2p\ 6s\ ^3P^o)$	cbb	-0.250
		55	→	94	$(2p\ 5d\ ^1D^o - 2s^2\ 2p\ ^2P^o\ \text{N III})$	cbf	0.223
		9	→	11	$(2p\ 3s\ ^1P^o - 2p\ 3p\ ^1P)$	stk	0.219
		56	→	94	$(2p\ 5d\ ^3D^o - 2s^2\ 2p\ ^2P^o\ \text{N III})$	cbf	-0.209
		9	→	11	$(2p\ 3s\ ^1P^o - 2p\ 3p\ ^1P)$	rbb	0.940
		14	→	73	$(2p\ 3p\ ^3S - 2p\ 6s\ ^3P^o)$	cbb	-0.257
		55	→	94	$(2p\ 5d\ ^1D^o - 2s^2\ 2p\ ^2P^o\ \text{N III})$	cbf	0.226
		20	→	43	$(2p\ 3d\ ^3D^o - 2p\ 4f\ ^3D)$	rbb	-0.216
		56	→	80	$(2p\ 5d\ ^3D^o - 2p\ 6p\ ^3P)$	stk	-0.207

Table C.12: Results of Monte Carlo Simulations for N II at $\log g=3.5$, and $\xi_t=5.0 \text{ km s}^{-1}$: Correlation Coefficients

λ (Å)	T_{eff} (K)	Perturbed Transition				Type	r
3995	19000	9	→	16	$(2p\ 3s\ ^1P^o \rightarrow 2p\ 3p\ ^1D)$	rbb	0.992
		37	→	55	$(2p\ 4f\ ^1F \rightarrow 2p\ 5d\ ^1D^o)$	cbb	-0.274
		28	→	35	$(2p\ 4p\ ^3P \rightarrow 2p\ 4d\ ^3D^o)$	cbb	0.231
		94	→	104	$(2s^2\ 2p\ ^2P^o\ \text{N III} \rightarrow 2s^2\ 2p\ ^2P^o\ \text{N IV})$	cbb	0.228
		32	→	89	$(2p\ 4p\ ^1S \rightarrow 2p\ 6d\ ^1P^o)$	rbb	0.221
	23000	9	→	16	$(2p\ 3s\ ^1P^o \rightarrow 2p\ 3p\ ^1D)$	rbb	0.976
		37	→	55	$(2p\ 4f\ ^1F \rightarrow 2p\ 5d\ ^1D^o)$	cbb	-0.268
		94	→	104	$(2s^2\ 2p\ ^2P^o\ \text{N III} \rightarrow 2s^2\ 3d\ ^2D\ \text{N IV})$	cbb	0.239
		8	→	49	$(2p\ 3s\ ^3P^o \rightarrow 2p\ 5p\ ^3D)$	cbb	-0.231
		28	→	35	$(2p\ 4p\ ^3P \rightarrow 2p\ 4d\ ^3D^o)$	cbb	0.227
	27000	9	→	16	$(2p\ 3s\ ^1P^o \rightarrow 2p\ 3p\ ^1D)$	rbb	0.968
		37	→	55	$(2p\ 4f\ ^1F \rightarrow 2p\ 5d\ ^1D^o)$	cbb	-0.267
		94	→	104	$(2s^2\ 2p\ ^2P^o\ \text{N III} \rightarrow 2s^2\ 3d\ ^2D\ \text{N IV})$	cbb	0.241
		8	→	49	$(2p\ 3s\ ^3P^o \rightarrow 2p\ 5p\ ^3D)$	cbb	-0.230
		28	→	35	$(2p\ 4p\ ^3P \rightarrow 2p\ 4d\ ^3D^o)$	cbb	0.228
	6482	9	→	11	$(2p\ 3s\ ^1P^o \rightarrow 2p\ 3p\ ^1P)$	rbb	0.984
		14	→	73	$(2p\ 3p\ ^3S \rightarrow 2p\ 6s\ ^3P^o)$	cbb	-0.246
		55	→	94	$(2p\ 5d\ ^1D^o \rightarrow 2s^2\ 2p\ ^2P^o\ \text{N III})$	cbf	0.232
		56	→	94	$(2p\ 5d\ ^3D^o \rightarrow 2s^2\ 2p\ ^2P^o\ \text{N III})$	cbf	-0.216
		47	→	77	$(2p\ 5s\ ^1P^o \rightarrow 2p\ 6p\ ^1P)$	rbb	-0.216
		9	→	11	$(2p\ 3s\ ^1P^o \rightarrow 2p\ 3p\ ^1P)$	rbb	0.941
		14	→	73	$(2p\ 3p\ ^3S \rightarrow 2p\ 6s\ ^3P^o)$	cbb	-0.253
		55	→	94	$(2p\ 5d\ ^1D^o \rightarrow 2s^2\ 2p\ ^2P^o\ \text{N III})$	cbf	0.229
		56	→	80	$(2p\ 5d\ ^3D^o \rightarrow 2p\ 6p\ ^3P)$	stk	-0.223
		5	→	45	$(2p^3\ ^3D^o \rightarrow -p2(3s\ ^3P))$	cbb	-0.213
		9	→	11	$(2p\ 3s\ ^1P^o \rightarrow 2p\ 3p\ ^1P)$	rbb	0.886
		11	→	19	$(2p\ 3p\ ^1P \rightarrow 2p\ 3d\ ^1D^o)$	rbb	-0.249
		14	→	73	$(2p\ 3p\ ^3S \rightarrow 2p\ 6s\ ^3P^o)$	cbb	-0.242
		55	→	94	$(2p\ 5d\ ^1D^o \rightarrow 2s^2\ 2p\ ^2P^o\ \text{N III})$	cbf	0.224
		3	→	9	$(2p^2\ ^1S \rightarrow 2p\ 3s\ ^1P^o)$	rbb	-0.223

Table C.13: Results of Monte Carlo Simulations for N II at $\log g=4.5$, and $\xi_t=5.0 \text{ km s}^{-1}$: Correlation Coefficients (r)

λ (Å)	T_{eff} (K)	Perturbed Transition				Type	r		
3995	19000	9	→	16	$(2p\ 3s\ ^1P^o$	$-2p\ 3p\ ^1D)$	rbb	0.981	
		9	→	16	$(2p\ 3s\ ^1P^o$	$-2p\ 3p\ ^1D)$	stk	0.267	
		37	→	55	$(2p\ 4f\ ^1F$	$-2p\ 5d\ ^1D^o)$	cbb	-0.266	
		28	→	35	$(2p\ 4p\ ^3P$	$-2p\ 4d\ ^3D^o)$	cbb	0.233	
		94	→	104	$(2s^2\ 2p\ ^2P^o\ \text{N III}$	$-2s^2\ 3d\ ^2D\ \text{N IV})$	cbb	0.215	
	23000	9	→	16	$(2p\ 3s\ ^1P^o$	$-2p\ 3p\ ^1D)$	rbb	0.974	
		9	→	16	$(2p\ 3s\ ^1P^o$	$-2p\ 3p\ ^1D)$	stk	0.292	
		37	→	55	$(2p\ 4f\ ^1F$	$-2p\ 5d\ ^1D^o)$	cbb	-0.263	
		28	→	35	$(2p\ 4p\ ^3P$	$-2p\ 4d\ ^3D^o)$	cbb	0.241	
		8	→	49	$(2p\ 3s\ ^3P^o$	$-2p\ 5p\ ^3D)$	cbb	-0.216	
	27000	9	→	16	$(2p\ 3s\ ^1P^o$	$-2p\ 3p\ ^1D)$	rbb	0.970	
		37	→	55	$(2p\ 4f\ ^1F$	$-2p\ 5d\ ^1D^o)$	cbb	-0.263	
		28	→	35	$(2p\ 4p\ ^3P$	$-2p\ 4d\ ^3D^o)$	cbb	0.233	
		8	→	49	$(2p\ 3s\ ^3P^o$	$-2p\ 5p\ ^3D)$	cbb	-0.228	
		94	→	104	$((2s^2\ 2p\ ^2P^o\ \text{N III}$	$-2s^2\ 3d\ ^2D\ \text{N IV})$	cbb	0.224	
	6482	19000	9	→	11	$(2p\ 3s\ ^1P^o$	$-2p\ 3p\ ^1P)$	rbb	0.992
			14	→	73	$(2p\ 3p\ ^3S$	$-2p\ 6s\ ^3P^o)$	cbb	-0.242
			55	→	94	$(2p\ 5d\ ^1D^o$	$-2s^2\ 2p\ ^2P^o\ \text{N III})$	cbf	0.225
			47	→	77	$(2p\ 5s\ ^1P^o$	$-2p\ 6p\ ^1P)$	rbb	-0.219
			56	→	94	$(2p\ 5d\ ^3D^o$	$-2s^2\ 2p\ ^2P^o\ \text{N III})$	cbf	-0.218
23000		9	→	11	$(2p\ 3s\ ^1P^o$	$-2p\ 3p\ ^1P)$	rbb	0.981	
		14	→	73	$(2p\ 3p\ ^3S$	$-2p\ 6s\ ^3P^o)$	cbb	-0.248	
		55	→	94	$(2p\ 5d\ ^1D^o$	$-2s^2\ 2p\ ^2P^o\ \text{N III})$	cbf	0.226	
		47	→	77	$(2p\ 5s\ ^1P^o$	$-2p\ 6p\ ^1P)$	rbb	-0.214	
		56	→	94	$(2p\ 5d\ ^3D^o$	$-2s^2\ 2p\ ^2P^o\ \text{N III})$	cbf	-0.212	
27000		9	→	11	$(2p\ 3s\ ^1P^o$	$-2p\ 3p\ ^1P)$	rbb	0.940	
		14	→	73	$(2p\ 3p\ ^3S$	$-2p\ 6s\ ^3P^o)$	cbb	-0.256	
		55	→	94	$(2p\ 5d\ ^1D^o$	$-2s^2\ 2p\ ^2P^o\ \text{N III})$	cbf	0.227	
		20	→	43	$(2p\ 3d\ ^3D^o$	$-2p\ 4f\ ^3D)$	rbb	-0.213	
		38	→	94	$(2p\ 4f\ ^3F$	$-2s^2\ 2p\ ^2P^o\ \text{N III})$	rbf	-0.209	

Table C.14: Results of Monte Carlo Simulations for N II atom at $\log(g)=3.5$, and $\xi_t=10.0$ km s^{-1} : Correlation Coefficients

λ (Å)	T_{eff} (K)	Perturbed Transition				Category	r		
3995	19000	9	→	16	$(2p\ 3s\ ^1P^o)$	$-2p\ 3p\ ^1D)$	rbb	0.996	
		37	→	55	$(2p\ 4f\ ^1F)$	$-2p\ 5d\ ^1D^o)$	cbb	-0.278	
		94	→	104	$(2s^2\ 2p\ ^2P^o\ \text{N III})$	$-2s^2\ 2p\ ^2P^o\ \text{N IV})$	cbb	0.230	
		28	→	35	$(2p\ 4p\ ^3P)$	$-2p\ 4d\ ^3D^o)$	cbb	0.226	
		32	→	89	$(2p\ 4p\ ^1S)$	$-2p\ 6d\ ^1P^o)$	rbb	0.224	
	23000	9	→	16	$(2p\ 3s\ ^1P^o)$	$-2p\ 3p\ ^1D)$	rbb	0.978	
		37	→	55	$(2p\ 4f\ ^1F)$	$-2p\ 5d\ ^1D^o)$	cbb	-0.270	
		94	→	104	$(2s^2\ 2p\ ^2P^o\ \text{N III})$	$-2s^2\ 2p\ ^2P^o\ \text{N IV})$	cbb	0.240	
		8	→	49	$(2p\ 3s\ ^3P^o)$	$-2p\ 5p\ ^3D)$	cbb	-0.229	
		28	→	35	$(2p\ 4p\ ^3P)$	$-2p\ 4d\ ^3D^o)$	cbb	0.224	
	27000	9	→	16	$(2p\ 3s\ ^1P^o)$	$-2p\ 3p\ ^1D)$	rbb	0.973	
		37	→	55	$(2p\ 4f\ ^1F)$	$-2p\ 5d\ ^1D^o)$	cbb	-0.268	
		94	→	104	$(2s^2\ 2p\ ^2P^o\ \text{N III})$	$-2s^2\ 2p\ ^2P^o\ \text{N IV})$	cbb	0.241	
		8	→	49	$(2p\ 3s\ ^3P^o)$	$-2p\ 5p\ ^3D)$	cbb	-0.230	
		28	→	35	$(2p\ 4p\ ^3P)$	$-2p\ 4d\ ^3D^o)$	cbb	0.230	
	6482	19000	9	→	11	$(2p\ 3s\ ^1P^o)$	$-2p\ 3p\ ^1P)$	rbb	0.984
			14	→	73	$(2p\ 3p\ ^3S)$	$-2p\ 6s\ ^3P^o)$	cbb	-0.245
			55	→	94	$(2p\ 5d\ ^1D^o)$	$-2s^2\ 2p\ ^2P^o\ \text{N III})$	cbf	0.230
			47	→	77	$(2p\ 5s\ ^1P^o)$	$-2p\ 6p\ ^1P)$	rbb	-0.218
			56	→	94	$(2p\ 5d\ ^3D^o)$	$-2s^2\ 2p\ ^2P^o\ \text{N III})$	cbf	-0.217
23000		9	→	11	$(2p\ 3s\ ^1P^o)$	$-2p\ 3p\ ^1P)$	rbb	0.940	
		14	→	73	$(2p\ 3p\ ^3S)$	$-2p\ 6s\ ^3P^o)$	cbb	-0.253	
		55	→	94	$(2p\ 5d\ ^1D^o)$	$-2s^2\ 2p\ ^2P^o\ \text{N III})$	cbf	0.228	
		56	→	80	$(2p\ 5d\ ^3D^o)$	$-2p\ 6p\ ^3P)$	stk	-0.219	
		5	→	45	$(2p^3\ ^3D^o)$	$-p2(3s\ ^3P)$	cbb	-0.215	
27000		9	→	11	$(2p\ 3s\ ^1P^o)$	$-2p\ 3p\ ^1P)$	rbb	0.884	
		11	→	19	$(2p\ 3p\ ^1P)$	$-2p\ 3d\ ^1D^o)$	rbb	-0.272	
		14	→	73	$(2p\ 3p\ ^3S)$	$-2p\ 6s\ ^3P^o)$	cbb	-0.246	
		55	→	94	$(2p\ 5d\ ^1D^o)$	$-2s^2\ 2p\ ^2P^o\ \text{N III})$	cbf	0.223	
		3	→	9	$(2p^2\ ^1S)$	$-2p\ 3s\ ^1P^o)$	rbb	-0.223	

Table C.15: Results of Monte Carlo Simulations for N II atom at $\log(g)=4.0$, and $\xi_i=10.0$ km s⁻¹: Correlation Coefficients

λ (Å)	T _{eff} (K)	Perturbed Transition				Category	r		
3995	19000	9	→	16	(2p 3s ¹ P ^o	-2p 3p ¹ D)	rbb	0.996	
		37	→	55	(2p 4f ¹ F	-2p 5d ¹ D ^o)	cbb	-0.276	
		28	→	35	(2p 4p ³ P	-2p 4d ³ D ^o)	cbb	0.228	
		94	→	104	(2s ² 2p ² P ^o N III	-2s ² 2p ² P ^o N IV)	cbb	0.226	
		32	→	89	(2p 4p ¹ S	-2p 6d ¹ P ^o)	rbb	0.224	
	23000	9	→	16	(2p 3s ¹ P ^o	-2p 3p ¹ D)	rbb	0.990	
		37	→	55	(2p 4f ¹ F	-2p 5d ¹ D ^o)	cbb	-0.276	
		94	→	104	(2s ² 2p ² P ^o N III	-2s ² 2p ² P ^o N IV)	cbb	0.232	
		28	→	35	(2p 4p ³ P	-2p 4d ³ D ^o)	cbb	0.227	
		8	→	49	(2p 3s ³ P ^o	-2p 5p ³ D)	cbb	-0.223	
	27000	9	→	16	(2p 3s ¹ P ^o	-2p 3p ¹ D)	rbb	0.971	
		37	→	55	(2p 4f ¹ F	-2p 5d ¹ D ^o)	cbb	-0.267	
		94	→	104	(2s ² 2p ² P ^o N III	-2s ² 2p ² P ^o N IV)	cbb	0.235	
		8	→	49	(2p 3s ³ P ^o	-2p 5p ³ D)	cbb	-0.230	
		28	→	35	(2p 4p ³ P	-2p 4d ³ D ^o)	cbb	0.224	
	6482	19000	9	→	11	(2p 3s ¹ P ^o	-2p 3p ¹ P)	rbb	0.988
			14	→	73	(2p 3p ³ S	-2p 6s ³ P ^o)	cbb	-0.243
			55	→	94	(2p 5d ¹ D ^o	-2s ² 2p ² P ^o N III)	cbf	0.227
			47	→	77	(2p 5s ¹ P ^o	-2p 6p ¹ P)	rbb	-0.222
			48	→	94	(2p 5p ¹ P	-2s ² 2p ² P ^o N III)	cbf	0.219
23000		9	→	11	(2p 3s ¹ P ^o	-2p 3p ¹ P)	rbb	0.968	
		14	→	73	(2p 3p ³ S	-2p 6s ³ P ^o)	cbb	-0.250	
		55	→	94	(2p 5d ¹ D ^o	-2s ² 2p ² P ^o N III)	cbf	0.230	
		47	→	77	(2p 5s ¹ P ^o	-2p 6p ¹ P)	rbb	-0.213	
		56	→	94	(2p 5d ³ D ^o	-2s ² 2p ² P ^o N III)	cbf	-0.207	
27000	9	→	11	(2p 3s ¹ P ^o	-2p 3p ¹ P)	rbb	0.908		
	14	→	73	(2p 3p ³ S	-2p 6s ³ P ^o)	cbb	-0.254		
	11	→	19	(2p 3p ¹ P	-2p 3d ¹ D ^o)	rbb	-0.225		
	55	→	94	(2p 5d ¹ D ^o	-2s ² 2p ² P ^o N III)	cbf	0.223		
	20	→	43	(2p 3d ³ D ^o	-2p 4f ³ D)	rbb	-0.216		

Table C.16: Results of Monte Carlo Simulations for N II atom at $\log(g)=4.5$, and $\xi_i=10.0$ km s^{-1} : Correlation Coefficients

λ (Å)	T_{eff} (K)			Perturbed Transition		Category	r
3995	19000	9	→	16	$(2p\ 3s\ ^1P^o - 2p\ 3p\ ^1D)$	rbb	0.995
		37	→	55	$(2p\ 4f\ ^1F - 2p\ 5d\ ^1D^o)$	cbb	-0.274
		28	→	35	$(2p\ 4p\ ^3P - 2p\ 4d\ ^3D^o)$	cbb	0.230
		32	→	89	$(2p\ 4p\ ^1S - 2p\ 6d\ ^1P^o)$	rbb	0.223
		94	→	104	$(2s^2\ 2p\ ^2P^o\ \text{N III} - 2s^2\ 2p\ ^2P^o\ \text{N IV})$	cbb	0.223
	23000	9	→	16	$(2p\ 3s\ ^1P^o - 2p\ 3p\ ^1D)$	rbb	0.991
		37	→	55	$(2p\ 4f\ ^1F - 2p\ 5d\ ^1D^o)$	cbb	-0.274
		28	→	35	$(2p\ 4p\ ^3P - 2p\ 4d\ ^3D^o)$	cbb	0.231
		94	→	104	$(2s^2\ 2p\ ^2P^o\ \text{N III} - 2s^2\ 2p\ ^2P^o\ \text{N IV})$	cbb	0.225
		8	→	49	$(2p\ 3s\ ^3P^o - 2p\ 5p\ ^3D)$	cbb	-0.219
	27000	9	→	16	$(2p\ 3s\ ^1P^o - 2p\ 3p\ ^1D)$	rbb	0.978
		37	→	55	$(2p\ 4f\ ^1F - 2p\ 5d\ ^1D^o)$	cbb	-0.269
		8	→	49	$(2p\ 3s\ ^3P^o - 2p\ 5p\ ^3D)$	cbb	-0.228
		94	→	104	$(2s^2\ 2p\ ^2P^o\ \text{N III} - 2s^2\ 2p\ ^2P^o\ \text{N IV})$	cbb	0.228
		28	→	35	$(2p\ 4p\ ^3P - 2p\ 4d\ ^3D^o)$	cbb	0.227
	6482	9	→	11	$(2p\ 3s\ ^1P^o - 2p\ 3p\ ^1P)$	rbb	0.993
		14	→	73	$(2p\ 3p\ ^3S - 2p\ 6s\ ^3P^o)$	cbb	-0.242
		55	→	94	$(2p\ 5d\ ^1D^o - 2s^2\ 2p\ ^2P^o\ \text{N III})$	cbf	0.225
		47	→	77	$(2p\ 5s\ ^1P^o - 2p\ 6p\ ^1P)$	rbb	-0.222
		48	→	94	$(2p\ 5p\ ^1P - 2s^2\ 2p\ ^2P^o\ \text{N III})$	cbf	0.221
		9	→	11	$(2p\ 3s\ ^1P^o - 2p\ 3p\ ^1P)$	rbb	0.982
		14	→	73	$(2p\ 3p\ ^3S - 2p\ 6s\ ^3P^o)$	cbb	-0.246
		55	→	94	$(2p\ 5d\ ^1D^o - 2s^2\ 2p\ ^2P^o\ \text{N III})$	cbf	0.227
		47	→	77	$(2p\ 5s\ ^1P^o - 2p\ 6p\ ^1P)$	rbb	-0.219
		56	→	94	$(2p\ 5d\ ^3D^o - 2s^2\ 2p\ ^2P^o\ \text{N III N III})$	cbf	-0.213
		9	→	11	$(2p\ 3s\ ^1P^o - 2p\ 3p\ ^1P)$	rbb	0.938
		14	→	73	$(2p\ 3p\ ^3S - 2p\ 6s\ ^3P^o)$	cbb	-0.256
		55	→	94	$(2p\ 5d\ ^1D^o - 2s^2\ 2p\ ^2P^o\ \text{N III})$	cbf	0.227
		38	→	94	$(2p\ 4f\ ^3F - 2s^2\ 2p\ ^2P^o\ \text{N III})$	rbf	-0.215
		20	→	87	$(2p\ 3d\ ^3D^o - \text{high l, n = 6})$	cbb	-0.213

Appendix D

H α Fitting Figures

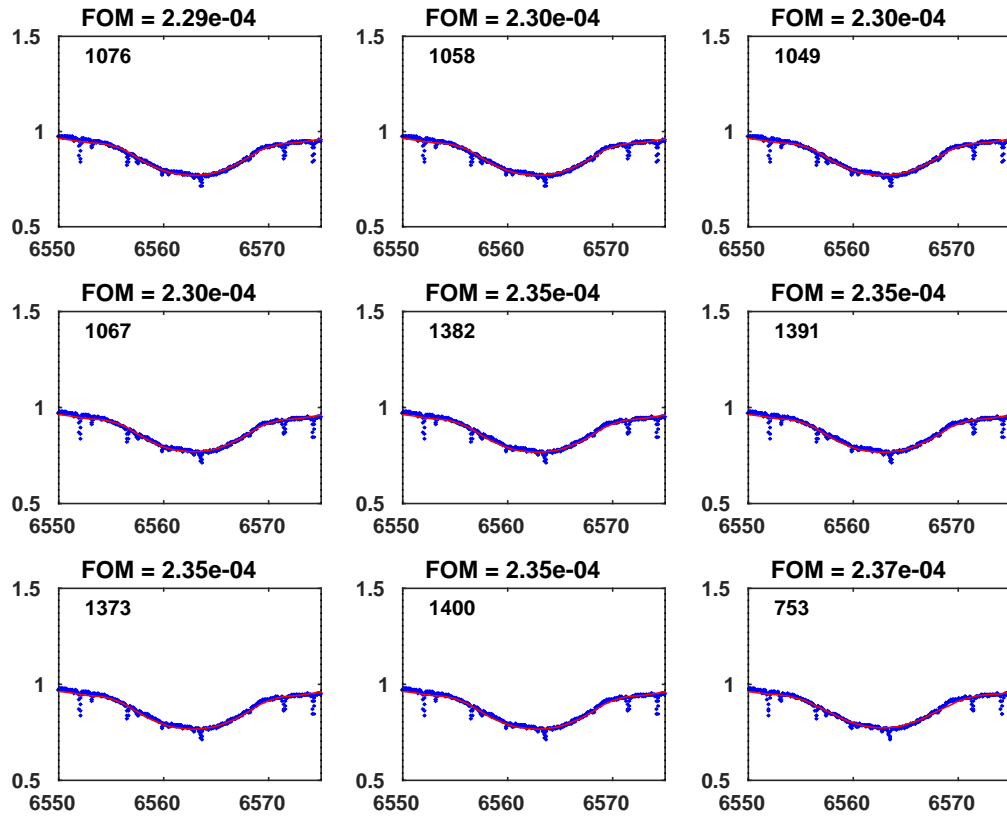


Figure D.1: The same as Figure (8.22) but for the Be star HD 33328.

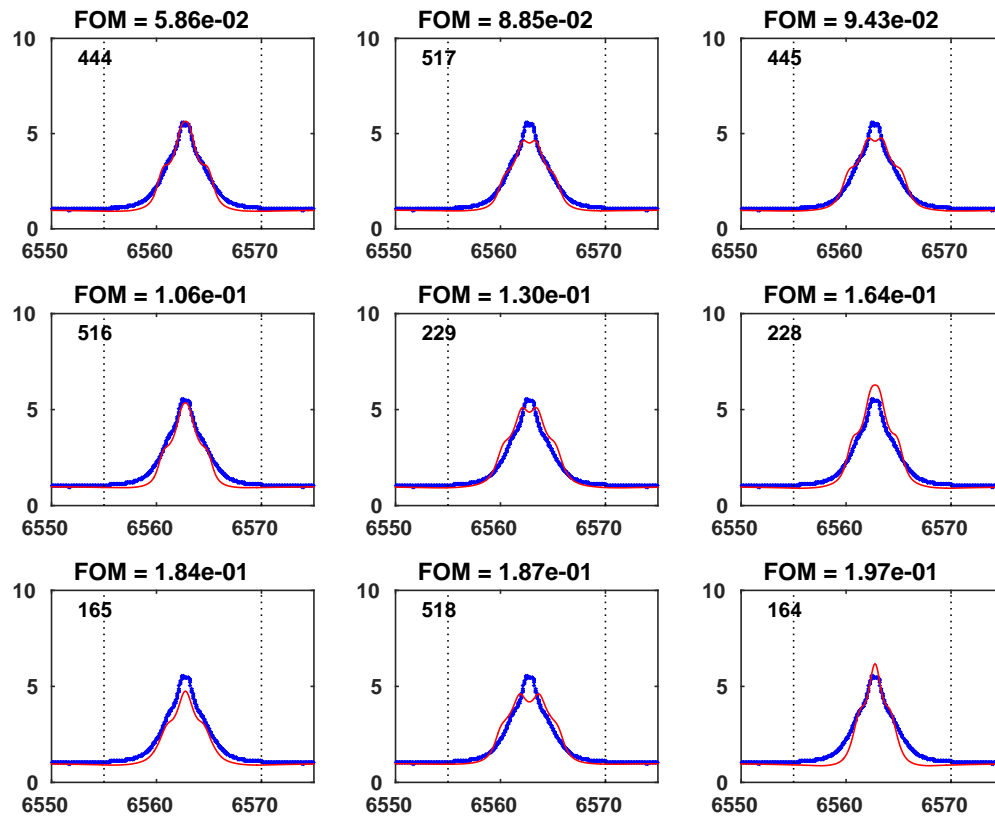


Figure D.2: The same as Figure (8.22) but for the Be star HD 56139.

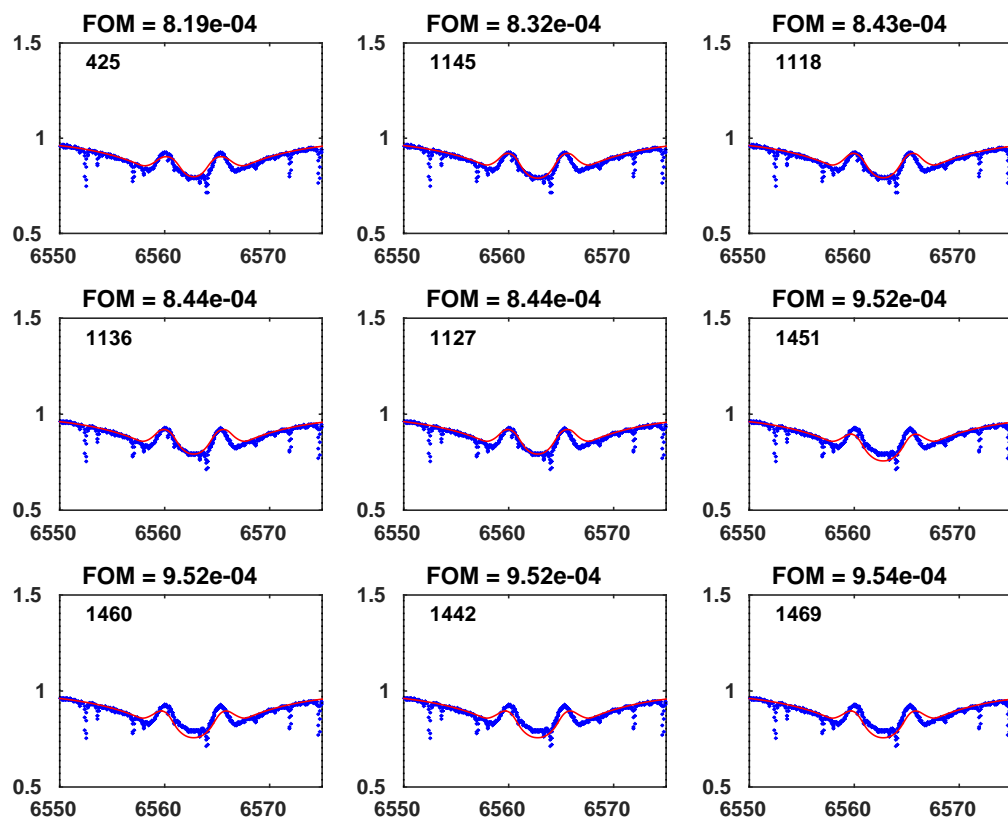


Figure D.3: The same as Figure (8.22) but for the Be star HD 58050.

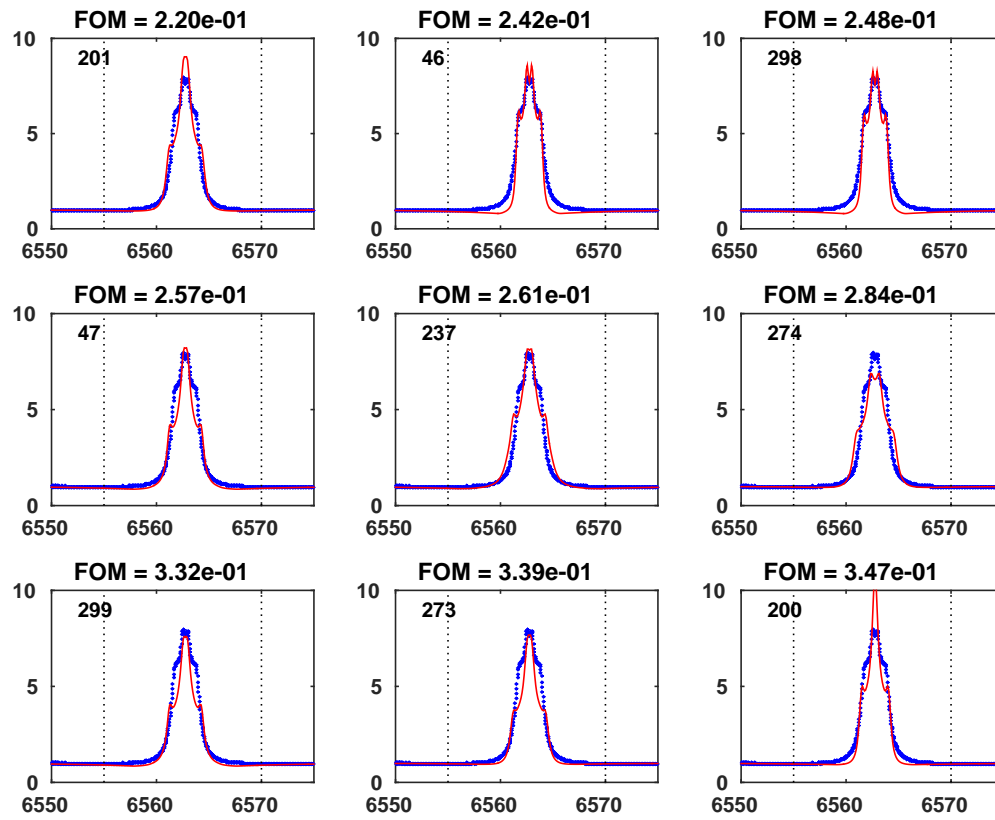


Figure D.4: The same as Figure (8.22) but for the Be star HD 58343.

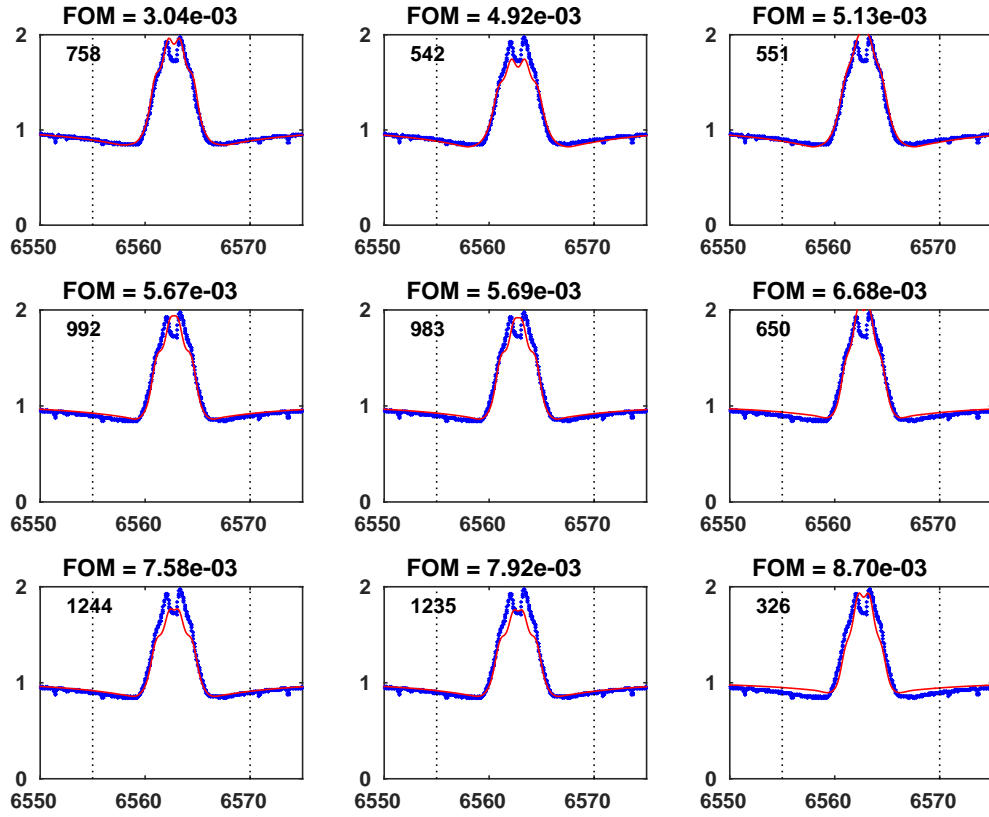


Figure D.5: The same as Figure (8.22) but for the Be star HD 67698.

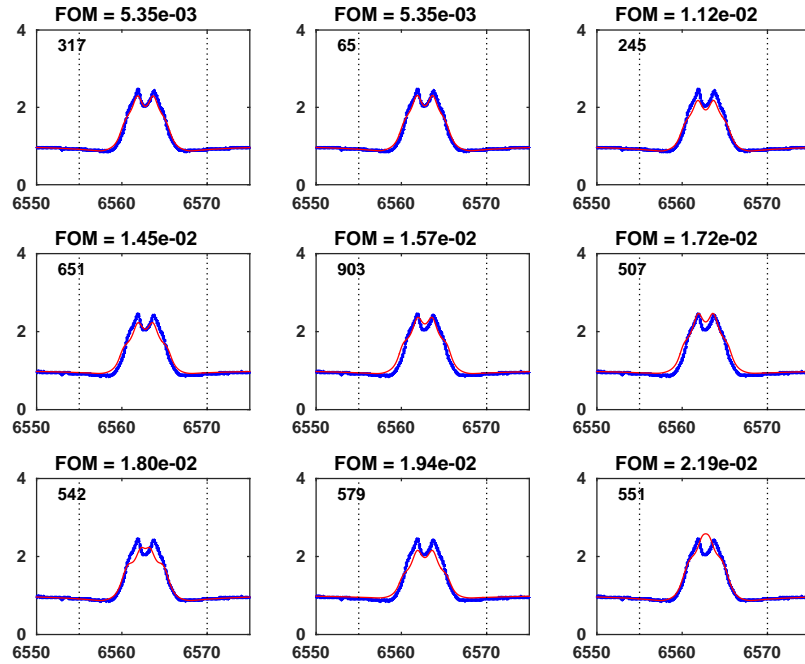


Figure D.6: The same as Figure (8.22) but for the Be star HD 120324.

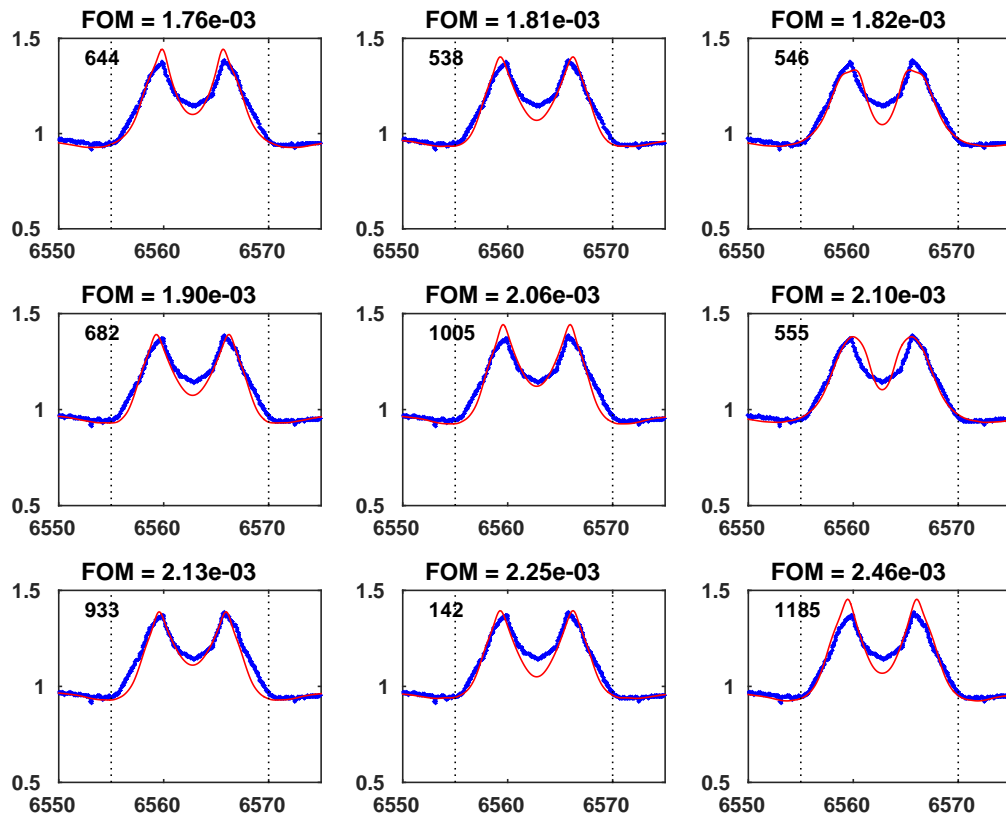


Figure D.7: The same as Figure (8.22) but for the Be star HD 187811.

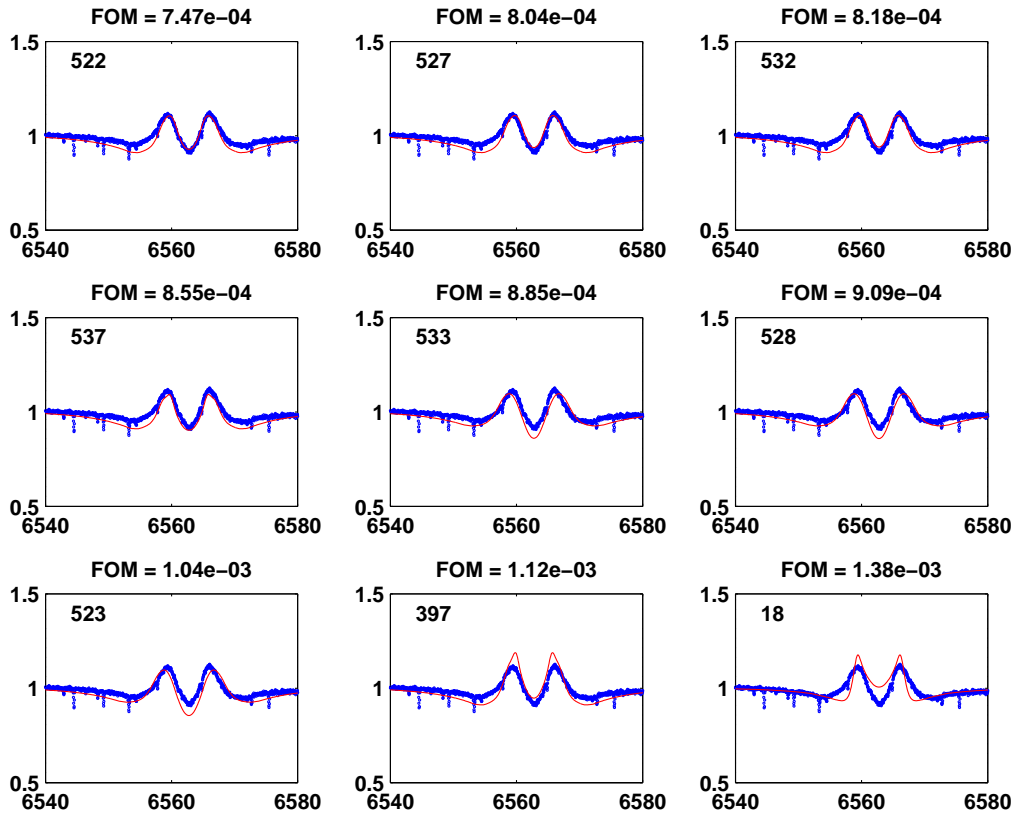


Figure D.8: The same as Figure (8.22) but for the Be star HD 191610.

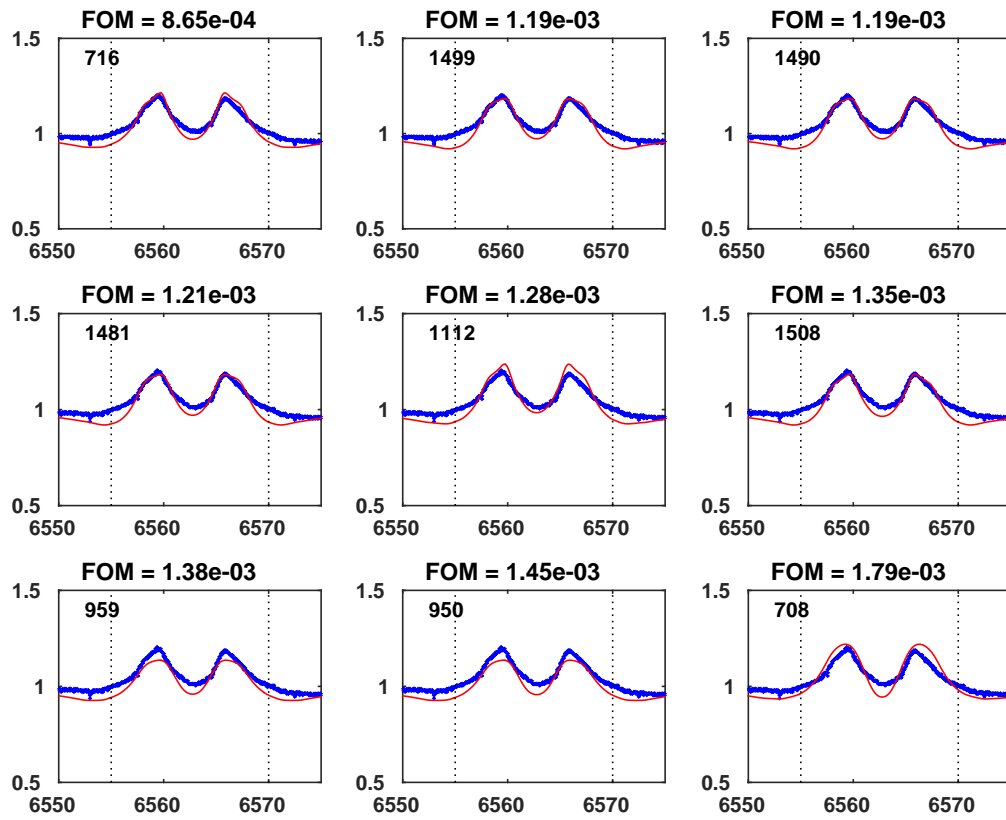


Figure D.9: The same as Figure (8.22) but for the Be star HD 192685.

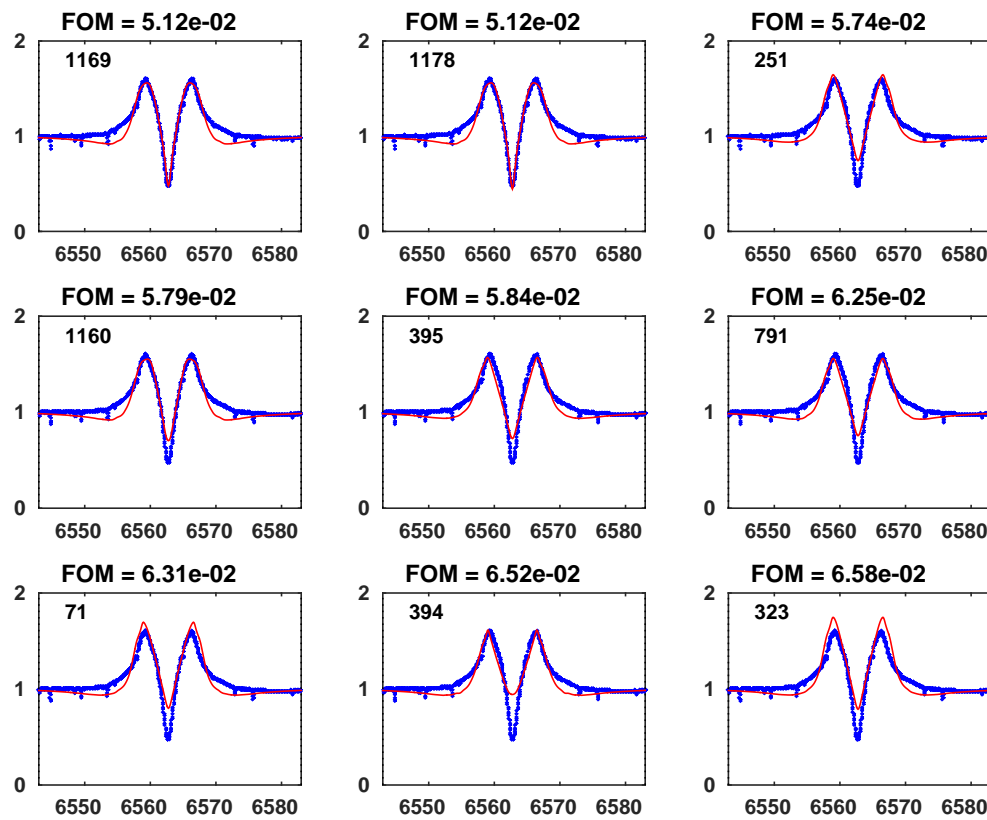


Figure D.10: The same as Figure (8.22) but for the Be star HD 205637.

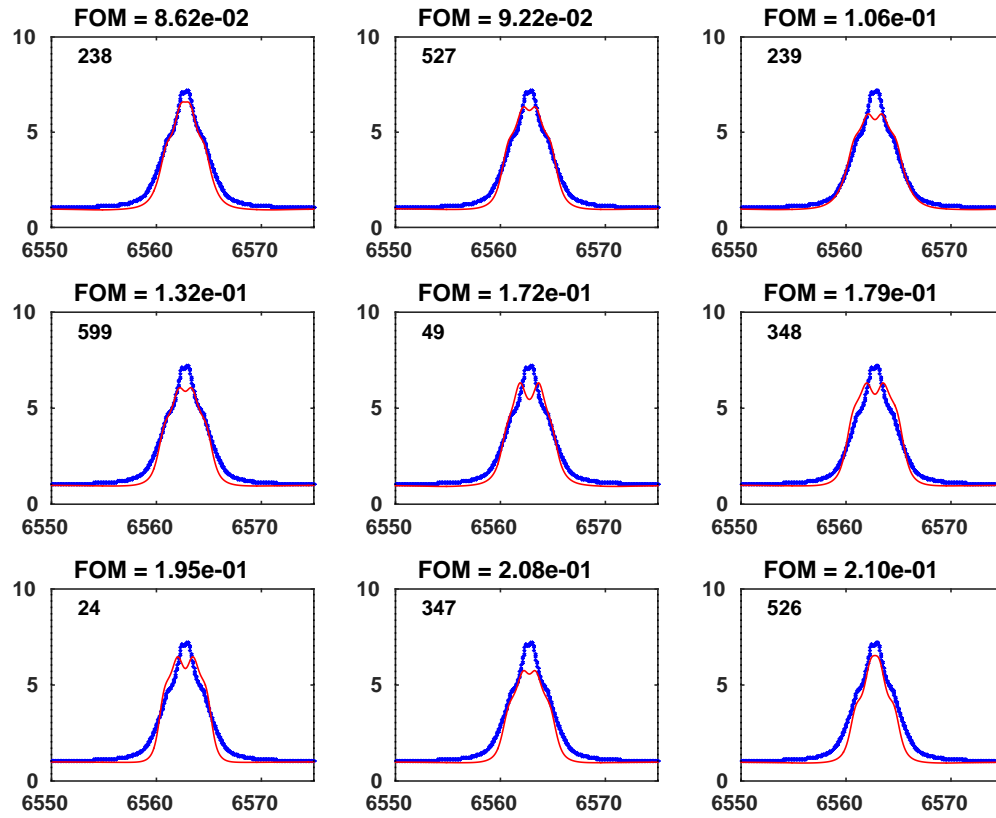


Figure D.11: The same as Figure (8.22) but for the Be star HD 212076.

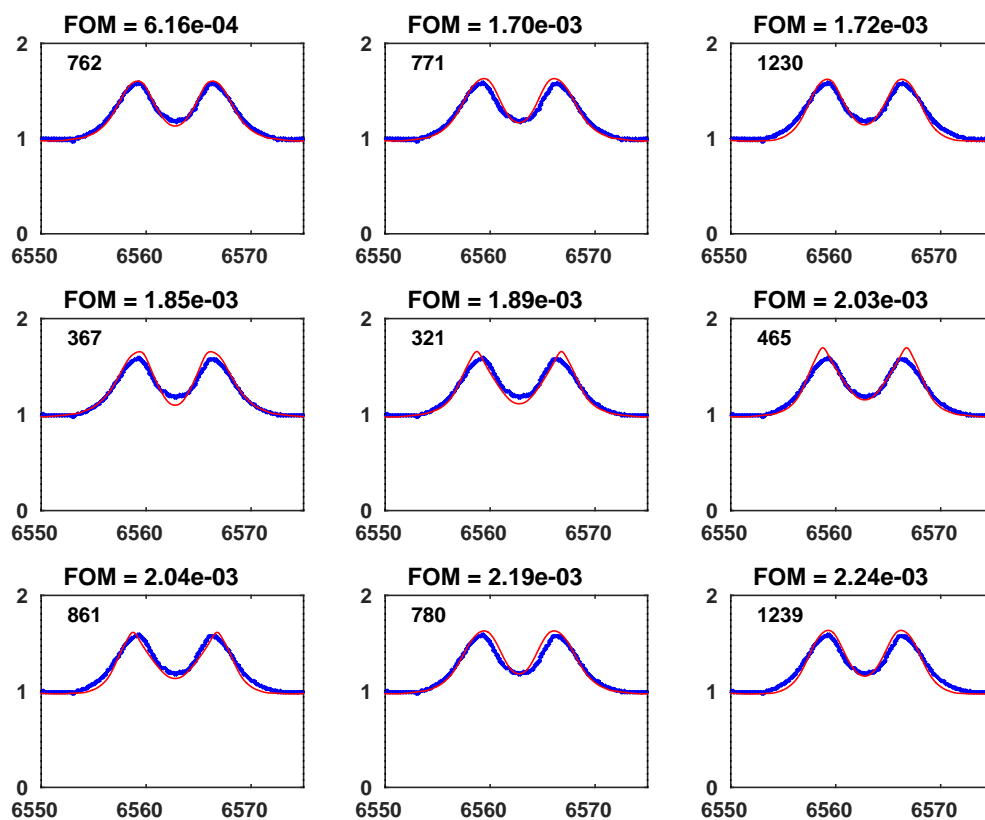


Figure D.12: The same as Figure (8.22) but for the Be star HD 212571.

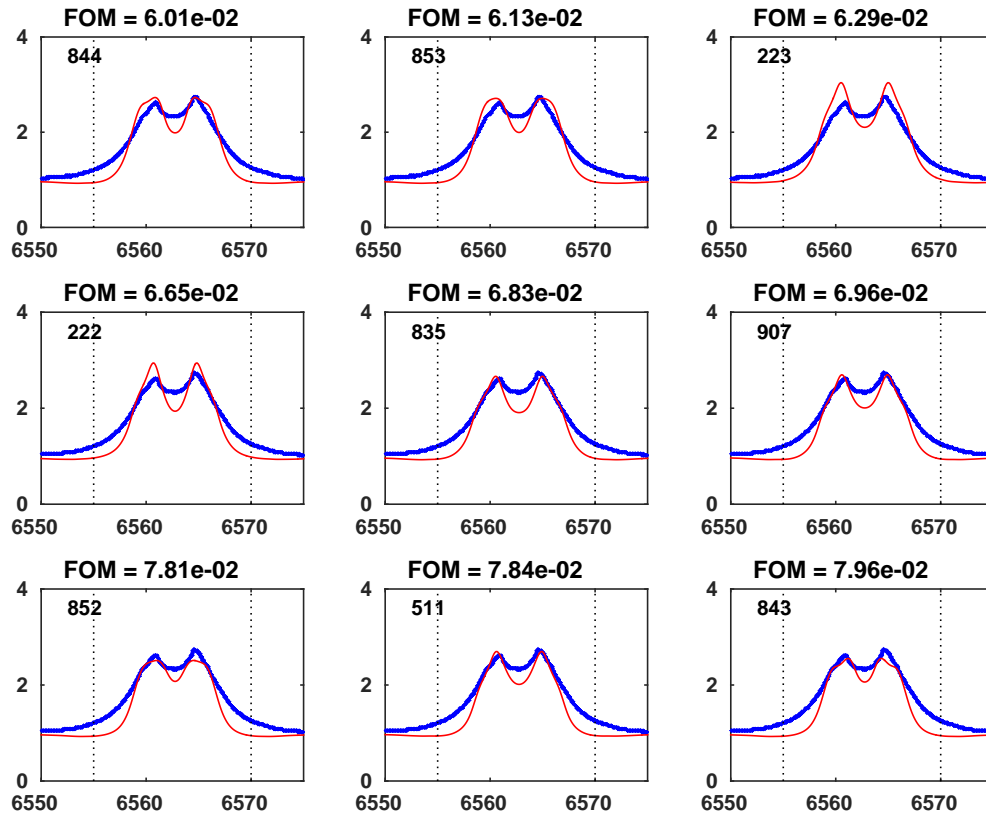


Figure D.13: The same as Figure (8.22) but for the Be star HD 20336.

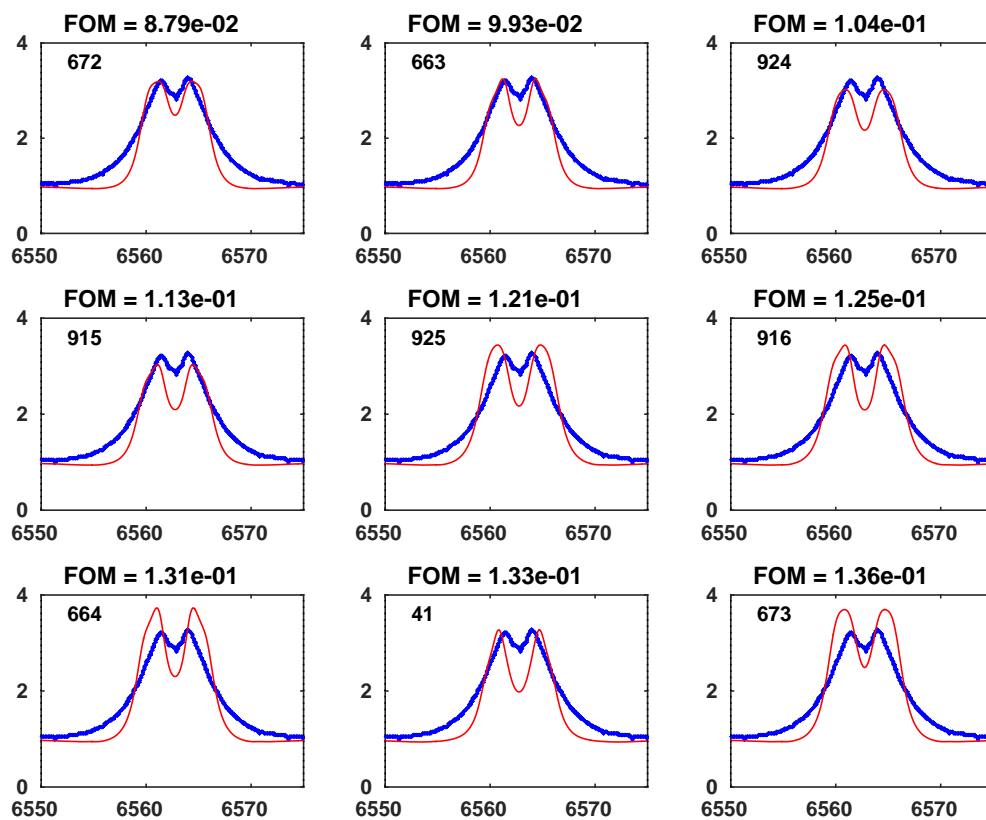


Figure D.14: The same as Figure (8.22) but for the Be star HD 54309.

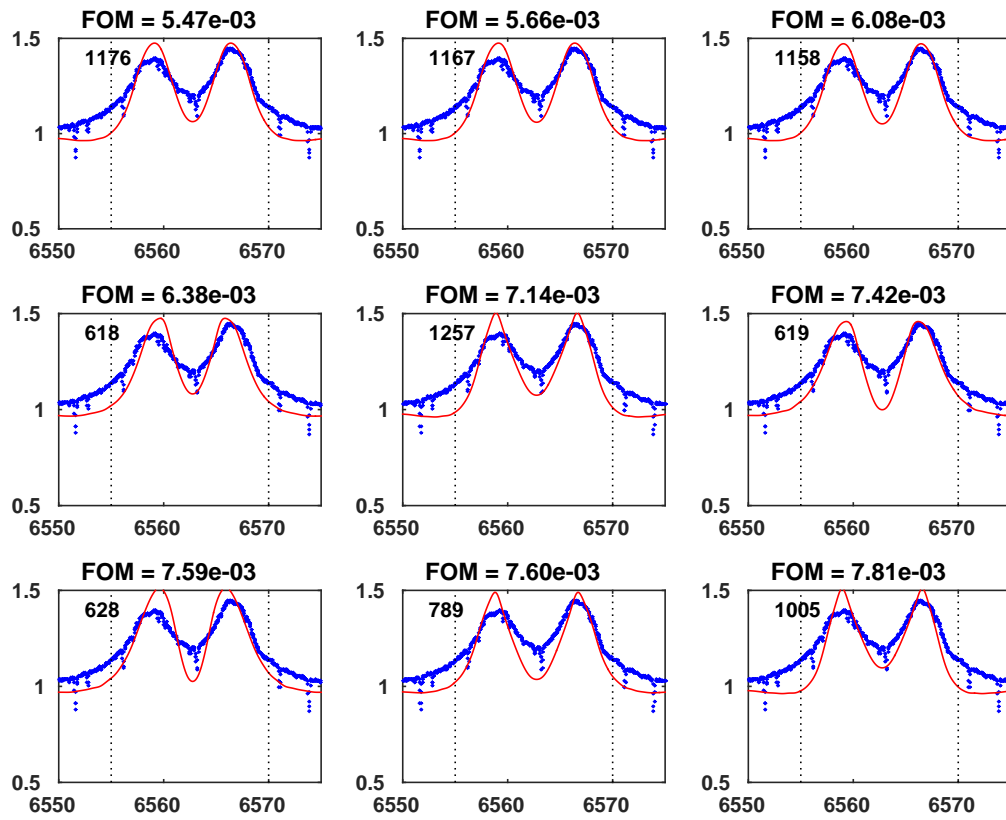


Figure D.15: The same as Figure (8.22) but for the Be star HD 58978.

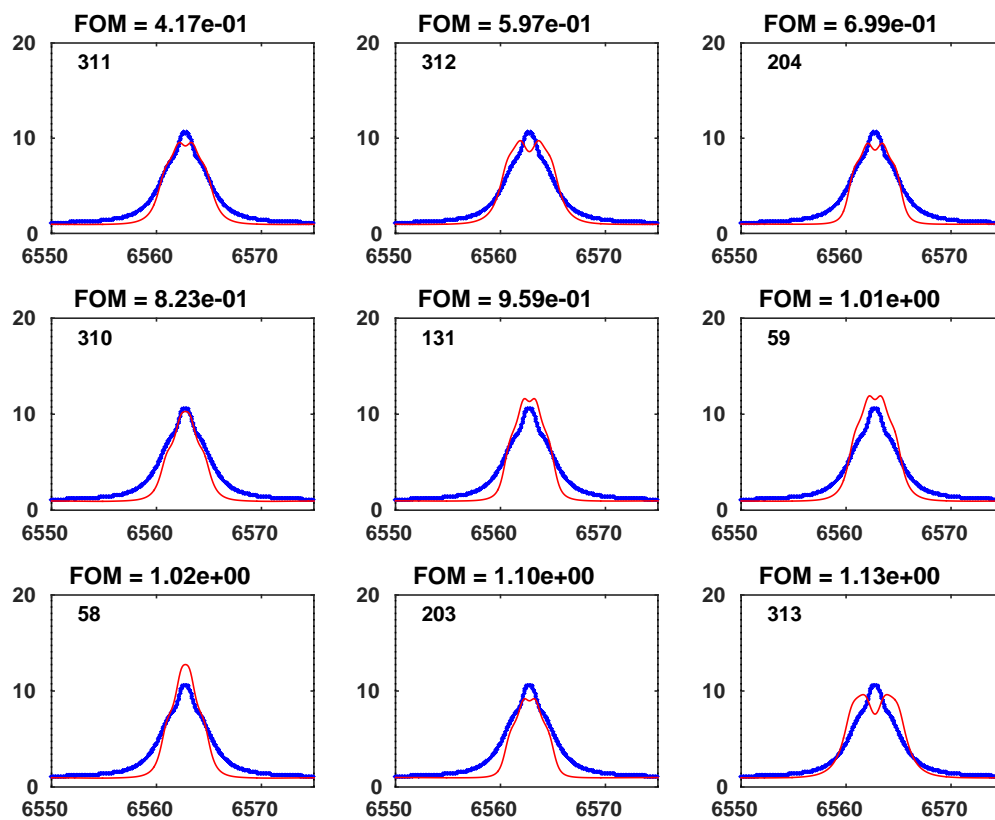


Figure D.16: The same as Figure (8.22) but for the Be star HD 65875.

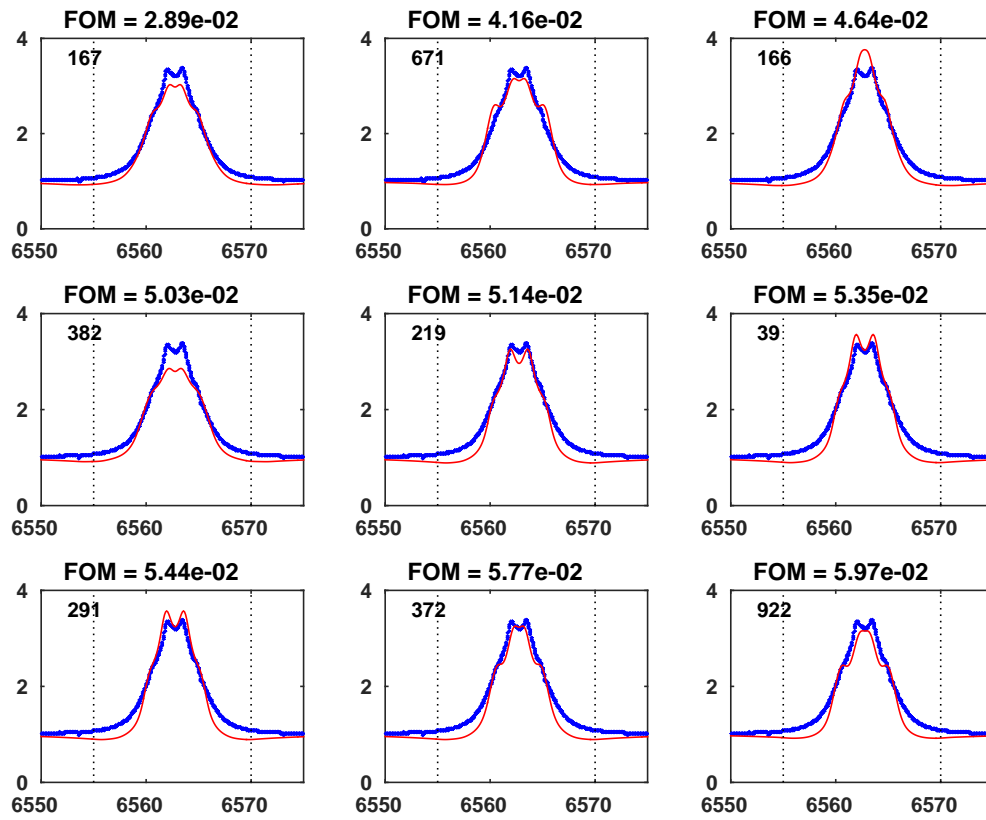


Figure D.17: The same as Figure (8.22) but for the Be star HD 178175.

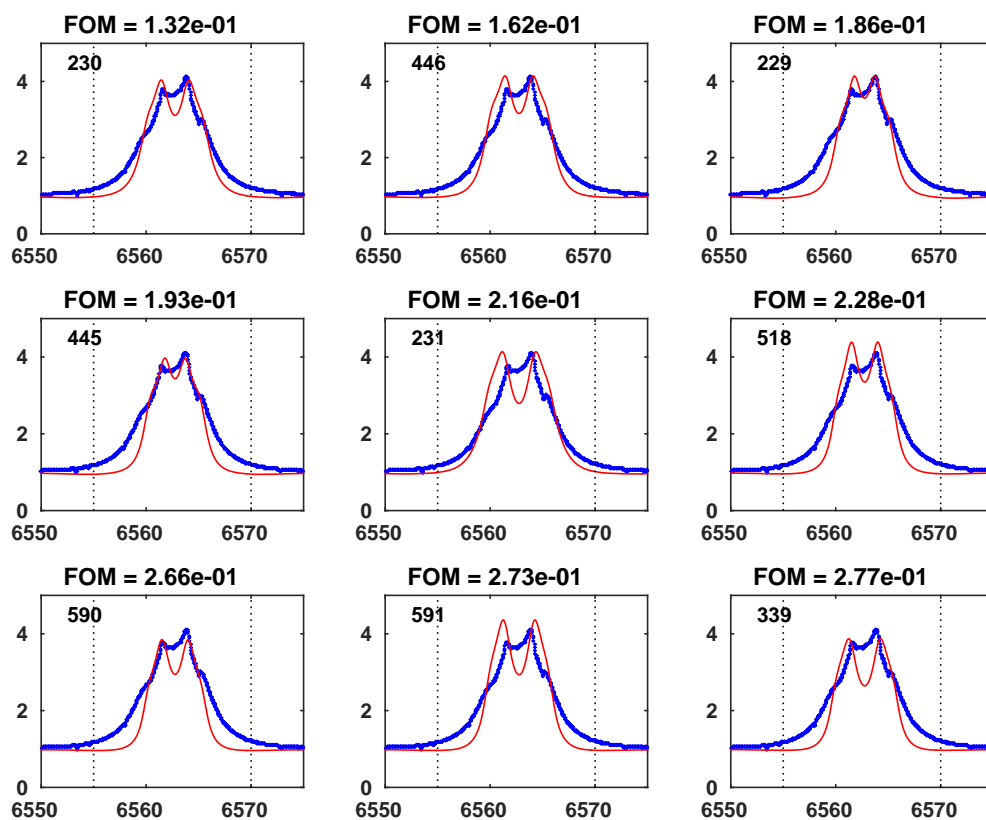


Figure D.18: The same as Figure (8.22) but for the Be star HD 187567.

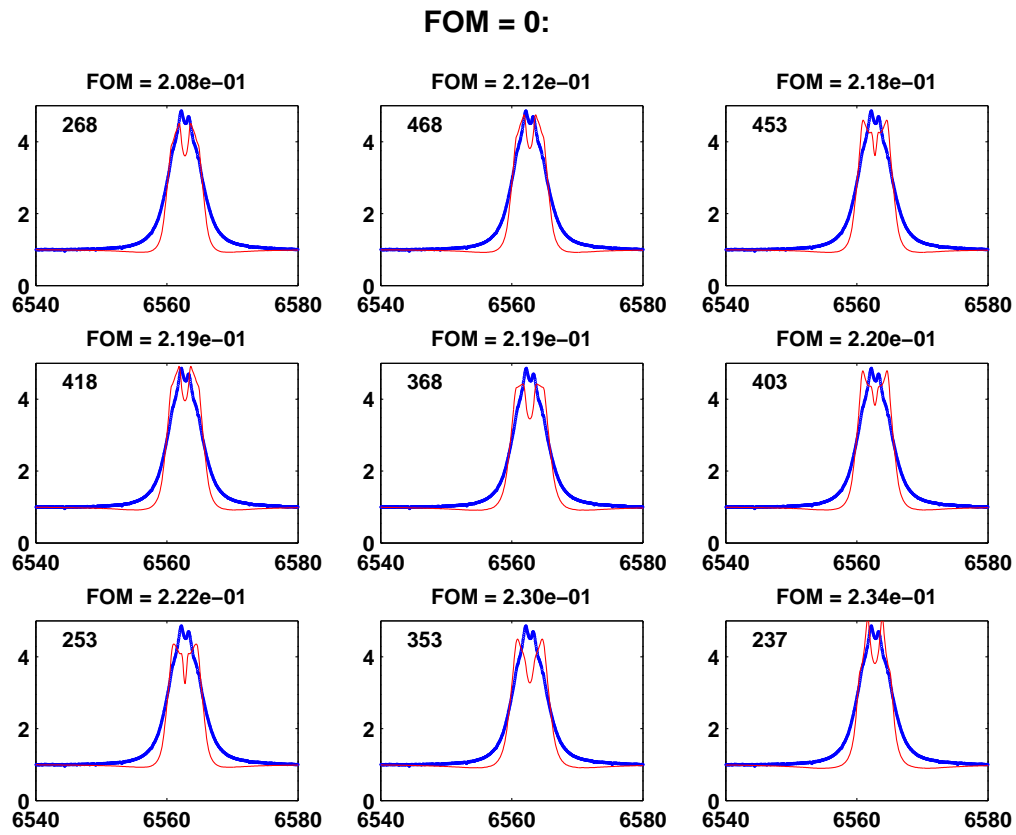


Figure D.19: The same as Figure (8.22) but for the Be star HD 203467.

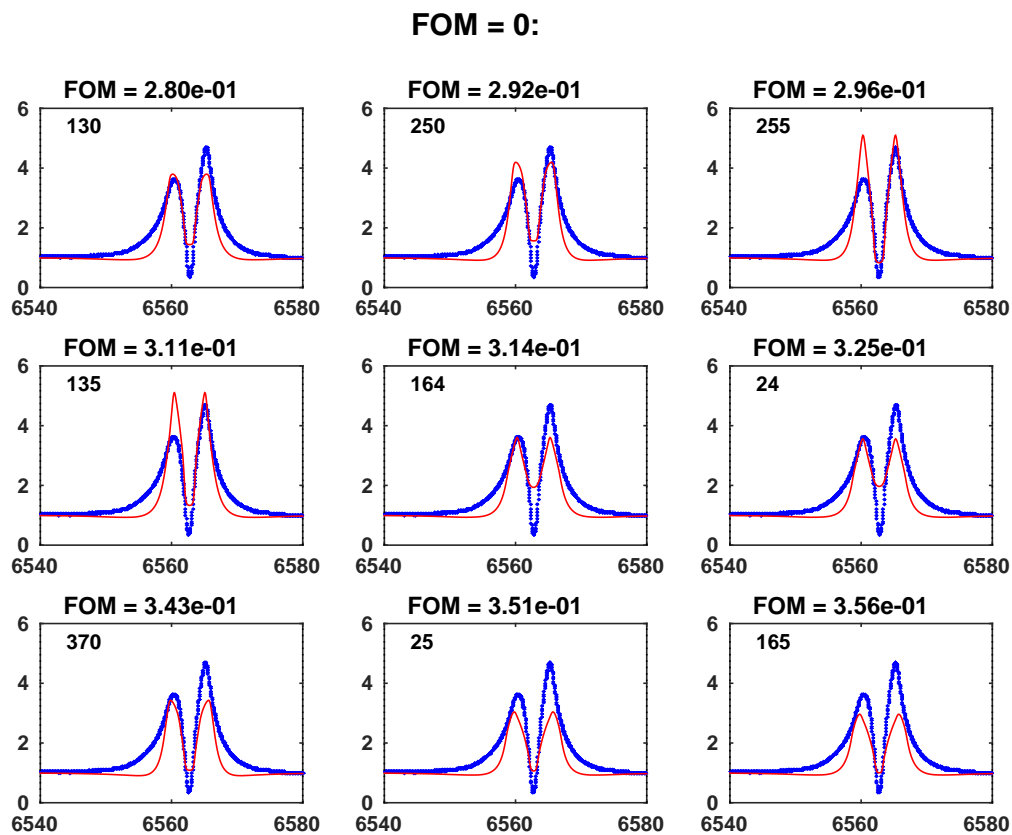


Figure D.20: The same as Figure (8.22) but for the Be star HD 217050.

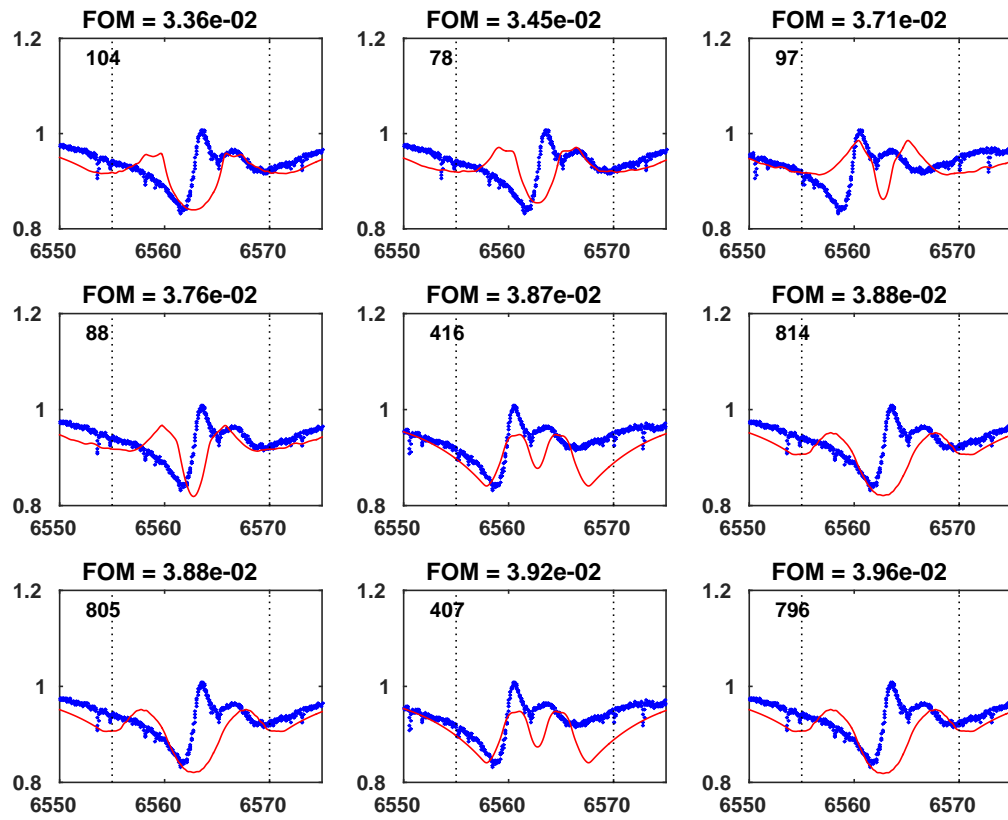


Figure D.21: The same as Figure (8.22) but for the Be star HD 174237.

Appendix E

N II Normalized Spectra

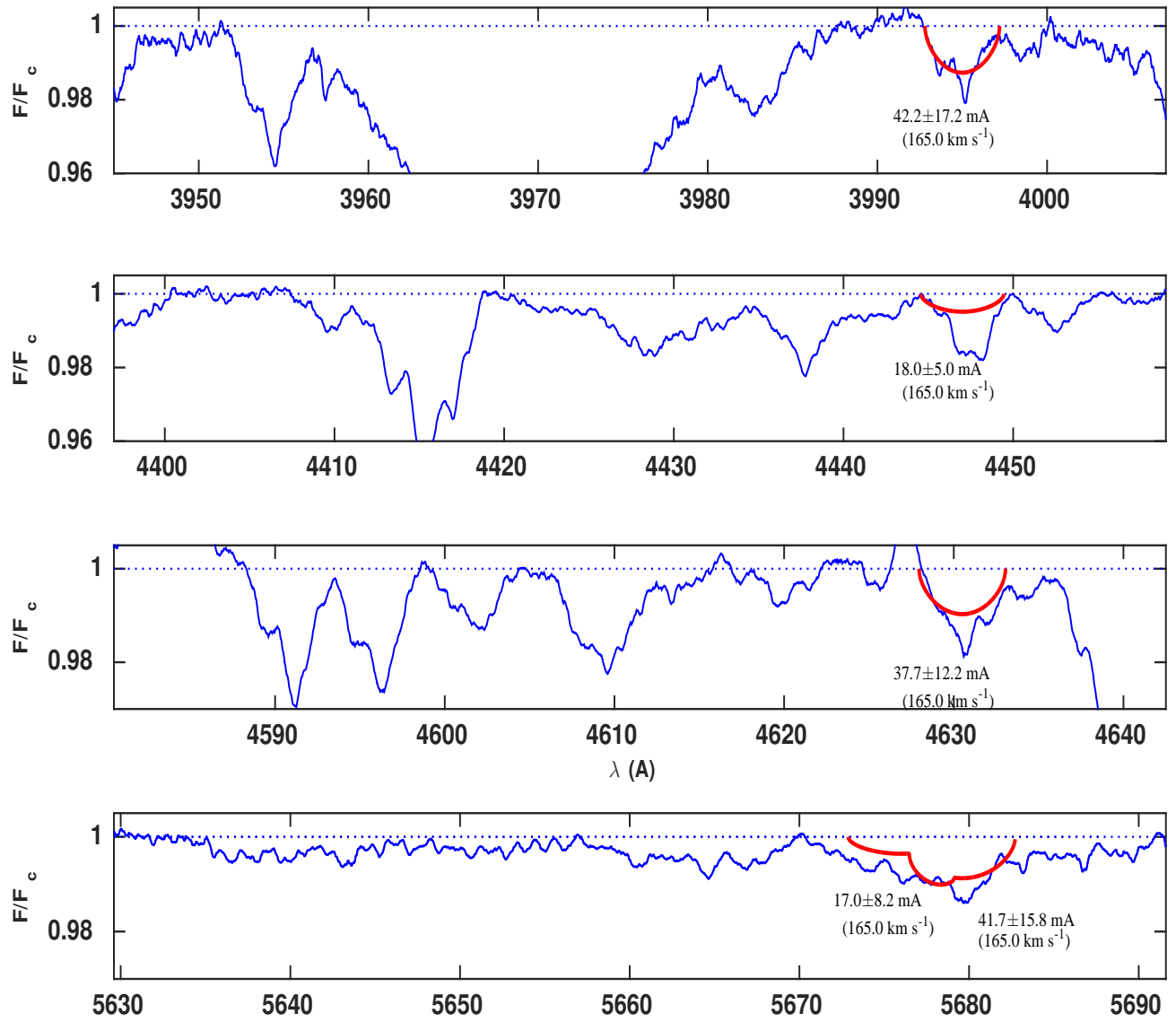


Figure E.1: The same as Figure (8.18) but for the Be star HD 143275.

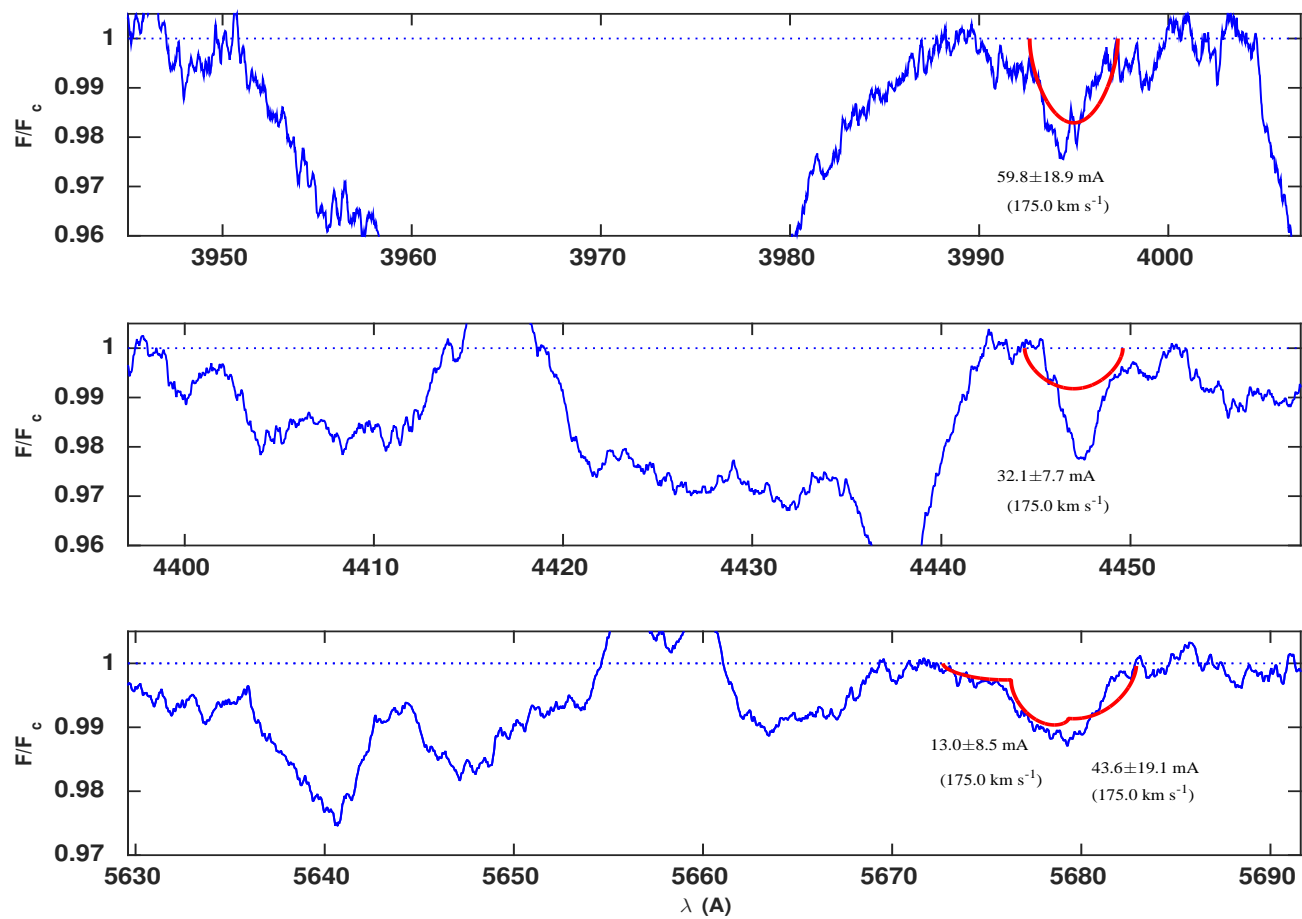


Figure E.2: The same as Figure (8.18) but for the Be star HD 65875.

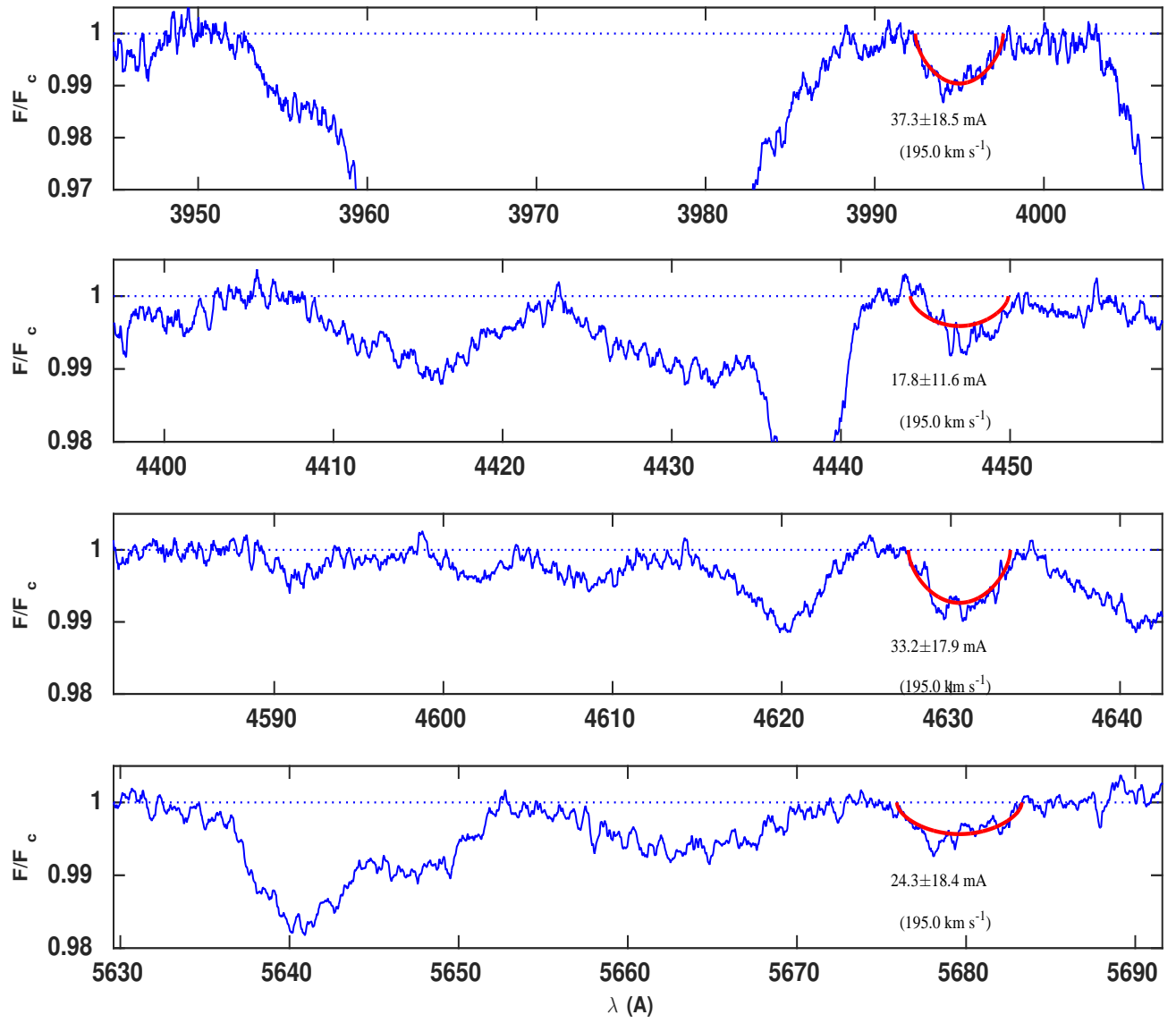


Figure E.3: The same as Figure (8.18) but for the Be star HD 189687.

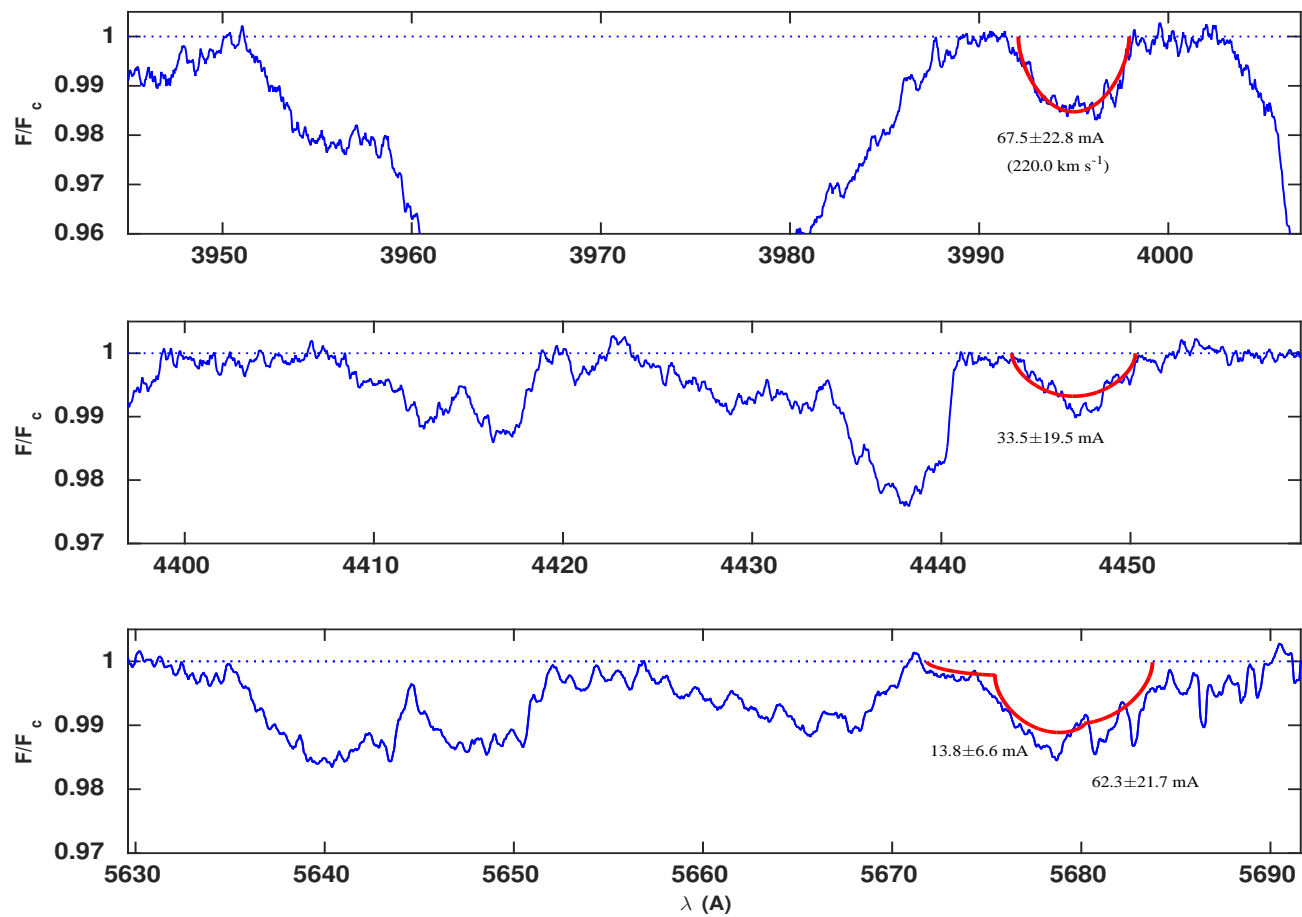


Figure E.4: The same as Figure (8.18) but for the Be star HD 54309.

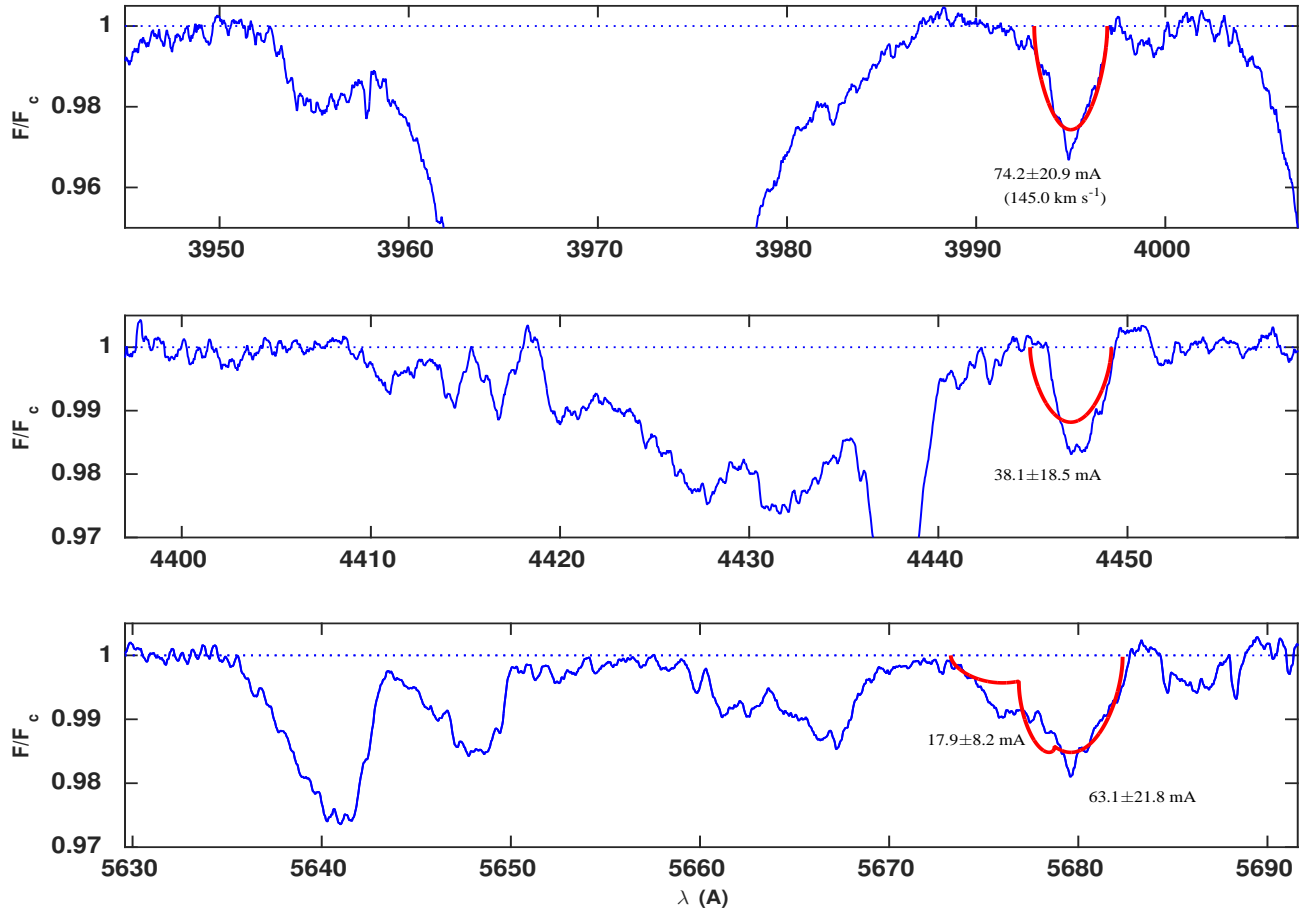


Figure E.5: The same as Figure (8.18) but for the Be star HD 178175.

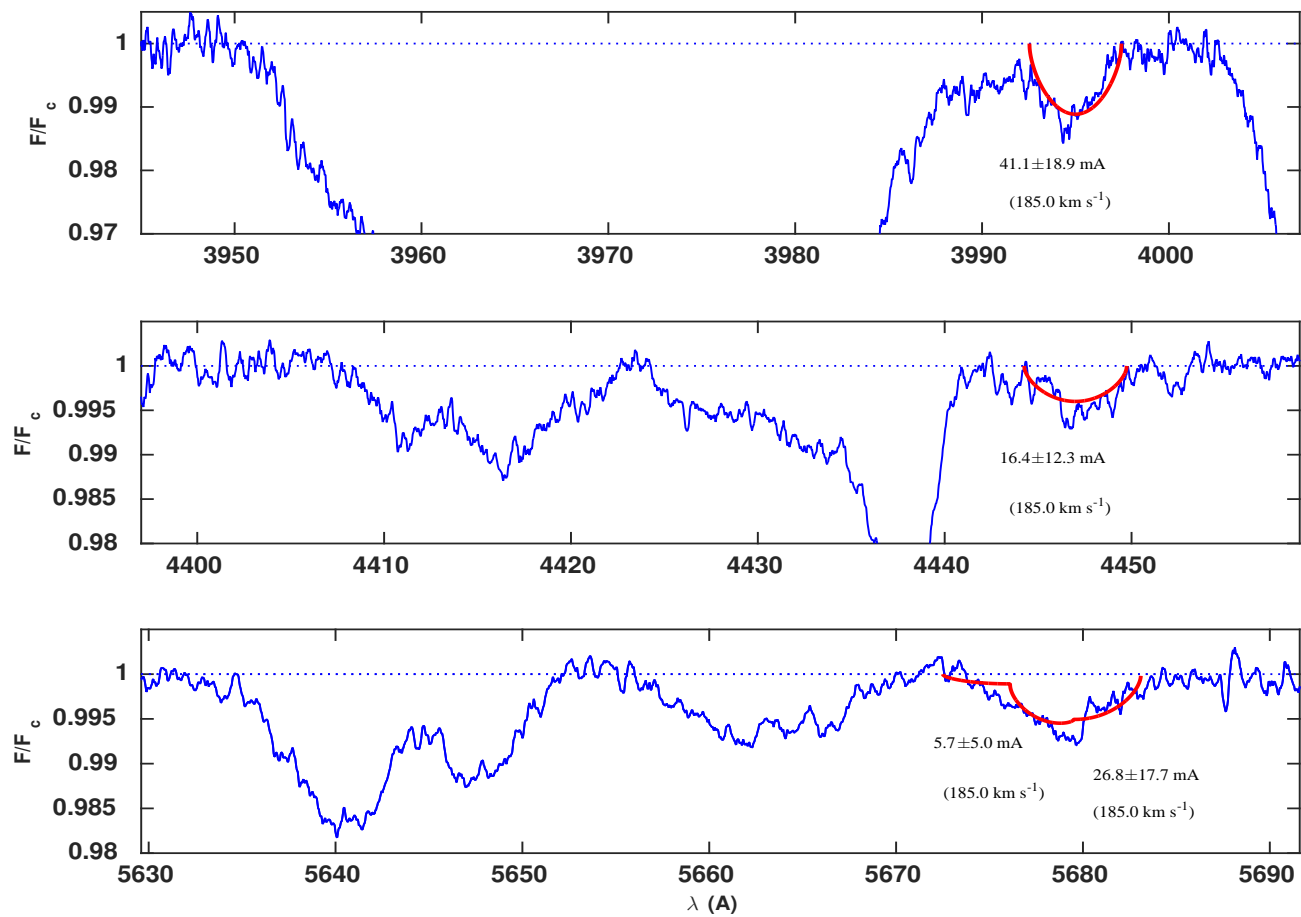


Figure E.6: The same as Figure (8.18) but for the Be star HD 192685.

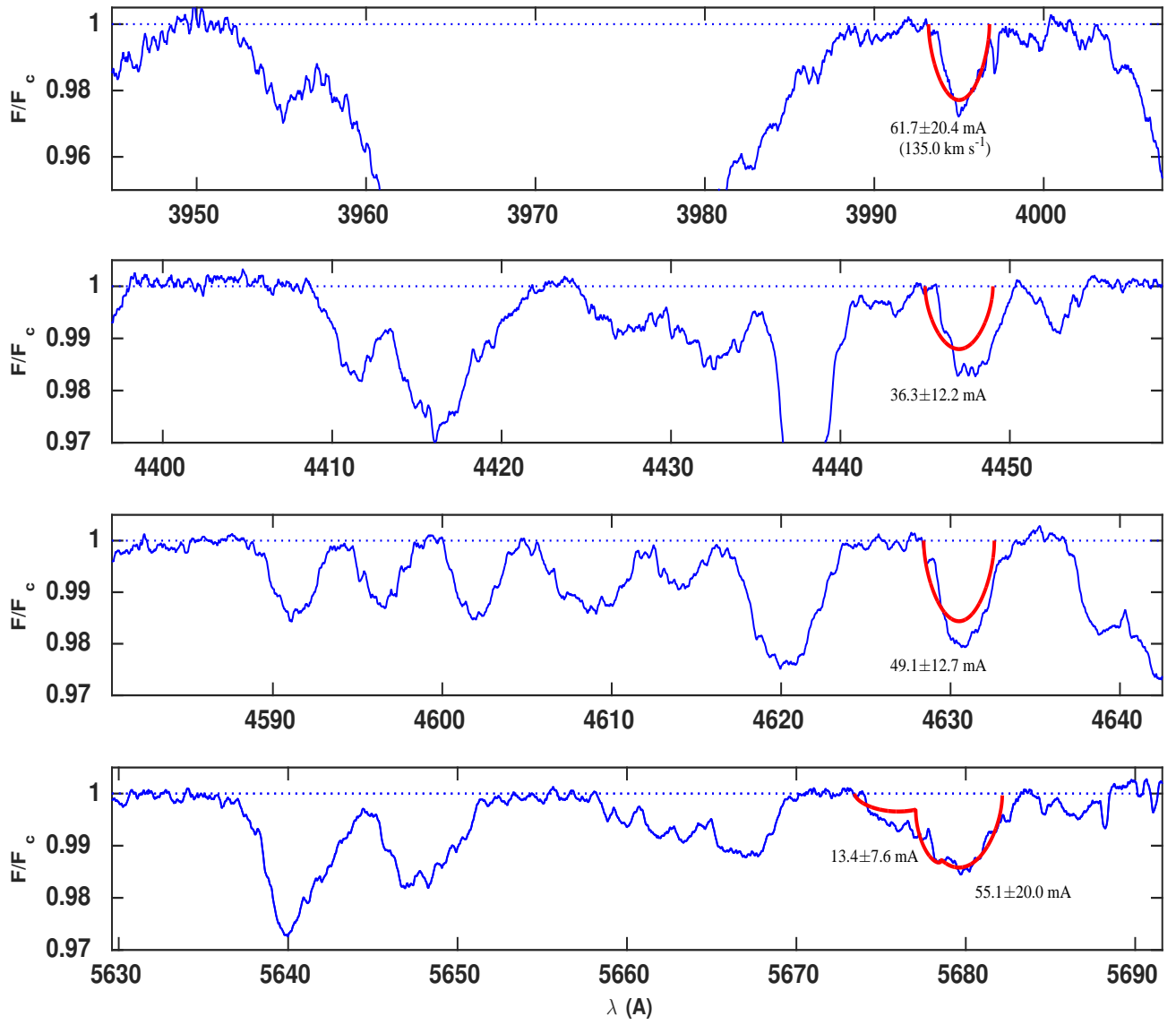


Figure E.7: The same as Figure (8.18) but for the Be star HD 120324.

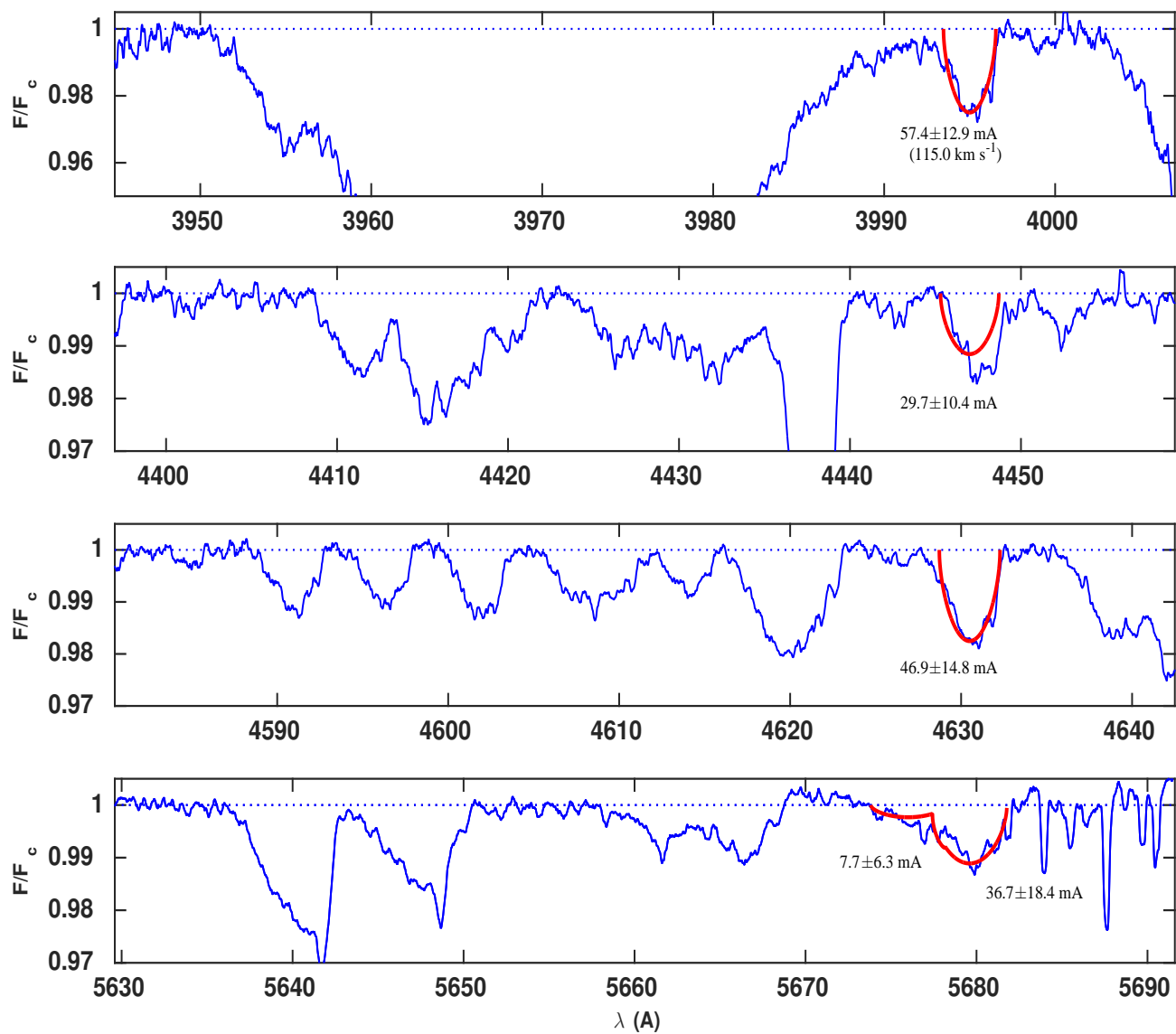


Figure E.8: The same as Figure (8.18) but for the Be star HD 58050.

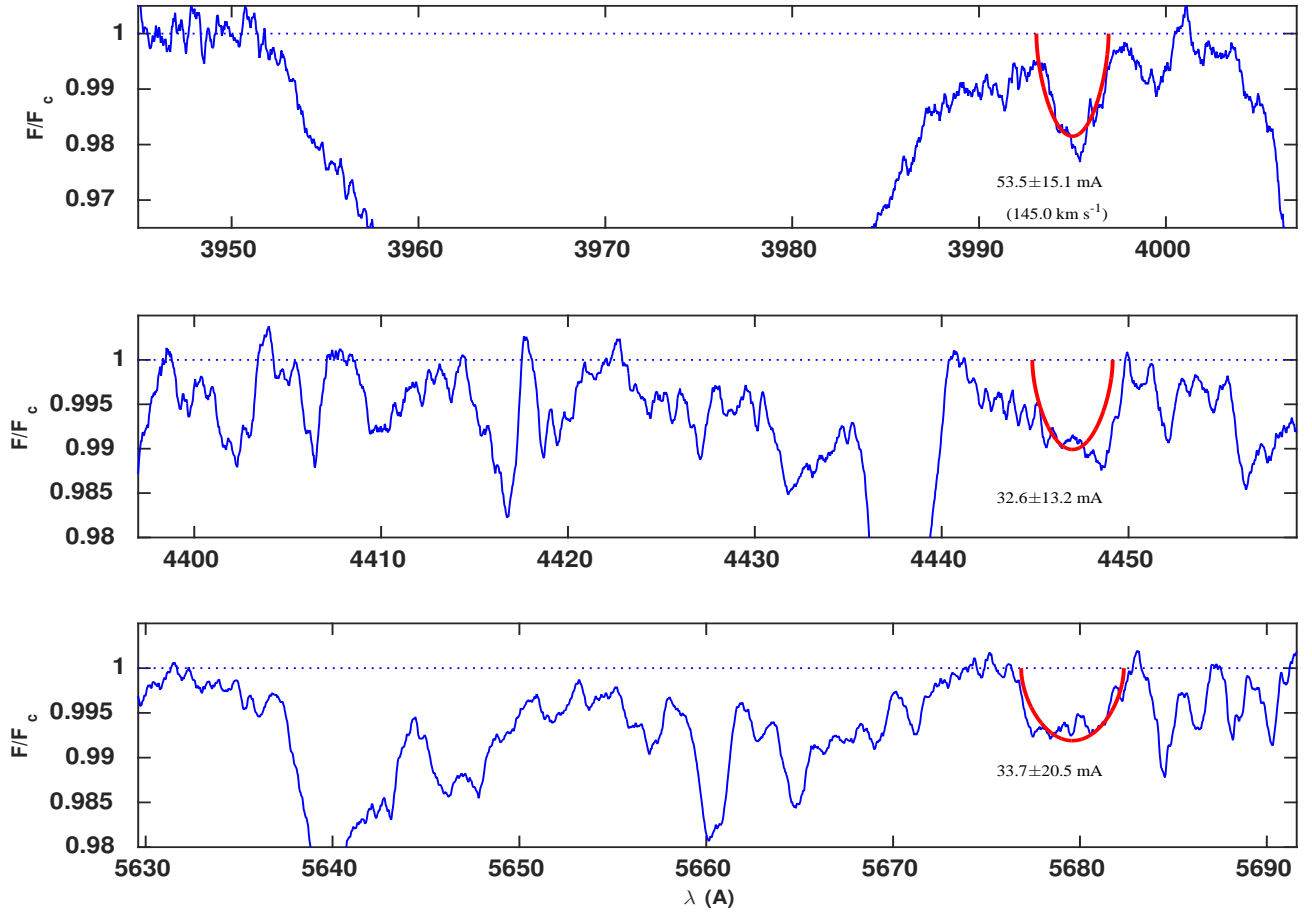


Figure E.9: The same as Figure (8.18) but for the Be star HD 174237.

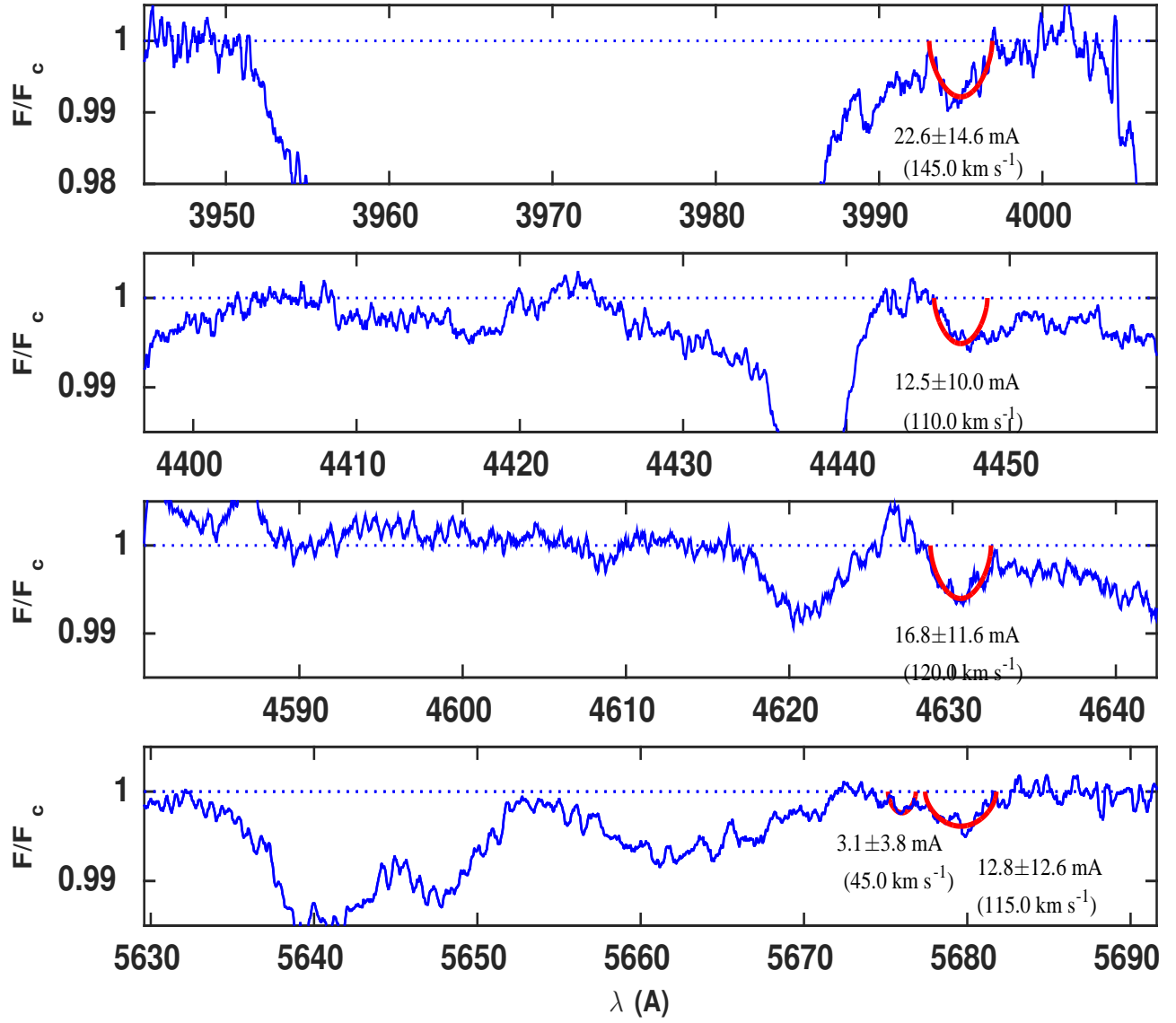


Figure E.10: The same as Figure (8.18) but for the Be star HD 187811.

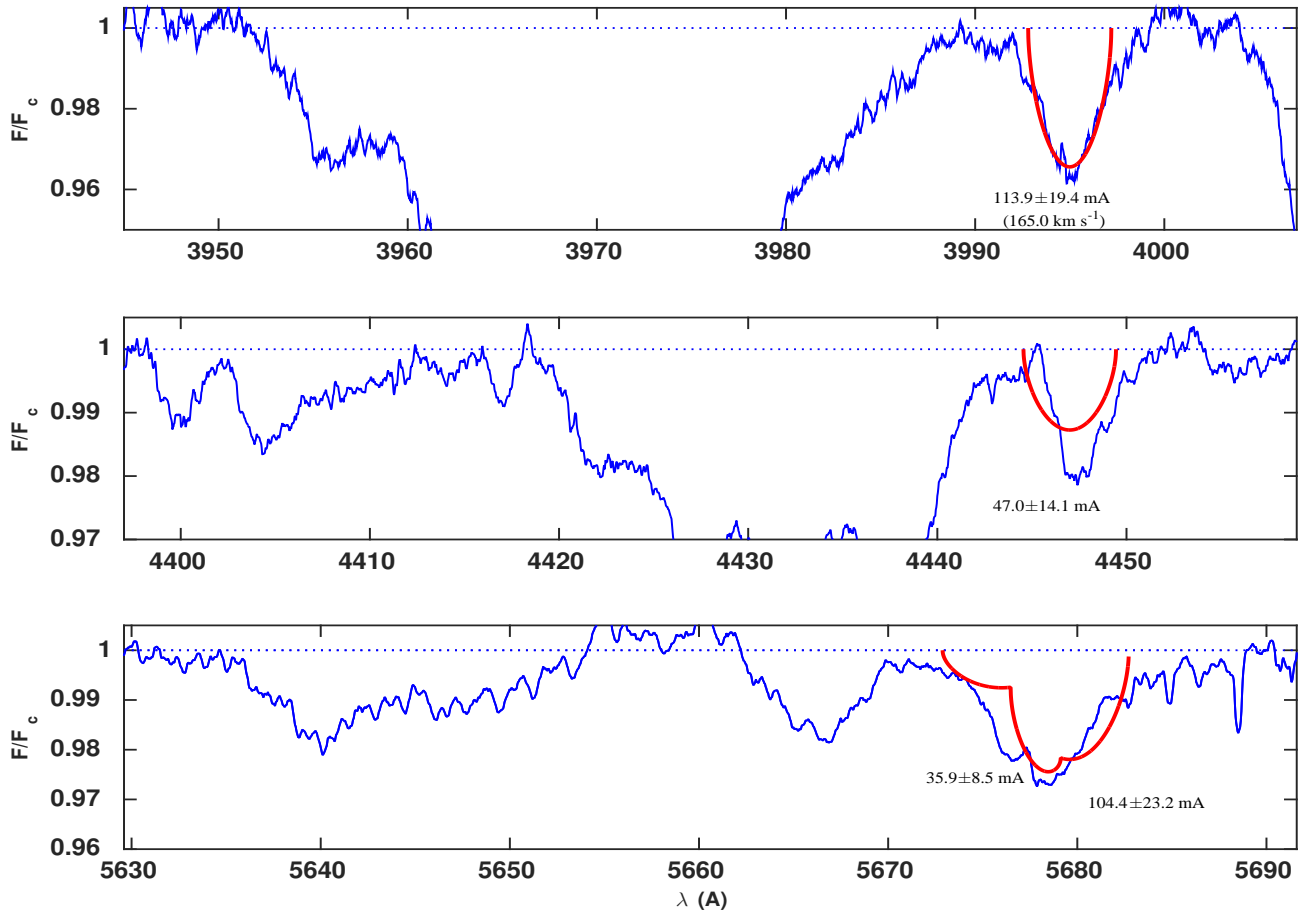


Figure E.11: The same as Figure (8.18) but for the Be star HD 187567.

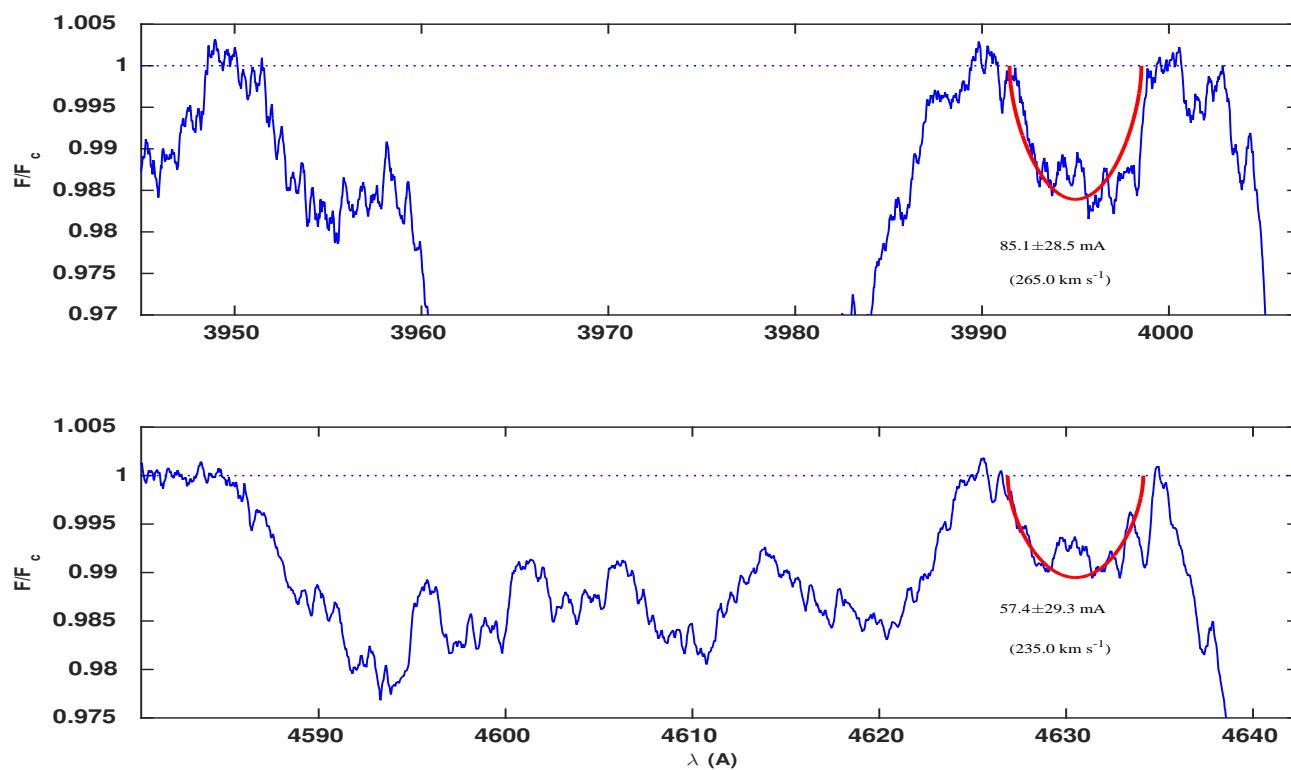


Figure E.12: The same as Figure (8.18) but for the Be star HD 33328.

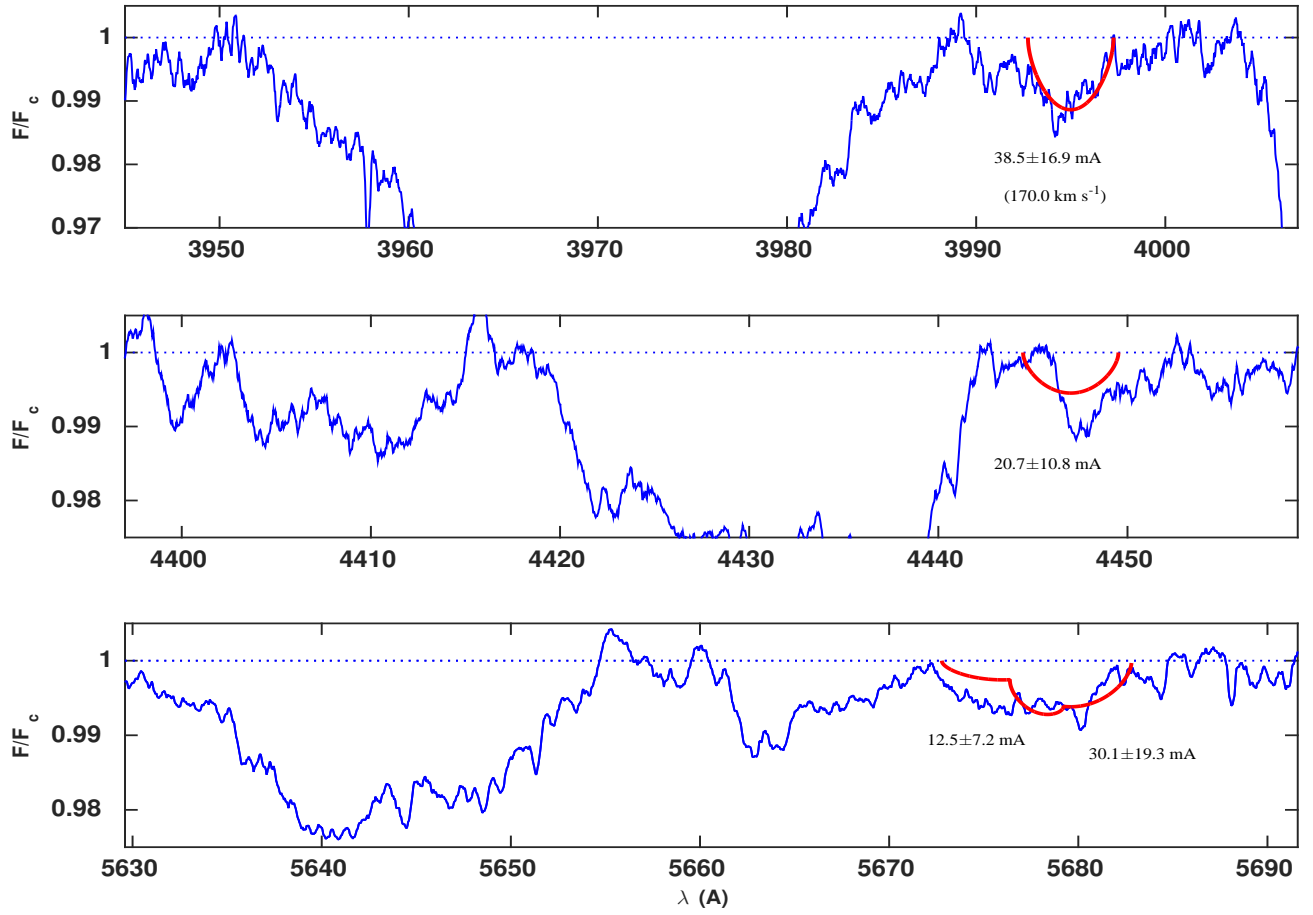


Figure E.13: The same as Figure (8.18) but for the Be star HD 203467.

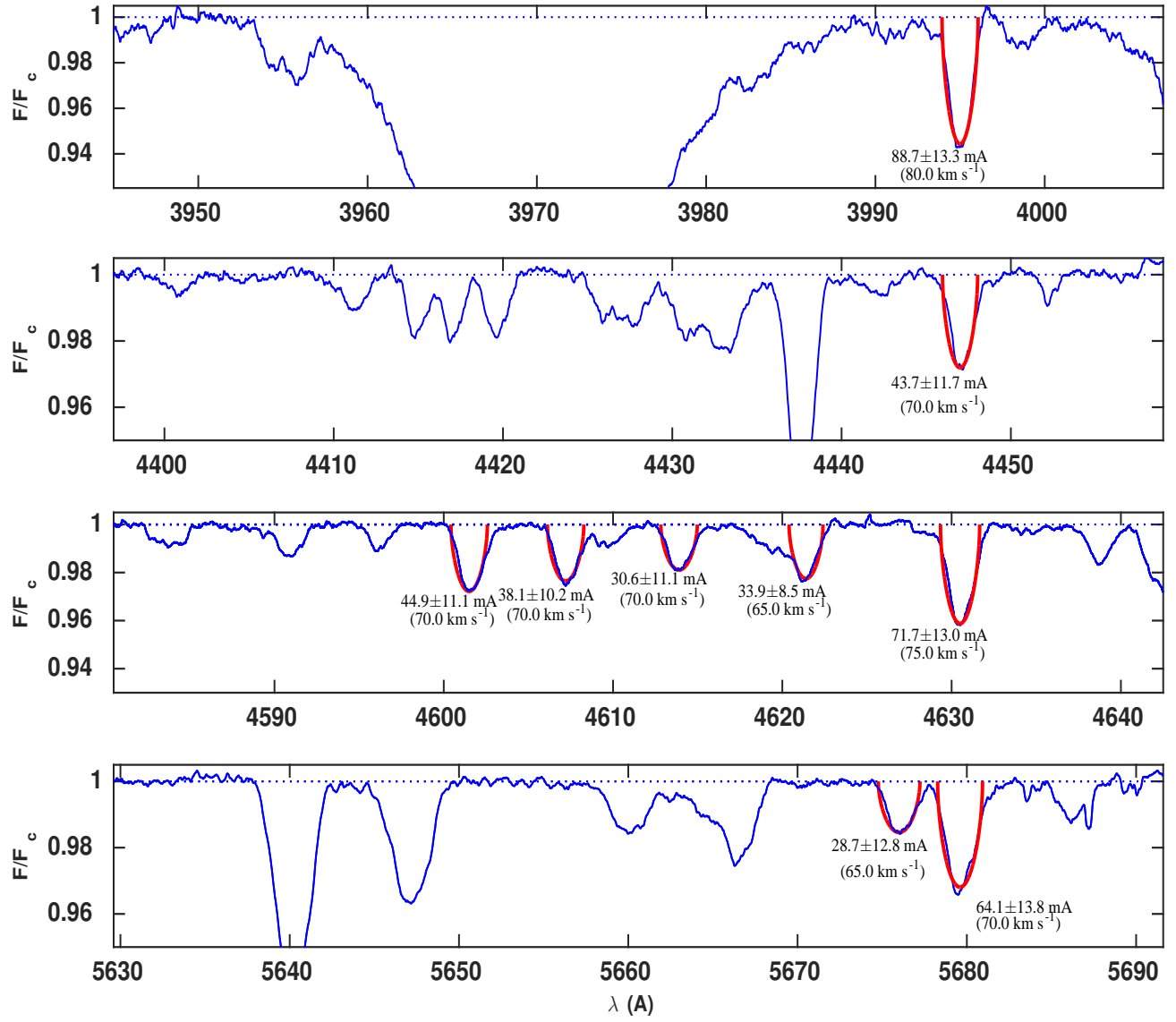


Figure E.14: The same as Figure (8.18) but for the Be star HD 49567.

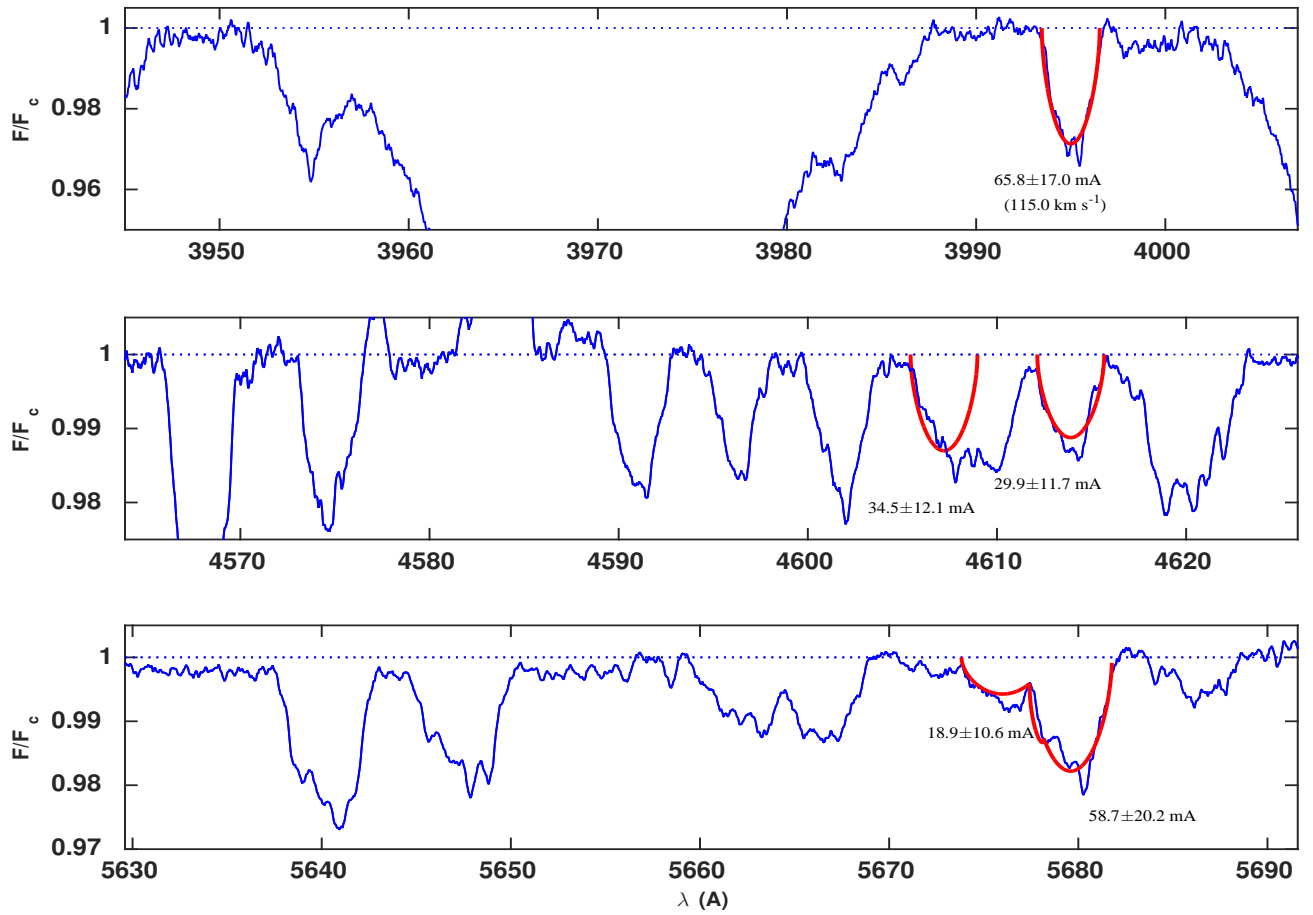


Figure E.15: The same as Figure (8.18) but for the Be star HD 212076.

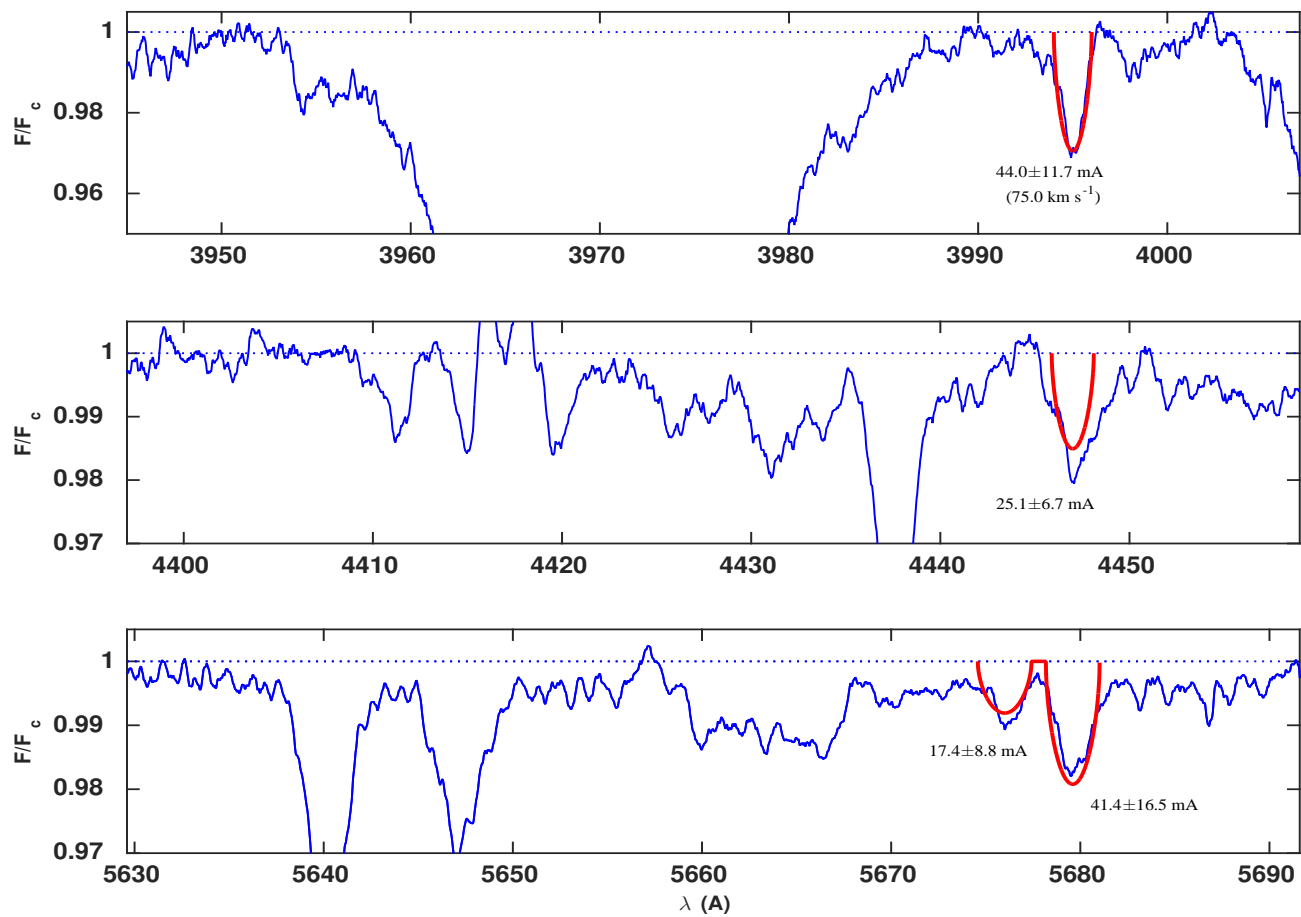


Figure E.16: The same as Figure (8.18) but for the Be star HD 56139.

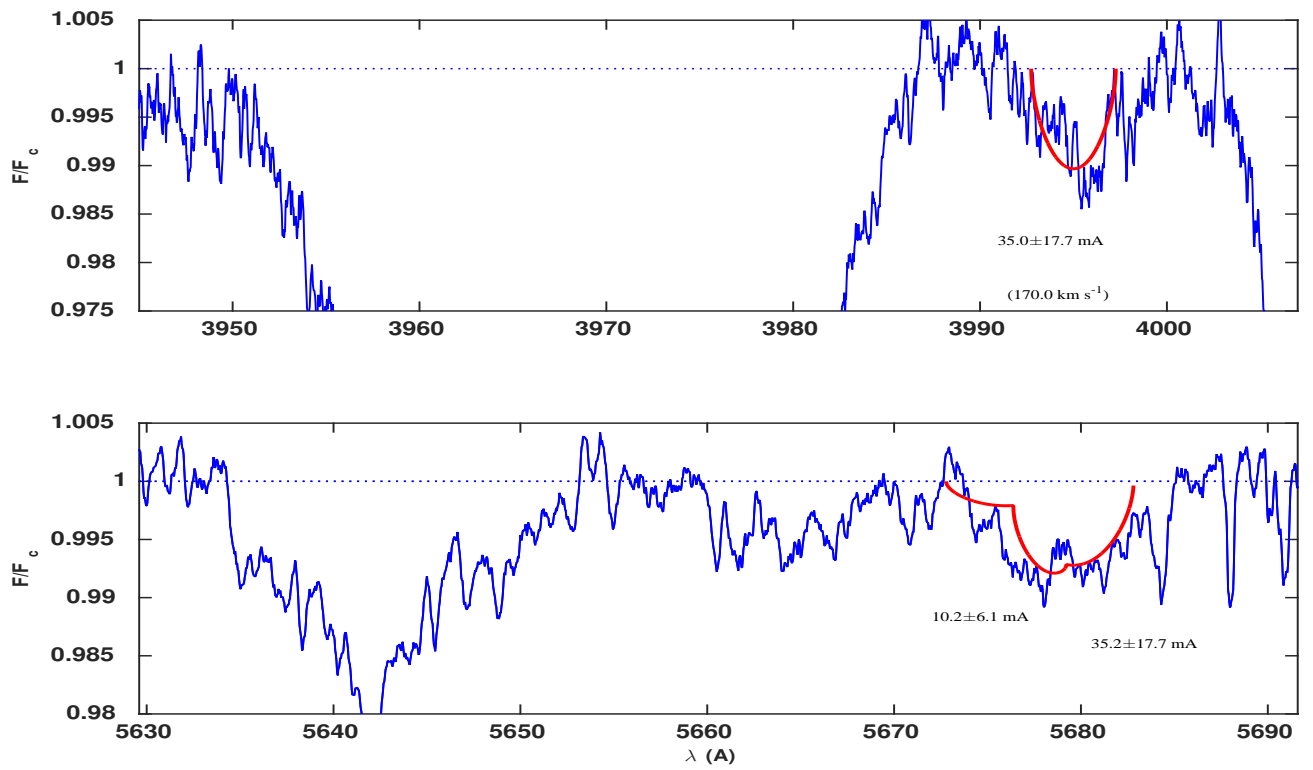


Figure E.17: The same as Figure (8.18) but for the Be star HD 191610.

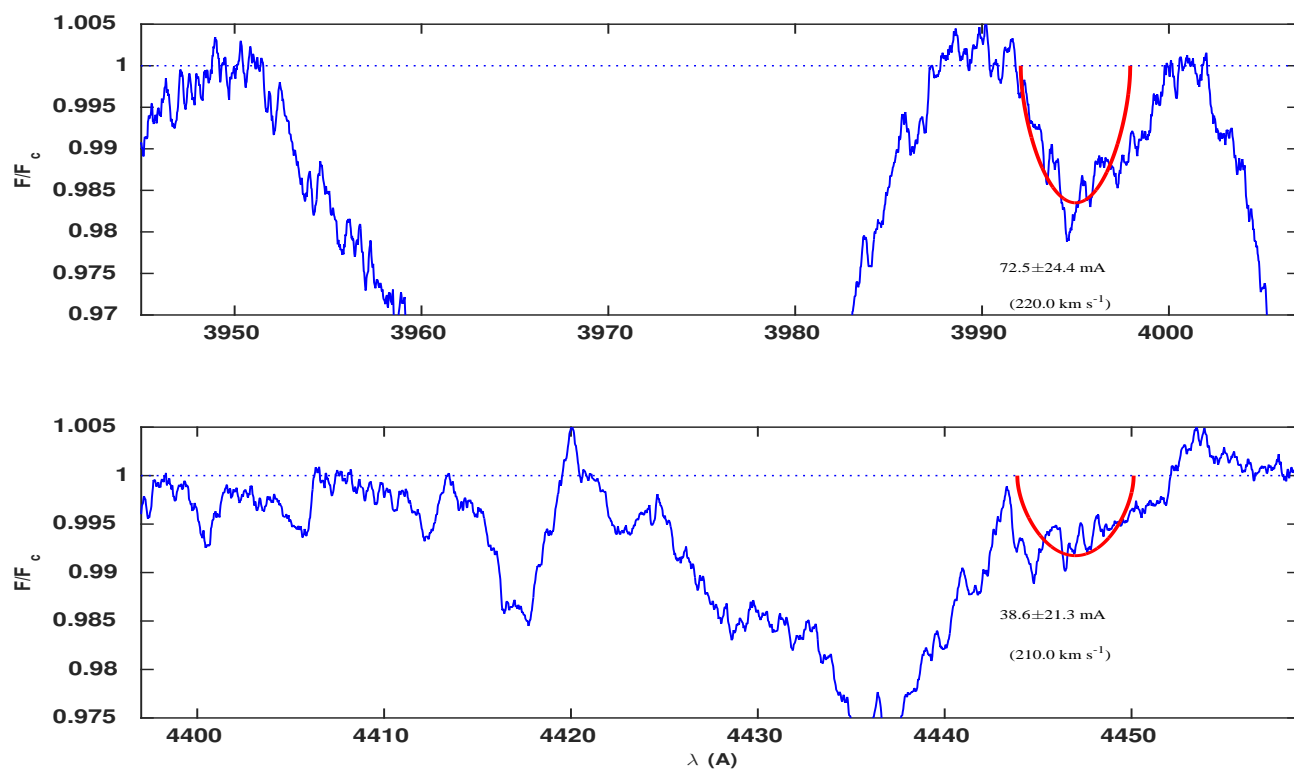


Figure E.18: The same as Figure (8.18) but for the Be star HD 20336.

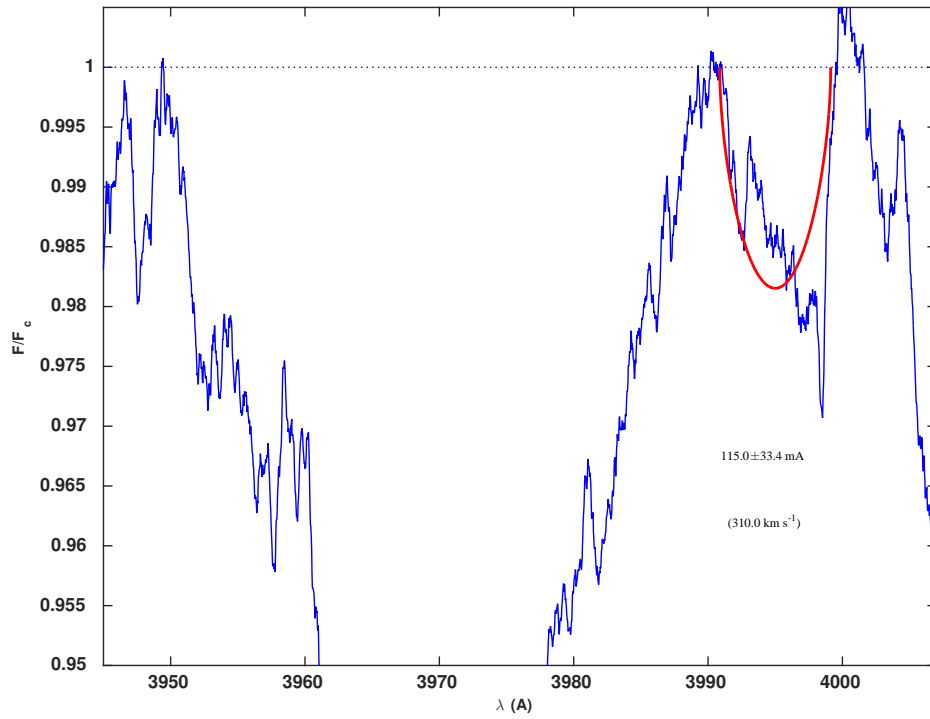


Figure E.19: The same as Figure (8.18) but for the Be star HD 58978.

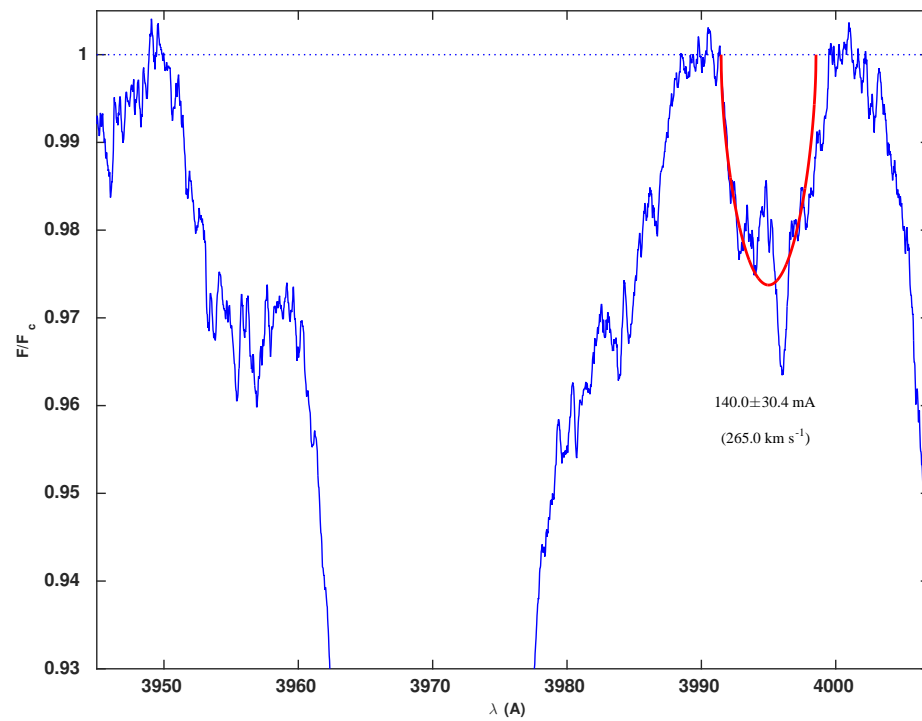


Figure E.20: The same as Figure (8.18) but for the Be star HD 212571.

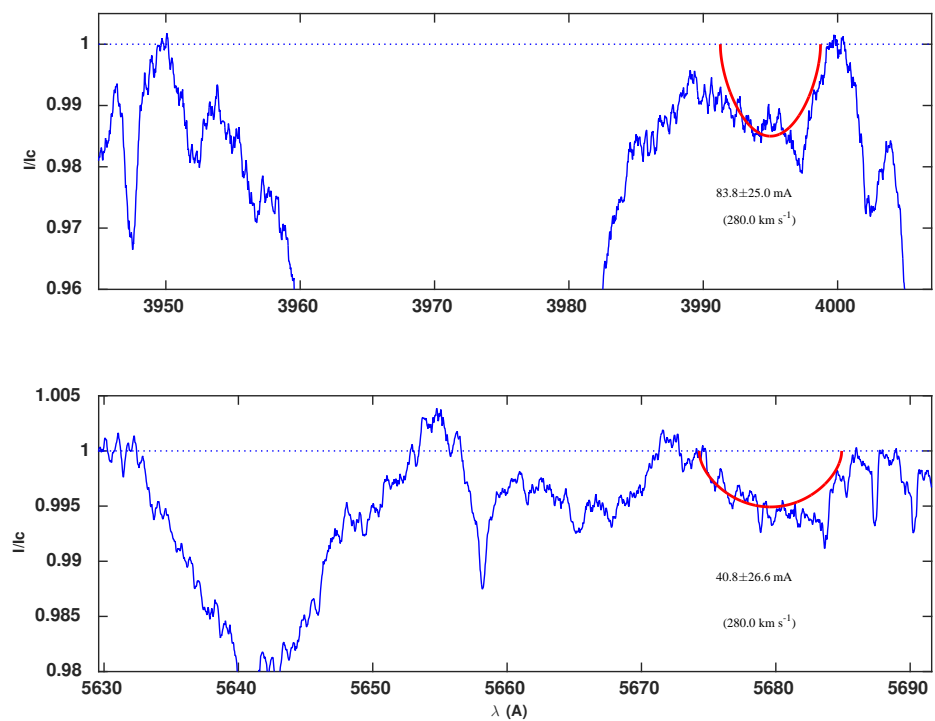


Figure E.21: The same as Figure (8.18) but for the Be star HD 45725.

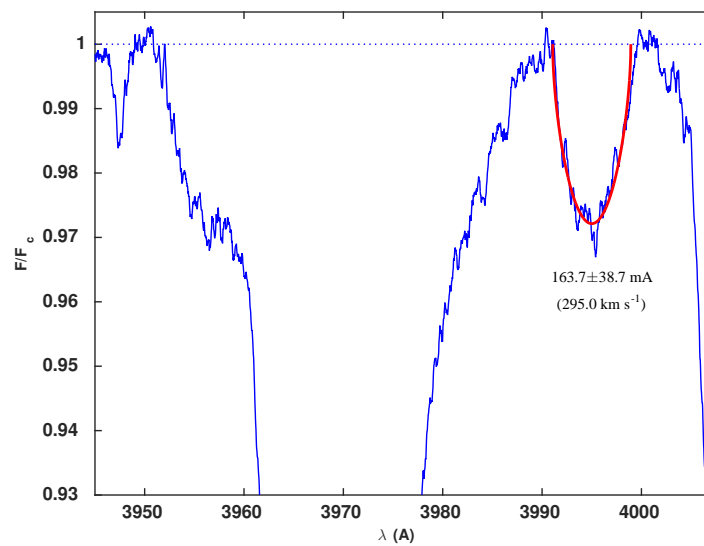


Figure E.22: The same as Figure (8.18) but for the Be star HD 205637.

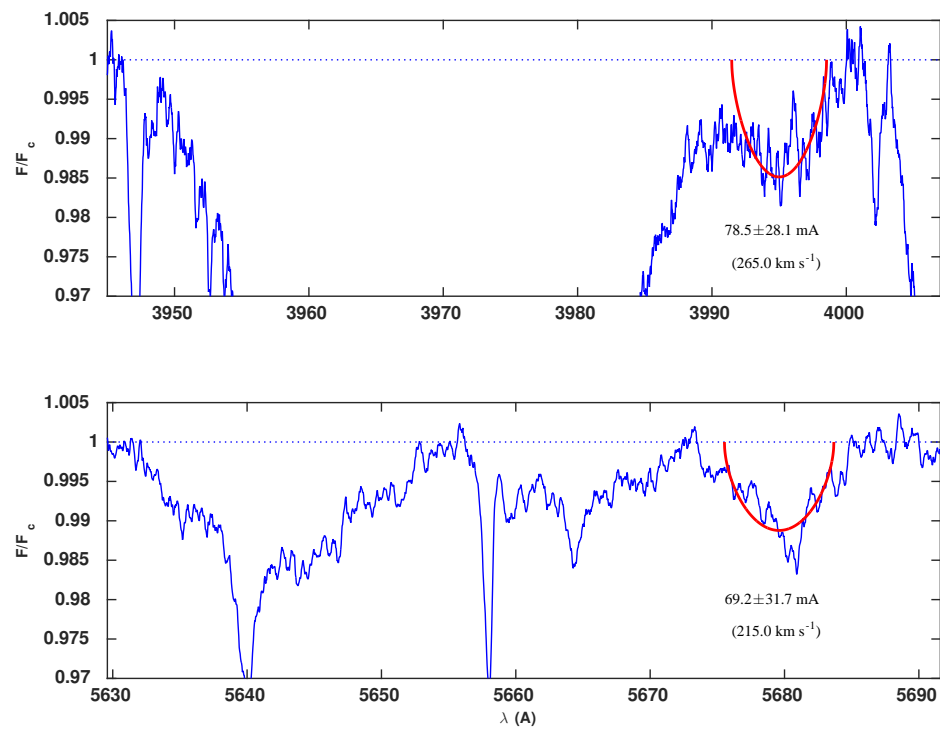


Figure E.23: The same as Figure (8.18) but for the Be star HD 217050.

Curriculum Vitae

Name: Ahmed Ahmed

Post-Secondary Education and Degrees: Cairo University, Cairo, Egypt
2000 - 2004 B.Sc.

University of Western Ontario, London, ON, Canada
2009 - 2011 M.Sc.

Honours and Awards: Awards of excellence from the ministry of higher education
2000-2004

Abd Alqawy Aiad award for excellent academic achievements
in Astronomy, May 2004

A governmental fellowship for graduate studies, Cairo University
December 2005 August 2009

Related Work Experience: Teaching Assistant Cairo University
2006 - 2009

Teaching Assistant, The University of Western Ontario
2009 - 2015

Publications:

Article: Refereed

- Non-LTE Equivalent Widths for N II with Error Estimates,
A. Ahmed, & T. A. A. Sigut, 2015, accepted for publication in MNRAS; Manuscript ID:
MN-15-2118-MJ
- The Temperature Structure of Be Star Disks in The Small Magellanic Cloud
A. Ahmed &, T. A. A. Sigut, 2012 ApJ 744, 191 (10pp).

Article: unrefereed

- The Motion of a Test Particle in The Gravitational Field of a Collapsing Shell
A. Eid &, A. M. Hamza, EJTP, May 2009.

Posters:

- Nitrogen Abundances in Rapidly Rotating B Stars , Ahmed and T.A.A. Sigut,
Bright Emissaries 2014, University of Western Ontario, London,
Ontario, Canada, August 11-13th, 2014.
- Be Stars Disks at Low Metallicity, Ahmed and T.A.A. Sigut, CASCA
2011, London, ON, Canada, May 30th June 2nd, 2011.

Conference talks:

- The Temperature Structure of Be Star Disks in the Small Magellanic
Cloud, CASCA 2012, Calgary, AB, Canada, June 4th -7th, 2012.